

**r-Process nucleosynthesis in neutron star mergers  
with the new nuclear reaction network *SkyNet***

Thesis by  
Jonas Lippuner

In Partial Fulfillment of the Requirements for the  
degree of  
Doctor of Philosophy

**Caltech**

CALIFORNIA INSTITUTE OF TECHNOLOGY  
Pasadena, California

2018  
Defended June 22, 2017

© 2018

Jonas Lippuner

[jonas@lippuner.ca](mailto:jonas@lippuner.ca)

ORCID: 0000-0002-5936-3485

All rights reserved

## ACKNOWLEDGEMENTS

First and foremost, I thank Luke Roberts for the extremely fruitful collaboration that led to *SkyNet*. It has been an enormous privilege to work with Luke and without him, the work presented in this thesis would not have happened. I also thank Luke for his mentorship, teaching me about nucleosynthesis and reaction networks, and the many productive hours we spent figuring out how to implement different physics in *SkyNet*.

I am extremely grateful to my parents, Stefan and Nelly Lippuner, my grandparents, Heinz and Eva Lippuner, and my great-uncle, Walter Lippuner, for their unwavering support throughout the last nine years that I spent in Canada and California.

I have been immensely blessed by Oasis Church and the Vineyard Pasadena (now Vineyard Eastside) community, who have been my family away from home. I am especially grateful to Brandon and Laura Henderson, Glen and Terri Taylor, and Sam Kim for their mentorship, encouragement, support, and fellowship. In addition, I thank Andrew Prawoto, Josh and Kirsten Taylor, Caleb Taylor, the Hightower clan, Jules Fink, Terry Williams, Ralph and Cathy Gómez, Jonathan and Kristen Gómez, Matthew and Ruth Patten, and Harold and Tami Toumayan for their friendship and their positive impact on me.

Being a part of the Graduate Christian Fellowship (GCF) at Caltech has also been a huge blessing. I thank everyone in GCF for creating a beautiful community that supports one another through the ups and downs of grad school, for providing a space for honest and mutually respectful dialogue about science and theology questions, and for allowing me to serve as president for two years. I especially thank Jamie Rankin, Rebekah Silva, Voon Hui Lai, Kimberley Mac Donald, Brandon Henderson, Chris Frick, Yong Sheng Soh, Janet Atkins, Janna Louie, and Jeff Liou for their leadership and service.

It has been a great pleasure to do grad school with the awesome grad students in the Theoretical Astrophysics including Relativity (TAPIR) group at Caltech. There has never been a dull moment in the office thanks to Kevin Barkett, Jonathan Blackman, Matthew Giesler, Dávid Guszejnov, Casey Handmer, Xiangcheng Ma, Elena Murchikova, Maria Okounkova, Matt Orr, Belinda Pang, Sherwood Richers, Denise Schmitz, Kung-Yi Su, Vijay Varma, Teja Venumadhav, Aaron Zimmerman, and many others in the physics and astronomy programs at Caltech.

I thank Kip Thorne for making TAPIR what it is and hosting awesome parties and Roland Haas for helping me get started in TAPIR. I am grateful to JoAnn Boyd for always being on top of things and processing my travel reimbursements very promptly.

I am indebted to the Joint Institute for Nuclear Astrophysics (JINA) community for providing a relevant network for nuclear astrophysics and for organizing many fruitful meetings.

I would not be where I am today without the excellent teachers and professors I have had over the last two decades. I especially thank Toni Kappeler, Bruno Gunterswiler, Bernhard Brunner, Christian Hänni, Lukas Lippert, Hansjakob Bischof, Alfred Vogelsanger, Jason Fiege, Can-Ming Hu, Kirill Kopotun, Shaun Lui, Eric Schippers, Jiri Sichler, Andreas Shalchi, Khodr Shamseddine, Kumar Sharma, Joe Williams, Nina Zorboska, Chris Hirata, Evan Kirby, Shri Kulkarni, and Sterl Phinney for challenging me, growing me, and fueling my passion for mathematics, physics, astronomy, and programming.

I am grateful to have had the opportunity to gain professional and research experience through numerous internships. I thank Manfred Linke, Idris Elbakri, Harry Ingleby, Nathan Luehr, Cliff Woolley, and Cyril Zeller for making these internships possible and mentoring me.

Last but not least, I owe a great debt to Christian Ott, my advisor. I am very grateful to Christian for his mentorship, guidance, and for making it possible for me to work on this project. I thank him for always taking the time to carefully read through my manuscripts and provide very insightful and helpful comments. Christian has been extremely generous with providing funding, so that I could concentrate on my research, and with paying for travel to many conferences, workshops, and visits, allowing me to form meaningful professional connections. Christian has always had my best interests in mind and he did not hesitate to let me take time off for not just one but two summer internships.

## ABSTRACT

At the Big Bang, only the lightest elements, mainly hydrogen and helium, were produced. Stars synthesize heavier elements, such as helium, carbon, and oxygen, from lighter ones through nuclear fusion. Iron-group elements are created in supernovae (both type Ia and core-collapse). It has been known for 60 years that the slow and rapid neutron capture processes (s- and r-process) are each responsible for creating about half of the elements beyond the iron group. The s-process is known to occur in asymptotic giant branch stars, but the astrophysical site of the r-process is still a mystery. Based on observations of heavy elements in old stars, it was theorized that r-process nucleosynthesis takes place in core-collapse supernovae (CCSNe). However, recent CCSN simulations indicate that the conditions required for the r-process are not obtained in CCSN. The focus has thus shifted to neutron star mergers (both binary neutron star and black hole–neutron star mergers), where the r-process easily synthesizes all the known heavy elements. Neutron star mergers are expected to be detected by the Laser Interferometer Gravitational Wave Observatory (LIGO) in the near future, which should either confirm or rule out their proposed association with radioactively powered transients called kilonovae or macronovae that are the observational signatures of r-process nucleosynthesis. To understand how the r-process operates in different astrophysical scenarios and what relative abundance patterns it produces, detailed nuclear reaction network calculations are needed that track thousands of isotopes and tens of thousands of nuclear reactions. In this thesis, I present *SkyNet*, a new general-purpose nuclear reaction network that can evolve an arbitrary list of nuclear species with an arbitrary set of nuclear reactions. I describe in detail the different physics that is implemented in *SkyNet* and I perform code tests and comparisons to other nuclear reaction networks. Then I use *SkyNet* to systematically investigate r-process nucleosynthesis as a function of the initial electron fraction, initial entropy, and expansion timescale of the fluid. Further, I present r-process nucleosynthesis calculations with *SkyNet* in the dynamical ejecta of a black hole–neutron star merger with varying levels of neutrino irradiation. Finally, I study the r-process in the outflow of a neutron star merger remnant disk as a function of the lifetime of the central hypermassive neutron star (HMNS). *SkyNet* is easy to use and flexible and it is publicly available as open-source software. Multiple researchers are already using *SkyNet* for their work, and I hope that *SkyNet* will be a useful tool for the broader nuclear astrophysics community.

## PUBLISHED CONTENT AND CONTRIBUTIONS

### Part of this thesis

- Lippuner, J. and L. F. Roberts (2015). “r-Process Lanthanide Production and Heating Rates in Kilonovae”. In: *Astrophysical Journal* 815, p. 82. DOI: [10.1088/0004-637X/815/2/82](https://doi.org/10.1088/0004-637X/815/2/82). arXiv: [1508.03133](https://arxiv.org/abs/1508.03133) [[astro-ph.HE](#)].  
*I am the primary author, wrote the vast majority of the text, performed all nucleosynthesis calculations and data analysis, and I created all the figures.*
- Roberts, L. F., J. Lippuner, M. D. Duez, J. A. Faber, F. Foucart, J. C. Lombardi Jr., S. Ning, C. D. Ott, and M. Ponce (2017). “The influence of neutrinos on r-process nucleosynthesis in the ejecta of black hole-neutron star mergers”. In: *Monthly Notices of the RAS* 464, p. 3907. DOI: [10.1093/mnras/stw2622](https://doi.org/10.1093/mnras/stw2622). arXiv: [1601.07942](https://arxiv.org/abs/1601.07942) [[astro-ph.HE](#)].  
*I set up the pipeline for the nucleosynthesis calculations from the tracer particles and performed all the nucleosynthesis calculations. I contributed significantly to the data analysis, figure creation, and writing.*
- Lippuner, J., R. Fernández, L. F. Roberts, F. Foucart, D. Kasen, B. D. Metzger, and C. D. Ott (2017). “Signatures of hypermassive neutron star lifetimes on r-process nucleosynthesis in the disk ejecta from neutron star mergers”. In: *accepted by Monthly Notices of the RAS*. arXiv: [1703.06216](https://arxiv.org/abs/1703.06216) [[astro-ph.HE](#)].  
*I am the primary author, wrote the majority of the text, performed all nucleosynthesis calculations and data analysis of the nucleosynthesis, and I created all the figures.*
- Lippuner, J. and L. F. Roberts (2017). “SkyNet: A modular nuclear reaction network library”. In: *submitted to Astrophysical Journal, Supplement*. arXiv: [1706.06198](https://arxiv.org/abs/1706.06198) [[astro-ph.HE](#)].  
*I am the primary author, wrote the vast majority of the text, performed all calculations and code comparisons, and I created all the figures. I also wrote almost all of the SkyNet code.*

### Other work

- Foucart, F., R. Haas, M. D. Duez, E. O’Connor, C. D. Ott, L. Roberts, L. E. Kidder, J. Lippuner, H. P. Pfeiffer, and M. A. Scheel (2016). “Low mass binary neutron star mergers: Gravitational waves and neutrino emission”. In: *Physical Review D* 93, p. 044019. DOI: [10.1103/PhysRevD.93.044019](https://doi.org/10.1103/PhysRevD.93.044019). arXiv: [1510.06398](https://arxiv.org/abs/1510.06398) [[astro-ph.HE](#)].  
*I helped with running some of the binary neutron star inspiral and merger simulations used in this paper.*

- Barkett, K., M. A. Scheel, R. Haas, C. D. Ott, S. Bernuzzi, D. A. Brown, B. Szilágyi, J. D. Kaplan, J. Lippuner, C. D. Muhlberger, F. Foucart, and M. D. Duez (2016). “Gravitational waveforms for neutron star binaries from binary black hole simulations”. In: *Physical Review D* 93, p. 044064. DOI: [10.1103/PhysRevD.93.044064](https://doi.org/10.1103/PhysRevD.93.044064). arXiv: [1509.05782](https://arxiv.org/abs/1509.05782) [gr-qc].  
*I helped with running the binary neutron star inspiral and merger simulations that are used in this paper.*
- Radice, D., F. Galeazzi, J. Lippuner, L. F. Roberts, C. D. Ott, and L. Rezzolla (2016). “Dynamical mass ejection from binary neutron star mergers”. In: *Monthly Notices of the RAS* 460, p. 3255. DOI: [10.1093/mnras/stw1227](https://doi.org/10.1093/mnras/stw1227). arXiv: [1601.02426](https://arxiv.org/abs/1601.02426) [astro-ph.HE].  
*I provided the nucleosynthesis data used in this paper and I assisted with editing the manuscript.*
- Haas, R., C. D. Ott, B. Szilágyi, J. D. Kaplan, J. Lippuner, M. A. Scheel, K. Barkett, C. D. Muhlberger, T. Dietrich, M. D. Duez, F. Foucart, H. P. Pfeiffer, L. E. Kidder, and S. A. Teukolsky (2016). “Simulations of inspiraling and merging double neutron stars using the Spectral Einstein Code”. In: *Physical Review D* 93, p. 124062. DOI: [10.1103/PhysRevD.93.124062](https://doi.org/10.1103/PhysRevD.93.124062). arXiv: [1604.00782](https://arxiv.org/abs/1604.00782) [gr-qc].  
*I performed a significant part of the binary neutron star inspiral and merger simulations presented in this paper. I also helped with the data analysis of the simulations and assisted with editing the manuscript.*
- Majid, W. A., A. B. Pearlman, T. Dobrev, S. Horiuchi, J. Kocz, J. Lippuner, and T. A. Prince (2017). “Post-outburst Radio Observations of the High Magnetic Field Pulsar PSR J1119-6127”. In: *Astrophysical Journal, Letters* 834, p. L2. DOI: [10.3847/2041-8213/834/1/L2](https://doi.org/10.3847/2041-8213/834/1/L2). arXiv: [1612.02868](https://arxiv.org/abs/1612.02868) [astro-ph.HE].  
*I created data processing software that was used for this project and I assisted with editing the manuscript.*
- Vlasov, A. D., B. D. Metzger, J. Lippuner, L. F. Roberts, and T. A. Thompson (2017). “Neutrino-heated winds from millisecond protomagnetars as sources of the weak r-process”. In: *Monthly Notices of the RAS* 468, p. 1522. DOI: [10.1093/mnras/stx478](https://doi.org/10.1093/mnras/stx478). arXiv: [1701.03123](https://arxiv.org/abs/1701.03123) [astro-ph.HE].  
*I provided access to and support for SkyNet that was used for the nucleosynthesis calculations. I wrote the section describing the reaction network calculations.*
- Kidder, L. E., S. E. Field, F. Foucart, E. Schnetter, S. A. Teukolsky, A. Bohn, N. Deppe, P. Diener, F. Hébert, J. Lippuner, J. Miller, C. D. Ott, M. A. Scheel, and T. Vincent (2017). “SpECTRE: A task-based discontinuous Galerkin code for relativistic astrophysics”. In: *Journal of Computational Physics* 335, p. 84. DOI: [10.1016/j.jcp.2016.12.059](https://doi.org/10.1016/j.jcp.2016.12.059). arXiv: [1609.00098](https://arxiv.org/abs/1609.00098) [astro-ph.HE].  
*I contributed to the code development of SpECTRE and I assisted with editing the manuscript.*

Fernández, R., F. Foucart, D. Kasen, J. Lippuner, D. Desai, and L. F. Roberts (2017). “Dynamics, nucleosynthesis, and kilonova signature of black hole - neutron star merger ejecta”. In: *Classical and Quantum Gravity, in press*. DOI: [10.1088/1361-6382/aa7a77](https://doi.org/10.1088/1361-6382/aa7a77). arXiv: [1612.04829](https://arxiv.org/abs/1612.04829) [astro-ph.HE].  
*I performed the nucleosynthesis calculations and I assisted with editing the manuscript.*

# TABLE OF CONTENTS

<b>Acknowledgements</b> . . . . .	<b>iii</b>
<b>Abstract</b> . . . . .	<b>v</b>
<b>Published Content and Contributions</b> . . . . .	<b>vi</b>
<b>Table of Contents</b> . . . . .	<b>ix</b>
<b>List of Illustrations</b> . . . . .	<b>xiii</b>
<b>List of Tables</b> . . . . .	<b>xvii</b>
<b>Chapter I: Introduction</b> . . . . .	<b>1</b>
1.1 Solar system abundances . . . . .	2
1.2 Nucleosynthesis up to the iron peak . . . . .	4
1.2.1 Big Bang nucleosynthesis . . . . .	4
1.2.2 Low-mass stellar burning . . . . .	4
1.2.3 Nuclear burning in massive stars . . . . .	7
1.2.4 Iron peak . . . . .	9
1.3 Nucleosynthesis beyond the iron peak . . . . .	10
1.4 Possible r-process sites . . . . .	14
1.4.1 Core-collapse supernovae . . . . .	14
1.4.2 Neutron star mergers . . . . .	17
1.5 Galactic chemical evolution . . . . .	19
1.6 Kilonovae . . . . .	23

<b>Chapter II: SkyNet</b> . . . . .	<b>28</b>
Abstract . . . . .	28
2.1 Introduction . . . . .	29
2.2 Nuclear reaction network basics . . . . .	33
2.2.1 Kinetic theory . . . . .	33
2.2.2 Reaction rates and velocity averaged cross-sections . . . . .	39
2.2.3 Nuclear Statistical Equilibrium (NSE) and inverse reaction rates . . . . .	40
2.3 Network evolution . . . . .	43
2.3.1 Implicit integration method . . . . .	43
2.3.2 Self-heating evolution . . . . .	44
2.3.3 Convergence criteria and time stepping . . . . .	48
2.3.4 NSE evolution mode . . . . .	52
2.4 Electron screening . . . . .	53
2.4.1 General screening factor . . . . .	55
2.4.2 Weak screening . . . . .	57
2.4.3 Strong and intermediate screening . . . . .	60
2.4.4 Combining the different screening regimes . . . . .	61
2.4.5 NSE with screening . . . . .	64
2.5 Implementation details . . . . .	67
2.5.1 Modularity and extendability . . . . .	67
2.5.2 Nuclear reaction libraries . . . . .	68
2.6 Code verification and tests . . . . .	70
2.6.1 Nuclear statistical equilibrium . . . . .	70
2.6.1.1 Consistency test . . . . .	70
2.6.1.2 Comparison with published results . . . . .	73
2.6.2 Network evolution . . . . .	73
2.6.2.1 Neutron-rich r-process . . . . .	75
2.6.2.2 X-ray burst . . . . .	79
2.6.2.3 Hydrostatic carbon-oxygen burning . . . . .	81
2.6.3 NSE evolution test . . . . .	83
2.7 Summary and future work . . . . .	84
Acknowledgments . . . . .	88
2.A Equation of state (EOS) . . . . .	89
2.A.1 Ideal Boltzmann gas . . . . .	89
2.A.2 Modified Timmes EOS . . . . .	91
2.B Calculating NSE . . . . .	94
2.B.1 From temperature and density . . . . .	94
2.B.2 With an unknown temperature . . . . .	97
2.C Neutrino interaction reactions . . . . .	99

<b>Chapter III: Lanthanides and heating rates in kilonovae</b> . . . . .	<b>103</b>
Abstract . . . . .	103
3.1 Introduction . . . . .	104
3.2 Parameterized ejecta nucleosynthesis . . . . .	106
3.2.1 Parameter space . . . . .	109
3.2.2 Lanthanide turnoff and heating rate as a function of $Y_e$ . . . . .	112
3.2.3 Fission cycling . . . . .	117
3.2.4 Lanthanide production and heating rate in the full parameter space . . . . .	119
3.2.5 Fitted nuclear heating rates . . . . .	126
3.2.6 Dominant nuclear decays . . . . .	127
3.3 Light curves . . . . .	133
3.3.1 Radiative transfer methods . . . . .	133
3.3.2 Dependence of kilonova light curves on the outflow properties . . . . .	135
3.3.3 Mass estimates of potential kilonova observations . . . . .	139
3.4 Conclusions . . . . .	141
Acknowledgments . . . . .	143
3.A Computing AB magnitude from light curve . . . . .	143
3.B Slice plots . . . . .	145
3.B.1 High-resolution <code>sym0</code> run . . . . .	146
3.B.2 <code>sym0</code> run . . . . .	164
3.B.3 <code>sym2</code> run . . . . .	174
3.B.4 <code>sym4</code> run . . . . .	184
3.B.5 <code>nonsym</code> run . . . . .	194
<b>Chapter IV: Neutrinos and BHNS r-process nucleosynthesis</b> . . . . .	<b>204</b>
Abstract . . . . .	204
4.1 Introduction . . . . .	205
4.2 Methods . . . . .	208
4.2.1 Relativistic merger simulations and binary systems . . . . .	208
4.2.2 SPH evolution of ejecta . . . . .	209
4.2.3 Nuclear reaction network and weak interactions . . . . .	213
4.3 Results and discussion . . . . .	216
4.3.1 The electron fraction of the ejecta . . . . .	216
4.3.2 Nucleosynthesis and neutrino induced production of the first r-process peak . . . . .	220
4.3.3 Details of the first peak production mechanism . . . . .	222
4.3.4 Isotopic and elemental abundances, galactic chemical evolution, and low metallicity halo stars . . . . .	228
4.4 Conclusions . . . . .	232
Acknowledgements . . . . .	234

<b>Chapter V: Nucleosynthesis in HMNS disk winds</b> . . . . .	<b>235</b>
Abstract . . . . .	235
5.1 Introduction . . . . .	236
5.2 Methods . . . . .	239
5.2.1 Disk outflow simulations and thermodynamic trajectories . .	239
5.2.2 Nuclear reaction network: <i>SkyNet</i> . . . . .	241
5.2.3 Investigated models . . . . .	241
5.3 Results and discussion . . . . .	244
5.3.1 Overview of disk evolution . . . . .	244
5.3.2 Neutrino emission . . . . .	245
5.3.3 Ejecta properties . . . . .	247
5.3.4 Nucleosynthesis . . . . .	252
5.3.4.1 Final abundances . . . . .	252
5.3.4.2 BH spin mimicking HMNS lifetime . . . . .	255
5.3.4.3 Lanthanides, actinides, and heating rates . . . . .	256
5.3.4.4 Comparison with r-process abundances in metal-poor halo stars . . . . .	261
5.3.5 Impact of angular momentum transport . . . . .	265
5.4 Conclusions . . . . .	268
Acknowledgments . . . . .	271
5.A Improvements to the hydrodynamic disk simulations . . . . .	272
<b>Chapter VI: Other work</b> . . . . .	<b>273</b>
6.1 Low mass binary neutron star mergers: Gravitational waves and neutrino emission . . . . .	273
6.2 Gravitational waveforms for neutron star binaries from binary black hole simulations . . . . .	275
6.3 Dynamical mass ejection from binary neutron star mergers . . . . .	277
6.4 Simulations of inspiraling and merging double neutron stars using the Spectral Einstein Code . . . . .	279
6.5 Post-outburst radio observations of the high magnetic field pulsar PSR J1119-6127 . . . . .	281
6.6 Neutrino-heated winds from millisecond protomagnetars as sources of the weak r-process . . . . .	282
6.7 SpECTRE: A task-based discontinuous Galerkin code for relativistic astrophysics . . . . .	283
6.8 Dynamics, nucleosynthesis, and kilonova signature of black hole–neutron star merger ejecta . . . . .	285
6.9 Fast and efficient multi-GPU collective communication . . . . .	287
<b>Chapter VII: Summary and outlook</b> . . . . .	<b>289</b>
<b>Bibliography</b> . . . . .	<b>292</b>

## LIST OF ILLUSTRATIONS

**Chapter I: Introduction**

1.1	Solar system abundances . . . . .	3
1.2	Lithium problem . . . . .	5
1.3	Early stages of stellar evolution . . . . .	6
1.4	Nuclear burning in massive stars . . . . .	7
1.5	Type Ia supernova nucleosynthesis . . . . .	10
1.6	Neutron capture processes . . . . .	12
1.7	s- and r-process contributions to the solar abundances . . . . .	13
1.8	Universality of the r-process abundance pattern . . . . .	13
1.9	r-Process in neutrino driven wind . . . . .	15
1.10	r-Process in a magnetorotational supernova . . . . .	16
1.11	Dynamical ejecta from a binary neutron star merger . . . . .	18
1.12	Neutrino-driven wind from a HMNS accretion disk . . . . .	19
1.13	Robustness of the r-process in neutron star mergers . . . . .	20
1.14	Galactic chemical evolution with neutron star mergers . . . . .	22
1.15	r-Process event rate versus yield . . . . .	23
1.16	r-Process enhanced ultrafaint dwarf galaxy Reticulum II . . . . .	24
1.17	Kilonova light curves . . . . .	27

**Chapter II: *SkyNet***

2.1	Convergence criteria comparison . . . . .	49
2.2	Adaptive time stepping mechanism . . . . .	51
2.3	Screening as a function of $Z$ . . . . .	62
2.4	Screening as a function of $T$ . . . . .	63
2.5	Impact of screening in NSE . . . . .	66
2.6	NSE consistency test . . . . .	72
2.7	NSE comparison with published results . . . . .	74
2.8	r-Process network comparison . . . . .	77
2.9	Explosive X-ray burst network comparison . . . . .	80
2.10	Hydrostatic C/O burning network comparison . . . . .	82
2.11	NSE evolution mode test . . . . .	85

### Chapter III: Lanthanides and heating rates in kilonovae

3.1	Final abundances of parametrized r-process calculations . . . . .	111
3.2	<i>SkyNet</i> movie frame . . . . .	113
3.3	Results of the high-resolution $Y_e$ runs . . . . .	114
3.4	Electron fraction slices . . . . .	120
3.5	Entropy slices . . . . .	122
3.6	Expansion timescale slices . . . . .	123
3.7	Heating rate fits . . . . .	128
3.8	Light curves and heating rates . . . . .	136
3.9	Light curve parameters as function of $Y_e$ . . . . .	138
3.10	Hi-res sym0 electron fraction slices of lanthanide mass fraction . . .	146
3.11	Hi-res sym0 electron fraction slices of heating rate . . . . .	149
3.12	Hi-res sym0 entropy slices of lanthanide mass fraction . . . . .	152
3.13	Hi-res sym0 entropy slices of heating rate . . . . .	155
3.14	Hi-res sym0 expansion timescale slices of lanthanide mass fraction .	158
3.15	Hi-res sym0 expansion timescale slices of heating rate . . . . .	161
3.16	sym0 electron fraction slices of lanthanide mass fraction . . . . .	164
3.17	sym0 electron fraction slices of heating rate . . . . .	165
3.18	sym0 entropy slices of lanthanide mass fraction . . . . .	167
3.19	sym0 entropy slices of heating rate . . . . .	169
3.20	sym0 expansion timescale slices of lanthanide mass fraction . . . . .	170
3.21	sym0 expansion timescale slices of heating rate . . . . .	172
3.22	sym2 electron fraction slices of lanthanide mass fraction . . . . .	174
3.23	sym2 electron fraction slices of heating rate . . . . .	175
3.24	sym2 entropy slices of lanthanide mass fraction . . . . .	177
3.25	sym2 entropy slices of heating rate . . . . .	179
3.26	sym2 expansion timescale slices of lanthanide mass fraction . . . . .	180
3.27	sym2 expansion timescale slices of heating rate . . . . .	182
3.28	sym4 electron fraction slices of lanthanide mass fraction . . . . .	184
3.29	sym4 electron fraction slices of heating rate . . . . .	185
3.30	sym4 entropy slices of lanthanide mass fraction . . . . .	187
3.31	sym4 entropy slices of heating rate . . . . .	189
3.32	sym4 expansion timescale slices of lanthanide mass fraction . . . . .	190
3.33	sym4 expansion timescale slices of heating rate . . . . .	192
3.34	nonsym electron fraction slices of lanthanide mass fraction . . . . .	194
3.35	nonsym electron fraction slices of heating rate . . . . .	195

3.36	nonsym entropy slices of lanthanide mass fraction . . . . .	197
3.37	nonsym entropy slices of heating rate . . . . .	199
3.38	nonsym expansion timescale slices of lanthanide mass fraction . . . . .	200
3.39	nonsym expansion timescale slices of heating rate . . . . .	202

#### **Chapter IV: Neutrinos and BHNS r-process nucleosynthesis**

4.1	Particle energy distribution . . . . .	212
4.2	Mass profiles . . . . .	213
4.3	Outflow structure . . . . .	214
4.4	Weak reaction rates . . . . .	218
4.5	Electron fraction distribution . . . . .	219
4.6	Final abundances . . . . .	220
4.7	First peak production details . . . . .	223
4.8	Final abundances from single particle . . . . .	225
4.9	First peak production details in different regime . . . . .	226
4.10	r-Process paths . . . . .	227
4.11	Final abundances of different models . . . . .	228
4.12	Final elemental abundances . . . . .	231

#### **Chapter V: Nucleosynthesis in HMNS disk winds**

5.1	Neutrino luminosities and energies . . . . .	246
5.2	Electron fraction distribution of HMNS models . . . . .	248
5.3	Ejecta properties of model H300 . . . . .	250
5.4	Final abundances . . . . .	253
5.5	Electron fraction distribution of BH models . . . . .	255
5.6	Lanthanides and heating vs. electron fraction . . . . .	258
5.7	Neutron-to-seed ratio vs. entropy . . . . .	259
5.8	Ejecta morphology . . . . .	262
5.9	Final abundances vs. charge number . . . . .	264
5.10	Ejecta properties without viscosity . . . . .	266
5.11	Final abundances without viscosity . . . . .	267

#### **Chapter VI: Other work**

6.1	Neutrino luminosities in a binary neutron star merger . . . . .	274
6.2	Gravitational waveform differences . . . . .	276
6.3	Density rendering of an eccentric binary neutron star merger . . . . .	278
6.4	Binary neutron star inspiral and merger waveform . . . . .	280

6.5	<i>SpECTRE</i> strong scaling . . . . .	284
6.6	Tidal tail and disk ejecta in a BHNS merger . . . . .	286
6.7	Multi-GPU communication . . . . .	288

## LIST OF TABLES

**Chapter II: *SkyNet***

2.1	Network comparison errors . . . . .	78
-----	-------------------------------------	----

**Chapter III: Lanthanides and heating rates in kilonovae**

3.1	Parameter grid . . . . .	110
3.2	Lanthanide and actinide turnoff . . . . .	115
3.3	Heating contributions . . . . .	131

**Chapter V: Nucleosynthesis in HMNS disk winds**

5.1	List of investigated models . . . . .	242
5.2	Summary of nucleosynthesis results . . . . .	249

*Chapter I*

## INTRODUCTION

The question of what the material world is made of and where it all came from has been pondered by humans since antiquity. Leucippus (ca. 430 BC) and Democritus (ca. 420 BC) were the first to propose an atomic theory where all matter consists of indivisible units (e.g., Bailey, 1928; Freeman, 1946; Shaviv, 2012). Throughout the middle ages, various researchers, commonly known as alchemists, made progress in developing experimental methods to investigate the constituents of matter. However, their research mainly consisted of futile attempts to transform ordinary metals (e.g. lead) into noble metals (particularly gold) and no progress was made towards developing a theory of how such a transformation could come about (e.g., Shaviv, 2012). It was not until the late 20th century that modern-day alchemists, commonly known as nuclear physicists, were successful in transforming bismuth into gold (albeit only in trace amounts and at commercially infeasible costs, Aleklett et al., 1981). The road that led to this momentous achievement includes the development of modern chemistry (e.g., Boyle, 1661; de Lavoisier, 1789), modern atomic theory (e.g., Dalton, 1808; Avogadro, 1811; Thomson, 1897), and nuclear physics (e.g., Rutherford, 1911; Chadwick, 1932; Fermi, 1934; Yukawa, 1935), which provide us with a good understanding of the building blocks of ordinary matter.

Having a good understanding of what makes up matter is a necessary first step to developing a theory of how this matter was created. Alpher et al. (1948) theorized that all elements were synthesized during the Big Bang. However, once more accurate neutron capture cross-sections for low-mass nuclei ( $A < 20$ ) became available, it was clear that nucleosynthesis during the early expanding universe would not be able to get past  $A = 8$  (e.g., Alpher and Herman, 1950; Shaviv, 2012). This set the stage for the seminal work of Burbidge et al. (1957), who proposed that only the lightest elements (mainly hydrogen and helium) were created in the Big Bang and all heavier elements are synthesized in stars. Although that theory has since been refined, the original idea of Burbidge et al. (1957) has stood the test of time. It is our current understanding that the various nuclear processes described by Burbidge et al. (1957) are indeed responsible for the synthesis of all elements heavier than hydrogen and helium.

In this thesis, I investigate the rapid neutron capture process (r-process), which is one of the nuclear processes proposed by Burbidge et al. (1957) to create elements heavier than iron. My focus is on computing r-process nucleosynthesis in neutron star mergers with a new nuclear reaction network code called *SkyNet* that I have developed. In the remainder of this introduction, I briefly summarize our current understanding of the origin of the elements, how the r-process works, where it could occur, and its expected observational signatures. In Chapter II, I present the physics that is implemented in *SkyNet* to evolve thousands of nuclear species under the influence of tens of thousands of nuclear reactions. I use *SkyNet* in Chapter III to systematically investigate the r-process and its possible optical counterparts in various parametrized scenarios. In Chapter IV, I discuss r-process nucleosynthesis in black hole–neutron star (BHNS) mergers, and in Chapter V, I consider the r-process in the disk outflow following a neutron star merger. In Chapter VI, I briefly summarize the other work I have done during my PhD that is not directly part of my thesis. Finally, I provide a summary and outlook in Chapter VII.

## 1.1 Solar system abundances

In order to test theories and models that predict how elements are created and in what ratios, a detailed inventory of the elements and their relative abundances in the universe is required. It is extremely challenging to obtain samples of matter from places other than the earth’s crust. The *Apollo* and *Luna* missions brought samples from the moon, and since then spacecrafts such as *Stardust*, *Genesis*, and *Hayabusa* have successfully returned samples from nearby asteroids and space dust to earth. However, the vast majority of extraterrestrial material available for chemical analysis comes from meteorites that naturally fall on earth. Therefore, to determine the composition of stars and other astrophysical objects, we are constrained to examining absorption and emission lines from these objects and infer elemental abundances from those (e.g., Shaviv, 2012).

Absorption lines in the solar spectrum were first discovered at the beginning of the 19th century (Wollaston, 1802; Fraunhofer, 1817). However, it was not until about 100 years later, after the development of quantum mechanics, that these absorption lines could be used to quantitatively determine the abundance of different elements in the sun. Pioneering work was done by Payne (1925) in her seminal PhD thesis and by Russell (1934). The important work of Suess and Urey (1956) was one of the first to also take isotope abundance measurements from meteorites into account. Since then, great progress has been made in measuring the abundances of the elements

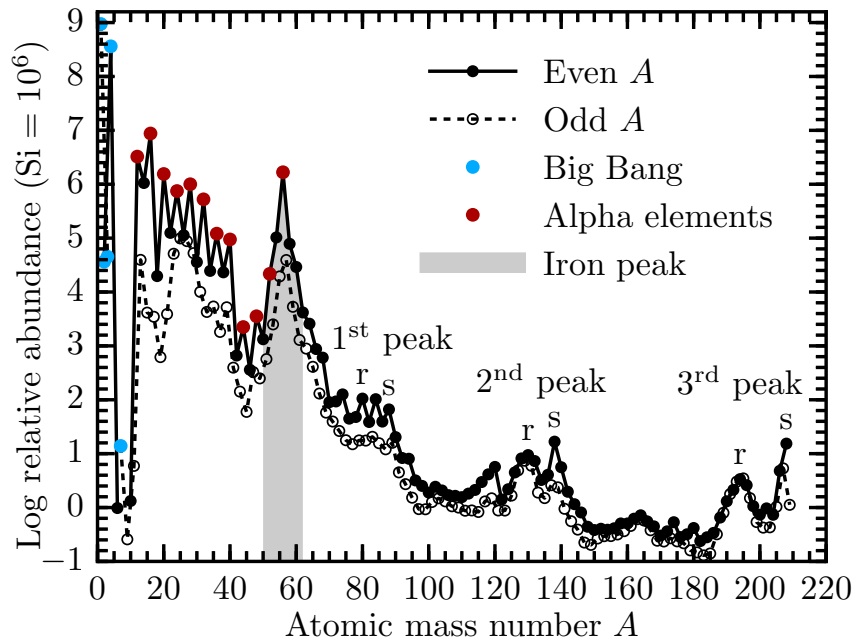


Figure 1.1: Observed abundances in our solar system as a function of mass number  $A$ . The lightest elements were created in the Big Bang and fusion in stars predominantly creates alpha elements. The iron peak is made in core-collapse and type Ia supernovae. Elements beyond the iron peak are synthesized by the slow ( $s$ ) and rapid ( $r$ ) neutron capture processes. These processes produce three distinct double peaks (see Section 1.3). Abundance data from Lodders (2003).

and isotopes in our solar system (e.g., Cameron, 1973; Anders and Grevesse, 1989; Grevesse and Sauval, 1998; Lodders, 2003).

Figure 1.1 shows the observed abundances as a function of atomic mass number  $A$  in our solar system (data from Lodders 2003). Nuclides with an even mass number tend to be more abundant than nuclides with an odd mass number because even mass nuclides are more bound. Due to spin pairing of nucleons, a nuclide with an even number of both neutrons and protons (hence an even  $A$ ) is more bound than a nuclide with an odd number of either neutrons or protons (hence an odd  $A$ , see e.g., Weizsäcker, 1935; Myers and Swiatecki, 1966; Möller et al., 1995). Nuclides with an odd number of both neutrons and protons (hence an even  $A$ ), have an even lower binding energy because neither all neutrons nor all protons can be spin-paired. It is thus no surprise that there are only a handful of odd-odd nuclides that are stable or long-lived:  ${}^2\text{H}$ ,  ${}^6\text{Li}$ ,  ${}^{10}\text{B}$ , and  ${}^{14}\text{N}$  are stable, and  ${}^{40}\text{K}$ ,  ${}^{50}\text{V}$ ,  ${}^{138}\text{La}$ , and  ${}^{176}\text{Lu}$  are the only odd-odd nuclides with a half-life of at least 1 Gyr.

There are a number of different nucleosynthesis processes that are dominant in different mass ranges. Very low-mass nuclides ( $A < 8$ ) were produced right after

the Big Bang, some  ${}^4\text{He}$  as well as most nuclides in the range  $12 \leq A \leq 56$  are produced in stars through hydrostatic nuclear burning, a significant fraction of the iron peak ( $50 \lesssim A \lesssim 62$ ) is produced by material going into nuclear statistical equilibrium (NSE) and then cooling down (e.g., during a type Ia supernova or explosive silicon burning in core-collapse supernovae (CCSNe)), and finally, almost all of the nuclides heavier than the iron peak are produced through capturing neutrons onto lighter seed nuclei (e.g., Burbidge et al., 1957). We will look at these different processes in the following sections.

## 1.2 Nucleosynthesis up to the iron peak

### 1.2.1 Big Bang nucleosynthesis

Big Bang nucleosynthesis (BBN) created mostly hydrogen ( $\sim 75\%$  by mass) and helium ( $\sim 25\%$  by mass) in the first tens of seconds to minutes after the Big Bang and some trace amounts of deuterium,  ${}^3\text{He}$ , and  ${}^7\text{Li}$  (e.g., Tytler et al., 2000, and references therein). 13.8 Gyr later, the chemical composition of the universe is still about 75% H and 25% He, because creating heavier elements requires extreme physical conditions.

Interestingly, even though BBN appears to be a straightforward problem to model because it only involves a handful of nuclides, there are presently large discrepancies between BBN models and observations. The predicted deuterium and  ${}^4\text{He}$  abundances agree well with observations, but BBN models over-predict the  ${}^7\text{Li}$  abundance by  $4 - 5 \sigma$  compared to observations, see Figure 1.2, which is Figure 1 from Coc et al. (2013). This discrepancy in the lithium abundance is not currently understood and referred to as the “lithium problem.” Suggested solutions include systematic errors in the  ${}^7\text{Li}$  abundance observations, unknown or poorly-measured nuclear properties of  ${}^7\text{Be}$ , and even unknown physics beyond the Standard Model. See, e.g., Fields (2011) and references therein.

### 1.2.2 Low-mass stellar burning

The main obstacle to combining helium and hydrogen into heavier elements is the strong Coulomb repulsion between nuclei, which are all positively charged. Furthermore, the most common way to fuse hydrogen, the p-p chain, involves the weak reaction  $p + p \rightarrow d + e^+ + \nu_e$ , which has an extremely small cross section (Rolfs and Rodney, 1988). Therefore, extremely high temperatures ( $\gtrsim 10$  MK) are necessary to burn hydrogen into helium and helium into heavier elements. Such conditions are reached inside stars, where nuclear fusion is going on (e.g., Bethe,

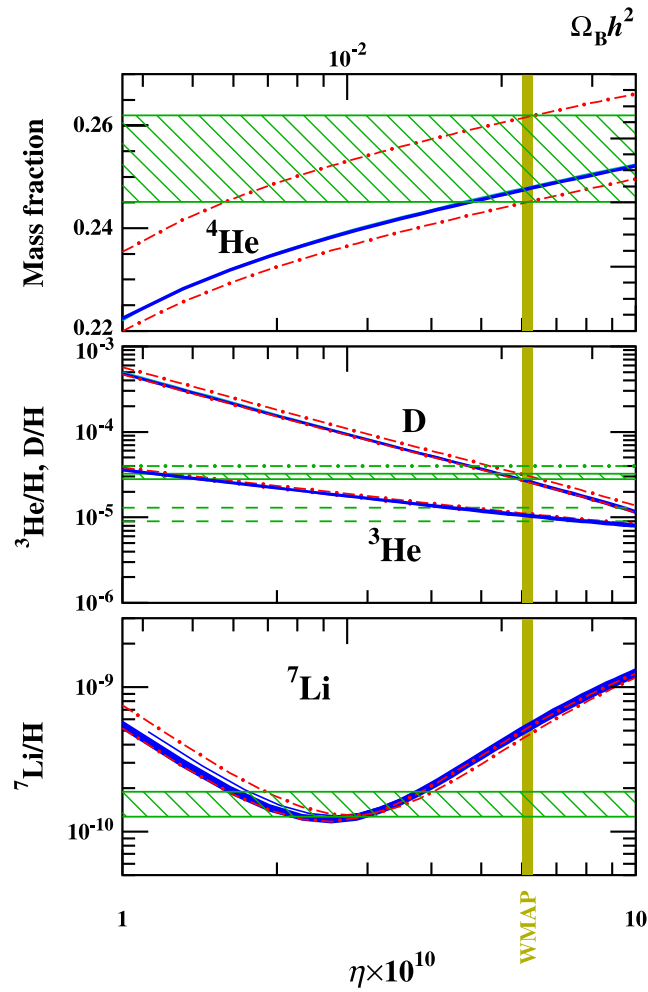


Figure 1.2: Computed abundances of  $^4\text{He}$ , D,  $^3\text{He}$ , and  $^7\text{Li}$  (blue lines) as a function of the baryon-to-photon ratio  $\eta$ . The green regions are the observed abundances and the yellow vertical strip is the observed value of  $\eta$ . The computed abundances of  $^4\text{He}$ , D, and  $^3\text{He}$  agree with the observations, but the  $^7\text{Li}$  abundance is over-predicted by 4–5  $\sigma$ . This is known as the “lithium problem.” Figure 1 from Coc et al. (2013); see that reference for details. © 2013 American Physical Society

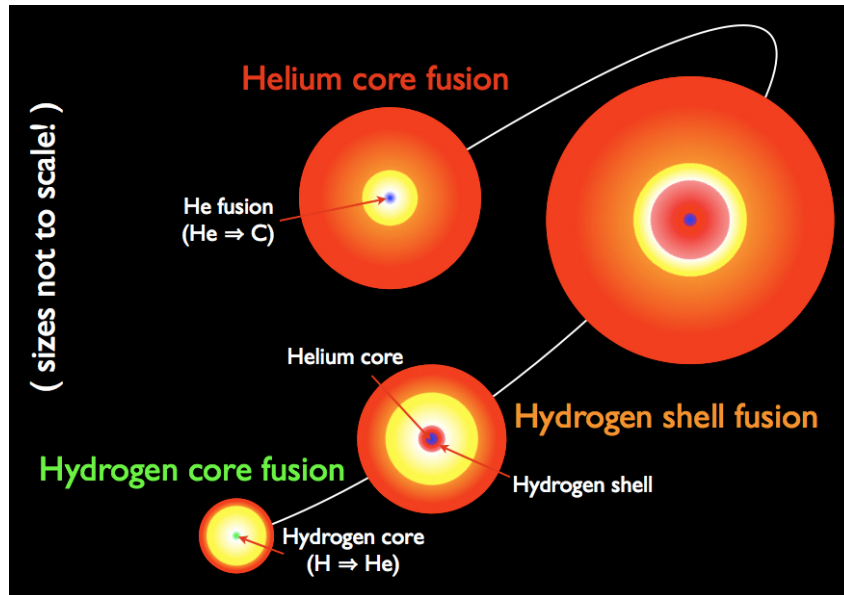


Figure 1.3: Cartoon of the early stages of stellar evolution. The star starts out fusing hydrogen to helium in its core. Once the hydrogen in the core is exhausted, the core contracts, which raises the temperature and ignites hydrogen fusion in a shell around the helium core. This expands the atmosphere of the star and turns it into a red giant. After the hydrogen fuel is burnt up, the core contracts again under gravitational pressure, which increases the temperature to the point where helium fusion initiates. Figure from [https://www.nasa.gov/mission\\_pages/kepler/news/giant\\_stars.html](https://www.nasa.gov/mission_pages/kepler/news/giant_stars.html). © 2011 Thomas Kallinger

1939), releasing nuclear binding energy in the form of heat, which keeps the star from collapsing and makes it shine.

Figure 1.3 depicts the early stages of stellar evolution. By definition, every star at least fuses hydrogen into helium in its core and stars spend most of their life in this hydrogen core burning phase. Once the hydrogen is exhausted in the core, the temperature is not high enough for helium burning, so the core contracts because the heat source from hydrogen burning is diminished. As the core contracts, it heats up and the temperature becomes high enough for hydrogen to burn in a shell around the helium core. At that point, the atmosphere of the star expands dramatically and the star enters the red-giant phase. When the hydrogen in the shell is exhausted and if the star is massive enough ( $\gtrsim 0.5 M_{\odot}$ , e.g. Rofls and Rodney, 1988), the core contracts again, which increases the temperature and allows the triple-alpha process to take place that fuses three  ${}^4\text{He}$  into  ${}^{12}\text{C}$ . Some helium can also be fused with the newly created  ${}^{12}\text{C}$  to make  ${}^{16}\text{O}$ , and in principle, it can also go further to produce  ${}^{20}\text{Ne}$ ,  ${}^{24}\text{Mg}$ ,  ${}^{28}\text{Si}$ , etc., which are called alpha elements because they are a

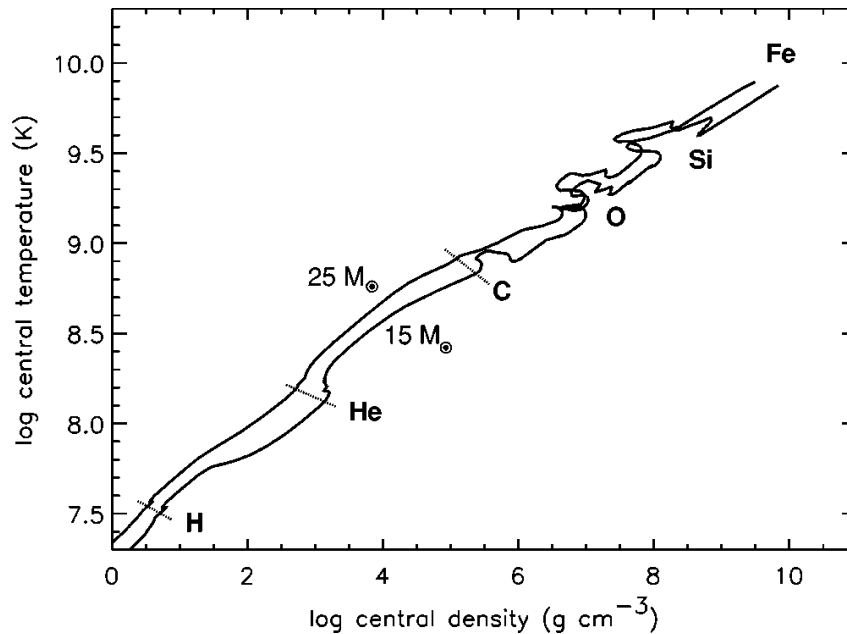


Figure 1.4: Central density and temperature of a  $15 M_{\odot}$  and  $25 M_{\odot}$  stellar model. As the star evolves, the central density and temperature increase, successively igniting hydrogen, helium, carbon, oxygen, and silicon burning. Figure 1 from Woosley et al. (2002); see that reference for details. © 2002 The American Physical Society

certain number of alpha nuclides fused together. However, in practice, the reaction  $^{16}\text{O} + ^4\text{He} \rightarrow ^{20}\text{Ne}$  is slow and so helium burning mostly produces  $^{12}\text{C}$  and  $^{16}\text{O}$  (e.g., Rolfs and Rodney, 1988; Hansen et al., 2004).

Once helium is exhausted, the core temperature is raised again by contraction. The highest temperature reached in the star depends on its initial mass. If the initial mass is above  $\sim 8 M_{\odot}$ , then carbon and oxygen can be burnt, otherwise the star ends its life as a carbon-oxygen white dwarf (e.g., Rolfs and Rodney, 1988; Hansen et al., 2004). If the star is only a few solar masses above  $8 M_{\odot}$ , it may be able to burn carbon and then become an oxygen-neon white dwarf.

### 1.2.3 Nuclear burning in massive stars

Stars with initial mass  $\geq 8 M_{\odot}$  go through multiple burning stages. After each stage, the core contracts under gravitational pressure because the nuclear fuel of that stage has been exhausted and thus the nuclear heat source is lost. As the core contracts, it heats up, which allows the next burning stage to start once the temperature is high enough. This is shown in Figure 1.4 (Figure 1 from Woosley et al., 2002), which shows the central density and temperature of two stellar models and the regions where the different burning stages happen. In the carbon burning phase, there are

a number of different possible outcomes of the reaction  $^{12}\text{C} + ^{12}\text{C}$ , but the most common are  $^{20}\text{Ne} + ^4\text{He}$  and  $^{23}\text{Na} + \text{p}$ . The free proton can capture on other existing nuclides to create non-alpha elements, and  $^{23}\text{Na}$  is also a non-alpha element that can be processed into other non-alpha elements. The helium produced by carbon burning is also burnt up as  $^{12}\text{C} + ^4\text{He} \rightarrow ^{16}\text{O}$  or  $^{16}\text{O} + ^4\text{He} \rightarrow ^{20}\text{Ne}$ . When carbon is exhausted, the core contracts until the very energetic photons form the tail of the Planck distribution can photodisintegrate  $^{20}\text{Ne}$ , which results in free alpha particles that can capture on undissociated  $^{20}\text{Ne}$  to form some  $^{24}\text{Mg}$ . The reaction with the smallest Coulomb barrier is now  $^{16}\text{O} + ^{16}\text{O}$ , which will mainly result in  $^{28}\text{Si} + ^4\text{He}$  and  $^{31}\text{P} + \text{p}$  (e.g., Rolfs and Rodney, 1988). The liberated alpha particles are captured on  $^{24}\text{Mg}$  and  $^{28}\text{Si}$  to make  $^{28}\text{Si}$  and  $^{32}\text{S}$ .

At the end of oxygen burning, the stellar core consists mostly of  $^{28}\text{Si}$ ,  $^{32}\text{S}$ , and smaller amounts of various other nuclides. This sets the stage for the final burning phase: silicon burning. Before the temperature required for  $^{28}\text{Si} + ^4\text{He}$  is reached, silicon nuclides are destroyed by photodissociation, which again creates a source for free alpha particles. These alpha particles are captured successively starting with  $^{28}\text{Si}$  to create  $^{32}\text{S}$ ,  $^{36}\text{Ar}$ ,  $^{40}\text{Ca}$ ,  $^{44}\text{Ti}$ ,  $^{48}\text{Cr}$ ,  $^{52}\text{Fe}$ , and  $^{56}\text{Ni}$ , which is called the alpha process or alpha ladder that occurs on the timescale of a day (e.g., Rolfs and Rodney, 1988; Hansen et al., 2004). Since the temperature during silicon burning is so high ( $\gtrsim 3.5$  GK), the nuclides heavier than silicon can also be photodissociated. The result is that reactions like  $^{28}\text{Si} + ^4\text{He} \rightarrow ^{32}\text{S}$  are in equilibrium with their inverse reactions. Thus there is a group of nuclides, namely nuclides with  $28 \leq A \leq 62$  and free alpha particles, neutrons, and protons, that are in equilibrium with each other. This is called quasi-equilibrium (QSE) and it differs from NSE (see next section) in that not all nuclides are in equilibrium with each other. Specifically,  $^{12}\text{C}$ ,  $^{16}\text{O}$ ,  $^{20}\text{Ne}$ , and  $^{24}\text{Mg}$  are not part of the QSE group described above (e.g., Bodansky et al., 1968; Woosley et al., 1973).

However, silicon burning can only produce nuclides up to an atomic mass number of  $A = 56$ , because the binding energy per nucleon (protons and neutrons) reaches a maximum at that mass. Therefore, heavier nuclides are more weakly bound (Rolfs and Rodney, 1988), which means one would have to add energy in order to make fusion work beyond  $A = 56$ . In other words, once all the matter in the core of massive stars is burnt up to  $^{56}\text{Ni}$  the core of the star now consists of nuclear ash, which cannot be burnt further, and the star loses its central heat source. The core remains supported against collapse by electron degeneracy pressure, but as soon as the mass of the core

exceeds the effective Chandrasekhar mass, it will collapse, triggering a CCSN (e.g., Woosley et al., 2002). The Chandrasekhar mass ( $\sim 1.4 M_{\odot}$ ) is the theoretical maximum mass of a white dwarf supported solely by electron degeneracy pressure. However, before the iron core reaches the Chandrasekhar mass, electrons capture on the nuclides, which removes electrons and hence pressure support, resulting in the collapse of the core before it reaches the Chandrasekhar mass. The maximum mass of the iron core before collapse starts is called the effective Chandrasekhar mass (e.g., Woosley et al., 2002).

Since stellar fusion preferentially produces alpha elements, it is not surprising that we observe alpha elements to be more abundant than the other nuclides below the iron peak (c.f. Figure 1.1).

#### 1.2.4 Iron peak

Above a temperature of  $\sim 5$  GK, fusion reactions become balanced by their inverse photodissociation reactions, which means that the reaction of fusing  $N$  neutrons and  $Z$  protons into a nuclide  $(N, Z)$  is balanced by the reaction of breaking up the nuclide  $(N, Z)$  into  $N$  free neutrons and  $Z$  free protons. This situation is called nuclear statistical equilibrium (NSE). When material is in NSE, the entire composition, i.e. the abundance of each nuclear species, is completely determined by the temperature, the density, and the electron fraction  $Y_e = n_p / (n_p + n_n)$ , where  $n_p$  is the total number density of protons (free or inside nuclides) and  $n_n$  is the same quantity for neutrons (e.g., Seitzzahl et al., 2009).

Nuclides that are more tightly bound will be more abundant than nuclides that are less tightly bound, because a more tightly bound nuclide is harder to break up via photodissociation, and so the equilibrium will allow for more such nuclides to remain intact. For this reason, the NSE distribution favors nuclides around  $A = 56$ , i.e. the iron peak, because those are the most tightly bound nuclides. This holds only, of course, if  $Y_e$  is close to 0.46, which is the electron fraction of  $^{56}\text{Fe}$ , and also only if the temperature is not too high (with respect to the density), because otherwise NSE will favor free neutrons and protons (e.g., Seitzzahl et al., 2009).

Those conditions are achieved in a type Ia supernova, where a white dwarf composed mostly of carbon and oxygen undergoes a thermonuclear explosion. The subsequent heating forces the material into NSE, which produces iron-peak nuclides that will persist once the material cools down again. Figure 1.5 (Figure 12 from Iwamoto et al., 1999) shows the final abundances from a type Ia supernova model. Type Ia

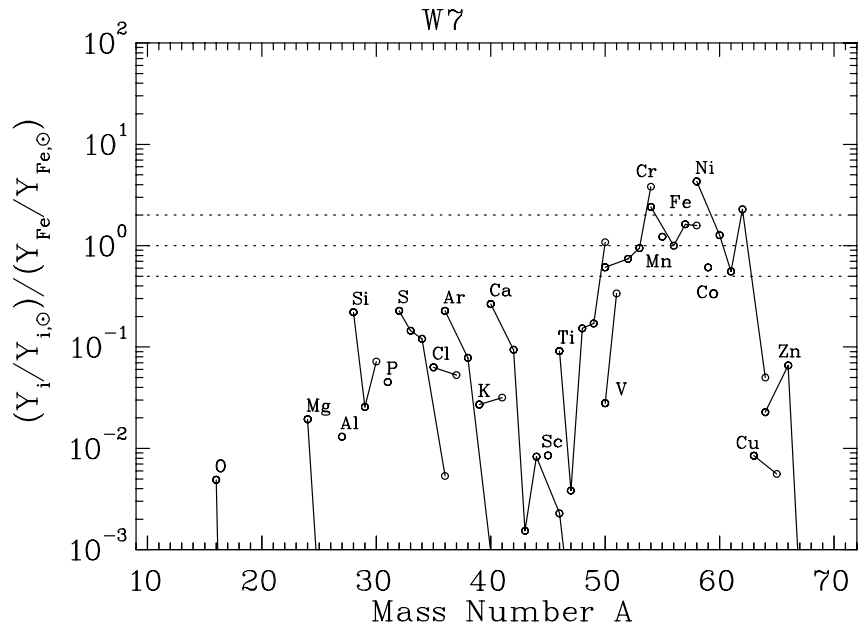


Figure 1.5: Final abundances in a type Ia supernova model. Iron peak elements are predominantly produced, along with some heavy alpha elements (silicon, sulfur, argon, calcium, and titanium). Figure 12 from Iwamoto et al. (1999); see that reference for details. © 1999 The American Astronomical Society

supernovae are a significant contributor to the iron peak along with explosive silicon burning in CCSNe and slow neutron capture (see next section) in massive stars (e.g., Timmes et al., 1996; Woosley et al., 2002)

### 1.3 Nucleosynthesis beyond the iron peak

Since fusion becomes endothermic for  $A \geq 56$  and the Coulomb barrier becomes insurmountably large, a different process is needed to produce elements beyond the iron peak. This process is neutron capture, which remains exothermic as long as the neutron binding energy  $Q_n$  remains large for the neutron-rich nuclei. At some point,  $Q_n$  is so small ( $\sim 1$  MeV) that the photodisintegration rate (a photon knocking out a neutron from the nucleus) is as large as the neutron capture rate, and so no additional neutrons remain bound to the nuclide. The point where this happens is called the neutron drip line and is typically 10 – 20 neutrons in excess of the most neutron-rich stable isotope (e.g., Rolfs and Rodney, 1988). The exact location of the neutron drip line depends on the temperature and neutron density. Obviously, there is no Coulomb barrier for neutron capture, since neutrons are electrically neutral.

Once a nuclide captures a neutron it may still be stable, in which case it can capture another neutron, but in most cases the new nuclide will be unstable to  $\beta$ -decay. An

important distinction is whether the timescale  $\tau_\beta$  for  $\beta$ -decay is shorter or longer than the timescale  $\tau_n$  for neutron capture. If  $\tau_\beta \ll \tau_n$ , then every unstable nuclide created by a neutron capture will decay to a stable nuclide before it has the chance to capture another neutron. Hence the neutron capture process is slow compared to the  $\beta$ -decays and so this is called the slow neutron capture process or s-process. The s-process never gets more than one nuclide away from stability and hence proceeds along the valley of stability (the region on the chart of nuclides where nuclides are stable, denoted by labeled squares in Figure 1.6). If, on the other hand,  $\tau_\beta \gg \tau_n$ , then there is time for multiple neutron captures before the first  $\beta$ -decay occurs. This is called the rapid neutron capture process or r-process, since neutron capture is proceeding rapidly. In this case, the nucleosynthesis runs along the neutron drip line, because neutron capture cannot cross the neutron drip line but it is forced to wait for a  $\beta$ -decay at that point (e.g., Rolfs and Rodney, 1988).

Figure 1.6 schematically shows the paths of the s- and r-processes on a section of the chart of nuclides. If a nucleus has a certain number of neutrons, called a magic number, then the neutrons can be arranged in a closed shell, which is energetically very favorable and drastically reduces the neutron capture cross section (Rolfs and Rodney, 1988). This is indicated in Figure 1.6 at  $N = 50$ . When the r-process reaches a closed neutron shell, it has to wait for several  $\beta$ -decays to happen before it can proceed past the closed neutron shell. Therefore, material will pile up where the neutron drip line intersects the closed neutron shell, which is indicated by the filled squares in Figure 1.6. Since those nuclides are all unstable, they will eventually decay back to stability when all the free neutrons have been captured, and the excess of material that was produced at the closed neutron shell will result in a peak in the abundance pattern at a mass where the nuclides have fewer neutrons than the magic number (because some of the neutrons decayed to protons). Similarly, when the s-process intersects with a closed neutron shell, there will also be an excess of material, but not because the s-process has to wait for additional  $\beta$ -decays (recall that  $\beta$ -decays always happen much faster than neutron captures for the s-process). Material piles up at the closed neutron shell because the neutron capture cross section is one or two orders of magnitude smaller there than for neighboring nuclides (Rolfs and Rodney, 1988). So the s-process will produce abundance peaks at masses where the number of neutrons is exactly the magic number, which is always a higher mass than the peaks produced by the r-process. The most relevant magic numbers are  $N = 50, 82, 126$ , which lead to abundance peaks at roughly  $A = 80, 130, 194$  for the r-process and around  $A = 88, 138, 208$  for the s-process. Figure 1.7 (Figure 1

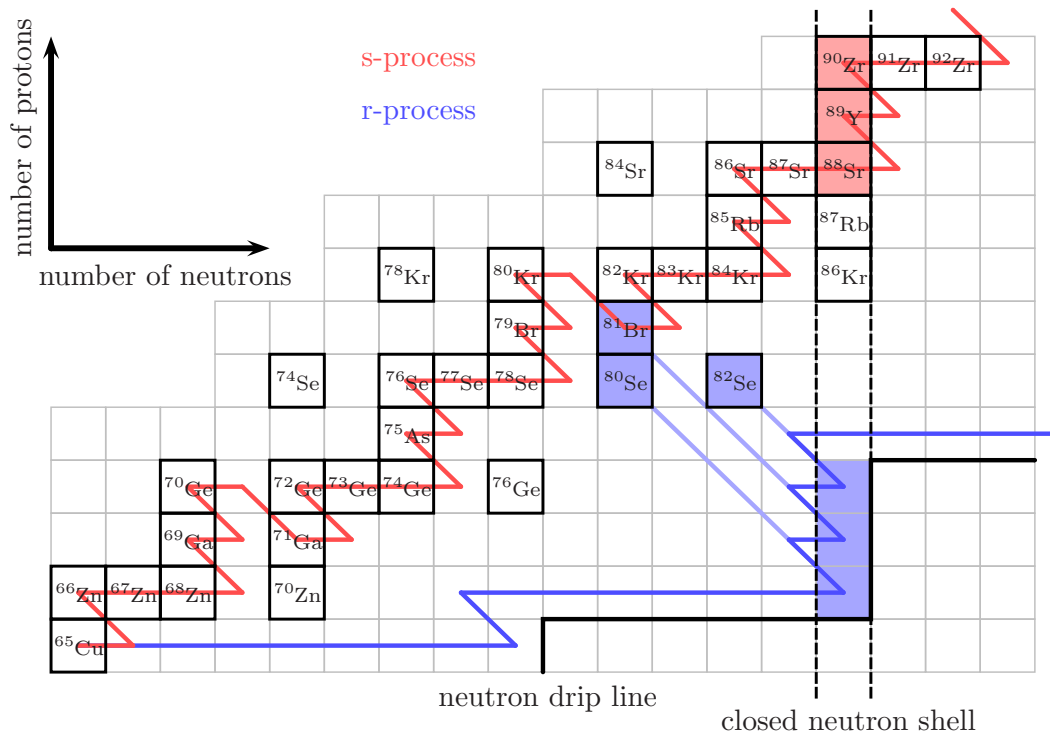


Figure 1.6: Schematic representation of the s- and r-process on a section of the chart of nuclides. The s-process (red) proceeds along the valley of stability and the r-process (blue) along the neutron drip line. At the closed neutron shell  $N = 50$ , the neutron capture cross section drops by several orders of magnitude, which leads to a pile up of material there that produces the double-peak features seen in Figure 1.1.

from Arnould et al., 2007) shows the contributions of the s- and r-processes to the solar abundances. The peaks at the different mass numbers are also clearly visible (especially the second and third), as in Figure 1.1.

When we investigate the r-process, we always compare the predicted abundance pattern to the solar r-process pattern shown in Figure 1.7. It turns out that the r-process abundance pattern is universal and the same relative abundances as in the sun are observed in metal-poor halo stars (e.g., Sneden et al., 2008; Roederer et al., 2010). r-Process abundances from five such stars are shown in Figure 1.8, which is Figure 8 from Sneden et al. (2009). Metal-poor halo stars formed early on in the life of our galaxy and so we expect that they are not significantly enriched in heavy elements produced by the s-process, because it had not enough time to operate by the time those stars were formed (see also Section 1.5). Therefore, any realistic r-process nucleosynthesis model must reproduce the solar r-process abundances shown in Figure 1.7.

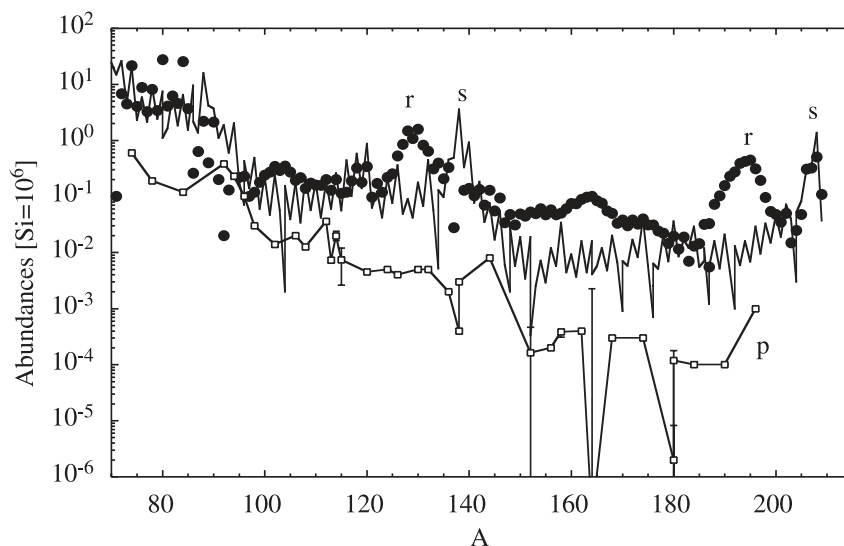


Figure 1.7: Contributions of the s-process (solid line), r-process (dots), and p-process (squares) to the solar abundances. Note that the r-process produces peaks at slightly lower masses than the s-process. Figure 1 from Arnould et al. (2007); see that reference for details. © 2007 Elsevier B.V.

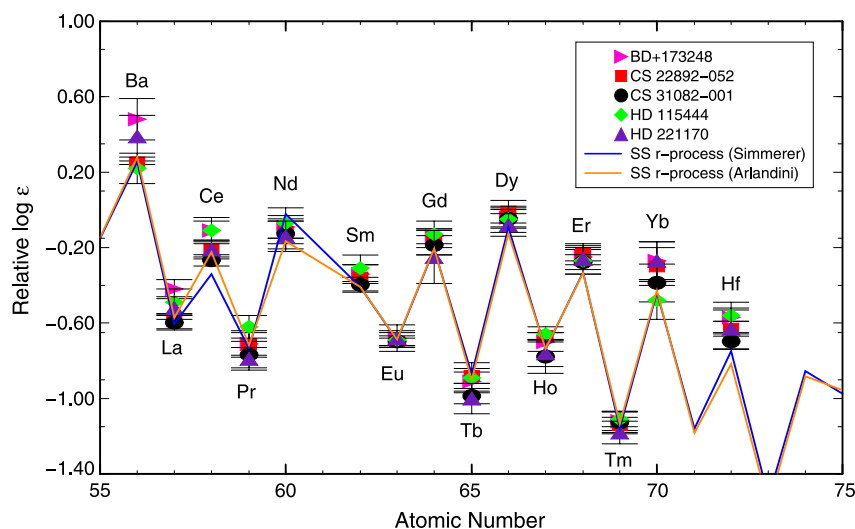


Figure 1.8: Observed abundances of some heavy elements in five metal-poor halo stars. The abundances are normalized at europium. All stars have virtually identical relative abundances and that pattern also agrees with what is observed in the solar system (lines). These stars are not expected to be enriched by s-process nucleosynthesis because they formed soon after the galaxy formed. Therefore, this finding indicates that the r-process produces a universal abundance pattern. Figure 8 from Sneden et al. (2009); see that reference for details. © 2009 The American Astronomical Society

Figure 1.7 also shows the p-process contribution to the solar abundances, which is several orders of magnitude less than the s- and r-process contributions. The p-process produces nuclides on the proton-rich side of the valley of stability (e.g.,  $^{74}\text{Se}$ ,  $^{78}\text{Kr}$ , and  $^{84}\text{Sr}$  in Figure 1.6). The p-process is an active area of research and not yet well-understood. Possible sites include massive stars in their pre-supernova phases and all types of supernovae. See Arnould and Goriely (2003) for a recent and comprehensive review.

Finally, some authors also consider an intermediate neutron capture process, called the i-process, between the slow and rapid one. The i-process proceeds on the neutron-rich side, reaching up to five nuclides away from stability (e.g., Cowan and Rose, 1977; Bertolli et al., 2013). The s-process and/or i-process occur inside low-mass asymptotic giant branch (AGB) stars ( $1.5 \leq M/M_{\odot} \leq 3$ ) and also more massive stars, which tend to have intense stellar winds that release some of the newly produced heavy elements to the interstellar medium (e.g., Peters, 1968; Couch et al., 1974; Käppeler et al., 1994; Woosley et al., 2002; Straniero et al., 2006; Herwig et al., 2011). The reactions  $^{13}\text{C} + ^4\text{He} \rightarrow ^{16}\text{O} + \text{n}$  and  $^{22}\text{Ne} + ^4\text{He} \rightarrow ^{25}\text{Mg} + \text{n}$  provide the free neutrons. The astrophysical site of the r-process is still an open question and the subject of the next section.

## 1.4 Possible r-process sites

The r-process requires a very neutron-rich environment. Numerous sites have been suggested where the right conditions for the r-process could be achieved. These include shock or jet ejecta in neutron-rich supernovae, inhomogeneous Big Bang cosmologies, ejecta from the coalescence and tidal disruption of binary neutron stars, nova outbursts, shock-induced explosive helium or carbon burning, core helium flashes in low-mass stars, or neutron star accretion disks (see Mathews and Cowan, 1990, and references therein). Based on observations of europium in metal-poor stars and galactic chemical evolution models, Mathews and Cowan (1990) concluded that CCSN were the most likely site for the r-process. Recent studies find that CCSN and neutron star mergers are the only viable r-process site candidates (e.g., Thielemann et al., 2011).

### 1.4.1 Core-collapse supernovae

After the iron core of a massive star collapses, a proto-neutron star (PNS) forms. This PNS deleptonizes to eventually form a neutron star. This process emits  $\sim 10^{53}$  erg of binding energy in the form of neutrinos. This large neutrino irradiation drives a

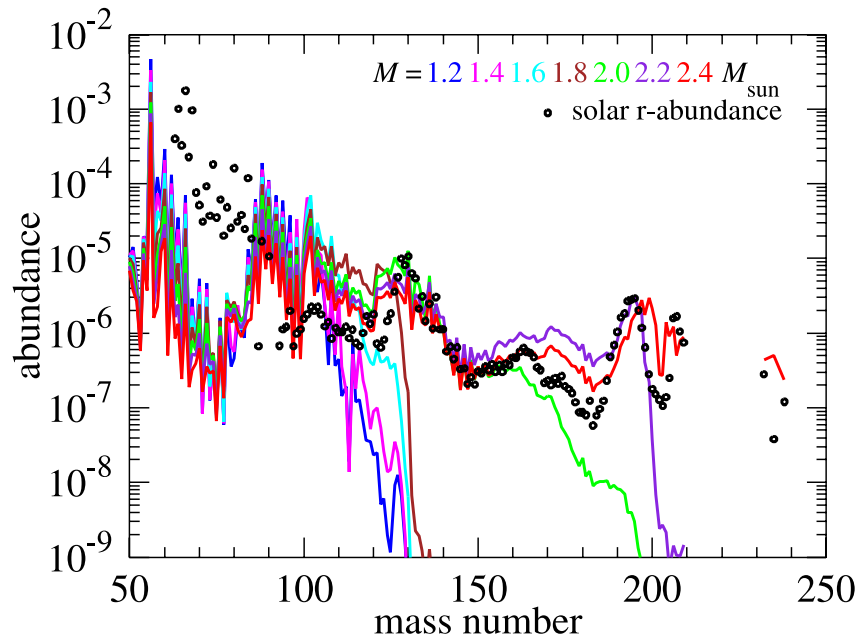


Figure 1.9: Final abundances of r-process nucleosynthesis calculations in the neutrino-driven wind from a PNS during a CCSN. The abundances are shown as a function of the PNS mass. To produce the full r-process up to the third peak ( $A \sim 195$ ),  $M \gtrsim 2 M_{\odot}$  is required, which is unrealistic based on the observed mass distribution of neutron stars. For smaller PNS masses, however, the r-process fairly robustly synthesizes elements up to  $A \sim 130$ . Figure 8 from Wanajo (2013); see that reference for details. © 2013 *The American Astronomical Society*

hot wind off the surface of the PNS, called a neutrino-driven wind (e.g., Qian and Woosley, 1996). Early simulations and models of this wind indicated that it could have the right conditions for the r-process to take place in some cases (e.g., Woosley et al., 1994; Wanajo, 2006).

However, the most recent investigations of r-process nucleosynthesis in neutrino-driven winds have shown that it is unlikely that the full r-process (producing nuclides up to the third peak, c.f. Figure 1.1) operates in those conditions, since the wind does not seem to be neutron-rich enough. It appears that only a weak version of the r-process (producing heavy elements up to  $A \sim 130$ ) can take place in the neutrino-driven wind from CCSNe (e.g., Qian and Woosley, 1996; Thompson et al., 2001; Fischer et al., 2010; Roberts et al., 2010; Martínez-Pinedo et al., 2012; Wanajo, 2013). Figure 1.9 (Figure 8 from Wanajo, 2013) shows a calculation of r-process nucleosynthesis in the neutrino-driven wind from a CCSN.

There is another process, though, the so-called  $\nu p$ -process, that can produce nuclides up to  $A \sim 110$  in a proton-rich neutrino-driven wind. In the hot, proton-rich wind,

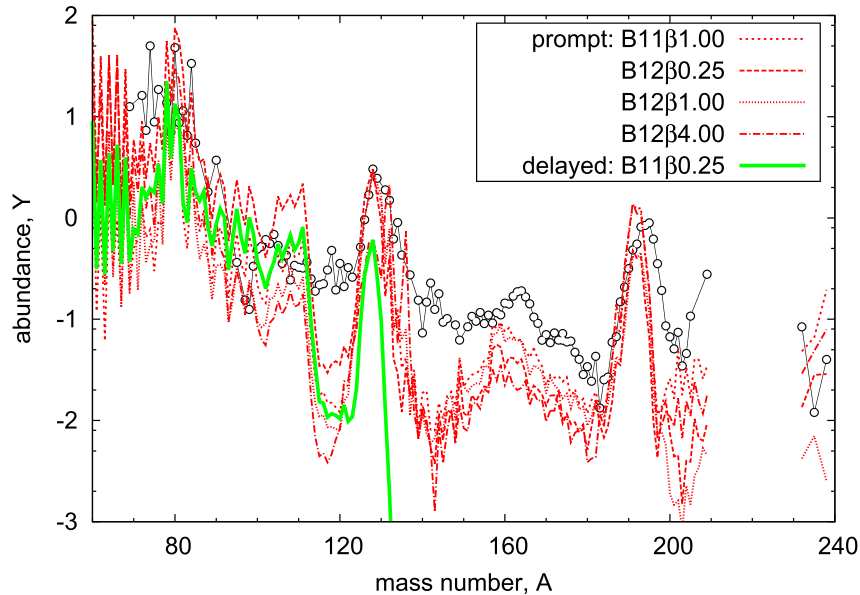


Figure 1.10: r-Process nucleosynthesis results in a special type of CCSN that is driven magnetorotationally. This type of supernova can produce the full r-process up to the third peak, but because of the large magnetic field and amount of rotation that is required, it is expected to be a very rare ( $\lesssim 0.1\%$ ) class of CCSN. Figure 13 from Nishimura et al. (2015); see that reference for details. © 2015 The American Astronomical Society

proton capture produces proton-rich nuclei but stops at  $^{64}\text{Ge}$ , which has a long  $\beta$ -decay half-life ( $\sim 64$  s) compared to the expansion time scale ( $\sim 10$  s) and a small proton capture cross section. The  $\nu p$ -process can get past this  $^{64}\text{Ge}$  barrier by converting a free proton to a neutron via electron antineutrino capture. The reaction  $^{64}\text{Ge} + n \rightarrow ^{64}\text{Ga} + p$  is much faster than proton capture on  $^{64}\text{Ge}$  and allows the nucleosynthesis to proceed past  $A = 64$  with subsequent proton captures (e.g., Fröhlich et al., 2006; Pruet et al., 2006; Wanajo et al., 2011; Arcones et al., 2012).

Finally, a certain rare type of CCSNe may be able to produce the full r-process. If the progenitor star has a strong magnetic field and its core rotates rapidly, then the supernova explosion could be powered by magnetorotational processes (possibly the magnetorotational instability), which could create a bipolar jet (e.g., Wheeler et al., 2000; Akiyama et al., 2003; Burrows et al., 2007; Mösta et al., 2014, 2015). It is possible that r-process nucleosynthesis takes place in this jet (e.g., Winteler et al., 2012; Nishimura et al., 2015) and creates all the heavy elements up to the third peak. Figure 1.10 shows an r-process nucleosynthesis calculation in such a magnetorotationally driven CCSN by Nishimura et al. (2015, their Figure 13). However, because an enormous magnetic field and large amount of rotation is

required in this type of supernova, it is expected that only a small fraction ( $\lesssim 0.1\%$ ) of all CCSNe would result in a magnetorotational supernova (Nishimura et al., 2015).

### 1.4.2 Neutron star mergers

Since an ordinary CCSN most likely cannot produce the full r-process, this leaves neutron star mergers as the only remaining viable site for r-process nucleosynthesis. We know that binary neutron star systems exist in our galaxy and that their orbit is shrinking due to gravitational wave emission (e.g., Hulse and Taylor, 1975; Lattimer and Prakash, 2005), which will eventually cause the two neutron stars to merge (e.g., Price and Rosswog, 2006). Numerous groups have performed hydrodynamical simulations of the merger of two neutron stars or the merger of a neutron star and a black hole. Such mergers can eject neutron-rich matter through a variety of processes. There are two types of dynamical ejecta, which are launched shortly before or during the merger. As the two neutron stars get close to each other, or a single neutron star gets close to its black hole companion, the neutron star(s) get tidally deformed and disrupted, which produces a stream of neutron star material that is flung out into space and unbound from the system (e.g., Price and Rosswog, 2006; Foucart et al., 2014; Sekiguchi et al., 2015; Kyutoku et al., 2015; Radice et al., 2016). This type of ejecta is referred to tidal tails and an example is shown in Figure 1.11. The second type of dynamical ejecta is material squeezed out from the collision interface of the two neutron stars. This type of dynamical ejecta only occurs in neutron star–neutron star (NSNS) mergers (e.g., Bauswein et al., 2013; Hotokezaka et al., 2013b). The dynamical ejecta mass ranges between  $10^{-4}$  to a few  $\times 10^{-2}$  solar masses and the electron fraction distribution ranges from  $Y_e \sim 0.05 - 0.45$  in the binary neutron star case. Black hole–neutron star binaries can eject up to  $\sim 0.1 M_\odot$ , but only if the black hole is of a similar mass as the neutron star and has a fairly high spin, otherwise there is typically no ejecta at all, because the neutron star gets disrupted inside the event horizon of the black hole. The electron fraction of the ejecta from a BHNS merger is typically below 0.2 (Foucart et al., 2014). I discuss r-process nucleosynthesis in the dynamical ejecta of a BHNS merger in detail in Chapter IV.

Neutron star mergers can produce additional outflows after the merger. In most cases, an accretion disk or torus forms around the central compact object, which is either a black hole or a hot hypermassive neutron star (HMNS). The lifetime of the HMNS before it collapses to a black hole ranges from a few milliseconds to

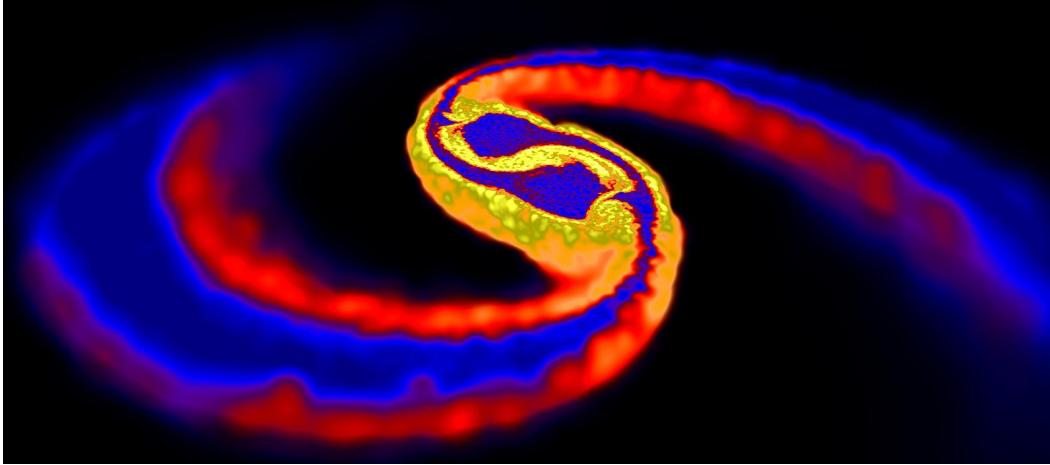


Figure 1.11: Density rendering of a binary neutron star merger simulation. The dark central blobs are the two neutron stars just before merging. The dynamical ejecta of neutron-rich matter in the form of two tidal tails can be seen clearly. This material is unbound and r-process nucleosynthesis takes place in the ejecta. Figure from <http://users.monash.edu.au/~dprice/research/nsmag>, see Price and Rosswog (2006) for details. © 2006 Daniel Price and Stephan Rosswog

much longer than 30 ms (e.g., Sekiguchi et al., 2011; Hotokezaka et al., 2013a). If there is a HMNS, it will emit neutrinos, and the hot accretion disk also cools via neutrino emission. This can drive a neutrino-driven wind from the disk surface, see Figure 1.12 (Figure 1 from Perego et al., 2014). An outflow from the disk can also be triggered by viscous heating and alpha recombination in the disk. Since this outflow happens at later times, the neutrino irradiation has enough time to significantly raise the electron fraction of the outflow, so that most simulations find  $Y_e \sim 0.2 - 0.45$  with a few  $\times 10^{-3} M_\odot$  ejected in these disk outflows (e.g., Surman et al., 2008; Wanajo and Janka, 2012; Fernández and Metzger, 2013; Perego et al., 2014; Just et al., 2015; Foucart et al., 2015). r-Process nucleosynthesis in the disk outflow after a NSNS merger is the subject of Chapter V.

Because the ejecta from neutron star mergers is so neutron-rich, the r-process can easily create all elements up to  $A \sim 250$ , which is beyond the third peak. In fact, during r-process nucleosynthesis even heavier nuclides ( $A > 300$ ) are produced, however, those nuclides are unstable to fission (either spontaneous or neutron-induced). Their fission products quickly capture more neutrons, grow to  $A > 300$ , and then fission themselves. This so-called fission cycle continues until the free neutrons are exhausted. The remarkable result is that the final r-process abundance pattern is very robust to variations in the detailed properties of the ejecta. If fission

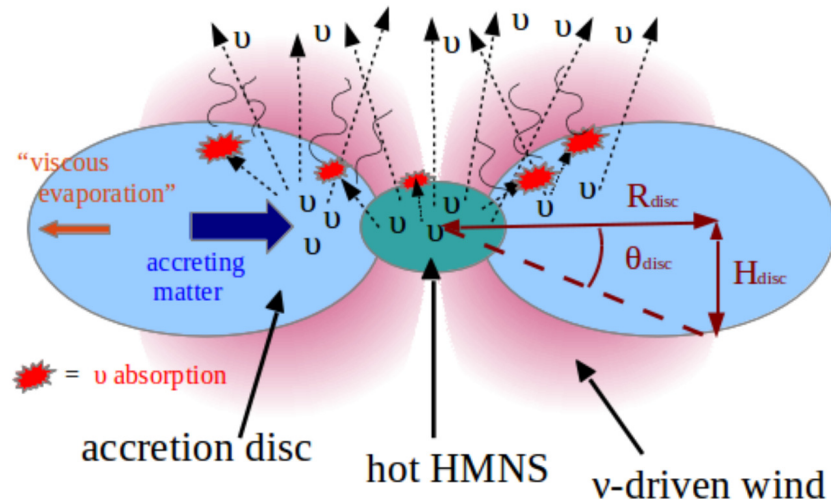


Figure 1.12: Cartoon of an accretion disk around a HMNS and the resulting neutrino-driven wind. Figure 1 from Perego et al. (2014); see that reference for details. © 2014 Albino Perego and coauthors

cycling is reached, the final abundances are independent of the exact number of cycles (e.g., Korobkin et al., 2012; Bauswein et al., 2013; Mendoza-Temis et al., 2015). Figure 1.13 (Figure 4 from Korobkin et al., 2012) shows the outcome of r-process nucleosynthesis in a variety of NSNS and BHNS mergers. All merger scenarios produce essentially identical final abundances, thus demonstrating the robustness of the r-process in neutron star mergers.

## 1.5 Galactic chemical evolution

Several groups have shown robust r-process nucleosynthesis in neutron star mergers that produce final abundance patterns that match the observed solar r-process pattern very well (e.g., Freiburghaus et al., 1999; Goriely et al., 2011; Wanajo et al., 2014; Goriely et al., 2015; Just et al., 2015; Radice et al., 2016). But there are still some challenges that need to be addressed before neutron star mergers can be accepted as the dominant site of the r-process (e.g., Qian, 2000; Argast et al., 2004; Matteucci et al., 2014). Those challenges stem from observations of r-process material in very metal-poor stars that were formed early in the galaxy’s lifetime, and the observed small scatter in the r-process abundances in the galaxy.

The galaxy is assumed to form from pristine gas containing only hydrogen and helium. As stars form, evolve, and die in supernova explosions, the interstellar gas gets enriched in heavier elements, especially iron. Out of this enriched gas, new stars are formed that start out with some heavy elements (heavier than helium).

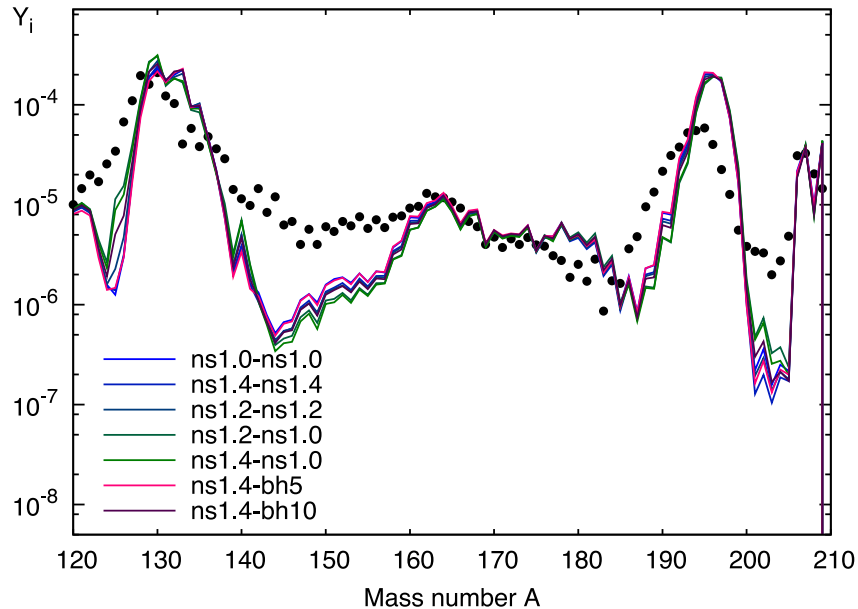


Figure 1.13: r-Process nucleosynthesis calculations in a wide range of NSNS and BHNS mergers. All mergers produce virtually identical final abundances, demonstrating the robustness of the r-process in neutron star mergers. Figure 4 from Korobkin et al. (2012); see that reference for details. © 2012 Oleg Korobkin and coauthors

The metallicity (a metal being anything other than H and He) of stars thus serves as a chronometer (e.g., Matteucci, 2012). An important caveat is, however, that the galaxy did not form from a single dark matter halo. Rather, the galaxy today is the product of merging sub-halos and within each sub-halo, the age–metallicity relationship depends on the mass of the sub-halo. Therefore, there may not be a universal age–metallicity relationship for the Milky Way. See Ishimaru et al. (2015) for details. Usually, the iron-to-hydrogen ratio  $[\text{Fe}/\text{H}]$  is used as a proxy for the metallicity. The notation  $[\text{X}/\text{H}]$  denotes the logarithm (base 10) of the abundance ratio of X to hydrogen, normalized to the solar ratio. I.e., the sun has  $[\text{X}/\text{H}] = 0$  and a star with  $[\text{Fe}/\text{H}] = -2$  has 100 times less iron compared to hydrogen than the sun. Large-scale spectroscopic surveys of stars that measure various abundances can thus provide valuable insights into the chemical evolution of the galaxy (e.g., Edvardsson et al., 1993; Suda et al., 2008).

Since compact object binaries take a long time, on average, to inspiral under gravitational wave emission (0.1 – 1 Gyr, e.g., Dominik et al., 2012), one might not expect to see r-process material in stars that were formed in the first 100 Myr or so. However, the observed metal-poor stars that contain r-process elements (e.g., Sneden

et al., 2009) were formed within the first 100 Myr of star formation in our galaxy. Furthermore, neutron star mergers are rare events that release r-process material and that material has to mix with the interstellar medium in the galaxy before it can be incorporated into new stars. Thus one might expect a significant scatter in the r-process abundances in different parts of the galaxy, depending on whether there was a neutron star merger nearby. The observed scatter in the r-process abundances might be lower than what one would expect from mergers (e.g., Argast et al., 2004).

However, even though the average delay time for compact object mergers is 0.1 – 1 Gyr, population synthesis models (e.g., De Donder and Vanbeveren, 2004; Dominik et al., 2012) predict that there are a few percent of binary neutron star systems that have delay times as short as a few Myr. These tight binaries can be created by unstable mass transfer due to Roche lobe overflow. The exact distribution of delay times and especially the minimum delay time depend strongly on the treatment of the common envelope phase of binary stellar evolution (e.g., Dominik et al., 2012). Using advanced population synthesis models and inhomogeneous mixing into account, several authors have found that neutron star mergers could be the dominant source of the r-process in the Milky Way, possibly with some early magnetorotationally-driven CCSNe, and can also account for the observed scatter of heavy elements (e.g., Ishimaru et al., 2015; Cescutti et al., 2015; Wehmeyer et al., 2015; van de Voort et al., 2015). Figure 1.14 shows a computation by van de Voort et al. (2015, their Figure 1) of galactic r-process enrichment in a cosmological simulation. They find that neutron star mergers alone can account for the observed r-process-to-iron ratios as a function of  $[\text{Fe}/\text{H}]$ .

A less theoretical argument for neutron star mergers to be the dominant site of the r-process comes from recent intriguing work by Wallner et al. (2015). They find that the current abundance of  $^{244}\text{Pu}$  (half-life of 81 Myr) in the interstellar medium, inferred from measuring  $^{244}\text{Pu}$  in the deep-sea crust, is much lower than its abundance in the early solar system. This points to a low-rate/high-yield process, like a neutron star merger, being responsible for the production of  $^{244}\text{Pu}$ . Hotokezaka et al. (2015) use the same data, but go a step farther. Given the total amount of r-process material in the galaxy, there is a degeneracy between a production site with a high rate and low yield (e.g., CCSN), or a site with a low rate and high yield (e.g., neutron star mergers). With a simple galactic mixing model, Hotokezaka et al. (2015) compute the number density of  $^{244}\text{Pu}$  a typical observer would measure given a certain  $^{244}\text{Pu}$  production rate. With this model, a relation between the production

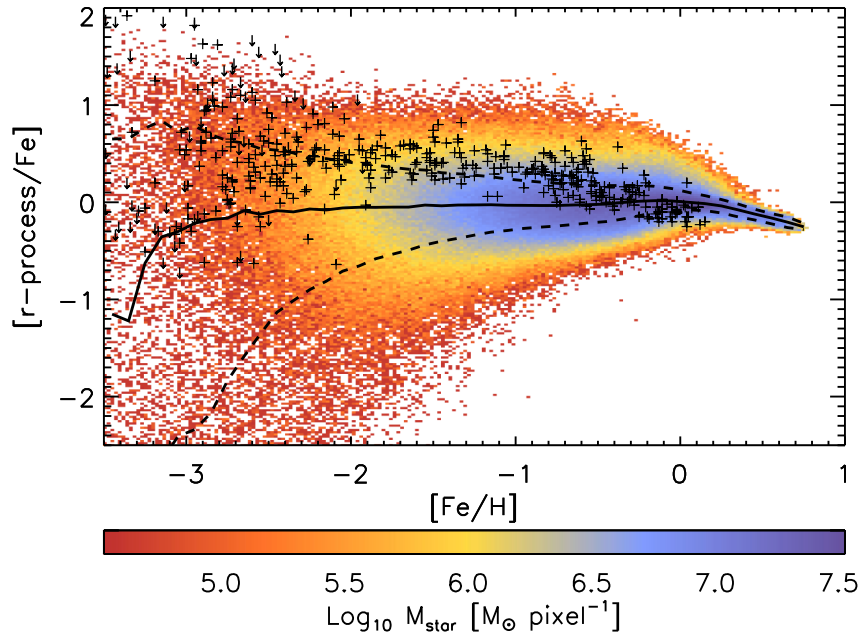


Figure 1.14: Results of a cosmological simulation with r-process enrichment by neutron star mergers. The colored pixels show the stellar mass of the galaxy that has a particular r-process-to-iron ratio and  $[\text{Fe}/\text{H}]$  value. The black line is the median and dashed lines are the 16th and 84th percentile. The black pluses and downward arrows are observed europium-to-iron ratios in galactic stars (europium is used as a proxy for r-process material since europium is almost exclusively produced by the r-process and readily measurable). The galactic chemical evolution simulation can account for the observations quite well. Figure 1 from van de Voort et al. (2015); see that reference for details. © 2014 Freeke van de Voort and coauthors

rate and production amount of  $^{244}\text{Pu}$  can be computed by requiring that the current  $^{244}\text{Pu}$  measurement is equal to what a typical observer would expect to see. This relation is shown in Figure 1.15 (Figure 1 from Hotokezaka et al., 2015) and it breaks the degeneracy of the total amount of r-process material. Hotokezaka et al. (2015) find that the  $^{244}\text{Pu}$  measurement in the deep sea crust agrees very well with the expected rate and yield of neutron star mergers. Tsujimoto et al. (2017) draw similar conclusions by studying the  $^{244}\text{Pu}$  abundance in meteorites.

Finally, a recent discovery by Ji et al. (2016) also points to neutron star mergers as the dominant r-process site. They discovered that the ultrafaint dwarf galaxy Reticulum II is highly enhanced in r-process elements compared to all other known ultrafaint dwarf galaxies. Ultrafaint dwarf galaxies are small galaxies that orbit the Milky Way and formed around the same time when the first stars in the Milky Way formed. Figure 1.16 (Figure 2 from Ji et al., 2016) shows that most of the stars in Reticulum II have an r-process enrichment that is two to three order of magnitude higher than

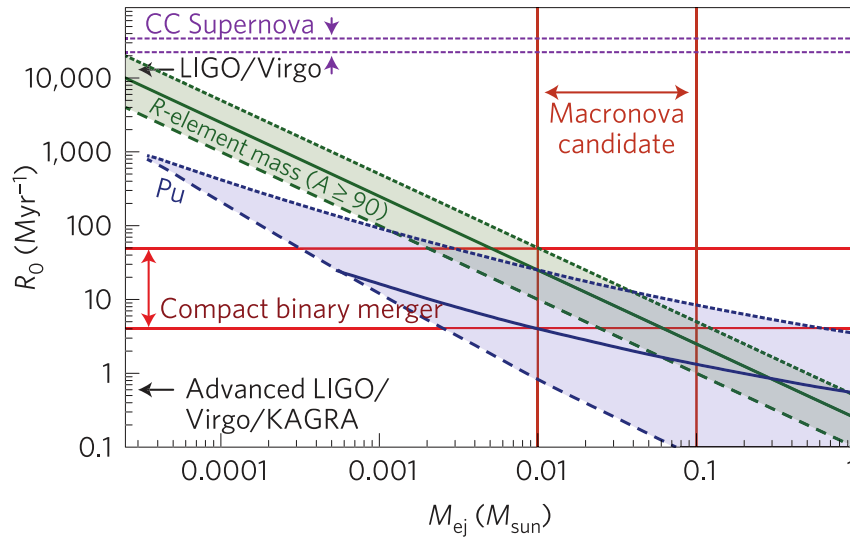


Figure 1.15: The green region is the allowed relationship between the r-process event rate  $R_0$  and yield  $M_{ej}$  per event to produce the total amount of r-process material in the galaxy. The blue region is the constraint obtained from a galactic mixing model and a measurement of  $^{244}\text{Pu}$  in the deep sea crust. The two constraints intersect at an event rate that is much lower than the CCSN rate but compatible with the expected neutron star merger rate. Furthermore, the predicted ejecta mass is also compatible with what we expect from neutron star mergers and what has been inferred from possible kilonova/macronova observations (see Section 1.6). Figure 1 from Hotokezaka et al. (2015); see that reference for details. © 2015 Macmillan Publishers Limited

the stars in other ultrafaint dwarf galaxies. And the measured abundances in these stars match the universal r-process abundance pattern. This implies that Reticulum II was enriched in r-process elements by a single, rare event, such as a neutron star merger, that has not happened in other ultrafaint dwarf galaxies. Furthermore, Ji et al. (2016) compute the total europium yield in Reticulum II and find that it is three orders of magnitude higher than what would be expected from a CCSN but the yield is compatible with a neutron star merger.

## 1.6 Kilonovae

After r-process nucleosynthesis has taken place, the resulting heavy nuclides are very neutron-rich and far away from stability. Over the following hours and days, those radioactively unstable nuclides decay back to stability, which releases energy into the expanding material and powers a transient in the optical or infrared band (e.g., Li and Paczyński, 1998; Kulkarni, 2005; Metzger et al., 2010; Roberts et al., 2011; Metzger, 2017; Wollaeger et al., 2017). Such a transient is called a kilonova

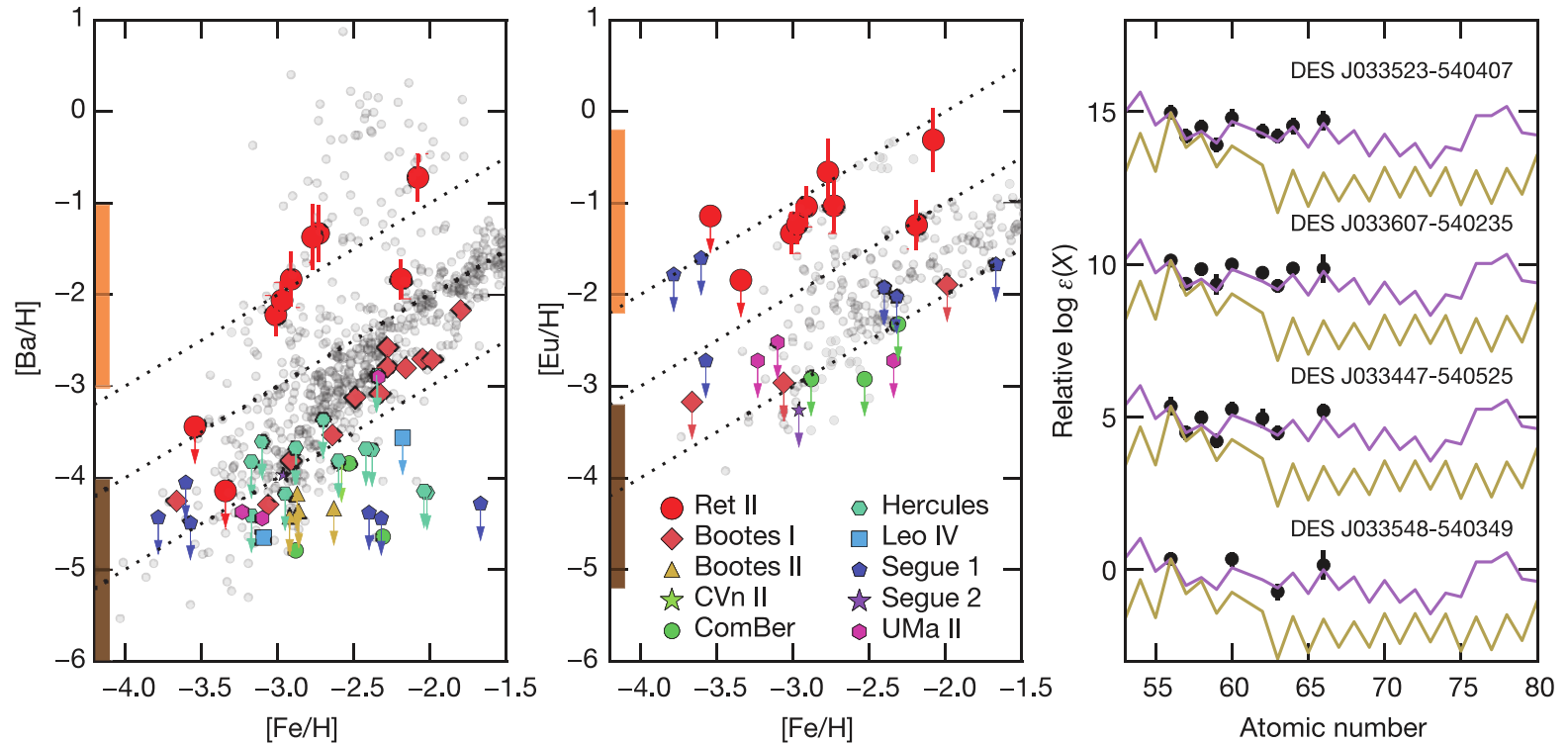


Figure 1.16: Barium (left) and europium (center) observations of stars in ultrafaint dwarf galaxies. Both of these elements are predominantly produced in the r-process and Reticulum II (Ret II) is highly enhanced in both of them compared to the other ultrafaint dwarf galaxies. Furthermore, the abundance pattern observed in some of the Reticulum II stars (right) matches the universal r-process pattern (purple line) but not the s-process pattern (yellow line). This suggests that Reticulum II has been enhanced in r-process elements by a single, rare event, such as neutron star merger. If frequent events like CCSNe were the main r-process site, then the amount of r-process material should be the same in all ultrafaint dwarf galaxies. Figure 2 from Ji et al. (2016); see that reference for details. © 2016 Macmillan Publishers Limited

or macronova. If r-process nucleosynthesis does indeed happen in the ejecta of neutron star mergers, then a kilonova would be an electromagnetic counterpart to the gravitational wave signal of the merger. The Laser Interferometer Gravitational Wave Observatory (LIGO) has recently detected gravitational waves from a binary black hole merger for the first time (Abbott et al., 2016a) and so it should not be long until we detect gravitational waves from neutron star mergers as well (e.g., LIGO Scientific Collaboration et al., 2015; Abbott et al., 2016b). If a kilonova can be found and tied to a gravitational wave event from a neutron star merger, then this would be concrete evidence that r-process nucleosynthesis happens in the ejecta of neutron star mergers. Furthermore, neutron star mergers are also thought to be the progenitors of short gamma ray bursts (sGRBs), in which case we would expect to see triple coincidence of a gravitational wave signal, an sGRB (provided it is beamed toward us), and a kilonova (e.g., Lee and Ramirez-Ruiz, 2007; Nakar, 2007; Gehrels et al., 2009; Fernández and Metzger, 2016).

The exact observational signature of kilonovae is subject to active investigation. Kasen et al. (2013) and Tanaka and Hotokezaka (2013) have pointed out that the presence of lanthanides ( $58 \leq Z \leq 71$ ) and actinides ( $90 \leq Z \leq 103$ ) significantly increases (by two orders of magnitude) the opacity of the material due to the open f-shells of those elements, which results in a huge number of absorption lines. This enhanced opacity increases the time it takes for photons to diffuse out and hence the transient will be dim (few  $\times 10^{40}$  erg s<sup>-1</sup>) and peak in the red/infrared band on the timescale of a week (e.g., Barnes and Kasen, 2013; Grossman et al., 2014; Lippuner and Roberts, 2015). However, lanthanides and actinides are only produced if  $Y_e \lesssim 0.25$  (Lippuner and Roberts, 2015) and so we expect them to be present in the dynamical ejecta. In the disk outflow, the electron fraction may be too high for the full r-process to happen in the bulk of the outflow, and hence that part of the ejecta might make a brighter, blue transient on the timescale of a few days (e.g., Kasen et al., 2015; Martin et al., 2015). Additionally, it is possible that a small fraction of the dynamical ejecta expands rapidly enough that the neutrons do not have enough time to capture on seed nuclei, thus producing a very short (hours) bright, ultraviolet precursor (Metzger et al., 2015). Example light curves of kilonovae with and without lanthanides and with and without a neutron precursor are shown in Figure 1.17, which is Figure 6 from Metzger (2017). Finally, a fraction of the  $\gamma$ -rays produced in the  $\beta$ -decays of the radioactive isotopes can escape without thermalizing (e.g., Barnes et al., 2016). However, detecting this  $\gamma$ -ray emission with current instruments seems unlikely, unless the kilonova is sufficiently close (a

few Mpc, but the event rate in this volume is small,  $\sim 10^{-3} \text{ yr}^{-1}$ , Hotokezaka et al., 2016).

There are reports of possible kilonova detections for three sGRBs: GRB130603B (Berger et al., 2013; Tanvir et al., 2013), GRB060614 (Jin et al., 2015; Yang et al., 2015), and GRB050709 (Jin et al., 2016). However, the observational data for these events seems too sparse to allow any strong conclusion about the exact nature of the observed transient. Nevertheless, kilonovae are actively being searched for and there exists a pipeline for searches in response to a gravitational wave trigger involving telescopes all around the world (e.g., Law et al., 2009; Singer et al., 2014; Bellm, 2014; Kasliwal et al., 2016). To aid with the detection, classification, and information extraction of and from kilonovae, it is important to have accurate models for the light curves and an understanding of the important mechanisms that affect them. This requires more work in simulating neutron star mergers and their outflows, simulating the subsequent nucleosynthesis, and finally modeling and/or simulating the light curve given the nucleosynthesis results and outflow morphology.

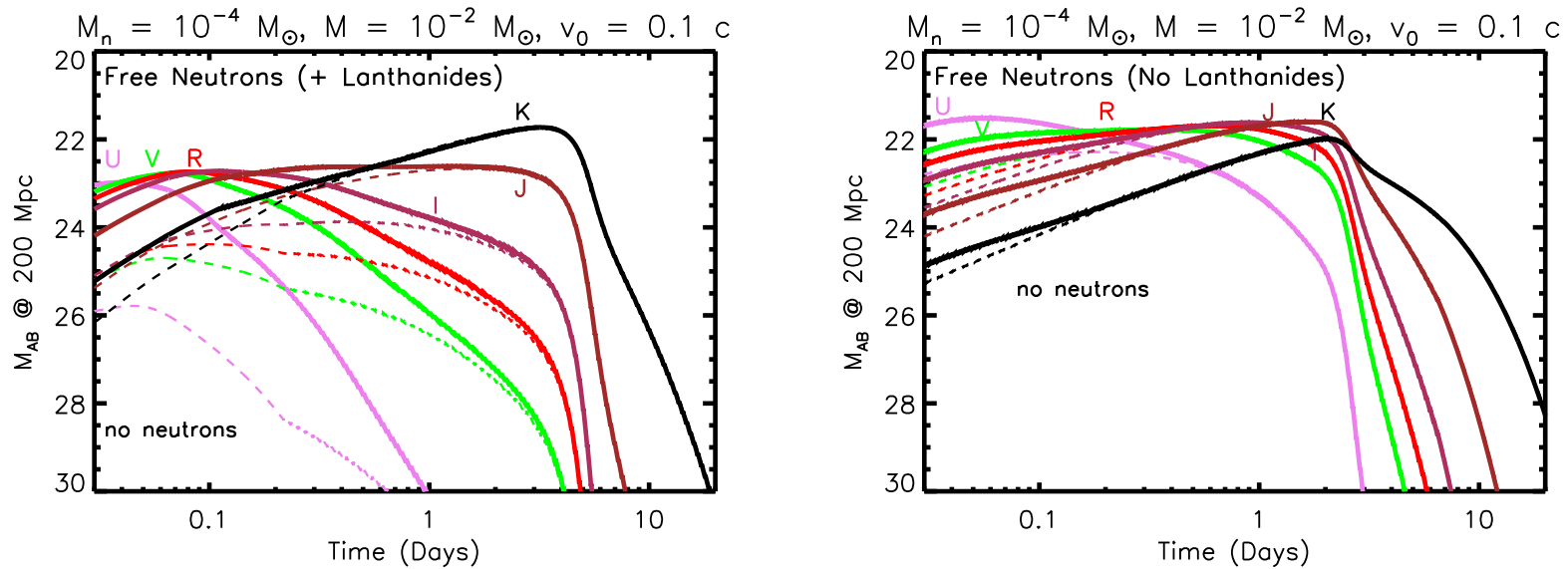


Figure 1.17: Computed kilonova light curves in bands spanning from ultraviolet (U) to infrared (K). Lanthanides are present in the left panel, and so the kilonova peaks in the infrared at a few days. In the right panel, there are no lanthanides and hence the light curves peaks in the optical bands at around one day. The solid lines include a neutron precursor, whereas the dashed lines do not. The neutron precursor is especially visible in the ultraviolet band in the left panel, where the UV emission at a few hours is enhanced by about 1.5 magnitudes. Figure 6 from Metzger (2017). © 2017 Brian D. Metzger

## Chapter II

### SKYNET

*This chapter was submitted to the Astrophysical Journal Supplement Series and a preprint version was published on the arXiv (1706.06198 [astro-ph.HE]). I am the primary author, wrote the vast majority of the text, performed all calculations and code comparisons, and I created all the figures. I also wrote almost all of the SkyNet code.*

© 2017 Jonas Lippuner and Luke F. Roberts

## **SkyNet: A modular nuclear reaction network library**

**Jonas Lippuner<sup>1</sup> and Luke F. Roberts<sup>2,3</sup>**

<sup>1</sup> TAPIR, Walter Burke Institute for Theoretical Physics, California Institute of Technology, MC 350-17, 1200 E California Blvd, Pasadena CA 91125, USA

<sup>2</sup> National Superconducting Cyclotron Laboratory, Michigan State University, East Lansing, MI 48824, USA

<sup>3</sup> Department of Physics and Astronomy, Michigan State University, East Lansing, MI 48824, USA

### **Abstract**

Almost all of the elements heavier than hydrogen that are present in our solar system were produced by nuclear burning processes either in the early universe or at some point in the life cycle of stars. In all of these environments, there are dozens to thousands of nuclear species that interact with each other to produce successively heavier elements. In this paper, we present *SkyNet*, a new general-purpose nuclear reaction network that evolves the abundances of nuclear species under the influence of nuclear reactions. *SkyNet* can be used to compute the nucleosynthesis evolution in all astrophysical scenarios where nucleosynthesis occurs. *SkyNet* is free and open-source and aims to be easy to use and flexible. Any list of isotopes can be evolved and *SkyNet* supports various different types of nuclear reactions. *SkyNet* is modular so that new or existing physics, like nuclear reactions or equations of state, can easily be added or modified. Here, we present in detail the physics implemented in *SkyNet* with a focus on a self-consistent transition to and from nuclear statistical equilibrium (NSE) to non-equilibrium nuclear burning, our implementation of electron screening, and coupling of the network to an equation of state. We also present comprehensive code tests and comparisons with existing nuclear reaction networks. We find that *SkyNet* agrees with published results and other codes to an accuracy of a few percent. Discrepancies, where they exist, can be traced to differences in the physics implementations.

*Subject headings:* methods: numerical – nuclear reactions, nucleosynthesis, abundances

## 2.1 Introduction

Nuclear and weak reactions play a crucial role in many astrophysical scenarios. Nuclear reactions typically occur at high temperatures and densities, because a large amount of energy is required to overcome the Coulomb repulsion between positively charged nuclei. Inside the cores of main sequence stars, nuclear fusion converts hydrogen into helium, which releases nuclear binding as heat, keeping the star from collapsing (Bethe, 1939). When massive stars undergo core collapse at the end of their lives, nuclear and weak reactions serve as important energy sinks and sources (neutrino cooling and heating). In core-collapse and type Ia supernovae, explosive nuclear burning mainly creates iron-group elements that are ejected into the interstellar medium (Nomoto et al., 1997; Woosley et al., 2002). According to our current understanding, a weak version of the rapid neutron capture process (r-process) can also occur (Wanajo, 2013) in core-collapse supernovae. However, it appears that the full r-process that can synthesize all the heavy elements predominantly happens during neutron star mergers (Freiburghaus et al., 1999). Heavy elements up to bismuth can also be created in stars via the slow neutron capture process (s-process, Burbidge et al., 1957). Finally, when hydrogen and helium gas accretes onto a white dwarf, the accumulated material can undergo a thermonuclear explosion that creates a short-lived bright flash of light called a nova. If the accretor is a neutron star instead, the thermonuclear explosion results in an X-ray burst (Boyd, 2008) or a superburst (Strohmayer and Brown, 2002).

To adequately understand these astrophysical objects and phenomena, one needs to account for the nuclear reactions that drive them. In some cases, reaction networks are mainly used to track the nuclear energy generation (e.g., Weaver et al., 1978; Müller, 1986; Timmes et al., 2000). But in most cases, the evolution of the entire composition due to nuclear reactions is of interest. Because of the many ways that nuclei can react with each other to form other nuclides, the number of nuclear species that are relevant for many astrophysical processes ranges from dozens to thousands, and the number of nuclear reactions involved is hundreds to tens of thousand. For this reason, a large number of variables (i.e., nuclide abundances) need to be evolved that are coupled together by the non-linear nuclear reaction rates (see Section 2.2). Mathematically and computationally, the ensemble of coupled nuclear reactions is described by a *nuclear reaction network*.

Large-scale (several dozen species or more) nuclear reaction networks were first developed in the late 60's and early 70's (e.g., Truran et al., 1966, 1967; Arnett and Truran, 1969; Woosley et al., 1973). These first networks were mainly for explosive nuclear burning in massive stellar evolution and supernovae, although earlier stellar evolution models also took nuclear reactions into account and evolved a handful of nuclear species (e.g., Hayashi et al., 1962; Hofmeister et al., 1964). Early networks ranged in size from a few dozen to around a hundred species with up to a few hundred reactions connecting the nuclei. Since then, nuclear reaction networks of different sizes have been used to study various astrophysical scenarios. Big Bang nucleosynthesis calculations require the smallest networks with typically fewer than a dozen nuclear species, although some authors utilize much bigger networks up to several dozen species (e.g., Wagoner, 1973; Orlov et al., 2000; Nollett and Burles, 2000; Coc et al., 2012; Cyburt et al., 2016). Networks with dozens to hundreds of species are employed in stellar evolution codes (e.g., Arnett, 1977; Weaver et al., 1978; Paxton et al., 2011; Bressan et al., 2012; Jones et al., 2015). Similar sized or larger (up to hundreds of species) networks are also used to compute explosive nucleosynthesis in type Ia supernovae (e.g., Thielemann et al., 1986; Iwamoto et al., 1999; Hillebrandt et al., 2013; Seitzzahl et al., 2013; Leung et al., 2015), core-collapse supernovae (e.g., Thielemann et al., 1986; Limongi and Chieffi, 2003; Heger and Woosley, 2010; Harris et al., 2014), novae (e.g., Weiss and Truran, 1990; José and Hernanz, 1998; Iliadis et al., 2002; Starrfield et al., 2016), and X-ray bursts (e.g., Schatz et al., 2001; Woosley et al., 2004; Cyburt et al., 2010; Parikh et al., 2013).

The largest nuclear networks are needed to simulate neutron capture processes. For the s-process in massive stars, it may be sufficient to use a few hundred to about a thousand nuclei (e.g., Prantzos et al., 1990; Käppeler et al., 2011; Nishimura et al., 2017). Larger nuclear reaction networks (typically thousands of isotopes) have been used for r-process nucleosynthesis calculations in neutrino driven winds from core-collapse supernovae (e.g., Woosley and Hoffman, 1992; Arcones et al., 2010; Wanajo, 2013), in the jets of magnetorotational core-collapse supernovae (e.g., Winteler et al., 2012; Nishimura et al., 2015), in the dynamical ejecta of neutron star mergers (e.g., Goriely et al., 2011; Bauswein et al., 2013; Wanajo et al., 2014; Just et al., 2015; Fernández et al., 2017), in accretion disk ejecta following neutron star mergers (e.g., Surman et al., 2008; Perego et al., 2014; Martin et al., 2015; Lippuner et al., 2017), and in broader astrophysical contexts (e.g., Blinnikov and Panov, 1996; Panov et al., 1995, 2001; Mumpower et al., 2012).

To evolve a nuclear reaction network, the rates of all reactions in the network are required. Most reaction rates, e.g. interactions between two or more nuclides, depend strongly on the energies of the incoming particles, due to Coulomb barrier penetration, resonances in the compound nuclear system, and other effects (e.g., Clayton, 1968, §4). The rates of reactions only involving a single particle in the entrance channel, like  $\beta$ -decays and spontaneous fission, are constant.<sup>1</sup> Some reaction rates involving nuclides sufficiently close to the valley of stability can be measured experimentally as a function of energy. Although in many cases, astrophysical reactions occur at energies that are much lower than the experimentally accessible energy ranges (e.g., Rolfs and Rodney, 1988, §4). Furthermore, most astrophysical processes involve unstable nuclei that may be very far away from stability and are not experimentally accessible for rate measurements. Therefore, theoretical models are necessary to compute reaction rates needed by the reaction network (e.g., Cyburt et al., 2010). The Hauser-Feshbach approach, which assumes that the reactants form a single compound nucleus that subsequently decays into the reaction products, has been used extensively to compute nuclear reaction rates for astrophysics applications (e.g., Hauser and Feshbach, 1952; Rauscher and Thielemann, 2000; Goriely et al., 2008).

Nuclear reaction networks also require properties such as masses and internal nuclear partition functions (e.g., Arcones and Martínez-Pinedo, 2011; Brett et al., 2012; Mendoza-Temis et al., 2015; Mumpower et al., 2016) of all nuclides evolved in the network. These properties are needed to compute nuclear statistical equilibrium (NSE) and inverse reaction rates (see Section 2.2.3), as well as  $\beta$ -decay rates. Some of these nuclear properties, such as the masses, also enter the theoretical reaction rate calculations. Since many of the nuclides of interest are extremely unstable, special radioactive ion beam facilities are needed to produce and measure these exotic nuclei (see, e.g., Lunney et al., 2003; Schatz, 2013; Mumpower et al., 2016, and references therein). Current radioactive beam facilities have made great progress in measuring unstable nuclei and new facilities or upgrades to current facilities are being built and planned. These new facilities will extend the reach to more exotic nuclei that are highly relevant to nuclear astrophysics scenarios (e.g., Schatz, 2013, 2016; Mumpower et al., 2016). For the foreseeable future, however, it is necessary to use theoretical models to compute nuclear masses and  $\beta$ -decay properties for

---

<sup>1</sup>Strictly speaking,  $\beta$ -decay rates are only constant in vacuum. In the medium, electron phase space blocking introduces a dependency on the electron chemical potential and temperature (e.g., Arnett, 1996, §11.3).

a large fraction of the nuclear species present in r-process networks (e.g., Lunney et al., 2003; Möller et al., 2003; Mumpower et al., 2016, and references therein).

Many authors who use nuclear reaction networks do not make the code of these networks publicly available. This makes it hard to reproduce and verify published results, and also presents a barrier to new researchers joining the field since they first have to write their own nuclear reaction network. Notable exceptions of nuclear reaction networks that are publicly available are: various networks by Timmes (1999)<sup>2</sup>, *XNet* by Hix and Thielemann (1999)<sup>3</sup>, and *NucNet* by Meyer and Adams (2007)<sup>4</sup>. In this paper, we present a new nuclear reaction network called *SkyNet* that is publicly available as open-source software at <https://bitbucket.org/jlippuner/skynet>.

*SkyNet* was initially designed for evolving large reaction networks for r-process nucleosynthesis calculations, but thanks to its modularity and flexibility, *SkyNet* can easily be used for nucleosynthesis computations in many other astrophysical situations. Besides correctness, the main design goals behind *SkyNet* are usability and flexibility, making *SkyNet* an easy to use and versatile nuclear reaction network that is available for anyone to use. *SkyNet* can evolve an arbitrary set of nuclear species under various different types of nuclear reactions (Section 2.5.2). *SkyNet* can also compute NSE compositions (Section 2.2.3) and switch between evolving NSE and the full network in an automated and self-consistent way (Section 2.3.4). *SkyNet* contains electron screening corrections (Section 2.4) and an equation of state (EOS) that takes the entire composition into account (Section 2.A.2). For ease of use, *SkyNet* can be used from within Python (Section 2.5), and *SkyNet* can make movies of the nucleosynthesis evolution (see examples at <http://stellarcollapse.org/lippunerroberts2015>).

*SkyNet* has been used for r-process nucleosynthesis calculations in different scenarios by various authors: Lippuner and Roberts (2015), Radice et al. (2016), Roberts et al. (2017), Lippuner et al. (2017), Siegel and Metzger (2017), Vlasov et al. (2017), and Fernández et al. (2017). Here we discuss the physics used in *SkyNet*, provide details how it is implemented, and perform code tests and comparisons with other nuclear reaction networks.

This paper is organized as follows. In Section 2.2, we derive the equations that

<sup>2</sup>[http://cococubed.asu.edu/code\\_pages/burn.shtml](http://cococubed.asu.edu/code_pages/burn.shtml)

<sup>3</sup><http://eagle.phys.utk.edu/xnet/trac>

<sup>4</sup><https://sourceforge.net/projects/nucnet-tools>

govern nuclear abundance evolution and equilibrium. Section 2.3 deals with the numerical implementation of the reaction network. We discuss in detail the electron screening corrections implemented in *SkyNet* in Section 2.4. In Section 2.5, we describe code implementation details. The code tests and comparisons are the subject of Section 2.6. We summarize in Section 2.7. In Appendix 2.A, we briefly present the physics of an ideal Boltzmann gas and the EOS implemented in *SkyNet*. We show how *SkyNet* computes NSE in Appendix 2.B, and in Appendix 2.C we discuss neutrino interaction reactions.

Throughout this paper, we set the Boltzmann constant  $k_B = 1$  (i.e., all temperatures are measured in energy), the speed of light  $c = 1$ , and the reduced Planck constant  $\hbar = 1$ .

## 2.2 Nuclear reaction network basics

Astrophysical nuclear reaction networks track the composition of a system containing many species of nuclei, electrons, positrons, photons, and sometimes neutrinos. Essentially, they evolve the numbers of different nuclei in a system given a set of reactions and rates for those reactions that transmute nuclei into other nuclei. Although it is straightforward to heuristically write down a system of rate equations (Hix and Meyer, 2006), it is useful to start from kinetic theory to tie the rate equations to the microscopic processes driving the nuclear transmutations.

### 2.2.1 Kinetic theory

Consider a homogenous system of different species particles (including nuclei, electrons, etc.) connected by a set of interactions, a subset of which change particles of one type into another. A reaction indexed by  $n$  converts a set of reactants to a set of products and vice versa. We write reaction  $n$  as

$$\sum_{\alpha \in \tilde{\mathcal{R}}_n} [\alpha] \rightleftharpoons \sum_{\beta \in \tilde{\mathcal{P}}_n} [\beta], \quad (2.1)$$

where  $[\alpha]$  is a reactant,  $[\beta]$  is a product, and  $\tilde{\mathcal{R}}_n$  and  $\tilde{\mathcal{P}}_n$  are the sets of all reactants and products, respectively. We emphasize that all particles are individually labeled, even if they are of the same species. For example, for the reaction  $^{12}\text{C} + ^4\text{He} \rightleftharpoons ^{16}\text{O} + \gamma$  we have  $\tilde{\mathcal{R}}_n = \{0, 1\}$  and  $\tilde{\mathcal{P}}_n = \{2, 3\}$  with  $[0] = ^{12}\text{C}$ ,  $[1] = ^4\text{He}$ ,  $[2] = ^{16}\text{O}$ , and  $[3] = \gamma$ . And for  $^{12}\text{C} + ^{12}\text{C} \rightleftharpoons ^{20}\text{Ne} + ^4\text{He} + \gamma$  we have  $\tilde{\mathcal{R}}_n = \{0, 1\}$  and  $\tilde{\mathcal{P}}_n = \{2, 3, 4\}$  with  $[0] = [1] = ^{12}\text{C}$ ,  $[2] = ^{20}\text{Ne}$ ,  $[3] = ^4\text{He}$ , and  $[4] = \gamma$ . Note that reaction  $n$  includes both the forward process (going from reactants to products) and the inverse process (going from products to reactants). Of course, it is arbitrary which set we

call reactants and which we call products. In the following, we use the convention that if we consider particle  $[\epsilon]$ , then we choose the reactants and products such that  $\epsilon \in \tilde{\mathcal{R}}_n$ .

If the particles are uncorrelated, the system can be described in terms of the individual particle distribution functions  $f_\epsilon$ . Kinetic theory then gives the time evolution of the distribution functions as (e.g., Danielewicz and Bertsch, 1991; Buss et al., 2012)

$$\begin{aligned}
& \left( \partial_t + \frac{\partial k_\epsilon^0}{\partial \mathbf{k}_\epsilon} \cdot \nabla \right) f_\epsilon(x^\mu, k_\epsilon^\mu) \\
&= - f_\epsilon \sum_n \mathcal{N}_n^{\text{forward}} \left[ \prod_{\alpha \in \tilde{\mathcal{R}}_n, \alpha \neq \epsilon} \int_{[\alpha]} f_\alpha \right] \left[ \prod_{\beta \in \tilde{\mathcal{P}}_n} \int_{[\beta]} (1 \pm f_\beta) \right] \\
& \quad \times \delta^4 \left( \sum_{\alpha \in \tilde{\mathcal{R}}_n} k_\alpha^\mu - \sum_{\beta \in \tilde{\mathcal{P}}_n} k_\beta^\mu \right) \mathcal{z}_n \left( k_{\{\alpha\}}^\mu, k_{\{\beta\}}^\mu \right) \\
&+ (1 \pm f_\epsilon) \sum_n \mathcal{N}_n^{\text{inverse}} \left[ \prod_{\alpha \in \tilde{\mathcal{R}}_n, \alpha \neq \epsilon} \int_{[\alpha]} (1 \pm f_\alpha) \right] \left[ \prod_{\beta \in \tilde{\mathcal{P}}_n} \int_{[\beta]} f_\beta \right] \\
& \quad \times \delta^4 \left( \sum_{\alpha \in \tilde{\mathcal{R}}_n} k_\alpha^\mu - \sum_{\beta \in \tilde{\mathcal{P}}_n} k_\beta^\mu \right) \mathcal{z}_n \left( k_{\{\alpha\}}^\mu, k_{\{\beta\}}^\mu \right), \tag{2.2}
\end{aligned}$$

where the sum over  $n$  only includes interactions that have  $\epsilon \in \tilde{\mathcal{R}}_n$ .  $\mathcal{N}_n^{\text{forward}}$  and  $\mathcal{N}_n^{\text{inverse}}$  are factors that avoid double counting if the interaction involves multiple particles of the same species. These will be defined later after introducing some additional notation.  $k_\epsilon^\mu = (k_\epsilon^0, \mathbf{k}_\epsilon)$  is the four-momentum of particle  $[\epsilon]$  and  $\delta^4$  is the 4-dimensional delta function that enforces conservation of momentum.  $\mathcal{z}_n$  denotes the differential rate of reaction  $n$ . The upper (+) signs are for Bosons and the lower (-) signs are for Fermions. We use the shorthand

$$\int_{[\epsilon]} = g_\epsilon \int \frac{d^3 k_\epsilon}{(2\pi)^3} \tag{2.3}$$

for the phase space integral of particle  $[\epsilon]$ , where  $g_\epsilon$  is the spin degeneracy factor. Note that the differential rate  $\mathcal{z}_n$  depends on the momenta of all particles (reactants and products). The second line in Equation (2.2) is due to the forward process of interaction  $n$  and the second line is due to the inverse process. The second line is required by the assumption of reversibility of interactions. Note that the differential rate is the same for the forward and inverse process, and the delta function is also identical since it is an even function.

For simple interactions, e.g., weak interactions between nucleons and neutrinos,  $\mathcal{z}$  is given by

$$\mathcal{z}\left(k_{\{\alpha\}}^{\mu}, k_{\{\beta\}}^{\mu}\right) = (2\pi)^4 \frac{\langle |\mathcal{T}^2| \rangle}{2 \prod_{\alpha \in \tilde{\mathcal{R}}} 2k_{\alpha}^0 \prod_{\beta \in \tilde{\mathcal{P}}} 2k_{\beta}^0}, \quad (2.4)$$

where  $\langle |\mathcal{T}^2| \rangle$  is the spin-averaged reduced matrix element (averaged over the spins of both the initial and final states) of the interaction (see Brown and Sawyer (1997) for a discussion in the non-relativistic context). For more complicated interactions between nuclei,  $\mathcal{z}_n$  could include transition probabilities between multiple internal states.

Generally, a reaction network only evolves some subset of the particles present in the system. For instance, photons are assumed to be in equilibrium at all times and the electron and positron densities are determined by charge neutrality, so their number evolution does not need to be tracked explicitly. Therefore, it is useful to define the part of a reaction that only includes particles that will be tracked by the network as

$$\sum_{j \in \mathcal{R}_n} N_j^n [j] \rightleftharpoons \sum_{l \in \mathcal{P}_n} N_l^n [l], \quad (2.5)$$

where  $[j]$  is a reactant species,  $[l]$  is a product species,  $\mathcal{R}_n$  and  $\mathcal{P}_n$  (without tildes) are the sets of distinct reactant species and product species including only species that are present in the network, respectively. The positive integers  $N_j^n$  and  $N_l^n$  are the numbers of particles of reactant species  $[j]$  destroyed and number of particles of product species  $[l]$  created, respectively. Note that we use Latin indices to refer to particle species and we use Greek indices to refer to individual particles. In the earlier example of  $^{12}\text{C} + ^4\text{He} \rightleftharpoons ^{16}\text{O} + \gamma$  we now have  $\mathcal{R}_n = \{0, 1\}$  and  $\mathcal{P}_n = \{2\}$  with  $[0] = ^{12}\text{C}$ ,  $[1] = ^4\text{He}$ ,  $[2] = ^{16}\text{O}$ , and  $N_0^n = N_1^n = N_2^n = 1$ . The photon that is contained in  $\tilde{\mathcal{P}}_n$  is not in  $\mathcal{P}_n$ , because it is not explicitly tracked in the network. Similarly, for  $^{12}\text{C} + ^{12}\text{C} \rightleftharpoons ^{20}\text{Ne} + ^4\text{He} + \gamma$  we get  $\mathcal{R}_n = \{0\}$  and  $\mathcal{P}_n = \{1, 2\}$  with  $[0] = ^{12}\text{C}$ ,  $[1] = ^{20}\text{Ne}$ , and  $[2] = ^4\text{He}$ . But in this case we have  $N_0^n = 2$  and  $N_1^n = N_2^n = 1$ .

Since Equation (2.2) essentially counts the pairs (or triplets, etc.) of reactants that can interact with each other (or pairs of products for the inverse process), we need to be careful to avoid double counting if the interaction involves multiple particles of the same species. If two distinct particles  $[0]$  and  $[1]$  interact with each other, then there are  $N_0 N_1$  distinct pairs, where  $N_0$  and  $N_1$  are the numbers of particles  $[0]$  and

[1], respectively. But if we have  $N$  particles of the same species where two react with each other, then the total number of distinct pairs is  $N^2/2$  and not  $N^2$ . If it is three identical particles that react with each other, the number of distinct triplets is  $N^3/6$ , since there are  $6 = 3!$  ways to order a set of three items. Thus we need to divide by the product of factorials of the multiplicities of the interacting particle species. With the notation introduced in Equation (2.5), we can write this as

$$\mathcal{N}_n^{\text{forward}} = \prod_{j \in \mathcal{R}_n} \frac{1}{N_j^{n_j}} \quad \text{and} \quad \mathcal{N}_n^{\text{inverse}} = \prod_{l \in \mathcal{P}_n} \frac{1}{N_l^{n_l}}. \quad (2.6)$$

We can now define the reaction rate of the forward process as

$$\begin{aligned} \lambda_n &= n_B^{-1} \mathcal{N}_n^{\text{forward}} \left[ \prod_{j \in \mathcal{R}_n} \left( \frac{n_B}{n_j} \right)^{N_j^{n_j}} \right] \left[ \prod_{\alpha \in \tilde{\mathcal{R}}_n} \int_{[\alpha]} f_\alpha \right] \left[ \prod_{\beta \in \tilde{\mathcal{P}}_n} \int_{[\beta]} (1 \pm f_\beta) \right] \\ &\times \delta^4 \left( \sum_{\alpha \in \tilde{\mathcal{R}}_n} k_\alpha^\mu - \sum_{\beta \in \tilde{\mathcal{P}}_n} k_\beta^\mu \right) z_n \left( k_{\{\alpha\}}^\mu, k_{\{\beta\}}^\mu \right), \end{aligned} \quad (2.7)$$

where

$$n_m = \int_{[m]} f_m = g_m \int \frac{d^3 k_m}{(2\pi)^3} f_m \quad (2.8)$$

is the number density of species  $[m]$  and  $n_B$  is the total baryon number density.  $\lambda_n$  is the forward process term of reaction  $n$  on the right-hand side of Equation (2.2) integrated over the phase space of particle  $[\epsilon]$  and normalized by the number densities of the particles in the entrance channel. The reaction rate is just the rate at which a reaction proceeds per particle in the entrance channel. These reaction rates are only non-zero when the particles in the entrance channel differ from those in the exit channel. The other interactions included in Equation (2.2) may change the momentum space distribution of the particles in the system, but they cannot change the total number of particles of any species. The reaction rate of the inverse process  $\lambda'_n$  is defined analogously to Equation (2.7) with the reactant and product sets switched.

Now, the standard reaction network equations follow from integrating over the phase space of particle  $[\epsilon]$  in Equation (2.2) to find

$$\partial_t n_\epsilon + \nabla \cdot (\langle \mathbf{v}_\epsilon \rangle n_\epsilon) = \sum_n \left[ -\lambda_n n_B^{1-N_n^{\mathcal{R}}} \prod_{j \in \mathcal{R}_n} n_j^{N_j^{n_j}} + \lambda'_n n_B^{1-N_n^{\mathcal{P}}} \prod_{l \in \mathcal{P}_n} n_l^{N_l^{n_l}} \right]. \quad (2.9)$$

Here,  $\langle \mathbf{v}_\epsilon \rangle = (2\pi)^{-3} n_\epsilon^{-1} \int d^3 k_\epsilon f_\epsilon \partial_{\mathbf{k}_\epsilon} k_\epsilon^0$  is the average velocity of particle  $[\epsilon]$  and we define

$$N_{\mathcal{R}}^n = \sum_{j \in \mathcal{R}_n} N_j^n \quad \text{and} \quad N_{\mathcal{P}}^n = \sum_{l \in \mathcal{P}_n} N_l^n. \quad (2.10)$$

Note that the left-hand side of Equation (2.9) is for an individual particle, not a particle species, but we need the evolution equations for the particle species. A reaction  $n$  that involves  $N_i^n$  particles of species  $[i]$  will contribute the right-hand side in Equation (2.9)  $N_i^n$  times to the derivative of  $n_i$  and so we multiply the right-hand side by  $N_i^n$ . Furthermore, due to the symmetry between the forward and inverse process in Equation (2.9), it makes sense to treat the forward and inverse processes separately. So far, we have indexed reactions with  $n$  and each reaction consisted of the forward and inverse direction. Let us now index reactions with  $\alpha$ , where the forward and inverse processes are counted separately. The set of reactions  $\{\alpha\}$  is thus twice as big as the set of reactions  $\{n\}$ . Although some inverse reactions may be ignored since they are extremely unlikely to occur. Equation (2.9) thus becomes

$$\partial_t n_i + \nabla \cdot (\langle \mathbf{v}_i \rangle n_i) = \sum_{\alpha} \lambda_{\alpha} (-R_i^{\alpha} + P_i^{\alpha}) N_i^{\alpha} n_B^{1-N_{\mathcal{R}}^{\alpha}} \prod_{m \in \mathcal{R}_{\alpha}} n_m^{N_m^{\alpha}}, \quad (2.11)$$

where

$$R_i^{\alpha} = \begin{cases} 1 & \text{if } i \in \mathcal{R}_{\alpha} \\ 0 & \text{otherwise} \end{cases} \quad \text{and} \quad P_i^{\alpha} = \begin{cases} 1 & \text{if } i \in \mathcal{P}_{\alpha} \\ 0 & \text{otherwise.} \end{cases} \quad (2.12)$$

For every interaction  $n$ , there is a forward reaction  $\alpha$  that has  $\lambda_{\alpha} = \lambda_n$ ,  $\mathcal{R}_{\alpha} = \mathcal{R}_n$ , and  $N_{\mathcal{R}}^{\alpha} = N_{\mathcal{R}}^n$ . For that reaction, Equation (2.11) contributes the forward part of Equation (2.9) with a multiplicative factor  $(-R_i^{\alpha} + P_i^{\alpha}) N_i^{\alpha} = -N_i^{\alpha}$ , since  $N_i^{\alpha}$  particles of species  $[i]$  are destroyed. Similarly, there is an inverse reaction  $\alpha'$  for the same interaction  $n$  that has  $\lambda_{\alpha'} = \lambda_n$ ,  $\mathcal{R}_{\alpha'} = \mathcal{P}_n$ , and  $N_{\mathcal{R}}^{\alpha'} = N_{\mathcal{P}}^n$ . This reaction contributes the inverse part of Equation (2.9) with a factor of  $(-R_i^{\alpha'} + P_i^{\alpha'}) N_i^{\alpha'} = N_i^{\alpha}$ , since  $N_i^{\alpha}$  particles of species  $[i]$  are created in the inverse reaction. Note that  $N_m^{\alpha} = N_m^{\alpha'} = N_m^n$  for all reactants and products  $[m]$ .

Finally, it is useful to define the *abundance*  $Y_i$  as

$$Y_i \equiv \frac{n_i}{n_B} = \frac{N_i/V}{N_B/V} = \frac{N_i}{N_B}, \quad (2.13)$$

where  $V$  is the volume of the fluid element and  $N_i$  and  $N_B$  are the total numbers of particles of species  $[i]$  and baryons, respectively. Since the number density  $n_i$

of species  $[i]$  changes with both the number of particles of species  $[i]$  and the total volume of the system, which is often changing in astrophysical systems undergoing nuclear burning, it is convenient to evolve the abundances  $Y_i$  instead of the number densities  $n_i$ . Assuming that all of the species move as a single fluid, i.e.,  $\langle \mathbf{v}_i \rangle = \mathbf{v}$ , and using the Lagrangian time derivative,  $d/dt = \partial_t + \mathbf{v} \cdot \nabla$ , we find

$$\begin{aligned}
\frac{dY_i}{dt} &= (\partial_t + \mathbf{v} \cdot \nabla) \left( \frac{n_i}{n_B} \right) \\
&= \frac{1}{n_B} \left[ \partial_t n_i - \frac{n_i}{n_B} \partial_t n_B + \nabla \cdot (\mathbf{v} n_i) - n_i \nabla \cdot \mathbf{v} - \frac{n_i}{n_B} (\nabla \cdot (\mathbf{v} n_B) - n_B \nabla \cdot \mathbf{v}) \right] \\
&= \frac{1}{n_B} \left[ \partial_t n_i + \nabla \cdot (\mathbf{v} n_i) - \frac{n_i}{n_B} (\partial_t n_B + \nabla \cdot (\mathbf{v} n_B)) \right] \\
&= \frac{1}{n_B} [\partial_t n_i + \nabla \cdot (\mathbf{v} n_i)], \tag{2.14}
\end{aligned}$$

where we used the identity  $\mathbf{v} \cdot \nabla f = \nabla \cdot (\mathbf{v} f) - f \nabla \cdot \mathbf{v}$  and the baryon number continuity equation  $\partial_t n_B + \nabla \cdot (\mathbf{v} n_B) = 0$ . But since  $\langle \mathbf{v}_i \rangle = \mathbf{v}$ , the above is the left-hand side of Equation (2.11) and so we get

$$\frac{dY_i}{dt} = \sum_{\alpha} \lambda_{\alpha} (-R_i^{\alpha} + P_i^{\alpha}) N_i^{\alpha} \prod_{m \in \mathcal{R}_{\alpha}} Y_m^{N_m^{\alpha}}, \tag{2.15}$$

which is the familiar abundance evolution equation (e.g., Hix and Thielemann, 1999). Essentially, for a given set of rates  $\lambda_{\alpha}$ , *SkyNet* solves this coupled, first-order, non-linear system of equations.

Even though it might look somewhat complicated, Equation (2.15) is very easy to understand. It says that the total time derivative of a species  $[i]$  is the sum over all reactions that involve that species and each reaction contributes a term consisting of the reaction rate multiplied by the abundances of the reactants and a factor that gives the number of particles of species  $[i]$  destroyed or created in the reaction. For example, for the forward and inverse reactions  $^{12}\text{C} + ^4\text{He} \rightleftharpoons ^{16}\text{O}$ , Equation (2.15) says

$$\frac{dY_{^{12}\text{C}}}{dt} = -\lambda_{\alpha} Y_{^{12}\text{C}} Y_{^4\text{He}} + \lambda_{\alpha'} Y_{^{16}\text{O}} + \dots, \tag{2.16}$$

$$\frac{dY_{^4\text{He}}}{dt} = -\lambda_{\alpha} Y_{^{12}\text{C}} Y_{^4\text{He}} + \lambda_{\alpha'} Y_{^{16}\text{O}} + \dots, \tag{2.17}$$

$$\frac{dY_{^{16}\text{O}}}{dt} = \lambda_{\alpha} Y_{^{12}\text{C}} Y_{^4\text{He}} - \lambda_{\alpha'} Y_{^{16}\text{O}} + \dots. \tag{2.18}$$

And for the reactions  $^{12}\text{C} + ^{12}\text{C} \rightleftharpoons ^{20}\text{Ne} + ^4\text{He}$  we get

$$\frac{dY^{12}\text{C}}{dt} = -2\lambda_\alpha Y_{^{12}\text{C}}^2 + 2\lambda_{\alpha'} Y^{20}\text{Ne} Y^4\text{He} + \dots, \quad (2.19)$$

$$\frac{dY^{20}\text{Ne}}{dt} = \lambda_\alpha Y_{^{12}\text{C}}^2 - \lambda_{\alpha'} Y^{20}\text{Ne} Y^4\text{He} + \dots, \quad (2.20)$$

$$\frac{dY^4\text{He}}{dt} = \lambda_\alpha Y_{^{12}\text{C}}^2 - \lambda_{\alpha'} Y^{20}\text{Ne} Y^4\text{He} + \dots. \quad (2.21)$$

### 2.2.2 Reaction rates and velocity averaged cross-sections

Specializing to astrophysical systems consisting of a range of nuclear species, scattering reactions mediated by the nuclear and electromagnetic forces bring particles into thermal equilibrium at temperature  $T$  on a much shorter timescale than nuclear reactions bring the particles into chemical equilibrium. In that case, the distribution functions only depend on temperature and the chemical potentials, i.e.,  $f_i = f_i(T, \mu_i)$ . As written, the rates defined in Equation (2.7) depend on the momentum space distribution functions of the particles involved in the reaction and may be quite complicated. Nevertheless, in thermal equilibrium the reaction rates depend only on the parameters of the distribution functions, i.e.,  $\lambda_\alpha = \lambda_\alpha(T, n_B, \mu_{\{m\}})$ , where the index  $m$  ranges over reactant and products.

If all of the particles involved in a reaction obey Boltzmann statistics or are photons with chemical potential zero, then we find that  $\lambda_\alpha = \lambda_\alpha(T, n_B)$  does not depend on the chemical potentials of the particles. This is because we can set the blocking factors  $(1 \pm f_i)$  of Boltzmann particles to 1, since quantum effects for Boltzmann particles are negligible. And for Boltzmann particles we have  $n_i \propto \exp(\mu_i/T)$  and  $f_i \propto \exp(\mu_i/T)$ , which means the dependence on  $\mu_i$  cancels for Boltzmann particles because every  $f_\alpha$  in Equation (2.7) is divided by an  $n_\alpha$ .<sup>5</sup> In most astrophysical scenarios, we can assume that the distribution functions  $f_i$  follow a thermal Maxwell-Boltzmann distribution, so the rates of reactions involving only nuclei and photons only depend on the temperature and density.

Nuclei can also undergo weak interactions that may involve leptons with non-zero chemical potentials. The leptons are generally not evolved in the network, but rather the electron (and positron) chemical potential is determined by the requirement of charge neutrality, or by the number of electrons per baryon  $Y_e$ . Neutrinos are also not evolved in reaction networks since their distribution functions are often non-thermal in astrophysical scenarios in which they play a role. Therefore, weak

<sup>5</sup>Actually, the  $f_\alpha$ 's are divided by  $n_j^{N_j}$ , but this is just an  $n_\alpha$  for every particle of species  $[j]$ .

interaction rates have a dependence  $\lambda_{\alpha,\text{weak}} = \lambda_{\alpha,\text{weak}}(T, n_B, Y_e, f_{\{\nu\}})$  where  $f_{\{\nu\}}$  are the externally specified neutrino distribution functions of the relevant neutrino species (see Appendix 2.C). Although, weak decay rates of nuclei are just constants when final state blocking by leptons can be safely ignored.

For two particle reactions, it is common to define the cross-section as Peskin and Schroeder, 1995, §4

$$\sigma_{\alpha}(k_1^{\mu} - k_2^{\mu}) = \frac{1}{v_{\text{rel}}} \left[ \prod_{l \in \mathcal{P}_{\alpha}} \int_{[l]} \right] \delta^4 \left( k_1^{\mu} + k_2^{\mu} - \sum_{l \in \mathcal{P}_{\alpha}} k_l^{\mu} \right) \mathcal{Z}_{\alpha} \left( k_1^{\mu}, k_2^{\mu}, k_{\{l\}}^{\mu} \right), \quad (2.22)$$

where  $v_{\text{rel}}$  is the relative velocity between particles [1] and [2]. Adopting the viewpoint that the [i]'s are stationary targets and the [j]'s are incoming projectiles impinging on the targets, the cross section  $\sigma_{\alpha}$  can be interpreted as (e.g., Clayton, 1968, §4)

$$\begin{aligned} \sigma_{\alpha} &= \frac{\text{number of reactions per second per target [i]}}{\text{flux of incoming projectiles [j]}} = \frac{R_{i,j}/(n_i V)}{v_{\text{rel}} n_j} \\ &= \frac{r_{i,j}}{v_{\text{rel}} n_i n_j}, \end{aligned} \quad (2.23)$$

where  $R_{i,j}$  is the number of reactions per second,  $r_{i,j} = R_{i,j}/V$  is the number of reactions per second per volume, and  $n_i, n_j$  are the number densities of [i] and [j]. Assuming Boltzmann statistics so that  $(1 \pm f_l) \rightarrow 1$  for the products, Equation (2.7) gives

$$\lambda_{\alpha} = \mathcal{N}_{\alpha} n_B \int_{[1]} \frac{f_1}{n_1} \int_{[2]} \frac{f_2}{n_2} v_{\text{rel}} \sigma_{\alpha} = \mathcal{N}_{\alpha} n_B \langle \sigma_{\alpha} v_{\text{rel}} \rangle, \quad (2.24)$$

where  $\mathcal{N}_{\alpha}$  is the double counting factor from Equation (2.6). Since the distribution functions are normalized by the densities of species [1] and [2], this expression shows that  $\lambda_{\alpha}$  is proportional to the cross-section averaged over the relative velocities between the two particles (after transforming to the center of mass frame, see e.g., Clayton 1968). Therefore, using Equation (2.23) one arrives at the standard relation between the reaction rate and the velocity averaged cross-section (e.g., Clayton 1968, §4; Rolfs and Rodney 1988, §3),

$$r_{i,j} = n_B^{-1} \lambda_{\alpha} n_1 n_2 = n_1 n_2 \mathcal{N}_{\alpha} \langle \sigma_{\alpha} v_{\text{rel}} \rangle. \quad (2.25)$$

### 2.2.3 Nuclear Statistical Equilibrium (NSE) and inverse reaction rates

Equation (2.2) shows that for every reaction, there is an inverse reaction. The relationship between the forward and reverse rates, which only depends on the

density, temperature, and the internal properties of the nuclei is generally called detailed balance. In some cases, for example for  $\beta$ -decays or fission reactions, the inverse reactions are extremely unlikely to occur and can be ignored. For other reactions, e.g., a neutron capture reaction, the inverse reaction can occur very frequently and sometimes even more often than the forward reaction. Thus it is important to take inverse reactions into account. At temperatures of about 5 GK and above, inverse strong reactions such as photodissociation of nuclides can be in equilibrium with their forward reactions. For example, the reactions  $^{196}\text{Au} + n \rightleftharpoons ^{197}\text{Au} + \gamma$  and  $^{20}\text{Ne} + \gamma \rightleftharpoons ^{16}\text{O} + ^4\text{He}$  can be in equilibrium at sufficiently high temperatures. The situation of all strong reactions being in equilibrium is called Nuclear Statistical Equilibrium (NSE). This situation can also be thought of as an equilibrium between the reaction of forming a nucleus  $(Z, N)$  from  $Z$  free protons and  $N$  free neutrons, and its inverse reaction, namely completely dissociating a nucleus  $(Z, N)$  into  $Z$  protons and  $N$  neutrons. In other words, if NSE holds, then the forward and inverse reactions,



are in equilibrium for all nuclides that are part of the composition. Of course, there are no reactions that directly create a nuclide  $(Z, N)$  out of  $Z$  protons and  $N$  neutrons. But there is a chain of strong reactions that connects  $(Z, N)$  to free neutrons and protons. So if all strong reactions are in equilibrium, then we effectively have the reactions shown above and they are also in equilibrium. When nucleons are in chemical equilibrium with all other nuclear species, the energetic cost of turning  $Z_i$  protons and  $N_i$  neutrons into a single nucleus must be zero, which requires

$$\mu_i = Z_i \mu_p + N_i \mu_n, \quad (2.27)$$

where  $\mu_i$  is the chemical potential of species  $[i]$ .

When the composition moves into NSE, the forward and inverse strong reactions approach equilibrium. In order to ensure that the equilibrium composition determined by the forward and inverse reaction rates is the same as the NSE composition computed from the equality of the chemical potentials, we need to compute the inverse reaction rates directly from the forward rates and nuclide properties. Consider the reaction  $\alpha$  and its inverse reaction  $\alpha'$ . In equilibrium, each set of terms on the right-hand side of Equation (2.2) must be zero. Then, by the symmetry of the

differential rate  $\lambda_\alpha = \lambda_{\alpha'}$  and casting Equation (2.2) into Equation (2.9), we have

$$\lambda_\alpha \prod_{j \in \mathcal{R}_\alpha} Y_{j,\text{eq}}^{N_j^\alpha} = \lambda_{\alpha'} \prod_{l \in \mathcal{P}_\alpha} Y_{l,\text{eq}}^{N_l^\alpha}, \quad (2.28)$$

where  $Y_{i,\text{eq}}$  is the abundance of species  $[i]$  in chemical equilibrium. For a Boltzmann gas, the abundance is given by (Equation 2.128)

$$Y_i = \frac{G_i(T)}{n_B} \left( \frac{m_i T}{2\pi} \right)^{3/2} \exp[(\mu_i - m_i)/T], \quad (2.29)$$

where  $G_i(T)$  is the internal partition function of species  $[i]$  (see Equation 2.120) and  $m_i$  is its rest mass. Substituting the above into Equation (2.28) yields

$$\begin{aligned} \frac{\lambda_{\alpha'}}{\lambda_\alpha} &= \frac{\prod_{j \in \mathcal{R}_\alpha} [G_j/n_B(m_j T/2\pi)^{3/2}]^{N_j^\alpha}}{\prod_{l \in \mathcal{P}_\alpha} [G_l/n_B(m_l T/2\pi)^{3/2}]^{N_l^\alpha}} \\ &\times \exp \left[ \frac{1}{T} \sum_{j \in \mathcal{R}_\alpha} N_j^\alpha (\mu_{j,\text{eq}} - m_j) - \frac{1}{T} \sum_{l \in \mathcal{P}_\alpha} N_l^\alpha (\mu_{l,\text{eq}} - m_l) \right]. \end{aligned} \quad (2.30)$$

Since the forward and reverse reactions are in equilibrium, the chemical potentials on both sides are equal, hence

$$\sum_{j \in \mathcal{R}_\alpha} N_j^\alpha \mu_{j,\text{eq}} = \sum_{l \in \mathcal{P}_\alpha} N_l^\alpha \mu_{l,\text{eq}}, \quad (2.31)$$

and the chemical potentials in the exponential of Equation (2.30) cancel. Then, the inverse reaction rate  $\lambda_{\alpha'}$  is

$$\lambda_{\alpha'}(T, \rho) = \lambda_\alpha(T, \rho) e^{-Q_\alpha/T} \Gamma_\alpha(T) M_\alpha^{3/2} \left( \frac{T}{2\pi} \right)^{3\Delta N_\alpha/2} n_B^{-\Delta N_\alpha}, \quad (2.32)$$

where we define

$$Q_\alpha = \sum_{j \in \mathcal{R}_\alpha} N_j^\alpha m_j - \sum_{l \in \mathcal{P}_\alpha} N_l^\alpha m_l, \quad (2.33)$$

$$\Gamma_\alpha(T) = \frac{\prod_{j \in \mathcal{R}_\alpha} G_j(T)^{N_j^\alpha}}{\prod_{l \in \mathcal{P}_\alpha} G_l(T)^{N_l^\alpha}}, \quad (2.34)$$

$$M_\alpha = \frac{\prod_{j \in \mathcal{R}_\alpha} m_j^{N_j^\alpha}}{\prod_{l \in \mathcal{P}_\alpha} m_l^{N_l^\alpha}}, \quad (2.35)$$

$$\Delta N_\alpha = \sum_{j \in \mathcal{R}_\alpha} N_j^\alpha - \sum_{l \in \mathcal{P}_\alpha} N_l^\alpha = N_{\mathcal{R}}^\alpha - N_{\mathcal{P}}^\alpha. \quad (2.36)$$

Although the above is derived under the assumption that the abundances are such that the two reactions are in equilibrium, it still holds for any abundances because the reaction rates only depend on the temperature and density. In Appendix 2.B, we show how calculating NSE is implemented in *SkyNet*.

## 2.3 Network evolution

In this section, we focus on the specific implementation of the physics described in the previous section in *SkyNet*. In essence, evolving the reaction network means solving the large coupled system of first order, non-linear ordinary differential equations (ODEs) given in Equation (2.15). But there are various other pieces that are needed to make the evolution robust and efficient, which are also discussed in this section.

### 2.3.1 Implicit integration method

The system of ODEs (Equation 2.15) we need to solve is extremely stiff because of the enormous range of reaction rates, which can span many orders of magnitude (e.g., Timmes, 1999; Hix and Meyer, 2006). Thus an explicit integration method would be constrained to taking extremely small time steps. This is why nuclear reaction networks are typically integrated with an implicit method (e.g., Timmes, 1999; Winteler, 2013; Longland et al., 2014). However, some authors have proposed various explicit methods specifically tuned to integrate stiff reaction networks (e.g., Feger, 2011; Guidry, 2012; Guidry and Harris, 2013; Guidry et al., 2013a,b; Brock et al., 2015). Currently, *SkyNet* uses the first-order implicit backward Euler method (e.g., Hix and Thielemann, 1999), but it is straightforward to implement higher-order implicit integration methods, as well. We plan to do this in the future, since Timmes (1999) recommends using higher-order methods, such as the variable-order Bader-Deuflhard method (Bader and Deuflhard, 1983). Let the vector  $\mathbf{Y}(t) = Y_i(t)$  denote the composition at time  $t$ . If we want to take a time step  $\Delta t$  using the first-order implicit backward Euler method, we write

$$\begin{aligned} \dot{\mathbf{Y}}(t + \Delta t) &= \frac{\mathbf{Y}(t + \Delta t) - \mathbf{Y}(t)}{\Delta t} \\ \Leftrightarrow \mathbf{0} &= \dot{\mathbf{Y}}(\mathbf{x}, T(t + \Delta t), \rho(t + \Delta t)) - \frac{\mathbf{x} - \mathbf{Y}(t)}{\Delta t} \\ &= \mathbf{F}(\mathbf{x}, T(t + \Delta t), \rho(t + \Delta t)), \end{aligned} \quad (2.37)$$

where  $\mathbf{x} = \mathbf{Y}(t + \Delta t)$  are the unknown abundances at the end of the time step we are trying to find, and  $\mathbf{Y}(t)$  are the known abundances at the beginning of the time step.  $\dot{\mathbf{Y}}(\mathbf{Y}, T, \rho)$  is the function defined in Equation (2.15) that gives the time derivatives of the abundances as a function of a given set of abundances  $\mathbf{Y}$ , a temperature  $T$ , and density  $\rho$ . Note that we need to know the temperature  $T$  and density  $\rho$  as a function of time. The function  $\mathbf{F}$  is simply the right-hand side of the above equation. We thus have a multi-dimensional root-finding problem  $\mathbf{0} = \mathbf{F}(\mathbf{x}, T, \rho)$ , where  $T$  and

$\rho$  are known functions of time. *SkyNet* uses the Newton–Raphson (NR) method to find the root. For every time step, the following iteration is performed to find the solution  $\mathbf{x}$  to Equation (2.37):

$$\mathbf{x}_{n+1} = \mathbf{x}_n - [J_{\mathbf{F}}(\mathbf{x}_n)]^{-1} \mathbf{F}(\mathbf{x}_n, T(t + \Delta t), \rho(t + \Delta t)), \quad (2.38)$$

where the iteration starts with  $\mathbf{x}_0 = \mathbf{Y}(t)$ , the abundances from the previous time step and

$$(J_{\mathbf{F}})_{ij} = \frac{\partial F_i}{\partial Y_j} = \frac{\partial \dot{Y}_i}{\partial Y_j} - \frac{\delta_{ij}}{\Delta t}, \quad (2.39)$$

is the Jacobian matrix and  $\delta_{ij}$  is the Kronecker delta. The partial derivatives  $\partial \dot{Y}_i / \partial Y_j$  are computed from Equation (2.15) as

$$\begin{aligned} \frac{\partial \dot{Y}_i}{\partial Y_j} &= \sum_{\alpha} \lambda_{\alpha} (-R_i^{\alpha} + P_i^{\alpha}) N_i^{\alpha} \sum_{n \in \mathcal{R}_{\alpha}} \delta_{nj} \frac{N_n^{\alpha}}{Y_n} \prod_{m \in \mathcal{R}_{\alpha}} Y_m^{N_m^{\alpha}} \\ &= \sum_{\alpha} \lambda_{\alpha} (-R_i^{\alpha} + P_i^{\alpha}) N_i^{\alpha} R_j^{\alpha} N_j^{\alpha} Y_j^{N_j^{\alpha} - 1} \prod_{m \in \mathcal{R}_{\alpha}, m \neq j} Y_m^{N_m^{\alpha}}. \end{aligned} \quad (2.40)$$

The size of the Jacobian matrix  $J_{\mathbf{F}}$  is  $N \times N$ , where  $N$  is the number of nuclear species in the network. For large networks ( $N \sim 8000$ ), inverting this large matrix can be quite costly, because the linear system in Equation (2.37) has to be solved for every NR iteration. Since the Jacobian matrix depends on the unknown abundances at the end of the time step, we have to recompute the Jacobian matrix after every NR iteration that updates our guess for the abundances at the end of the time step. Fortunately, however, the Jacobian matrix is very sparse (only 0.24% of the  $N^2$  entries are non-zero for large networks), because most nuclear species are not directly connected by a single reaction. By exploiting the sparseness of the Jacobian, we drastically reduce the memory requirement to store the Jacobian and we can also use matrix solver packages that are specifically designed for sparse systems (see Section 2.5). The most expensive parts of the evolution are computing the Jacobian entries from Equation (2.40) and then solving the sparse linear system given by Equation (2.37). These two operations have to be performed at every NR iteration. The method for choosing the time step  $\Delta t$  and when to terminate the NR iteration will be discussed in Section 2.3.3.

### 2.3.2 Self-heating evolution

In the previous section, we showed how *SkyNet* integrates the nuclear abundances forward in time if both the temperature and density are given as functions of time. In

most applications, the density history  $\rho(t)$  is given (for example when *SkyNet* is used to post-process nucleosynthesis for tracer particles from a hydro simulation), but the temperature is not necessarily known as a function of time. And even if we do have a temperature history available, it most likely would not include heating due to the nuclear reactions that *SkyNet* evolves. But based on the kinetic theory description of the reaction network equations in Section 2.2.1, as well as the discussion of detailed balance in Section 2.2.3, it is clear that the reaction network and the thermodynamic state of the fluid are intimately related and need to be treated consistently. Therefore, we want the temperature to be evolved in the network under the influence of the nuclear reactions, which release nuclear binding energy as heat. This is referred to as a self-heating network evolution (e.g., Freiburghaus et al., 1999). We still require to know the density as a function of time, though.

Recall the First Law of thermodynamics,

$$dU = \delta Q - \delta W = \delta Q - PdV, \quad (2.41)$$

where  $dU$  is the infinitesimal change in internal energy,  $\delta Q$  is the infinitesimal heat added to the system from the surroundings, and  $\delta W$  is the infinitesimal mechanical work performed by the system. If the system expands or contracts, the work performed is  $\delta W = PdV$ , where  $P$  is the pressure and  $dV$  is the infinitesimal change in volume. We use the entropy  $S$ , volume  $V$ , and composition  $\{N_k\}$  as our independent thermodynamic variables. Note that the index  $k$  ranges over all particles in the system, not just nuclides. The total differential of the internal energy is thus

$$\begin{aligned} dU &= \left(\frac{\partial U}{\partial S}\right)_{V,\{N_k\}} dS + \left(\frac{\partial U}{\partial V}\right)_{S,\{N_k\}} dV + \sum_k \left(\frac{\partial U}{\partial N_k}\right)_{S,V,\{N_{l \neq k}\}} dN_k \\ &= TdS - PdV + \sum_k \mu_k dN_k, \end{aligned} \quad (2.42)$$

where  $T$  is the temperature and  $\mu_k$  is the chemical potential of particle  $k$ . Equating Equation (2.41) and Equation (2.42) yields

$$\delta Q = TdS + \sum_k \mu_k dN_k. \quad (2.43)$$

If we divide the above by  $N_B$ , the total number of baryons, and replace the infinitesimal changes by the differences of the quantities from one time step to the next (i.e.,  $\Delta X = X(t + \Delta t) - X(t)$ ), we find

$$\Delta q = T\Delta s + \sum_k \mu_k dY_k, \quad (2.44)$$

since  $Y_k = N_k/N_B$  (Equation 2.13). Note that the sum over  $k$  includes all particles, hence also electrons, which can be created or destroyed in weak nuclear reactions.  $\Delta q$  is the change in the heat per baryon due to external heating sources. Let  $\dot{\epsilon}_{\text{ext}}$  be an imposed external heating rate (per baryon), then

$$\Delta q = (\dot{\epsilon}_{\text{ext}} - \dot{\epsilon}_\nu)\Delta t, \quad (2.45)$$

where  $\dot{\epsilon}_\nu$  is the neutrino heating/cooling rate of the system on the environment given by Equation (2.194). Since we do not include neutrinos in the internal state of the system, the neutrino heating/cooling must be treated as an external source of heat. And because we define  $\dot{\epsilon}_\nu$  as the heating/cooling on the environment, it has a minus sign in Equation (2.44). Combining Equation (2.44) with Equation (2.45) and solving for  $\Delta s$  yields

$$\begin{aligned} \Delta s &= \frac{\Delta q}{T} - \frac{1}{T} \sum_i \Delta Y_i (\mu_i + Z_i \mu_{e^-}) \\ &= (\dot{\epsilon}_{\text{ext}} - \dot{\epsilon}_\nu) \frac{\Delta t}{T} - \sum_i \Delta Y_i \left( \frac{m_i}{T} + \frac{Z_i \mu_{e^-}}{T} + \ln \left[ \frac{n_i}{G_i(T)} \left( \frac{2\pi}{m_i T} \right)^{3/2} \right] \right), \end{aligned} \quad (2.46)$$

where we used Equation (2.128) and switched to index  $i$  that runs only over the nuclides. So we explicitly include the contribution from the  $Z_i$  electrons that come with nuclide  $i$ . To make the rest mass terms in the sum closer to unity, we define the mass excess  $\mathcal{M}_i$  as

$$\mathcal{M}_i = m_i - A_i m_u, \quad (2.47)$$

where  $A_i$  is the number of neutrons and protons of species  $i$  and  $m_u$  is the atomic mass unit, defined such that the mass excess of  $^{12}\text{C}$  is exactly 0 (i.e.,  $m_u = m^{12}\text{C}/12$ ). Since  $Y_i = N_i/N_B$  (with  $N_i$  being the number of particles of species  $[i]$ , see Equation 2.13), we find

$$\sum_i Y_i A_i = \frac{1}{N_B} \sum_i N_i A_i = \frac{N_B}{N_B} = 1, \quad (2.48)$$

because species  $[i]$  is made up of  $A_i$  neutrons and protons, hence  $A_i$  baryons. Thus we have  $\sum_i Y_i(t) A_i = 1$  for all times  $t$ , which is another way of saying that the total baryon number  $N_B$  is conserved. Using this, we find

$$\begin{aligned} \sum_i \Delta Y_i m_i &= \sum_i \Delta Y_i (\mathcal{M}_i + m_u A_i) \\ &= \sum_i \Delta Y_i \mathcal{M}_i + m_u \left( \sum_i Y_i(t + \Delta t) A_i - \sum_i Y_i(t) A_i \right) \\ &= \sum_i \Delta Y_i \mathcal{M}_i + m_u (1 - 1) = \sum_i \Delta Y_i \mathcal{M}_i. \end{aligned} \quad (2.49)$$

Using the above and the fact that  $n_i = Y_i n_B$ , we can write Equation (2.46) as

$$\Delta s = (\dot{\epsilon}_{\text{ext}} - \dot{\epsilon}_\nu) \frac{\Delta t}{T} - \sum_i \Delta Y_i \left( \frac{\mathcal{M}_i}{T} + \frac{Z_i \mu_{e^-}}{T} + \ln \left[ \frac{Y_i n_B}{G_i(T)} \left( \frac{2\pi}{m_i T} \right)^{3/2} \right] \right). \quad (2.50)$$

Note that the external heating is accounted for with a first-order forward Euler method. We plan to improve this in the future when we implement higher-order integration methods for the network itself. With the above, *SkyNet* can update the entropy after every time step and then obtain the new temperature at the end of the time step from the EOS. Therefore, we only need to know the initial entropy (or temperature, from which the entropy is determined). This changes the evolution (Equation 2.37) slightly, because we now have to use the entropy at the beginning of the time step to estimate the temperature at the end of the time step. That is, we solve

$$\mathbf{0} = \mathbf{F}(\mathbf{x}, T^*, \rho(t + \Delta t)), \quad (2.51)$$

where  $T^*$  is given by the EOS as

$$T^* = \text{EOS}(s(t), \rho(t + \Delta t), \mathbf{Y}(t)). \quad (2.52)$$

Equation (2.51) is solved with the NR method, as described in the previous section. Note that  $\Delta t$  is fixed during the NR iterations, which means the temperature and density are also fixed. After the NR iterations have converged, we have found the new abundances  $Y_i(t + \Delta t)$  and then we can compute  $\Delta s$  according to Equation (2.50) and update the entropy as

$$s(t + \Delta t) = s(t) + \Delta s. \quad (2.53)$$

Hence we have a hybrid implicit/explicit scheme where the abundances are evolved implicitly but the entropy is evolved explicitly. One could also evolve the entropy implicitly together with the abundances, which would require computing  $\partial \dot{Y}_i / \partial s$  and  $\partial \dot{s} / \partial Y_i$  and adding these terms to the Jacobian. We may extend *SkyNet* in the future to support such a fully implicit scheme, but for now, we have achieved good results with the hybrid approach.

The energy released in nuclear binding energy due to nuclear reactions is

$$\dot{\epsilon}_{\text{nuc}} = -\frac{1}{\Delta t} \sum_i \Delta Y_i m_i = -\frac{1}{\Delta t} \sum_i \Delta Y_i \mathcal{M}_i, \quad (2.54)$$

where we used Equation (2.49) and  $\Delta Y_i / \Delta t$  is an approximation for  $\dot{Y}_i$  over the time step. Note that the minus sign comes from the fact that rest mass (or mass excess) is converted into energy, hence the heating rate is positive if there is a net reduction in rest mass. Some authors (e.g., Hix and Thielemann, 1999) treat  $\dot{\epsilon}_{\text{nuc}}$  as an external heat source. This is necessary if the EOS does not depend on the entire composition but only on  $\bar{A}$  and  $\bar{Z}$ , the average mass and charge numbers, for example. In order to compare the nuclear heating in *SkyNet* to other codes, *SkyNet* computes and records a total heating rate  $\dot{\epsilon}_{\text{tot}}$ , regardless of whether self-heating is enabled.  $\dot{\epsilon}_{\text{tot}}$  is computed as

$$\dot{\epsilon}_{\text{tot}} = \frac{\Delta q}{\Delta t} + \dot{\epsilon}_{\text{nuc}} = -\dot{\epsilon}_\nu + \dot{\epsilon}_{\text{ext}} - \frac{1}{\Delta t} \sum_i \Delta Y_i \mathcal{M}_i. \quad (2.55)$$

Note that the above has units of  $\text{erg s}^{-1} \text{baryon}^{-1}$ , to convert it to more commonly used units of  $\text{erg s}^{-1} \text{g}^{-1}$ , we simply multiply  $\dot{\epsilon}_{\text{tot}}$  by the Avogadro constant  $N_A$ .

Currently, *SkyNet* records the total heating rate shown above. In reality, this heating rate is composed of multiple components that are thermalized in the material in different ways (e.g., Barnes et al., 2016). For example, emitted electrons and positrons, as well as kinetic energy of fission fragments thermalize with very high efficiency, while only a small fraction of the energy released as neutrinos might thermalize. In a future version of *SkyNet* we plan to record the different heating rate components, so that thermalization can be taken into account in kilonova light curve calculations, for example.

### 2.3.3 Convergence criteria and time stepping

The time step for the network evolution needs to be adjusted depending on how well the NR iteration (Equation 2.38) converges. All the default values and thresholds mentioned in this section are adjustable by the user. To check that the NR iterations have completely converged, a standard criterion is (Press et al., 2007)

$$\sum_{x_i^{(n+1)} \geq Y_{\text{thr}}} \left| \frac{x_i^{(n+1)} - x_i^{(n)}}{x_i^{(n+1)}} \right| < \epsilon_{\text{tol}, \Delta x}, \quad (2.56)$$

where  $x_i^{(n+1)}$  is the  $i$ -th component of the vector  $\mathbf{x}_{n+1}$  and  $\mathbf{x} = \mathbf{Y}(t + \Delta t)$  are the unknown abundances at the end of the current time steps that we want to find. The sum only runs over the indices  $i$  for which  $x_i^{(n+1)} \geq Y_{\text{thr}}$  for some abundance threshold  $Y_{\text{thr}}$ , which we usually set to  $10^{-20}$ . The default value is  $\epsilon_{\text{tol}, \Delta x} = 10^{-6}$ . While this convergence criterion ensures that any subsequent NR iterations would

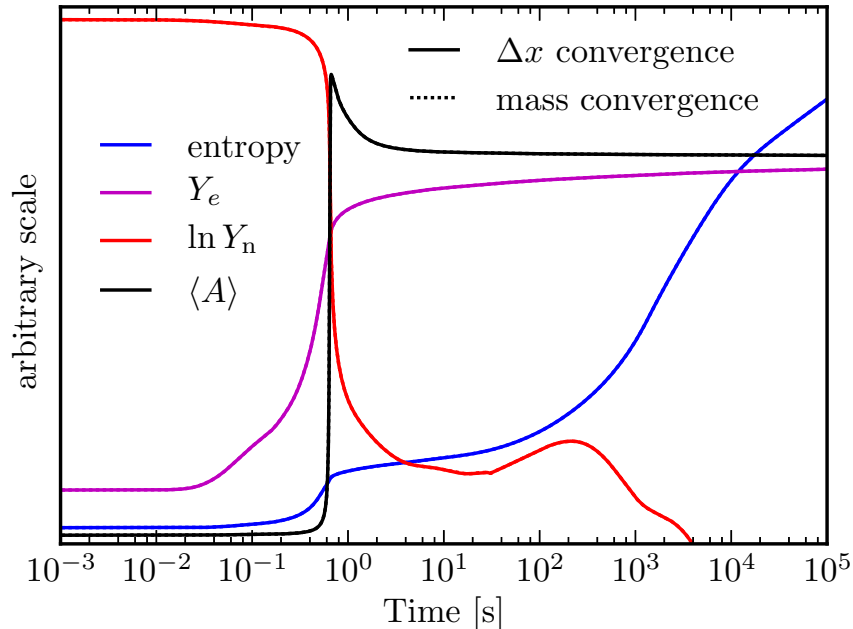


Figure 2.1: Comparison of the two convergence criteria. The solid lines show the entropy, electron fraction  $Y_e$ , logarithm of the neutron abundance  $Y_n$ , and average mass number  $\langle A \rangle$  as a function of time using the  $\Delta x$  convergence criterion (Equation 2.56) with  $\varepsilon_{\text{tol},\Delta x} = 10^{-6}$ . The dotted lines plotted on top of the solid lines are the same quantities using the mass conservation convergence criterion (Equation 2.57) with  $\varepsilon_{\text{tol},\text{mass}} = 10^{-10}$ . For all quantities, the two lines are exactly on top of each other and so the dotted lines are not visible. All quantities have been scaled by an arbitrary amount to fit on one figure. The networks evolve an r-process starting at 6 GK with initial  $Y_e = 0.1$ ,  $s = 10 k_B \text{ baryon}^{-1}$ , and an analytic density profile described in Lippuner and Roberts (2015) with expansion timescale 7.1 ms. The networks contain 7843 nuclides and 140,000 reactions.

not change the solution  $\mathbf{x}_{n+1}$  any more, we found that this criterion is too strict in practice. Instead, *SkyNet* typically uses mass conservation as a heuristic convergence criterion (which is also used by Hix and Thielemann, 1999), which takes the form

$$\left| 1 - \sum_i x_i^{(n+1)} A_i \right| < \varepsilon_{\text{tol},\text{mass}}, \quad (2.57)$$

where we usually use  $\varepsilon_{\text{tol},\text{mass}} = 10^{-10}$ . Note that the sum now runs over all nuclear species and there is no threshold for  $x_i^{(n+1)}$ . Since  $x_i^{(n+1)} = Y_i(t + \Delta t)$ , this convergence criterion is simply conservation of total baryon number. The user of *SkyNet* can choose to use Equation (2.56), Equation (2.57), or both as the convergence criterion for Equation (2.38).

Figure 2.1 shows an r-process evolution with the two different convergence criteria using  $\varepsilon_{\text{tol},\Delta x} = 10^{-6}$  and  $\varepsilon_{\text{tol},\text{mass}} = 10^{-10}$ . These convergence thresholds result in

almost exactly the same time step sizes, but if we made  $\varepsilon_{\text{tol},\Delta x}$  smaller, that would result in much smaller time steps. However, using the  $\Delta x$  convergence criterion requires an average of 3.1 NR iterations per time step, while mass conservation only needs 1.1 NR iterations per time step. Since the total number of time steps is almost the same, using mass conservation as the convergence criterion is almost about 2.4 times faster for this particular case. As Figure 2.1 shows, however, the nucleosynthesis evolution is identical in the two cases. No differences are visible in the entropy, electron fraction, neutron abundance, or average mass number as a function of time. And the maximum absolute difference in the final abundances of the two cases (using the  $\Delta x$  or mass conservation convergence criteria) is less than  $10^{-7}$ .

*SkyNet* adjusts the time step size  $\Delta t$  dynamically. Once the NR iterations have converged according to the chosen criterion, *SkyNet* checks that the composition did not change too much over the last time step. The temperature and entropy are allowed to change by at most 1%. If either of them changes by more than this threshold, then the time step is considered failed and  $\Delta t$  is reduced by a factor of two and the whole step is attempted again with the reduced time step size. *SkyNet* also considers the time step as failed if the NR iterations are not converged after 10 iterations, or if the error measure used for the NR convergence criterion increases compared to the error of the previous iteration, or if the error decreases by less than 10%. In all of those cases,  $\Delta t$  is reduced and the time step is attempted again. A simplified schematic of this mechanism is shown in Figure 2.2.

After a successful time step, *SkyNet* attempts to increase the step size for the next time step. *SkyNet* tries to double  $\Delta t$  after every successful step, but this new time step can be limited if the abundance of a particular nuclide changed by a large amount in the previous time step. If that is the case, then the new time step is limited to the approximate step size necessary to keep the abundance of the nuclide that changed the most over the last time step from changing by more than 10%. Hence the new time step is computed as

$$\Delta t^{(n+1)} = \min \left\{ \Delta t_{\text{max}}, 2\Delta t^{(n)}, \frac{10\% \Delta t^{(n)}}{\max_i(\Delta Y_i/Y_i)} \right\}, \quad (2.58)$$

where  $\Delta t_{\text{max}}$  is the maximum allowed time step and  $\Delta t^{(n)}$  is the previous time step. Using this adaptive time stepping mechanism, we typically get a time step size that grows exponentially with time in freely expanding trajectories, while keeping the error measure used for the convergence criterion below its prescribed tolerance.

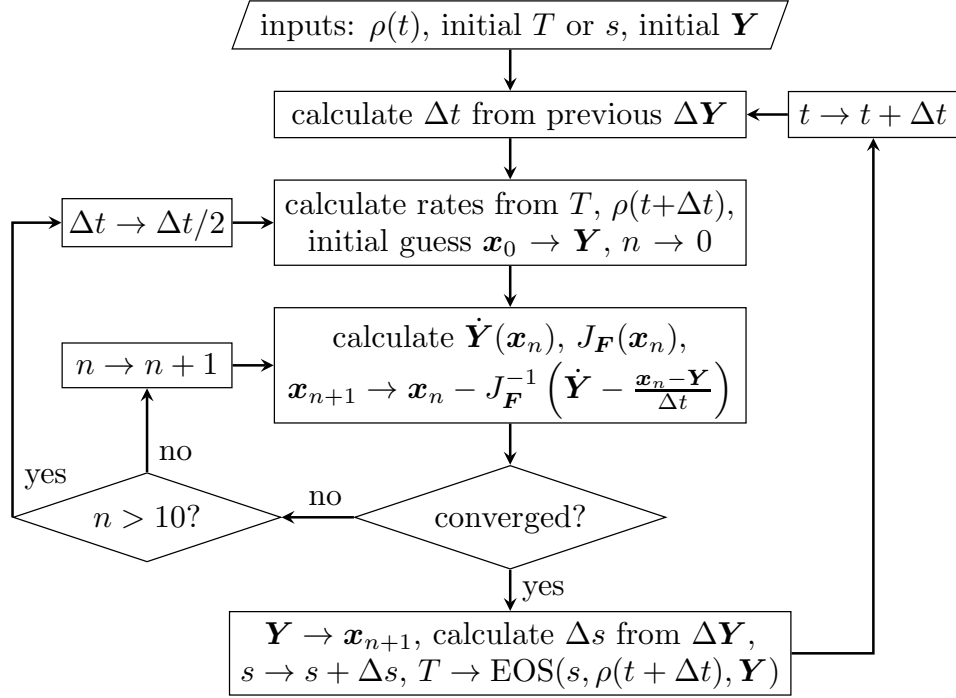


Figure 2.2: Simplified overview of the adaptive time stepping mechanism used in *SkyNet*. If the NR iterations do not converge after 10 iterations, the time step size  $\Delta t$  is cut in half and the time step is attempted again. There are other conditions that can result in a failed step and a subsequent retry with a smaller time step size. See the text for details. After a successful time step, the next  $\Delta t$  is computed from the size of the abundance changes  $\Delta \mathbf{Y}$  (Equation 2.58), and at that point  $\Delta t$  can increase or decrease.

Very rarely, it is necessary to renormalize the composition. In that case, every abundance is divided by the total mass, i.e.,

$$Y_{i,\text{new}} = \frac{Y_i}{\sum_i A_i Y_i}, \quad (2.59)$$

and then the new composition satisfies  $\sum_i A_i Y_i = 1$  exactly. While this artificially injects or removes energy from the system, it is useful as a last resort if the time step size is kept small because the composition is far away from mass conservation (but still within the error tolerance). After renormalization, the evolution usually proceeds normally with a larger time step than before. We renormalize if the time step falls below a certain limit (usually  $10^{-16}$ ), or if there are more than 25 time steps in a row that tried to increase the step size but subsequently failed and had to keep the step size constant. In such cases, it could be that the time step is small because the mass conservation convergence criterion is preventing the time step from increasing. If this is the case, then renormalizing the abundances usually

helps to increase the time step, because after renormalizing, mass conservation in Equation (2.57) is fulfilled exactly. But in some cases, for example when trying to evolve the network near NSE with reaction rates that are inconsistent with NSE (see Section 2.6.1.1), the time step is small because the abundances are changing rapidly and so renormalizing the composition does not help.

### 2.3.4 NSE evolution mode

If the abundances approach the NSE composition, the forward and inverse strong rates exactly balance (Section 2.2.3). In that case, all the partial derivatives in the Jacobian (Equation 2.40) would be zero, resulting in a singular Jacobian. The Jacobian is not exactly singular, however, because the weak reactions (that are not in equilibrium with their inverses) contribute non-zero derivatives to the Jacobian. Nevertheless, as the strong reactions move into equilibrium, the network time step becomes very small as the Jacobian becomes close to being numerically singular. To alleviate this problem, *SkyNet* automatically switches from a full network evolution to an NSE evolution scheme, if the strong nuclear reaction time scale becomes shorter than the time scale over which the density changes, and if the temperature is above some threshold (a user setting with default value of 7 GK). The full network is turned back on when these conditions are no longer satisfied.

If *SkyNet* determines that switching to NSE evolution is appropriate, it computes the NSE composition from the current internal energy, density, and electron fraction. If the entropy and temperature of that NSE composition differs by less than 1% (user setting) from the current network entropy and temperature, then the switch to NSE is allowed. Otherwise the full network evolution will continue and *SkyNet* will try to switch to NSE evolution mode again after the next step. A test of NSE evolution mode that demonstrates its necessity and consistency is present in Section 2.6.3.

In NSE evolution mode, *SkyNet* no longer evolves the abundances of all nuclear species. Instead, *SkyNet* only evolves the entropy  $s$  and electron fraction  $Y_e$  of the composition, which can change due to weak reactions, such as  $\beta$ -decays or neutrino interactions, that can change the charge of nuclides and heat the material. Recall that the electron fraction is  $Y_e = \sum_i Z_i Y_i$ , and so

$$\dot{Y}_e = \sum_i Z_i \dot{Y}_i, \quad (2.60)$$

where  $\dot{Y}_i$  is given by Equation (2.15) as a function of  $T$ ,  $\rho$ , and  $\mathbf{Y}$ . The temperature is given by the EOS as a function of  $s$ ,  $\rho$ , and  $\mathbf{Y}$ .  $\mathbf{Y}$  is given by NSE as a function

of  $s$ ,  $\rho$ , and  $Y_e$  (see Section 2.B.2). Thus we have

$$\mathbf{Y} = \text{NSE}(s, \rho, Y_e), \quad (2.61)$$

$$T = \text{EOS}(s, \rho, \mathbf{Y}), \quad (2.62)$$

$$\dot{\mathbf{Y}} = [\text{weak reactions}](T, \rho, \mathbf{Y}), \quad (2.63)$$

$$\dot{Y}_e = \sum_i Z_i \dot{Y}_i. \quad (2.64)$$

The rate of change of the entropy is obtained from dividing Equation (2.50) by  $\Delta t$ , namely

$$\begin{aligned} \dot{s} &= \frac{\dot{\epsilon}_{\text{ext}} - \dot{\epsilon}_v}{T} - \sum_i \dot{Y}_i \left( \frac{M_i}{T} + \frac{Z_i \mu_{e^-}}{T} + \ln \left[ \frac{Y_i n_B}{G_i(T)} \left( \frac{2\pi}{m_i T} \right)^{3/2} \right] \right) \\ &= \dot{s}(\dot{\epsilon}_v, \dot{\epsilon}_{\text{ext}}, T, \dot{\mathbf{Y}}, \mathbf{Y}, \rho) = \dot{s}(\dot{\epsilon}_v, \dot{\epsilon}_{\text{ext}}, s, \rho, Y_e). \end{aligned} \quad (2.65)$$

Since  $\dot{\epsilon}_v(t)$ ,  $\dot{\epsilon}_{\text{ext}}(t)$ , and  $\rho(t)$  are known, we thus have two coupled ODEs for  $Y_e$  and  $s$ , which *SkyNet* integrates with the Runge–Kutta–Fehlberg 4(5) method (e.g., Burden et al., 2015, §5.5). This is a 4-th order explicit integration method that also computes a 5-th order error estimate that is used to adaptively control the integration time step. The heating rate can be calculated analogous to Equation (2.55) as

$$\dot{\epsilon} = -\dot{\epsilon}_v + \dot{\epsilon}_{\text{ext}} - \sum_i \dot{Y}_i M_i. \quad (2.66)$$

Note that in NSE evolution mode, we only evolve two variables and they are changing on similar timescales because they are both influenced by the weak reactions. In this case, however, even though the weak reactions span a large range of timescales, this does not introduce any stiffness because we only deal with the sum of the abundance derivatives in both Equations (2.60) and (2.65). Thus we can safely use an explicit integration method.

## 2.4 Electron screening

Nuclear reaction rates strongly depend on the Coulomb interaction between the nuclides in the entrance channel (e.g., Salpeter, 1954). In conditions where nuclear burning can occur, the nuclides are almost all fully ionized. Therefore, nuclear reaction rates can be computed assuming that bare nuclei of charge  $Z_i$  interact with each other. At high temperature, the background gas of free electrons is uniform and has no impact on the Coulomb interactions between nuclei, but at lower temperatures the electron gas can become correlated with the nuclei and screen their Coulomb

interactions. Thus, electron screening is likely to be important if the density of the medium is sufficiently high and the temperature sufficiently low. In these conditions, a nucleus will repel neighboring nuclei and attract nearby electrons, thus creating an electron charge cloud around the nucleus. This charge cloud partially screens or shields the nuclear charge  $Z_i e$ , where  $e$  is the elementary charge unit. Thus the Coulomb repulsion between the two positively charged nuclei is reduced by the screening effect, which can enhance the nuclear reaction rates which depend strongly on the probability of Coulomb barrier penetration. Obviously, screening corrections are only important for charged particle reactions. Neutron capture reactions are unaffected by the polarization of the electron gas.

In this section, we present how electron screening is implemented in *SkyNet*. Our focus will be on writing down the equations that *SkyNet* uses to compute the screening corrections in a useful way with adequate justification. We will not develop the screening theory from first principles but refer the reader to the established literature on this subject (e.g., Salpeter, 1954; Dewitt et al., 1973; Graboske et al., 1973; Itoh et al., 1979; Ichimaru and Utsumi, 1984; Brown and Sawyer, 1997, to name but a few). For a handful of reactions, screening has been investigated experimentally (e.g., Engstler et al., 1988; Rolfs and Somorjai, 1995; Chen et al., 2004; Gatu Johnson et al., 2017). We use Gaussian CGS units throughout this section.

The strength of the electron screening effect depends mainly on the ratio of the Coulomb interaction energy between a nucleus and the nearby electrons to the thermal energy. If the thermal energy is large compared to the Coulomb interaction energy, then the electron charge cloud around the nucleus will be large and diffuse, providing less screening to the nuclear charge. We define the ion density

$$n_I = \sum_i n_i = \sum_i Y_i n_B = n_B \sum_i Y_i. \quad (2.67)$$

The average inter-ionic spacing is

$$a = \left( \frac{3}{4\pi n_I} \right)^{1/3}. \quad (2.68)$$

Now we define the dimensionless screening parameter  $\Lambda_0$  as

$$\Lambda_0 = \sqrt{4\pi n_I} e^3 \beta^{3/2}, \quad (2.69)$$

where  $\beta = 1/T$ . For some average (dimensionless) charge per ion  $\zeta$  (defined later on in Equation 2.92), let

$$\Lambda = \zeta^3 \Lambda_0 = \left( \frac{3^{1/3} \zeta^2 e^2}{aT} \right)^{3/2}. \quad (2.70)$$

Thus  $\Lambda$  is a measure of the ratio of the average Coulomb interaction energy  $\zeta^2 e^2/a$  to the average thermal energy  $T$ . If  $\Lambda$  is large, we expect the screening effect to be strong and when  $\Lambda$  is small, screening should be weak. The screening corrections in these two regimes, as well as the intermediate regime where  $\Lambda \sim 1$ , are the subject of the following sections, after we introduce the general screening factor that modifies the nuclear reaction rate.

### 2.4.1 General screening factor

For the two-body reaction  $[1] + [2] \rightarrow [3]$ , the total Coulomb potential can be written as

$$U_{\text{tot}}(r_{12}) = \frac{Z_1 Z_2 e^2}{r_{12}} + U(r_{12}), \quad (2.71)$$

where  $U(r_{12})$  is a potential correction to the bare Coulomb interaction between the two nuclei due to screening,  $r_{12}$  is the separation of the two reactants, and  $Z_1$  and  $Z_2$  are the charge numbers. Salpeter (1954) showed that the screening correction to the nuclear reaction rate  $\lambda_{12}$  is given by

$$\lambda_{12} = e^{-U_0/T} \lambda_{12,\text{no-sc}} = f_{\text{sc}} \lambda_{12,\text{no-sc}}, \quad (2.72)$$

where  $U_0 = U(r_{12} = 0)$ ,  $\lambda_{12,\text{no-sc}}$  is the unscreened reaction rate, and  $f_{\text{sc}} = e^{-U_0/T}$  is the general screening factor. Note that  $f_{\text{sc}}$  is sometimes written as  $\exp(H_{12}(0))$  in the literature. An approximation for the screening factor  $f_{\text{sc}}$  can be found in terms of  $Z_1$ ,  $Z_2$ , density, temperature, and other quantities determined by the composition. However, it is advantageous to (equivalently) write down the screening factor in terms of a chemical potential correction  $\mu_{\text{sc}}(Z)$  that depends on the charge of a single nucleus. This way, we can apply the screening corrections in NSE as well and we are not constrained to only correcting reaction rates with two reactants. In this section, we show how to compute the reaction screening factor if we have the chemical potential correction  $\mu_{\text{sc}}(Z)$ . In the following sections, we will show how to compute  $\mu_{\text{sc}}(Z)$  in different screening regimes.

For the same two-body reaction  $[1] + [2] \rightarrow [3]$ , Dewitt et al. (1973) found that the screening factor can also be written as

$$f_{\text{sc}} = \exp(\beta \mu_{\text{sc}}(Z_1) + \beta \mu_{\text{sc}}(Z_2) - \beta \mu_{\text{sc}}(Z_3)), \quad (2.73)$$

where  $\beta = 1/T$ ,  $\mu_{\text{sc}}(Z)$  is the correction to the chemical potential for the addition of a charge  $Z$  to the system when the electron gas is non-uniform, and  $Z_3 = Z_1 + Z_2$  is

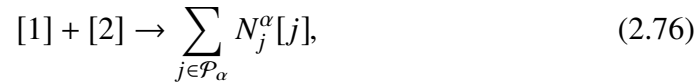
the charge of the product. It is straightforward to generalize this result to an arbitrary (i.e. not just two-body) reaction  $\alpha$  as

$$f_{\text{sc}} = \exp \left( \sum_{i \in \mathcal{R}_\alpha} N_i^\alpha \beta \mu_{\text{sc}}(Z_i) - \beta \mu_{\text{sc}}(Z_{\mathcal{R}}^\alpha) \right), \quad (2.74)$$

where  $\mathcal{R}_\alpha$  is the set of reactant species of the reaction and  $N_i^\alpha$  is the number of species  $[i]$  destroyed or produced in the reaction (see Section 2.2.1 and Equation 2.5). We also define

$$Z_{\mathcal{R}}^\alpha = \sum_{i \in \mathcal{R}_\alpha} N_i^\alpha Z_i. \quad (2.75)$$

The above expression for the screening factor  $f_{\text{sc}}$  for reactions with an arbitrary number of particles in the entrance channel holds for multi-step reactions. This can be shown by breaking up the multi-body reaction into two-body reactions, e.g., treating  $[1] + [2] + [3] \rightarrow X$  as  $[1] + [2] \rightarrow [12]$  followed by  $[12] + [3] \rightarrow X$ , and then calculating the overall screening factor. To justify the general form of  $f_{\text{sc}}$ , consider a two-body reaction that produces an arbitrary set of products  $\mathcal{P}_\alpha$ , i.e.



where  $Z_1 + Z_2 = \sum_{j \in \mathcal{P}_\alpha} N_j^\alpha Z_j$  due to charge conservation. Let  $\lambda_{\alpha, \text{no-sc}}$  and  $\lambda_{\alpha', \text{no-sc}}$  be the reaction rates of the forward and inverse reactions without the screening corrections. The corrected forward rate is

$$\lambda_\alpha = \lambda_{\alpha, \text{no-sc}} \exp(\beta \mu_{\text{sc}}(Z_1) + \beta \mu_{\text{sc}}(Z_2) - \beta \mu_{\text{sc}}(Z_1 + Z_2)). \quad (2.77)$$

Equation (2.128) gives the chemical potential of nuclear species  $[i]$  without the screening correction, which we call  $\mu_{i, \text{no-sc}}$ . The corrected chemical potential is  $\mu_i = \mu_{i, \text{no-sc}} + \mu_{\text{sc}}(Z_i)$ . Note that the chemical potential correction  $\mu_{\text{sc}}(Z_i)$  enters on the same level as the term  $m_i$  in Equation (2.128) and therefore,  $\mu_{\text{sc}}(Z_i)$  can be absorbed into  $Q_\alpha$ , the rest mass difference between the reactants and products, defined in Equation (2.33).  $Q_\alpha$  thus becomes

$$\begin{aligned} Q_\alpha &= Q_{\alpha, \text{no-sc}} + \sum_{i \in \mathcal{R}_\alpha} N_i^\alpha \mu_{\text{sc}}(Z_i) - \sum_{j \in \mathcal{P}_\alpha} N_j^\alpha \mu_{\text{sc}}(Z_j) \\ &= Q_{\alpha, \text{no-sc}} + \mu_{\text{sc}}(Z_1) + \mu_{\text{sc}}(Z_2) - \sum_{j \in \mathcal{P}_\alpha} N_j^\alpha \mu_{\text{sc}}(Z_j). \end{aligned} \quad (2.78)$$

Substituting the above corrected expressions for  $\lambda_\alpha$  and  $Q_\alpha$  into Equation (2.32) yields

$$\begin{aligned}
\lambda_{\alpha'} &= \lambda_{\alpha', \text{no-sc}} \exp(\beta\mu_{\text{sc}}(Z_1) + \beta\mu_{\text{sc}}(Z_2) - \beta\mu_{\text{sc}}(Z_1 + Z_2)) \\
&\quad \times \exp\left(\sum_{j \in \mathcal{P}_\alpha} N_j^\alpha \beta\mu_{\text{sc}}(Z_j) - \beta\mu_{\text{sc}}(Z_1) - \beta\mu_{\text{sc}}(Z_2)\right) \\
&= \lambda_{\alpha', \text{no-sc}} \exp\left(\sum_{j \in \mathcal{P}_\alpha} N_j^\alpha \beta\mu_{\text{sc}}(Z_j) - \beta\mu_{\text{sc}}(Z_1 + Z_2)\right) \\
&= \lambda_{\alpha', \text{no-sc}} \exp\left(\sum_{j \in \mathcal{P}_\alpha} N_j^\alpha \beta\mu_{\text{sc}}(Z_j) - \beta\mu_{\text{sc}}(Z_\varphi^\alpha)\right), \tag{2.79}
\end{aligned}$$

where we used charge conservation, i.e.,  $Z_1 + Z_2 = \sum_{j \in \mathcal{P}_\alpha} N_j^\alpha Z_j = Z_\varphi^\alpha$ . Thus the screening factor for the inverse reaction (whose set of reactants is  $\mathcal{P}_\alpha$ ) is indeed exactly the generalized screening factor postulated in Equation (2.74). Thus we only need to know how to compute  $\mu_{\text{sc}}(Z)$ , which is the subject of the following sections. Note that in terms of the screened forward rate, we combine the above with detailed balance (Equation 2.32) to obtain the screened inverse rate

$$\begin{aligned}
\lambda_{\alpha'} &= \lambda_\alpha(T, \rho) \exp\left(\sum_{j \in \mathcal{P}_\alpha} N_j^\alpha \beta\mu_{\text{sc}}(Z_j) - \sum_{i \in \mathcal{R}_\alpha} N_i^\alpha \beta\mu_{\text{sc}}(Z_i)\right) \\
&\quad \times e^{-Q_\alpha/T} \Gamma_\alpha(T) M_\alpha^{3/2} \left(\frac{T}{2\pi}\right)^{3\Delta N_\alpha/2} (\rho N_A)^{-\Delta N_\alpha}, \tag{2.80}
\end{aligned}$$

where we used  $Z_\varphi^\alpha = Z_{\mathcal{R}}^\alpha$  since strong reactions conserve charge.

It now remains to find the screening chemical potential correction  $\mu_{\text{sc}}(Z)$  for a nuclide of charge  $Z$ . Thanks to *SkyNet*'s modularity, arbitrary expressions for  $\mu_{\text{sc}}(Z)$  can be plugged into the general screening framework. In the following sections, we describe the current implementation of  $\mu_{\text{sc}}(Z)$  in *SkyNet*.

## 2.4.2 Weak screening

The weak screening limit is the limiting case where the Coulomb interaction energy is much lower than the thermal energy, hence where  $\Lambda \ll 1$ . In this case, the electrostatic Poisson-Boltzmann equation describing the screening can be solved approximately to find (Salpeter, 1954)

$$-\frac{U_0}{T} = \frac{Z_1 Z_2 e^2}{\lambda_D T}, \tag{2.81}$$

where  $\lambda_D$  is the Debye screening length.  $\kappa_D = \lambda_D^{-1}$  is called the Debye wave number, and it is given by (Brown and Sawyer, 1997)

$$\kappa_D^2 = \sum_i \kappa_{D,i}^2, \quad (2.82)$$

where the Debye wave number of species  $[i]$  is

$$\kappa_{D,i}^2 = 4\pi(Z_i e)^2 \int \frac{d^3 p}{(2\pi)^3} \frac{\partial f_i(p, \mu_i)}{\partial \mu_i}, \quad (2.83)$$

where  $Z_i e$  is the charge,  $\mu_i$  is the chemical potential (defined in Equation 2.128), and  $f_i(p, \mu_i)$  is the distribution function of species  $[i]$ .

*SkyNet* assumes that the ions (nuclides) are non-degenerate and non-relativistic. Therefore, they obey Boltzmann statistics with  $E(p) = p^2/(2m_i) + m_i$ , where  $p$  is the momentum and  $m_i$  the mass of species  $[i]$ . Hence,

$$f_i(p, \mu_i) = \exp(-\beta(E(p) - \mu_i)) = \exp\left(\beta\mu_i - \frac{p^2\beta}{2m_i} - \beta m_i\right), \quad (2.84)$$

and so

$$\int \frac{d^3 p}{(2\pi)^3} \frac{\partial f_i(p, \mu_i)}{\partial \mu_i} = \int \frac{d^3 p}{(2\pi)^3} \beta f_i(p, \mu_i) = \beta n_i, \quad (2.85)$$

and hence,

$$\kappa_{D,i}^2 = 4\pi Z_i^2 e^2 \beta n_i, \quad (2.86)$$

where  $n_i$  is the number density of ion species  $[i]$ .

The electrons and positrons are allowed to be arbitrarily degenerate and arbitrarily relativistic. They are both fermions and thus follow Fermi-Dirac statistics, so

$$f_{e^\pm}(p, \mu_{e^\pm}) = \frac{1}{\exp(\beta(E(p) - \mu_{e^\pm})) + 1}, \quad (2.87)$$

where  $E(p)$  is the total energy

$$E(p) = \sqrt{m_e^2 + p^2}. \quad (2.88)$$

We find

$$\frac{\partial f_{e^\pm}(p, \mu_{e^\pm})}{\partial \mu_{e^\pm}} = \frac{\beta \exp(\beta(E(p) - \mu_{e^\pm}))}{[\exp(\beta(E(p) - \mu_{e^\pm})) + 1]^2} = \beta f_{e^\pm}(1 - f_{e^\pm}), \quad (2.89)$$

and so

$$\kappa_{D,e^\pm}^2 = 4\pi e^2 \beta \int \frac{d^3 p}{(2\pi)^3} 2f_{e^\pm}(1 - f_{e^\pm}), \quad (2.90)$$

where the extra factor of 2 in the phase space integral comes from the fact that fermions have two spin states, and we used  $Z_{e^\pm} = \pm 1$ .

The Debye length is thus

$$\lambda_D = \kappa_D^{-1} = \sqrt{\frac{1}{4\pi e^2 \beta n_I \zeta^2}}, \quad (2.91)$$

where

$$\zeta^2 = \frac{n_B}{n_I} \left[ \sum_i Z_i^2 Y_i + \frac{2}{n_B} \int \frac{d^3 p}{(2\pi)^3} (f_{e^-}(1 - f_{e^-}) + f_{e^+}(1 - f_{e^+})) \right]. \quad (2.92)$$

Note that the factor of  $n_B/n_I$  in  $\zeta$  occurs because we define  $\zeta$  as the RMS charge per ion rather than per nucleon. The two-body screening potential in Equation (2.81) becomes

$$-\frac{U_0}{T} = \frac{Z_1 Z_2 e^2}{\lambda_D T} = Z_1 Z_2 \zeta e^3 \sqrt{4\pi n_I} \beta^{3/2} = Z_1 Z_2 \zeta \Lambda_0, \quad (2.93)$$

and so the screening factor is

$$f_{\text{sc}} = e^{-U_0/T} = \exp(-Z_1 Z_2 \zeta \Lambda_0). \quad (2.94)$$

This is consistent with the result from Dewitt et al. (1973), who showed that in the weak screening case, the chemical potential correction due to screening is

$$\beta \mu_{\text{sc,weak}}(Z) = -\frac{1}{2} Z^2 \zeta \Lambda_0. \quad (2.95)$$

Combining the above with the expression for the general screening factor (Equation 2.74) yields

$$\begin{aligned} f_{\text{sc}} &= \exp(\beta \mu_{\text{sc,weak}}(Z_1) + \beta \mu_{\text{sc,weak}}(Z_2) - \beta \mu_{\text{sc,weak}}(Z_1 + Z_2)) \\ &= \exp\left(-\frac{1}{2} \zeta \Lambda_0 [Z_1^2 + Z_2^2 - (Z_1 + Z_2)^2]\right) \\ &= \exp(-Z_1 Z_2 \zeta \Lambda_0), \end{aligned} \quad (2.96)$$

as shown in Equation (2.94).

The integral in Equation (2.92) has to be evaluated numerically. First note that

$$\beta E(p) = \beta \sqrt{m_e^2 + p^2} = \beta m_e \sqrt{1 + \left(\frac{p}{m_e}\right)^2} = \gamma_e \sqrt{1 + y^2}, \quad (2.97)$$

where we define  $\gamma_e = \beta m_e = m_e/T$  and  $y = p/m_e$ . Performing the change of variable from  $p$  to  $y$  and using the fact that the integrand only depends on the magnitude of the momentum  $p$ , we find

$$\begin{aligned} \int \frac{d^3 p}{(2\pi)^3} f_{e^\pm}(1 - f_{e^\pm}) &= \frac{4\pi}{(2\pi)^3} \int_0^\infty dp p^2 f_{e^\pm}(1 - f_{e^\pm}) \\ &= 4\pi \left(\frac{m_e}{2\pi}\right)^3 \int_0^\infty dy y^2 f_{e^\pm}(y, \mu_{e^\pm})(1 - f_{e^\pm}(y, \mu_{e^\pm})), \end{aligned} \quad (2.98)$$

where

$$f_{e^\pm}(y, \mu_{e^\pm}) = \frac{1}{\exp\left(\gamma_e \sqrt{1 + y^2} - \beta \mu_{e^\pm}\right) + 1}. \quad (2.99)$$

Recall that the electron and positron chemical potentials  $\mu_{e^\pm}$  are given by the EOS (Equations 2.134 and 2.135), and so we have all the ingredients to evaluate the integral in Equation (2.92) numerically. *SkyNet* uses the adaptive QAG integration routines provided by the GNU Scientific Library<sup>6</sup> to evaluate the integral.

### 2.4.3 Strong and intermediate screening

In the strong screening limit, the Poisson-Boltzmann equation governing screening has to be solved numerically. Dewitt et al. (1973) found that

$$\begin{aligned} \beta \mu_{\text{sc, strong}}(Z) &= -\frac{Z}{\bar{Z}} \left[ Z^{2/3} \bar{Z}^{4/3} \Gamma_0 \left( c_0 + c_1 \left(\frac{\bar{Z}}{Z}\right)^{1/3} + c_2 \left(\frac{\bar{Z}}{Z}\right)^{2/3} \right) \right. \\ &\quad \left. + d_0 + d_1 \left(\frac{\bar{Z}}{Z}\right)^{1/3} \right], \end{aligned} \quad (2.100)$$

where  $c_0 = 9/10$ ,  $c_1 = 0.2843$ ,  $c_2 = -0.054$ ,  $d_0 = -9/16$ , and  $d_1 = 0.4600$ . The parameter  $\Gamma_0$  is

$$\Gamma_0 = \Lambda_0^{2/3} / 3^{1/3}, \quad (2.101)$$

and the applicable average charge per ion is the arithmetic mean  $\bar{Z}$ , instead of the RMS  $\zeta$ , which is given by

$$\bar{Z} = \frac{\sum_i Z_i Y_i}{\sum_i Y_i}. \quad (2.102)$$

<sup>6</sup>[https://www.gnu.org/software/gsl/manual/html\\_node/Numerical-Integration.html](https://www.gnu.org/software/gsl/manual/html_node/Numerical-Integration.html)

We can write Equation (2.100) in terms of  $\Lambda_0$  as

$$\begin{aligned} \beta\mu_{\text{sc,strong}}(Z) = & -\Lambda_0^{2/3} \left( 0.6240 Z^{5/3} \bar{Z}^{1/3} + 0.1971 Z^{4/3} \bar{Z}^{2/3} - 0.0374 Z \bar{Z} \right) \\ & + \frac{9}{16} \frac{Z}{\bar{Z}} - 0.4600 \left( \frac{Z}{\bar{Z}} \right)^{2/3}, \end{aligned} \quad (2.103)$$

which is valid when  $\Gamma = \bar{Z}^2 \Gamma_0 \gg 1$ . Alternatively, if  $\zeta \sim \bar{Z}$ , then  $\Gamma \sim \Lambda^{2/3}$  and so the strong screening limit applies if  $\Lambda \gg 1$ . The strong screening limit is also applicable if  $\Lambda \ll 1$  but the charge  $Z$  is such that  $Z\zeta^2\Lambda_0 \gg 1$ . Then strong screening applies for charge  $Z$  (Dewitt et al., 1973).

The intermediate screening regime is where  $\Lambda = \zeta^3 \Lambda_0 \sim 1$ , in which case Dewitt et al. (1973) found

$$\beta\mu_{\text{sc,intermediate}}(Z) = -0.380 \Lambda_0^b \eta_b Z^{b+1}, \quad (2.104)$$

where  $b = 0.860$  and

$$\eta_b = \frac{\sum_i Z_i^{3b-1} n_i / n_I}{\zeta^{3b-2} \bar{Z}^{2-2b}} = \frac{n_B \sum_i Z_i^{3b-1} Y_i}{n_I \zeta^{3b-2} \bar{Z}^{2-2b}}. \quad (2.105)$$

#### 2.4.4 Combining the different screening regimes

Equations (2.95), (2.103), and (2.104) give the chemical potential corrections in the limit of weak, strong, and intermediate screening, respectively. To smoothly transition between these three regimes, we need a single parameter that determines which regime is applicable and a function that smoothly interpolates between the regimes based on said parameter.

Weak screening applies if  $\Lambda = \zeta^3 \Lambda_0 \ll 1$  and strong screening if  $\Lambda \gg 1$  or  $\Lambda \ll 1$  but  $Z\zeta^2\Lambda_0 = \Lambda Z/\zeta \gg 1$ . We thus define the dimensionless parameter

$$p(Z) = \Lambda + \Lambda \frac{Z}{\zeta} = (\zeta + Z)\zeta^2 \Lambda_0. \quad (2.106)$$

Note that  $p(Z) \ll 1$  if and only if  $\Lambda \ll 1$  and  $\Lambda Z/\zeta \ll 1$ , in which case weak screening applies. If and only if  $\Lambda \gg 1$  or  $\Lambda Z/\zeta \gg 1$  is  $p(Z) \gg 1$ , in which case we are in the strong screening regime. If  $p(Z) \sim 1$ , then intermediate screening applies. To ensure a smooth transition of  $\beta\mu_{\text{sc}}$  from one regime to another, we will compute the screening correction as a weighted sum of the corrections computed in the different regimes. Hence we compute

$$\beta\mu_{\text{sc}}(Z) = f_w \beta\mu_{\text{sc,weak}}(Z) + f_s \beta\mu_{\text{sc,strong}}(Z) + f_i \beta\mu_{\text{sc,intermediate}}(Z), \quad (2.107)$$

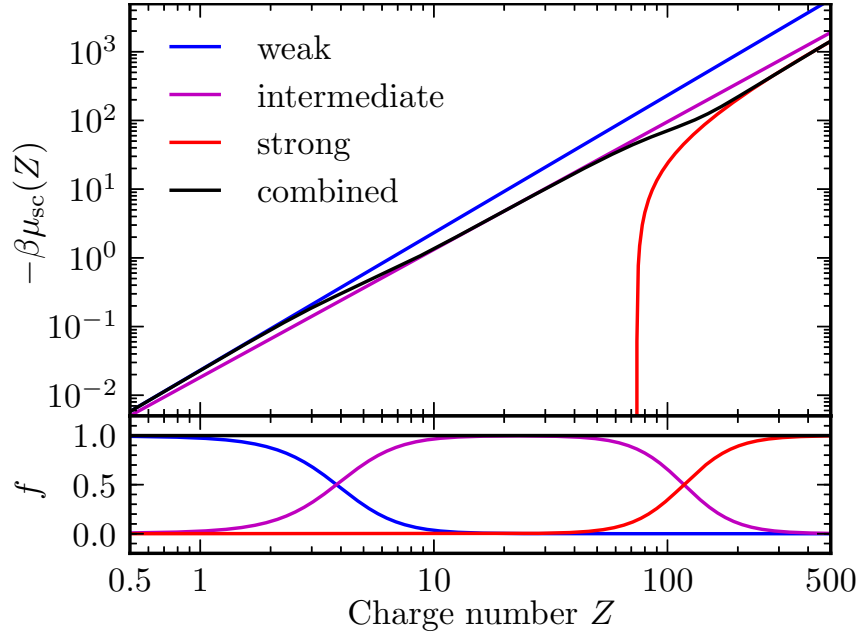


Figure 2.3: Screening correction to the chemical potential for a test particle with charge  $Z$ . The upper panel shows the corrections from the weak, intermediate, and strong regimes, as well as the combined correction. The bottom panel shows the functions  $f_w$ ,  $f_i$ , and  $f_s$  that are used to weight the chemical potential corrections due to weak, intermediate, and strong screening. These screening corrections are computed at  $T = 3$  GK,  $\rho = 2 \times 10^9$  g cm $^{-3}$  with a composition consisting of 59% neutrons, 40% protons, and 1% U $^{238}$  (by mass).

where each coefficient  $f_j$  is between 0 and 1 and defined as

$$f_w(p) = \frac{1}{2} [\tanh(-2 \ln p - \ln 25) + 1], \quad (2.108)$$

$$f_s(p) = \frac{1}{2} [\tanh(2 \ln p - \ln 25) + 1], \quad (2.109)$$

$$f_i(p) = \frac{1}{2} [\tanh(2 \ln p + \ln 25) + \tanh(-2 \ln p + \ln 25)]. \quad (2.110)$$

Note that  $f_w(p) + f_s(p) + f_i(p) = 1$  for all values of  $p$ . The transition from weak to intermediate screening occurs at  $p(Z) = 1/\sqrt{25} = 0.2$  and the transition from intermediate to strong screening at  $p(Z) = \sqrt{25} = 5$ .

Figure 2.3 demonstrates the transition between the different screening regimes. We choose a composition consisting of 59% neutrons, 40% protons, and 1% U $^{238}$  (by mass) at  $T = 3$  GK and  $\rho = 2 \times 10^9$  g cm $^{-3}$ . In this composition, all three screening regimes occur as the charge number of a test particle ranges from  $Z = 1$  to  $Z \sim 100$ . In order to show the transitions more clearly, we plot the chemical potential corrections from the different regimes for  $Z$  ranging from 0.5 to 500 in Figure 2.3.

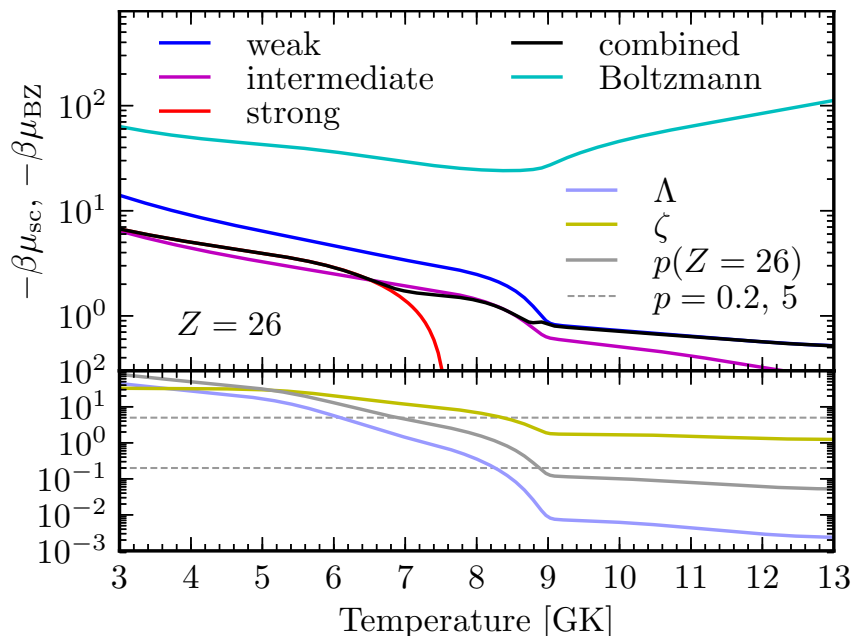


Figure 2.4: Screening correction to the chemical potential as a function of temperature for a fixed charge  $Z = 26$ . The composition is computed from NSE with screening corrections with the given temperature,  $\rho = 10^8 \text{ g cm}^{-3}$ , and  $Y_e = 0.4$ . The upper panel shows the screening corrections from the weak, intermediate, and strong screening regimes, as well as the combined correction. The Boltzmann chemical potential  $\mu_{BZ}$  of  $^{56}\text{Fe}$  (Equation 2.128 without the rest mass) is also shown for comparison. The lower panel shows the screening parameter  $\Lambda$  (Equation 2.70) and average charge per ion  $\zeta$  (Equation 2.92) computed from the composition, and the  $p(Z)$  parameter used to transition between the different regimes for  $Z = 26$ . The dashed gray lines show the values of  $p$  at which the transitions from strong to intermediate screening ( $p = 5$ ) and from intermediate to weak screening ( $p = 0.2$ ) happen.

Such charge numbers are not expected to occur in reality, but the expressions for the chemical potential corrections are valid nonetheless. The chosen composition results in  $\Lambda_0 = 0.05089$ ,  $\zeta = 0.9104$ ,  $\bar{Z} = 0.4079$ ,  $\eta_b = 0.6214$ , and  $\Lambda = 0.03840$ .

Whereas Figure 2.3 shows the screening correction for different ion charges in a fixed composition, Figure 2.4 shows the screening correction for a fixed charge ( $Z = 26$ ) in different compositions determined by the temperature  $T$ . Also shown is the Boltzmann chemical potential (Equation 2.128 without the rest mass) for  $^{56}\text{Fe}$ . The composition is determined from NSE with screening corrections (Section 2.4.5) using a temperature ranging from 3 to 13 GK,  $\rho = 10^8 \text{ g cm}^{-3}$ , and  $Y_e = 0.4$ . At low temperatures ( $T \lesssim 7 \text{ GK}$ ), strong screening is applicable since the thermal energy is small and Coulomb interactions dominate. Electron screening provides

a 10% correction over the unscreened Boltzmann chemical potential. Intermediate screening is applicable between 7 and 9 GK. At 9 GK,  ${}^4\text{He}$  nuclei are broken up and free neutrons and protons start to dominate the composition. Thus  $\zeta$  remains roughly constant at 1, and so  $\Lambda$  and  $p(26)$  also stop changing rapidly because  $\Lambda_0$  does not depend strongly on the temperature.  $T \sim 9$  GK is also where weak screening sets in, because the thermal energy now overcomes the Coulomb interaction energy, which has been reduced by the smaller average charge per ion provided by the free protons. In that regime, the screening effect is at the 4% to 0.5% level.

Figure 2.4 also shows that our screening corrections are indeed approximate. The weak and intermediate screening corrections never meet, so any scheme to transition between them is necessarily approximate and arbitrary to some degree. But considering the fact that our transition scheme needs to work robustly for a wide range of compositions and ion charges, it seems to do reasonably well in interpolating between the different (somewhat disjoint) screening regimes. While progress has been made in improving screening calculations in various regimes, a unifying theory for screening across all regimes still eludes (e.g., Itoh et al., 1977; Shaviv and Shaviv, 1996; Shaviv and Shaviv, 2000; Chugunov et al., 2007).

### 2.4.5 NSE with screening

As was noted above, in addition to screening nuclear reactions electronic correlations also change the free energetic cost of adding or removing a charged particle from the medium. Therefore, the chemical potentials of the nuclides have an ‘additional correction due to screening, i.e.,  $\mu_i = \mu_{i,\text{no-sc}} + \mu_{\text{sc}}(Z_i)$ , where  $\mu_{i,\text{no-sc}}$  is the unscreened chemical potential given by Equation (2.128) and  $\mu_{\text{sc}}(Z_i)$  is the screening correction given by Equation (2.107) with  $Z_i$  being the charge number of nuclide  $i$ . Thus Equation (2.148) becomes

$$\hat{\mu}_i = \mu_{i,\text{no-sc}} + \mu_{\text{sc}}(Z_i) - m_i - \text{BE}_i, \quad (2.111)$$

which means Equation (2.154) gives

$$Y_i = e^{\eta_i - \beta \mu_{\text{sc}}(Z_i) + \beta \text{BE}_i} \frac{G_i(T)}{n_B} \left( \frac{m_i T}{2\pi} \right)^{3/2}, \quad (2.112)$$

where  $\beta = 1/T$ . Note that  $\mu_{\text{sc}}(Z_i)$  depends on all  $Y_i$  because the screening corrections depend on different types of average ion charges ( $\bar{Z}$ ,  $\zeta$ , and  $\eta_b$ ). Thus the screening corrections introduce a large number of complicated partial derivatives to the Jacobian, which we will not attempt to write down. We have experimented with

using numerical derivatives to compute the Jacobian, with limited success. Another complication is that Equation (2.112) itself depends on all  $Y_i$  on the right-hand side and thus has to be solved iteratively.

We find that it is much more robust to keep the screening corrections fixed during the NR iterations. This does not introduce any additional derivatives in the Jacobian. NSE is computed exactly as shown in Appendix 2.B, with the only difference that Equation (2.112) is used to compute  $Y_i$  from  $\eta_i$ , but the terms  $\beta\mu_{\text{sc}}(Z_i)$  are constant throughout the NR iterations. In this case, to obtain an NSE composition that is self-consistent with the screening corrections it is based on, the NSE computation itself needs to be iterated.

We start by computing the NSE composition without screening (i.e.,  $\mu_{\text{sc}}(Z_i) = 0$ ). We denote the resulting composition by  $\mathbf{Y}^{(0)}$ . Then we compute  $\mu_{\text{sc}}(Z_i)$  based on  $\mathbf{Y}^{(0)}$  and use these as the constant screening corrections for the next NSE computation that yields  $\mathbf{Y}^{(1)}$ . From this new composition we compute new screening corrections, which are used to compute  $\mathbf{Y}^{(2)}$  and so on. This iteration stops once  $\max_i(|Y_i^{(n+1)} - Y_i^{(n)}|) < 10^{-12}$  or  $n$  reaches 20 (both of these criteria can be changed by the user). This method of iteratively updating the screening corrections and computing NSE with them being fixed is not guaranteed to converge (but neither is the NR method itself). However, in practice we find that this method works very well and converges quite quickly in a large region of parameter space.

Figure 2.5 shows the NSE abundance distribution as a function of mass number  $A$  for three different temperatures. For all temperatures,  $\rho = 10^8 \text{ g cm}^{-3}$  and  $Y_e = 0.4$ , so this is the same composition as the one shown in Figure 2.4. To show the impact of the screening corrections, the NSE compositions with and without screening are shown in the left panel. Screening is strongest for  $T = 3 \text{ GK}$  and the effect of screening is to reduce the abundances below  $A \sim 80$  and slightly increase them above that mass number. Screening is weaker at  $T = 8 \text{ GK}$ , but still enhances the high-mass abundances above  $A \sim 60$ . Finally, for  $T = 13 \text{ GK}$ , screening has virtually no effect. In the right panel of Figure 2.5 we show the ratio of the screening chemical potential  $\mu_{\text{sc}}$  to the Boltzmann chemical potential  $\mu_{\text{BZ}}$  (Equation 2.128 without the rest mass).  $\mu_{\text{sc}}$  depends on the composition and the charge, hence it is the same for all isotopes of a given element. But the Boltzmann chemical potential also depends on the mass, partition function, and the abundance of a given isotope. Thus for a given charge number  $Z$ , the ratio  $\mu_{\text{sc}}/\mu_{\text{BZ}}$  varies for the isotopes of that charge. In Figure 2.5, we show the range of the chemical potential ratios as colored bands. The

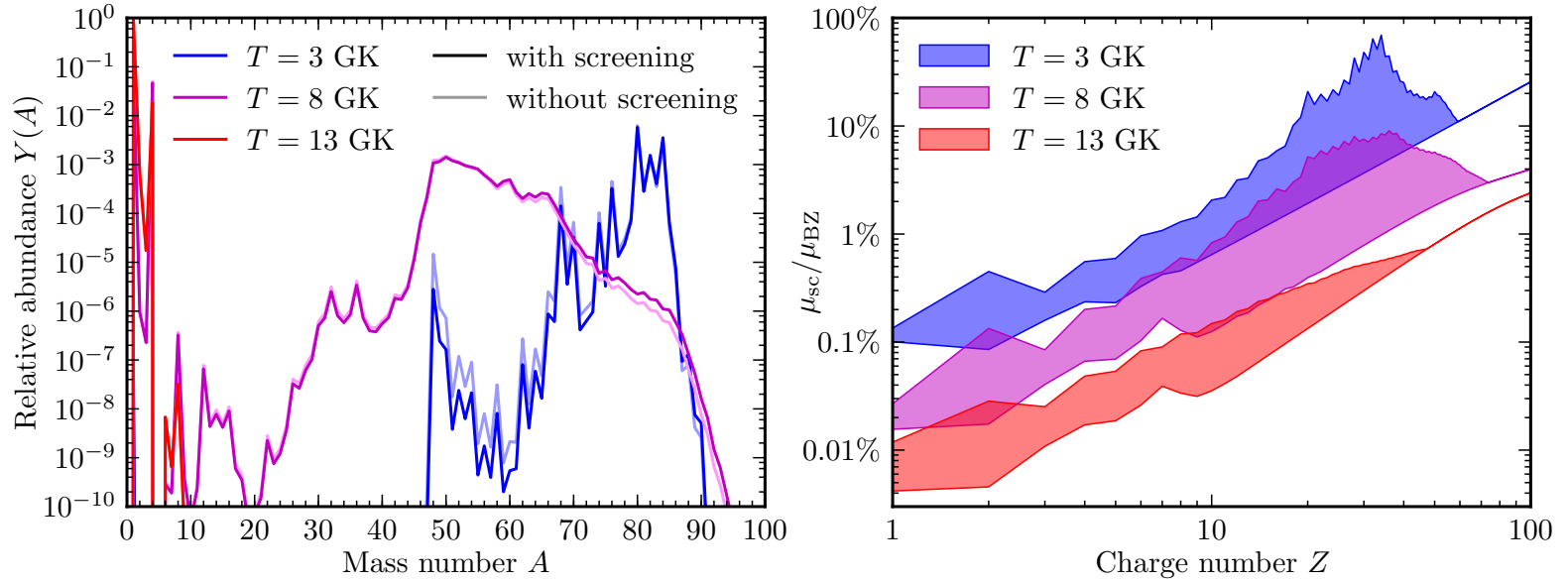


Figure 2.5: NSE compositions with and without screening at different temperatures. In all cases,  $\rho = 10^8 \text{ g cm}^{-3}$  and  $Y_e = 0.4$ . **Left:** Abundances as a function of mass number  $A$  of the compositions with and without screening. Screening pushes the abundance distribution to slightly higher masses. The effect at  $T = 3$  GK is clearly visible. At  $T = 8$  GK the screening effect is quite small and at  $T = 13$  GK it is practically absent. **Right:** The ratio of the screening chemical potential correction to the Boltzmann chemical potential (Equation 2.128 without the rest mass). The bands show the range of this ratio for all isotopes with the same charge number  $Z$ . The screening correction can be as large as 70% in the  $T = 3$  GK case, and as low as 0.004% for  $T = 13$  GK. At high  $Z$  where the bands collapse, all isotopes of the same element have the same screening to Boltzmann chemical potential ratio, because their abundances are all extremely small.

bands collapse to a line at large  $Z$ , because there the abundances of all isotopes are essentially zero. In the strongest screening case ( $T = 3$  GK), the screening effect ranges from 0.1% to 70%. For  $T = 8$  GK, it ranges from about 0.02% to 10%. And for  $T = 13$  GK, the screening effect is much less than 1% except for very large  $Z$ .

## 2.5 Implementation details

The main design goals of *SkyNet* are usability and flexibility. Since *SkyNet* is built in a modular fashion, different physics implementations can easily be switched out or new physics can be added, making *SkyNet* very flexible (see next sections for details). To achieve the modularity, *SkyNet* is written in object-oriented C++ and makes use of some C++11 features. *SkyNet* contains a small amount of Fortran code to provide a minimal interface for *SkyNet* to be called from Fortran. CMake (<http://www.cmake.org>) provides a cross-platform, compiler-independent build system for *SkyNet* that automatically finds the required external libraries. CMake also provides an automated testing facility and *SkyNet* comes with a suite of tests that check basic functionality and correctness of *SkyNet*.

To make it easy to use, *SkyNet* comes with Python bindings that make it possible to use all parts of *SkyNet* from an interactive Python shell or a Python script. Therefore, one can use standard Python libraries like *NumPy* (<http://www.numpy.org>) to read in and manipulate input data, like the list of nuclides to be evolved, the initial composition, density vs. time history, etc., and this data can be passed to *SkyNet* using standard Python data structures. This means that one does not have to deal with C++ to run *SkyNet*. But of course, *SkyNet* can also be used from a C++ or Fortran application. One can even run multiple copies of *SkyNet* in parallel within Python, using Python's `multiprocessing` module—a facility we use extensively whenever post-processing nucleosynthesis on many tracer particles from hydro simulations (e.g., Roberts et al., 2017; Lippuner et al., 2017). An example of how to run *SkyNet* in parallel with Python is included with the *SkyNet* source code available at <https://bitbucket.org/jlippuner/skynet>. The *SkyNet* Python bindings are provided by SWIG (<http://www.swig.org>) and using Python is the most convenient and most flexible way to run *SkyNet*.

### 2.5.1 Modularity and extendability

*SkyNet* is a modular library of different C++ classes rather than a monolithic program. Some of the most important classes in *SkyNet* are: various reaction library classes that contain different types of nuclear reactions (see next section), a nu-

clide library class that contains all nuclear data, and a reaction network class that implements the actual nuclear reaction network. There are various other types of classes that implement specific functionalities. For example, there are different function interpolation classes, ODE integrators, and general numerical method classes (bisection, line search). On the physics side, there are different classes that are responsible for different pieces of physics. The NSE class computes NSE given an electron fraction and two of the following properties: temperature, density, entropy, or internal energy. And there are separate classes that are responsible for the EOS and screening corrections.

Since *SkyNet* is built in an object-oriented fashion, different parts of the code are separated from each other and only interact via well-defined interfaces. This makes *SkyNet* extremely modular, because the implementation of a certain class can be changed or extended, without having to modify the rest of the code. For example, one could easily extend the nuclide library class to support reading in nuclear data from a different file format. Since all the nuclear data is handled by this one class, only this class has to be modified to support the new file format. Furthermore, some classes are implemented as abstract base classes, meaning they only specify the interface for a particular physics module without tying it to a specific implementation. Examples of this are the EOS class and the screening corrections class. For both of these, *SkyNet* currently has one implementation, namely the extended Timmes EOS described in Section 2.A.2 and the screening corrections discussed in Section 2.4. One can easily add a new EOS class that implements a different EOS but has the same interface as the abstract EOS base class. This new EOS class then plugs into the existing *SkyNet* framework. In a similar way, one can add additional screening implementations to *SkyNet*.

The various classes provided in *SkyNet* can be used individually through the Python bindings. For instance, one can use the NSE class in Python to compute NSE in various conditions, or use the nuclide library class to access the nuclear data and partition functions from Python.

### 2.5.2 Nuclear reaction libraries

*SkyNet* supports different types of nuclear reactions. Reactions of the same type or from the same data source are grouped into reaction library classes. The network class contains an arbitrary list of reaction library classes that collectively contain all the reactions that are evolved in the network. The reaction library classes have

a common interface that allows the network to be agnostic to how the reaction rate is determined. Via this interface, the network can tell the reaction libraries to recompute the reaction rates for a given thermodynamic state (temperature, density, electron fraction, electron degeneracy parameter, etc.), to get the contributions to all  $\dot{Y}_i$  from the reactions in the network, and to get the contributions to  $\partial\dot{Y}_i/\partial Y_j$ . This makes *SkyNet* extremely flexible because many different types of reactions can be evolved at the same time, and furthermore, the data for reactions of the same type can be split across multiple files, allowing the user to quickly switch out certain reactions. Finally, thanks to the abstract interface of reaction library classes, it is easy to add new types of reactions to *SkyNet*.

The following reaction types of nuclear reactions are currently implemented in *SkyNet*.

- **Constant:** These reactions have a constant rate that does not depend on any properties of the thermodynamic state.
- **REACLIB:** These are reactions that come from the REACLIB database (Cyburt et al., 2010). The rates of these reactions are given by parametric fitting formulae that depend on temperature and density.
- **FFN:** This reaction library contains the tabulated  $\beta$ -decay (both  $\beta^-$  and  $\beta^+$ ) and electron/positron capture rates from Fuller et al. (1982). The rates are tabulated as a function of temperature and  $Y_e\rho$ .
- **Neutrino interactions:** These are neutrino emission and absorption reactions on free neutrons and protons. The rates are calculated according to Equations (2.184) to (2.187) given the electron neutrino and electron antineutrino distribution functions.
- **Arbitrary rate functions:** This reaction library contains reactions whose rates are given by arbitrary, user-specified functions. This can be used to quickly test a new or modified reaction rate that can depend on various thermodynamic quantities and also time.

Since the different reaction types and rate sources can be used concurrently in *SkyNet*, care must be taken to ensure that no reaction rate is contained multiple times in the network, since that would effectively multiply the reaction rate by the number of times it occurs. *SkyNet* provides a facility to remove all reactions in one

reaction library that also occur in another library. However, in some cases, there are supposed to be multiple rates for the same reaction. In this case, the total reaction rate is the sum of the individual rates. REACLIB uses this mechanism to capture different resonant and non-resonant parts of a reaction rate with its limited fitting formula.

## 2.6 Code verification and tests

In order to verify the correctness of *SkyNet*, we compare its results to the results of other existing reaction network codes, specifically *WinNet* (Winteler, 2013) and *XNet* (Hix and Thielemann, 1999), and also to results published in the literature. The scripts and input files to reproduce these code tests are distributed with *SkyNet* in the directory `examples/code_tests`. *SkyNet* also has a test suite that contains simple code tests, regression tests, and tests that compare very simple networks to analytic solutions. The main purpose of that test suite is to ensure that changes to the code do not break the functionality or correctness of *SkyNet*.

### 2.6.1 Nuclear statistical equilibrium

To verify the NSE solver in *SkyNet*, we perform a consistency test and comparison to literature results of the NSE abundances computed by *SkyNet*. We use nuclear masses and partition functions distributed with REACLIB (Cyburt et al., 2010), which contains experimental data where available and finite-range droplet macroscopic model (FRDM, see, e.g., Möller et al., 2016) data otherwise. The temperature dependent partition functions are from Rauscher and Thielemann (2000).

#### 2.6.1.1 Consistency test

In this section, we verify that the abundances computed with the NSE solver in *SkyNet* are consistent with the strong reactions. We perform a test evolution starting with purely free neutrons and protons and let only strong reactions take place. We use the strong reaction rates from REACLIB and the default fission rates distributed with *SkyNet*. The network contains 7824 nuclear species, ranging from free neutron and protons to  $^{337}\text{Cn}$  ( $Z = 112$ ). We keep the temperature constant at  $T = 7$  GK and the density  $\rho = 10^9$  g cm $^{-3}$  is also fixed. We pick these values to ensure that the composition achieves NSE within a reasonable amount of time. We set  $Y_e = 0.4$ , so the initial composition is  $Y_n = 0.6$  and  $Y_p = 0.4$ , and since the network does not contain any weak reactions, the electron fraction remains constant at  $Y_e = 0.4$ . Screening corrections are enabled for both the NSE solver and the

network evolution. At every step, we compare the network abundances to the NSE abundances and compute the error  $\Delta Y$  as

$$\Delta Y = \max_i |Y_i^{\text{network}} - Y_i^{\text{NSE}}|. \quad (2.113)$$

We perform two different network evolutions. One where the strong inverse rates are computed from detailed balance (Section 2.2.3) and another one where the inverse rates from REACLIB are used. We never use inverse fission reactions.

The results are shown in Figure 2.6. After evolving the network for about one second using detailed balance to compute the inverse rates, the network reaches the NSE composition. The error between NSE and the network composition is  $\Delta Y \sim 10^{-11}$  and the deviation of  $Y_e$  from 0.4 is on the same level. We note that this is comparable to the mass conservation limit of  $10^{-10}$  that *SkyNet* uses as the NR iteration convergence criterion. The neutron, proton, and helium abundances also match the values from the NSE composition with very high precision. This demonstrates that the NSE solver in *SkyNet* and the implementation of detailed balance for the inverse rates are consistent. The NSE compositions computed with *SkyNet* are indeed the compositions that the network produces if the strong reactions are in equilibrium.

Furthermore, Figure 2.6 also shows that the inverse rates provided in REACLIB are not completely consistent with the NSE composition that is computed from the nuclear data (masses and partition functions) distributed together with REACLIB. If the REACLIB inverse rates are used (“*SkyNet* no DB” in Figure 2.6), the network evolution is extremely slow. We stopped the network evolution after 420,000 steps at  $t \sim 0.152$  s when it became clear that  $\Delta Y$  converged to  $2.5 \times 10^{-4}$  (black arrow in Figure 2.6). But the deviation in  $Y_e$  from 0.4 is still growing rapidly at that point. The evolution without detailed balance becomes very slow because the inverse rates from REACLIB try to push the composition into a certain equilibrium configuration, but chemical potential balance predicts a different equilibrium composition. This makes the evolution very difficult and drives the time step down to  $\sim 10^{-14}$  s. Computing the inverse rates from detailed balance so that the inverse rates exactly cancel the forward rates when the chemical potentials balance is therefore necessary for the network evolution to be consistent with NSE (see Section 2.2.3). Detailed balance also makes the evolution much more straightforward, requiring only about 800 time steps to reach  $\Delta Y \sim 10^{-11}$  at  $t \sim 1$  s. We suspect that some of the inverse rates in REACLIB are not consistent with NSE because different nuclear data was

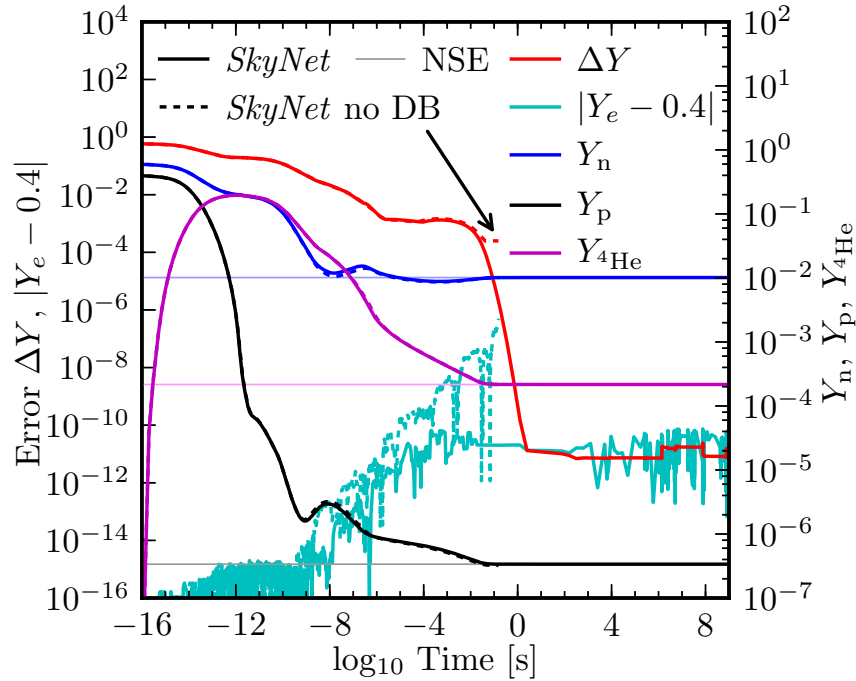


Figure 2.6: Evolving pure neutrons and protons to NSE with a fixed temperature  $T = 7$  GK, density  $\rho = 10^9$  g cm $^{-3}$ , and  $Y_e = 0.4$ . The evolution only includes strong reactions, because weak reactions would change the electron fraction. The thin light lines show the neutron, proton, and helium abundances of the NSE composition. The *SkyNet* evolutions are done with screening correction turned on. The solid lines are the quantities from the *SkyNet* evolution where the inverse rates are computed from detailed balance, while the dashed lines are from *SkyNet* without detailed balance, i.e., the inverse rates are taken from REACLIB. The error  $\Delta Y$  is the maximum abundance difference between the network and the NSE composition. We stop the network evolution without detailed balance after 420,000 time steps because the time step remained at around  $10^{-14}$  s after roughly 10,000 steps. Hence the dashed lines only extend to about 0.15 s. The error  $\Delta Y$  without detailed balance appears to converge to a few  $\times 10^{-4}$  (black arrow). In contrast, the evolution with detailed balance only requires about 800 steps to reach  $\Delta Y \sim 10^{-11}$ .

used to compute the REACLIB inverse rates than the data that is distributed with REACLIB, which we use to compute NSE.

### 2.6.1.2 Comparison with published results

We compare the *SkyNet* NSE solver to the NSE results with and without electron screening by Seitzzahl et al. (2009). The composition includes 443 nuclides ranging from free neutrons and protons to multiple isotopes of krypton (see Figure 1 in Seitzzahl et al., 2009). We compute NSE with and without screening at a fixed density of  $\rho = 5 \times 10^8 \text{ g cm}^{-3}$  and fixed  $Y_e = 0.5$  for temperatures ranging from 4 to 10 GK. The results are shown in Figure 2.7 along with the results from Seitzzahl et al. (2009, Figures 3 to 6, data used with permission).

We find excellent agreement between the *SkyNet* results and those presented in Seitzzahl et al. (2009). When screening corrections are included, the deviation between the two results is slightly larger, because Seitzzahl et al. (2009) use a different screening implementation. The effect of the different screening implementation is most pronounced for the proton mass fraction at  $T \gtrsim 9$  GK, but even then, the difference is less than 5%. Seitzzahl et al. (2009) use a fit for the screening corrections that has a significant correction even in the weak screening regime at  $T \gtrsim 8$  GK. On the other hand, the weak screening correction in *SkyNet* becomes much smaller at those temperatures. Hence the differences in the NSE mass fractions is due to the increased disagreement between the different screening corrections as the temperature increases. Furthermore, Seitzzahl et al. (2009) use different nuclear masses, so that could account for the small differences between our results and theirs when screening is turned off.

### 2.6.2 Network evolution

In this section, we present comparisons of nucleosynthesis evolutions with *SkyNet* and other nuclear reaction networks. We compare *SkyNet* to *WinNet* and *XNet*. *WinNet* was originally developed at the University of Basel by Winteler (2013) based on the earlier *BasNet* by Thielemann et al. (2011). *WinNet* has been used by various authors for r-process nucleosynthesis calculations in core-collapse supernovae and neutron star mergers, and to investigate the impact of nuclear physics on the r-process (e.g., Winteler et al., 2012; Korobkin et al., 2012; Martin et al., 2015; Eichler et al., 2015; Martin et al., 2016). *XNet* was developed at Oak Ridge National Laboratories by Hix and Thielemann (1999) and has been used for r-process nucleosynthesis in

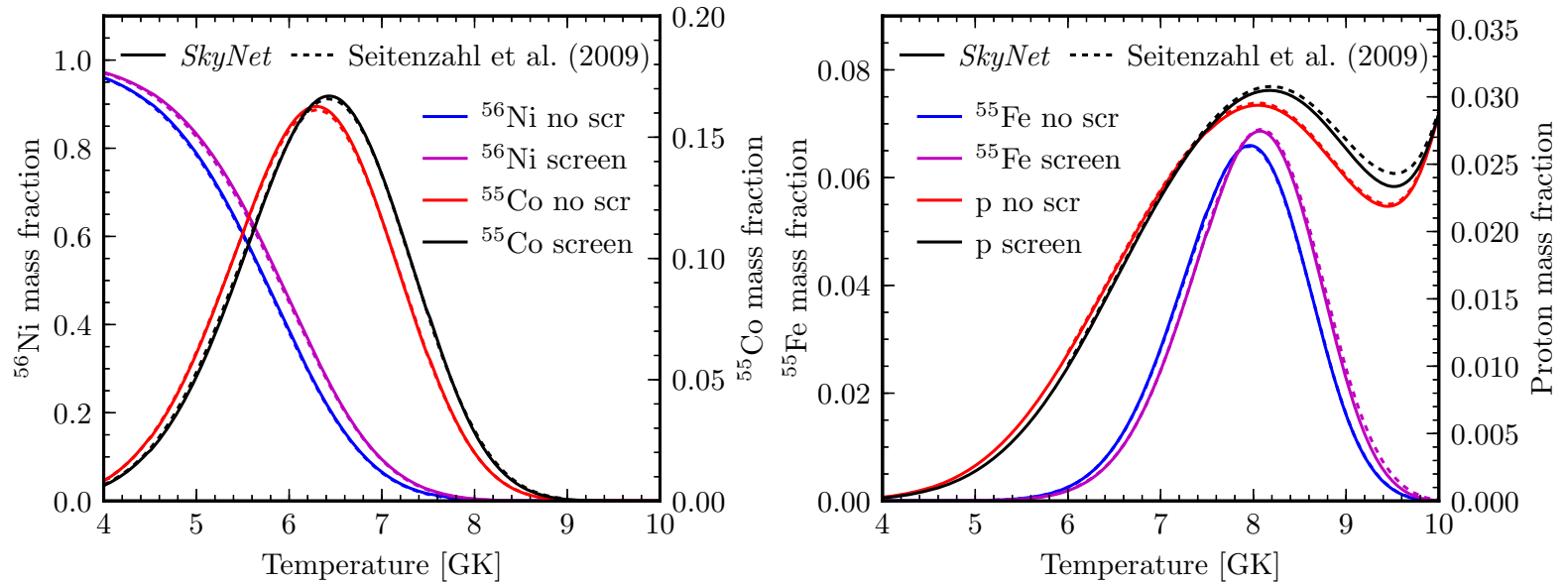


Figure 2.7: The  $^{56}\text{Ni}$ ,  $^{55}\text{Co}$ ,  $^{55}\text{Fe}$ , and proton mass fractions in an NSE composition with varying temperatures and fixed  $\rho = 5 \times 10^8 \text{ g cm}^{-3}$  and  $Y_e = 0.5$ . The composition includes 443 species and NSE is computed with and without screening corrections. The results are compared to those published in Seitenzahl et al. (2009) (data used with permission). We see excellent agreement between *SkyNet* and the published results. The differences are slightly enhanced when screening is turned on, due to the different screening implementations.

accretion disk outflows and neutron star mergers, and for explosive nucleosynthesis in type I X-ray bursts and core-collapse supernovae (e.g., Surman et al., 2006; Fisker et al., 2008; Roberts et al., 2011; Harris et al., 2017).

Since nuclear physics data, such as nuclear masses, partition functions, and nuclear reaction rates, have a significant influence on the nucleosynthesis calculations, we take care in ensuring that exactly the same nuclear physics input data are used for all the different codes that we consider. However, this means that we are restricted to using the greatest common denominator of nuclear physics data sources that can be used by all codes. For the comparisons in this section, we use the strong and weak reaction rates distributed in REACLIB (Cyburt et al., 2010), neutron induced fission reactions with symmetric fission fragments from Panov et al., 2010, and spontaneous fission rates calculated from the approximation of Frankel and Metropolis, 1947 using the spontaneous fission barriers of Mamdouh et al., 2001. The nuclear masses and partition functions are again the ones distributed with REACLIB, as in Section 2.6.1.

### 2.6.2.1 Neutron-rich r-process

We run an r-process nucleosynthesis calculation in a neutron-rich environment with all three networks. We use 7836 nuclear species and about 93,000 reactions. The density history is a trajectory from the ejecta of a black hole–neutron star merger (Roberts et al., 2017). The initial composition is NSE with  $T = 6.1$  GK,  $\rho = 7.4 \times 10^9$  g cm<sup>-3</sup>, and  $Y_e = 0.07$ . We run all combinations of screening and self-heating turned on and off. For each case, we perform two separate *SkyNet* evolutions: one where the inverse rates are computed from detailed balance, and another where the inverse rates from REACLIB are used. We consider these two cases because *SkyNet* is usually run with inverse rates computed from detailed balance, but *WinNet* and *XNet* use the inverse rates from REACLIB, and so we also run *SkyNet* with those inverse rates for a more direct comparison.

The self-heating method currently implemented in *XNet* only applies in the case of constant density (Harris, 2017). Hence for this r-process computation with an evolving density, we cannot use the self-heating capability of *XNet*. Instead, to compare *XNet* to *SkyNet* and *WinNet* when self-heating is turned on, we use the *SkyNet* temperature history (from the *SkyNet* run without detailed balance) in *XNet*. However, the temperature provided to *XNet* has to be limited to a lower bound of 0.01 GK. At temperatures lower than that, the reaction rate fits from REACLIB no

longer apply and some of the rates blow up. *SkyNet* internally also uses a lower bound 0.01 GK for the REACLIB reactions, but the network temperature used in the EOS is allowed to drop below that bound, until the lower limit of the EOS is reached at around  $4 \times 10^5$  K (this lower bound is due to the tabulated electron/positron part of the Timmes EOS).

Figure 2.8 shows the results of running the neutron-rich r-process with the three reaction networks with screening and self-heating turned on. We find excellent agreement between the different networks with the temperature evolution of *SkyNet* and *WinNet* being virtually indistinguishable (for *XNet* we prescribe the *SkyNet* temperature). The final abundances (at  $t = 5 \times 10^8$  s) also agree very well. To compare the results of the three networks quantitatively, we compute the numeric error between the final mass-summed abundances as

$$\text{error} = \frac{\sum_{A=1}^{A_{\max}} |Y_{\text{net1}}(A) - Y_{\text{net2}}(A)|}{\sum_{A=1}^{A_{\max}} \frac{Y_{\text{net1}}(A) + Y_{\text{net2}}(A)}{2}}, \quad (2.114)$$

where the mass-summed abundance  $Y(A)$  is given by

$$Y(A) = \sum_{\substack{i \text{ where} \\ A_i=A}} Y_i. \quad (2.115)$$

This error measure is the average absolute difference between the abundance results divided by the average abundances. This effectively measures the fractional error in the final abundances, averaged over all mass numbers  $A$ . However, we compute the quotient of the sums rather than the sum of quotients, because the latter would be dominated by tiny abundances ( $\sim 10^{-20}$ ) that may differ by a factor of several between the two networks. This would result in a large overall error, but abundance differences at the  $10^{-20}$  level are not important, even if it is by a factor of several.

Table 2.1 shows the errors in percent between the different networks. Since this is a neutron-rich environment, we expect that screening plays no important role in the nucleosynthesis evolution. The fact that the errors between the different networks are almost the same regardless whether screening is turned on or off confirms that screening is not important in this case. Furthermore, the error between *SkyNet* without detailed balance and *WinNet* or *XNet* are comparable to the errors between *WinNet* and *XNet*. For example, with screening and self-heating turned on (first

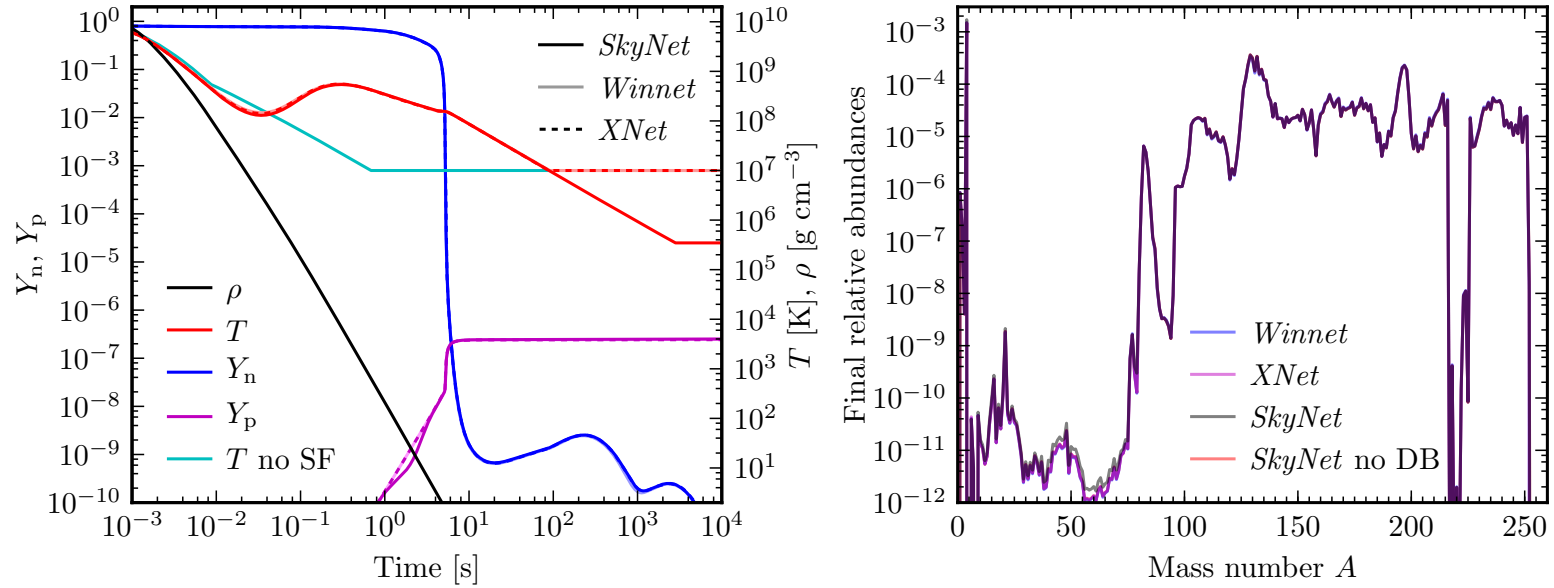


Figure 2.8: Neutron-rich r-process calculation with three different reaction networks: *SkyNet*, *WinNet*, and *XNet*. Screening corrections are turned on. *SkyNet* and *WinNet* evolve the temperature, but *XNet*'s temperature was fixed to that computed by *SkyNet* (with a lower bound of 0.01 GK). **Left:** Prescribed density  $\rho$  as a function of time, resulting temperature  $T$ , neutron abundance  $Y_n$ , and proton abundance  $Y_p$ . For comparison, the temperature without self-heating (SF) from the trajectory is also shown to illustrate the importance of self-heating. The solid dark lines show the *SkyNet* results, solid light lines are the *WinNet* results, and the dashed lines are the *XNet* results. The three networks agree extremely well with each other, with the lower temperature floor in *SkyNet* being the largest difference. The small deviation in  $Y_p$  at  $t \sim 2$  s is because *SkyNet* uses detailed balance to compute the inverse rates. Detailed balance also accounts for the small temperature difference around  $t = 0.01 - 0.1$  s. **Right:** Final abundances as a function of mass number  $A$  after  $5 \times 10^8$  s. Showing two *SkyNet* results: with detailed balance (DB) and without. We again see excellent agreement between the networks and the small differences around  $A = 50$  are again because of detailed balance. *SkyNet* without detailed balance matches *WinNet* and *XNet* in that region.

Table 2.1: Errors between the final mass-summed abundances between the different networks (Equation 2.114). S: *SkyNet* with detailed balance, SnoDB: *SkyNet* without detailed balance, W: *WinNet*, X: *XNet*. The error measures the average fractional difference between the final abundances. The numbers shown are in %. The three networks generally agree very well with each other. The error between *SkyNet* without detailed balance (SnoDB), *WinNet* (W), and *XNet* (X) are usually of similar magnitude and on the few percent level. The only exception are the self-heating runs of the hydrostatic C/O burn test case, which highlights the different self-heating implementations in the networks. We also see that using detailed balance for the inverse rates has a big impact in the first two test cases, especially when self-heating is turned off. Since *WinNet* and *XNet* do not use detailed balance, the error is bigger when they are compared to *SkyNet* with detailed balance (S).

Test case	screening	self-heating	S – SnoDB	S – W	SnoDB – W	S – X	SnoDB – X	X – W
Neutron-rich r-process (Section 2.6.2.1, Figure 2.8)	yes	yes/no*	3.2	5.8	3.3	3.2	0.061	3.4
	yes	no	34	35	4.5	33	2.5	3.6
	no	yes/no*	3.4	6.0	3.4	3.4	0.035	3.4
	no	no	33	36	3.3	33	0.77	3.3
Explosive X-ray burst (Section 2.6.2.2, Figure 2.9)	yes	yes/no*	0.40	1.3	0.92	1.3	1.0	1.2
	yes	no	13	14	4.0	11	3.5	3.3
	no	yes/no*	0.38	1.4	1.0	0.47	0.090	0.93
	no	no	17	18	1.5	18	1.2	0.40
Hydrostatic C/O burn (Section 2.6.2.3, Figure 2.10)	yes	yes	0.61	9.6	9.4	5.8	5.5	3.9
	yes	no	0.10	0.22	0.18	0.16	0.22	0.13
	no	yes	0.56	7.6	7.5	5.1	5.0	2.5
	no	no	0.10	0.27	0.17	0.10	0.00036	0.17

\* Self-heating is turned on in *SkyNet* and *WinNet*, but not in *XNet*, because its self-heating method does not apply in these test cases. Instead, *XNet* uses the temperature computed by the self-heating *SkyNet* run without detailed balance (SnoDB).

row in Table 2.1), the error between *SkyNet* without detailed balance and *WinNet* is 3.3%, while the error between *WinNet* and *XNet* is 3.4%, and the error between *XNet* and *SkyNet* without detailed balance is 0.061%. *SkyNet* is closer to *XNet* in this case because *XNet* uses the same temperature as *SkyNet* whereas *WinNet* evolves its own temperature. This demonstrates that *SkyNet* produces results that are compatible with *WinNet* and *XNet*. The errors between *SkyNet* and *WinNet* or *XNet* are larger if detailed balance is used to compute the inverse rates in *SkyNet*. For example, again for the first row in Table 2.1, the error between *WinNet* and *SkyNet* with detailed balance is 5.8%, but only 3.3% when compared to *SkyNet* without detailed balance. This is not surprising, because *SkyNet* is effectively evolving slightly different reaction rates when inverse rates are computed from detailed balance. It does illustrate, however, that using detailed balance, which produces inverse rates that are consistent with the nuclear masses and partition functions, has a significant impact and might be a reasonable standard practice. In the self-heating runs, *SkyNet* is much closer to *XNet* than *WinNet*, because *XNet* uses the temperature from *SkyNet*.

### 2.6.2.2 X-ray burst

In Figure 2.9, we show a comparison between the three networks for a different type of trajectory. This trajectory captures the situation of unstable hydrogen burning on the surface of a neutron star, which produces a type I X-ray burst, presented in Schatz et al. (2001). The density and temperature histories as well as the initial and final abundances were graciously provided by Schatz et al. (2001). The temperature starts at 0.2 GK and peaks at 1.9 GK during the burst. The density starts at  $1.1 \times 10^6 \text{ g cm}^{-3}$ . The initial composition is 66.0% hydrogen (by mass), 33.6% helium, and 0.4% heavier elements, mostly oxygen. For this test, we use a small network containing only 686 species going up to  $^{136}\text{Xe}$  and 8400 reactions.

We again see good agreement in Figure 2.9 between the three networks in the proton and helium abundance evolution (left panel of Figure 2.9). But there are a handful of mass numbers at which *SkyNet* with detailed balance produces final abundances that deviate from the other networks by up to two orders of magnitude (right panel of Figure 2.9). This indicates that it is vital to compute the inverse reaction rates correctly with detailed balance in this scenario. However, the average fractional abundance errors shown in Table 2.1 are still at the few percent level, and the differences between *SkyNet* and *WinNet* or *XNet* are comparable to the differences between *WinNet* and *XNet*. We note that the errors between *SkyNet* without detailed

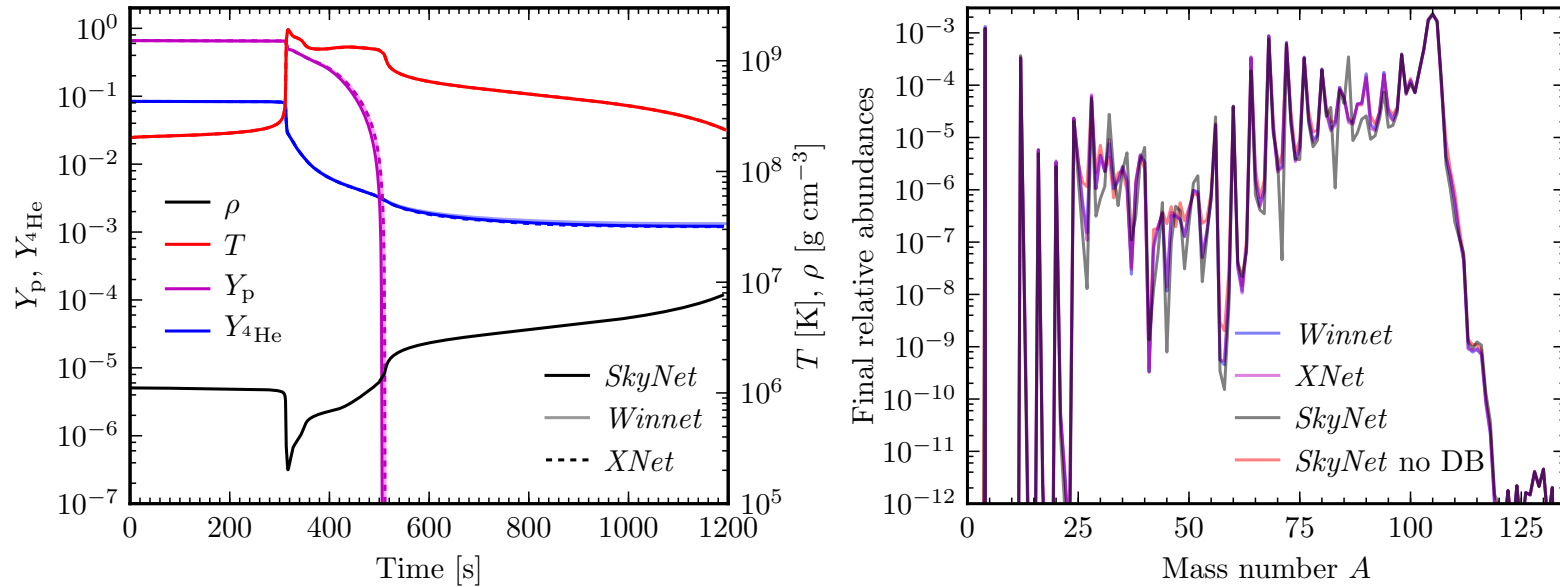


Figure 2.9: Explosive nucleosynthesis in an X-ray burst with three different reaction networks: *SkyNet*, *WinNet*, and *XNet*. Screening corrections are included, but self-heating is turned off for the computations shown in this figure so that the impact of screening can be presented. We use the temperature and density history from Schatz et al. (2001). **Left:** Prescribed density  $\rho$  and temperature  $T$  as a function of time, resulting proton abundance  $Y_p$ , and helium abundance  $Y_{4\text{He}}$ . All three networks agree very well with each other. **Right:** Final abundances as a function of mass number  $A$  at  $t = 1242.6$  s. Showing two *SkyNet* results: with detailed balance (DB) and without. *SkyNet* with detailed balance produces final abundances at some specific values of  $A$  that differ by up to two orders of magnitude from the other networks. This shows the importance of using detailed balance to compute inverse rates.

balance and *WinNet* or *XNet* are smaller if screening is turned off. This indicates that screening is somewhat important in this case and we expect the discrepancy between the different codes to increase if screening is turned on due to the different screening implementations. The effect is especially noticeable when comparing *SkyNet* to *XNet* with self-heating turned on, because in this case *XNet* uses the temperature computed from *SkyNet*, but if screening is switched off, the error between the two codes decreases from 1% to 0.09%.

*SkyNet*'s screening implementation is presented in Section 2.4. *WinNet* uses a single fit of the two-body screening factor by Chugunov et al. (2007) across all screening regimes. *XNet* computes the two-body screening function provided by Graboske et al. (1973) for weak and intermediate screening and the one provided by Dewitt and Slattery (1999) for strong screening. *XNet* then uses a selection rule to select one of the three screening regimes without interpolating between them.

### 2.6.2.3 Hydrostatic carbon-oxygen burning

In order to compare the self-heating methods implemented in the three networks, we perform a hydrostatic burn at constant density. We keep  $\rho = 10^7 \text{ g cm}^{-3}$  fixed and start with  $T = 3 \text{ GK}$  and the initial composition consists of half  $^{12}\text{C}$  and half  $^{16}\text{O}$  (by mass). As a baseline comparison, we also perform non-self-heating runs, where we keep the temperature fixed at 3 GK. The increase in the errors between the networks with self-heating enabled compared to with it disabled, must then be due to the difference in the self-heating implementations in the codes. We use a mid-size network containing all nuclides from the full network (Section 2.6.2.1) with  $A \leq 100$ . This results in a network with 1530 species and 20,000 reactions.

Figure 2.10 shows results of this test case with self-heating and screening turned on. We find good qualitative agreement between the three networks, but quantitatively, the differences are much larger than in the previous test cases. These discrepancies come from the different self-heating implementations in the three codes. *WinNet* uses the same self-heating method as *SkyNet* (described in Section 2.3.2), but *WinNet* does not include the entropy change due to the electron chemical potential. Also, *WinNet* uses the original Timmes EOS, which computes the entropy with a single representative heavy ion species, while *SkyNet* computes the entropy by considering all species in the network separately (Section 2.A.2). These two differences cause the temperatures of *SkyNet* and *WinNet* to disagree slightly, which then results in somewhat different abundances. *XNet*, on the other hand, uses a different self-

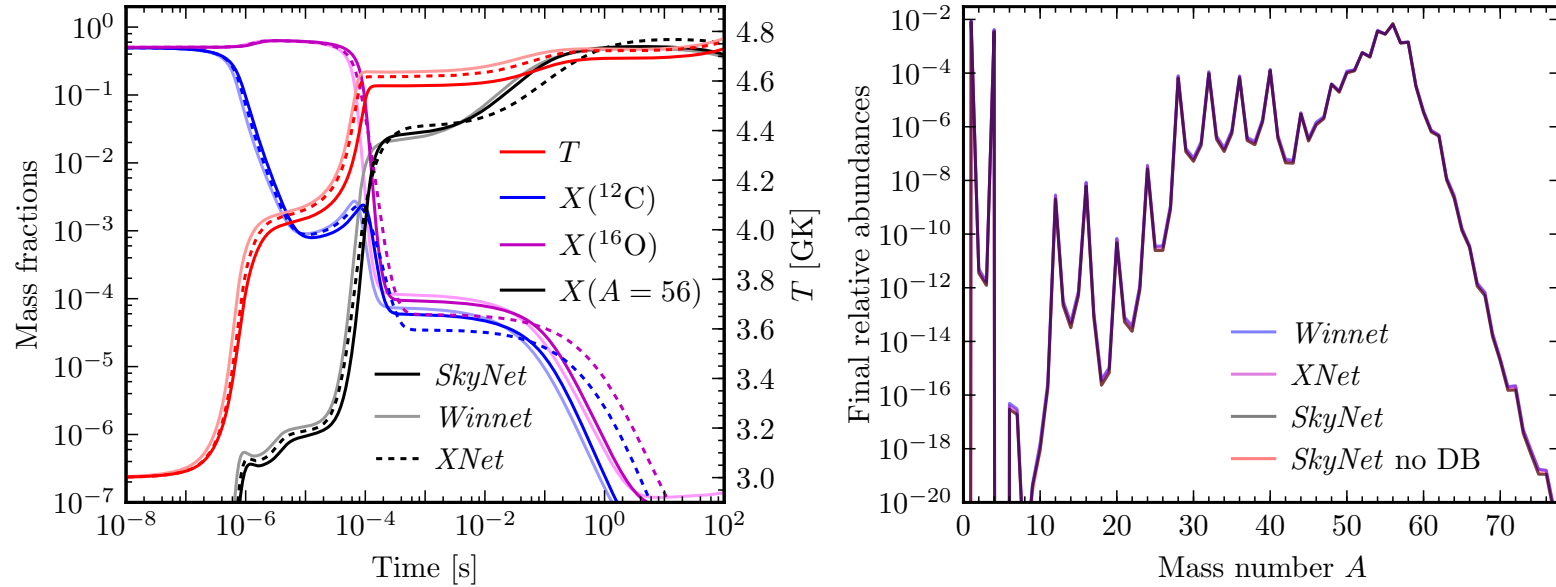


Figure 2.10: Hydrostatic burning of carbon and oxygen with three different reaction networks: *SkyNet*, *WinNet*, and *XNet*. The density is fixed at  $\rho = 10^7 \text{ g cm}^{-3}$  and the evolution starts with  $T = 3 \text{ GK}$  and half  $^{12}\text{C}$ , half  $^{16}\text{O}$  (by mass). Screening and self-heating are enabled in all three networks. **Left:** Resulting temperature  $T$ ,  $^{12}\text{C}$  and  $^{16}\text{O}$  mass fractions, and sum of the mass fractions of all isotopes with  $A = 56$ . We clearly see the difference in the self-heating implementations in the three codes. *SkyNet* and *WinNet* evolve the entropy and compute the temperature from it, which takes composition changes into account. *XNet* evolves the temperature directly solely based on the released nuclear binding energy, which becomes small after  $t \sim 10^{-4} \text{ s}$  and so the temperature stops changing in *XNet*. **Right:** Final abundances as a function of mass number  $A$  at  $t = 100 \text{ s}$ . Showing two *SkyNet* results: with detailed balance (DB) and without. The *XNet* results stand out due to the substantially different temperature in *XNet* after  $t \sim 10^{-4} \text{ s}$ .

heating method. It evolves the temperature directly using (Harris, 2017)

$$\frac{dT}{dt} = \frac{\dot{\epsilon}_{\text{nuc}}}{c_V} = -\frac{1}{c_V} \sum_i \dot{Y}_i \mathcal{M}_i, \quad (2.116)$$

where  $c_V$  is the specific heat capacity at constant volume (provided by the Timmes EOS),  $\dot{Y}_i = dY_i/dt$  is the abundance time derivative of species  $i$ , and  $\mathcal{M}_i$  is the mass excess. As can be seen in the left panel of Figure 2.10, this method is comparable to the methods in *SkyNet* and *WinNet*. Note that *XNet* is using exactly the same EOS as *WinNet*. We see only very small differences in the final abundances of the three networks in the right panel of Figure 2.10.

The differences in the self-heating implementations are also very apparent in Table 2.1. When self-heating is turned on, *XNet* differs from *SkyNet* and *WinNet* by about 3 to 6%, and *WinNet* differs from *SkyNet* by about 10% (slightly less if screening is turned off). However, when self-heating is disabled, the three networks agree at the 0.2% level, and if screening is turned off, *SkyNet* without detailed balance and *XNet* agree to an astounding precision of 0.0004%.

### 2.6.3 NSE evolution test

To ensure that the NSE evolution mode in *SkyNet* produces the correct results, we perform a test that evolves a trajectory with and without NSE evolution mode. Of course, the trajectory must experience some heating that forces the composition into NSE at some point during the evolution, otherwise the NSE evolution mode would not be triggered. We first attempt this test with a trajectory from a neutron star merger accretion disk outflow simulation (Lippuner et al., 2017). That trajectory experiences late-time fallback, which causes a spike in the density that results in late-time heating and forces the composition into NSE. While *SkyNet* is able to evolve this trajectory without issues using the NSE evolution mode, when NSE evolution mode is turned off, *SkyNet* gets stuck with a time step of  $\sim 10^{-16}$  s for at least 350,000 steps at the time when the heating occurs. Thus we cannot use this trajectory for this test, since we cannot evolve it without NSE evolution mode. However, this trajectory serves as an illustration of the necessity of the NSE evolution mode in order to evolve certain trajectories.

Since it is challenging to evolve a trajectory without NSE evolution mode that moves into NSE during the evolution, we use an artificial trajectory that has a temperature peak that is less than 8 GK. In practice, we found that a trajectory with a peak of 7.6 GK can be evolved without NSE evolution mode, but anything hotter becomes

problematic. So we use an imposed temperature history that starts out at 5.5 GK and remains constant at that value, except for a short peak up to 7.6 GK at 10 s. We keep the density fixed at  $\rho = 10^8 \text{ g cm}^{-3}$ . We evolve *SkyNet* without screening or self-heating, but with inverse rates from detailed balance, as these are important for consistency with NSE (Section 2.6.1.1). We use the same full network (7836 species and 93,000 reactions) as in Section 2.6.2.1. The initial composition is NSE with  $Y_e = 0.1$ . Figure 2.11 shows the results of this test. From the left panel we see that the free neutrons are captured in the first second to make heavy nuclei, raising the average mass number  $\bar{A}$  to about 60. The nuclei synthesized are mainly around the first r-process peak and the composition decays toward stability until the temperature starts to rise at around 8 s. The rising temperature forces the material into NSE, which liberates neutrons and protons from nuclei, quickly reducing  $\bar{A}$  to around 10. When the temperature drops back to 5.5 GK, the free neutrons and protons are absorbed into nuclei again and the iron peak is formed. In the left panel of Figure 2.11, there are no visible differences between the *SkyNet* evolution with and without NSE evolution mode. They produce exactly the same results. The right panel of Figure 2.11 contains the time step  $\Delta t$  and temperature as a function of time. We see that the time steps with and without NSE evolution mode are the same until *SkyNet* turns on NSE evolution mode when the temperature is sufficiently high. With NSE evolution mode, *SkyNet* evolves with  $\Delta t \sim 10^{-1}$  s until the temperature drops again and NSE evolution mode is turned off. Without NSE evolution mode, however, the time step drops to a few  $\times 10^{-5}$  s. After the temperature has returned to 5.5 GK, the time steps in both cases are virtually identical again. Not shown are the final abundances of the two *SkyNet* evolutions, but we find no discernible differences down to a level of  $10^{-30}$ . The error according to Equation (2.114) between the two *SkyNet* evolutions is 0.0098%, indicating that the NSE evolution mode in *SkyNet* produces correct results, i.e., exactly the same results as would be obtained with the full network, but NSE evolution mode prevents the time step from getting stuck at a very small value.

## 2.7 Summary and future work

We have presented the new nuclear reaction network *SkyNet* and the physics that it currently implements. Details are provided of how the abundance evolution equations implemented in *SkyNet* are derived from kinetic theory. We discuss how inverse reaction rates are computed with detailed balance and how this is related to NSE. A detailed description is given of the numerical methods used in *SkyNet* for the

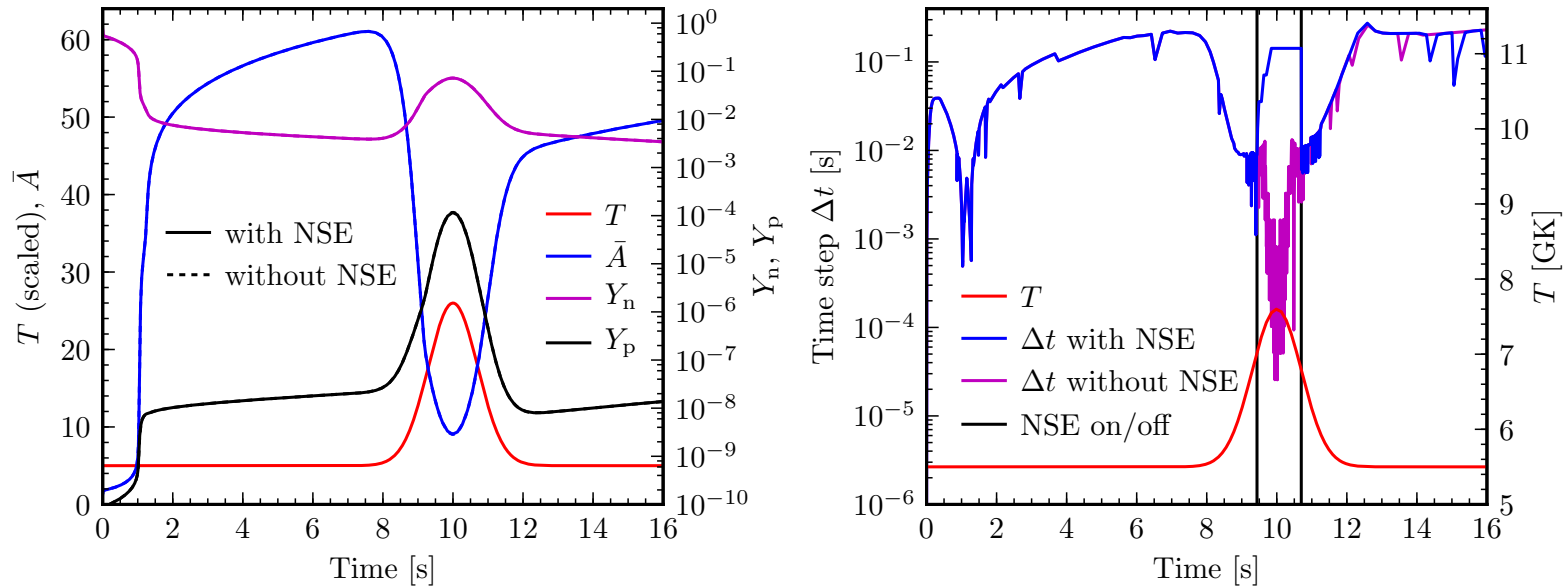


Figure 2.11: Test of the *SkyNet* NSE evolution mode. *SkyNet* is evolved with a constant density of  $\rho = 10^8 \text{ g cm}^{-3}$  and a constant temperature of 5.5 GK except for a bump up to 7.6 GK at 10 s. Self-heating and screening corrections are turned off and inverse rates are computed from detailed balance. The initial composition is NSE with  $Y_e = 0.1$ . **Left:** The temperature  $T$ , average mass number  $\bar{A}$ , and neutron and proton abundances  $Y_n$  and  $Y_p$  as a function of time. In the first second or so, neutrons are captured onto seed nuclei and heavy nuclei around the first r-process peak are synthesized with  $\bar{A}$  increasing to about 60. Then at 8 s as the temperature begins to rise, the heavy nuclei are destroyed again as the material is being forced into NSE. This increases  $Y_n$  and  $Y_p$  and the average nuclear mass drops to around 10. As the temperature returns back to 5.5 GK, the iron peak is formed and  $\bar{A}$  increases to 56 at  $T \sim 50$  s, eventually settling around 54. Only the first 16 seconds are shown to highlight the region around  $t = 10$  s. We see absolutely no differences between the evolution with and without NSE evolution mode. **Right:** The imposed temperature  $T$  and resulting time step size  $\Delta t$  as a function of time showing that using NSE evolution mode allows *SkyNet* to evolve more quickly. The vertical black lines indicate the times at which  
*(figure caption continued on next page)*

(continued caption of Figure 2.11)

*SkyNet* decides to turn NSE evolution mode on and off. As the temperature increases, the composition moves into NSE and the time step decreases because the reaction rates become faster. With NSE evolution mode, *SkyNet* can turn off the strong reactions that are all in equilibrium now and hence do not change the composition. The composition is only evolved under the influence of weak reactions that change the electron fraction and entropy. Without NSE evolution mode, the time step keeps decreasing to a few  $\times 10^{-5}$ , until the temperature decreases again.

network integration and the self-heating evolution that accounts for heating due to nuclear reactions. Further, we show how *SkyNet* automatically transitions between evolving the full network and evolving only the entropy and electron fraction under the influence of weak reactions when the composition is in NSE and all the strong reactions are in equilibrium. A general treatment of electron screening is presented that computes the screening factors for arbitrary strong reactions from chemical potential corrections that only depend on the nucleus charge and the composition. We then show in detail how *SkyNet* computes these chemical potential corrections in the weak, strong, and intermediate screening regimes and how it smoothly transitions between the regimes. These screening corrections are also taken into account when computing NSE compositions.

After providing some code implementation details that highlight the modularity and expandability of *SkyNet*, we present comprehensive code tests and comparisons. The NSE compositions computed by *SkyNet* are shown to be consistent with the evolved strong reactions, but only if detailed balance is used to compute the inverse rates. Furthermore, we show that *SkyNet*'s NSE results are compatible with results in the published literature. *SkyNet* is compared to two other nuclear reaction networks in three different cases: a neutron-rich r-process, a proton-rich, explosive X-ray burst, and hydrostatic carbon/oxygen burning. All three tests are conducted with and without electron screening and with and without self-heating. We find that all three networks agree with each other at the few percent level in most cases, although there are some situations where the disagreement is larger due to somewhat different implementations of the physics in the codes. Finally, in the appendices we discuss the physics of ideal Boltzmann gases and how this is implemented in the *SkyNet* EOS that accounts for all nuclear species individually. Technical details of how NSE is calculated in *SkyNet* and how the neutrino interactions are implemented are also presented in the appendices.

We hope that *SkyNet* will be a useful tool for the nuclear astrophysics community to compute nucleosynthesis in various scenarios. And we also hope that the theoretical and experimental nuclear physics communities will find *SkyNet* useful as a low-barrier entry point to running nucleosynthesis models. *SkyNet* can be used for testing the impact of newly measured or calculated reaction rates or nuclear properties, or to conduct sensitivity studies in order to determine which nuclides should be the focus of future experiments. *SkyNet* is available as open-source software at <https://bitbucket.org/jlippuner/skynet>. We value any feedback,

whether it be bug reports, feature requests, or code contributions.

In the future, we plan to extend the electron screening implementation in *SkyNet* in a way that screening corrections can be consistently accounted for in the EOS as well. We are also thinking of investigating different screening prescriptions and making them available in *SkyNet*. Currently, only the first-order backward Euler method is implemented in *SkyNet*, but we intend to add higher-order integration methods in the future. *SkyNet* is limited to evolving a one-zone model right now (i.e., there is only one density and temperature). We plan to add support for multiple zones in *SkyNet* and couple it to existing hydrodynamical simulations. Finally, we plan to investigate offloading some or most of the computations in *SkyNet* to GPUs, which could significantly speed up the network evolution and might be necessary to efficiently evolve large hydro simulations that are coupled to *SkyNet*.

### **Acknowledgments**

We thank J. Austin Harris and W. Raph Hix for giving us access to *XNet*, for assisting us with running the code comparison tests with *XNet*, and for helpful discussion of the test results. We are also very grateful to Moritz Reichert, Dirk Martin, Oleg Korobkin, and Marius Eichler for giving us access to *WinNet* and for helping us run the code comparisons with it. We thank Hendrik Schatz for providing the X-ray burst trajectories and Ivo Seitenzahl for allowing us to use his NSE data. We are very grateful to Christian D. Ott for carefully reading the manuscript and providing helpful comments and suggestions. LR thanks W. Raph Hix and Stan Woosley for many useful discussions concerning nuclear reaction networks and nucleosynthesis. We are indebted to the authors of the sparse linear solver package PARDISO (Schenk and Gärtner, 2004, 2006; Karypis and Kumar, 1998) for making their code available for free for academic uses. This work was supported in part by the Sherman Fairchild Foundation and NSF awards NSF CAREER PHY-1151197, TCAN AST-1333520, and AST-1205732. The calculations were performed on the *Zwicky* compute cluster at Caltech, supported by NSF under MRI award PHY-0960291 and by the Sherman Fairchild Foundation. This work benefited from access to the NSF XSEDE computing network under allocation TG-PHY100033 and to NSF/NCSA Blue Waters under NSF PRAC award ACI-1440083. This work was supported in part by NSF grant PHY-1430152 (JINA Center for the Evolution of the Elements).

## 2.A Equation of state (EOS)

*SkyNet* requires an EOS in order to relate different thermodynamic quantities, such as temperature, entropy, chemical potential, etc. to each other. Ions behave as non-relativistic, non-degenerate particles in the majority of situations where nuclear burning occurs and so the EOS in *SkyNet* treats all ions as non-interacting, non-degenerate, non-relativistic ideal Boltzmann gases. Electrons and positrons, on the other hand, can be both degenerate and relativistic. An important exception to the assumption that the ions are non-interacting is electron screening, which is discussed in detail in Section 2.4.

In this section, we present a brief summary of the most relevant properties of ideal Boltzmann gases and introduce the notation used in this paper. We also describe the EOS implemented in *SkyNet*.

### 2.A.1 Ideal Boltzmann gas

The grand partition function  $\mathcal{Z}$  of a Maxwell-Boltzmann gas is given by (e.g., Reichl, 1980, §9.D.3)

$$\ln \mathcal{Z} = \sum_k e^{-\beta(\epsilon_k - \mu)}, \quad (2.117)$$

where the sum runs over all single-particle states  $k$  with energy  $\epsilon_k$ ,  $\beta = 1/T$ , and  $\mu$  is the chemical potential. Let the particles be non-relativistic with rest mass  $m$  and kinetic energy  $E = p^2/(2m)$ . Also let the particles have internal states with excitation energies  $\Delta_l$  (with respect to the ground state  $l = 0$ , so  $\Delta_0 = 0$ ) and spins  $J_l$ , so that the multiplicity factor is  $2J_l + 1$ . Thus a state  $k$  is described by the internal state label  $l$  and momentum  $p$ , and the energy is given by

$$\epsilon_k = \epsilon(l, p) = \frac{p^2}{2m} + m + \Delta_l. \quad (2.118)$$

Recalling that the momentum phase space volume element is  $V/h^3 d^3 p$ , we find

$$\begin{aligned} \ln \mathcal{Z} &= \sum_l (2J_l + 1) \frac{V}{h^3} \int d^3 p e^{-\beta(p^2/(2m) + m + \Delta_l - \mu)} \\ &= 4\pi \frac{V}{(2\pi)^3} e^{\beta(\mu - m)} \sum_l (2J_l + 1) e^{-\beta\Delta_l} \int_0^\infty dp p^2 e^{-\beta p^2/(2m)} \\ &= \frac{V}{2\pi^2} e^{\beta(\mu - m)} G(T) \sqrt{\frac{\pi}{2}} \left(\frac{m}{\beta}\right)^{3/2} = VG(T) \left(\frac{mT}{2\pi}\right)^{3/2} e^{\beta(\mu - m)}, \end{aligned} \quad (2.119)$$

where  $(2J_l + 1)$  is the multiplicity of the internal state  $l$ , we used  $\int d^3p = 4\pi \int_0^\infty dp p^2$  and  $h = 2\pi\hbar = 2\pi$  since  $\hbar = 1$ , and we define the internal partition function

$$G(T) = \sum_l (2J_l + 1)e^{-\beta\Delta_l}. \quad (2.120)$$

Note that the internal partition function is sometimes given normalized to the ground state spin factor, i.e.,

$$G(T) = (2J_0 + 1)g(T), \quad (2.121)$$

where  $J_0$  is the ground state spin of the nuclide and  $g(T)$  is a tabulated function (e.g., Rauscher and Thielemann, 2000).

The grand potential  $\Omega$  is defined as

$$\Omega(T, V, \mu) = -T \ln \mathcal{Z} = -VG(T) \left(\frac{m}{2\pi}\right)^{3/2} T^{5/2} e^{\beta(\mu-m)}, \quad (2.122)$$

and the particle number  $N$ , pressure  $P$ , entropy  $S$ , and internal energy  $U$  are given by (e.g., Reichl, 1980, §9.B.3)

$$N = - \left( \frac{\partial \Omega}{\partial \mu} \right)_{V,T} \quad (2.123)$$

$$P = - \left( \frac{\partial \Omega}{\partial V} \right)_{T,\mu} \quad (2.124)$$

$$S = - \left( \frac{\partial \Omega}{\partial T} \right)_{V,\mu} \quad (2.125)$$

$$U = \Omega + TS + \mu N. \quad (2.126)$$

We find

$$N = -\beta\Omega = VG(T) \left(\frac{mT}{2\pi}\right)^{3/2} e^{\beta(\mu-m)}, \quad (2.127)$$

which we can solve for the chemical potential  $\mu$  to find

$$\mu = m + T \ln \left[ \frac{n}{G(T)} \left(\frac{2\pi}{mT}\right)^{3/2} \right], \quad (2.128)$$

where  $n = N/V$  is the number density. The pressure  $P$  becomes

$$P = -\frac{\Omega}{V} = \frac{NT}{V} = nT, \quad (2.129)$$

since  $\Omega = -NT$ . For the entropy  $S$  we obtain

$$S = -\frac{\partial G(T)}{\partial T} \frac{\Omega}{G(T)} - \frac{5\Omega}{2T} - \Omega \left( -\frac{\mu - m}{T^2} \right) = -\frac{5\Omega}{2T} - \frac{\Omega}{T} \left( -\frac{\mu - m}{T} \right) - \frac{\Omega}{T} \frac{\partial \ln G(T)}{\partial \ln T}, \quad (2.130)$$

and since  $N = -\Omega/T$ , the specific entropy per particle  $s = S/N$  is

$$s = \frac{5}{2} + \ln \left[ \frac{G(T)}{n} \left( \frac{mT}{2\pi} \right)^{3/2} \right] + \frac{\partial \ln G(T)}{\partial \ln T}, \quad (2.131)$$

where we used Equation (2.128). And finally, the internal energy per particle is

$$\begin{aligned} u &= \frac{U}{N} = \frac{\Omega}{N} + Ts + \mu \\ &= -\Omega \frac{T}{\Omega} + \frac{5}{2}T - (\mu - m) + T \frac{\partial \ln G(T)}{\partial \ln T} + \mu \\ &= \frac{3}{2}T + m + T \frac{\partial \ln G(T)}{\partial \ln T}. \end{aligned} \quad (2.132)$$

### 2.A.2 Modified Timmes EOS

In the previous section, we found the most relevant thermodynamic properties of a non-interacting, non-relativistic, non-degenerate Boltzmann gas. In this section, we describe the complete EOS implemented in *SkyNet*. *SkyNet* uses a modified Timmes EOS developed in Timmes and Arnett (1999) and Timmes and Swesty (2000). The Timmes EOS consists of three independent parts: a photon gas, an arbitrarily degenerate and relativistic electron/positron gas, and a non-degenerate, non-relativistic Boltzmann gas for the heavy ions (Timmes and Arnett, 1999). The electron/positron part is implemented via table interpolation of the Helmholtz free energy (Timmes and Swesty, 2000).

For the photon gas and electron/positron gas, the code from the original author of the Timmes EOS is used, which is available at <http://cococubed.asu.edu/codes/eos/helmholtz.tbz>. That code also provides the electron/positron chemical potential  $\eta_{e^-, \text{Timmes}} = \mu_{e^-, \text{Timmes}}/T$ , which we need to compute neutrino interactions (Appendix 2.C) and electron screening corrections (Section 2.4). Note that the electron/positron chemical potential  $\mu_{e^-, \text{Timmes}}$  in the Timmes EOS is defined with the electron rest mass subtracted out (Timmes and Arnett, 1999, §2). And the positron chemical potential is

$$\mu_{e^+, \text{Timmes}} = -\mu_{e^-, \text{Timmes}} - 2m_e. \quad (2.133)$$

So the electron and positron chemical potentials that include the rest masses are

$$\mu_{e^-} = \mu_{e^-, \text{Timmes}} + m_e = T\eta_{e^-, \text{Timmes}} + m_e, \quad (2.134)$$

$$\mu_{e^+} = \mu_{e^+, \text{Timmes}} + m_e = -T\eta_{e^-, \text{Timmes}} - m_e = -\mu_{e^-}. \quad (2.135)$$

For the heavy ions, Timmes EOS Implementation uses a single representative ion species with mass  $\bar{A}$  and charge  $\bar{Z}$ , which are the average mass and charge of all nuclides, respectively. Since *SkyNet* has the complete composition information at all times, we decided to extend the original Timmes EOS to take into account all ion species individually. Furthermore, we use the expressions derived in the previous section for the ion quantities, which take the internal nuclear partition functions into account.

The overall specific entropy of the system is computed in units of  $k_B$  baryon $^{-1}$  as

$$s_{\text{tot}} = \frac{s_{e^\pm, \text{Timmes}} + s_{\gamma, \text{Timmes}}}{k_B N_A} + s_{\text{ions}}, \quad (2.136)$$

where  $s_{e^\pm, \text{Timmes}}$  and  $s_{\gamma, \text{Timmes}}$  are the electron/positron and photon entropies provided by the Timmes EOS, respectively. We divide them by  $k_B N_A$ , where  $N_A \approx 6.022 \times 10^{23}$  baryon  $\text{g}^{-1}$  is the Avogadro constant, because the Timmes EOS returns the entropies in units of  $\text{erg g}^{-1} \text{K}^{-1}$ . The specific entropy of the ions  $s_{\text{ions}}$  is calculated by *SkyNet* itself according to Equation (2.131) as

$$s_{\text{ions}} = \sum_i \frac{N_i s_i}{N_B} = \sum_i Y_i s_i = \sum_i Y_i \left( \frac{5}{2} + \ln \left[ \frac{G_i(T)}{n_i} \left( \frac{m_i T}{2\pi} \right)^{3/2} \right] + \frac{\partial \ln G_i(T)}{\partial \ln T} \right), \quad (2.137)$$

where the sum runs over all nuclear species labeled by  $i$ ,  $N_i$  is the number of particles of species  $i$ ,  $N_B$  is the total number of baryons, and  $s_i$  is the entropy per particle of species  $i$  given by Equation (2.131). Recall that the abundance  $Y_i$  is (Equation 2.13)

$$Y_i \equiv \frac{n_i}{n_B} = \frac{N_i/V}{N_B/V} = \frac{N_i}{N_B}, \quad (2.138)$$

where  $N_i$  and  $N_B$  are the total number of particles species  $i$  and total number of baryons, respectively, and  $V$  is the volume. Thus the abundance  $Y_i$  is the fraction of particles of species  $i$  compared to the total number of baryons. Note that  $N_i s_i$  is the total entropy contribution of species  $i$  and so  $N_i s_i / N_B$  is the entropy per baryon contribution of species  $i$ . Also note that

$$n_B = \rho N_A, \quad (2.139)$$

where  $\rho$  is the mass density.

In Section 2.B.2, we require the partial derivative of the entropy with respect to temperature. From Equation (2.131) we get

$$\frac{\partial s}{\partial T} = \frac{1}{k_B N_A} \left( \frac{\partial s_{e^\pm, \text{Timmes}}}{\partial T} + \frac{\partial s_{\gamma, \text{Timmes}}}{\partial T} \right) + \frac{\partial s_{\text{ions}}}{\partial T}. \quad (2.140)$$

The first two partial derivatives are provided by the Timmes EOS, and from Equation (2.137) we find

$$\begin{aligned} \frac{\partial s_{\text{ions}}}{\partial T} &= \sum_i Y_i \left( 0 + \frac{1}{G_i(T)} \frac{\partial G_i(T)}{\partial T} + \frac{3}{2} \frac{1}{T} + \frac{\partial}{\partial T} \left[ \frac{\partial \ln G_i(T)}{\partial \ln T} \right] \right) \\ &= \sum_i \frac{Y_i}{T} \left( \frac{3}{2} + \frac{\partial \ln G_i(T)}{\partial \ln T} + \frac{\partial^2 \ln G_i(T)}{\partial (\ln T)^2} \right), \end{aligned} \quad (2.141)$$

since  $\partial f / \partial \ln T = T \partial f / \partial T$ . In the current *SkyNet* implementation, however, we ignore the second derivative of  $\ln G_i(T)$ , because the partition functions we currently have available do not have continuous second derivatives. This will be fixed in a future version of *SkyNet*.

Similar to Equation (2.136), the specific internal energy is computed as

$$u_{\text{tot}} = u_{e^\pm, \text{Timmes}} + u_{\gamma, \text{Timmes}} + u_{\text{ions}} \quad (2.142)$$

in units of  $\text{erg g}^{-1}$ . The ion internal energy is computed as

$$u_{\text{ions}} = N_A \sum_i Y_i \left[ T \left( \frac{3}{2} + \frac{\partial \ln G_i(T)}{\partial \ln T} \right) - \text{BE}_i - Z_i(m_n - m_p) \right] + N_A Y_e m_e, \quad (2.143)$$

where  $m_n$  and  $m_p$  are the neutron and proton mass, respectively,  $Z_i$  is the charge number of nuclide  $i$  and  $\text{BE}_i$  is its binding energy. Note that the sum in the above expression gives the internal energy per baryon, so we multiply by  $N_A$  to convert this to internal energy per gram. We need to add the electron rest mass because it is not accounted for in  $u_{e^\pm, \text{Timmes}}$  (Timmes and Arnett, 1999). The binding energy  $\text{BE}_i$  is defined as

$$\text{BE}_i = N_i m_n + Z_i m_p - m_i, \quad (2.144)$$

with  $N_i$  being the number of neutrons of nuclide  $i$  (not to be confused with the same symbol used above for the total number of particles of species  $i$  in the composition) and  $m_i$  being the rest mass of nuclide  $i$ . Thus the term  $-\text{BE}_i - Z_i(m_n - m_p)$  in

Equation (2.143) is

$$\begin{aligned} -BE_i - Z_i(m_n - m_p) &= m_i - N_i m_n - Z_i m_p - Z_i m_n + Z_i m_p \\ &= m_i - A_i m_n, \end{aligned} \quad (2.145)$$

where  $A_i = Z_i + N_i$  is the mass number of nuclide  $i$ . Thus Equation (2.143) differs from the expression for the specific internal energy of a single species (Equation 2.132) only by the subtraction of  $A_i m_n$  from the particle rest mass  $m_i$ . Thus the specific internal energy we calculate is relative to the neutron rest mass, which has the advantage that the numerical value of the specific internal energy is not too large but may be comparable to the thermal energy. However, if we ignored the rest mass altogether, the internal energy would not be conserved under nuclear reactions. Nuclear reactions change particles from one species to another that have different binding energies, and so we have to account for the binding energy and mass difference between neutrons and protons, as we do in Equation (2.143). Other EOSs use the same convention (e.g., Lattimer and Swesty, 1991). Note that we have

$$u_{\text{ions}} = N_A \sum_i Y_i (u_i - A_i m_n) = N_A \sum_i Y_i u_i - N_A m_n \sum_i Y_i A_i, \quad (2.146)$$

where  $u_i$  is given by Equation (2.132). But since  $\sum_i Y_i A_i = 1$  (Equation 2.48), we find  $u_{\text{ions}} = N_A \sum_i Y_i u_i - N_A m_n$ , which means our definition of specific internal energy only differs by a constant ( $N_A m_n c^2 \approx 9.065 \times 10^{20} \text{ erg g}^{-1}$ ) from the specific internal energy we would calculate by using Equation (2.132) directly.

Currently, the electron screening corrections implemented in *SkyNet* (Section 2.4) are not yet included in the modified Timmes EOS. Since screening is implemented as a correction to the ion chemical potential (Equation 2.128), it is not straightforward to propagate those corrections to the other thermodynamic quantities of the ions, let alone the electron/positron gas. We plan to incorporate screening into the EOS in a future version of *SkyNet*.

## 2.B Calculating NSE

In this section, we show in detail how NSE is computed in *SkyNet* given a temperature and density (Section 2.B.1) and with an unknown temperature (Section 2.B.2).

### 2.B.1 From temperature and density

NSE evolution mode requires a robust method for calculating NSE. We have a list of nuclides for which we want to calculate the NSE composition, given a temperature  $T$ ,

density  $\rho$ , and electron fraction  $Y_e$ . Recall that NSE is governed by Equation (2.27)

$$\mu_i = Z_i\mu_p + N_i\mu_n, \quad (2.147)$$

where  $\mu_i$ ,  $\mu_p$ , and  $\mu_n$  are the chemical potentials of nuclide  $i$ , protons, and neutrons, respectively. To make the values of the chemical potentials closer to unity, we introduce a renormalized chemical potential  $\hat{\mu}$  given by

$$\hat{\mu}_i = \mu_i - m_i - \text{BE}_i, \quad (2.148)$$

where  $\text{BE}_i$  is the binding energy of the nuclide  $i$  defined in Equation (2.144). Recall that

$$\text{BE}_i = Z_im_p + N_im_n - m_i, \quad (2.149)$$

where the proton and neutron masses  $m_p$  and  $m_n$  are generally chosen such that the binding energies of the neutron and proton are exactly zero. Equation (2.147) now becomes

$$\begin{aligned} \hat{\mu}_i + m_i + \text{BE}_i &= Z_i\hat{\mu}_p + Z_im_p + N_i\hat{\mu}_n + N_im_n \\ \Leftrightarrow \hat{\mu}_i &= Z_i\hat{\mu}_p + N_i\hat{\mu}_n, \end{aligned} \quad (2.150)$$

where we used the definition of  $\text{BE}_i$ , Equation (2.149), and the fact that  $\text{BE}_p = \text{BE}_n = 0$ .

It is always possible to choose any two chemical potentials as the basis vectors and express all other chemical potentials in terms of those two. In terms of species  $l$  and  $m$  that have  $Z_l$  and  $Z_m$  protons and  $N_l$  and  $N_m$  neutrons, we find

$$\begin{aligned} \begin{bmatrix} Z_l & N_l \\ Z_m & N_m \end{bmatrix} \cdot \begin{bmatrix} \hat{\mu}_p \\ \hat{\mu}_n \end{bmatrix} &= \begin{bmatrix} \hat{\mu}_l \\ \hat{\mu}_m \end{bmatrix} \\ \Leftrightarrow \begin{bmatrix} \hat{\mu}_p \\ \hat{\mu}_n \end{bmatrix} &= \frac{1}{Z_lN_m - Z_mN_l} \begin{bmatrix} N_m & -N_l \\ -Z_m & Z_l \end{bmatrix} \cdot \begin{bmatrix} \hat{\mu}_l \\ \hat{\mu}_m \end{bmatrix}. \end{aligned} \quad (2.151)$$

And so

$$\begin{aligned} \hat{\mu}_i &= Z_i\hat{\mu}_p + N_i\hat{\mu}_n \\ &= \frac{1}{Z_lN_m - Z_mN_l} (Z_i(N_m\hat{\mu}_l - N_l\hat{\mu}_m) + N_i(-Z_m\hat{\mu}_l + Z_l\hat{\mu}_m)) \\ &= \frac{Z_iN_m - N_lZ_m}{Z_lN_m - N_lZ_m} \hat{\mu}_l + \frac{Z_iN_l - N_lZ_l}{Z_mN_l - N_mZ_l} \hat{\mu}_m \\ &= \alpha_i\hat{\mu}_l + \beta_i\hat{\mu}_m, \end{aligned} \quad (2.152)$$

where

$$\alpha_i = \frac{Z_i N_m - N_i Z_m}{Z_l N_m - N_l Z_m} \quad \text{and} \quad \beta_i = \frac{Z_i N_l - N_i Z_l}{Z_m N_l - N_m Z_l}. \quad (2.153)$$

Clearly, the species  $l$  and  $m$  must be chosen to have different proton fractions  $Z/N$ . However, they do not have to be nuclei in the network. We have had reasonable success with  $Z_l = 0$ ,  $N_l = 1$  and  $Z_m = -1$ ,  $N_m = 1$ .

Using Equation (2.128), the abundance  $Y_i = n_i/n_B$  in terms of the chemical potential  $\hat{\mu}_i$  is given by

$$\begin{aligned} \hat{\mu}_i &= -BE_i + T \ln \left[ \frac{n_i}{G_i(T)} \left( \frac{2\pi}{m_i T} \right)^{3/2} \right] \\ \Leftrightarrow e^{(\hat{\mu}_i + BE_i)/T} &= \frac{Y_i n_B}{G_i(T)} \left( \frac{2\pi}{m_i T} \right)^{3/2} \\ \Leftrightarrow Y_i &= e^{(\hat{\mu}_i + BE_i)/T} \frac{G_i(T)}{n_B} \left( \frac{m_i T}{2\pi} \right)^{3/2} \\ &= e^{\eta_i + BE_i/T} \frac{G_i(T)}{n_B} \left( \frac{m_i T}{2\pi} \right)^{3/2}, \end{aligned} \quad (2.154)$$

where we define  $\eta_i = \hat{\mu}_i/T$ .

This system of equations is subject to baryon number conservation and charge conservation,

$$f_A = 1 - \sum_i A_i Y_i = 0, \quad (2.155)$$

$$f_Z = Y_e - \sum_i Z_i Y_i = 0. \quad (2.156)$$

These equations can be zeroed by a two-dimensional NR iteration, where the Jacobian is given by

$$J_{\text{NSE}} = \begin{bmatrix} \frac{\partial f_A}{\partial \eta_l} & \frac{\partial f_A}{\partial \eta_m} \\ \frac{\partial f_Z}{\partial \eta_l} & \frac{\partial f_Z}{\partial \eta_m} \end{bmatrix}, \quad (2.157)$$

so that the chemical potential updates are given by

$$\Delta \boldsymbol{\eta} = -J_{\text{NSE}}^{-1} \cdot \begin{bmatrix} f_A \\ f_Z \end{bmatrix}. \quad (2.158)$$

From Equations (2.155) and (2.156) we find

$$\frac{\partial f_A}{\partial \eta_l} = - \sum_i A_i \frac{\partial Y_i}{\partial \eta_l} = - \sum_i A_i Y_i \alpha_i, \quad (2.159)$$

and similarly

$$\frac{\partial f_A}{\partial \eta_m} = - \sum_i A_i Y_i \beta_i, \quad (2.160)$$

$$\frac{\partial f_Z}{\partial \eta_l} = - \sum_i Z_i Y_i \alpha_i, \quad (2.161)$$

$$\frac{\partial f_Z}{\partial \eta_m} = - \sum_i Z_i Y_i \beta_i. \quad (2.162)$$

The trickiest part about calculating NSE is choosing the basis nuclides  $l$  and  $m$  and the starting guess for  $\eta = (\eta_l, \eta_m)$ . If one of the basis nuclides is  $(Z, N) = (-1, 1)$ , then the corresponding  $\eta$  can be set to zero in most cases. To choose the second basis nuclide, compute the chemical potential of the most bound nuclide if it had a mass fraction of 1 and compare this to the chemical potential of the neutron if it had mass fraction 1. The second basis nuclide will be the nuclide corresponding to the larger of those two chemical potentials and the starting guess for that  $\eta$  comes from that chemical potential. While this method may not work in every case, we have found it to work robustly in a large region of parameter space.

### 2.B.2 With an unknown temperature

In the previous section, we described how to calculate NSE given a temperature  $T$ , density  $\rho$  (from which we get the baryon number density  $n_B = N_A \rho$ ), and electron fraction  $Y_e$ . However, there are cases where the temperature is unknown but the entropy  $s_0$  is given instead. In that case, we have an additional unknown variable  $T$ , and the additional constraint equation

$$f_s = \frac{s(T, \eta_l, \eta_m)}{s_0} - 1 = 0, \quad (2.163)$$

where  $s_0$  is the given target entropy and  $s(T, \eta_l, \eta_m)$  is the entropy given by the EOS from the current guess for  $T$ ,  $\eta_l$ , and  $\eta_m$ . The Jacobian becomes

$$J_{\text{NSE}} = \begin{bmatrix} \frac{\partial f_A}{\partial \eta_l} & \frac{\partial f_A}{\partial \eta_m} & \frac{\partial f_A}{\partial T} \\ \frac{\partial f_Z}{\partial \eta_l} & \frac{\partial f_Z}{\partial \eta_m} & \frac{\partial f_Z}{\partial T} \\ \frac{\partial \eta_l}{\partial f_s} & \frac{\partial \eta_m}{\partial f_s} & \frac{\partial T}{\partial f_s} \\ \frac{\partial \eta_l}{\partial T} & \frac{\partial \eta_m}{\partial T} & \frac{\partial T}{\partial T} \end{bmatrix}. \quad (2.164)$$

Note that Equation (2.154) gives

$$\frac{\partial Y_i}{\partial T} = \frac{Y_i}{T} \left( \frac{3}{2} - \frac{\text{BE}_i}{T} + \frac{\partial \ln G_i(T)}{\partial \ln T} \right) \quad (2.165)$$

and so

$$\frac{\partial f_A}{\partial T} = - \sum_i A_i \frac{Y_i}{T} \left( \frac{3}{2} - \frac{\text{BE}_i}{T} + \frac{\partial \ln G_i(T)}{\partial \ln T} \right), \quad (2.166)$$

$$\frac{\partial f_Z}{\partial T} = - \sum_i Z_i \frac{Y_i}{T} \left( \frac{3}{2} - \frac{\text{BE}_i}{T} + \frac{\partial \ln G_i(T)}{\partial \ln T} \right). \quad (2.167)$$

Recall that the entropy is calculated as (Equation 2.136)

$$s = s_{e^\pm} + s_\gamma + s_{\text{ions}}. \quad (2.168)$$

The EOS provides  $\partial s / \partial T$  (Equation 2.140), so

$$\frac{\partial f_s}{\partial T} = \frac{1}{s_0} \frac{\partial s}{\partial T} + \frac{1}{s_0} \sum_i \frac{\partial s}{\partial Y_i} \frac{\partial Y_i}{\partial T}. \quad (2.169)$$

The electron entropy  $s_{e^\pm}$  and photon entropy  $s_\gamma$  only depend on the temperature and electron fraction. Thus they do not depend on the composition  $\mathbf{Y}$  and so also not on  $\eta_l$  and  $\eta_m$ . The ion entropy is calculated as (Equation 2.137)

$$s_{\text{ion}} = \sum_i Y_i \left( \frac{5}{2} + \ln \left[ \frac{G_i(T)}{n_B Y_i} \left( \frac{m_i T}{2\pi} \right)^{3/2} \right] + \frac{\partial \ln G_i(T)}{\partial \ln T} \right), \quad (2.170)$$

so

$$\begin{aligned} \frac{\partial s}{\partial Y_i} &= \frac{5}{2} + \ln \left[ \frac{G_i(T)}{n_B Y_i} \left( \frac{m_i T}{2\pi} \right)^{3/2} \right] + \frac{\partial \ln G_i(T)}{\partial \ln T} + Y_i \left( -\frac{1}{Y_i} \right) \\ &= \frac{3}{2} + \ln \left[ \frac{G_i(T)}{n_B Y_i} \left( \frac{m_i T}{2\pi} \right)^{3/2} \right] + \frac{\partial \ln G_i(T)}{\partial \ln T}. \end{aligned} \quad (2.171)$$

From Equation (2.154) we get

$$\ln \left[ \frac{G_i(T)}{n_B Y_i} \left( \frac{m_i T}{2\pi} \right)^{3/2} \right] = - \left( \eta_i + \frac{\text{BE}_i}{T} \right). \quad (2.172)$$

Combining the above with Equation (2.165) yields

$$\frac{\partial f_s}{\partial T} = \frac{1}{s_0} \frac{\partial s}{\partial T} + \frac{1}{s_0} \sum_i \left( \frac{3}{2} - \left( \eta_i + \frac{\text{BE}_i}{T} \right) + \frac{\partial \ln G_i(T)}{\partial \ln T} \right) \frac{Y_i}{T} \left( \frac{3}{2} - \frac{\text{BE}_i}{T} + \frac{\partial \ln G_i(T)}{\partial \ln T} \right), \quad (2.173)$$

where the first partial derivative is provided by the EOS (Equation 2.140). We also find

$$\frac{\partial f_s}{\partial \eta_l} = \frac{1}{s_0} \sum_i \frac{\partial s}{\partial Y_i} \frac{\partial Y_i}{\partial \eta_l} = \frac{1}{s_0} \sum_i \left( \frac{3}{2} - \left( \eta_i + \frac{BE_i}{T} \right) + \frac{\partial \ln G_i(T)}{\partial \ln T} \right) Y_i \alpha_i \quad (2.174)$$

and similarly

$$\frac{\partial f_s}{\partial \eta_m} = \frac{1}{s_0} \sum_i \left( \frac{3}{2} - \left( \eta_i + \frac{BE_i}{T} \right) + \frac{\partial \ln G_i(T)}{\partial \ln T} \right) Y_i \beta_i. \quad (2.175)$$

Unfortunately, the NR iterations with three variables are much less stable than if the temperature is fixed, unless a good initial guess for the temperature is available. For this reason, if NSE is computed from a given entropy and density, *SkyNet* first uses the bisection method (e.g., Burden et al., 2015, §2.1) to find a good guess for the temperature. The bisection attempts to find a guess temperature such that Equation (2.163) is close to zero. Then the NR iterations are performed as described in this section, which may lead to a temperature that satisfies the three constraint equations better than the guess temperature found by the bisection method. However, it can also happen that the bisection already found the best temperature.

If NSE needs to be calculated from a given temperature, entropy, and electron fraction, then the bisection method is used to find the density that produces the desired entropy. Similarly, if the internal energy, density, and electron fraction are given, *SkyNet* uses the bisection method to find the temperature that produces an NSE distribution with the desired internal energy.

## 2.C Neutrino interaction reactions

The rate for a two-particle charged current weak interaction is given by (see Equation 2.7)

$$\begin{aligned} \lambda_w = & \frac{1}{n_2} g_1 \int \frac{d^3 k_1}{(2\pi)^3} g_2 \int \frac{d^3 k_2}{(2\pi)^3} \int \frac{d^3 k_3}{(2\pi)^3} \int \frac{d^3 k_4}{(2\pi)^3} \\ & \times \delta^{(4)}(k_1^\mu + k_2^\mu - k_3^\mu - k_4^\mu) z_w f_1 f_2 (1 - f_3)(1 - f_4), \end{aligned} \quad (2.176)$$

where particles [1] and [3] are the incoming and outgoing neutrino and lepton, particles [2] and [4] are the incoming and outgoing nucleon. Under the astrophysical conditions relevant for reaction networks (see, e.g., Reddy et al., 1998) we have

$$z_w \approx (2\pi)^4 G_F^2 (g_V^2 + 3g_A^2) (1 + h_{wm} E_3), \quad (2.177)$$

where  $G_F$  is the Fermi coupling constant,  $g_V$  and  $g_A$  are the vector and axial vector couplings of the weak current to the nucleons, and the energy-dependent correction factor  $(1 + h_{wm}E_3)$  comes from weak magnetism and recoil corrections (Horowitz, 2002). Due to the large mass of the nucleons relative to the energy scale of neutrinos emitted from sites undergoing nuclear burning, we can assume there is no momentum transfer from the nucleons to the leptons. Also neglecting final state nucleon blocking, we then have

$$\lambda_w = G_F^2(g_V^2 + 3g_A^2)g_1 \int \frac{d^3k_1}{(2\pi)^3} \int \frac{d^3k_3}{(2\pi)^3} f_1(1 - f_3)2\pi\delta(E_1 - E_3 + q_0)(1 + h_{wm}E_3), \quad (2.178)$$

where  $q_0$  is the energy difference between the incoming and outgoing nucleons. The angular integrals in momentum space are trivially integrated, we have  $E_i dE_i = k_i dk_i$ , and the delta function gets rid of the integral over  $k_3$ . This gives

$$\lambda_w = G_F^2(g_V^2 + 3g_A^2)\frac{g_1}{2\pi^3} \int_0^\infty dE_3 k_1 E_1 k_3 E_3 (1 + h_{wm}E_3) \theta(E_1 - m_1) f_1(1 - f_3), \quad (2.179)$$

where  $E_1 = E_3 - q_0$ ,  $k_1 = \sqrt{E_1^2 - m_1^2}$ , and  $\theta(x) = 1$  if  $x > 0$  and 0 otherwise.

*SkyNet* contains neutrino interactions on free nucleons. Currently, the following reactions are implemented:

$$\lambda_{ec} : p + e^- \rightarrow n + \nu_e, \quad (2.180)$$

$$\lambda_{pc} : n + e^+ \rightarrow p + \bar{\nu}_e, \quad (2.181)$$

$$\lambda_{\nu_e} : n + \nu_e \rightarrow p + e^-, \quad (2.182)$$

$$\lambda_{\bar{\nu}_e} : p + \bar{\nu}_e \rightarrow n + e^+. \quad (2.183)$$

Thus we compute

$$\begin{aligned} \lambda_{ec} = C \int_{\omega_{ec}}^\infty dE E \sqrt{E^2 - m_e^2} (E - Q_{ec})^2 (1 + E h_{wm}) \\ \times f_e(E, \mu_e) (1 - f_{\nu_e}(E - Q_{ec}, \mu_{\nu_e})), \end{aligned} \quad (2.184)$$

$$\begin{aligned} \lambda_{pc} = C \int_{\omega_{pc}}^\infty dE E \sqrt{E^2 - m_e^2} (E - Q_{pc})^2 (1 + E h_{wm}) \\ \times f_p(E, -\mu_e) (1 - f_{\bar{\nu}_e}(E - Q_{pc}, \mu_{\bar{\nu}_e})), \end{aligned} \quad (2.185)$$

$$\begin{aligned}\lambda_{\nu_e} &= C \int_{\omega_{ec}}^{\infty} dE E \sqrt{E^2 - m_e^2} (E - Q_{ec})^2 (1 + E h_{wm}) \\ &\quad \times (1 - f_e(E, \mu_e)) f_{\nu_e}(E - Q_{ec}, \mu_{\nu_e}),\end{aligned}\quad (2.186)$$

$$\begin{aligned}\lambda_{\bar{\nu}_e} &= C \int_{\omega_{pc}}^{\infty} dE E \sqrt{E^2 - m_e^2} (E - Q_{pc})^2 (1 + E h_{wm}) \\ &\quad \times (1 - f_p(E, -\mu_e)) f_{\bar{\nu}_e}(E - Q_{pc}, \mu_{\bar{\nu}_e}),\end{aligned}\quad (2.187)$$

where  $Q_{ec} = -Q_{pc} = m_n - m_p = 1.29333 \text{ MeV}$ ,  $\omega_x = \max(m_e, Q_x)$  for  $x = ec$  or  $x = pc$ ,  $f_e$  and  $f_p$  are the electron and positron distribution functions with the electron chemical potential  $\mu_e$  given by Equation (2.134), and  $f_{\nu_e}$  and  $f_{\bar{\nu}_e}$  are the electron neutrino and antineutrino distributions functions, which are usually Fermi-Dirac with  $\mu_{\nu_e} = \mu_{\bar{\nu}_e} = 0$ , but could be set to something else too. We also use the Fermi-Dirac distribution for the electrons and positrons, hence

$$f_{e,p}(E, \mu) = \frac{1}{e^{\beta(E-\mu)} + 1}, \quad (2.188)$$

where  $\beta = 1/T$ . The factor  $C$  is give by (Arcones et al., 2010)

$$C = \frac{B \ln 2}{K m_e^5}, \quad (2.189)$$

where the matrix element is  $B = g_V^2 + 3g_A^2 = 5.76$  and  $K = 6144 \text{ s}$ .

Note that the factor  $(E - Q_x)$  in Equations (2.184) to (2.187) is the (anti) neutrino energy. We neglect nucleon recoils so that  $E_{\nu_e} = E + m_p - m_n = E - Q_{ec}$  for electron capture and neutrino absorption, and for positron capture and antineutrino absorption we get  $E_{\bar{\nu}_e} = E + m_n - m_p = E + Q_{ec} = E - Q_{pc}$ . Therefore, to compute the neutrino heating or cooling rates due to these reactions, we simply multiply the integrand by another factor of  $(E - Q_x)$  and we get

$$\begin{aligned}\dot{\epsilon}_{ec} &= C \int_{\omega_{ec}}^{\infty} dE E \sqrt{E^2 - m_e^2} (E - Q_{ec})^3 (1 + E h_{wm}) \\ &\quad \times f_e(E, \mu_e) (1 - f_{\nu_e}(E - Q_{ec}, \mu_{\nu_e})),\end{aligned}\quad (2.190)$$

$$\begin{aligned}\dot{\epsilon}_{pc} &= C \int_{\omega_{pc}}^{\infty} dE E \sqrt{E^2 - m_e^2} (E - Q_{pc})^3 (1 + E h_{wm}) \\ &\quad \times f_p(E, -\mu_e) (1 - f_{\bar{\nu}_e}(E - Q_{pc}, \mu_{\bar{\nu}_e})),\end{aligned}\quad (2.191)$$

$$\begin{aligned} \dot{\epsilon}_{\nu_e} = & -C \int_{\omega_{ec}}^{\infty} dE E \sqrt{E^2 - m_e^2} (E - Q_{ec})^3 (1 + E h_{wm}) \\ & \times (1 - f_e(E, \mu_e)) f_{\nu_e}(E - Q_{ec}, \mu_{\nu_e}), \end{aligned} \quad (2.192)$$

$$\begin{aligned} \dot{\epsilon}_{\bar{\nu}_e} = & -C \int_{\omega_{pc}}^{\infty} dE E \sqrt{E^2 - m_e^2} (E - Q_{pc})^3 (1 + E h_{wm}) \\ & \times (1 - f_p(E, -\mu_e)) f_{\bar{\nu}_e}(E - Q_{pc}, \mu_{\bar{\nu}_e}), \end{aligned} \quad (2.193)$$

where the negative sign for the (anti) neutrino absorption reactions comes from the fact that in those reactions the neutrino energies are absorbed and they thus provide cooling instead of heating. The total neutrino heating/cooling rate is thus

$$\dot{\epsilon}_{\nu} = \dot{\epsilon}_{ec} + \dot{\epsilon}_{pc} + \dot{\epsilon}_{\nu_e} + \dot{\epsilon}_{\bar{\nu}_e}. \quad (2.194)$$

The integrals shown in this section are evaluated numerically in *SkyNet* using the adaptive QAG integration routines provided by the GNU Scientific Library<sup>7</sup>. As usual, all the reaction rates and heating rates need to be multiplied by the product of reactant abundances. So the electron capture and antineutrino absorption rates are multiplied by  $Y_p$  and the positron capture and neutrino absorption rates are multiplied by  $Y_n$ .

Alternatively, instead of computing the rates from the integrals provided here, one can also specify the rates  $\lambda_{ec}$ ,  $\lambda_{pc}$ ,  $\lambda_{\nu_e}$ , and  $\lambda_{\bar{\nu}_e}$  directly as a function of time, and *SkyNet* will use these externally given rates. In that case, the neutrino heating/cooling rate also has to be specified directly. This capability is useful if the (anti) neutrino absorption and emission rates are computed in a hydrodynamical simulation and the same rates should be used for the nucleosynthesis calculations in *SkyNet* for consistency.

---

<sup>7</sup>[https://www.gnu.org/software/gsl/manual/html\\_node/Numerical-Integration.html](https://www.gnu.org/software/gsl/manual/html_node/Numerical-Integration.html)

## LANTHANIDES AND HEATING RATES IN KILONOVAE

*This chapter was published in December 2015 in the Astrophysical Journal, 815, 82, doi:10.1088/0004-637X/815/2/82. The appendices were not included with that publication. I am the primary author, wrote the vast majority of the text, performed all nucleosynthesis calculations and data analysis, and I created all the figures.*

© 2015 The American Astronomical Society

## r-Process lanthanide production and heating rates in kilonovae

Jonas Lippuner<sup>1</sup> and Luke F. Roberts<sup>1,2</sup>

<sup>1</sup> TAPIR, Walter Burke Institute for Theoretical Physics, California Institute of Technology, MC 350-17, 1200 E California Blvd, Pasadena CA 91125, USA

<sup>2</sup> NASA Einstein Fellow

### Abstract

r-Process nucleosynthesis in material ejected during neutron star mergers may lead to radioactively powered transients called kilonovae. The timescale and peak luminosity of these transients depend on the composition of the ejecta, which determines the local heating rate from nuclear decays and the opacity. Kasen et al. (2013, ApJ, 774, 25) and Tanaka & Hotokezaka (2013, ApJ, 775, 113) pointed out that lanthanides can drastically increase the opacity in these outflows. We use the new general-purpose nuclear reaction network *SkyNet* to carry out a parameter study of r-process nucleosynthesis for a range of initial electron fractions  $Y_e$ , initial specific entropies  $s$ , and expansion timescales  $\tau$ . We find that the ejecta is lanthanide-free for  $Y_e \gtrsim 0.22 - 0.30$ , depending on  $s$  and  $\tau$ . The heating rate is insensitive to  $s$  and  $\tau$ , but certain, larger values of  $Y_e$  lead to reduced heating rates, due to individual nuclides dominating the heating. We calculate approximate light curves with a simplified gray radiative transport scheme. The light curves peak at about a day (week) in the lanthanide-free (-rich) cases. The heating rate does not change much as the ejecta becomes lanthanide-free with increasing  $Y_e$ , but the light curve peak becomes about an order of magnitude brighter because it peaks much earlier when the heating rate is larger. We also provide parametric fits for the heating rates between 0.1 and 100 days, and we provide a simple fit in  $Y_e$ ,  $s$ , and  $\tau$  to estimate whether the ejecta is lanthanide-rich or not.

*Subject headings:* gamma-ray burst: general – gravitational waves – nuclear reactions, nucleosynthesis, abundances – stars: neutron

### 3.1 Introduction

The merger of a compact binary system that includes at least one neutron star, hence the merger of a neutron star with a black hole (NSBH) or the merger of two neutron stars (NSNS), is likely to eject a significant amount of material during the final stages of coalescence (Lattimer et al., 1977) in addition to emitting gravitational waves that may be observed by gravitational wave detectors such as advanced LIGO (LIGO Scientific Collaboration et al., 2015) and possibly powering short gamma ray bursts (sGRBs) (e.g. Lee and Ramirez-Ruiz, 2007; Nakar, 2007; Gehrels et al., 2009). The material that is unbound during the merger is of interest for two main reasons. First, the majority of the mass ejected in these events is very neutron-rich. Once the material decompresses from initial densities close to nuclear density, the large number of neutrons can rapidly capture on the few heavy nuclides present and produce nuclei up to nuclear mass 300. This process is called the r-process because neutrons are captured rapidly compared to the  $\beta$ -decay timescale of the unstable nuclides produced by neutron capture. Thus the r-process quickly creates heavy, very neutron-rich nuclides that eventually decay back to stability after the neutron capture ceases (Burbidge et al., 1957). Depending on the rate of NSBH and NSNS mergers and the amount of neutron-rich material ejected during these events, they can be the dominant source of r-process nucleosynthesis in the universe (Argast et al., 2004; Shen et al., 2015; van de Voort et al., 2015; Ramirez-Ruiz et al., 2015).

Second, observable electromagnetic signals may be associated with these ejecta. A radio transient that occurs on a timescale of a few weeks can be powered by the interaction of the ejecta with the surrounding medium (Nakar and Piran, 2011). Additionally, radioactive decay of unstable nuclides formed during decompression of the ejecta can power a transient in the optical or infrared that peaks on a timescale of a day to a week (Li and Paczyński, 1998; Kulkarni, 2005; Metzger et al., 2010; Kasen et al., 2013; Tanaka and Hotokezaka, 2013). These are often referred to as either “kilonovae” (Metzger et al., 2010) or “macronovae” (Kulkarni, 2005). In fact, one of these events may have been observed. An excess in the infrared afterglow of nearby GRB130603B, which was an sGRB, has been interpreted by some authors as a strong indicator of a transient powered by the decay of r-process material (Tanvir et al., 2013; Berger et al., 2013). A similar kilonova like excess has recently been observed in the afterglow of GRB060614 (Yang et al., 2015; Jin et al., 2015).

Although almost all of the ejected material will be neutron-rich, there can be a significant spread in the electron fraction of this neutron-rich material. The compo-

sition will depend on whether the material was ejected tidally (Lattimer et al., 1977; Freiburghaus et al., 1999), dynamically from the region where the two neutron stars collide (Bauswein et al., 2013; Hotokezaka et al., 2013b), or from the accretion disk that forms after the merger (Fernández and Metzger, 2013; Perego et al., 2014; Just et al., 2015). Since the material ejected by all of these mechanisms starts out as cold, catalyzed material in a neutron star, the final electron fraction of the material depends on the weak interaction timescale relative to the dynamical timescale of the ejecta. If the temperature and local neutrino density are low, and therefore weak interactions are slow, the electron fraction is unaltered. This is the case for the tidal ejecta, which is predicted to have a very low electron fraction (Korobkin et al., 2012). Conversely, material ejected from the disk stays near the compact object for a long period and can achieve beta-equilibrium at lower density and higher temperature (Just et al., 2015; Richers et al., 2015). The dynamical ejecta from the contact region sits somewhere in between, as it is ejected rapidly but shocked to high temperatures and irradiated strongly by neutrinos, which can significantly alter the initial electron fraction (Wanajo et al., 2014; Goriely et al., 2015).

At low initial electron fractions ( $Y_e \lesssim 0.2$ ), the final composition of the ejecta is relatively insensitive to the initial electron fraction of the material because a strong r-process occurs and fission cycling produces a robust pattern (Metzger et al., 2010; Roberts et al., 2011; Goriely et al., 2011). But for higher electron fractions ( $0.2 \lesssim Y_e \lesssim 0.3$ ), an incomplete r-process can occur and the composition will be much more sensitive to the properties of the outflow (Korobkin et al., 2012; Grossman et al., 2014; Kasen et al., 2015). In addition to the total mass and velocity of the ejecta, the composition of the ejecta at around a day—which determines the nuclear heating rate and opacity of the material—plays a large role in determining the properties of the kilonova (Li and Paczyński, 1998). Since losses due to adiabatic expansion rob all of the initial energy from the outflow, almost all of the energy that powers the transient must come from thermalizing the products of nuclear decay (Metzger et al., 2010). This in turn implies that the peak luminosity of a kilonova is sensitive to the composition.

The opacity of the material determines the timescale on which the ejecta becomes optically thin and therefore the timescale on which the transient will peak. Kasen et al., 2013 and Tanaka and Hotokezaka, 2013 have shown that continuum opacity is very sensitive to the presence of lanthanides, and possibly actinides, in the outflow. Due to their large atomic complexity, lanthanides and actinides have a very large

number of lines relative to iron group elements and therefore their presence drastically increases the opacity of the material and causes predicted kilonovae to peak on timescales of around a week (Barnes and Kasen, 2013; Tanaka and Hotokezaka, 2013). Older models that assumed iron-like opacities predicted a peak timescale of around a day (Metzger et al., 2010; Roberts et al., 2011; Goriely et al., 2011). Significant lanthanide and actinide production requires very neutron-rich conditions, so Metzger and Fernández, 2014 have suggested that measurement of the peak time of a kilonova might provide insight into the composition of the outflow.

In this work, we present a parameter study of detailed nucleosynthesis calculations in NSBH or NSNS merger scenarios and their associated kilonova light curves. We focus in particular on the mass fraction of lanthanides and actinides present in the ejecta, the radioactive heating rate at 1 day, and how these properties depend on the initial conditions of the outflow. As expected, the lanthanide and actinide abundances depend strongly on the electron fraction, but the entropy and expansion timescale can also play an important role in certain cases. In contrast, we find that the nuclear decay heating rate does not depend as strongly on the initial electron fraction and it changes relatively smoothly when going from lanthanide-rich to lanthanide-free cases. The peak timescale, peak luminosity, and spectral temperature of our modeled kilonovae differ substantially due to the effect of the lanthanides and actinides on the opacity. In some cases, we also find very early and bright transients due to a neutron-rich freeze-out, which was proposed by Kulkarni, 2005 and Metzger et al., 2015.

In Section 3.2, we describe our parametrized nucleosynthesis calculations and discuss how lanthanide production and the nuclear heating rate varies over our chosen parameter space. In Section 3.3, we present simplified kilonova light curve models and examine how these transients vary with outflow properties. We then conclude in Section 3.4. Lanthanides and actinides both have open  $f$ -shells and thus a similar valence electron structure, which means their impact on the opacity is similar (Kasen et al., 2013). Therefore, we will use the term “lanthanides” to refer to both lanthanides and/or actinides, unless otherwise noted.

### 3.2 Parameterized ejecta nucleosynthesis

The details of the  $r$ -process abundance pattern, especially the position of the third peak, can be sensitive to the nuclear mass model, reaction rates, and fission fragment distributions that are used (e.g. Goriely et al., 2005; Arcones and Martínez-Pinedo,

2011; Mumpower et al., 2012; Mendoza-Temis et al., 2015; Eichler et al., 2015). Here, we are less interested in the detailed final abundance patterns at high mass and more interested in the surfaces in our parameter space at which lanthanide production ceases. Therefore, we employ a single mass model and set of reaction rates. We use two models for fission fragments, but our main results are insensitive to this choice.

Rather than post-processing full hydrodynamic models as was done in Goriely et al. (2011), Korobkin et al. (2012), Grossman et al. (2014), Wanajo et al. (2014), Just et al. (2015), and Martin et al. (2015), we use a parametrized approach that allows us to systematically study the impact of different ejecta properties on the properties of the ejected material relevant to kilonovae. Kasen et al. (2015) performed preliminary investigations of the electron fraction at which lanthanide production ceases, but they did not investigate how this influences the nuclear decay heating rate and only considered a small region of the parameter space.

We use the following three parameters to characterize the expanding material that undergoes r-process nucleosynthesis and produces a kilonova.

(i) The initial **electron fraction**  $Y_e = N_p/N_B$ , where  $N_p$  is the total number of protons (free or inside nuclei) and  $N_B$  is the total number of baryons. We sample  $Y_e$  uniformly between 0.01 (very neutron-rich matter) and 0.5 (symmetric matter). We do not consider  $Y_e > 0.5$  because the r-process requires a neutron-rich environment.

(ii) The initial **specific entropy**  $s$ , which we sample logarithmically between 1 and  $100 k_B$  baryon<sup>-1</sup>.

(iii) The **expansion timescale**  $\tau$ , which determines how fast the density decreases during nuclear burning. We sample  $\tau$  logarithmically between 0.1 and 500 ms. We choose an analytic density profile that initially decreases exponentially with time, i.e.  $\rho \propto e^{-t/\tau}$ , and then transitions smoothly to a homologous,  $\rho \propto t^{-3}$ , expansion. Requiring continuity of  $\rho$  and  $d\rho/dt$  fixes the matching point at  $t = 3\tau$  and gives

$$\rho(t) = \begin{cases} \rho_0 e^{-t/\tau} & \text{if } t \leq 3\tau, \\ \rho_0 \left(\frac{3\tau}{et}\right)^3 & \text{if } t \geq 3\tau, \end{cases} \quad (3.1)$$

where  $\rho_0$  is the initial density and  $e$  is Euler's number. This parameterization of the density is chosen because it gives us direct control over the dynamical timescale at the time of r-process nucleosynthesis but still matches smoothly to the density profile expected for homologous ejecta. We have also found that this profile gives a

good approximation to density histories of Lagrangian fluid elements in the ejecta of BHNS mergers simulations (Duez, 2015; Foucart et al., 2014)

We determine  $\rho_0$  by setting the initial temperature to  $T = 6 \times 10^9$  K and then finding the density for which nuclear statistical equilibrium (NSE) (with the given  $Y_e$ ) produces a set of abundances that has the prescribed initial entropy  $s$ . The entropy is calculated from the NSE distribution using a modified version of the Helmholtz equation of state (EOS) based on Timmes and Swesty, 2000. The EOS has been modified to calculate the entropy for each nuclear species separately, rather than using average mass and charge numbers, and it also includes the internal partition functions of all nuclear species, which we obtained from the WebNucleo database distributed<sup>1</sup> with REACLIB (see below). The resulting initial densities range from  $7.1 \times 10^5$  to  $1.4 \times 10^{12}$  g cm<sup>-3</sup>.

Given  $Y_e$ ,  $s$ , and  $\tau$ , NSE determines  $\rho_0$  (and thus  $\rho(t)$ ) and the initial abundances. We then use the newly developed nuclear reaction network *SkyNet* for the abundance evolution. *SkyNet* is a general-purpose, modular nuclear reaction network that keeps track of entropy and temperature changes due to the nuclear reactions it is evolving. A detailed code description of the functionality and features of *SkyNet* is forthcoming (Lippuner and Roberts, 2017, in prep.), and the source code will be publicly released together with that paper. In the meantime, anyone who wishes to use *SkyNet* can contact the authors and request access to the code.

We run *SkyNet* with nuclear reaction rates from the JINA REACLIB database<sup>2</sup> (Cyburt et al., 2010). The nuclear data (masses and partition functions) were taken from the associated WebNucleo XML file distributed with REACLIB. Although REACLIB includes inverse rates for the strong reactions, *SkyNet* calculates these inverse rates from detailed balance, so that the rates are consistent with NSE. We also include different sets of spontaneous and neutron-induced fission rates, as REACLIB does not presently include any fission reactions. There are three sets of symmetric neutron-induced fission reactions: *sym0*, *sym2*, and *sym4*, which produce 0, 2, and 4 free neutrons, respectively, for each fission event. There is also a set

<sup>1</sup><https://groups.nscf.msu.edu/jina/reaclib/db/library.php?action=viewsnapshots>

<sup>2</sup>At the time of writing, the latest REACLIB snapshot (2013-04-02) contains 83 incorrect  $\beta$ -decay rates, which we corrected for this study. It appears that some lower limits of the half-lives published in the Nuclear Wallet Cards (<http://www.mndc.bnl.gov/wallet>) were put into REACLIB, but those lower limits can be very far away from realistic estimates of the half-lives. For example, REACLIB gives a half-life of 300 ns for <sup>216</sup>Pb because the Nuclear Wallet Cards state the half-life is “> 300 ns”, but Möller et al. (2003) gives a half-life of about 850 s, which is much closer to the half-lives of similar nuclides.

nonsym of non-symmetric fission reactions that do not produce any free neutrons. Each nucleosynthesis calculation includes one of the four neutron-induced fission reaction sets and the spontaneous fission reaction set. All the fission reactions and their rates are taken from the same sources used in Roberts et al., 2011.

We use beta-decay and electron capture rates from Fuller et al., 1982, Oda et al., 1994 and Langanke and Martínez-Pinedo, 2000 whenever they are available. For nuclei for which these rates are not available, the effects of electron blocking and positron capture are approximately included by assuming that only a ground state to ground state transition occurs as described in Arcones et al., 2010. These rates are then normalized such that they are equal to the vacuum decay rates given in REACLIB at low temperature and density, which can be thought of as setting the effective matrix element for the ground state to ground state transition. Because this procedure assumes a maximal  $Q$ -value for these weak rates, this provides a lower limit on the effect of the surrounding medium on the combined beta-decay and lepton capture rate. For this study, we run *SkyNet* with 7843 nuclear species, ranging up to  $Z = 112$  and  $A = 337$ , and 110,793 nuclear reactions.

### 3.2.1 Parameter space

We use a  $9 \times 9 \times 9$  grid to cover the entire parameter space and run *SkyNet* for each point with all four sets of neutron-induced fission reactions (sym0, sym2, sym4, nonsym). We also run the sym0 fission reactions with a finer  $17 \times 17 \times 17$  grid. The parameter values at the grid points are shown in Table 3.1. The different fission reactions only result in small quantitative and no qualitative differences. Thus we only discuss and show plots of the high-resolution sym0 runs. Finally, we carry out a set of runs with high  $Y_e$  resolution ( $\Delta Y_e = 0.005$  resulting in 99  $Y_e$  points) for  $s = 1, 10, 30, 100 k_B \text{ baryon}^{-1}$  and  $\tau = 0.1, 1, 10 \text{ ms}$  with the sym0 fission reactions. The data underlying all the results shown and discussed here (nucleosynthesis results, heating rate fit coefficients, light curve model results, and integrated fractional heating contributions of all nuclides) are available at <http://stellarcollapse.org/lippunerroberts2015>.

Figure 3.1 shows the final abundances of a few selected cases, which span the whole range of  $Y_e$  and  $s$  at intermediate values of the other two parameters. For the  $s = 10 k_B \text{ baryon}^{-1}$  and  $\tau = 7.1 \text{ ms}$  trajectories (left panel of Figure 3.1), the full r-process up to the third peak ( $A \sim 190$ ) for  $Y_e = 0.01$  and  $Y_e = 0.19$  is produced. We note good agreement of the second, third, and rare-earth peak positions with

Table 3.1: Parameter Values at Grid Points

Low-resolution points <sup>a</sup>			Additional high-resolution points <sup>b</sup>		
$Y_e$	$s$ ( $k_B$ baryon <sup>-1</sup> )	$\tau$ (ms)	$Y_e$	$s$ ( $k_B$ baryon <sup>-1</sup> )	$\tau$ (ms)
0.01	1.0	0.10			
			0.04	1.3	0.17
0.07	1.8	0.29			
			0.10	2.4	0.49
0.13	3.2	0.84			
			0.16	4.2	1.4
0.19	5.6	2.4			
			0.22	7.5	4.2
0.25	10	7.1			
			0.29	13	12
0.32	18	21			
			0.35	24	35
0.38	32	59			
			0.41	42	100
0.44	56	170			
			0.47	75	290
0.50	100	500			

<sup>a</sup> The low-resolution runs of the entire parameter space use only these grid points.

<sup>b</sup> For the high-resolution runs of the entire parameter space we double the number of grid points. The high-resolution runs include the grid points shown in this column in addition to the the same points as the low-resolution runs.

the solar r-process abundances, although the third peak is slightly overproduced relative to the second peak. The abundance patterns of  $Y_e = 0.01$  and  $Y_e = 0.19$  are very similar because both cases are neutron-rich enough to produce nuclides with  $A \gtrsim 250$ , which eventually undergo fission. As the ejecta becomes less neutron-rich ( $Y_e = 0.25$  and  $Y_e = 0.50$ ), the full r-process is no longer produced; there are not enough neutrons available per seed nucleus to reach the third peak. At  $Y_e = 0.25$ , the first and second r-process peaks are produced. The right panel of Figure 3.1 shows the final abundances of cases with  $Y_e = 0.25$ ,  $\tau = 7.1$  ms, and different initial entropies. Here, the electron fraction is too high to get to the third r-process peak at most entropies (all the cases with entropies between 10 and  $75 k_B$  baryon<sup>-1</sup> have virtually identical final abundances as the  $s = 10 k_B$  baryon<sup>-1</sup>

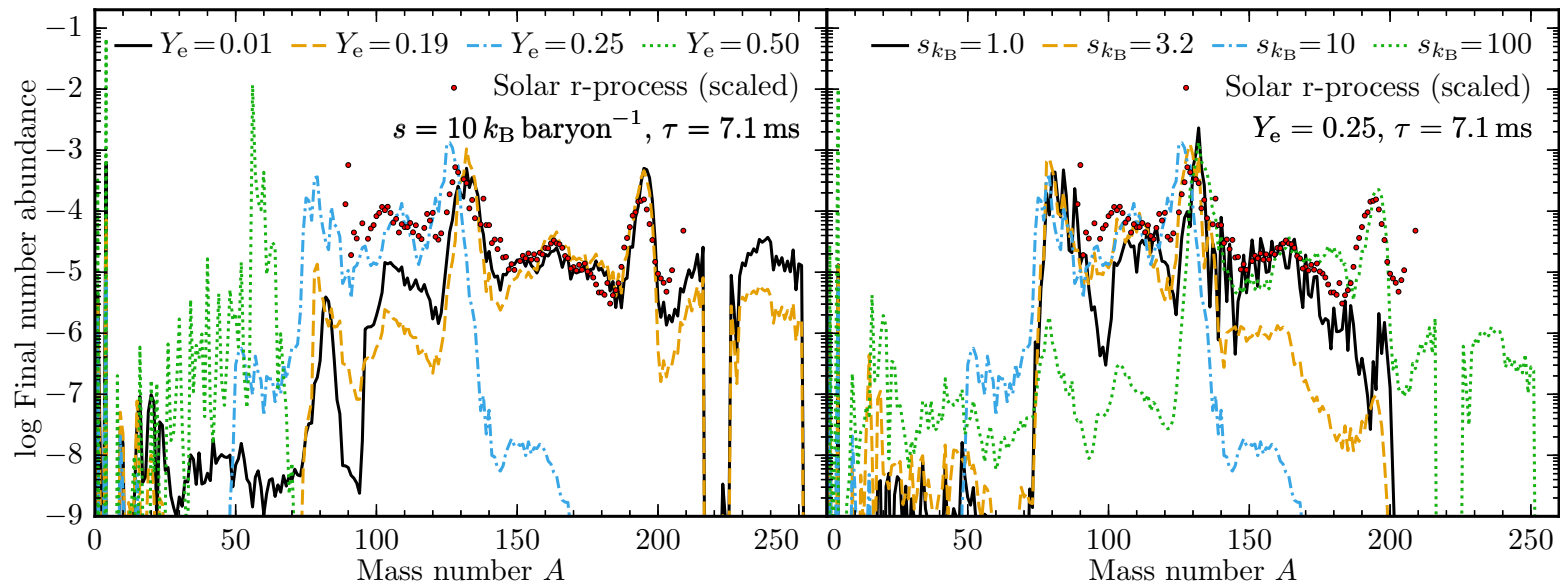


Figure 3.1: The final abundances of some selected nucleosynthesis calculations. **Left:**  $Y_e = 0.01, 0.19, 0.25, 0.50$ ,  $s = 10 k_B \text{ baryon}^{-1}$ , and  $\tau = 7.1 \text{ ms}$ . The full r-process is made, with substantial amounts of lanthanides and actinides, for  $Y_e = 0.01$  and  $Y_e = 0.19$ . The  $Y_e = 0.25$  trajectory is neutron-rich enough to make the second r-process peak, but not the third and not a significant amount of lanthanides. In the symmetric case ( $Y_e = 0.5$ ), mostly  ${}^4\text{He}$  and iron-peak elements are produced. **Right:**  $Y_e = 0.25$ ,  $s = 1.0, 3.2, 10, 100 k_B \text{ baryon}^{-1}$ , and  $\tau = 7.1 \text{ ms}$ . With  $s = 1 k_B \text{ baryon}^{-1}$  a jagged r-process is obtained because there are only few free neutrons per seed nucleus available and nuclides with even neutron numbers are favored. Even though there are not many free neutrons available, there is still a significant amount of lanthanides in the  $s = 1 k_B \text{ baryon}^{-1}$  case because the initial seed nuclei are very heavy. At higher entropies, the initial seeds become lighter and the initial free neutron abundance increases. However, the increase in the initial free neutron abundance is not enough to offset the decrease in the initial mass of the seeds and so we obtain a less complete r-process. The situation is reversed at  $s = 100 k_B \text{ baryon}^{-1}$ , where there is a very high neutron-to-seed ratio. In that case, a significant fraction of  $\alpha$  particles are also captured on the seed nuclei. This leads to a full r-process in the  $s = 100 k_B \text{ baryon}^{-1}$  case.

case). At  $s = 100 k_B \text{ baryon}^{-1}$  the third r-process peak is obtained because the initial composition contains few seed nuclei and alpha particles are unable to efficiently combine to produce seed nuclei. Thus, the neutron-to-seed ratio is significantly enhanced.

Animations of the full nucleosynthesis calculations for all seven cases shown in Figure 3.1 are available at <http://stellarcollapse.org/lippunerroberts2015>. Figure 3.2 shows a frame from one of the animations.

### 3.2.2 Lanthanide turnoff and heating rate as a function of $Y_e$

Figure 3.3 shows the final lanthanide and actinide mass fractions  $X_{\text{La}}$  and  $X_{\text{Ac}}$ , respectively, along with the neutron mass fraction  $X_n$  at 10 minutes, which is the mean lifetime of a free neutron. Also shown is  $\bar{A}_{\text{fin}}$ , which is an estimate of the final average mass number  $A$  of the material. It is defined as

$$\bar{A}_{\text{fin}} = \frac{1}{Y_{\text{seed}}(0) + Y_{\alpha}(0)/18}, \quad (3.2)$$

where  $Y_{\alpha}(0)$  is the initial  $\alpha$ -particle abundance and  $Y_{\text{seed}}(0)$  is the initial seed abundance (sum of abundances of all nuclides with  $A \geq 12$ ). Since the  $\alpha$ -process ceases around Kr in neutron rich conditions (Woosley and Hoffman, 1992), it takes around eighteen  $\alpha$  particles to make a seed nucleus. Therefore, the quantity in the denominator of Equation (3.2) is approximately the number abundance of heavy nuclei present at the end of the r-process. We then arrive at Equation (3.2) by assuming that the total mass fraction of heavy nuclei at the end of the calculation is unity. Clearly, this assumption breaks down if there is fission cycling, because then the number of seeds at the end is much larger than the number of initial seeds plus those produced by the  $\alpha$ -process. However, we are interested in the value of  $\bar{A}_{\text{fin}}$  at the actinide and lanthanide turnoff, which preclude significant fission cycling because fission cycling only happens if nuclides heavier than actinides are produced, and so there is no problem in using the definition in Equation (3.2). At low electron fractions,  $\alpha$ -rich freeze-out does not occur due to the low initial abundance of  $\alpha$  particles. We emphasize that  $\bar{A}_{\text{fin}}$  only depends on the initial abundances, and thus it is useful to determine whether a certain trajectory is likely to produce large quantities of lanthanides or actinides, without having to perform any nucleosynthesis calculation.

Table 3.2 shows the values of  $Y_e$  and  $\bar{A}_{\text{fin}}$  at which lanthanide and actinide production ceases (mass fraction goes below  $10^{-3}$ ). In other words, if  $Y_e$  is lower than or  $\bar{A}_{\text{fin}}$

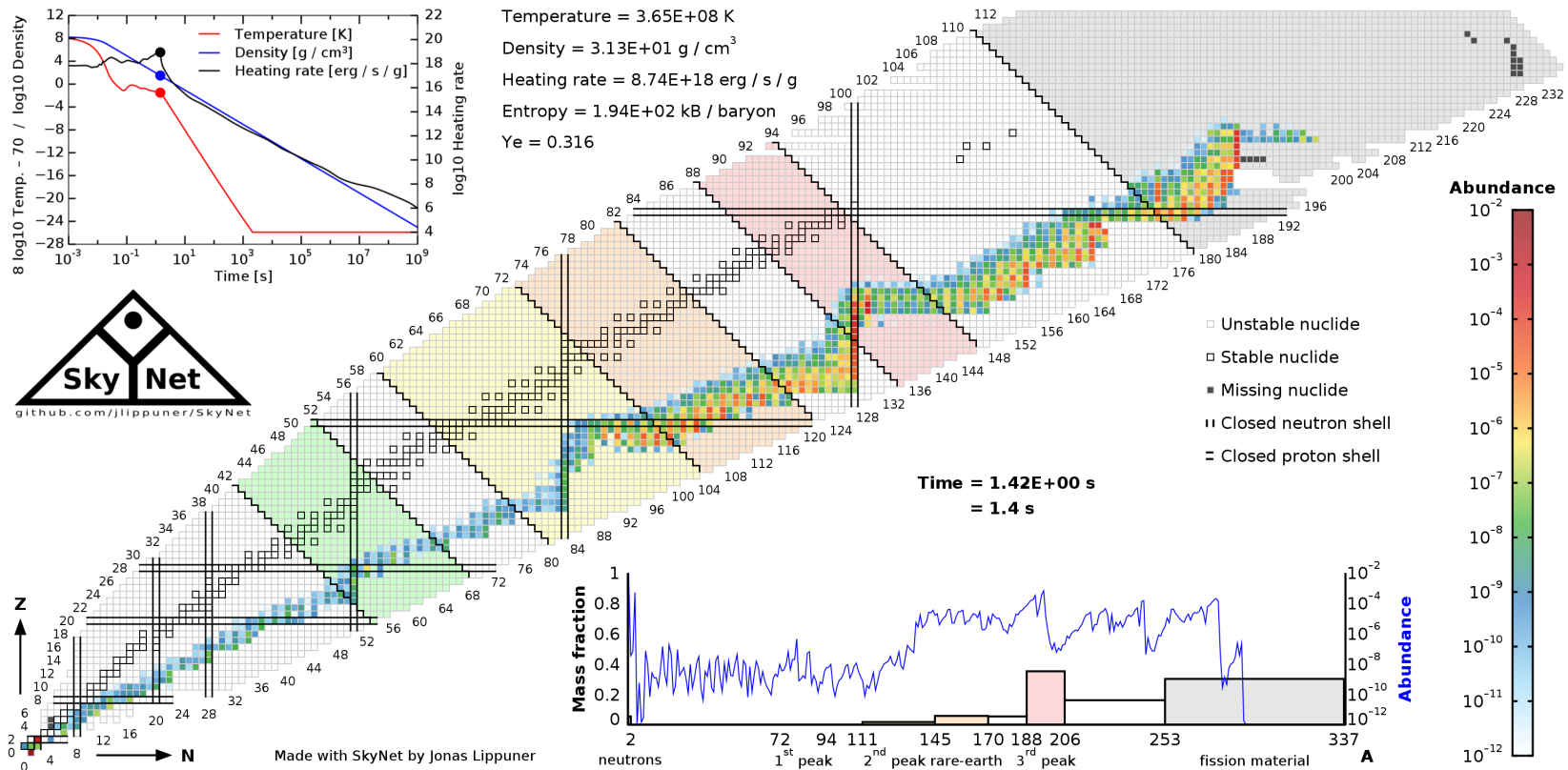


Figure 3.2: A frame from the animation of the nucleosynthesis calculation for  $Y_e = 0.01$ ,  $s = 10 k_B \text{ baryon}^{-1}$ , and  $\tau = 7.1 \text{ ms}$ . The frame shows the full extent of the r-process just when free neutrons get exhausted. The plot in the upper left corner shows the temperature, density, and heating rate as function of time. The colored bands in the chart of nuclides correspond to the mass bins in the histogram at the bottom. The histogram shows the mass fractions on a linear scale while the blue curve shows the abundances as a function of mass on a logarithmic scale. The full animations are available at <http://stellarcollapse.org/lippunerroberts2015>.

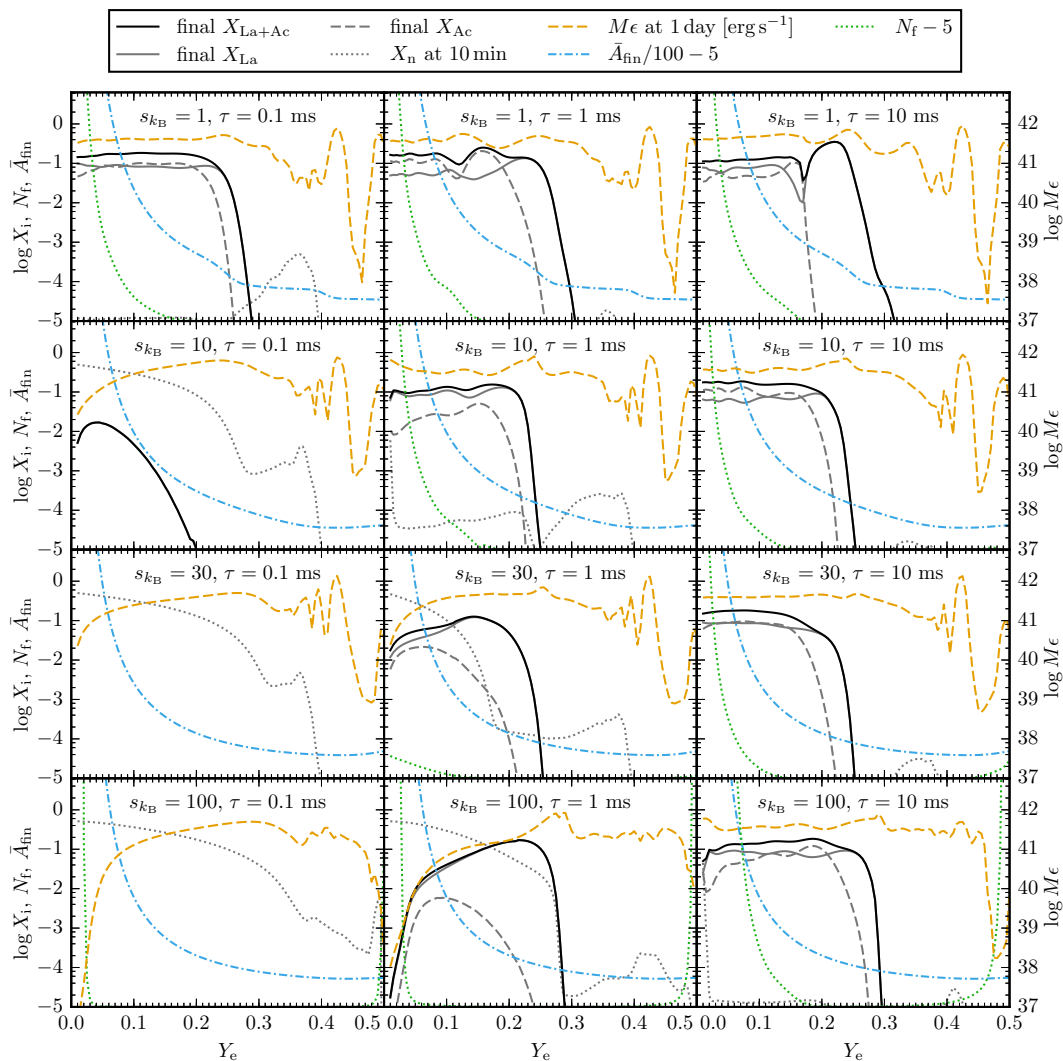


Figure 3.3: Results of the high-resolution  $Y_e$  runs. The lanthanide and actinide mass fractions,  $X_{\text{La}}$  and  $X_{\text{Ac}}$ , and their sum,  $X_{\text{La+Ac}}$ , are fairly constant up to some critical value of  $Y_e$  in most cases because of fission cycling. The neutron abundance  $X_n$  at 10 minutes (the mean lifetime of a free neutron) is an indicator for a neutron-rich freeze-out, which occurs at high initial entropies and short expansion timescales, where the neutrons do not have time to capture on the seed nuclei. The heating rate  $M\epsilon$  at 1 day with  $M = 10^{-2} M_\odot$  is fairly insensitive to  $Y_e$ , except at high electron fractions ( $Y_e \gtrsim 0.4$ ) where some individual nuclides start to dominate the heating. The estimated final average mass number  $\bar{A}_{\text{fin}}$  falls off monotonically with  $Y_e$  in all cases except  $s = 100 k_B$  baryon $^{-1}$ , where it rebounds at  $Y_e$  very close to 0.5. There, the number of seed nuclei decreases drastically because  $\alpha$ -particles are initially produced in higher quantities, which increases the neutron-to-seed ratio. In those cases, the predicted number of fission cycles  $N_f$  is artificially increased at high  $Y_e$ , because of production of seed nuclei by the triple- $\alpha$  process. Where Equation (3.3) accurately predicts the number of fission cycles,  $N_f$  falls off rapidly with  $Y_e$  and the point  
(figure caption continued on next page)

(continued caption of Figure 3.3)

where it becomes zero is correlated with the actinide turnoff, because actinides are at the low end of the fissionable material mass range. Note that we plot  $\bar{A}_{\text{fin}}$  and  $N_f$  on linear scales rather than log scales as all the other quantities. Also, we added a negative offset of 5 to both  $\bar{A}_{\text{fin}}$  and  $N_f$  and we scaled  $\bar{A}_{\text{fin}}$  by 1/100 so that they fit onto our left vertical axis.

Table 3.2:  $\bar{A}_{\text{fin}}$  and  $Y_e$  at Lanthanide and Actinide Turnoff

$s$	$\tau$	Lanthanide turnoff <sup>a</sup>		Actinide turnoff <sup>a</sup>	
		$Y_e$	$\bar{A}_{\text{fin}}$	$Y_e$	$\bar{A}_{\text{fin}}$
(k <sub>B</sub> baryon <sup>-1</sup> ) (ms)					
1.0	0.1	0.27	94	0.25	123
1.0	1	0.28	91	0.24	137
1.0	10	0.28	93	0.18	192
1.8	0.1	0.25	106	0.21	123
1.8	1	0.27	100	0.21	125
1.8	10	0.27	98	0.17	170
3.0	0.1	0.23	118	0.20	135
3.0	1	0.25	111	0.21	130
3.0	10	0.27	106	0.18	150
5.6	0.1	0.22	135	0.14	196
5.6	1	0.23	127	0.21	138
5.6	10	0.24	124	0.21	140
10	0.1	0.13	223	–	–
10	1	0.24	121	0.21	139
10	10	0.24	120	0.21	139
18	0.1	–	–	–	–
18	1	0.24	102	0.20	130
18	10	0.24	102	0.21	125
30	0.1	–	–	–	–
30	1	0.24	93	0.18	132
30	10	0.24	93	0.20	113
56	0.1	–	–	–	–
56	1	0.24	94	0.16	143
56	10	0.24	94	0.21	109
100	0.1	–	–	–	–
100	1	0.28	94	0.18	148
100	10	0.29	92	0.26	102

<sup>a</sup> Turnoff is when the mass fraction  $X_{\text{La}}$  or  $X_{\text{Ac}}$  drops below  $10^{-3}$ . The columns show the maximum  $Y_e$  and corresponding minimum  $\bar{A}_{\text{fin}}$  for which  $X_i \geq 10^{-3}$ . A dash (–) denotes that  $X_i < 10^{-3}$  for all  $Y_e$ , which means there is a neutron-rich freeze-out.

larger than what is shown in Table 3.2, then  $X_{\text{La}} \geq 10^{-3}$  or  $X_{\text{Ac}} \geq 10^{-3}$ . The lanthanide turnoff is at  $\bar{A}_{\text{fin}} \sim 100$  and the actinide turnoff is at  $\bar{A}_{\text{fin}} \sim 130$ . The cases where  $X_{\text{La}} < 10^{-3}$  or  $X_{\text{Ac}} < 10^{-3}$  for all  $Y_e$  are denoted by “–” in Table 3.2, and they correspond to the strong neutron-rich freeze-outs in Figure 3.3, which means that the r-process did not happen (or at least not efficiently) in those cases because after about 10 min we are just left with free neutrons that will now decay to protons. In the case  $s10\tau0.1$  (which stands for  $s = 10 k_B \text{ baryon}^{-1}$  and  $\tau = 0.1 \text{ ms}$ ) where lanthanides are made, but no actinides above a mass fraction of  $10^{-3}$ , we see a weaker neutron-rich freeze-out in Figure 3.3. The neutron-rich freeze-outs happen at high initial entropies and short expansion timescales, where the ejecta is very hot and expands quickly, which leaves little time for neutrons to capture on seed nuclides. There is also a neutron-rich freeze-out in  $s30\tau1$  and  $s100\tau1$  models, but the freeze-out is weak enough to allow lanthanides and actinides to be produced, albeit in lower quantities. Metzger et al. (2015) suggested that a kilonova containing some mass with such short dynamical timescales could be preceded by an ultraviolet transient powered by these frozen-out neutrons.

Figure 3.3 shows that the heating rate from decay at 1 day is quite insensitive to  $Y_e$  at  $Y_e \lesssim 0.35$  and also fairly insensitive to the amount of lanthanides and actinides produced. As long as  $X_{\text{La+Ac}}$  is more or less constant as a function of  $Y_e$ ,  $M\epsilon$  at 1 day is also fairly constant. When the lanthanides turn off, there is a small bump in the heating rate in most cases and at larger  $Y_e$ , after lanthanides have completely gone away, the heating rate drops only slightly (an order of magnitude or less). One might expect a larger decline of the heating rate once the full r-process stops happening, because the material is less neutron-rich overall, more stable nuclei are produced directly, and thus the total radioactive decay energy should be lower. This is indeed true and we verified it by looking at the integrated nuclear heating amount as a function of  $Y_e$  (for fixed  $s$  and  $\tau$ ). We find that in most cases the total amount of heating drops by 1.5 to 2 orders of magnitude as  $Y_e$  goes from low values to high values. There is a smaller drop in the heating rates shown in Figure 3.3, because there we only plot the instantaneous heating rate at 1 day. Since the  $\beta$ -decay energy is correlated with the decay timescale, we always see a similar instantaneous decay rate at the same point in time, as long as we have a collection of nuclides with half-lives at around a day. The picture changes at  $Y_e \gtrsim 0.35$  because there the final composition is dominated by one or a few individual nuclides, as opposed to a large ensemble of nuclides, which then determine the heating rate. This is discussed in detail in Section 3.2.4.

Since our parameter space is three-dimensional, we can go beyond giving a simple  $Y_e$  cutoff for lanthanide production. We use a heuristic method to fit for the coefficients of three inequalities in  $Y_e$ ,  $\ln s$ , and  $\ln \tau$  that separate the lanthanide-rich and lanthanide-free regions of the parameter space. We find that

$$\begin{aligned}
 X_{\text{La+Ac}} &\geq 10^{-3} \text{ if and only if} \\
 -1.00 Y_e - 0.00744 \ln s_{k_B} + 0.000638 \ln \tau_{\text{ms}} + 0.259 &\geq 0 \\
 \text{and} \\
 -0.990 Y_e + 0.117 \ln s_{k_B} - 0.0783 \ln \tau_{\text{ms}} + 0.452 &\geq 0 \\
 \text{and} \\
 -0.799 Y_e - 0.288 \ln s_{k_B} + 0.528 \ln \tau_{\text{ms}} + 1.88 &\geq 0,
 \end{aligned}$$

where  $s_{k_B}$  is the entropy  $s$  in units of  $k_B$  baryon<sup>-1</sup> and  $\tau_{\text{ms}}$  is the expansion timescale  $\tau$  in units of milliseconds. The above statement only fails for 97 out of 4913 points in our parameter space, i.e. it is true for 98% of the parameter space. Most of the points where the above fails are very close to one of the planes, but there are a few points further away from the boundaries that fail too. Those points are all at very low  $Y_e$ , high entropy, and very short expansion timescale, where we get strong neutron-rich freeze-out. The results of the full parameter space are discussed in detail in Section 3.2.4.

### 3.2.3 Fission cycling

If the r-process is strong enough to produce nuclides with masses near 300, these nuclides fission and the fission products then capture more neutrons, eventually getting up to  $A \sim 300$  and fissioning again, creating a fission cycle. Thus fission cycling limits the maximum mass of nuclides produced in the r-process, which washes out the initial conditions of the ejecta and hence the final abundances are determined by nuclear physics rather than the properties of the outflow.

The quantity  $N_f$  shown in Figure 3.3 is an estimate for the number of fission cycles that occurred during nucleosynthesis. It is defined as

$$N_f = \frac{Y_{\text{seed}}(t = t_n)}{Y_{\text{seed}}(t = 0)} - 1, \quad (3.3)$$

where  $Y_{\text{seed}}(t = t_n)$  is the abundance of all seed nuclides ( $A \geq 12$ ) at the time that neutrons are exhausted (when  $X_n \leq 10^{-4}$ ) and  $Y_{\text{seed}}(t = 0)$  is the initial abundance of seed nuclei. This estimate for the number of fission cycles rests on the assumption

that only fission can create additional seed nuclides. When a neutron captures on a seed nuclide, it creates a heavier nuclide, but it will not increase the total number (and hence abundance) of seed nuclides in the ejecta. However, if a heavy nuclide (which is counted as a seed nuclide) fissions, then there are two seed nuclides in its place. Thus comparing the number of heavy nuclides at the time when neutron capture ceases to the initial number of heavy nuclides tells us how many additional heavy nuclides were produced. For example, if  $Y_{\text{seed}}(t = t_n) = Y_{\text{seed}}(t = 0)$ , then no additional heavy nuclides were produced and thus there was no fission cycling, hence  $N_f = 0$ . But if  $Y_{\text{seed}}(t = t_n) = 3Y_{\text{seed}}(t = 0)$ , for example, then (on average) each initial heavy nuclide produced two additional heavy nuclides and so there were two fission cycles, hence  $N_f = 2$ . Note that this method of estimating the number of fission cycles breaks down if nuclides with  $A \geq 12$  are produced from nuclides with  $A < 12$ , e.g.  $^{12}\text{C}$  from three  $^4\text{He}$ . This happens most prominently at  $Y_e$  close to 0.5 and at high entropies, where fission will clearly not occur.

As expected, there are many fission cycles at low  $Y_e$  where large amounts of lanthanides and actinides are produced. In the regions with significant fission cycling,  $X_{\text{La}}$ ,  $X_{\text{Ac}}$ , and  $\epsilon$  are fairly insensitive to  $Y_e$  because fission cycling effectively limits the maximum mass of nuclides that are produced to  $A \sim 300$ . As the ejecta becomes less neutron-rich, fewer fission cycles occur because there are not enough free neutrons to produce fissionable material with  $A \gtrsim 250$ .

In most panels in Figure 3.3 we see that the production of actinides is closely tied to fission cycling; actinides go away just after fission cycling stops. If the r-process cannot get to  $A \sim 250$ , it cannot create actinides and it cannot create fissionable material. Furthermore, in most panels, but especially in  $s1\tau1$  and  $s1\tau10$  there is an increase in  $X_{\text{Ac}}$  and decrease in  $X_{\text{La}}$  at the electron fraction where fission cycling stops and just before actinides are not produced. Just as fission cycling stops, the r-process can get to about  $A = 250$ , but not much above. This means that actinides can still be produced, but they are not being fissioned (because only lighter actinides are produced or there are no more free neutrons to initiate fission). Lanthanides have a mass around 150 and so they can be created from fission products. When fission is just turning off, we lose a small source of lanthanides leading to the (small) decline in  $X_{\text{La}}$  that can be prominently seen in  $s1\tau10$  in Figure 3.3 at  $Y_e = 0.17$ .

### 3.2.4 Lanthanide production and heating rate in the full parameter space

Since the amount of lanthanides determines the opacity of the ejecta and the nuclear heating rate determines the amount of energy available for the electromagnetic transient, we are especially interested in how these two quantities are correlated in our parameter space. Figures 3.4 to 3.6 show slices of the final lanthanide and actinide mass fractions,  $X_{\text{La+Ac}}$ , and heating rates at 1 day for the extreme and intermediate values of  $Y_e$ ,  $s$ , and  $\tau$ . All the other slice plots are available at <http://stellarcollapse.org/lippunerroberts2015>. In the following, the term “lanthanide” will stand for both lanthanides and actinides, unless actinides are specifically mentioned. Unsurprisingly,  $X_{\text{La+Ac}}$  depends most strongly on  $Y_e$  and the ejecta is lanthanide-free for  $Y_e \gtrsim 0.26$ . However, even for a very low  $Y_e$  of 0.01, there are some combinations of  $s$  and  $\tau$  that yield a lanthanide-free ejecta (see upper left panel of Figure 3.4). Specifically, at high entropies ( $s \gtrsim 20 k_B \text{ baryon}^{-1}$ ) and small expansion timescales ( $\tau \lesssim 1 \text{ ms}$ ), no lanthanides are produced. The reason for this is that neutron capture begins at a lower density because of the high entropy (for a fixed temperature at which neutron capture begins) and therefore the neutron capture timescale is increased. This—in combination with light seed nuclei, a large initial neutron abundance, a potentially  $\alpha$ -rich freeze-out, and a short dynamical timescale—prevents production of lanthanides and sometimes results in a neutron-rich freeze-out. At lower entropies, the seed nuclei are heavier and the density is higher during the neutron capture period, allowing neutrons to capture on them even at small expansion timescales. And at larger expansion timescales, there is more time for the neutrons to capture on the light seed nuclei even at very high entropies. This is reflected in the upper right panel of Figure 3.5 where no lanthanides are produced at small expansion timescales at  $s = 100 k_B \text{ baryon}^{-1}$ , and in the upper left panel of Figure 3.6 where no lanthanides are produced at high entropies at  $\tau = 0.1 \text{ ms}$ .

There is another lanthanide-free corner in the upper left panel of Figure 3.4 at very large expansion timescales ( $\tau \gtrsim 400 \text{ ms}$ ) and low entropies ( $s \lesssim 3 k_B \text{ baryon}^{-1}$ ). Here, the full r-process is being made, since the material is very neutron-rich, but because the expansion timescale is so long, the density is still quite high (about  $10^{10} \text{ g cm}^{-3}$ ) when neutron burning ceases. All the heavy elements then decay and considerably heat up the material (to above 7 GK), which destroys all heavy nuclides via photodissociation and brings the composition back to NSE. Only after tens of seconds has the material cooled down enough for neutron captures to happen again, but by then,  $\beta$ -decays have raised  $Y_e$  to about 0.3. Thus we now get an r-process

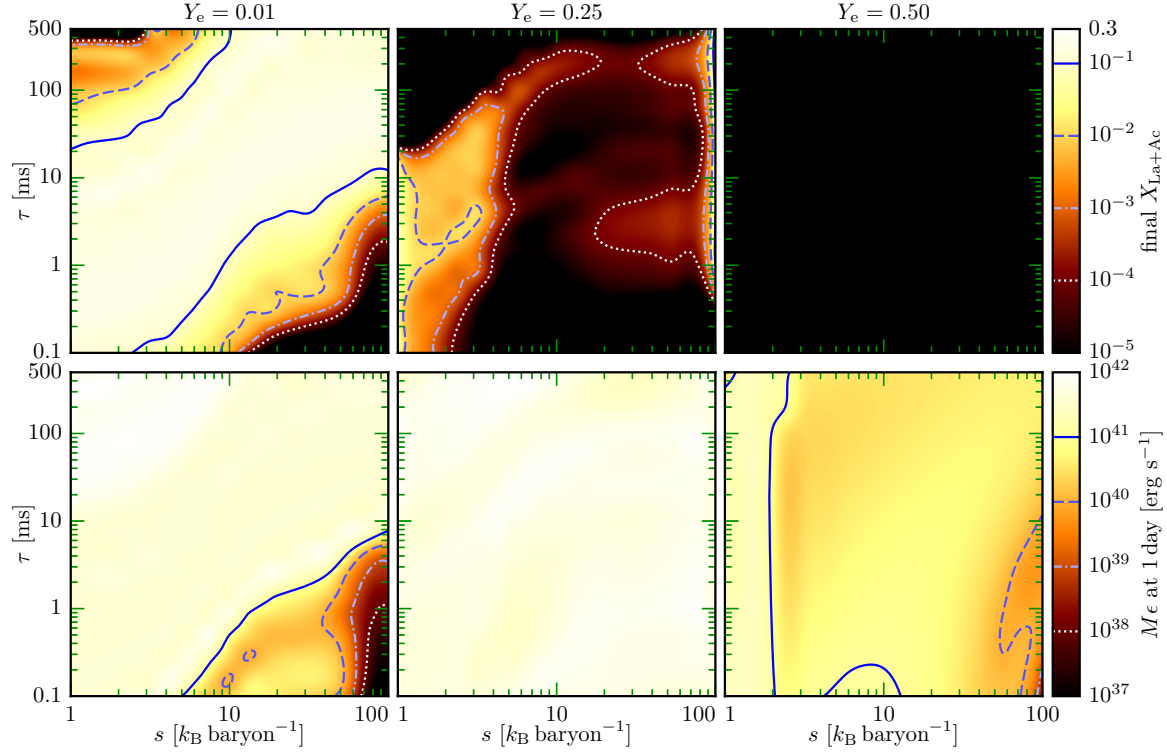


Figure 3.4: Slices of constant electron fraction showing the lanthanide and actinide mass fraction  $X_{\text{La+Ac}}$  and the heating rate  $M\epsilon$  at 1 day with  $M = 10^{-2} M_{\odot}$ . For  $Y_e = 0.01$ , the high- $s$ /small- $\tau$  corner is lanthanide-free because the high entropy produces very light seed nuclides, fewer seed nuclei are produced due to an  $\alpha$ -rich freeze-out, and neutron capture begins at low density due to the high entropy (see the text for more discussion). The low- $s$ /large- $\tau$  corner is lanthanide-free because the slow expansion timescale results in significant late-time heating, which drives the ejecta back to NSE, but at those late times,  $\beta$ -decays have significantly raised the electron fraction and so the r-process starts again but at a much higher  $Y_e$ , which does not produce lanthanides. The  $Y_e = 0.25$  slice is the transition between  
*(figure caption continued on next page)*

*(continued caption of Figure 3.4)*

lanthanide-rich and lanthanide-free. At low entropies we can still make significant amounts of lanthanides because the seed nuclides are heavy, and at very high entropies we initially have a lot of free neutrons and  $\alpha$  particles, which can produce significant amounts of heavy elements. Finally, at  $Y_e = 0.50$  the material is simply not neutron-rich enough to make any lanthanides. The heating rate at 1 day is quite insensitive to  $s$  and  $\tau$ , except at low  $Y_e$ , where it is significantly smaller at high entropies and fast expansion timescales because a neutron-rich freeze-out happens. The uniformity in the heating rate is due to the fact that there is an ensemble of nuclides contributing to the heating. And since we are considering the heating at 1 day, we tend to pick up nuclides with similar decay energies (because the decay energy is correlated with the half-life), leading to similar heating rates even if the composition varies.

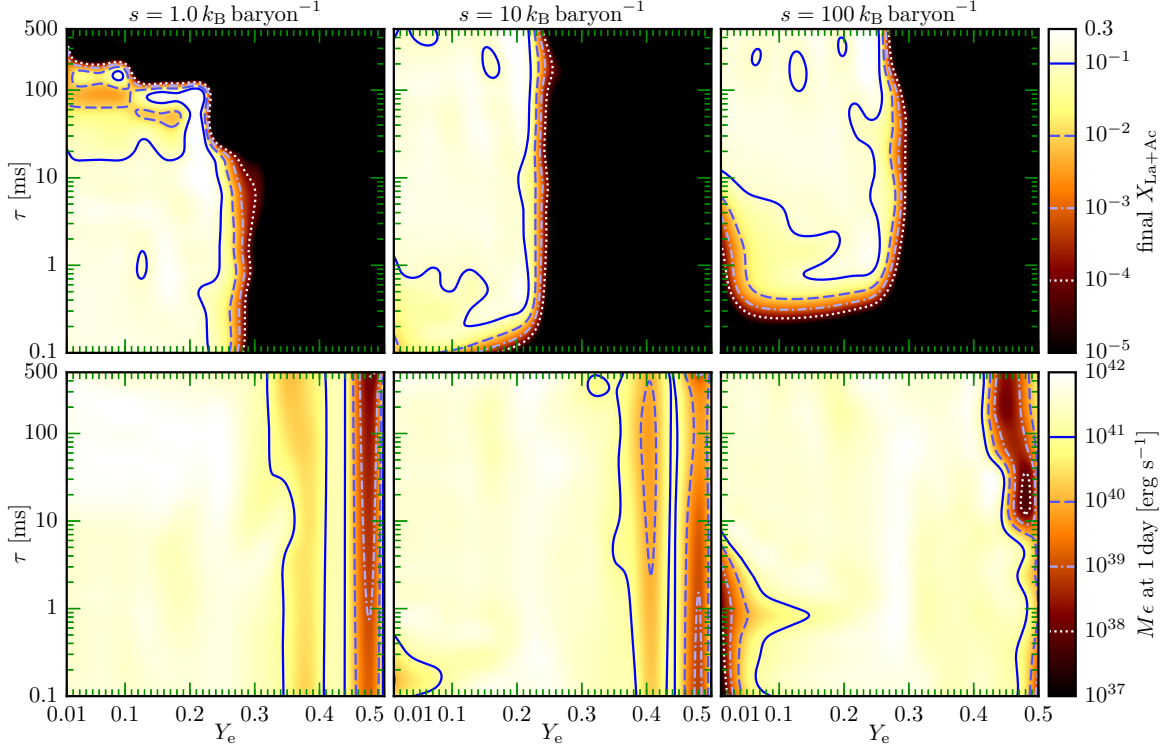


Figure 3.5: Slices of constant entropy showing the lanthanide and actinide mass fraction  $X_{\text{La+Ac}}$  and the heating rate  $M\epsilon$  at 1 day with  $M = 10^{-2} M_{\odot}$ . At  $s = 1 k_B \text{ baryon}^{-1}$ , no lanthanides are produced at large expansion timescales because the material heats up significantly at late times, which restarts the r-process at late times after  $Y_e$  has risen to about 0.3. At  $s = 100 k_B \text{ baryon}^{-1}$ , no lanthanides are produced when the dynamical timescale is short for the reasons discussed in the caption of Figure 3.4. In all cases, there is a critical value of  $Y_e$  where lanthanide production abruptly ceases. The heating rate at 1 day only shows some structure at high  $Y_e$  where certain individual nuclides dominate the heating. The reduced heating in the low- $Y_e$ /small- $\tau$  corner of  $s = 100 k_B \text{ baryon}^{-1}$  is due to a neutron-rich freeze-out that occurs there.

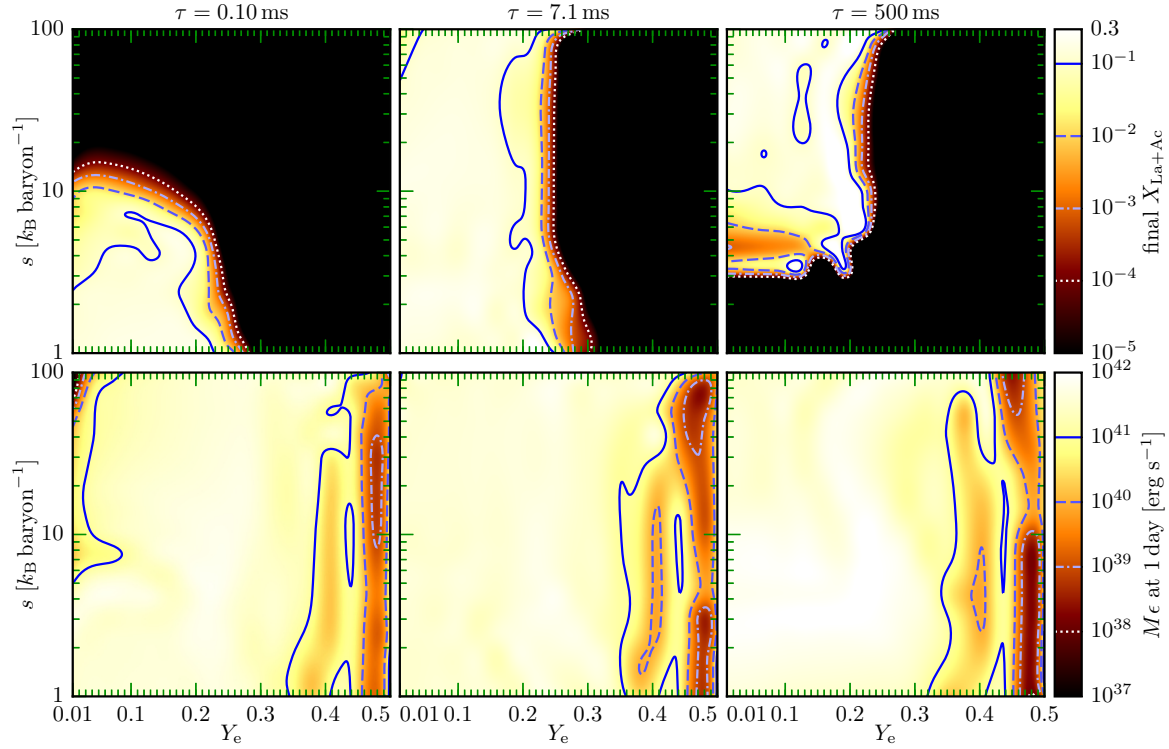


Figure 3.6: Slices of constant expansion timescale showing the lanthanide and actinide mass fraction  $X_{\text{La+Ac}}$  and the heating rate  $M\epsilon$  at 1 day with  $M = 10^{-2} M_{\odot}$ . At  $\tau = 0.10$  ms, there are no lanthanides at high entropies because the neutrons have no time to capture on the light seed nuclides. At  $\tau = 500$  ms, there are no lanthanides at low entropies because the heavy, neutron-rich seed nuclei lead to substantial late-time heating, which restarts the r-process at  $Y_e \sim 0.3$ , which is not neutron-rich enough to produce lanthanides. In all cases, there is a fairly uniform lanthanide cutoff as  $Y_e$  goes beyond a critical value. The heating rate at 1 day only shows structure at high  $Y_e$  where certain individual nuclides dominate the heating.

with an initial  $Y_e$  of 0.3, which is not neutron-rich enough to produce lanthanides. At faster expansion rates (smaller  $\tau$ ) the density falls off faster, resulting in less dramatic heating that cannot force the composition into NSE. Because we obtain the initial density from solving for NSE at the prescribed entropy,  $Y_e$ , and  $T = 6$  GK, the initial density is lower at higher entropies ( $s \gtrsim 3 k_B \text{ baryon}^{-1}$ ) and so even though the density remains close to the initial value at  $\tau = 500$  ms, the density is not high enough to produce heating that results in NSE. This is reflected in the upper left panel of Figure 3.5 where the ejecta is lanthanide-free at large expansion timescales at  $s = 1 k_B \text{ baryon}^{-1}$ , and in the upper right panel of Figure 3.6 where no lanthanides are produced at low entropies at  $\tau = 500$  ms.

The  $Y_e = 0.25$  slice in Figure 3.4 is right at the transition from lanthanide-rich to lanthanide-free ejecta. The upper panels of Figures 3.5 and 3.6 show clearly that this transition is very sharp at  $Y_e \sim 0.22 - 0.30$ . In the upper middle panel of Figure 3.4, the low- $s$ /large- $\tau$  corner that is lanthanide-free has expanded and so has the high- $s$ /small- $\tau$  corner, relative to the  $Y_e = 0.01$  panel. Additionally, lanthanide production is suppressed at intermediate entropies ( $5 k_B \text{ baryon}^{-1} \lesssim s \lesssim 90 k_B \text{ baryon}^{-1}$ ). At low entropies, we still get an r-process because the seed nuclei are very heavy and thus require fewer neutrons to capture on them to make the r-process distribution. At very high entropies, the initial composition includes a large fraction of free neutrons and  $\alpha$  particles. At high entropies, production of seed nuclei via neutron catalyzed triple- $\alpha$  is suppressed (Hoffman et al., 1997), which reduces the number of seed nuclei and thereby increases the neutron-to-seed ratio. These conditions allow for the production of the r-process nuclei. With  $Y_e \gtrsim 0.3$ , lanthanides are not produced at any entropy and expansion timescale combination, since the ejecta is not neutron-rich enough. In Section 3.2.2 we discussed in detail how the final lanthanide and actinide mass fractions depend on  $Y_e$ .

The lower row of panels in Figures 3.4 to 3.6 shows the heating rate (actually  $M\epsilon$  where  $M = 10^{-2} M_\odot$ ) at 1 day. For  $0.04 \lesssim Y_e \lesssim 0.35$  all the  $Y_e$  slices are very similar to the lower middle panel of Figure 3.4, with virtually no structure. At  $Y_e = 0.01$ , the high- $s$ /small- $\tau$  corner has significantly less heating because the initial density is very low ( $\rho_0 \sim 8 \times 10^5 \text{ g cm}^{-3}$ ) and this, coupled with the rapid expansion timescale ( $\tau = 0.1$  ms) and the fact that the initial composition contains few seed nuclei (98% of the mass is neutrons), means there is little opportunity for neutron capture. For larger expansion timescales, the initial conditions remain the same (low initial density and 98% of the mass is neutrons), but because the density decreases

more slowly, there is sufficient time for neutrons to capture on the few seed nuclei available and make a full r-process. At lower initial entropies, the initial density is larger (e.g.  $4 \times 10^6 \text{ g cm}^{-3}$  at  $s = 32 k_B \text{ baryon}^{-1}$ ) so that the density remains higher even with a rapid expansion, giving the neutrons a better chance to capture on seed nuclei—of which there are slightly more available—leading to a moderate r-process. This is reflected in the low- $Y_e$ /small- $\tau$  corner of the lower right panel in Figure 3.5 and in the low- $Y_e$ /high- $s$  corner of the lower left panel in Figure 3.6.

For  $Y_e \gtrsim 0.35$  we start to see large variations in the heating rate at 1 day as a function of  $Y_e$ , which can be seen in all lower panels in Figures 3.5 and 3.6. But the heating is still quite insensitive to  $s$  and  $\tau$ , as the lower right panel of Figure 3.4 shows. This variation as a function of  $Y_e$  at high  $Y_e$  can also be seen in Figure 3.3. There is a pronounced peak in the heating rate at 1 day at  $Y_e = 0.425$  in all but the  $s = 100 k_B \text{ baryon}^{-1}$  cases. This peak is due to the decay of  $^{66}\text{Cu}$  (half-life of 5 minutes) which comes from the decay of  $^{66}\text{Ni}$ , which has a half-life of 55 hours.  $^{66}\text{Ni}$  has 28 protons and 38 neutrons and so its electron fraction is  $28/66 \approx 0.424$ , which is very close to  $Y_e = 0.425$ , the initial electron fraction of the material. Thus the initial NSE distribution contains a larger quantity of  $^{66}\text{Ni}$  at  $Y_e = 0.425$  than at different  $Y_e$ , which leads to excessive heating via the decay chain described above because  $^{66}\text{Cu}$  has a fairly large  $Q$ -value of 2.6 MeV. At  $s = 100 k_B \text{ baryon}^{-1}$  the initial neutron-to-seed ratio is much larger than at lower entropies and so significant neutron burning occurs even at high  $Y_e$ , which washes out the strong dependence of the heating rate at 1 day on  $Y_e$ .

In Figure 3.3, there are also large minima in the heating rate at 1 day in all but the  $s = 100 k_B \text{ baryon}^{-1}$  cases at electron fractions between 0.45 and 0.48, depending on  $s$  and  $\tau$ . These minima can also be seen in Figures 3.5 and 3.6. In those cases, NSE preferentially produces stable isotopes in the initial composition, which drastically reduces the heating. For example, the cases with  $s = 1 k_B \text{ baryon}^{-1}$  have the minima at  $Y_e = 0.465$  and over 80% of the initial mass is either stable or has a half-life of more than 100 days. The most abundant nuclide (37% of the mass) is  $^{56}\text{Fe}$ , which is stable and has  $Y_e = 26/56 \approx 0.464$ , which is why the minimum occurs at  $Y_e = 0.465$ , because that favors  $^{56}\text{Fe}$  the most. As another example, the  $s = 10 k_B \text{ baryon}^{-1}$  cases have the minima at  $Y_e = 0.45$ , where  $^{58}\text{Fe}$  and  $^{62}\text{Ni}$  are preferentially produced by NSE, which have electron fractions of 0.448 and 0.452, respectively.

As in Section 3.2.2, we do not find a significant correlation between the amount of

lanthanides and actinides produced with the heating rate at 1 day. The heating rate at 1 day is very uniform at values of  $Y_e$  where lanthanides are produced. Since we are looking at the heating rate at a specific time, we will always pick out the nuclides with a half-life of about 1 day (or decay products of nuclides that decay on a one-day timescale). Because the decay energy is correlated with the half-life and because we always have a collection of different nuclides, we obtain roughly the same heating rate at 1 day regardless of the exact composition of the ejecta. This is no longer true at higher  $Y_e$ , where the composition can be dominated by individual nuclides, which then determine the heating rate.

### 3.2.5 Fitted nuclear heating rates

For each nucleosynthesis calculation, we calculate a parametric fit for the nuclear heating rate  $\epsilon(t)$  between 0.1 and 100 days (the fit window). The fit has the form

$$\hat{\epsilon}(t) = At^{-\alpha} + B_1e^{-t/\beta_1} + B_2e^{-t/\beta_2} + B_3e^{-t/\beta_3}, \quad (3.4)$$

where  $t$  and  $\beta_i$  are in days and  $\hat{\epsilon}(t)$  is in  $\text{erg s}^{-1} \text{g}^{-1}$ . We use at most six parameters for the fit, so either  $A$  and  $\alpha$  are zero or one or more of  $B_i$  and  $\beta_i$  are zero. We use a weighted fit where the range 0.1 to 100 days has a weight of one and the weight decreases linearly to zero in logspace from 0.1 to 0.05 days and from 100 to 200 days. We use a heuristic method to find the global best fit for all six types of fits (power law with 0, 1, or 2 exponentials, or 1, 2, or 3 exponentials without a power law term). The best of these six fits is then selected with a small penalty term for the number of parameter pairs. The fitting error is multiplied by 1.1 for each parameter pair in excess of one, so that we do not pick up meaningless parameters that improve the fit by less than 10%.

For consistency, we calculate the fitting error at the same times  $t_i$  for all cases and we interpolate the actual heating rate to those times, which are 500 points uniformly sampled in logspace between  $10^{-2}$  and  $10^3$  days (however, points before 0.05 days and after 200 days have zero weight and thus do not contribute to the fitting error, as explained above). The fit error used for finding the optimal fit parameters is the sum of squares of the log difference, i.e.

$$\text{fit error} = \sum_i w_i (\ln \epsilon(t_i) - \ln \hat{\epsilon}(t_i))^2, \quad (3.5)$$

where  $w_i$  is the weight of time  $t_i$ . This error measure works well for the optimization algorithm to find the best parameters, but it carries little physical meaning. To be

able to intuitively judge the quality of a particular fit, we define the mean fractional log error as

$$\left\langle \frac{\Delta \ln \epsilon}{\ln \epsilon} \right\rangle = \left\langle \frac{|\ln \epsilon(t_i) - \ln \hat{\epsilon}(t_i)|}{\ln \epsilon(t_i)} \right\rangle, \quad (3.6)$$

where the average runs over all times  $t_i$  such that  $0.1 \text{ days} \leq t_i \leq 100 \text{ days}$ . We only fit the total heating rate, but we also provide the average heating contribution due to fission reactions in the fit window.

The best and worst heating rate fits, as well as some fits of intermediate quality, are shown in Figure 3.7. About 80% of all high-resolution `sym0` fits have  $\langle \Delta \ln \epsilon / \ln \epsilon \rangle \leq 0.5\%$  and about 95% have a mean fractional log error of at most 1%. Since we do not include  $\beta$ -delayed fission reactions, the heating due to fission in our fit window (0.1 to 100 days) is solely due to spontaneous fission and it is close to constant during the fit window because there is usually one nuclide that dominates the fission heating. In 85% of all cases it varies by less than a factor of two within the fit window, and in 99% of all cases it varies by less than a factor of three. Thus it is sufficient to report the geometric mean of the heating rate due to fission over the fit window. Fits to the heating rates over our entire parameter space are available at <http://stellarcollapse.org/lippunerroberts2015>.

### 3.2.6 Dominant nuclear decays

To determine the particular nuclei that are likely to power kilonovae, we integrate the fractional heating contributions of all nuclides to find out which nuclides contribute most to the heating. For a single nucleosynthesis calculation, we know the total heating rate  $\epsilon(t)$  as a function of time and we can calculate the heating rate  $\epsilon_i(t)$  due to nuclide  $i$  as a function of time.  $\epsilon_i(t)$  is calculated as

$$\epsilon_i(t) = N_A \sum_{\alpha \in \mathcal{D}_i} \lambda_\alpha(t) Q_\alpha Y_i(t), \quad (3.7)$$

where  $\alpha$  is an index of a reaction in the reaction network and it runs over the set  $\mathcal{D}_i$ , which is the set of all reactions that destroy exactly one nuclide  $i$ .  $N_A$  is the Avogadro constant in baryon  $\text{g}^{-1}$ ,  $\lambda_\alpha(t)$  is the reaction rate of reaction  $\alpha$  in  $\text{s}^{-1}$ ,  $Q_\alpha$  is the energy released in reaction  $\alpha$  in erg, and  $Y_i(t)$  is the number abundance of nuclide  $i$  in baryon  $^{-1}$ . Note that the total heating rate is  $\epsilon(t) = \sum_i \epsilon_i(t)$ , where  $i$  runs over all nuclear species in the network.

At any given time  $t$ , we can now calculate the fractional heating contribution of nuclide  $i$  as  $\epsilon_i(t)/\epsilon(t)$ , which is the fraction of the total heating rate at time  $t$  that is

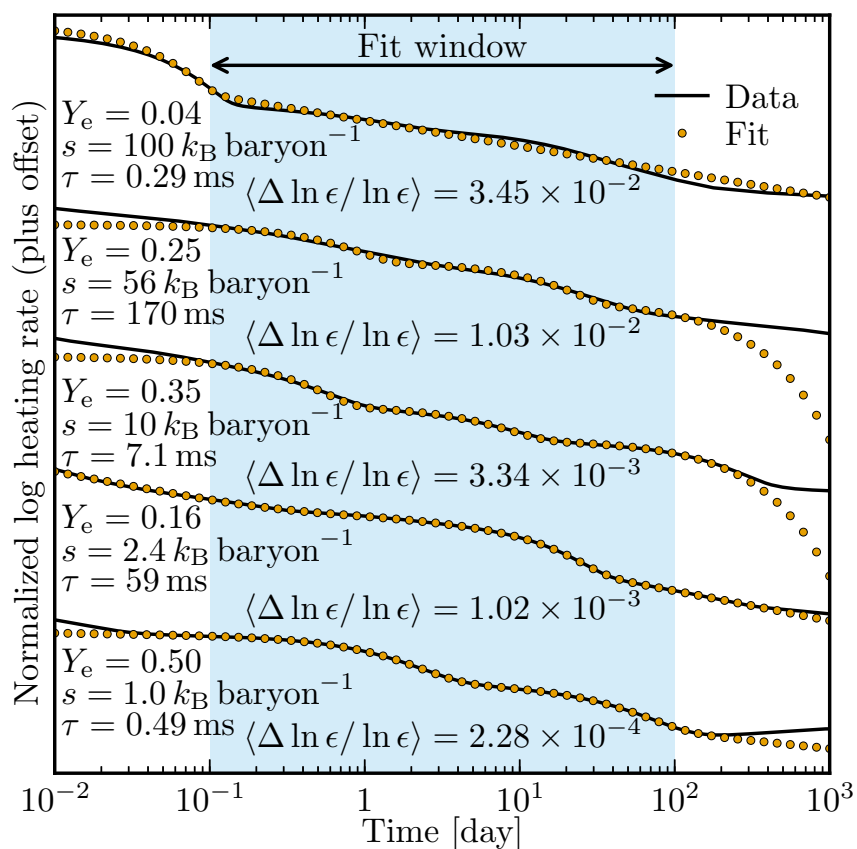


Figure 3.7: Some heating rate fits showing the fits with the largest and smallest error, and fits with errors in between. The heating rate is only fitted inside the fit window (0.1 to 100 days). We use a power law with up to two exponential terms, or up to three exponential terms without a power law show in Equation (3.4), whichever produces the best fit. The fit error  $\langle \Delta \ln \epsilon / \ln \epsilon \rangle$  is defined in Equation (3.6). As the second and third case from the top show, the fit can be quite bad outside the fit window. This is no surprise since we do not fit the data outside the fit window and because we only use up to three exponential terms. In reality, there are hundreds of individual nuclides contributing to the total heating rate and each one contributes a different exponential term.

solely due to the decay of nuclide  $i$ . These fractional heating contributions tell us which nuclides dominate the heating at a given time. To quantify which nuclides dominate the heating over a period of time, we define the *integrated fractional heating contribution*  $f_i$  as

$$f_i = \frac{1}{\ln t_1/t_0} \int_{t_0}^{t_1} \frac{\epsilon_i(t)}{\epsilon(t)} d \ln t, \quad (3.8)$$

where  $t_0 = 0.1$  days and  $t_1 = 100$  days are the beginning and end of our heating rate fit window. We integrate in logspace to equally weigh contributions at early and late times. Since we know  $\epsilon_i$  and  $\epsilon$  only at specific time steps  $t_k$ , we approximate the integral as

$$f_i \sim \frac{1}{\ln t_1/t_0} \sum_{t_0 \leq t_k \leq t_1} \frac{\epsilon_i(t_k)}{\epsilon(t_k)} \ln \frac{t_{k+1}}{t_k}. \quad (3.9)$$

If no  $t_k$  is equal to  $t_0$  or  $t_1$ , we add these two endpoints to the sum and interpolate  $\epsilon_i$  and  $\epsilon$  at those points.

Note that we calculate  $f_i$  for each nuclide  $i$  in a single nucleosynthesis calculation. So we should really say  $f_i(Y_e, s, \tau)$ , because  $f_i$  will be different for the same nuclide  $i$  in different nucleosynthesis calculations since different amounts of nuclide  $i$  are produced, depending on  $Y_e$ ,  $s$ , and  $\tau$ . To get an idea of which nuclides have the biggest influence on the heating rate over a range of  $Y_e$ ,  $s$ , and  $\tau$ , we average  $f_i$  over multiple nucleosynthesis calculations in our parameter space. We call this the *average integrated fractional heating contribution*  $\bar{f}_i$  and calculate it as

$$\bar{f}_i = \frac{1}{|\mathcal{Y}||\mathcal{S}||\mathcal{T}|} \sum_{Y_e \in \mathcal{Y}} \sum_{s \in \mathcal{S}} \sum_{\tau \in \mathcal{T}} f_i(Y_e, s, \tau), \quad (3.10)$$

where  $\mathcal{Y}$ ,  $\mathcal{S}$ , and  $\mathcal{T}$  are the sets of values of  $Y_e$ ,  $s$ , and  $\tau$ , respectively, that we are averaging over, and  $|\mathcal{Y}|$ ,  $|\mathcal{S}|$ , and  $|\mathcal{T}|$  are the cardinalities of those sets, i.e. the number of elements in the sets. Note that this method of averaging is meaningful because we are considering the fractional heating contribution of nuclide  $i$  and not the absolute heating contribution, and furthermore, we normalize  $f_i(Y_e, s, \tau)$  in the same way for each nucleosynthesis calculation. The final number  $\bar{f}_i$  that we obtain is a number between 0 and 1 and it tells us that nuclide  $i$  is responsible for this fraction of the total heating rate between 0.1 and 100 days averaged over a certain set of parameters  $Y_e$ ,  $s$ , and  $\tau$ . Note that  $\bar{f}_i$  is not intended to be used to estimate the absolute amount of heating due to nuclide  $i$ , because the absolute amount of heating can vary greatly between the different nucleosynthesis cases over which we

averaged to obtain  $\bar{f}_i$ . Rather,  $\bar{f}_i$  is intended to quantify how important different nuclides are in the makeup of the total radioactive heating rate over a wide range of possible kilonovae. This can help inform experiments that are measuring the  $\beta$ -decay properties of nuclides produced in the r-process. To model the r-process and associated kilonovae more accurately, it would be more beneficial to have precise measurements of the  $\beta$ -decay properties of nuclides that have a larger  $\bar{f}_i$  than of nuclides with smaller  $\bar{f}_i$ .

Table 3.3 shows the 10 most dominant heating nuclides and their average integrated fractional heating contributions  $\bar{f}_i$ . The  $\bar{f}_i$ 's are averaged over different high-resolution sym0 (symmetric fission with no free neutrons) runs in different  $Y_e$  bins and over the entire range of entropies ( $1 k_B \text{ baryon}^{-1} \leq s \leq 100 k_B \text{ baryon}^{-1}$ ) and expansion timescales ( $0.1 \text{ ms} \leq \tau \leq 500 \text{ ms}$ ). In each  $Y_e$  bin, the nuclides are sorted with decreasing  $\bar{f}_i$ . We only look at the  $Y_e$ -dependence of the dominant heating nuclides because the r-process depends very strongly on  $Y_e$ , while it is quite insensitive to entropy (e.g. Freiburghaus et al., 1999, also see Figure 3.1). Only the 10 most dominant heating nuclides are shown here, the full table, and the tables of the runs with different fission reactions, are available at <http://stellarcollapse.org/lippunerroberts2015>. The single most important nuclide for heating between 0.1 and 100 days is  $^{132}\text{I}$ . It dominates over all other nuclides by a factor of at least 3 to 10 and it especially dominates at low initial  $Y_e$ .  $^{132}\text{Sn}$  is doubly magic (50 protons and 82 neutrons) and so it gets produced in high quantities in the r-process. Within minutes,  $^{132}\text{Sn}$  decays to  $^{132}\text{Sb}$  which decays to  $^{132}\text{Te}$ .  $^{132}\text{Te}$  has a half-life of 3.2 days and so it decays in the middle of our fit window where we are looking at the heating contributions. But the decay of  $^{132}\text{Te}$  to  $^{132}\text{I}$  has a  $Q$ -value of only about 500 keV, while  $^{132}\text{I}$  decays to the stable isotope  $^{132}\text{Xe}$  (which is in the middle of the second r-process peak) with a half-life of only 2.3 hours and a  $Q$ -value of 3.6 MeV. Thus we get a large heating contribution from  $^{132}\text{I}$ .

As is to be expected, at very low  $Y_e$  (between 0 and 0.125), most of the heating comes from nuclei that form the second ( $A \sim 130$ ) and third ( $A \sim 200$ ) r-process peaks. A few very heavy nuclides ( $A \sim 250$ ) contribute. At higher  $Y_e$  (between 0.125 and 0.25), the 10 most significantly contributing nuclides are all in the second peak, since anything in the third peak and beyond is more difficult to produce. The nuclides we find to be the dominant source of heating at low initial  $Y_e$  are consistent with the dominant  $\beta$ -decay nuclei that Metzger et al., 2010 found. They only investigated

Table 3.3: Average Integrated Fractional Heating Contributions  $\bar{f}_i$  of the High-Resolution sym0<sup>a</sup> Runs

Y <sub>e</sub> Bins <sup>b</sup>								Overall <sup>c</sup>	
0 < Y <sub>e</sub> ≤ 0.125		0.125 < Y <sub>e</sub> ≤ 0.250		0.250 < Y <sub>e</sub> ≤ 0.375		0.375 < Y <sub>e</sub> ≤ 0.5		(0 < Y <sub>e</sub> ≤ 0.5)	
Nuclide	$\bar{f}_i$	Nuclide	$\bar{f}_i$	Nuclide	$\bar{f}_i$	Nuclide	$\bar{f}_i$	Nuclide	$\bar{f}_i$
<sup>132</sup> I	22.59%	<sup>132</sup> I	26.49%	<sup>89</sup> Sr	9.01%	<sup>66</sup> Cu	13.21%	<sup>132</sup> I	13.99%
<sup>200</sup> Au	4.46%	<sup>131</sup> I	5.52%	<sup>72</sup> Ga	5.91%	<sup>57</sup> Ni	10.83%	<sup>66</sup> Cu	4.42%
<sup>128</sup> Sb	4.26%	<sup>128</sup> Sb	4.66%	<sup>132</sup> I	5.00%	<sup>59</sup> Fe	7.47%	<sup>89</sup> Sr	3.51%
<sup>249</sup> Bk	4.23%	<sup>132</sup> Te	3.78%	<sup>59</sup> Fe	4.77%	<sup>89</sup> Sr	5.21%	<sup>57</sup> Ni	3.18%
<sup>132</sup> Te	3.22%	<sup>125</sup> Sn	3.37%	<sup>78</sup> As	4.65%	<sup>77</sup> As	4.79%	<sup>59</sup> Fe	3.04%
<sup>131</sup> I	3.13%	<sup>133</sup> I	3.06%	<sup>125</sup> Sn	3.64%	<sup>77</sup> Ge	4.18%	<sup>128</sup> Sb	2.67%
<sup>252</sup> Cf	3.09%	<sup>129</sup> Sb	2.85%	<sup>103</sup> Ru	3.24%	<sup>61</sup> Cu	3.20%	<sup>131</sup> I	2.59%
<sup>133</sup> I	3.09%	<sup>127</sup> Sb	2.79%	<sup>91</sup> Y	3.08%	<sup>62</sup> Cu	3.04%	<sup>78</sup> As	2.27%
<sup>202</sup> Au	2.89%	<sup>140</sup> La	2.56%	<sup>66</sup> Cu	2.97%	<sup>56</sup> Ni	3.00%	<sup>72</sup> Ga	2.05%
<sup>135</sup> I	2.65%	<sup>129</sup> Te	2.25%	<sup>112</sup> Ag	2.96%	<sup>72</sup> Ga	2.95%	<sup>77</sup> Ge	2.02%

<sup>a</sup> Symmetric fission reactions that do not create free neutrons.

<sup>b</sup> The  $\bar{f}_i$ 's shown in these columns are averaged over all nucleosynthesis calculations (with different initial electron fractions, entropies, and expansion timescales) whose Y<sub>e</sub> falls within the Y<sub>e</sub> bin.

<sup>c</sup> The  $\bar{f}_i$ 's shown in this column are averaged over the entire parameter space.

a  $Y_e = 0.1$  outflow and we confirm that this result holds for a range of electron fractions below 0.25.

At  $Y_e$  between 0.25 and 0.375 there is a mix of significant contributors from the first ( $A \sim 88$ ) and second peaks. There are also some iron peak elements, but most isotopes on the neutron-rich side of the iron peak have half-lives that are either too short or too long for our fit window. Notable exceptions are  $^{59}\text{Fe}$ ,  $^{66}\text{Ni}$ ,  $^{67}\text{Cu}$ , and  $^{72}\text{Ga}$ . We do indeed see significant contributions from  $^{72}\text{Ga}$  and  $^{59}\text{Fe}$ . Instead of  $^{66}\text{Ni}$ , we see its  $\beta$ -decay product,  $^{66}\text{Cu}$ , which has a much larger  $Q$ -value (2.6 MeV instead of 250 keV) and a half-life of 5 minutes.  $^{67}\text{Cu}$  does not contribute significantly because of its relatively low  $Q$ -value of 560 keV. Finally, at very high  $Y_e$  (between 0.375 and 0.5) there are significant contributors from the proton-rich side of stability around the iron peak.  $^{57}\text{Ni}$  dominates over  $^{56}\text{Ni}$  because it has one more neutron—thus it is a bit easier to produce in slightly neutron rich conditions ( $Y_e < 0.5$ )—and the  $\beta^+$ -decay  $Q$ -value of  $^{57}\text{Ni}$  is a bit larger than that of  $^{56}\text{Ni}$  (3.3 MeV vs. 2.1 MeV). Both nuclides, however, have a half-life that is right inside our fit window, which is why both contribute significantly to the total heating rate.

The cases that produce significant amounts of actinides also produce nuclides that undergo spontaneous fission. In those cases, the heating due to fission becomes dominant toward the end of the fit window (at about 100 days) but it is subdominant throughout the rest of the fit window. The nuclides that contribute the most to fission induced heating across the entire parameter space are  $^{249}\text{Bk}$ ,  $^{252}\text{Cf}$ , and  $^{241}\text{Pu}$ , which have average integrated fractional fission heating contributions of 33%, 21%, and 19%, respectively. These numbers are  $\bar{f}_i$  defined in Equation (3.10) averaged over the entire parameter space, but the  $f_i$ 's of the individual nucleosynthesis calculations defined in Equation (3.8) were calculated using only fission reactions in  $\epsilon_i(t)$  (cf. Equation (3.7)) and with  $\epsilon(t)$  being the total heating rate due to fission alone. In other words, averaged over all runs in the entire parameter space and averaged in logspace over all times between 0.1 and 100 days,  $^{249}\text{Bk}$  accounts for 33% of the entire heating due to fission, and similarly for the other nuclides. If  $\beta$ -delayed fission were included in our reaction network, it would likely significantly alter the contribution of fission to the heating rate at low electron fraction. For higher electron fractions, the neglect of beta-delayed fission is unlikely to be important since very little fissionable material is produced.

### 3.3 Light curves

To test how variations in the late-time nuclear heating rate and composition affect possible electromagnetic transients associated with neutron star mergers, we calculate light curves using a simplified gray radiative transport scheme in a spherically symmetric outflow.

#### 3.3.1 Radiative transfer methods

The ejecta is assumed to expand homologously, such that  $r = vt$ . The density structure of the outflow is then described by

$$\rho(t, r) = \rho_0(r/t) \left(\frac{t}{t_0}\right)^{-3}. \quad (3.11)$$

*SkyNet* gives a heating rate  $\epsilon(t)$ , which is the total amount of energy released per unit mass and per unit time due to nuclear reactions. The majority of this energy is carried away by neutrinos, but some fraction, say  $f$ , is thermalized in the material. So  $f\epsilon(t)$  is the heating rate of the material due to nuclear reactions and decays.

For homologous outflows, the velocity can be taken as a Lagrangian coordinate. Writing down the gray, Lagrangian radiative transport equations to first order in  $v/c$  (e.g. Mihalas and Weibel-Mihalas, 1999), using the velocity as the Lagrangian coordinate, and including energy release from nuclear reactions gives

$$\frac{dE}{dt} + \frac{2E}{t} + \frac{1}{v^2 t} \frac{\partial}{\partial v} (v^2 F) = \rho c \kappa (aT^4 - E), \quad (3.12)$$

$$\frac{dF}{dt} + \frac{1}{t} \frac{\partial}{\partial v} (\mathcal{F} E) + \frac{3\mathcal{F} - 1}{vt} E = -\rho c \kappa F, \quad (3.13)$$

$$\frac{du}{dt} + \frac{3P}{\rho t} = f\epsilon + c\kappa (E - aT^4), \quad (3.14)$$

where  $E$  is the radiation energy density,  $t$  is the time since merger,  $v$  is the velocity measured in units of the speed of light  $c$ ,  $F$  is the radiation flux,  $\rho$  is the density given in Equation (3.11),  $\kappa$  is the opacity,  $a = 4\sigma/c$  is the radiation constant where  $\sigma$  is the Stefan–Boltzmann constant,  $T$  is the temperature of the fluid,  $\mathcal{F}$  is the Eddington factor (i.e. the ratio of the radiation pressure to the radiation energy density),  $u$  is the specific internal energy of the fluid,  $p$  is the fluid pressure,  $f$  is the fraction of the heating rate  $\epsilon$  that is thermalized. The heating rate is not entirely thermalized because a large fraction of the nuclear decay energy goes into neutrinos and gamma rays; neutrinos are lost from the system and gamma rays are only partially thermalized. To accurately calculate the thermalization fraction, one would need much more detailed information about the  $\beta$ -decays than what is

available in REACLIB and one would also have to do  $\gamma$ -ray transport. Following Barnes and Kasen, 2013, we adopt  $f = 0.3$ .

The fluid is assumed to be a non-relativistic, non-degenerate ideal gas with molecular weight  $\mu$ , so that the specific internal energy is  $u = 3T/(2\mu)$ . The gray transport equations are discretized in space on a staggered grid, with  $E$  and  $u$  defined on zone centers and  $F$  defined on zone edges. The resulting system of ordinary differential equations is then solved in time using a backward Euler method. Eddington factors are obtained by solving the static Boltzmann transport equation on a tangent ray grid at the beginning of a timestep. This method is similar to the one described in Ensman, 1994, specialized to an homologous outflow. The zones are chosen to be logarithmically increasing in size moving away from the maximum radius. This is done to ensure that the radiation decoupling layer is resolved even at high densities.

The density structure is assumed to be described by a broken power law as argued in Chevalier and Soker (1989). This choice was made mainly to facilitate comparison with Barnes and Kasen, 2013. The power law break and density scale are fixed to give the desired total mass and total kinetic energy of the outflow. We use  $M = 10^{-2} M_{\odot}$  and  $v = 0.1 c$ , where  $c$  is the speed of light, for all light curve models (e.g. Hotokezaka et al., 2013b; Rosswog, 2013; Foucart et al., 2014).

We note that the density evolution in the transport model and the one given in Equation (3.1) are both proportional to  $t^{-3}$ , but they have different scale factors. The main point of  $\rho(t)$  given in Equation (3.1) is to control the timescale over which the density changes at the time of nucleosynthesis ( $t \lesssim 1$  s), but extrapolating this density to late times and assuming that it was the uniform density of a ball of gas expanding with a fixed velocity would lead to superluminal expansion velocities in many cases. Equation (3.11) gives a much more reasonable estimate of the density at late times after nucleosynthesis is over.

Calculating the exact wavelength and temperature dependent opacity of a mixture is extremely difficult because of the large number of elements and absorption lines involved. Especially the lanthanide and actinide element groups have very complicated line structures and the most sophisticated line structure and opacity calculations have only been done for a few representative nuclides (e.g. Kasen et al., 2013). Such detailed opacity calculations are beyond the scope of this work and we use a simple prescription to compute the gray opacity  $\kappa$  as a function of temperature

$T$  and composition as

$$\kappa = \kappa_{\text{Fe}}(T) + \sum_i \max[\kappa_{\text{Nd}}(T, X_i) - \kappa_{\text{Fe}}(T), 0], \quad (3.15)$$

where  $\kappa_{\text{Fe}}(T)$  and  $\kappa_{\text{Nd}}(T, X_i)$  are the iron and neodymium opacities given in Kasen et al., 2013. The sum runs over all lanthanide and actinide species with  $X_i$  being the mass fraction of a particular lanthanide or actinide species. We subtract the iron opacity from the neodymium opacity because  $\kappa_{\text{Nd}}(T, X_i)$  given in Kasen et al. (2013) is actually the opacity of a mixture containing  $X_i$  neodymium and  $1 - X_i$  iron. Our approximation assumes that every lanthanide and actinide contributes the same number of lines with the same distribution in energy. The opacity used in the gray calculation is taken to be the Planck mean opacity, which is appropriate when the wavelength dependent opacity is calculated in the Sobolev approximation (Kasen, 2015). At temperatures above  $10^4$  K, the opacities are held constant since ionization states which would have been accessed at those temperatures were not included in the original opacity calculation and the opacities there are artificially low (Kasen, 2015).

### 3.3.2 Dependence of kilonova light curves on the outflow properties

Figure 3.8 shows the light curves and heating rates of the cases whose final abundances are shown in Figure 3.1. In the left panel, the lanthanide-rich cases ( $Y_e = 0.01, 0.19$ ) are about an order of magnitude dimmer than the lanthanide-free case ( $Y_e = 0.25$ ) and they peak at about a week instead of about a day. The effective temperature at peak of the lanthanide-rich cases is also much lower ( $\sim 1600$  K vs.  $\sim 5700$  K) than the temperature of the lanthanide-free case. The heating rates between 0.01 and 100 days, however, are almost identical for those three cases, so the significant differences in the light curves are solely due to the amount of lanthanides present in the ejecta and their effect on the opacity. Comparing the cases  $Y_e = 0.25$  and  $Y_e = 0.50$ , which are both lanthanide-free, the impact of the heating rate on the light curve can be seen. The heating rate is lower for the  $Y_e = 0.50$  case, because mostly stable nuclei are produced, leading to less heating. The result is that the light curve of the  $Y_e = 0.50$  case peaks slightly later (2.6 days vs. 1.2 days for  $Y_e = 0.25$ ), is about an order of magnitude dimmer, and redder (spectral temperature is  $\sim 3000$  K compared to  $\sim 5700$  K).

In the left panel of Figure 3.8, the light curves for  $Y_e = 0.01$  and  $Y_e = 0.19$  have a small peak at very early times (about 0.04 days). This early peak comes from our underestimate of the opacity at high temperatures. There is also a small bump at

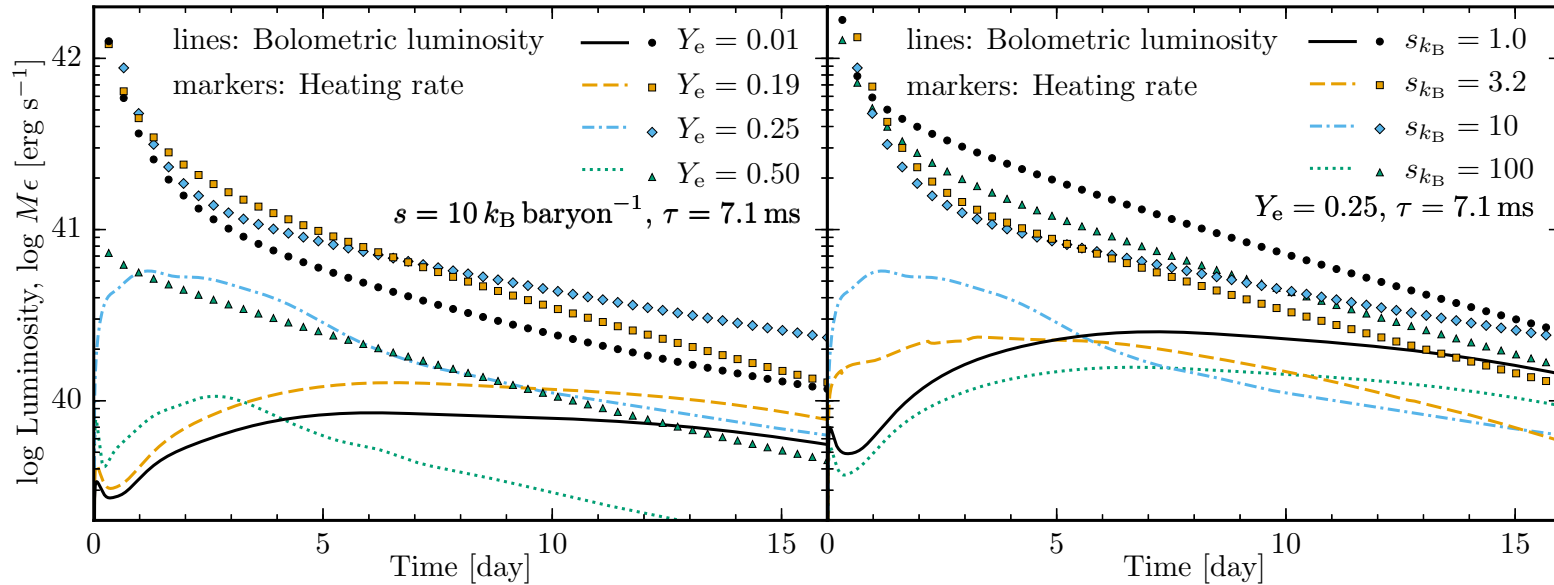


Figure 3.8: The light curves and heating rates of some selected nucleosynthesis calculations. **Left:**  $Y_e = 0.01, 0.19, 0.25, 0.50$ ,  $s = 10 k_B \text{ baryon}^{-1}$ , and  $\tau = 7.1 \text{ ms}$ . With  $Y_e = 0.01$  and  $Y_e = 0.19$  we obtain the full r-process and so the ejecta is lanthanide-rich, which drastically increases the opacity, resulting in a dim transient that peaks about a week after the nucleosynthesis event. This is in contrast to the  $Y_e = 0.25$  case, which has a very similar heating rate as the low- $Y_e$  cases, but does not produce lanthanides, and thus the transient is brighter and peaks earlier. The  $Y_e = 0.50$  transient is also lanthanide-free and peaks at a few days, but because a significant amount of stable nuclides are produced, the heating is much less, which leads to a dim transient. **Right:**  $Y_e = 0.25$ ,  $s = 1.0, 3.2, 10, 100 k_B \text{ baryon}^{-1}$ , and  $\tau = 7.1 \text{ ms}$ . As we saw in Figure 3.1, the  $s = 1.0 k_B \text{ baryon}^{-1}$  and  $s = 100 k_B \text{ baryon}^{-1}$  cases are lanthanide-rich, while  $s = 3.2 k_B \text{ baryon}^{-1}$  and  $s = 10 k_B \text{ baryon}^{-1}$  are lanthanide-free, which is clearly visible in the light curves. Even though  $s = 3.2 k_B \text{ baryon}^{-1}$  and  $s = 10 k_B \text{ baryon}^{-1}$  have essentially the same heating rate, the  $s = 3.2 k_B \text{ baryon}^{-1}$  case is significantly dimmer because it has a small amount of lanthanides. The ejecta of a binary neutron star merger is expected to have entropies between 1 and  $10 k_B \text{ baryon}^{-1}$  (e.g. Goriely et al., 2011; Just et al., 2015).

early times in the light curve of the  $Y_e = 0.50$  case, which is due to the behavior of the heating rate at early times. When determining the actual peak of the light curve, we neglect all peaks earlier than 0.5 days, unless they are more than three times brighter than all peaks after 0.5 days. If there are no peaks after 0.5 days, we pick the brightest peak that is more than three times brighter than the latest peak (which is also before 0.5 days).

The right panel of Figure 3.8 shows selected light curves with  $Y_e = 0.25$  and various initial entropies. The cases  $s = 1 k_B \text{ baryon}^{-1}$  and  $s = 100 k_B \text{ baryon}^{-1}$  produce very typical lanthanide-rich light curves, whereas  $s = 10 k_B \text{ baryon}^{-1}$  produces a typical lanthanide-free light curve, and  $s = 3.2 k_B \text{ baryon}^{-1}$  produces a light curve that has trace amounts of lanthanides.

In the cases where we make lanthanides at lower  $Y_e$ , we expect the peak luminosity to increase and move to earlier times at higher  $Y_e$  when the ejecta transitions from lanthanide-rich to lanthanide-free, because the large contribution to the opacity from the lanthanides suddenly goes away (Kasen et al., 2013; Tanaka and Hotokezaka, 2013). This is shown in Figure 3.9. When lanthanides are not produced, the transient generally becomes brighter, shorter, and bluer. We recall from Figure 3.3 that the heating rate at 1 day tends to decrease a little when lanthanides go away. Thus the peak luminosity  $L_p$  in the lanthanide-free cases is larger not because there is more heating in those cases, but because the peak occurs earlier (due to the smaller opacity) and the heating rate is always larger at earlier times than at later times.

Looking at the time  $t_p$  of the light curve in Figure 3.9, we see that the light curve peaks at about 6 days if the ejecta is lanthanide-rich and at about 1 day if the ejecta is lanthanide-free, which is consistent with earlier work (e.g. Roberts et al., 2011; Barnes and Kasen, 2013; Tanaka and Hotokezaka, 2013). At high  $Y_e$ , where we see some oscillations in the heating rate due to specific nuclides being produced (as explained in Section 3.2.4), the variation in the heating rate is reflected in the peak luminosity  $L_p$  and the peak time  $t_p$ . More heating results in a brighter transient at later times because the heating keeps the ejecta hotter, and thus the opacity remains high since more excited levels are populated, which increases the number of optically thick lines (Kasen et al., 2013). Conversely, less heating leads to a dimmer transient at earlier times because the ejecta is cooler and thus the opacity is lower. This variation is also reflected in the effective temperature  $T_{\text{eff}}$  of the transient, but to a lesser degree. In general, lanthanide-rich transients have  $T_{\text{eff}} \sim 1600 \text{ K}$ , which peaks at  $\lambda \sim 1.8 \mu\text{m}$  in the infrared H and K bands. Lanthanide-free transients have

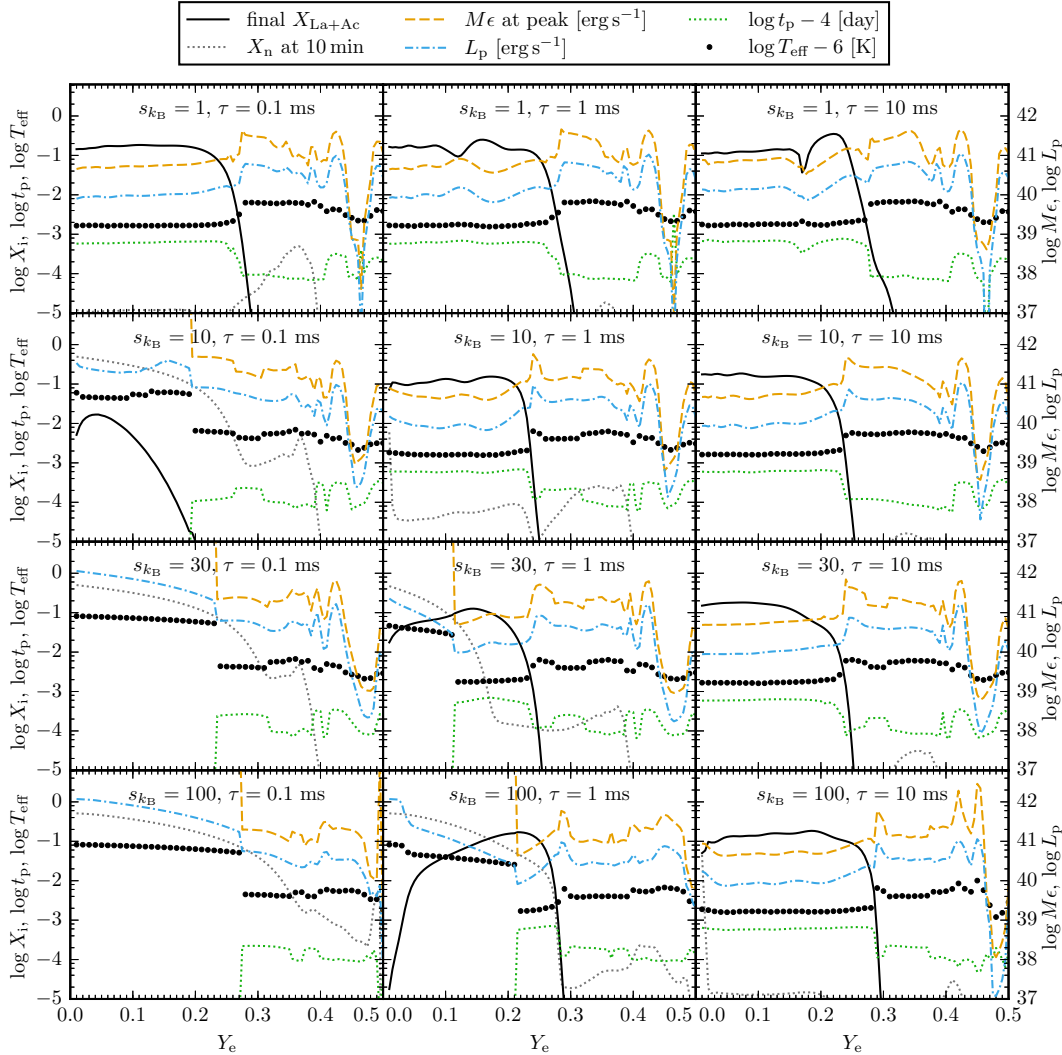


Figure 3.9: The light curve results as a function of  $Y_e$  for selected values of  $s$  and  $\tau$ . To show how lanthanides and neutron-rich freeze-out impact the light curve, we again show the lanthanide and actinide abundance  $L_{\text{La+Ac}}$  at peak and the neutron abundance  $X_n$  at 10 minutes, which were already shown in Figure 3.3. Additionally, we plot the heating rate  $M\epsilon$  at peak, with  $M = 10^{-2} M_\odot$ , the peak luminosity  $L_p$ , peak time  $t_p$ , and the effective blackbody temperature  $T_{\text{eff}}$  at peak of the light curve. Note that in the neutron-rich freeze-out cases, the heating rate  $M\epsilon$  and the peak timescale  $t_p$  go off the scales, their values are  $10^{44} - 10^{45} \text{ erg s}^{-1}$  and  $15 - 30 \text{ min}$ , respectively. As expected,  $L_p$  follows the heating rate quite closely, except in the cases where we get a neutron-rich freeze-out. In those cases, we get a bright, very blue transient at early times. The exact point in  $Y_e$  of the transition from a neutron-powered transient to an ordinary kilonova in this figure is somewhat arbitrary, since it depends on the exact method of finding the light curve peak that we choose, as explained in the text. Apart from the neutron-powered transients, the general trend is that we see a slightly dimmer, redder transient at later times if the ejecta is lanthanide-rich, and a brighter, bluer transient at earlier times if it is lanthanide-free. This is consistent with earlier work (e.g. Barnes and Kasen, 2013).

$T_{\text{eff}} \sim 6000$  K (although this is a bit lower at very high  $Y_e$  where the radioactive heating is reduced), which peaks at  $\lambda \sim 480$  nm in the optical B band.

In Figure 3.9, we can also clearly see that neutron-rich freeze-out produces very bright, very early, and very ultraviolet transients. The cleanest examples are  $s30\tau0.1$  and  $s100\tau0.1$ . There the luminosity ranges from  $2 \times 10^{41}$  to  $10^{42}$  erg  $s^{-1}$ , the effective temperature is about  $7 \times 10^4$  K, which peaks at  $\lambda \sim 40$  nm (extreme ultraviolet), and the peak occurs about an hour after the nucleosynthesis event. These results are very similar to what Metzger et al. (2015) found, however, they found peak effective temperatures of  $\sim 10^4$  K, because they used higher opacities ( $\kappa = 30$  cm<sup>2</sup> g<sup>-1</sup>) since their trajectories still contained a significant amount of lanthanides and actinides (Metzger, 2015). In our case, we do not find significant amounts of lanthanides or actinides if we obtain a strong neutron-rich freeze-out, and thus we get a lower opacity, which raises the effective temperature (Li and Paczyński, 1998), making such a transient even harder to detect because it peaks deeper in the ultraviolet. It appears that more work is needed to consistently model these neutron-powered transients.

Note that the transition point in  $Y_e$  in Figure 3.9 where the light curve peaks at about 1 hour to where it peaks at a few days is somewhat arbitrary because it depends on how we determine the peak in the light curve. As explained above, we arbitrarily decided to only consider peaks occurring earlier than 0.5 days if they are more than three times brighter than any later peaks. The justification for this is that early peaks are very short and thus hard to detect, but in the cases where we only obtain a short, bright early peak, we do not want to pick out any later peaks that are really just the highest points of very shallow and long plateaus.

We emphasize that the outflows used in this section were assumed to have homogeneous compositions. In nature, outflows from compact object mergers will have some spread in electron fraction and therefore have inhomogeneous compositions. Nonetheless, our simplified models provide guidance on the sensitivity of kilonova light curves to variations in the average electron fraction, entropy, and dynamical timescale during r-process nucleosynthesis.

### 3.3.3 Mass estimates of potential kilonova observations

Since the ejecta mass is a parameter in our simplified light curve model, we can attempt to put a lower bound on the ejecta mass necessary to reproduce the possible kilonova observations. For the possible kilonova associated with GRB130603B,

there is one observation in the infrared, one upper limit in the optical, and another upper limit in the infrared at late times (Berger et al., 2013; Tanvir et al., 2013). For every point in our low-resolution  $\text{sym}0$  parameter space we compute nine light curves with all combinations of  $v/c = 0.1, 0.2, 0.3$  and  $M/M_{\odot} = 0.01, 0.05, 0.15$ . We then compute the observed AB magnitudes that would result from the light curve at the rest frame time when the observations were made, taking into account redshift and the actual filter response of the Hubble Space Telescope (HST)<sup>3</sup> (Section 3.A). Finally, we interpolate the resulting observed magnitudes as a function of the ejecta mass to find the minimum mass that reproduces the observed magnitude in the near-infrared band (HST filter WFC3/F160W, roughly J-band in the rest frame) and produces an optical signal (HST filter WFC3/F606W, roughly B-band in rest frame) that is below the observed upper limits.

We repeat the above procedure for light curves calculated with different heating efficiencies  $f$  (see Equation (3.14)), as the exact value of  $f$  is not known but has a direct influence on the brightness of the kilonova. For  $f = 0.1, 0.3, \text{ and } 0.5$ , we find that the minimum (over our entire parameter space) ejecta masses necessary to match the possibly observed kilonova after GRB130603B are 0.09, 0.03, and 0.02 solar masses, respectively. This is a reasonable result, as we expect the minimum mass necessary to produce a kilonova of equal brightness to decrease as the heating efficiency increases.

If we repeat the same procedure with the potentially observed kilonova after GRB060614 (where there are detections in both the near-infrared (HST filter WFPC2/F814W, roughly R-band in rest frame) and optical (HST filter WFPC2/F606W, roughly V-band in rest frame), two infrared upper limits at late times, and an optical upper limit at late times (Yang et al., 2015; Jin et al., 2015)), we find that none of our light curves calculated with  $f = 0.1$  can match the observations, and for  $f = 0.3$  and  $0.5$  we require a minimum mass of 0.04 and 0.05 solar masses, respectively. We note that a larger ejecta mass is needed when a larger heating efficiency is assumed. Because there are observations in two bands for GRB060614, our fits are more sensitive to the spectral temperature found in the light curve models than in the case of GRB130603B. Qualitatively, the spectral temperature scales inversely with the mass and proportionally to the heating efficiency (Li and Paczyński, 1998). Therefore, to keep a fixed spectral temperature when increasing the heating efficiency the total mass also must be increased. Our simple method for calculating the

<sup>3</sup><http://svo2.cab.inta-csic.es/svo/theory/fps3/index.php?mode=browse&gname=HST>

effective temperature is likely inadequate for detailed confrontation with multi-band observations, so these minimum masses are necessarily approximate. Another issue with this method of finding the minimum allowed mass is that the outflow does not have a homogeneous composition (e.g. Kasen et al., 2015; Just et al., 2015; Metzger et al., 2015; Wanajo et al., 2014). Therefore, to acquire more accurate estimates of the minimum ejected mass in these potential kilonova events, more sophisticated light curve model and hydrodynamical simulations are required. Such an analysis was performed in Hotokezaka et al., 2013c for GRB130603B, where they found preferred ejecta masses between 0.02 and 0.1  $M_{\odot}$ .

Nevertheless, the work we have presented here will be very useful to estimate the masses and maybe even other parameters from future observations of kilonovae. With a sophisticated radiation transport method, one can calculate accurate light curves using our heating rates and lanthanide and actinide abundances. A consequence of our finding that the heating rate does not strongly depend on  $Y_e$  in the lanthanide-rich regime (and not even on  $s$  and  $\tau$  except at very low  $Y_e$ ) is that one will be able to quite accurately estimate the ejecta mass of future observed kilonovae without precisely knowing the values of  $Y_e$ ,  $s$ , and  $\tau$ . A caveat is, however, that one needs to know the heating efficiency and lanthanide and actinide opacities well.

### 3.4 Conclusions

We have systematically performed nucleosynthesis calculations with our new nuclear reaction network *SkyNet* for a wide range of three parameters: initial electron fraction ( $0.01 \leq Y_e \leq 0.5$ ), initial entropy  $1 k_B \text{ baryon}^{-1} \leq s \leq 100 k_B \text{ baryon}^{-1}$ , and the expansion timescale  $0.1 \text{ ms} \leq \tau \leq 500 \text{ ms}$  during nuclear burning. We ran the full parameter space with different fission reactions, but found that there were only small quantitative and no qualitative differences between the different fission reactions. We focused our attention on the amount of lanthanides and actinides produced and the heating rate between 0.1 and 100 days after the start of the nucleosynthesis calculation, because kilonova transients are expected to occur in this time frame. With a spherically symmetric, gray radiation transport scheme we estimated the peak time, peak luminosity, and peak spectral temperature of the kilonova light curves.

We find that the final amount of lanthanides and actinides depends most strongly on  $Y_e$  and the ejecta is lanthanide-free for  $Y_e \gtrsim 0.26$ . However, there are some regions of the parameter space where the ejecta is lanthanide-free even for very low electron

fractions. Specifically, at high initial entropies and small expansion timescales we get a neutron-rich freeze-out, which does not produce lanthanides, but may result in a very bright, very blue transient on the timescale of an hour. At small initial entropies and very large expansion timescales, there is significant late-time heating, which causes the composition to go back to NSE and effectively restart the r-process at a much higher electron fraction, which was raised by  $\beta$ -decays.

Since the lanthanides and actinides can increase the opacity of the material by a factor of  $\sim 100$ , we find that the peak luminosity increases by about one order of magnitude and the light curve peak timescale goes from about a week to about a day as the ejecta becomes lanthanide-free. This is consistent with previous works by Roberts et al. (2011), Kasen et al. (2013), Tanaka and Hotokezaka (2013), and Grossman et al. (2014). The heating rate at 1 day, however, remains largely unchanged and decreases by no more than one order of magnitude as the ejecta becomes lanthanide-free. Thus the increase in the kilonova luminosity is due to the decrease in the opacity when lanthanides are no longer present, which pushes the peak to earlier times when the heating is stronger. At very high  $Y_e$  ( $\gtrsim 0.4$ ), there are large variations in the heating rate because single nuclides dominate the heating. At lower  $Y_e$ , the heating rate at 1 day is very uniform in entropy and expansion timescale because it is dominated by an ensemble of nuclides that average out to the same heating rate at 1 day even though the exact composition may be very different. This has already been found in Metzger et al., 2010 and we are now confirming it for a larger parameter space.

Overall, we find only weak correlation between the lanthanide production and heating rate. Both quantities are quite strongly correlated with  $Y_e$ , but not so much with one another. The heating rate at 1 day is not affected much when the lanthanide abundance suddenly drops by many order of magnitude, but it slowly declines at higher  $Y_e$ .

In Section 3.2.4, we provided three linear inequalities involving  $Y_e$ ,  $\ln s$ , and  $\ln \tau$  that can be used to determine if the ejecta with those properties is lanthanide-rich or lanthanide-free. Those inequalities give the correct answer in 98% of all cases. We also provide parametric fits for the heating rates between 0.1 and 100 days for all cases at <http://stellarcollapse.org/lippunerroberts2015>. The mean fractional log difference between the actual heating rate and our fit is no more than 1% in 95% of all cases. On the same website, we also provide an integrated fractional heating contribution to give an idea of which specific nuclides contribute

the most to the radioactive heating.

Our nucleosynthesis code *SkyNet* will be released as free and open-source code soon. In the meantime, those interested can contact the authors about getting early access to the code. Future versions of *SkyNet* will also include neutrino interactions. Much more work needs to be done to accurately model the light curves of kilonovae and especially to calculate the line structure and hence opacity of the lanthanide and actinide elements. We hope that our heating rate fits will be useful to other researchers to calculate kilonova light curves that could aid with detecting such events.

### Acknowledgments

We thank Dan Kasen for helpful discussions on light curve modeling and for graciously providing us with temperature-dependent mean opacities for various mixtures of neodymium and iron. We thank Christian Ott for numerous useful discussions and for a careful reading of the manuscript. We thank Brian Metzger for a number of useful comments on the manuscript. And we also thank Shri Kulkarni for discussion about computing observed magnitudes.

The calculations presented here were performed on the Caltech “Zwicky” compute cluster (NSF MRI award No. PHY-0960291), on the NSF XSEDE network under allocation TG-PHY100033, and on NSF/NCSA Blue Waters under allocation jr6 (NSF PRAC award No. ACI-1440083). Support for LR during this work was provided by NASA through an Einstein Postdoctoral Fellowship grant numbered PF3-140114 awarded by the Chandra X-ray Center, which is operated by the Smithsonian Astrophysical Observatory for NASA under contract NAS8-03060. JL is partially supported by NSF under award Nos. TCAN AST-1333520, CAREER PHY-1151197, and AST-1205732, and by the Sherman Fairchild Foundation.

### 3.A Computing AB magnitude from light curve

The observed AB magnitude is defined as

$$m_{\text{AB}} = -\frac{5}{2} \log_{10} \left( \frac{\int f_{\nu}(\nu) T_{\nu}(\nu) d\nu}{3631 \text{ Jy} \int T_{\nu}(\nu) d\nu} \right), \quad (3.16)$$

where  $f_{\nu}(\nu)$  is the observed spectral flux density (energy per unit time per unit area per unit frequency) at frequency  $\nu$ ,  $T_{\nu}(\nu)$  is the filter throughput per unit frequency at frequency  $\nu$ , and Jy is the unit Jansky, where  $1 \text{ Jy} = 10^{-23} \text{ erg s}^{-1} \text{ cm}^{-2} \text{ Hz}^{-1}$ . The

HST filters are given as throughput per wavelength as a function of wavelength<sup>4</sup>, i.e.  $T_\lambda(\lambda)$ . To convert from  $T_\lambda(\lambda)$  to  $T_\nu(\nu)$ , we note that

$$\begin{aligned} T_\nu(\nu)d\nu &= -T_\lambda(\lambda)d\lambda \\ \Leftrightarrow T_\nu(\nu) &= -T_\lambda(\lambda)\frac{d\lambda}{d\nu} = T_\lambda(c/\nu)\frac{c}{\nu^2}, \end{aligned} \quad (3.17)$$

since  $\lambda = c/\nu$ , where  $c$  is the speed of light in vacuum, and the minus sign comes from the fact that the wavelength decreases as the frequency increases. The observed spectral flux density is given by

$$f_\nu(\nu) = \frac{L_\nu(\nu)}{4\pi D^2}, \quad (3.18)$$

where  $L_\nu(\nu)$  is the radiated spectral flux (radiated energy per unit time per unit frequency) at frequency  $\nu$  and  $D$  is the distance between the source and the observer. This assumes that the source is radiating isotropically. Our light curve model gives us the bolometric luminosity  $L_{\text{bol}}$  and the effective temperature  $T_{\text{eff}}$  as a function of time. We then assume that the radiated spectrum is a black body spectrum with total luminosity  $L_{\text{bol}}$ , hence we get

$$L_\nu(\nu) = L_{\text{bol}} \frac{B_\nu(\nu, T_{\text{eff}})}{\int B_\nu(\nu, T_{\text{eff}}) d\nu}, \quad (3.19)$$

where  $B_\nu(\nu, T_{\text{eff}})$  is the spectral radiance given by Planck's law.

The above is true for a source that is close to the observer compared to cosmological distances, but if the source is sufficiently far away, we need to take redshift into account. Recall that the emitted frequency is given by

$$\nu_{\text{emit}} = (1 + z)\nu_{\text{obs}}, \quad (3.20)$$

where  $z$  is the redshift of the source. Since (3.16) is calculated at the observer, we have  $f_\nu(\nu) = f_{\nu_{\text{obs}}}(\nu_{\text{obs}})$ , and since this power per unit area per unit frequency, it follows that

$$\begin{aligned} f_{\nu_{\text{obs}}}(\nu_{\text{obs}})d\nu_{\text{obs}} &= f_{\nu_{\text{emit}}}(\nu_{\text{emit}})d\nu_{\text{emit}} \\ \Leftrightarrow f_{\nu_{\text{obs}}}(\nu_{\text{obs}}) &= f_{\nu_{\text{emit}}}(\nu_{\text{emit}})\frac{d\nu_{\text{emit}}}{d\nu_{\text{obs}}} = (1 + z)f_{\nu_{\text{emit}}}((1 + z)\nu_{\text{obs}}). \end{aligned} \quad (3.21)$$

Note that there are additional corrections to  $f_\nu$  due to the photon energy and their arrival rate both being reduced by a factor of  $(1 + z)$ . However, we will absorb these

<sup>4</sup><http://svo2.cab.inta-csic.es/svo/theory/fps3/index.php?mode=browse&gname=HST>

to factors of  $(1 + z)$  into the definition of the distance between the source and the observer, which is called the luminosity distance  $D_L$ . Thus we finally have

$$m_{AB} = -\frac{5}{2} \log_{10} \left( \frac{(1+z)L_{\text{bol}}}{4\pi D_L^2 \int B_\nu(\nu, T_{\text{eff}}) d\nu} \frac{\int B_\nu((1+z)\nu, T_{\text{eff}}) T_\lambda(c/\nu) \nu^{-2} d\nu}{3631 \text{ Jy} \int T_\lambda(c/\nu) \nu^{-2} d\nu} \right). \quad (3.22)$$

The luminosity distance as a function of redshift  $z$  can be calculated as follows (Hogg, 1999). Define

$$E(z) = \sqrt{\Omega_m(1+z)^3 + \Omega_k(1+z)^2 + \Omega_\Lambda}, \quad (3.23)$$

where  $\Omega_m$  is the total matter density,  $\Omega_\Lambda$  is the dark energy density, and  $\Omega_k = 1 - \Omega_m - \Omega_\Lambda$  is the curvature. Also define the Hubble distance  $D_H = c/H_0$ , where  $H_0$  is the Hubble parameter. Then, the comoving distance  $D_C$  is

$$D_C(z) = D_H \int_0^z \frac{dz'}{E(z')}, \quad (3.24)$$

the transverse comoving distance  $D_M(z)$  is

$$D_M(z) = \begin{cases} \frac{D_H}{\sqrt{\Omega_k}} \sinh \left( \sqrt{\Omega_k} D_C(z)/D_H \right) & \text{if } \Omega_k > 0, \\ D_C(z) & \text{if } \Omega_k = 0, \\ \frac{D_H}{\sqrt{|\Omega_k|}} \sin \left( \sqrt{|\Omega_k|} D_C(z)/D_H \right) & \text{if } \Omega_k < 0, \end{cases} \quad (3.25)$$

and finally, the luminosity distance is

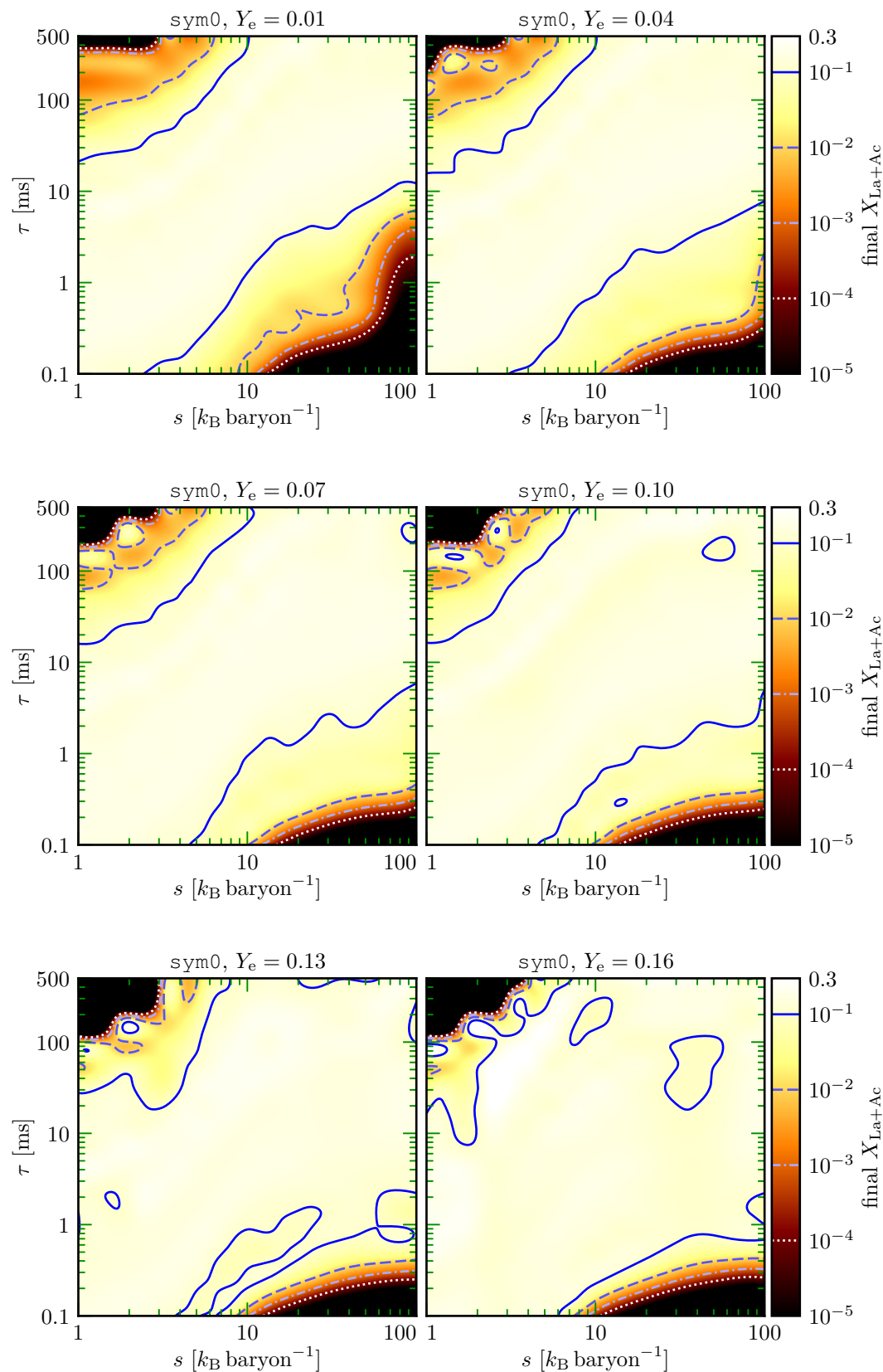
$$D_L(z) = (1+z)D_M(z). \quad (3.26)$$

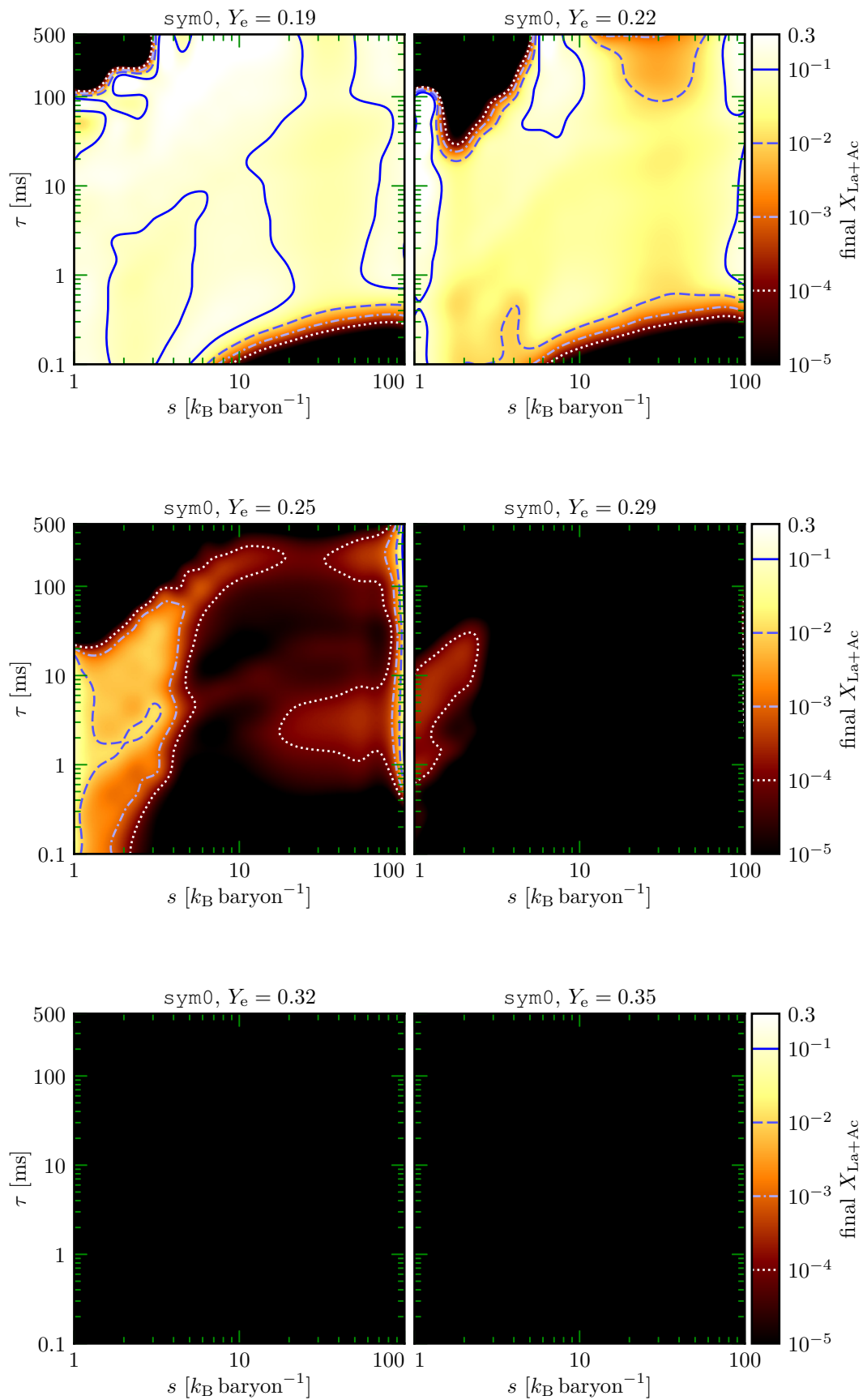
In this paper, we use the most recent Planck values (Planck Collaboration et al., 2016) for the cosmological parameters, i.e.  $H_0 = 67.74 \text{ km s}^{-1} \text{ Mpc}^{-1}$ ,  $\Omega_m = 0.3089$ ,  $\Omega_\Lambda = 0.6911$ , and  $\Omega_k = 0$ .

### 3.B Slice plots

In this section we show all the slice plots from our runs, which have also been made available at <http://stellarcollapse.org/lippunerroberts2015>.

### 3.B.1 High-resolution sym0 run





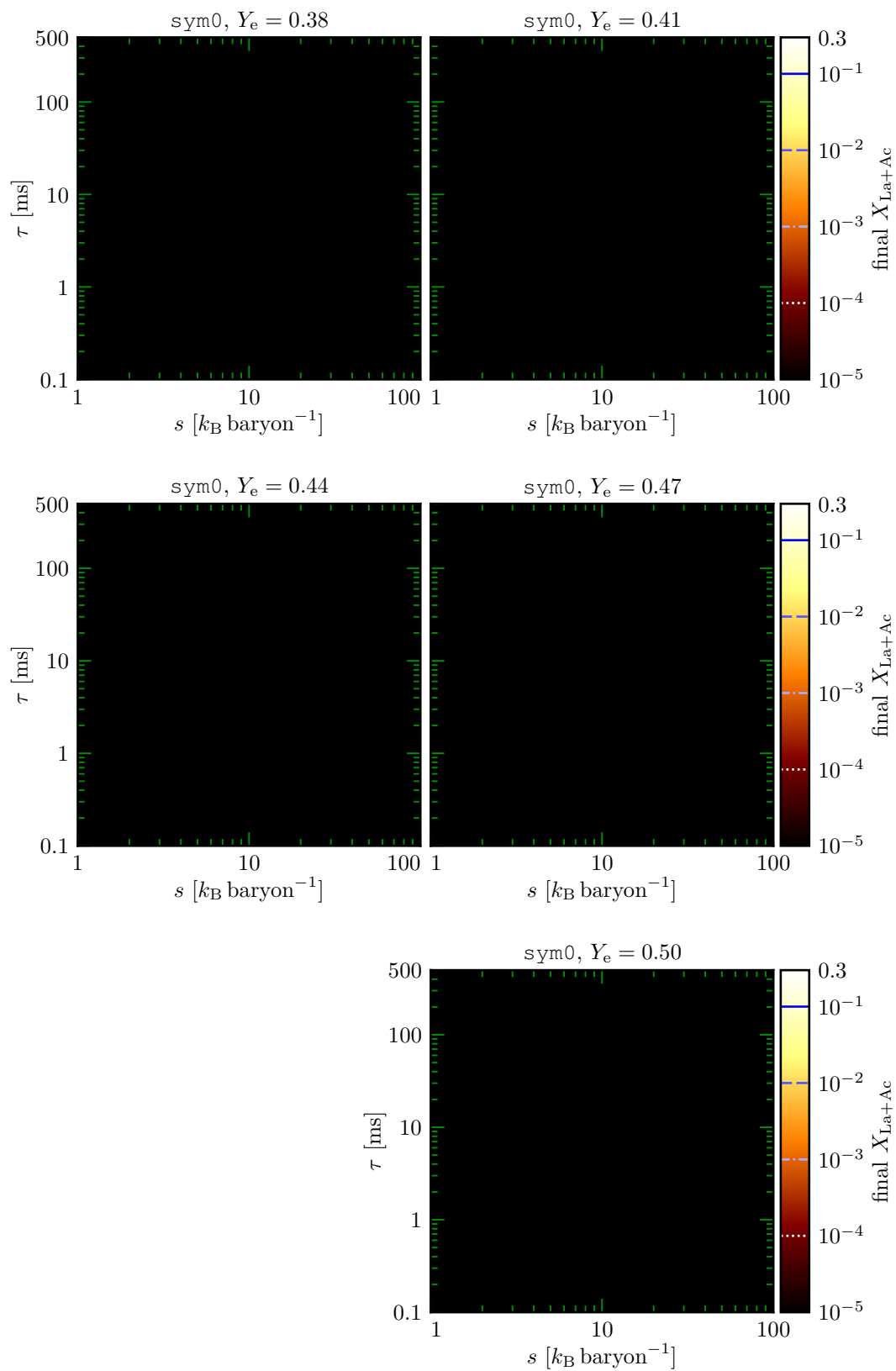
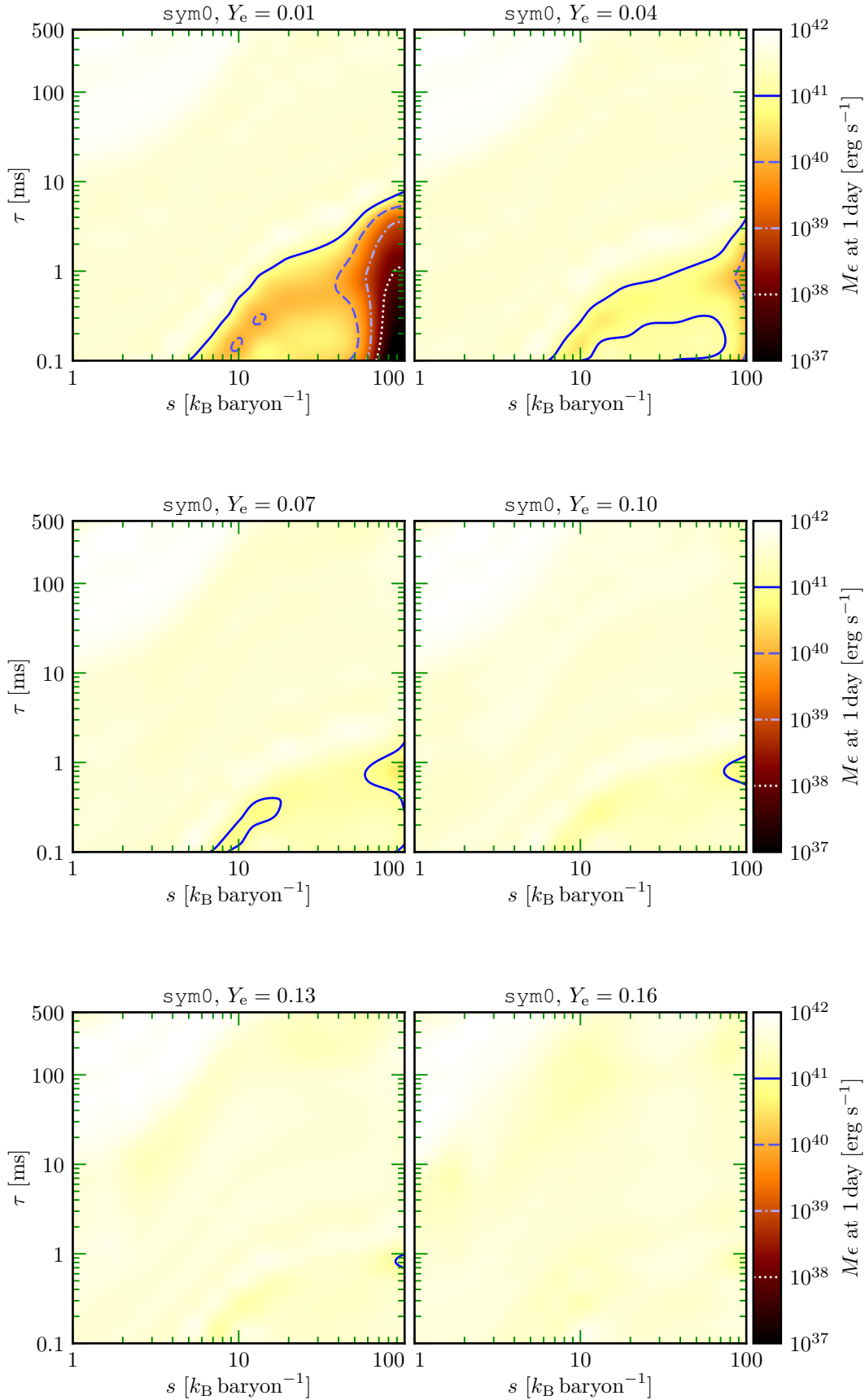
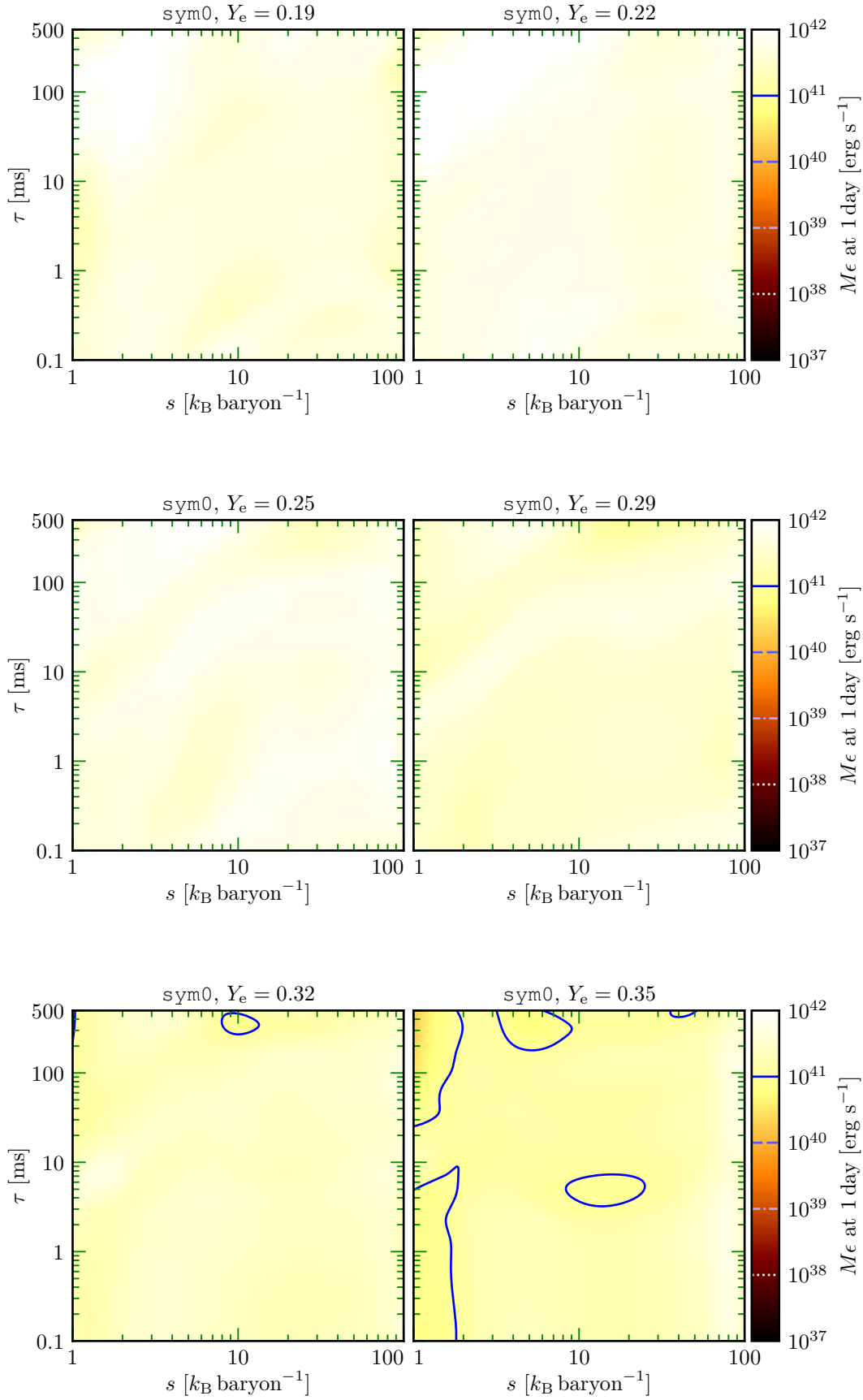


Figure 3.10: All the  $Y_e$  slices showing the final lanthanide and actinide mass fraction of the high-resolution `sym0` run.





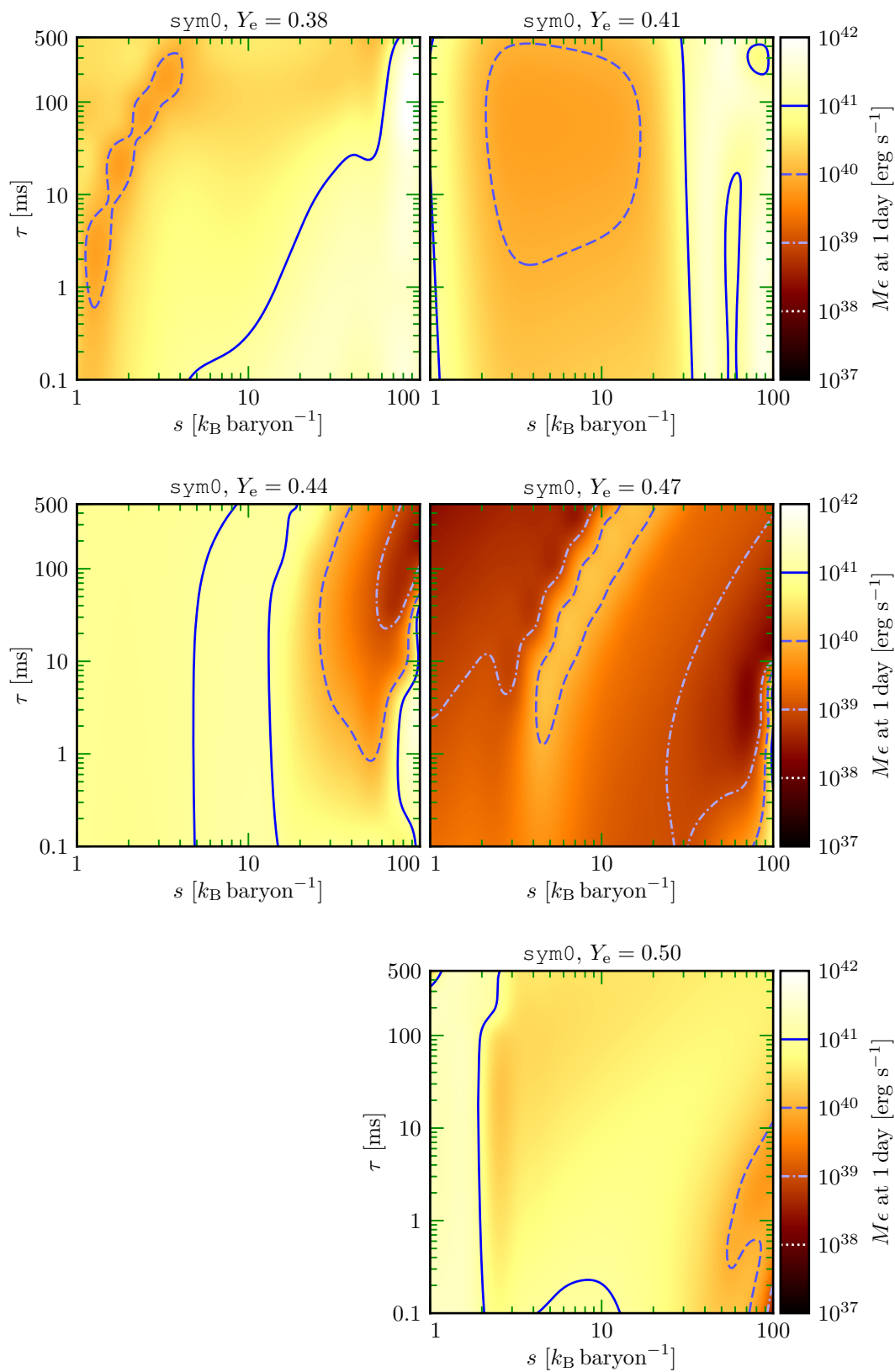
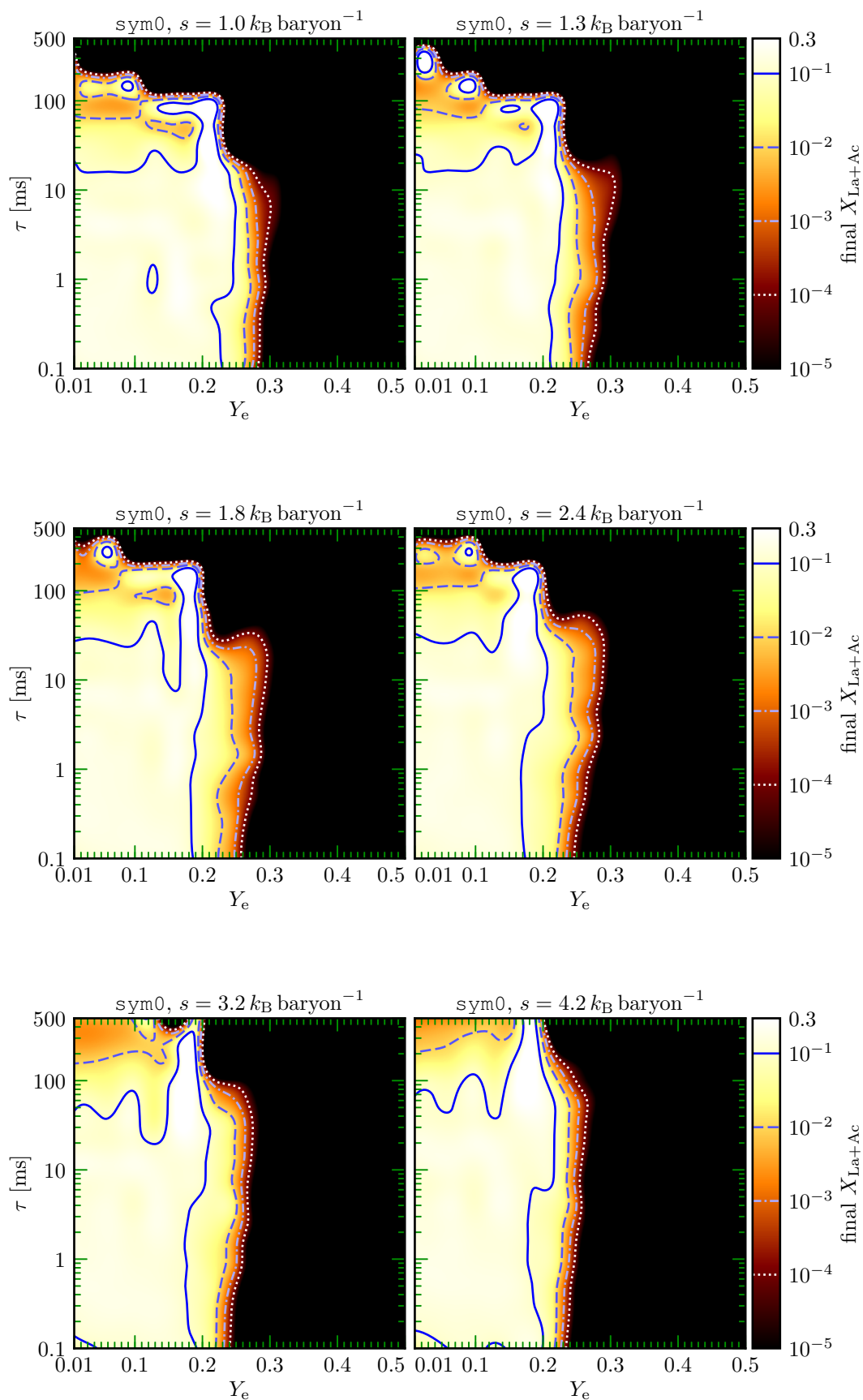
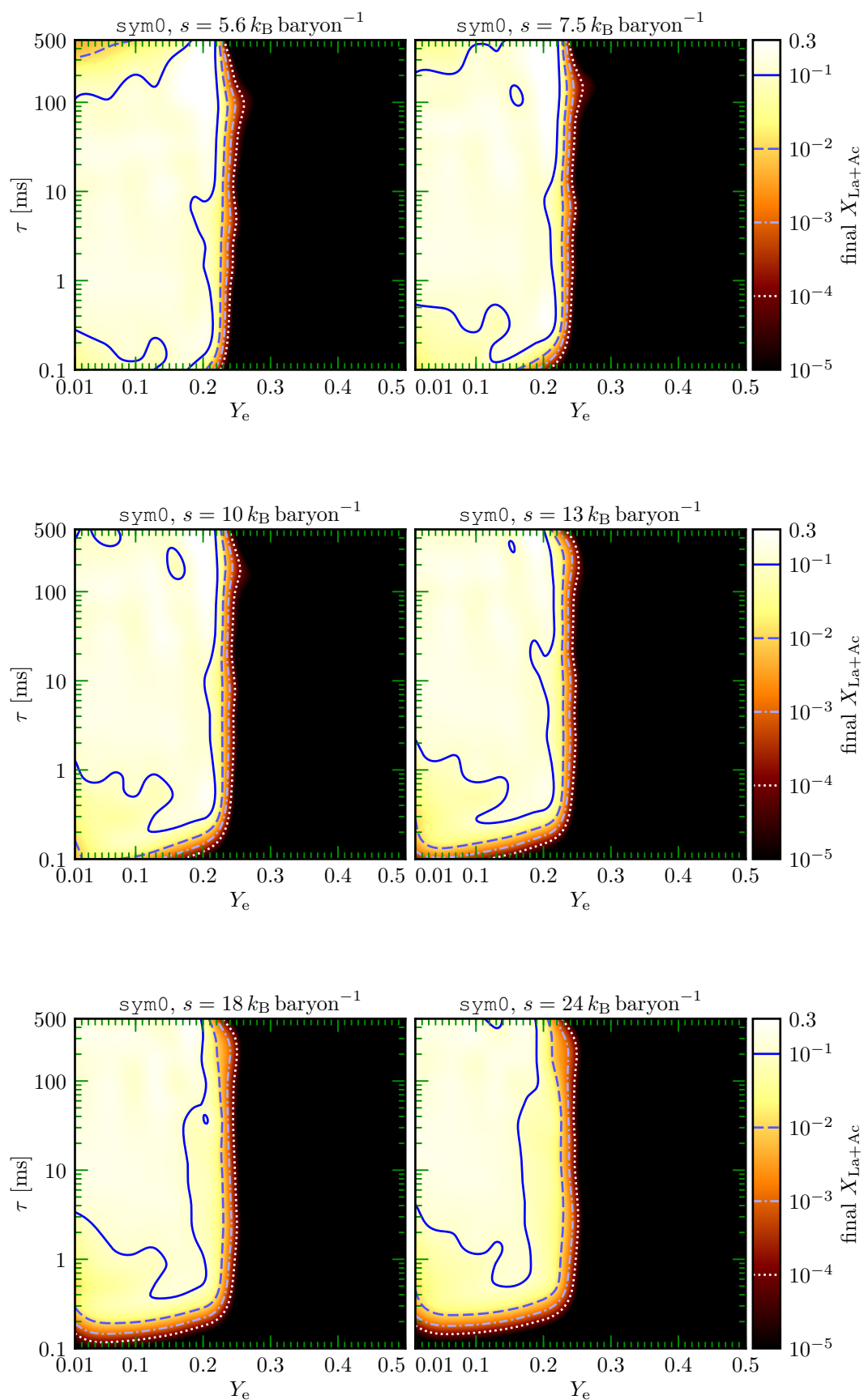


Figure 3.11: All the  $Y_e$  slices showing the heating rate at 1 day of the high-resolution sym0 run.





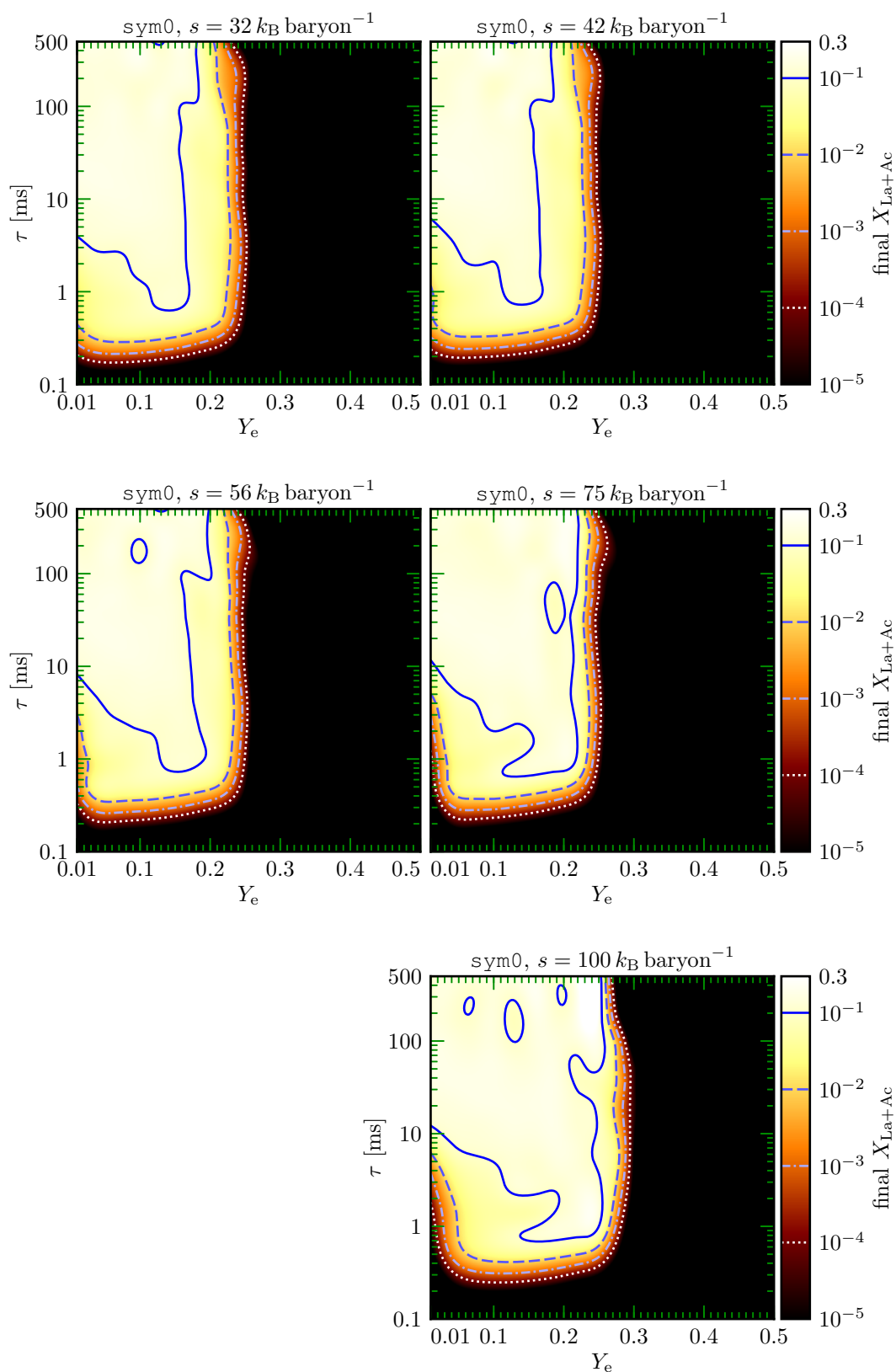
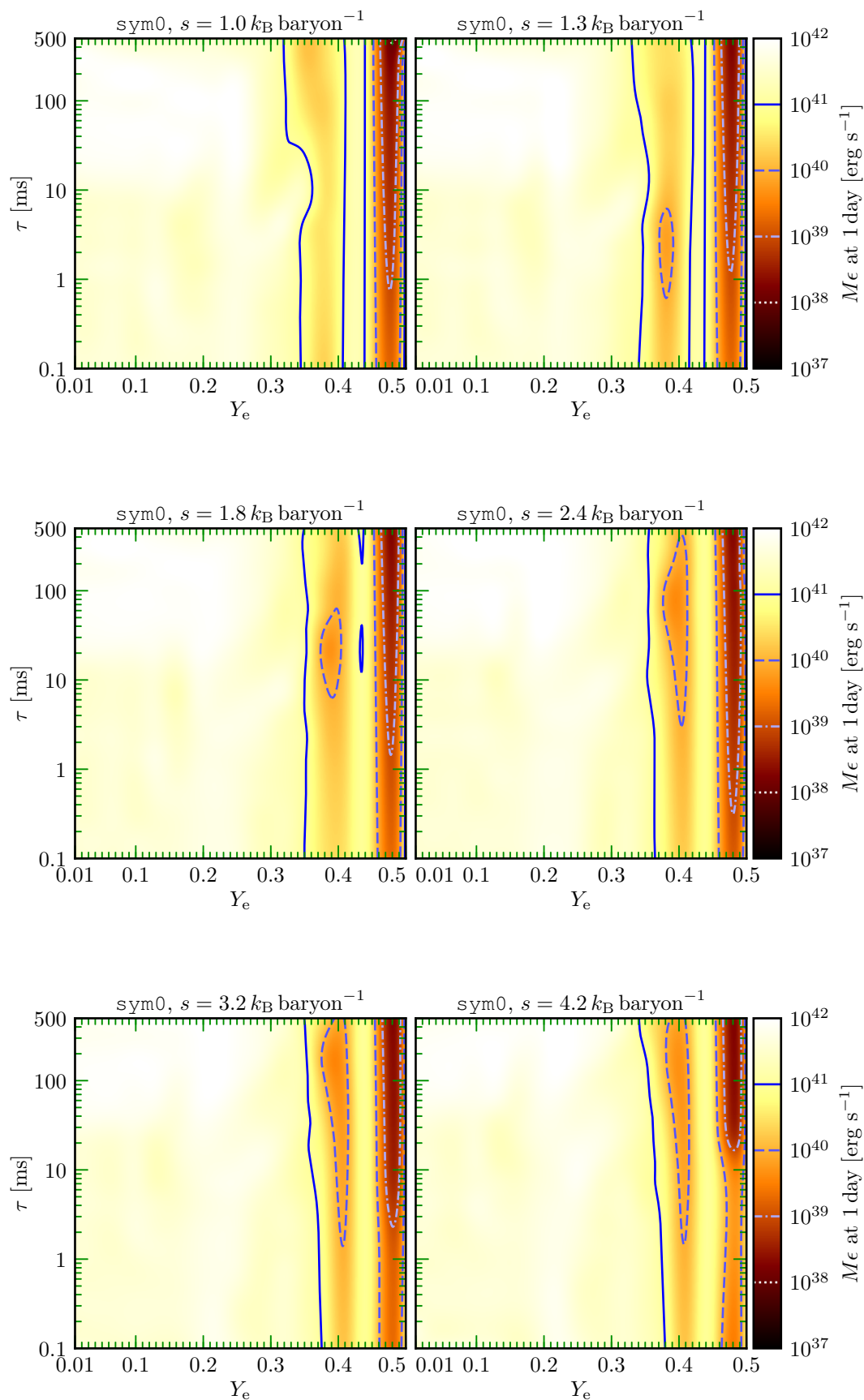
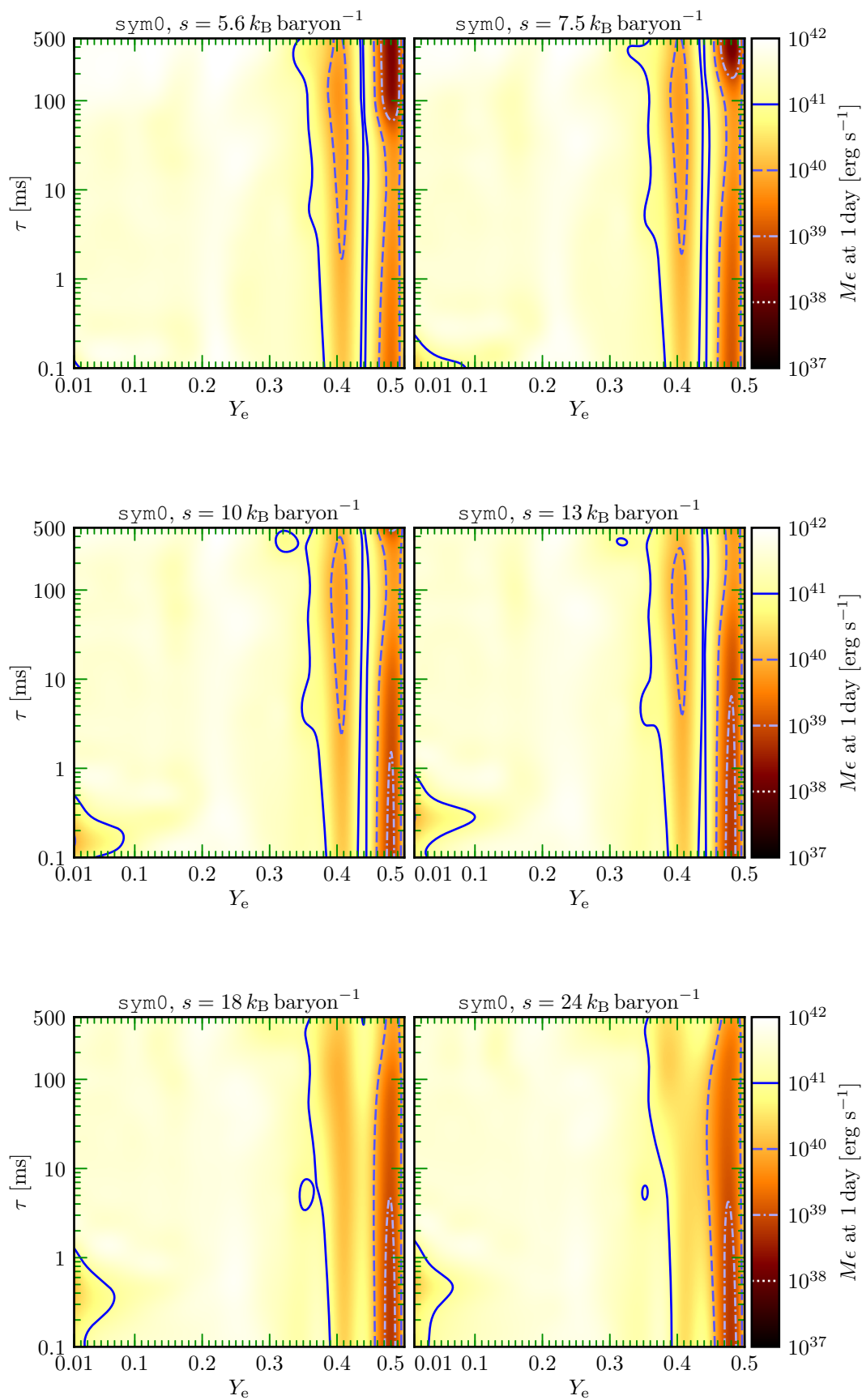


Figure 3.12: All the  $s$  slices showing the final lanthanide and actinide mass fraction of the high-resolution `sym0` run.





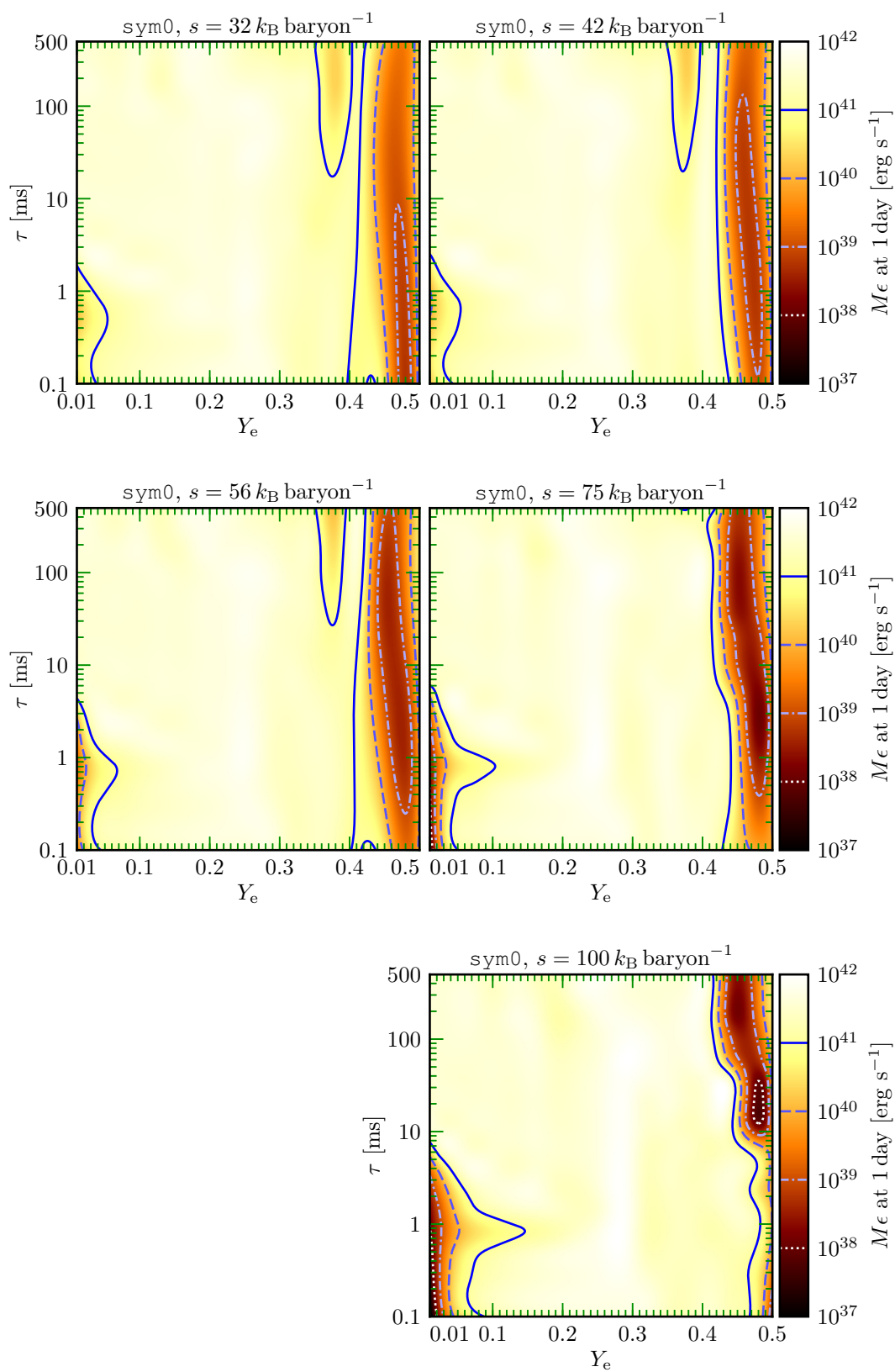
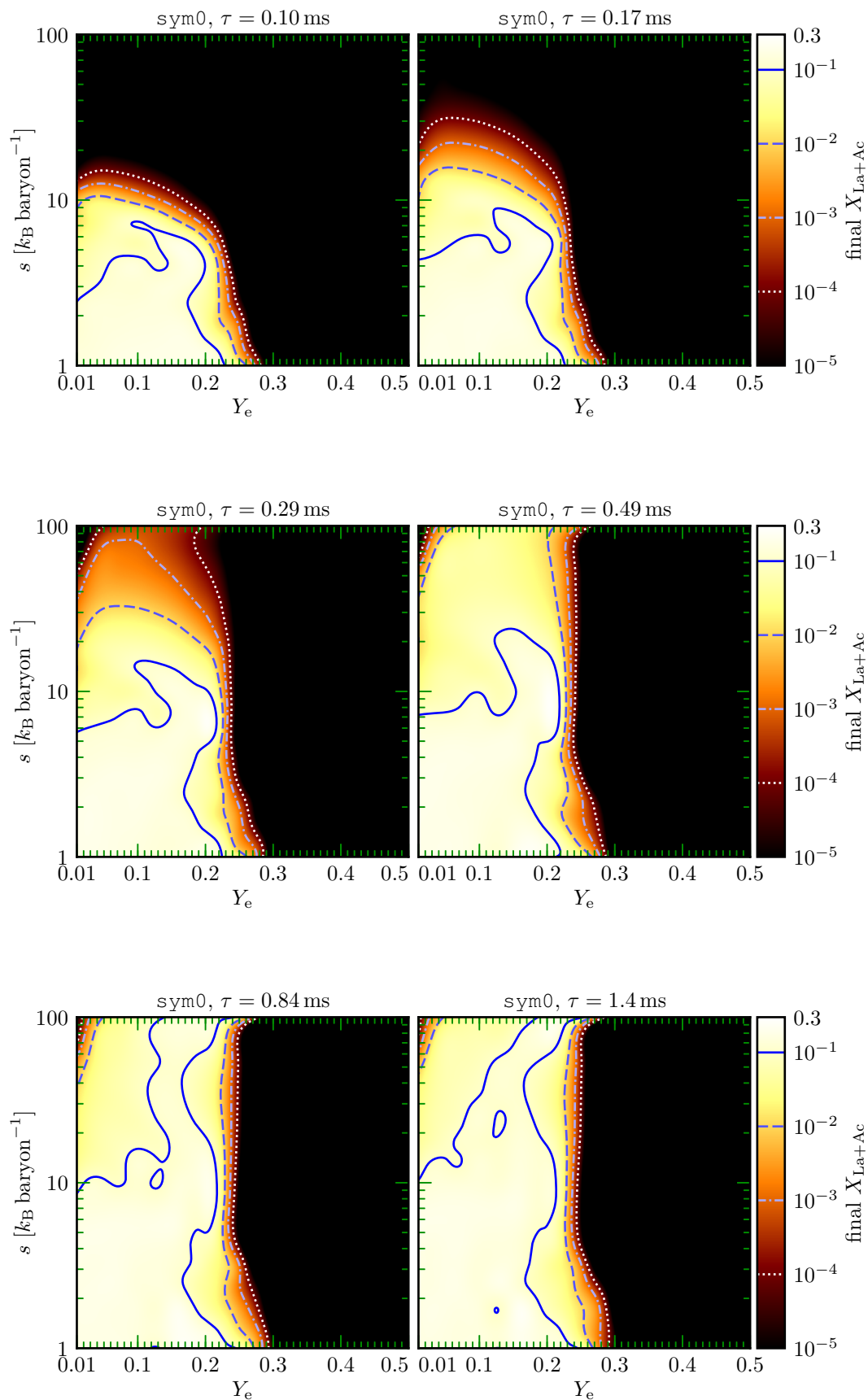
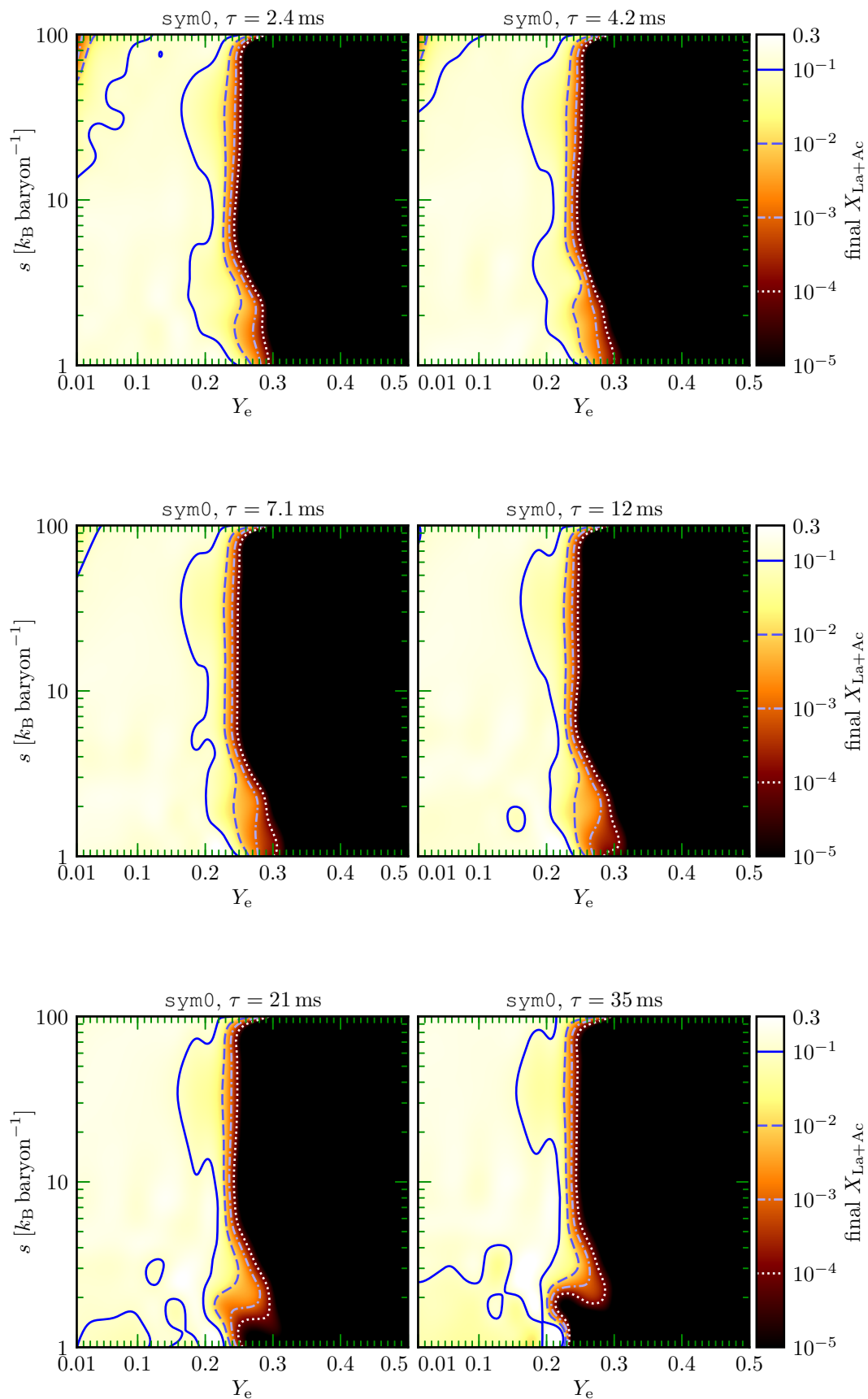


Figure 3.13: All the  $s$  slices showing the heating rate at 1 day of the high-resolution `sym0` run.





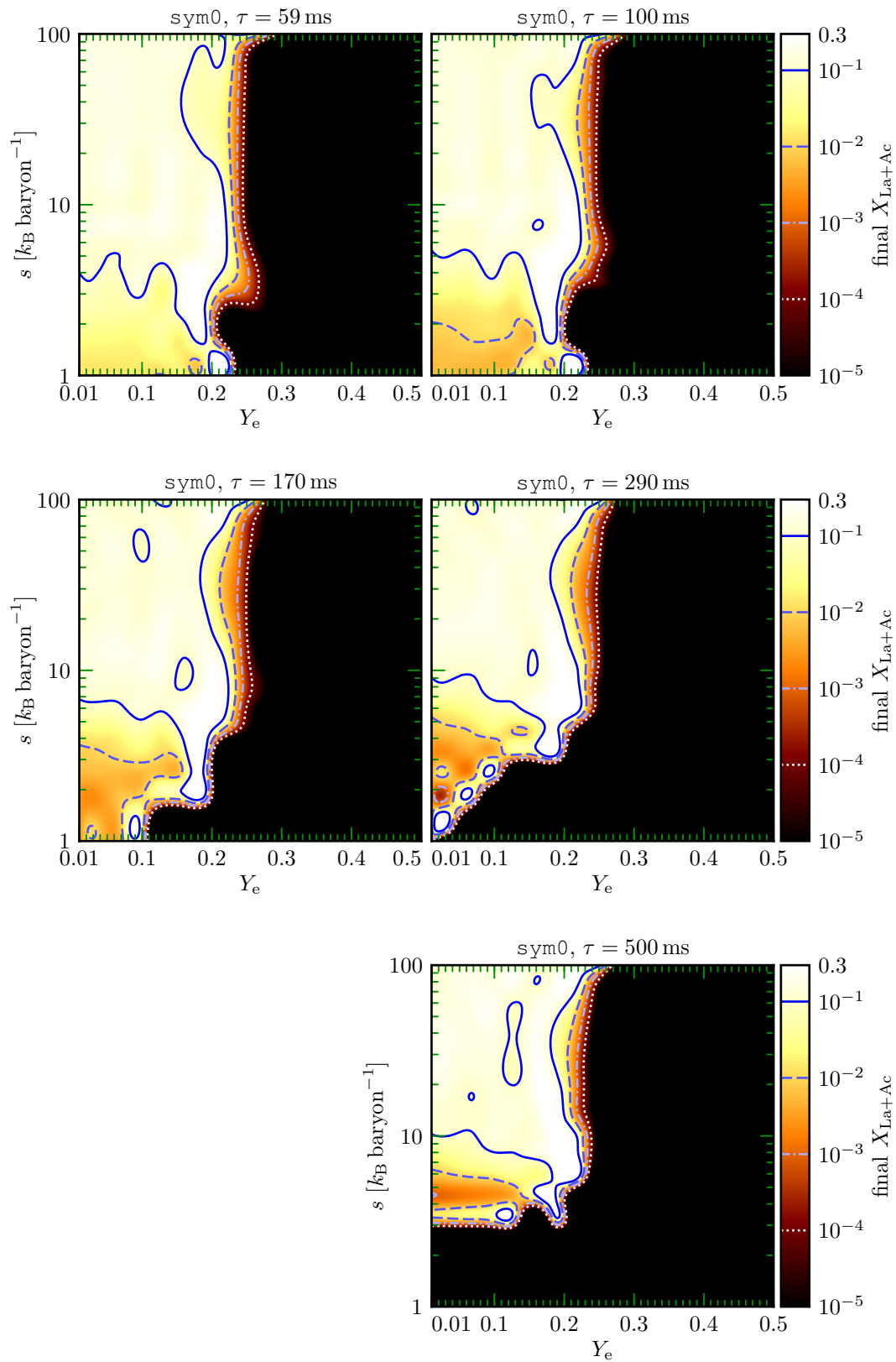
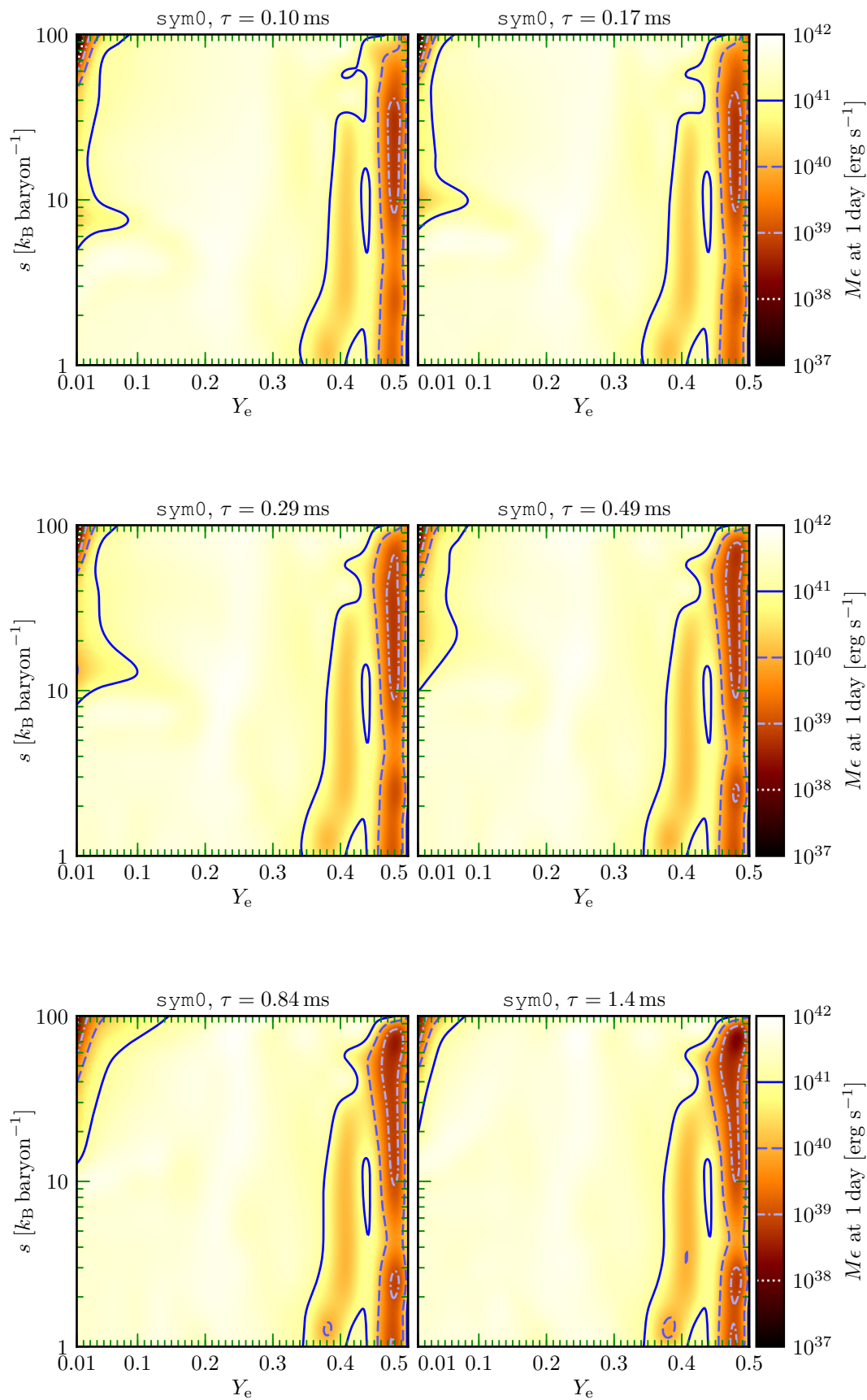
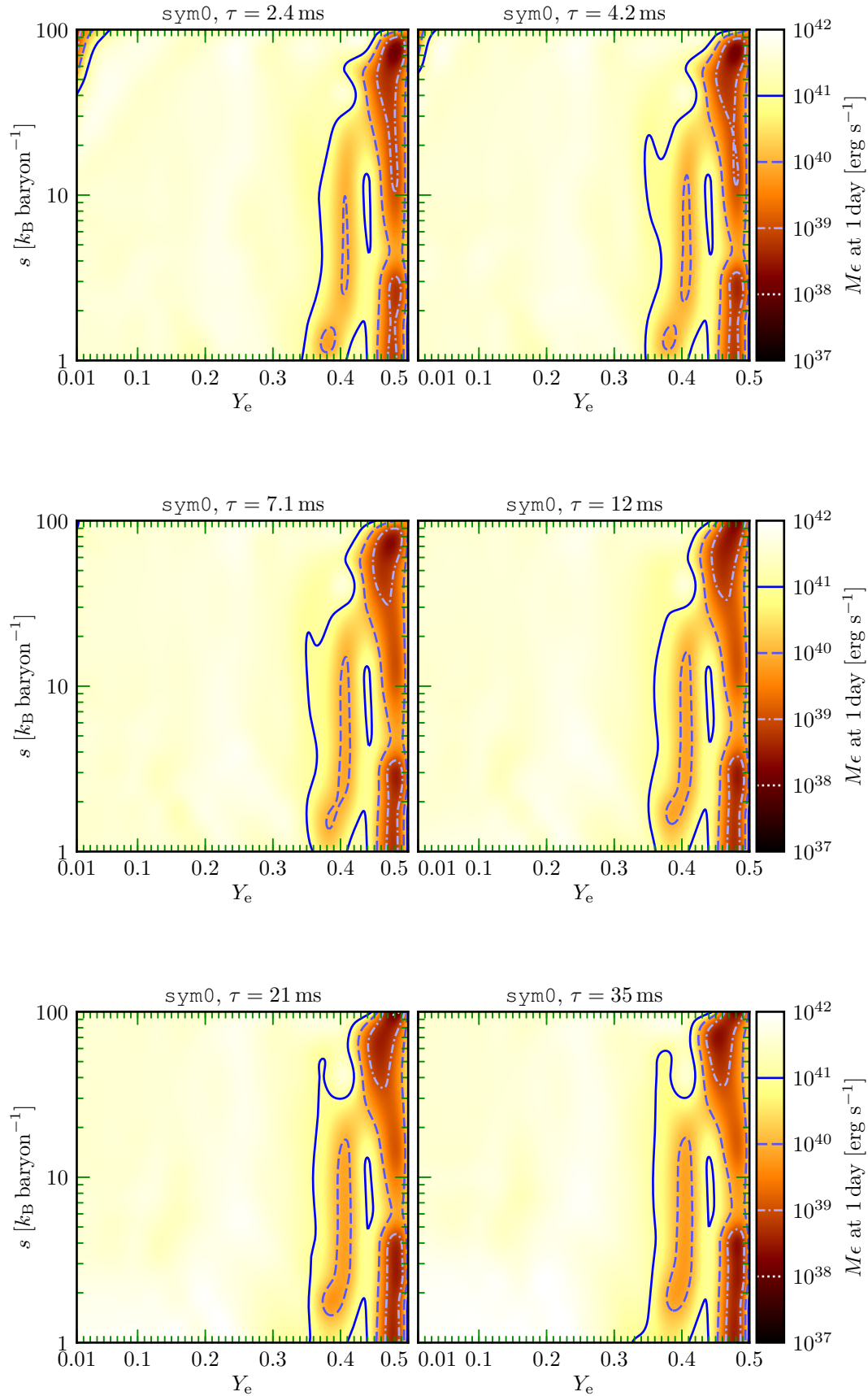


Figure 3.14: All the  $\tau$  slices showing the final lanthanide and actinide mass fraction of the high-resolution `sym0` run.





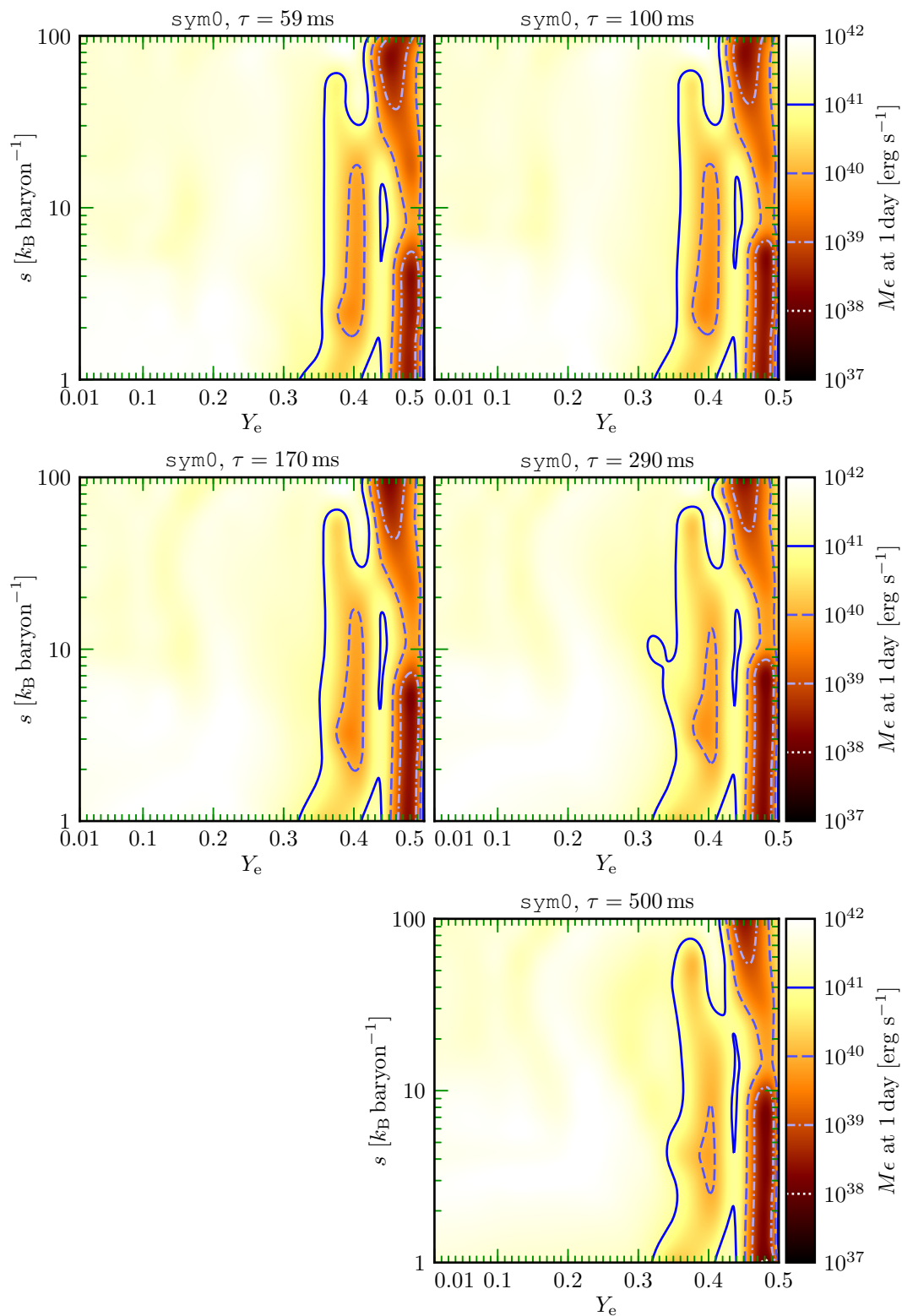
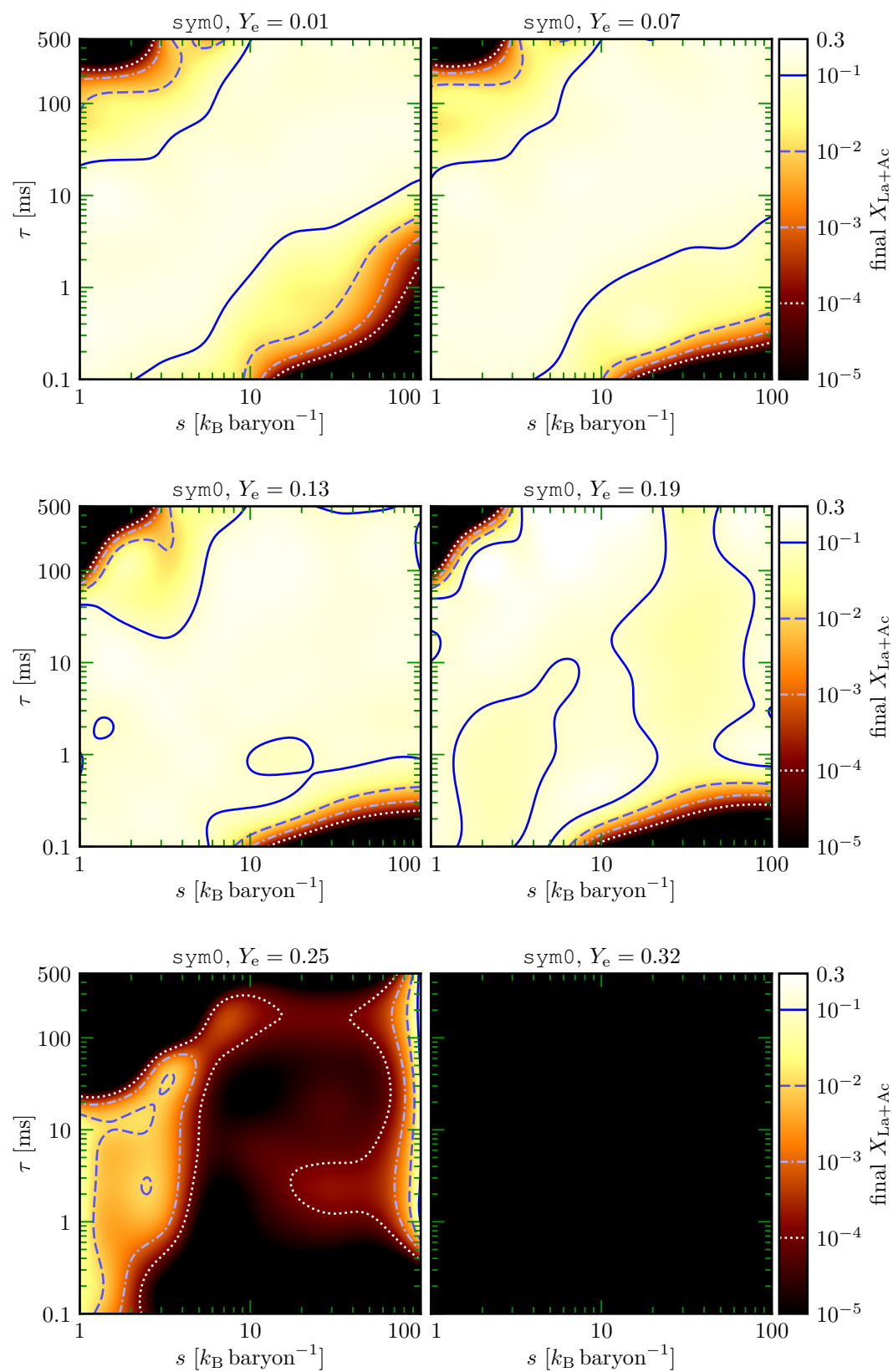


Figure 3.15: All the  $\tau$  slices showing the heating rate at 1 day of the high-resolution `sym0` run.

## 3.B.2 sym0 run



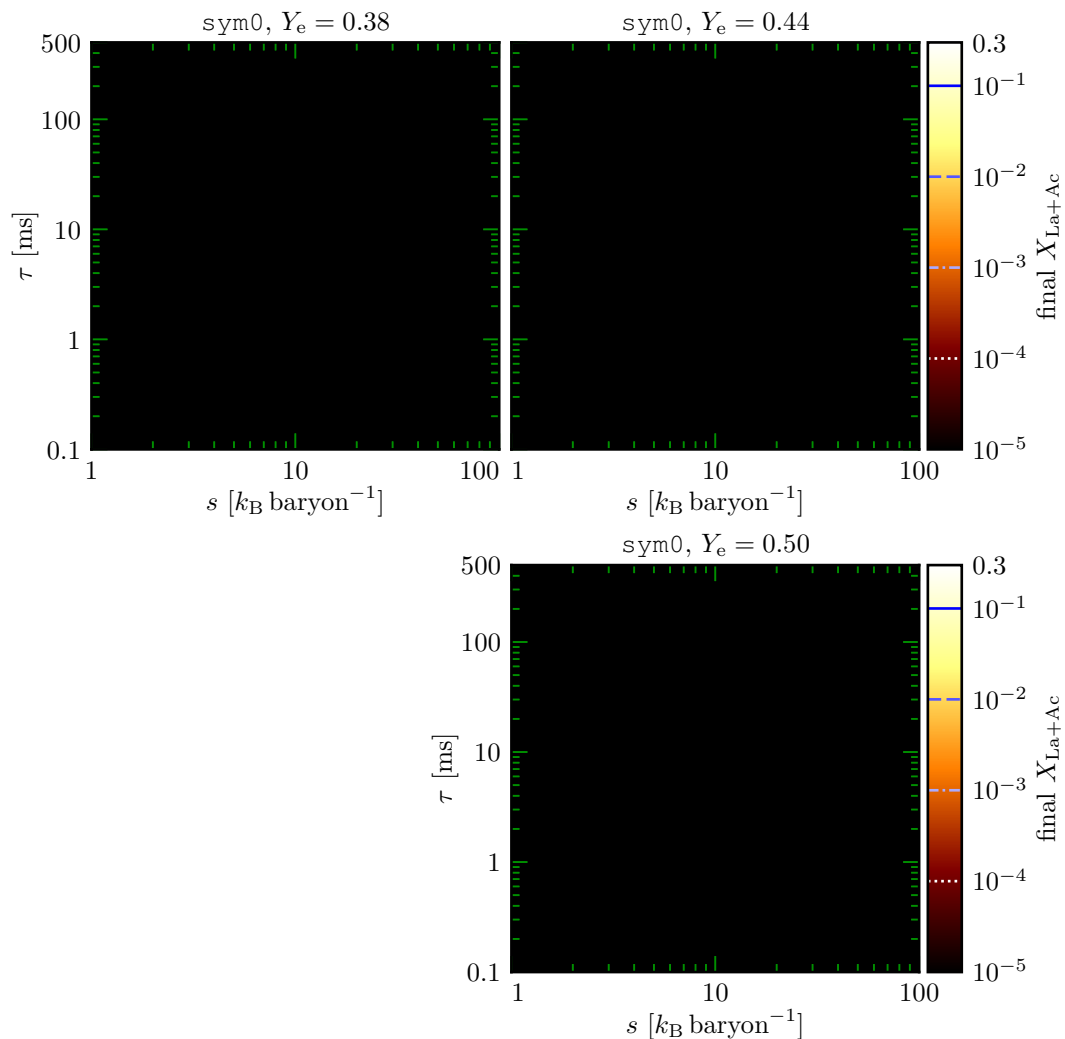
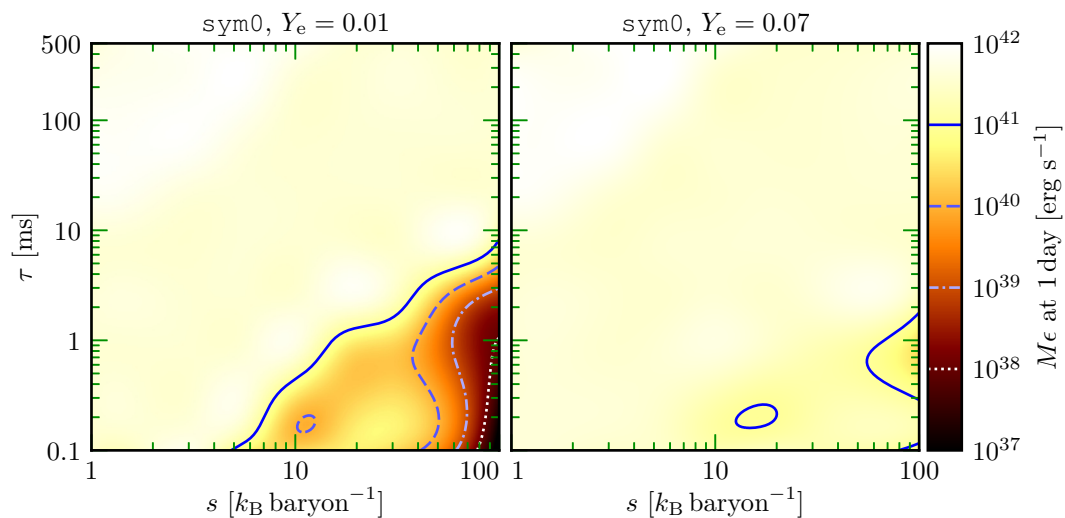
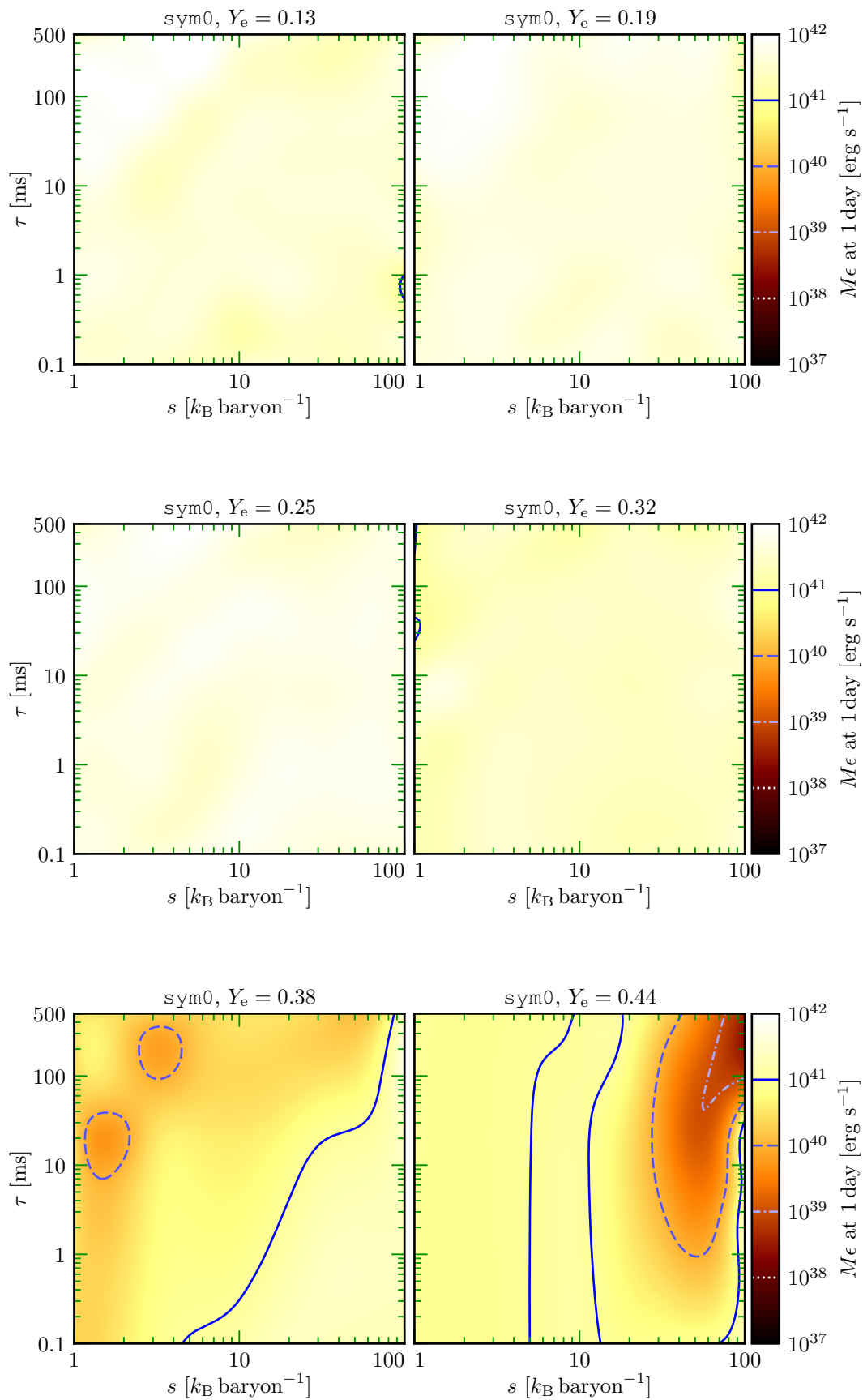


Figure 3.16: All the  $Y_e$  slices showing the final lanthanide and actinide mass fraction of the `sym0` run.





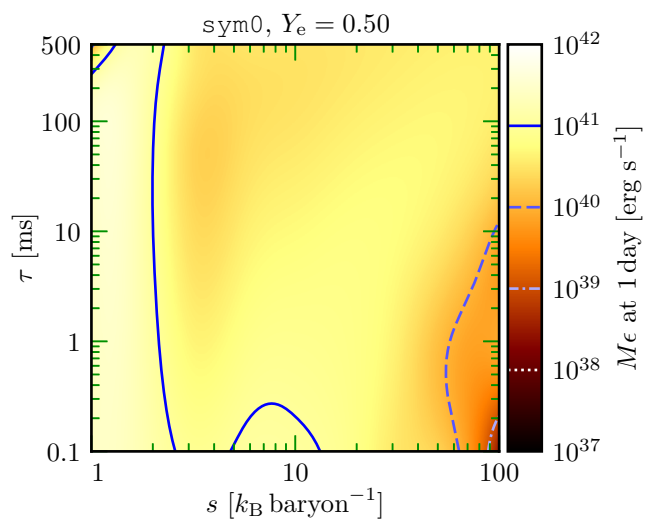
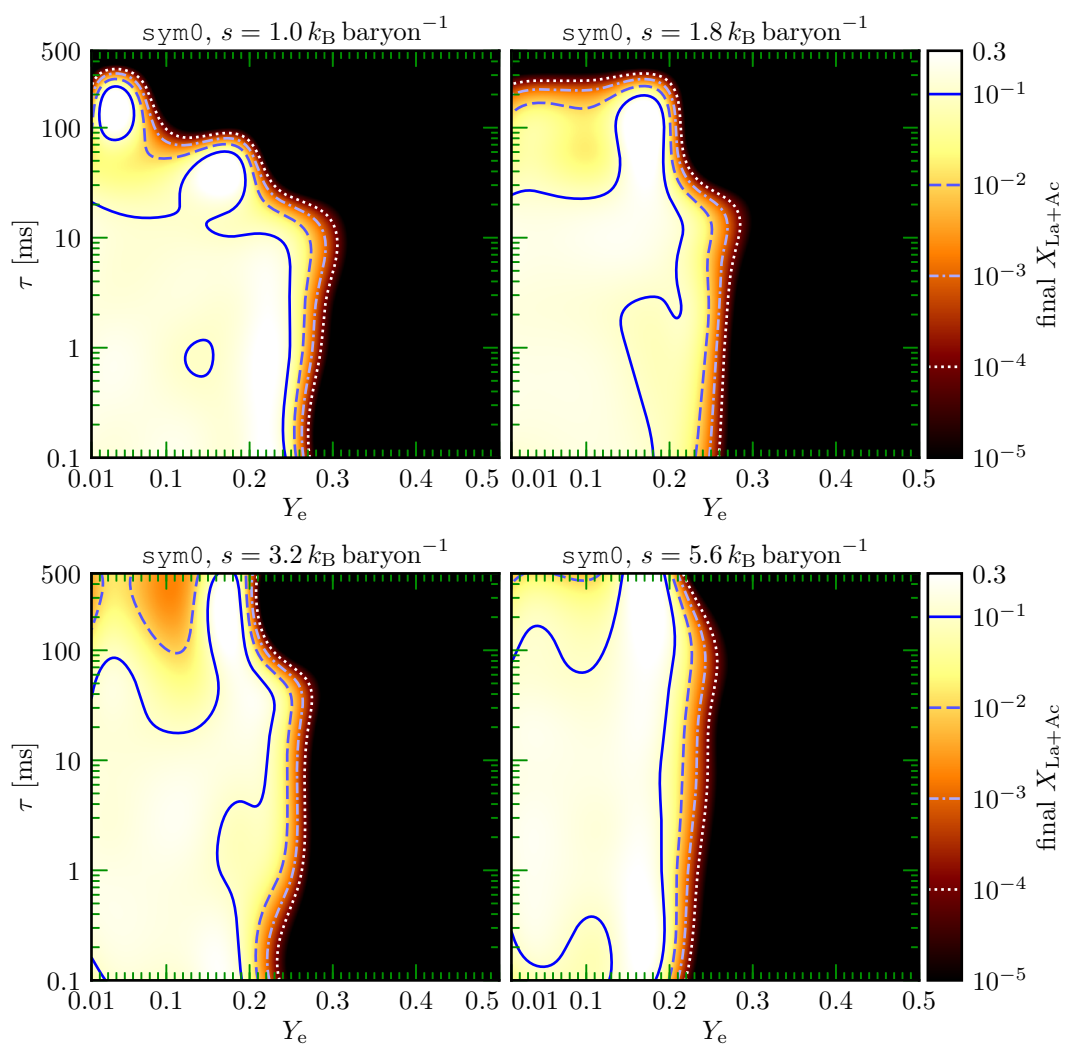


Figure 3.17: All the  $Y_e$  slices showing the heating rate at 1 day of the sym0 run.



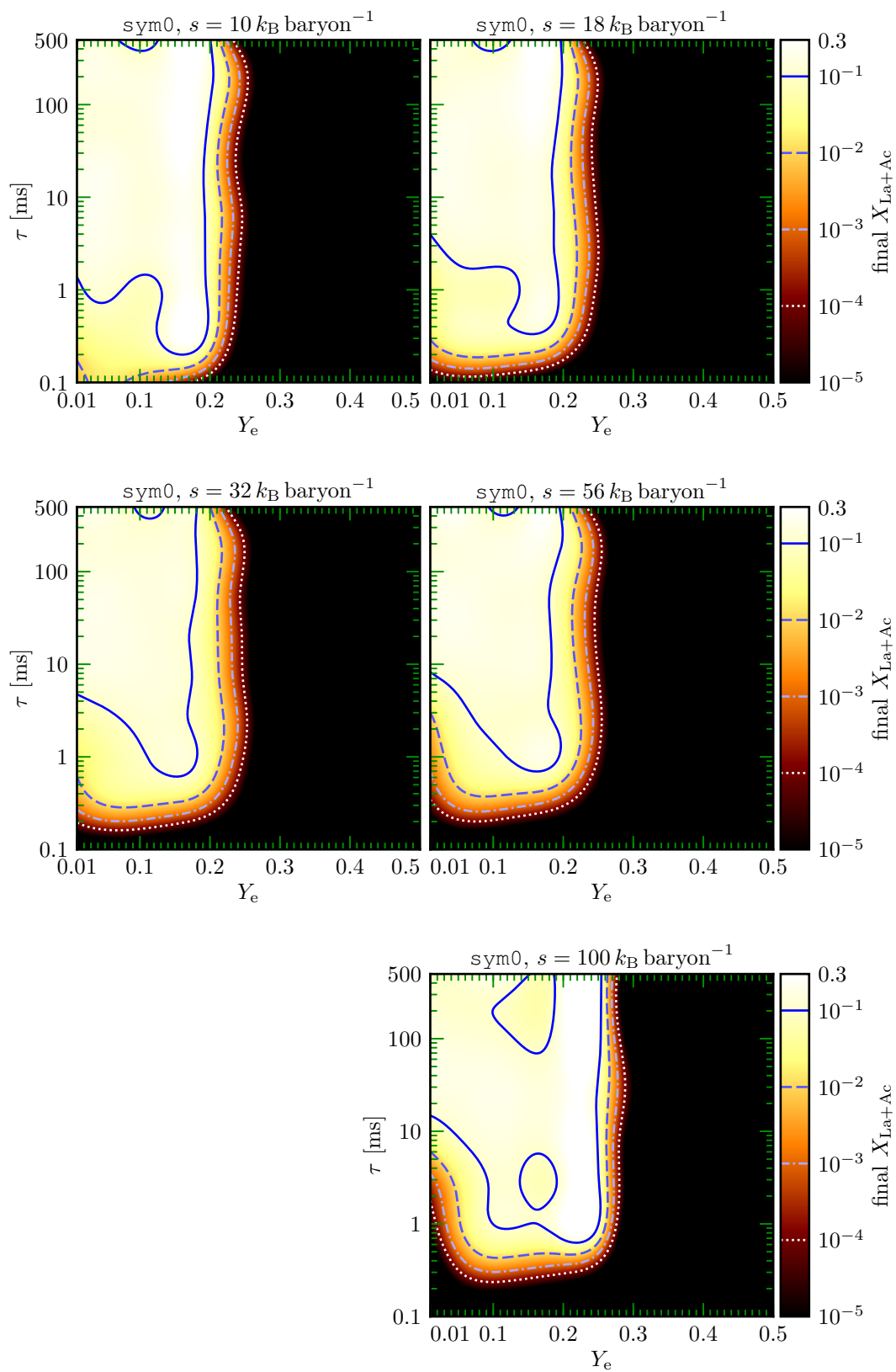
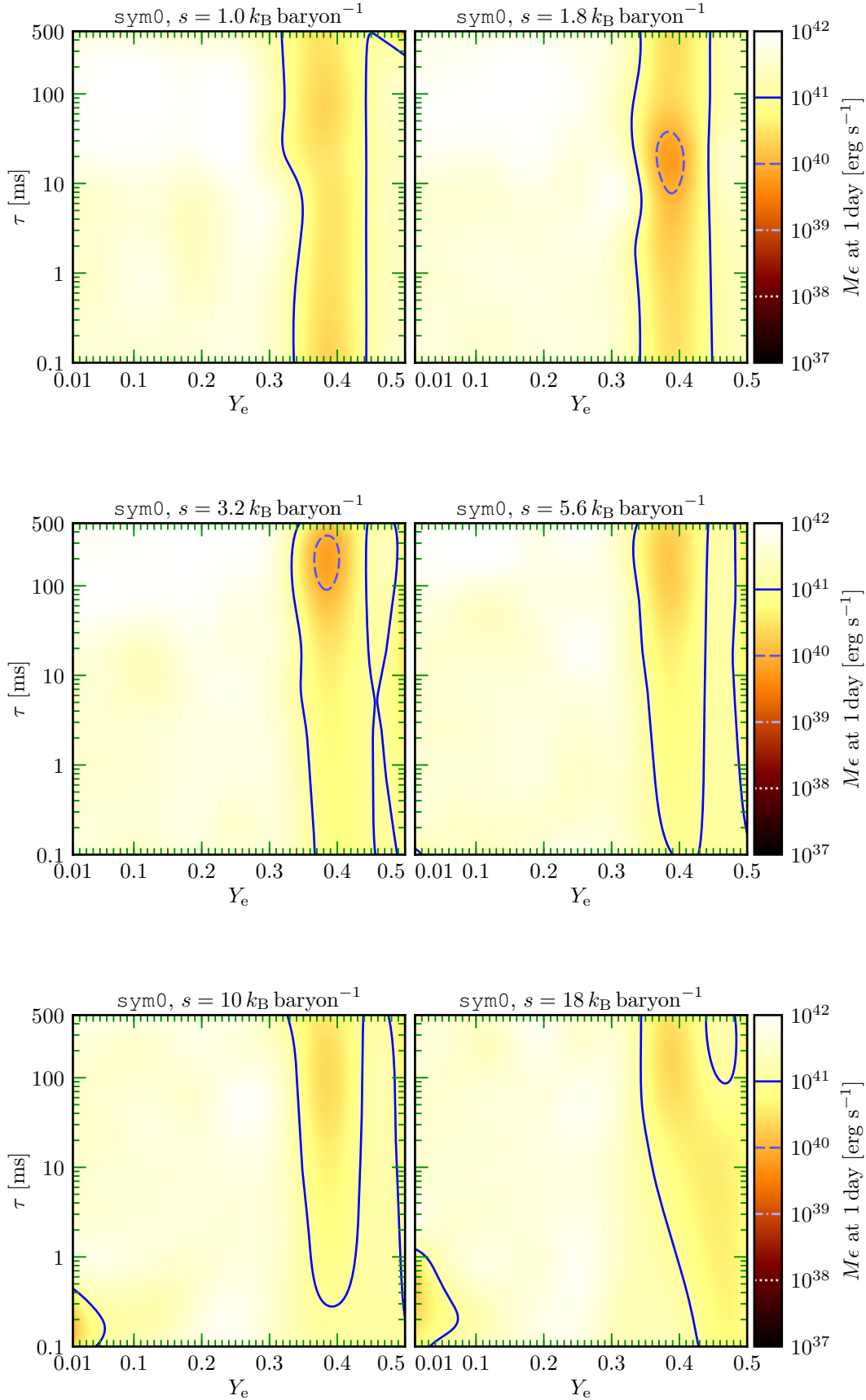


Figure 3.18: All the  $s$  slices showing the final lanthanide and actinide mass fraction of the `sym0` run.



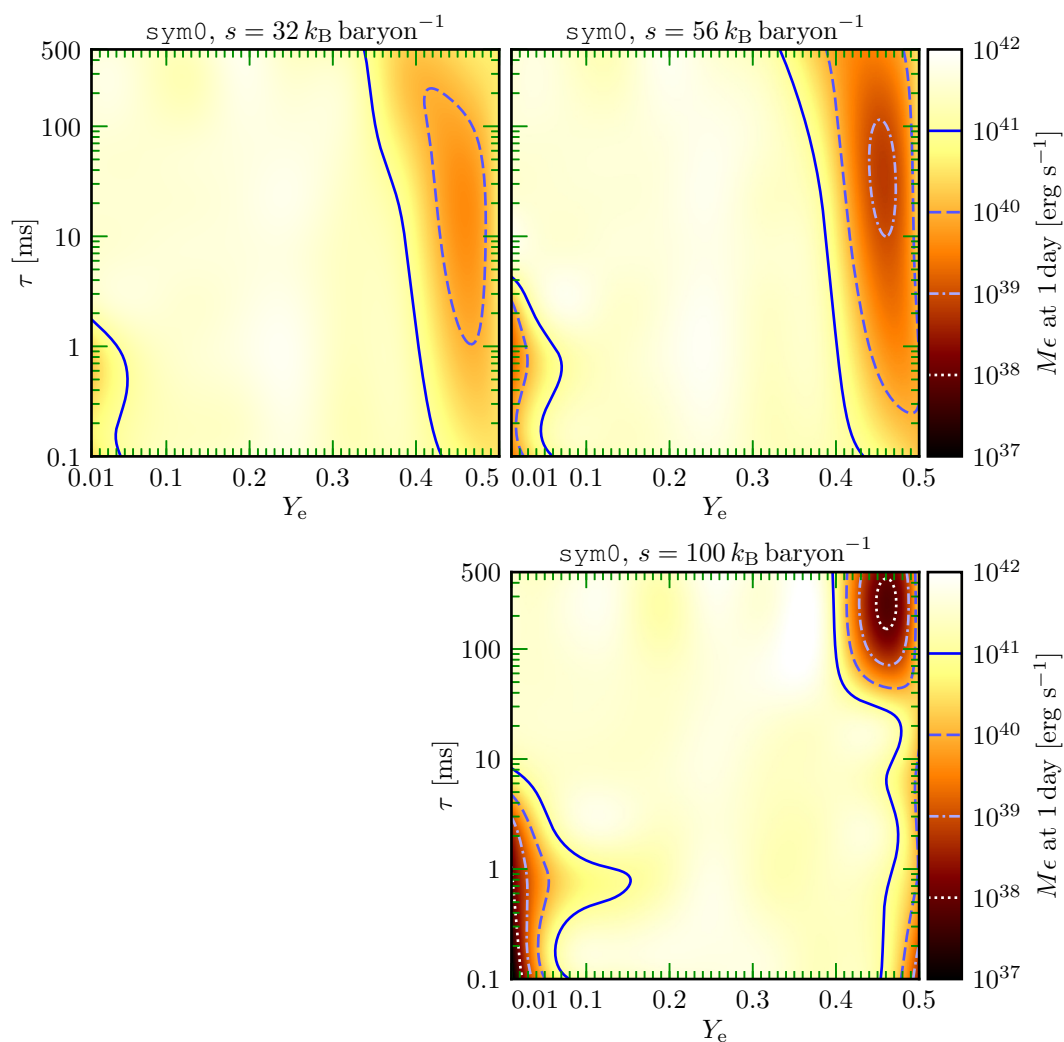
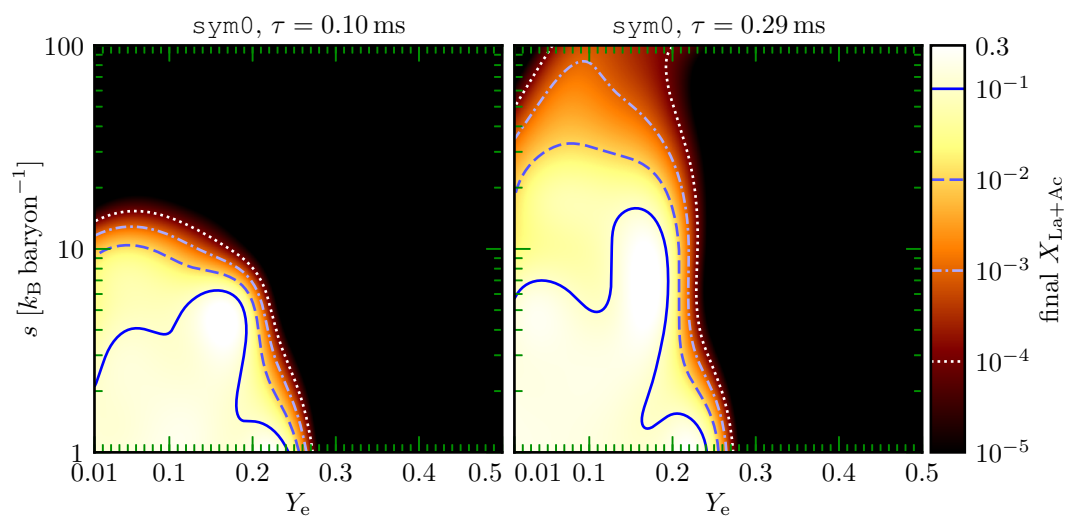
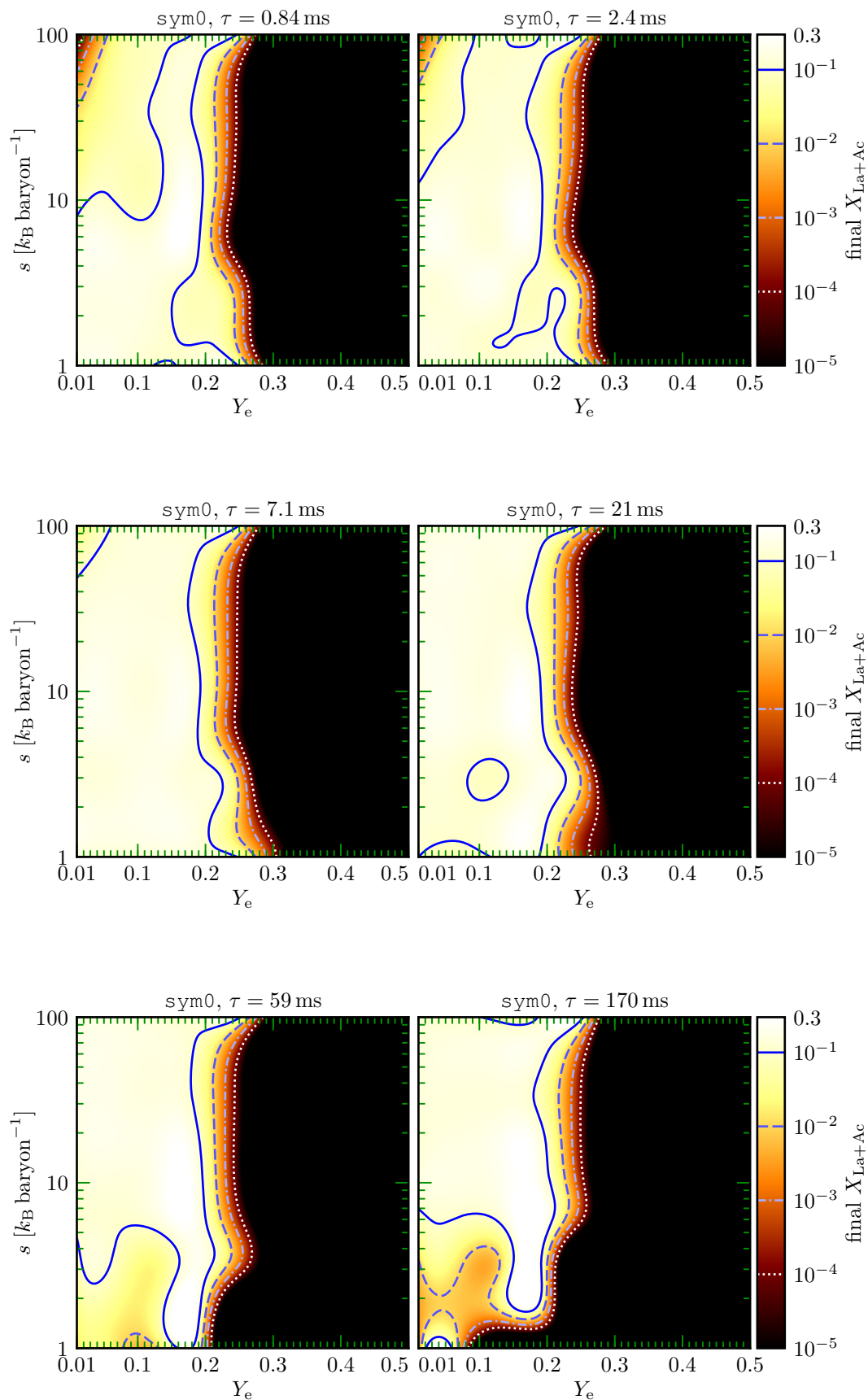


Figure 3.19: All the  $s$  slices showing the heating rate at 1 day of the  $\text{sym0}$  run.





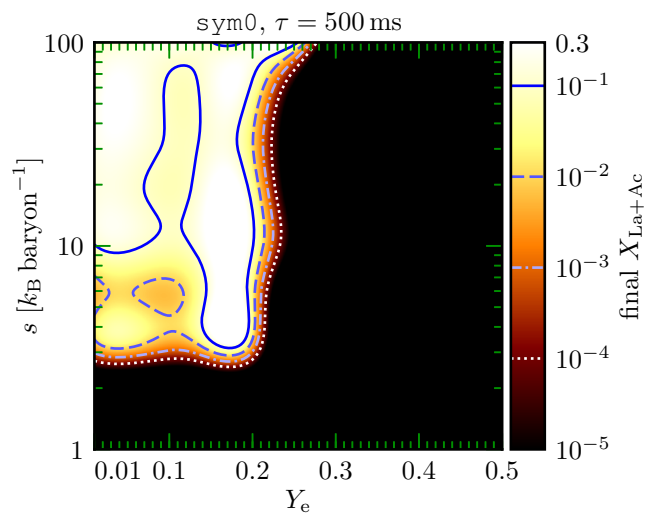
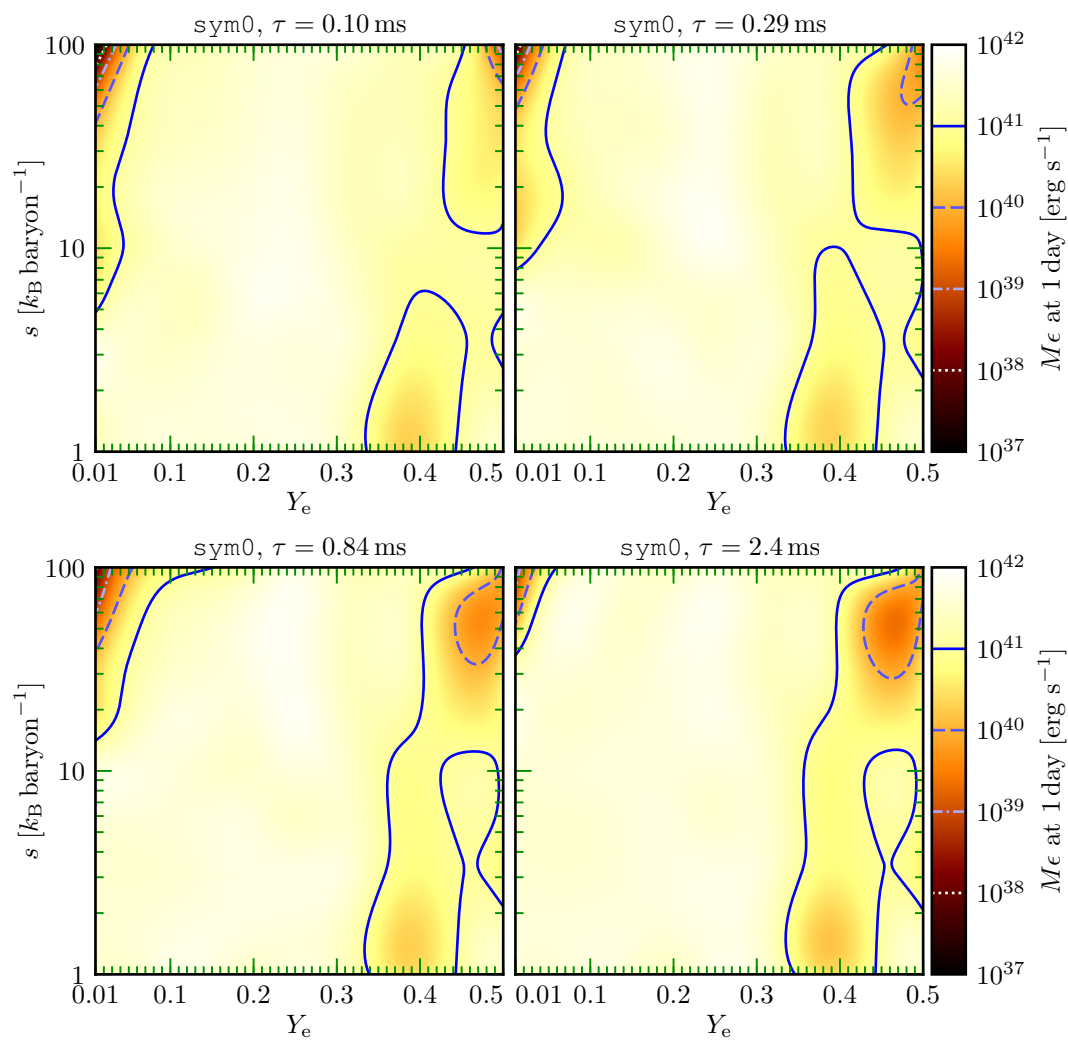


Figure 3.20: All the  $\tau$  slices showing the final lanthanide and actinide mass fraction of the sym0 run.



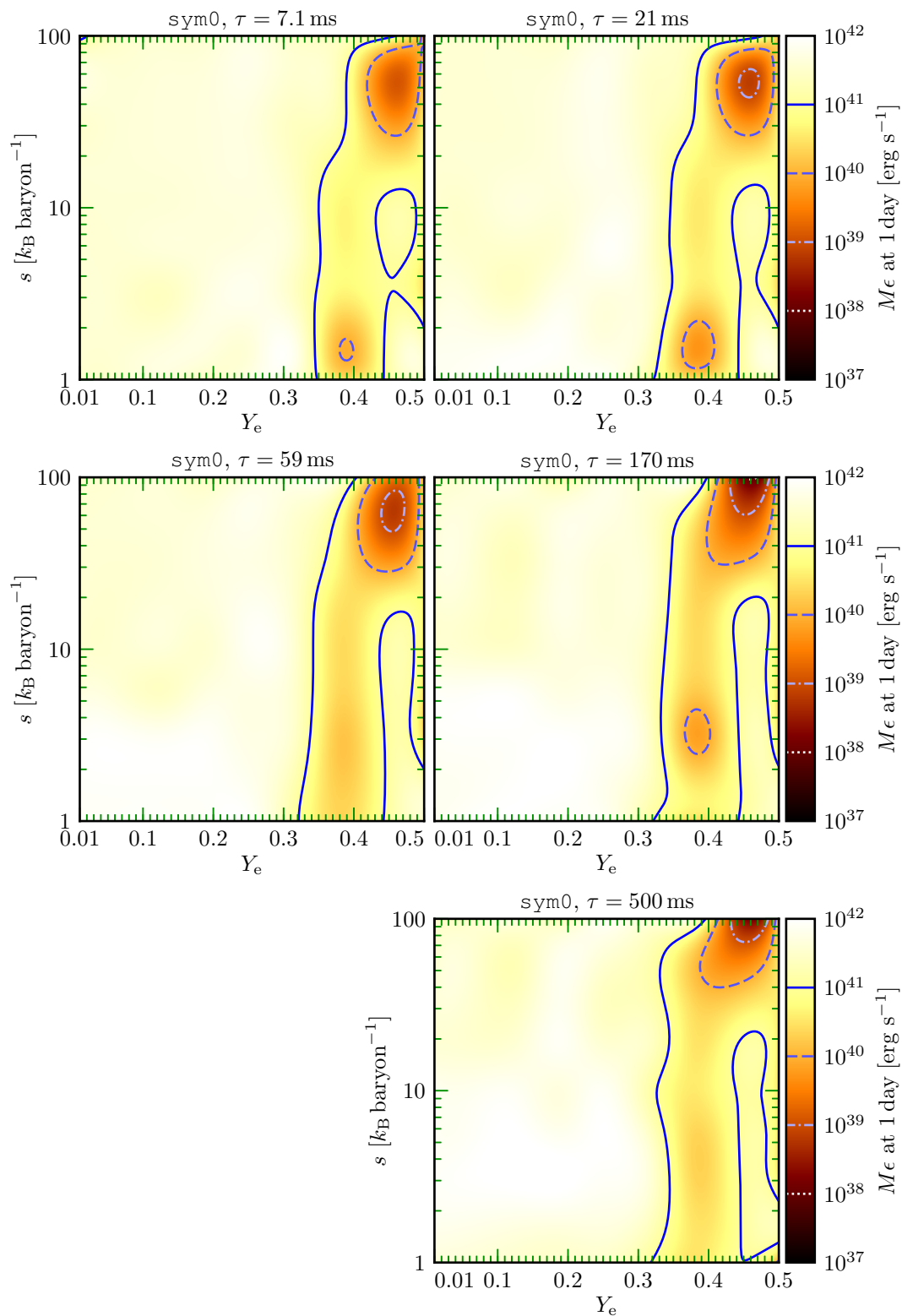
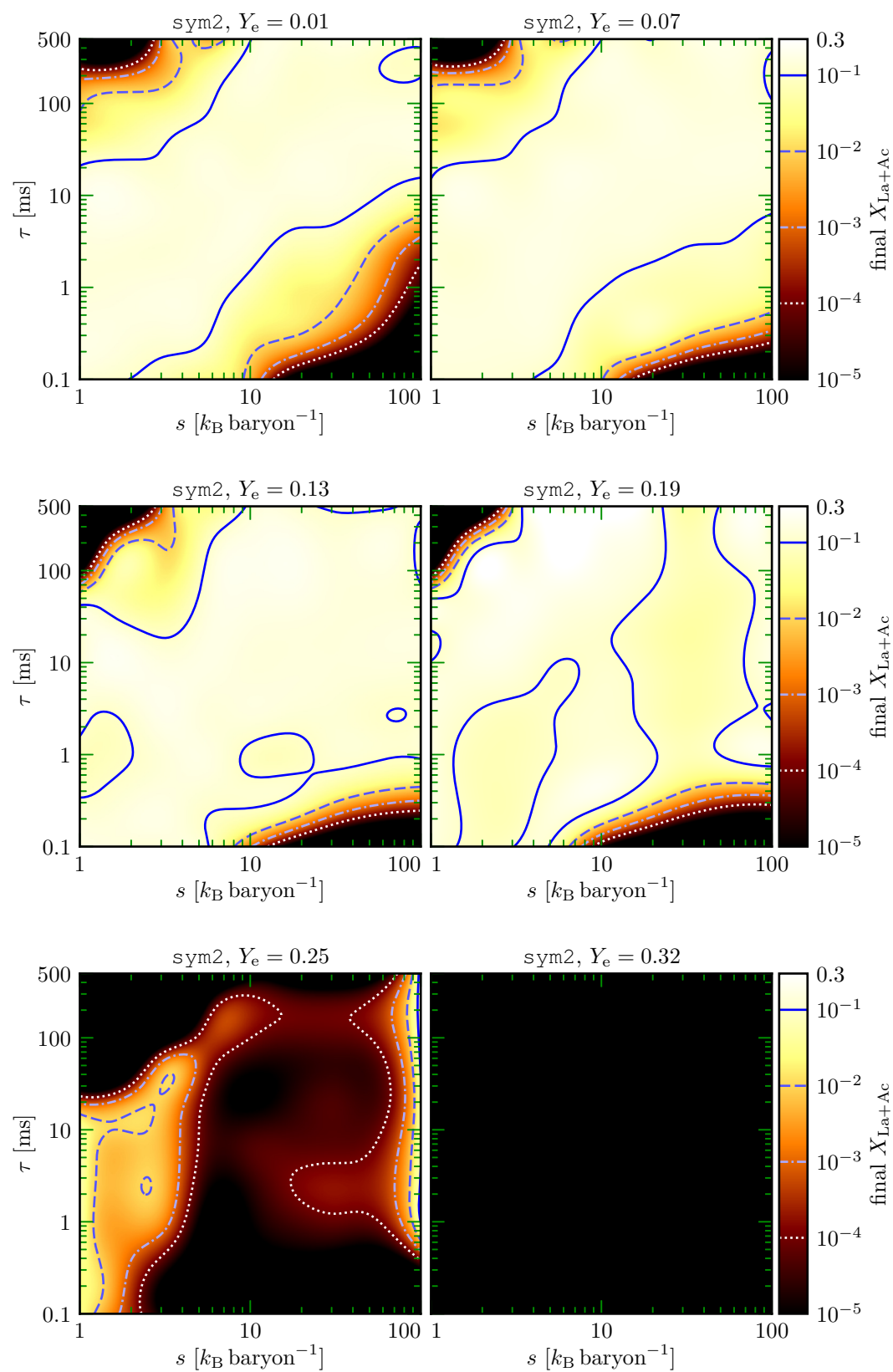


Figure 3.21: All the  $\tau$  slices showing the heating rate at 1 day of the `sym0` run.

## 3.B.3 sym2 run



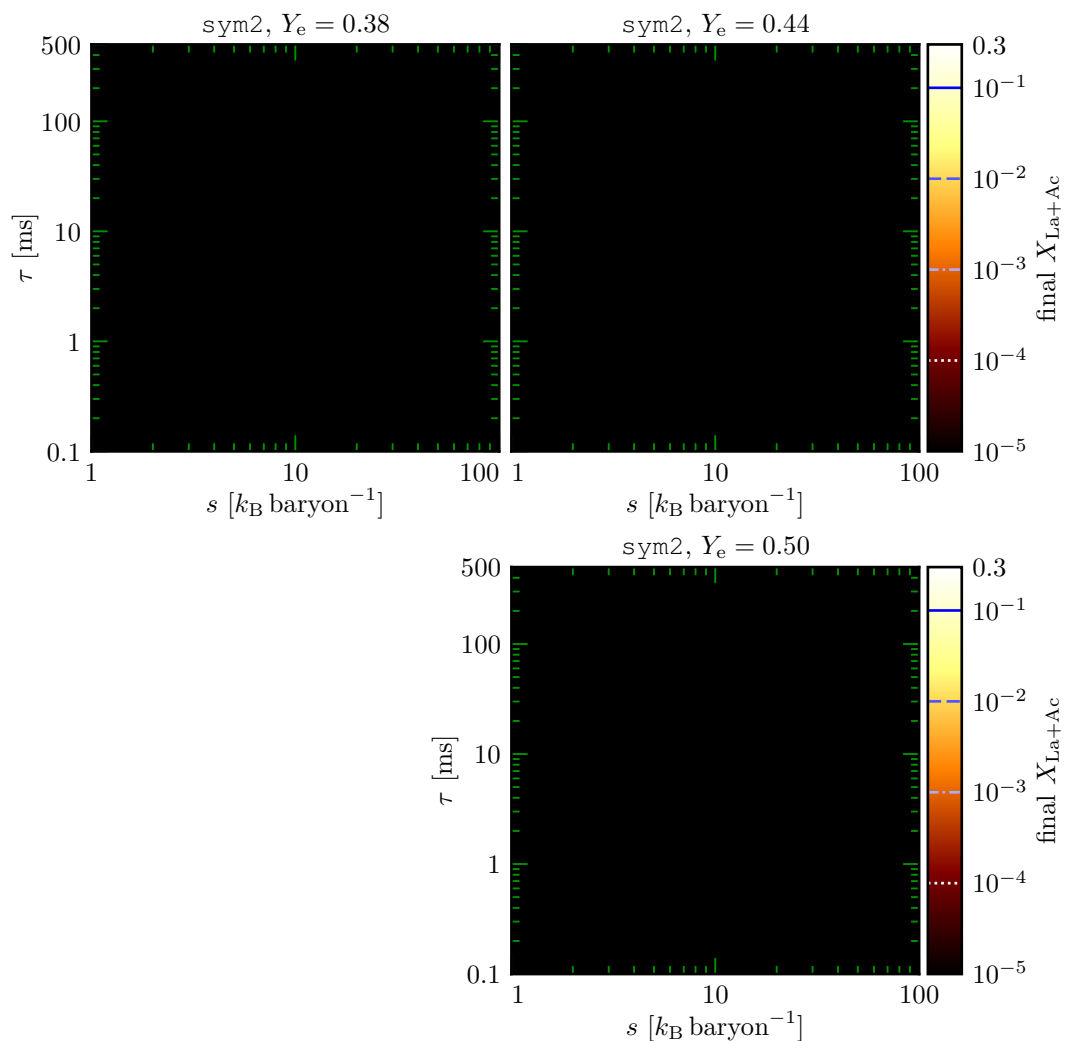
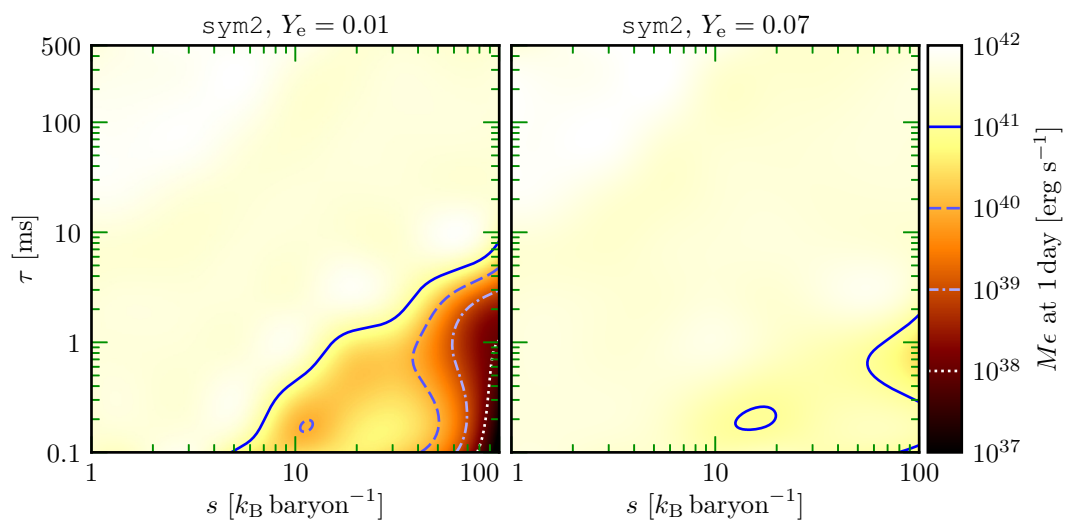
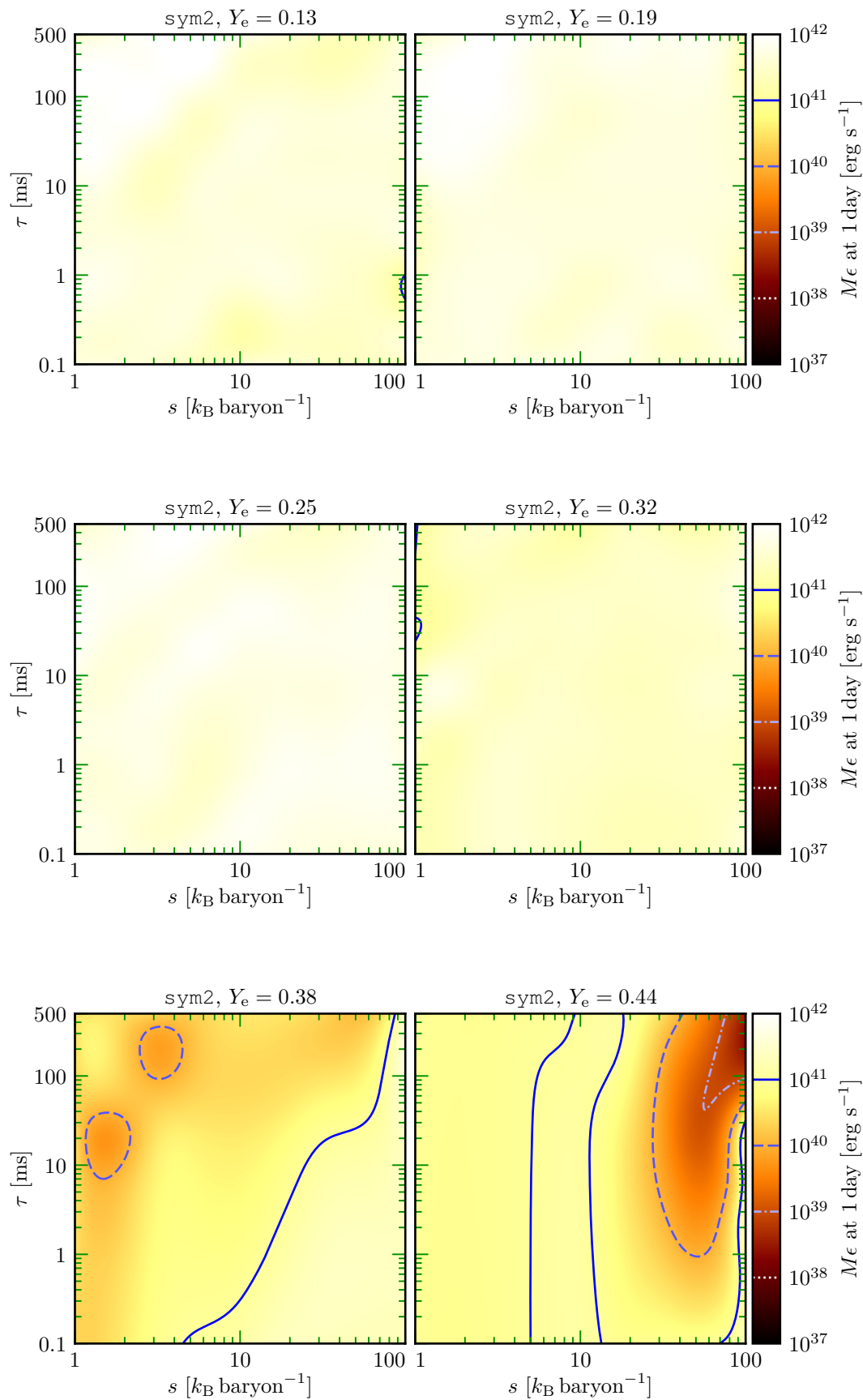


Figure 3.22: All the  $Y_e$  slices showing the final lanthanide and actinide mass fraction of the sym2 run.





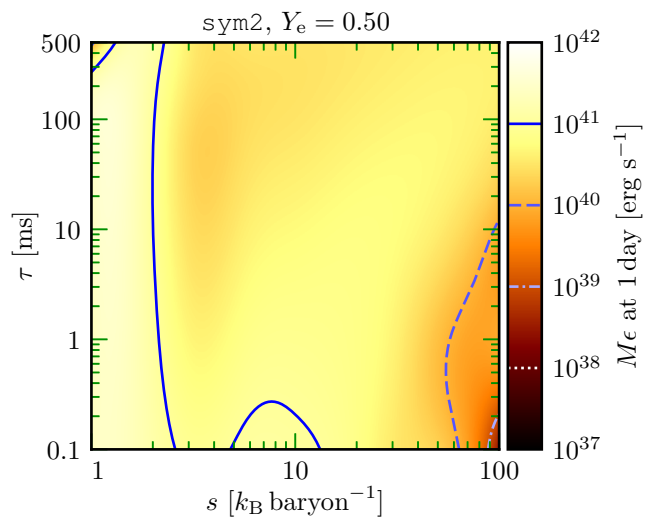
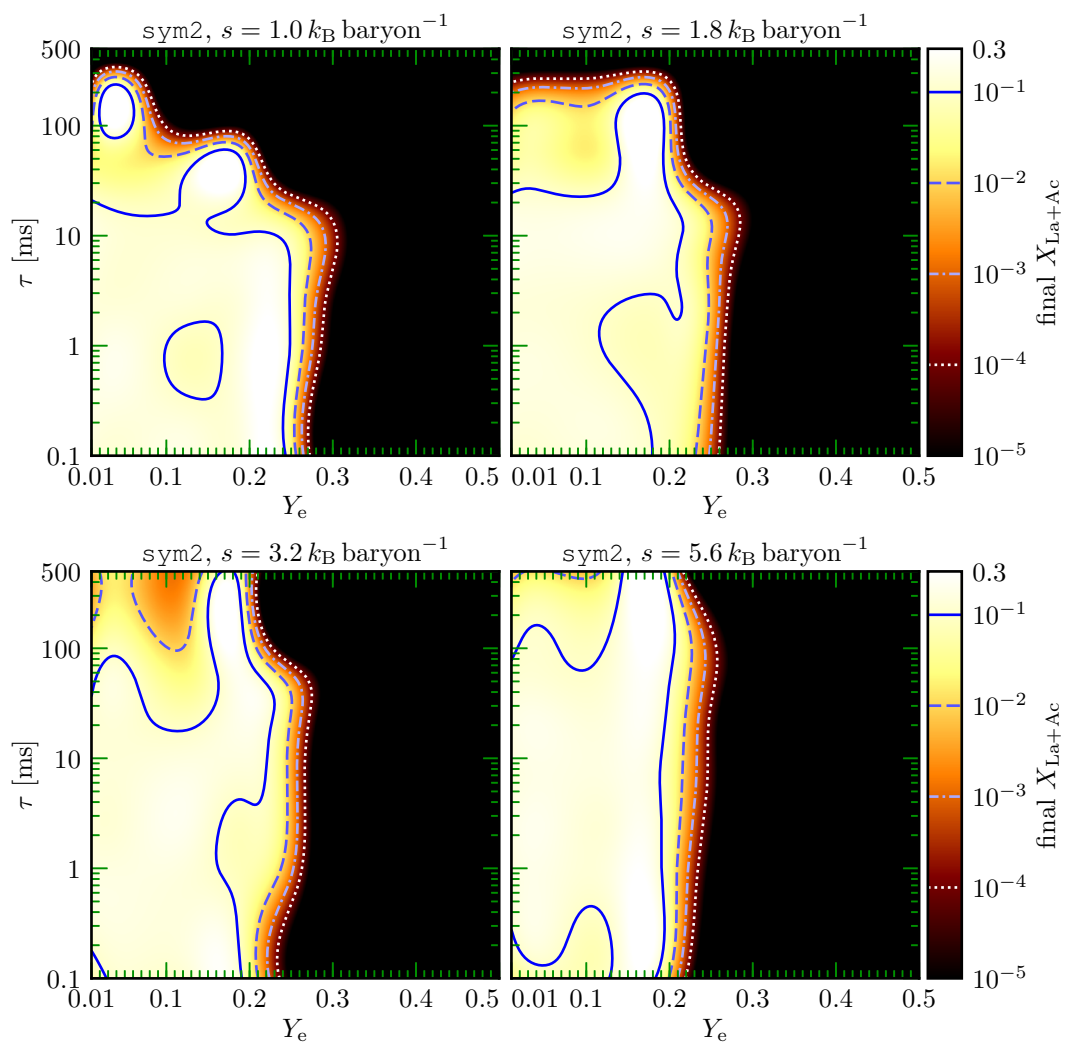


Figure 3.23: All the  $Y_e$  slices showing the heating rate at 1 day of the sym2 run.



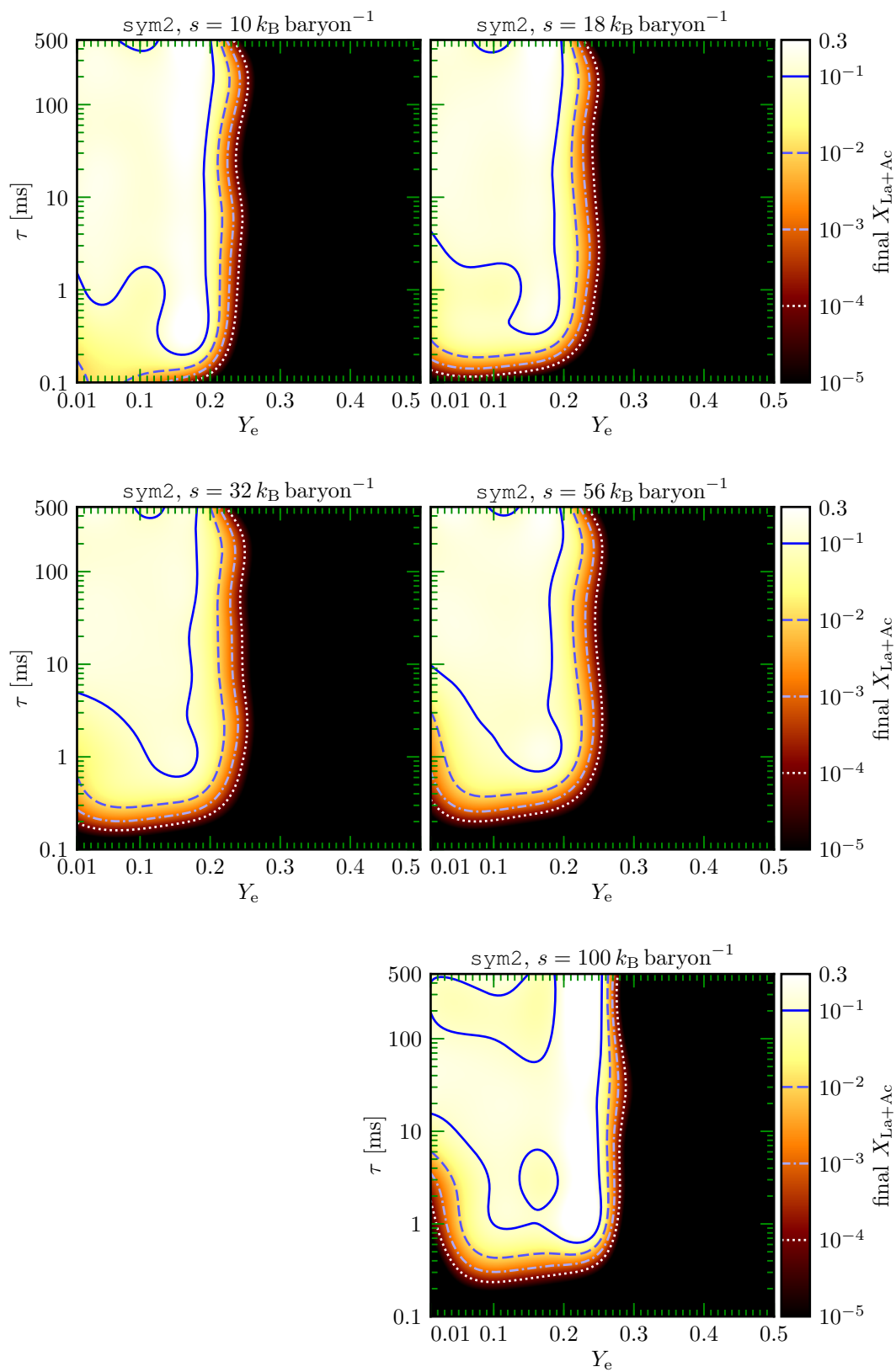
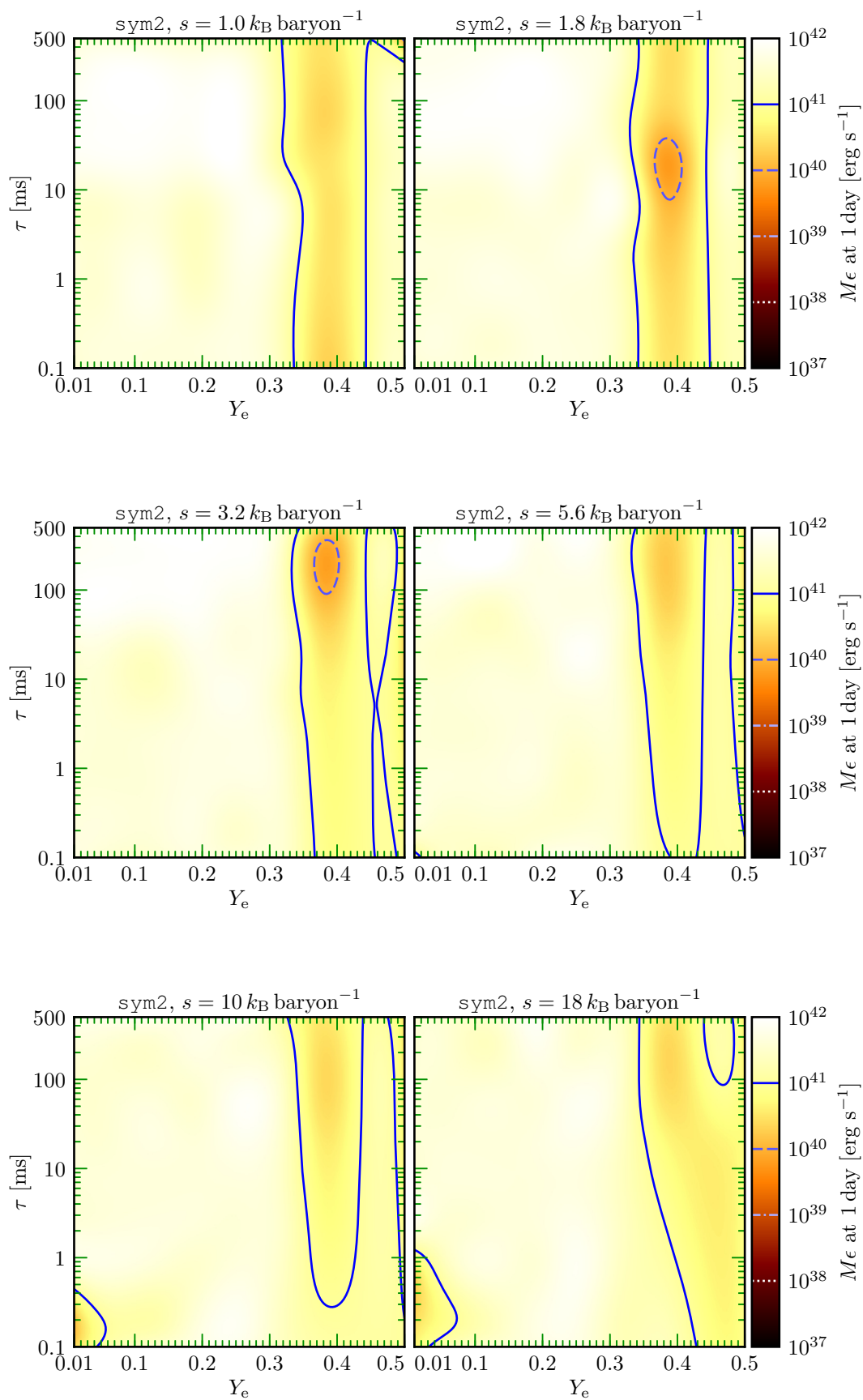


Figure 3.24: All the  $s$  slices showing the final lanthanide and actinide mass fraction of the sym2 run.



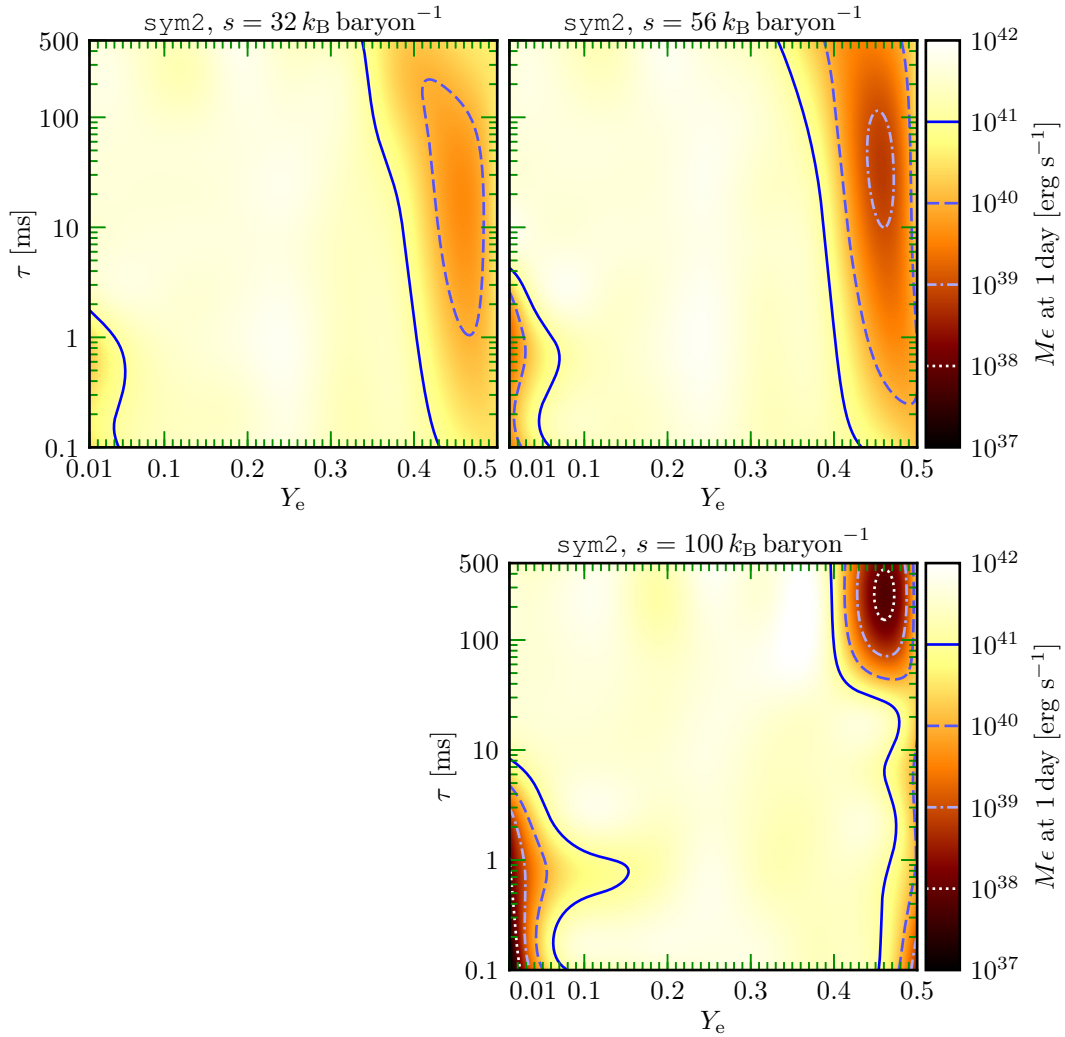
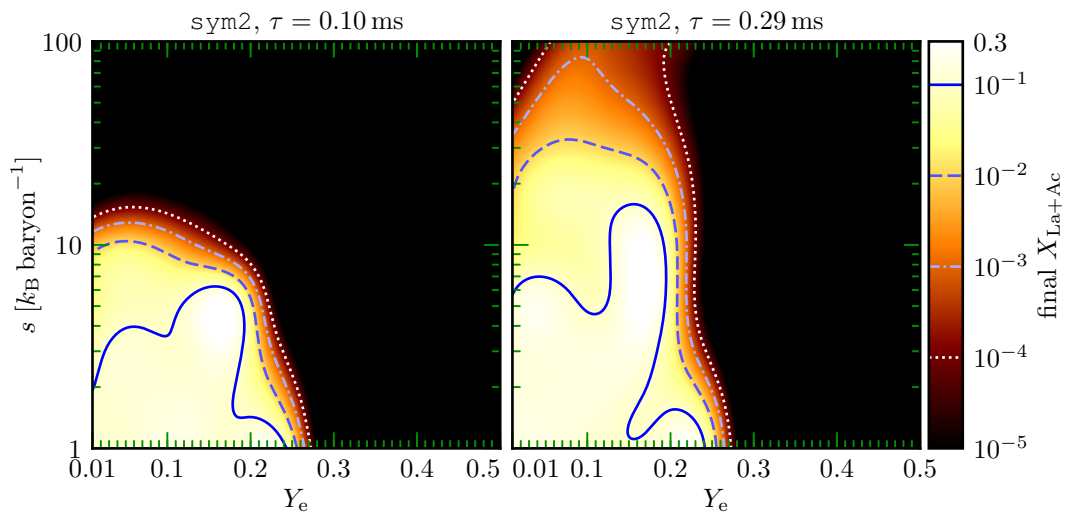
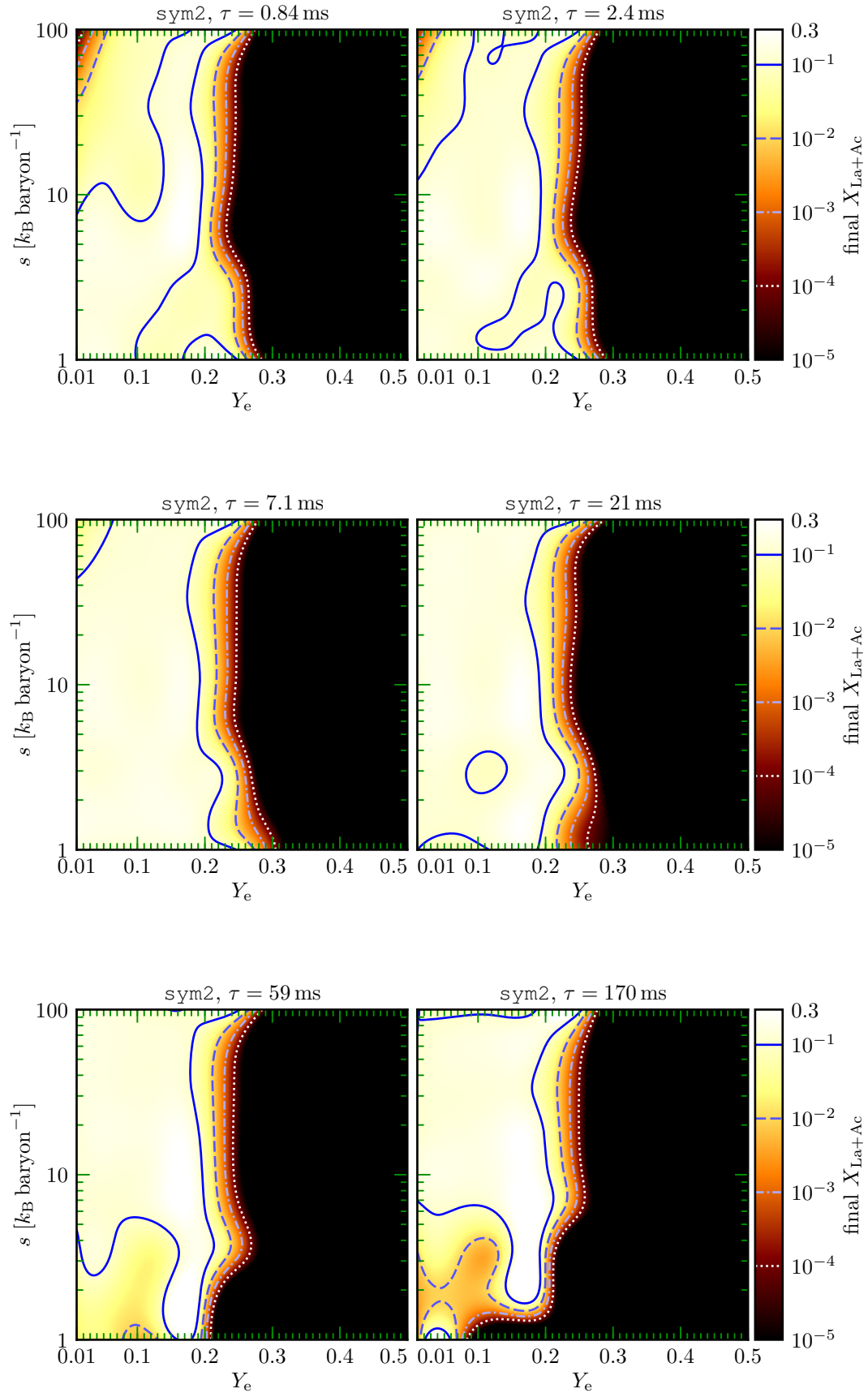


Figure 3.25: All the  $s$  slices showing the heating rate at 1 day of the sym2 run.





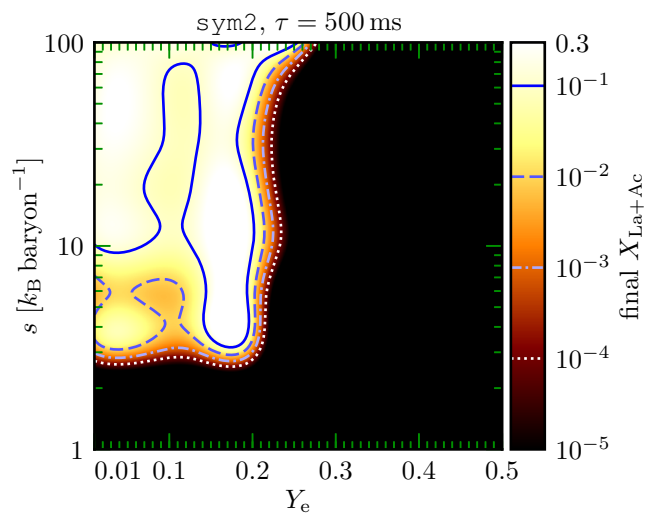
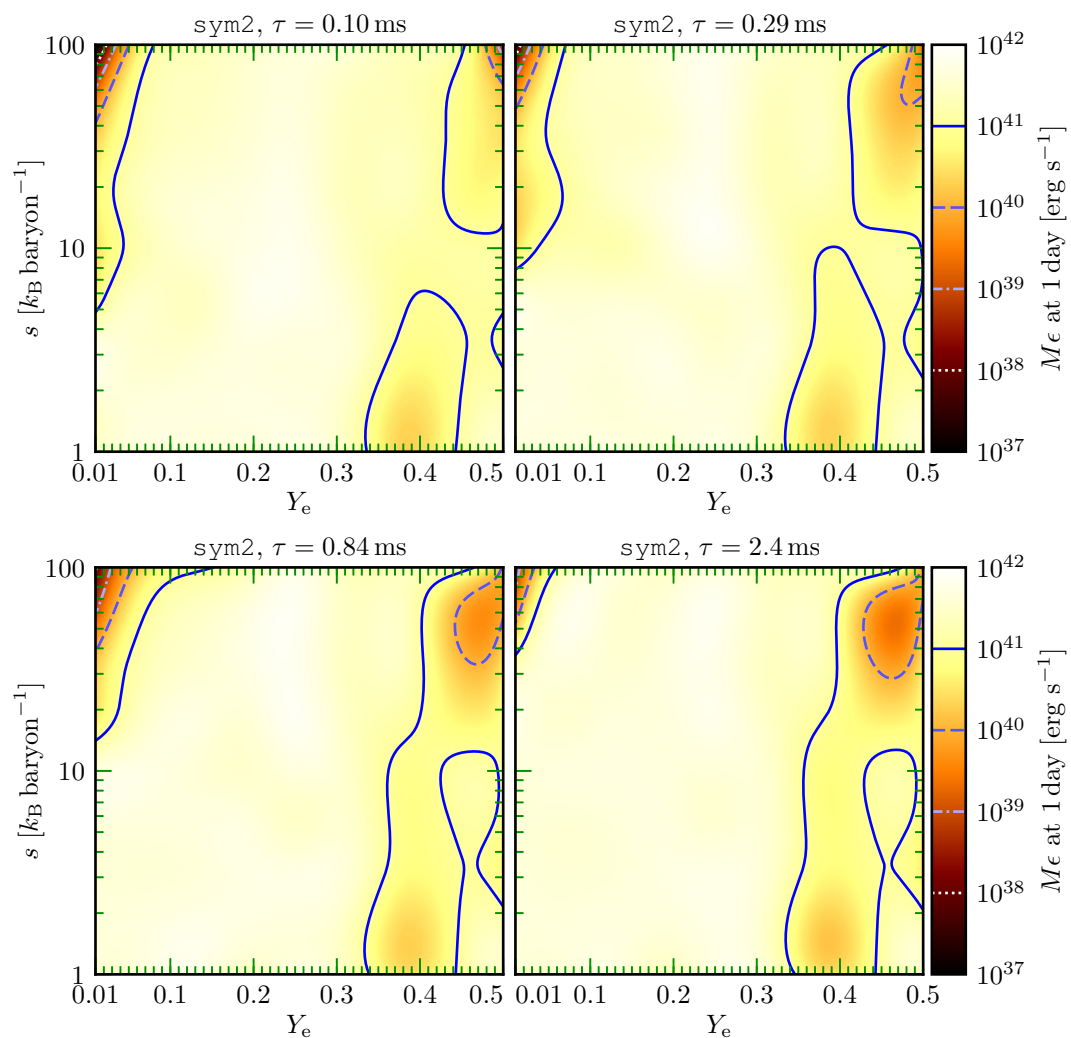


Figure 3.26: All the  $\tau$  slices showing the final lanthanide and actinide mass fraction of the sym2 run.



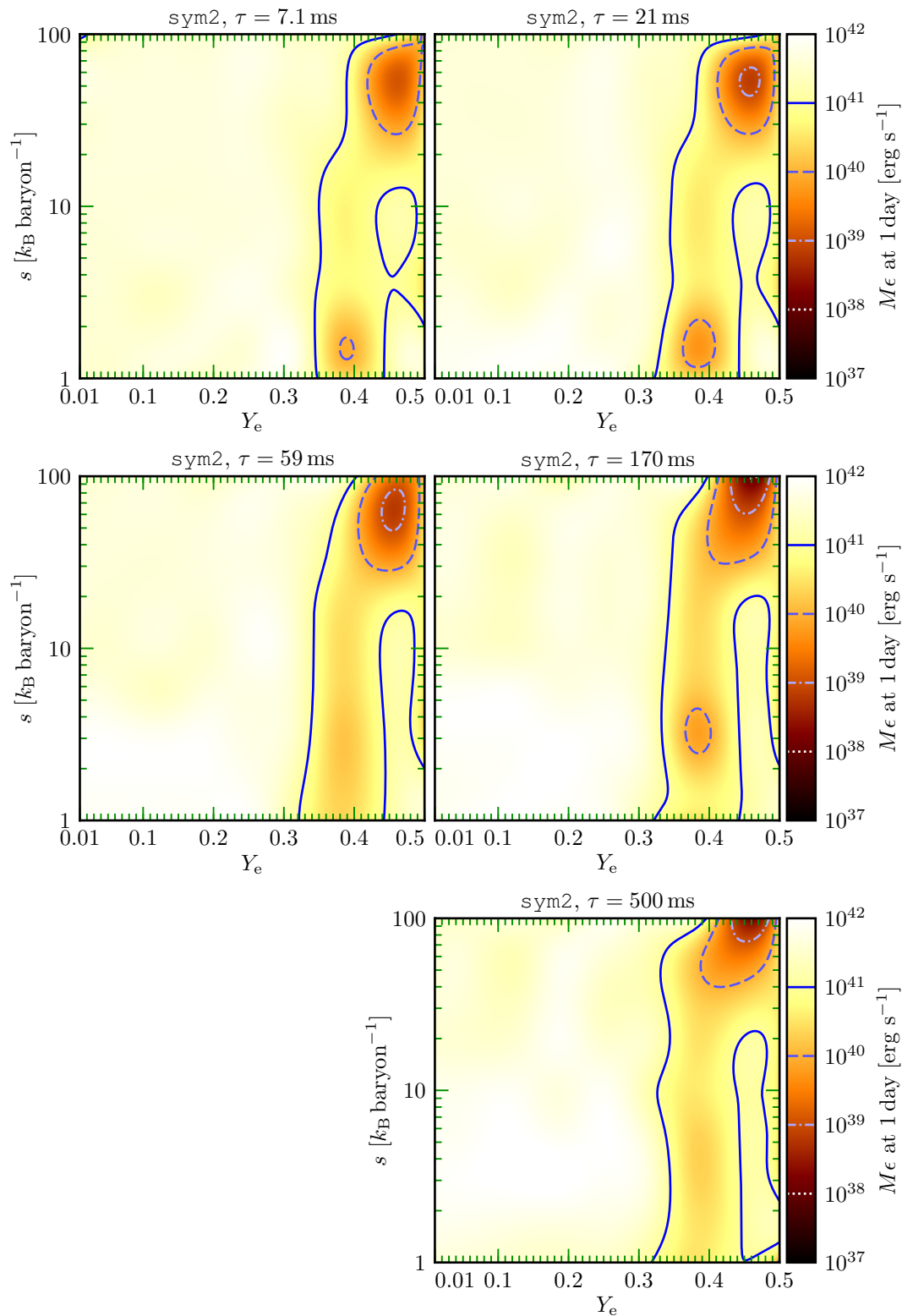
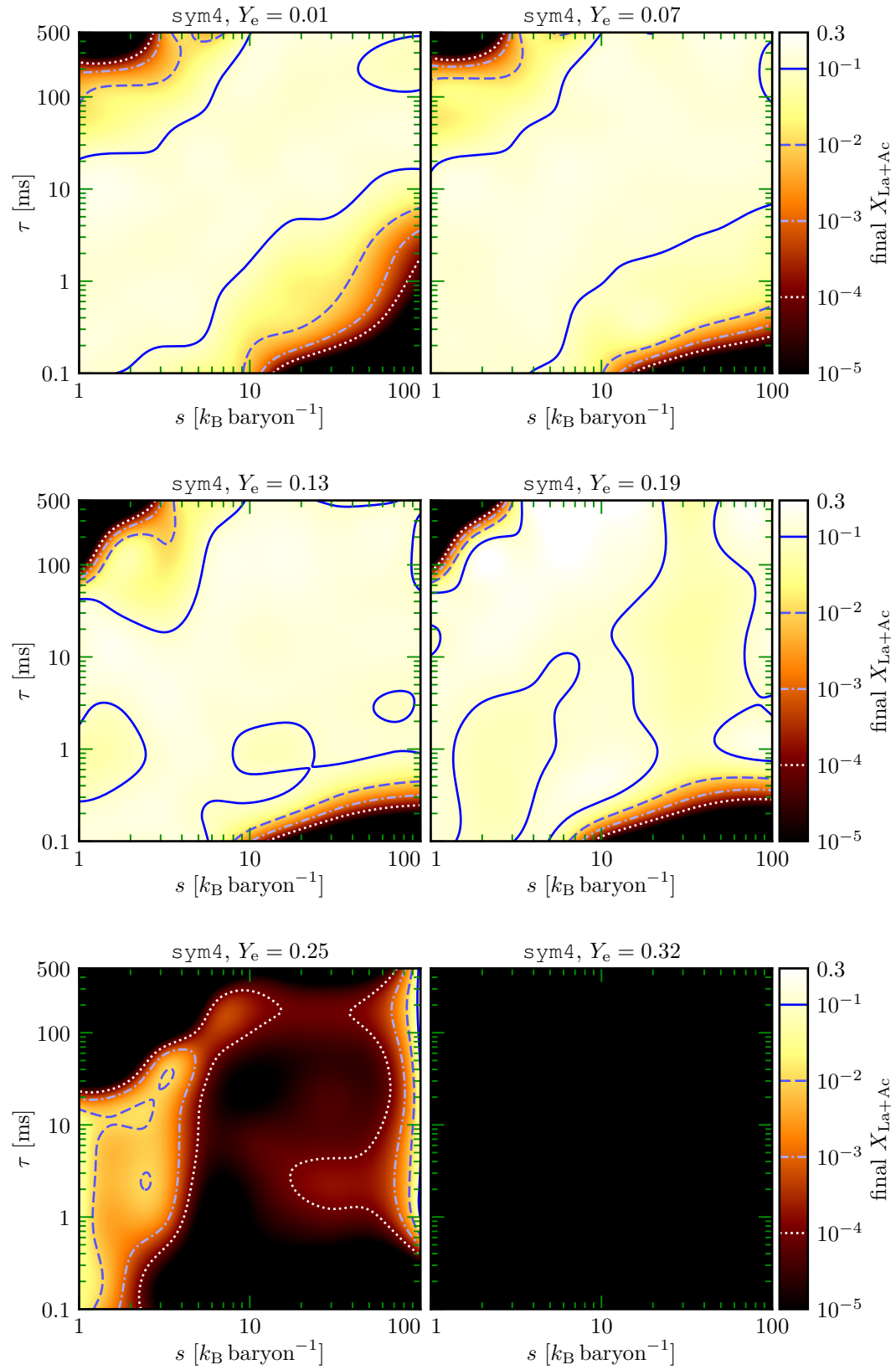


Figure 3.27: All the  $\tau$  slices showing the heating rate at 1 day of the sym2 run.

### 3.B.4 sym4 run



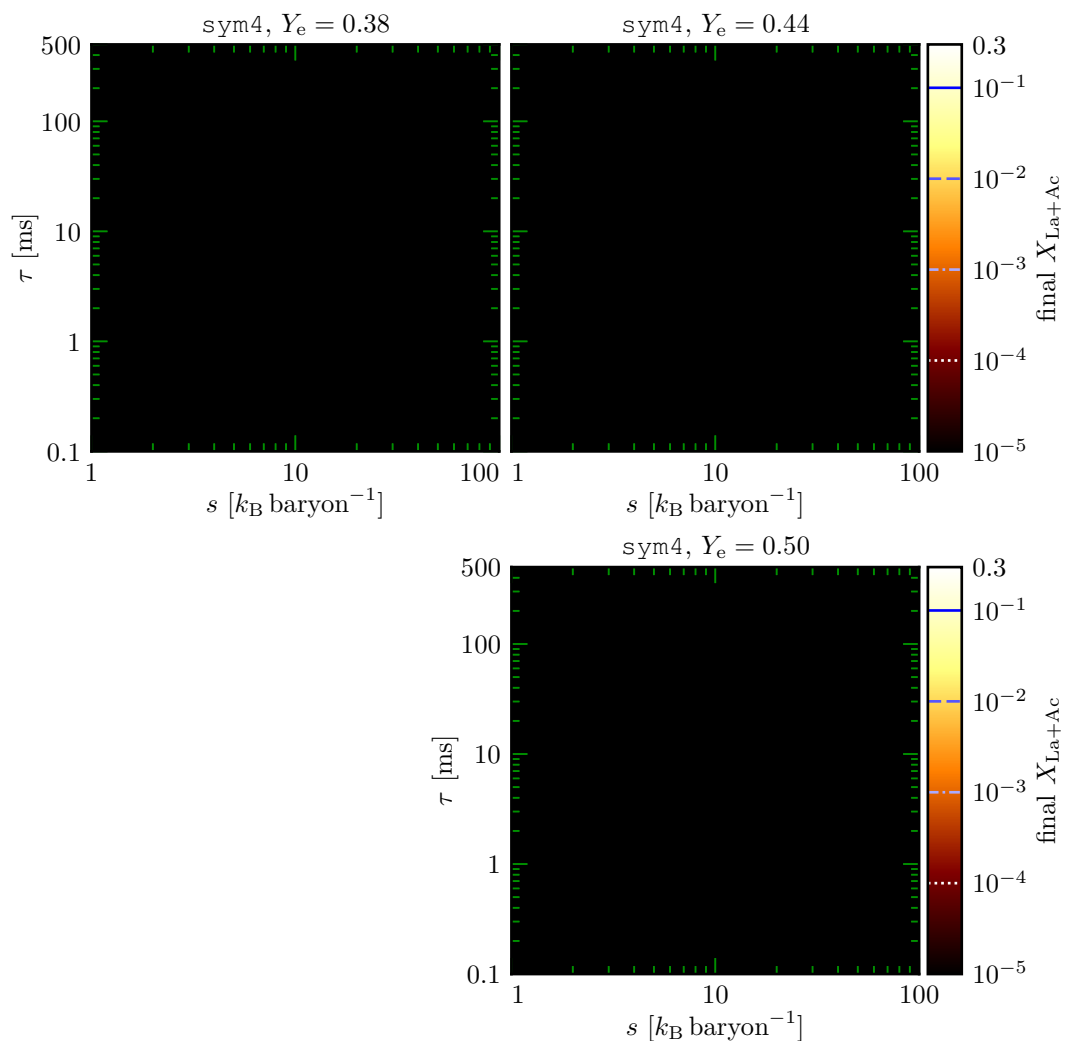
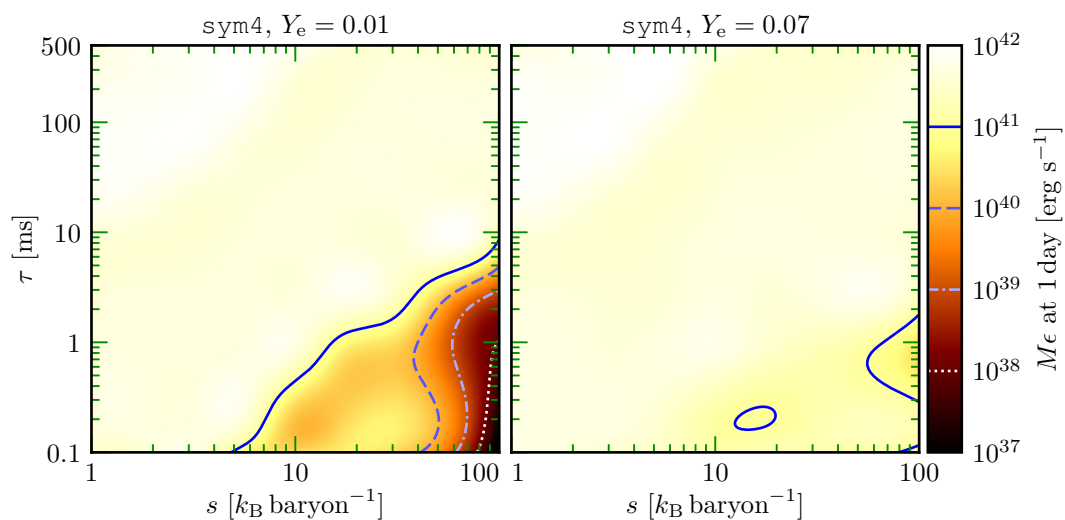
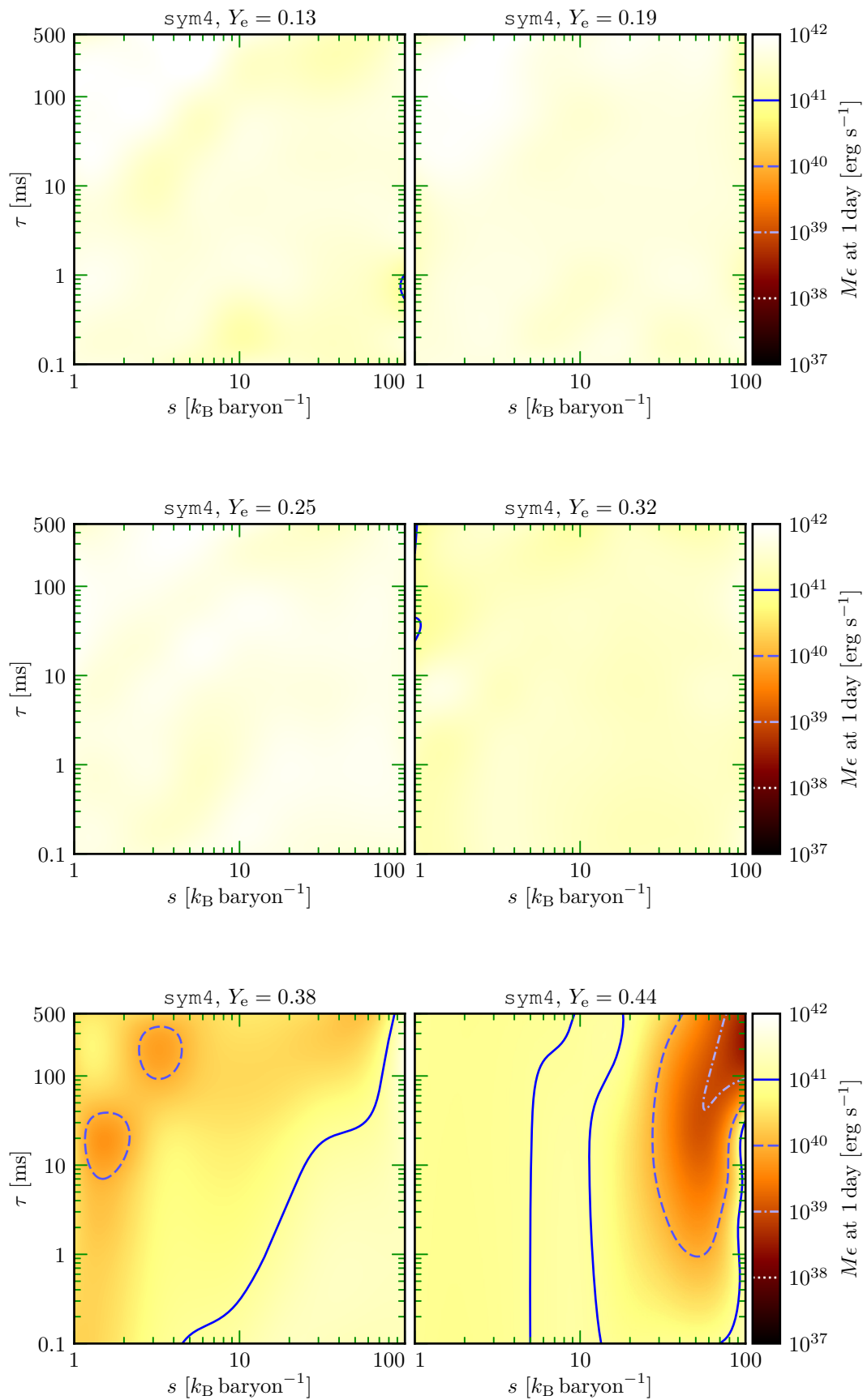


Figure 3.28: All the  $Y_e$  slices showing the final lanthanide and actinide mass fraction of the sym4 run.





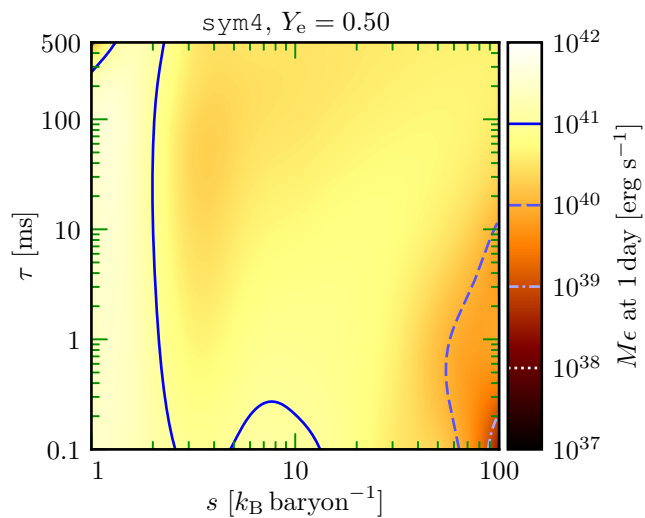
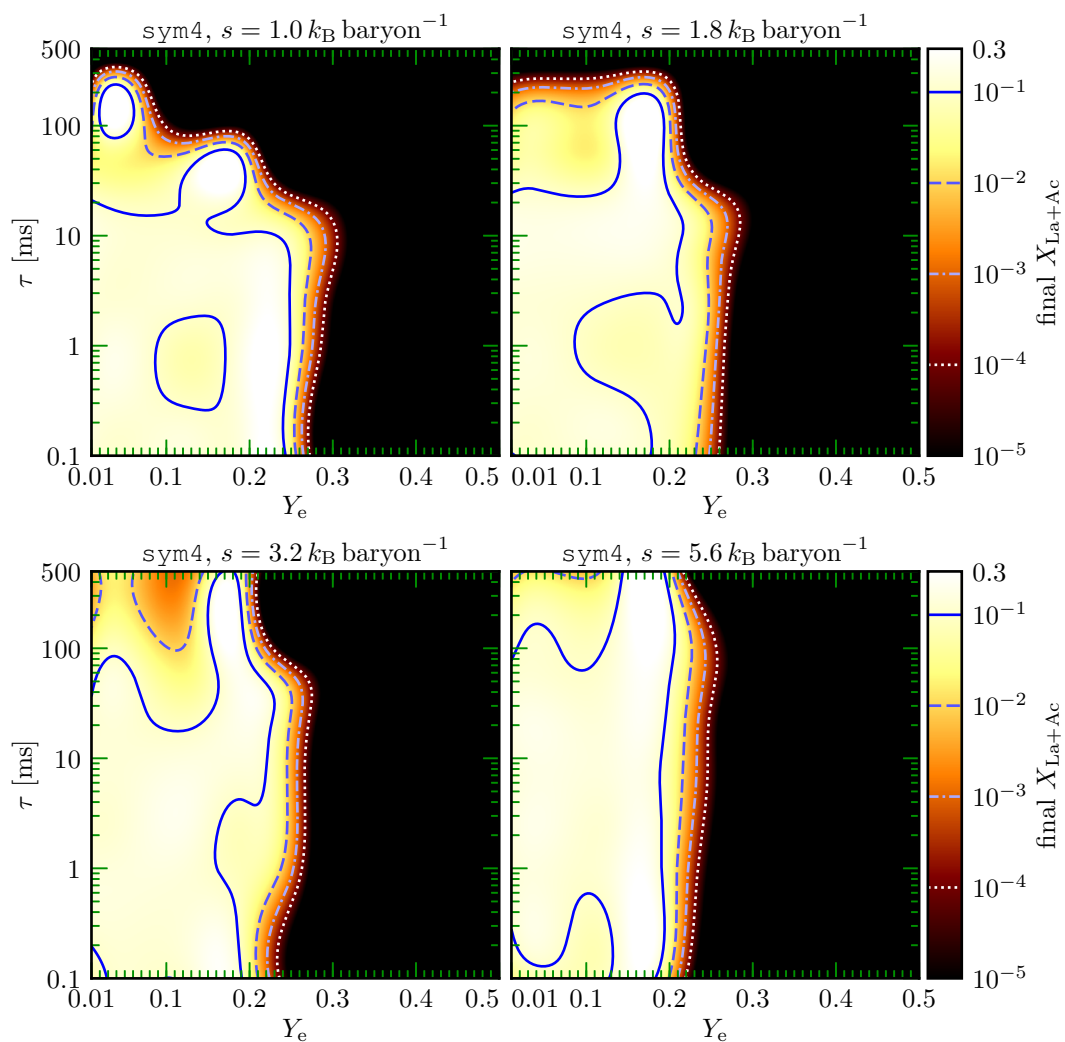


Figure 3.29: All the  $Y_e$  slices showing the heating rate at 1 day of the sym4 run.



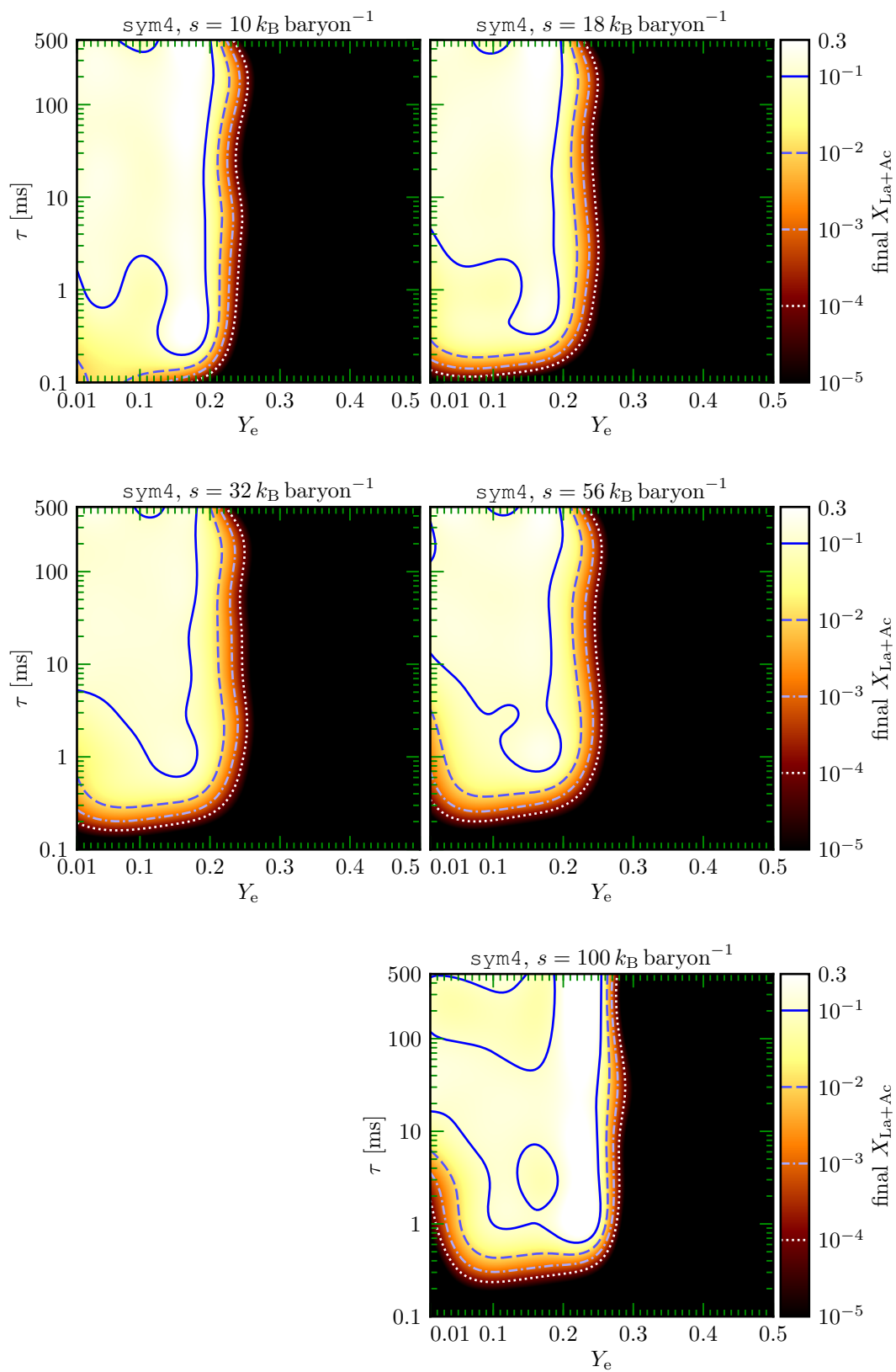
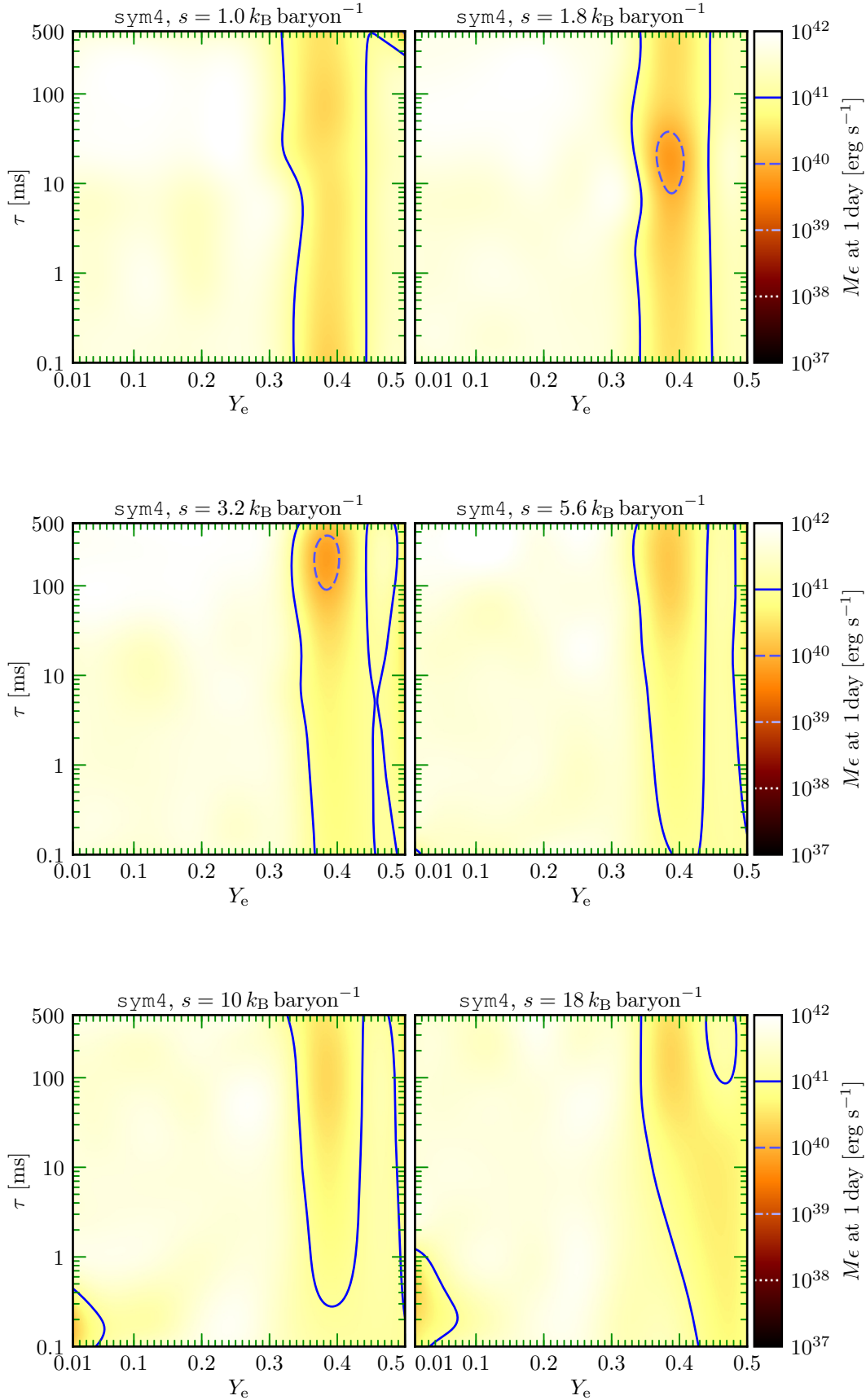


Figure 3.30: All the  $s$  slices showing the final lanthanide and actinide mass fraction of the sym4 run.



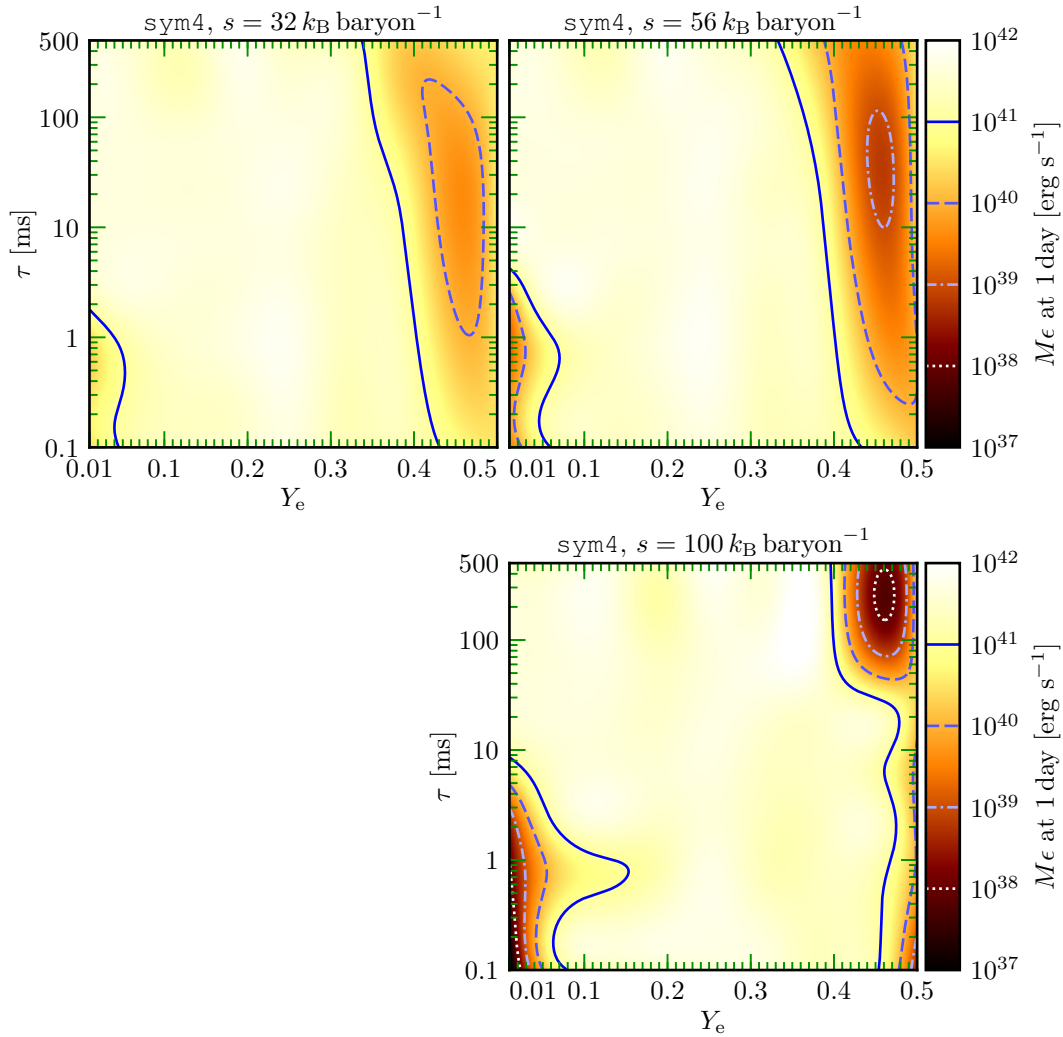
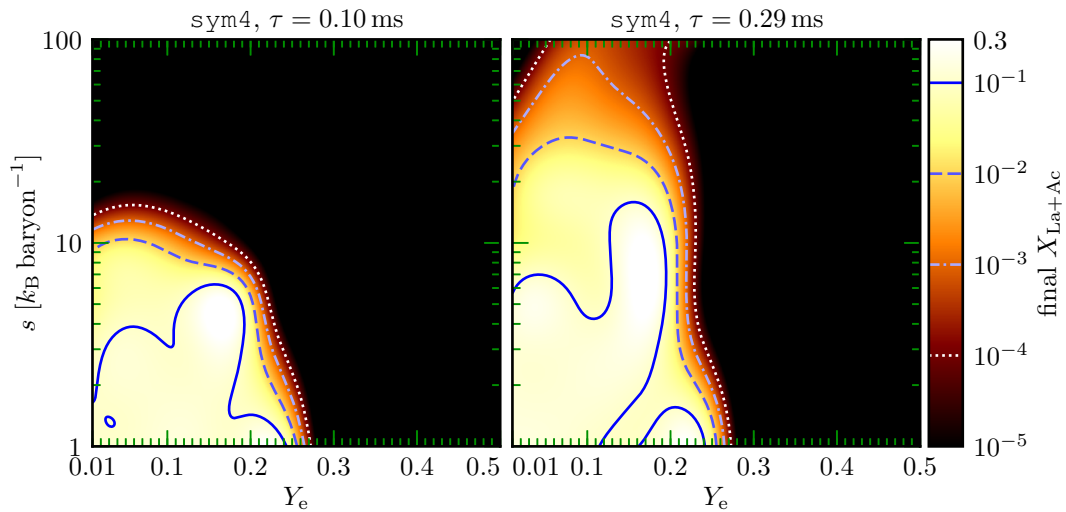
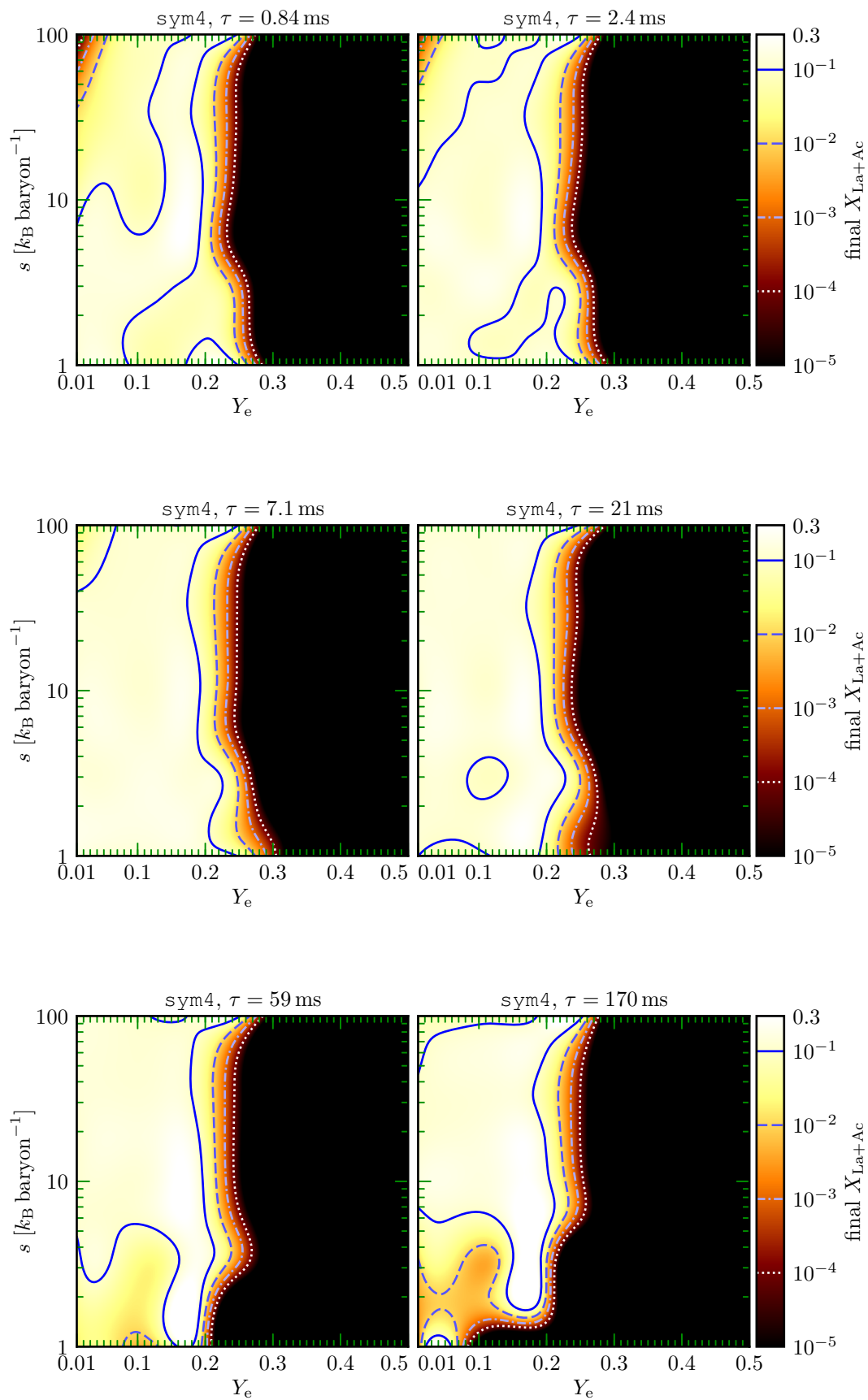


Figure 3.31: All the  $s$  slices showing the heating rate at 1 day of the sym4 run.





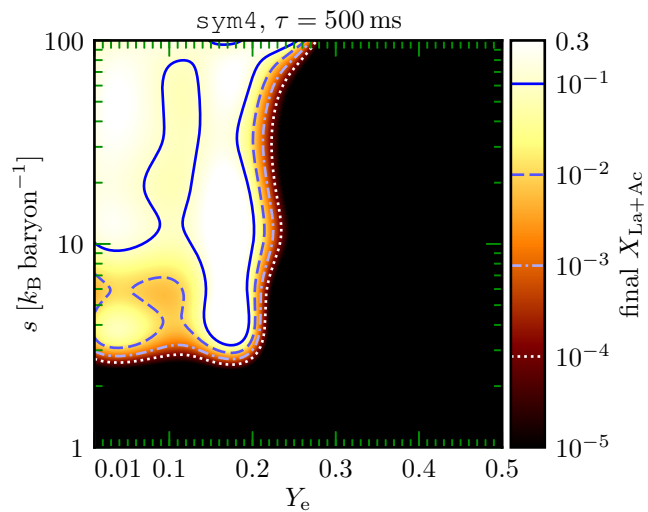
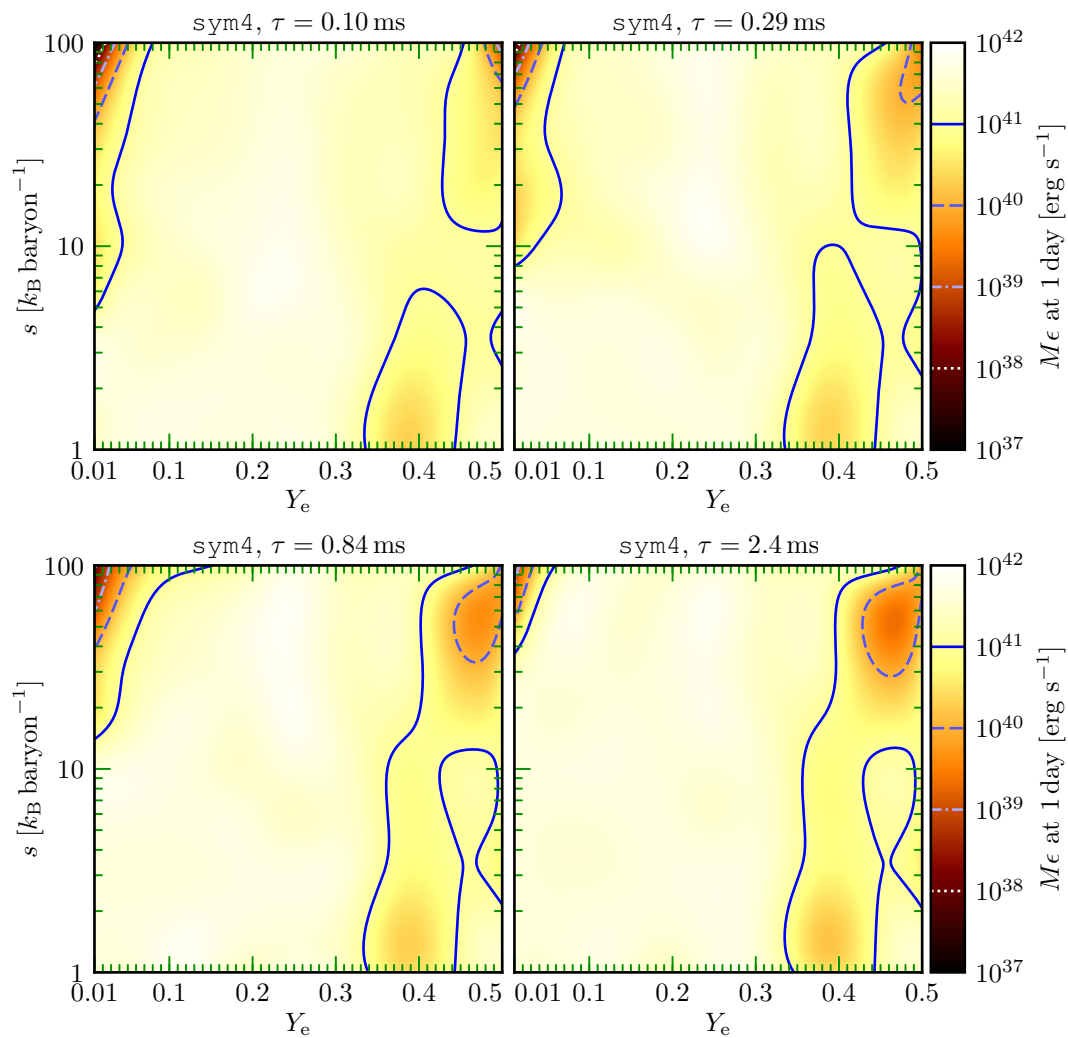


Figure 3.32: All the  $\tau$  slices showing the final lanthanide and actinide mass fraction of the sym4 run.



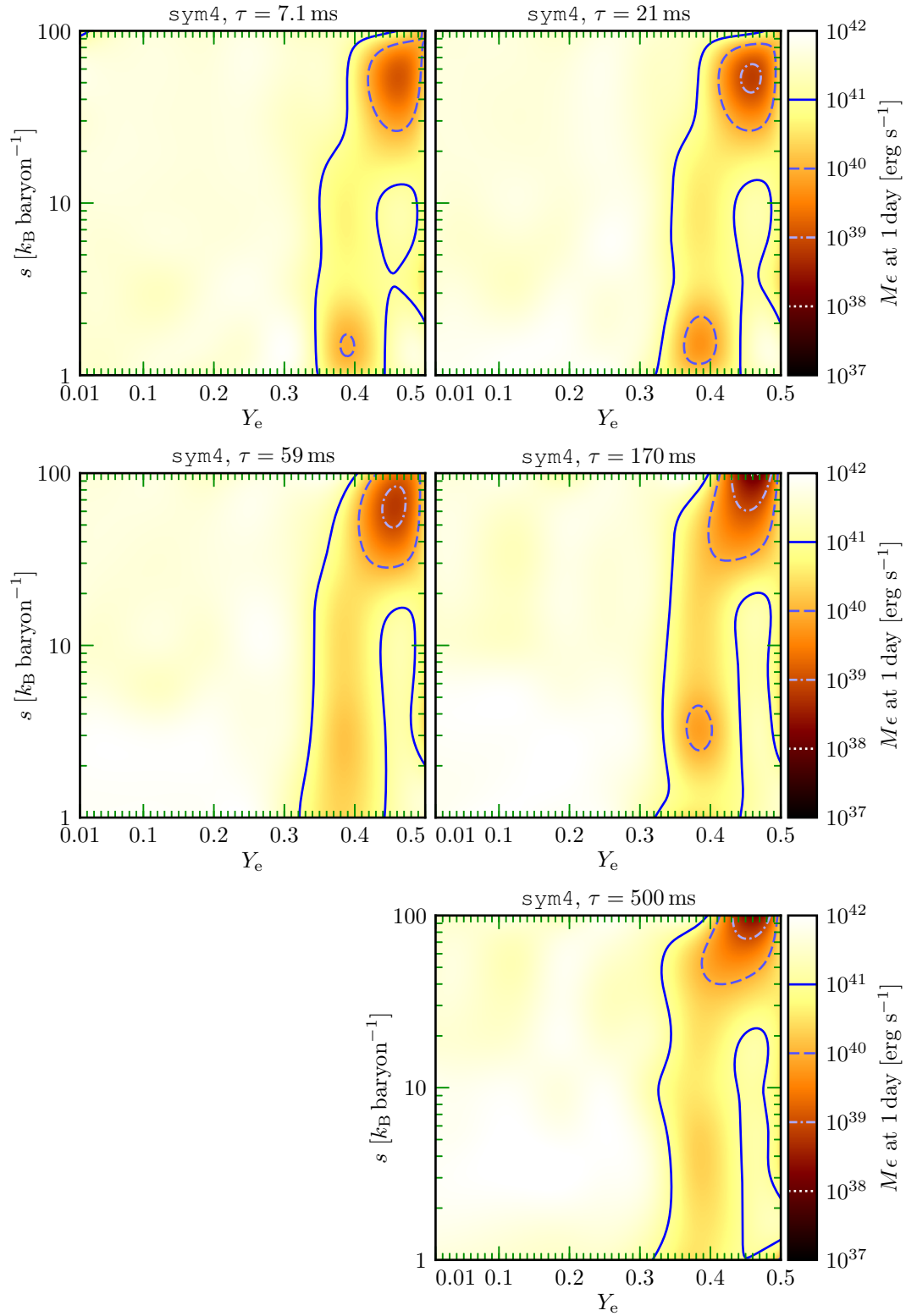
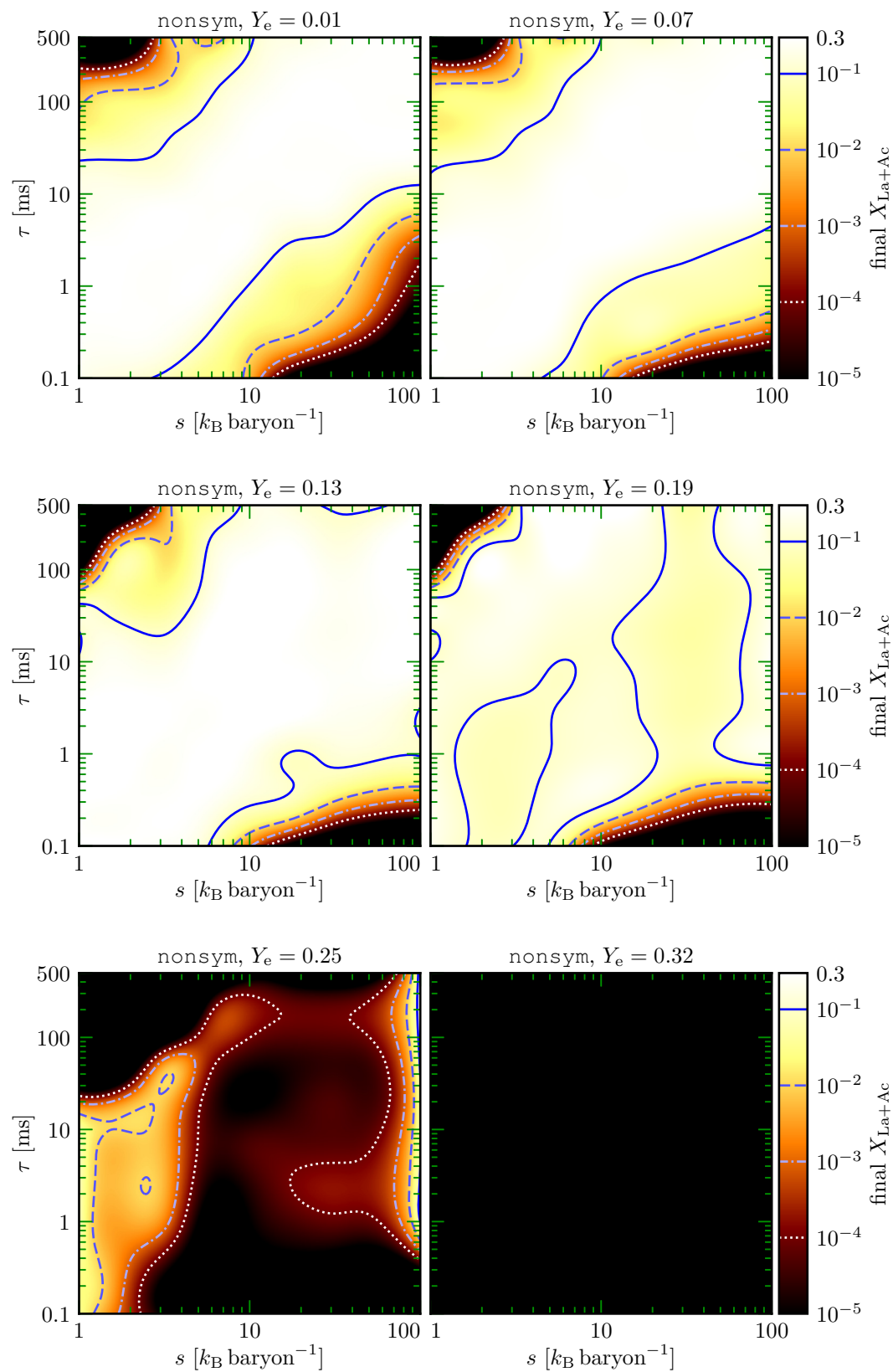


Figure 3.33: All the  $\tau$  slices showing the heating rate at 1 day of the sym4 run.

### 3.B.5 nonsym run



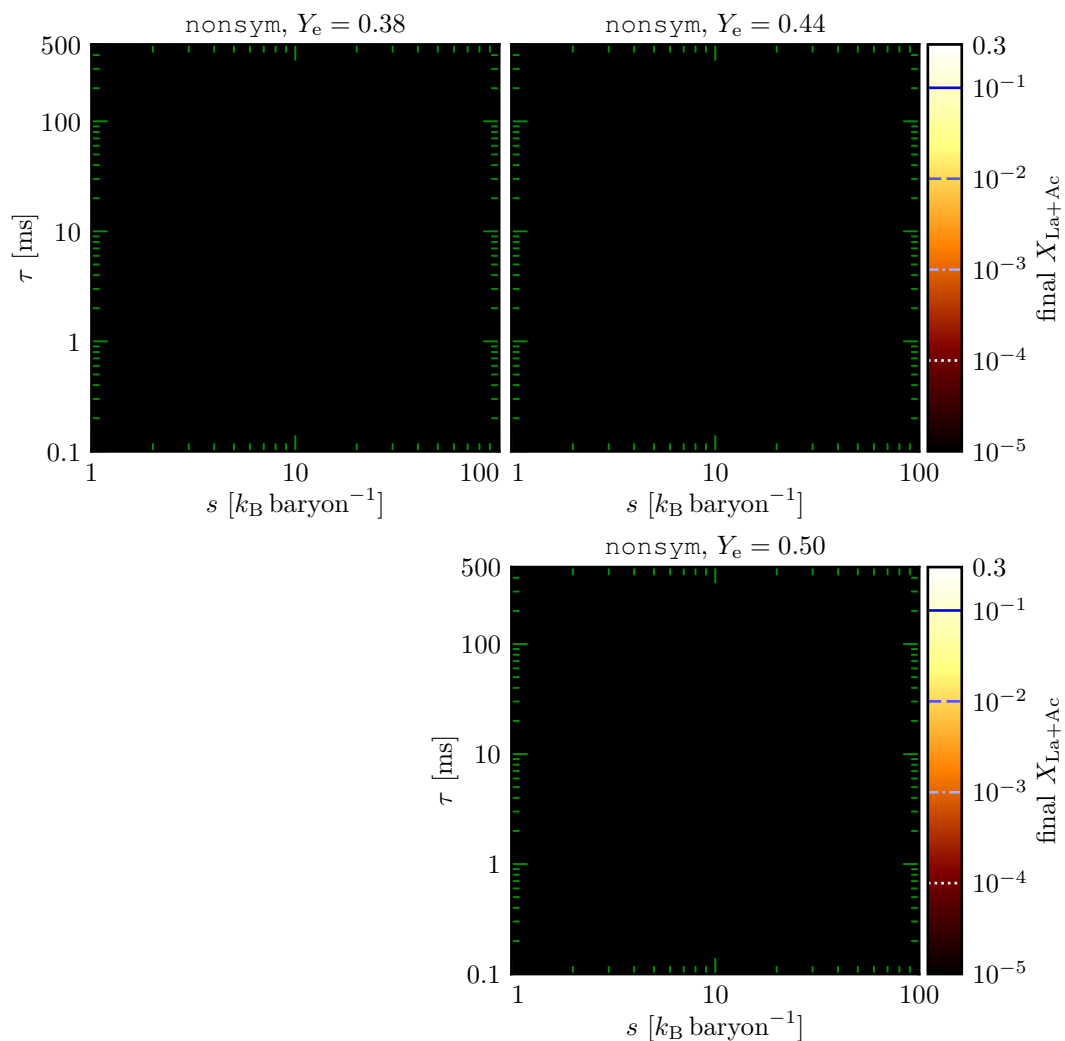
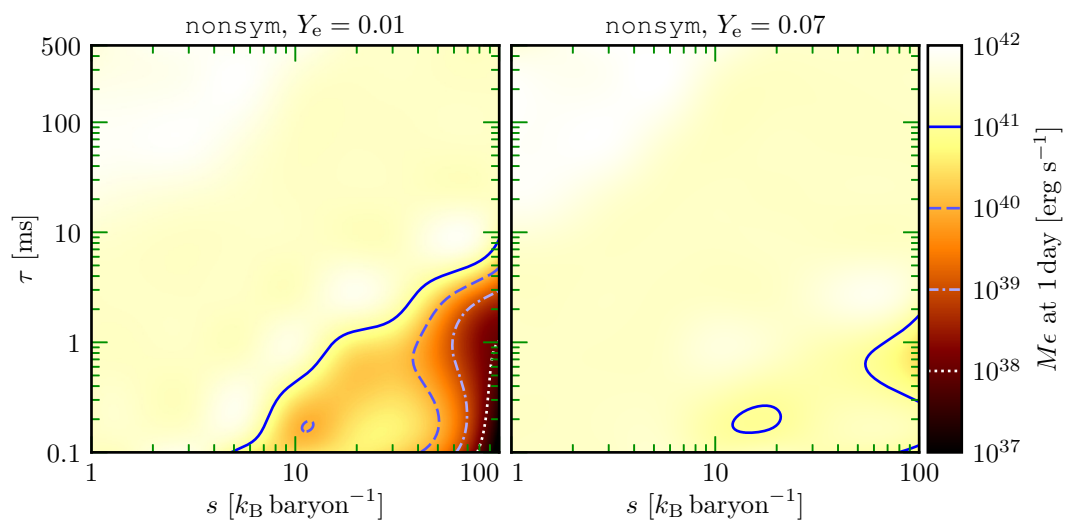
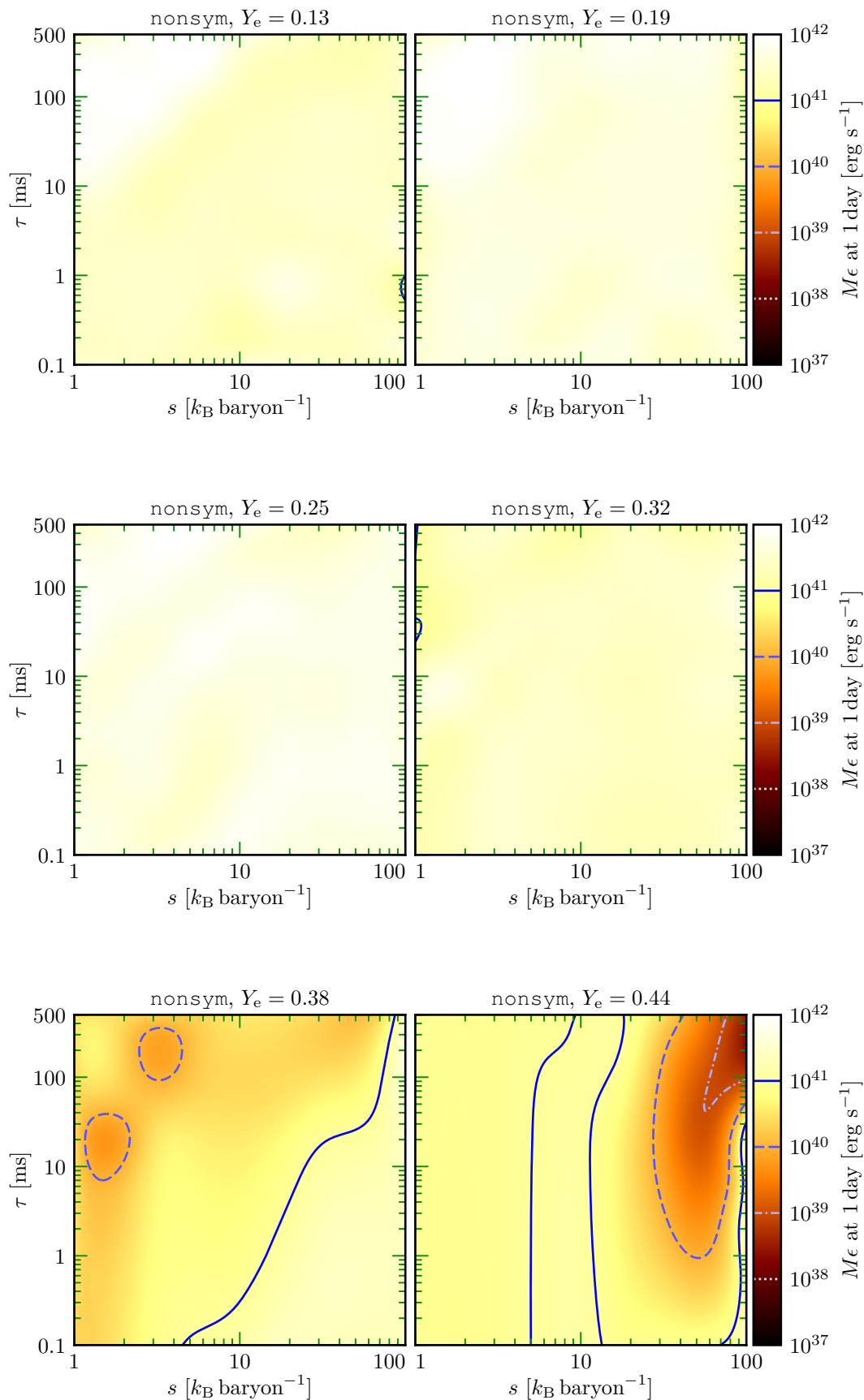


Figure 3.34: All the  $Y_e$  slices showing the final lanthanide and actinide mass fraction of the nonsym run.





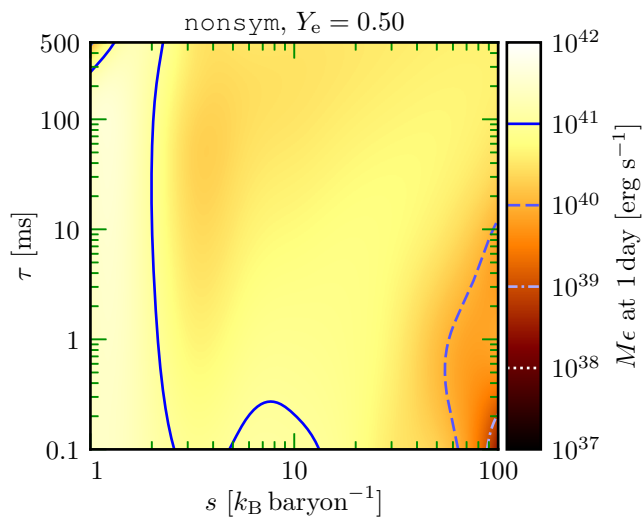
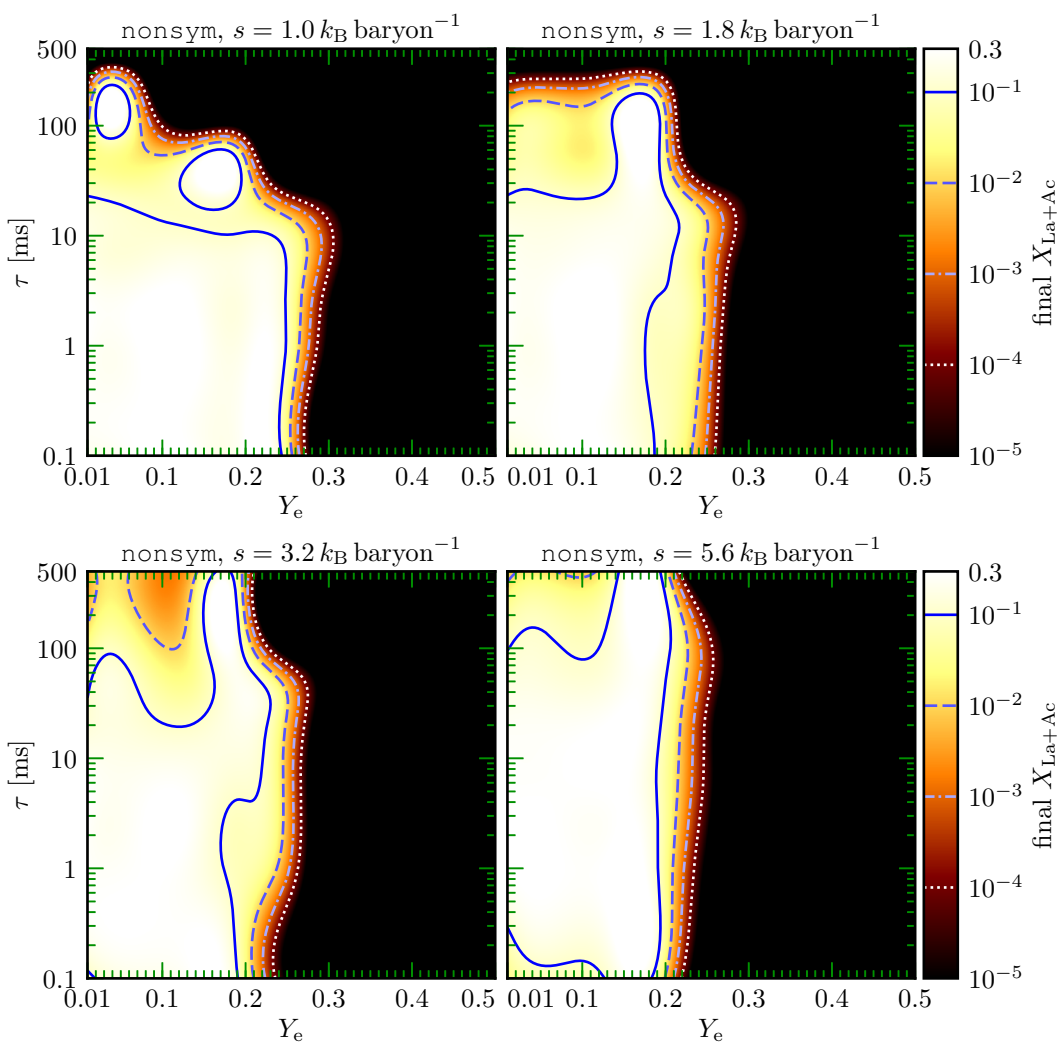


Figure 3.35: All the  $Y_e$  slices showing the heating rate at 1 day of the nonsym run.



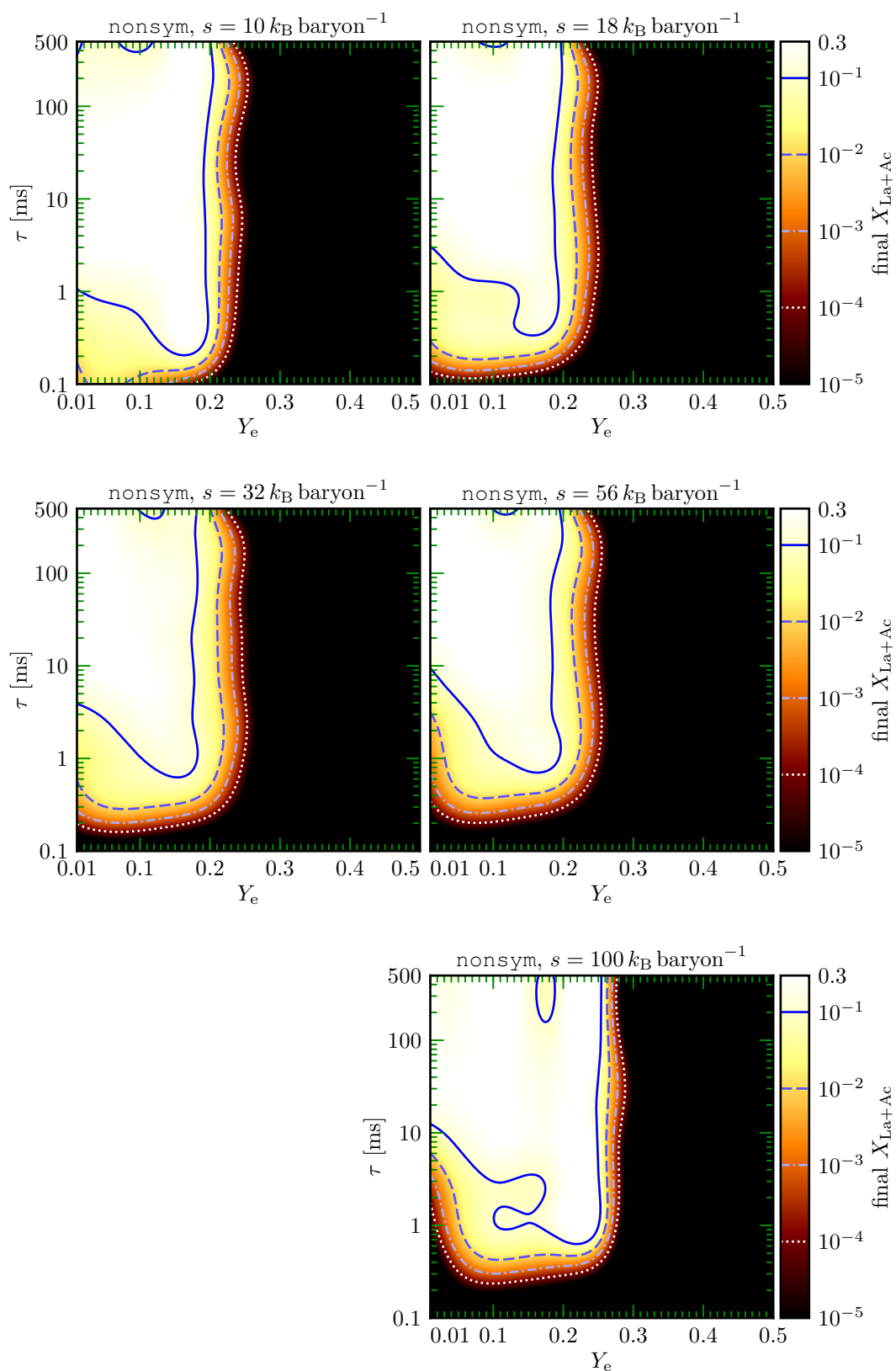
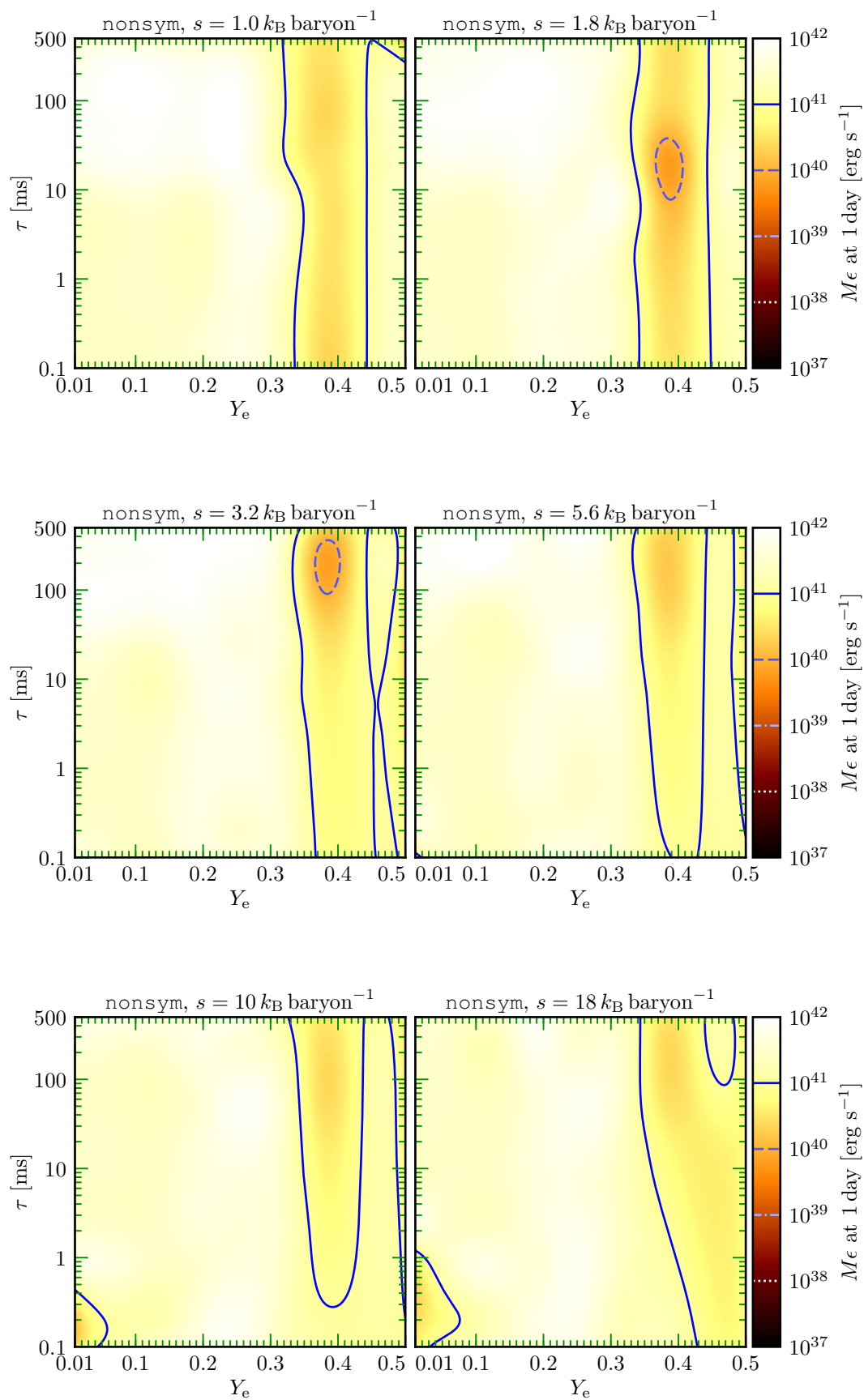


Figure 3.36: All the  $s$  slices showing the final lanthanide and actinide mass fraction of the nonsym run.



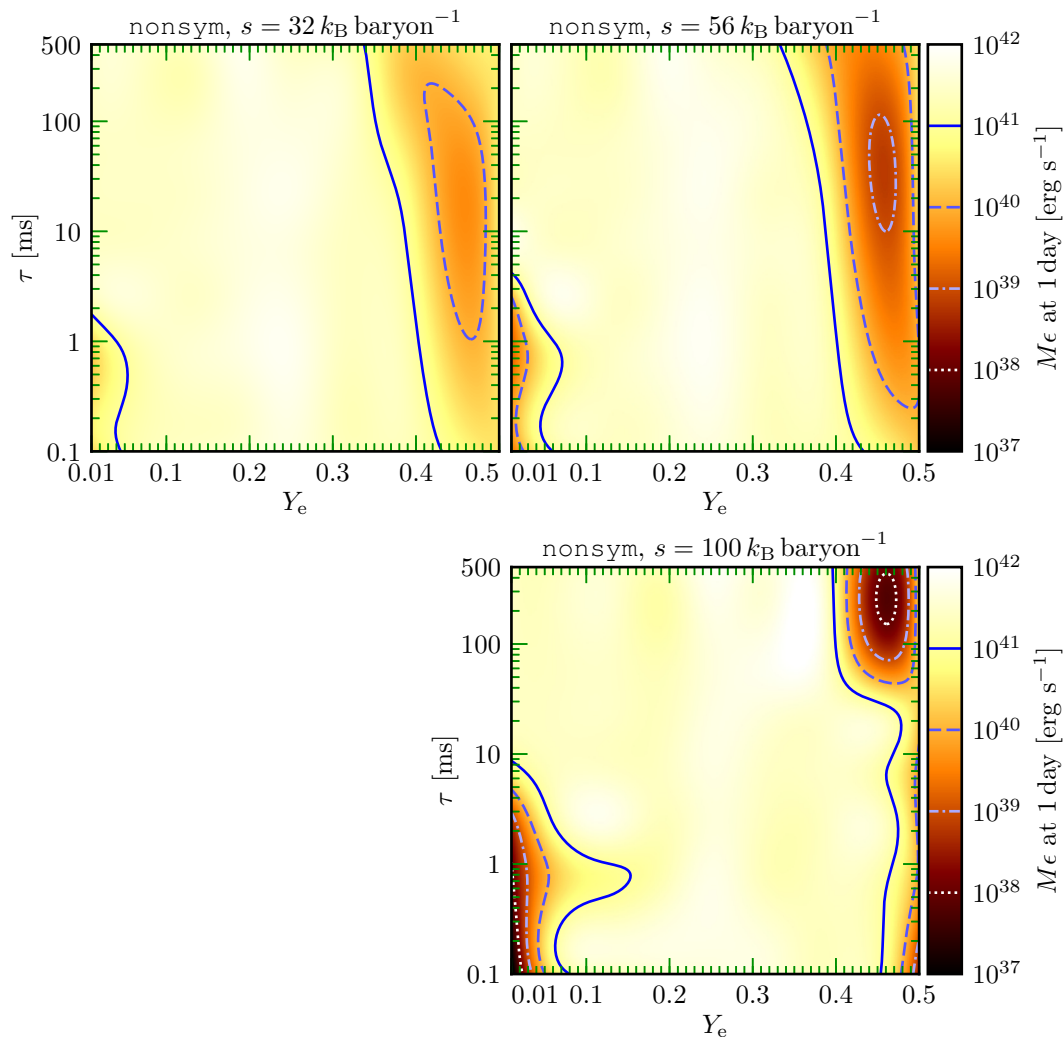
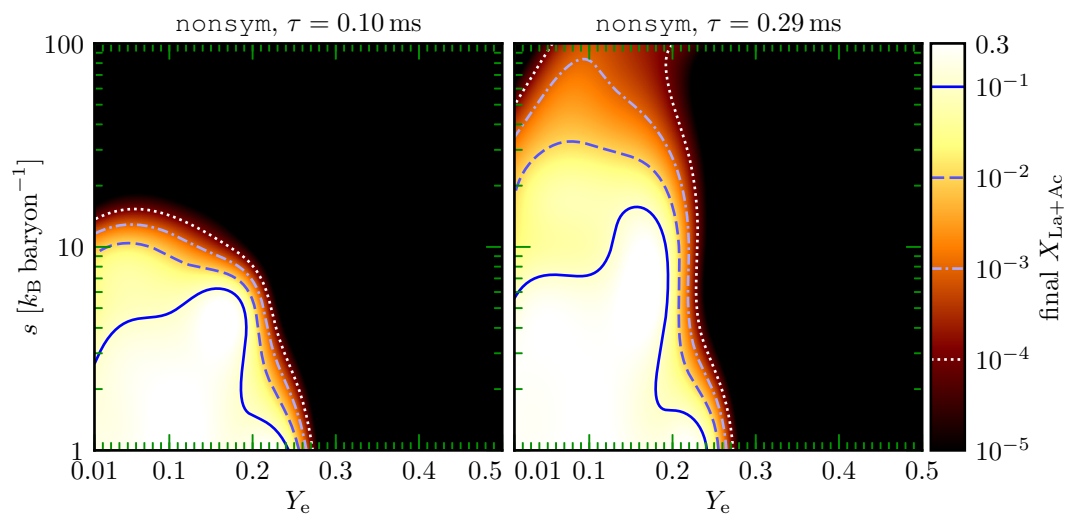
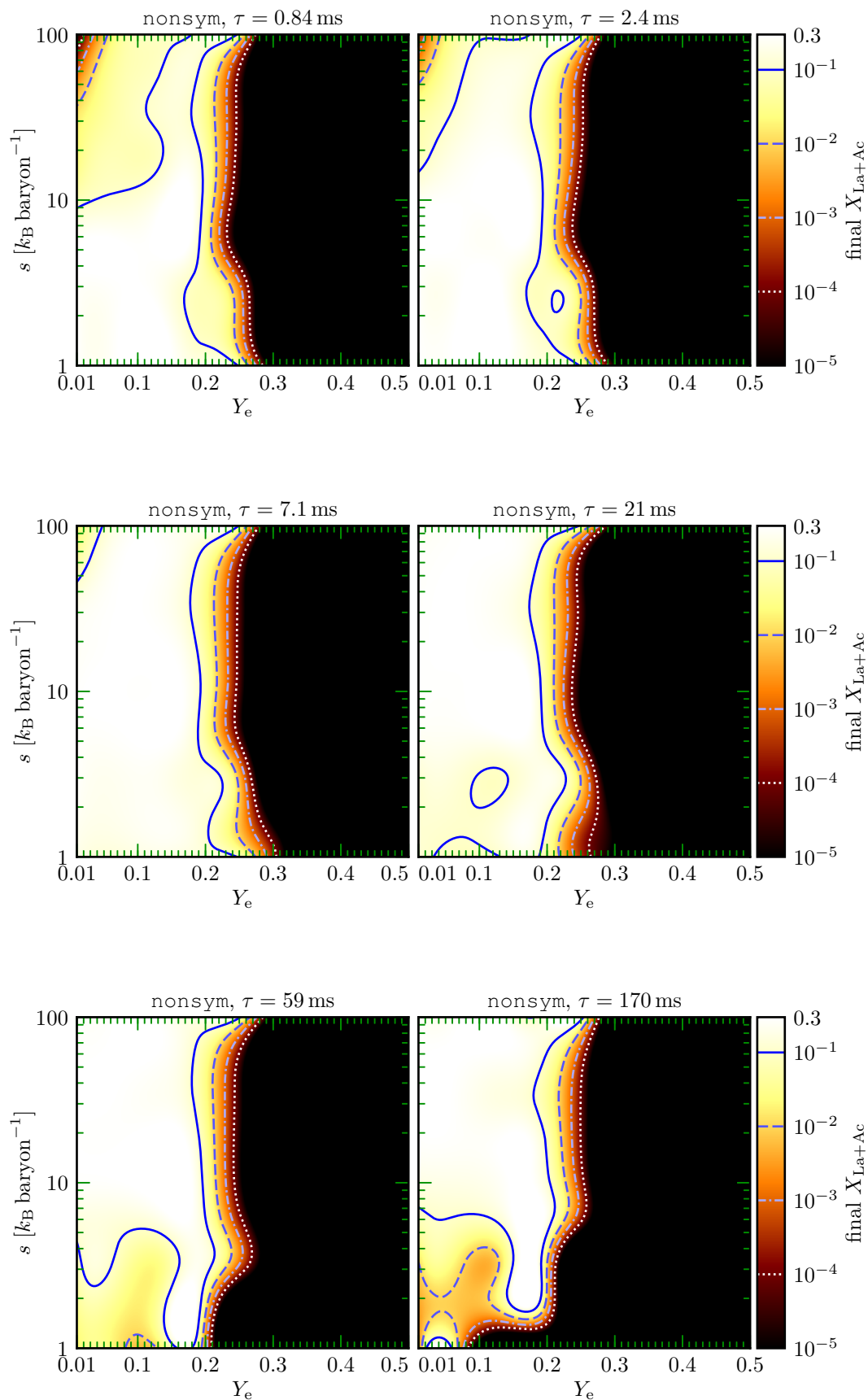


Figure 3.37: All the  $s$  slices showing the heating rate at 1 day of the nonsym run.





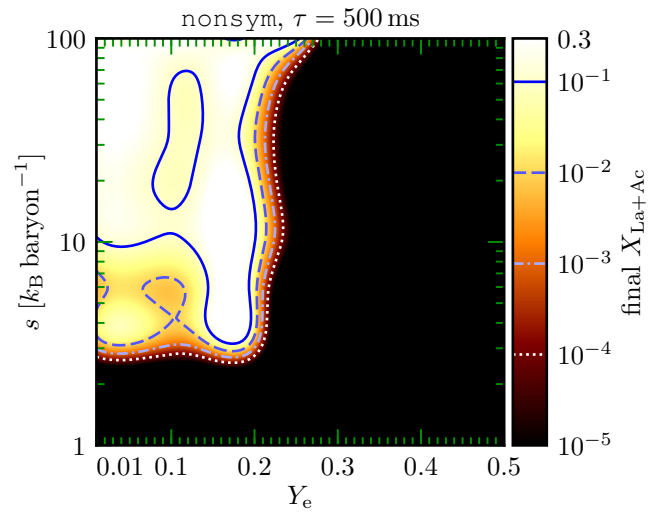
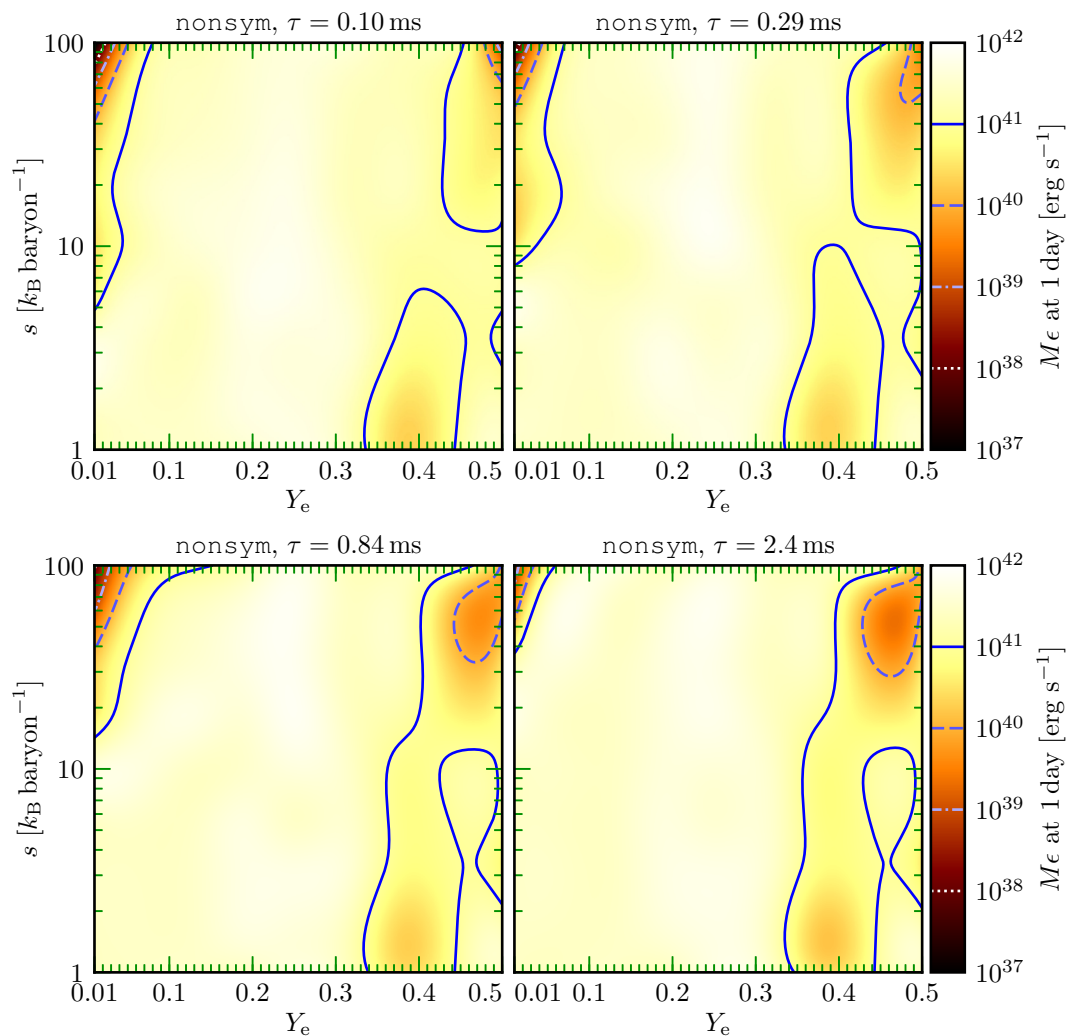


Figure 3.38: All the  $\tau$  slices showing the final lanthanide and actinide mass fraction of the nonsym run.



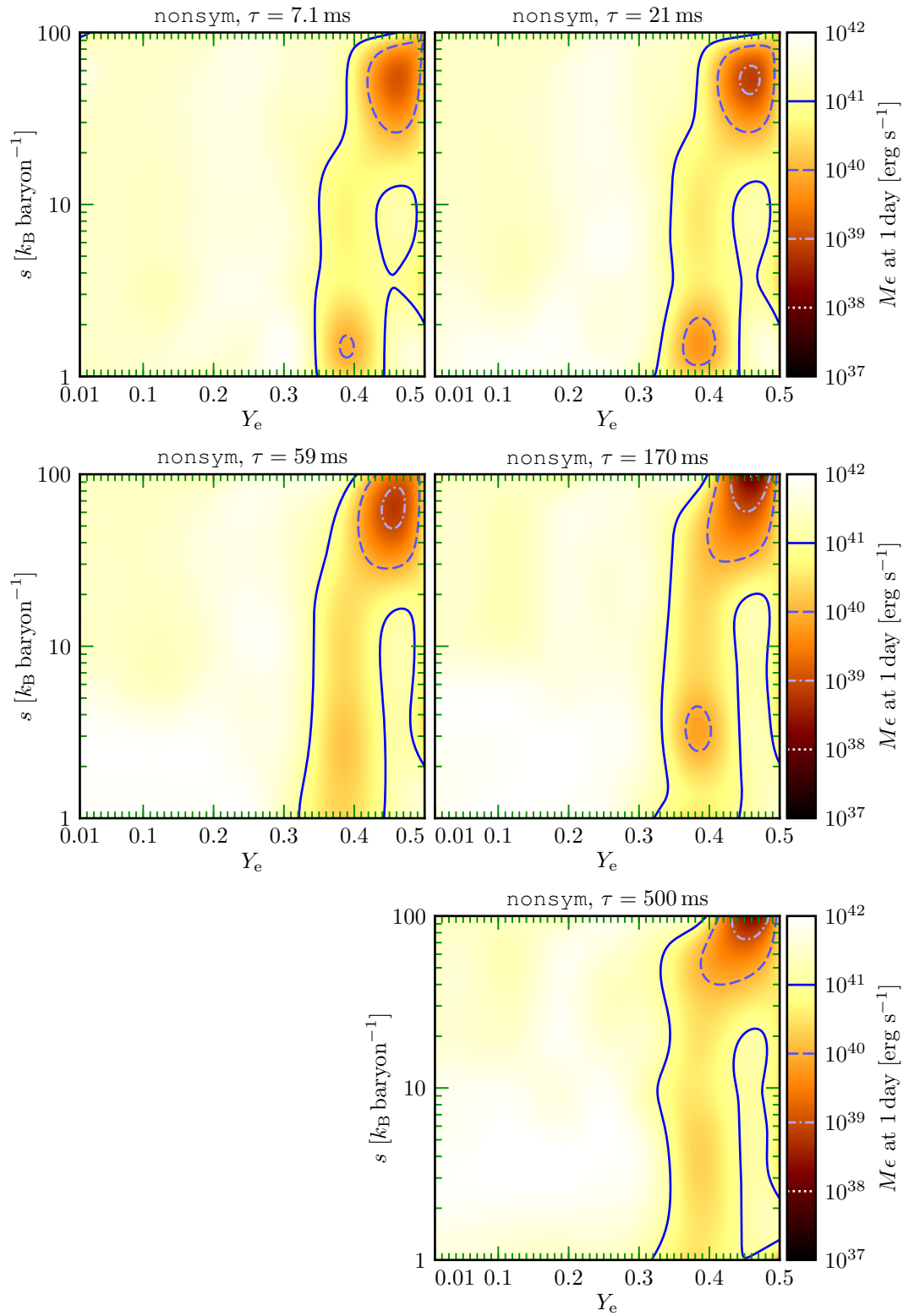


Figure 3.39: All the  $\tau$  slices showing the heating rate at 1 day of the nonsym run.

*Chapter IV*

## NEUTRINOS AND BHNS R-PROCESS NUCLEOSYNTHESIS

*This chapter was published in February 2017 (October 2016 online) in the Monthly Notices of the Royal Astronomical Society, 464, 3907, [doi:10.1093/mnras/stw2622](https://doi.org/10.1093/mnras/stw2622). I set up the pipeline for the nucleosynthesis calculations from the tracer particles and performed all the nucleosynthesis calculations. I contributed significantly to the data analysis, figure creation, and writing.*

© 2016 Luke F. Roberts and coauthors

## **The influence of neutrinos on r-process nucleosynthesis in the ejecta of black hole–neutron star mergers**

**Luke F. Roberts<sup>1,8</sup>, Jonas Lippuner<sup>1</sup>, Matthew D. Duez<sup>2</sup>, Joshua A. Faber<sup>3</sup>, Francois Foucart<sup>4,8</sup>, James C. Lombardi Jr.<sup>5</sup>, Sandra Ning<sup>1</sup>, Christian D. Ott<sup>1</sup>, and Marcelo Ponce<sup>6,7</sup>**

<sup>1</sup> TAPIR, Walter Burke Institute for Theoretical Physics, MC 350-17, California Institute of Technology, Pasadena, California 91125, USA

<sup>2</sup> Department of Physics & Astronomy, Washington State University, Pullman, Washington 99164, USA

<sup>3</sup> Center for Computational Relativity and Gravitation and School of Mathematical Sciences, Rochester Institute of Technology, Rochester, New York 14623, USA

<sup>4</sup> Lawrence Berkeley National Laboratory, 1 Cyclotron Rd, Berkeley, California 94720, USA

<sup>5</sup> Department of Physics, Allegheny College, Meadville, Pennsylvania 16335, USA

<sup>6</sup> Department of Physics, University of Guelph, Guelph, Ontario N1G 2W1, Canada

<sup>7</sup> SciNet HPC Consortium, University of Toronto, Toronto, Ontario M5T 1W5, Canada

<sup>8</sup> NASA Einstein Fellow

### **Abstract**

During the merger of a black hole and a neutron star, baryonic mass can become unbound from the system. Because the ejected material is extremely neutron-rich, the r-process rapidly synthesizes heavy nuclides as the material expands and cools. In this work, we map general relativistic models of black hole–neutron star (BHNS) mergers into a Newtonian smoothed particle hydrodynamics (SPH) code and follow the evolution of the thermodynamics and morphology of the ejecta until the outflows become homologous. We investigate

how the subsequent evolution depends on our mapping procedure and find that the results are robust. Using thermodynamic histories from the SPH particles, we then calculate the expected nucleosynthesis in these outflows while varying the level of neutrino irradiation coming from the postmerger accretion disk. We find that the ejected material robustly produces r-process nucleosynthesis even for unrealistically high neutrino luminosities, due to the rapid velocities of the outflow. Nonetheless, we find that neutrinos can have an impact on the detailed pattern of the r-process nucleosynthesis. Electron neutrinos are captured by neutrons to produce protons while neutron capture is occurring. The produced protons rapidly form low mass seed nuclei for the r-process. These low mass seeds are eventually incorporated into the first r-process peak at  $A \sim 78$ . We consider the mechanism of this process in detail and discuss if it can impact galactic chemical evolution of the first peak r-process nuclei.

*Subject headings:* nuclear reactions, nucleosynthesis, abundances – neutrinos – stars: neutron – stars: black holes – hydrodynamics

#### 4.1 Introduction

Black hole–neutron star (BHNS) binary mergers are a likely candidate for Advanced LIGO and Advanced VIRGO detections of gravitational waves (LIGO Scientific Collaboration et al., 2015; Acernese et al., 2015), they may be responsible for short gamma ray bursts (sGRBs) (e.g. Lee and Ramirez-Ruiz, 2007), and they may provide a significant fraction of the r-process material found in our galaxy (e.g. Lattimer and Schramm, 1976; Korobkin et al., 2012; Bauswein et al., 2014b). Within the next few years, it is likely that Advanced LIGO will detect gravitational waves from these systems and constrain the BHNS merger rate. If electromagnetic counterparts are detected, the merger-sGRB connection may be confirmed and production of the r-process nuclei may be observed *in situ* (Metzger and Berger, 2012).

The origin of the r-process nuclei has been a long standing question in nuclear astrophysics (Burbidge et al., 1957). Core-collapse supernovae are appealing as a possible site because of galactic chemical evolution considerations (e.g. Qian, 2000; Argast et al., 2004), but there is significant difficulty finding the requisite conditions for r-process nucleosynthesis in this environment (e.g. Arcones and Thielemann, 2013). Conversely, it is relatively easy to find conditions neutron-rich enough for r-process nucleosynthesis in the material ejected from binary neutron star (NS) and BHNS mergers (Freiburghaus et al., 1999). Due to the long delay time from binary formation to merger and the large amount of material ejected per merger event, it is challenging to get simple models of galactic chemical evolution, which invoke compact object mergers for r-process production to agree with the observed

distribution of r-process elements in low metallicity halo stars (Qian, 2000; Argast et al., 2004). Nevertheless, recent works taking into account more complex models of galaxy formation get reasonable agreement with the observed distribution of r-process elements (Matteucci et al., 2014; Shen et al., 2015; van de Voort et al., 2015; Ishimaru et al., 2015) and it is possible to get r-process enrichment at very low metallicity when different channels of binary formation are considered (Ramirez-Ruiz et al., 2015). Therefore, it is plausible that compact object mergers could be a significant source of the galactic r-process nuclei.

Recently, it has been recognized that weak interactions can significantly affect the final composition of binary NS outflows (Wanajo et al., 2014; Goriely et al., 2015; Sekiguchi et al., 2015; Foucart et al., 2016a; Palenzuela et al., 2015; Radice et al., 2016). Likewise, the final state and remnant product of binary NS mergers has been shown to depend on several properties of the system, e.g. important roles are played by the microphysical nuclear equation of state (EOS), electromagnetic fields and neutrino effects (Neilsen et al., 2014; Palenzuela et al., 2015). In contrast to binary NS mergers, the material ejected during BHNS mergers is unlikely to undergo significant numbers of weak interactions. Electron and positron captures are suppressed relative to the rates in the shock heated ejecta of binary NS mergers due to the low entropy present in the tidal ejecta. The high outflow speeds and low neutrino luminosities encountered in these events—compared to binary NS mergers—also make it unlikely that neutrino interactions will drastically change the number of neutrons present at the onset of r-process nucleosynthesis (Foucart et al., 2014, 2015). Therefore, the dynamical ejecta of BHNS mergers have been long thought to be likely sites for production of heavy r-process nucleosynthesis (Lattimer and Schramm, 1976; Lattimer et al., 1977; Korobkin et al., 2012; Bauswein et al., 2014a). Understanding how BHNS mergers contribute to galactic chemical evolution requires knowledge of the merger rate, predictions for the amount of mass ejected per merger, the kinetic energy of the ejecta, and predictions of nuclei synthesized in these outflows. Although there are no observed BHNS binaries, theoretical predictions suggest that the rate of BHNS binary mergers could be up to a tenth of the rate of double neutron star binary mergers (LIGO Scientific Collaboration, 2010; Bauswein et al., 2014a). The amount of mass ejected during BHNS mergers can depend sensitively on the binary parameters, especially the black hole (BH) spin and mass (Foucart et al., 2013; Hotokezaka et al., 2013c; Bauswein et al., 2014a; Kyutoku et al., 2015). More mass is ejected as the BH spin increases in the direction of the orbital angular momentum (Foucart et al., 2014).

Increasing the spin decreases the radius of the innermost stable orbit and decreases gravitational binding at the radius at which the NS is tidally disrupted. Increasing the BH mass reduces the amount of material remaining outside of the BH after merger (for fixed NS properties), since the tidal radius scales as  $(M_{\text{BH}}/M_{\text{NS}})^{1/3}R_{\text{NS}}$  while the innermost stable orbit of the BH scales as  $M_{\text{BH}}$  for fixed BH spin. The fraction of the mass outside the horizon which is unbound, however, also increases with the BH mass, making the relation between BH mass and unbound mass nontrivial (Kyutoku et al., 2015).

Because the mass and spin distributions of stellar mass BHs and the expected number of BHNS system in our galaxy are not well known (e.g. LIGO Scientific Collaboration, 2010), it is difficult to estimate the contribution of these events to the r-process material found in the galaxy (Bauswein et al., 2014a). Nonetheless, it is timely to investigate the detailed composition of the ejecta because the merger rate is likely to soon be constrained by Advanced LIGO (LIGO Scientific Collaboration et al., 2015). Additionally, there are some hints that the infrared excess associated with GRB130603B (Tanvir et al., 2013; Berger et al., 2013) is consistent with that event being powered by the radioactive decay of r-process products in the ejecta of a BHNS merger (Hotokezaka et al., 2013c). A similar excess has recently been observed in the afterglow of GRB060614 (Yang et al., 2015; Jin et al., 2015).

In this work, we investigate the long term hydrodynamics of the BHNS ejecta and the nucleosynthesis that occurs therein. For the first time, we focus on how neutrinos might affect the detailed nucleosynthesis patterns that are produced. Even for unrealistically large neutrino luminosities, we find that the distribution of the pre-neutron capture electron fraction is not significantly altered and the second and third r-process peaks are robustly produced in almost all of the material. This is in contrast to the dynamical ejecta of binary NS mergers, where weak processing may prevent an r-process from occurring in a significant amount of the material (Wanajo et al., 2014; Goriely et al., 2015). Of course, the BHNS result is expected because the outflows happen relatively early before the remnant disk can start to emit neutrinos, there is no hypermassive NS contributing to the neutrino flux, and the tidal ejecta possesses a very high velocity. More interestingly, we find that electron neutrino captures by neutrons can provide seed nuclei for a low mass r-process that produces material in the first r-process peak at  $A \sim 78$ . Nonetheless, in our models, the ratio of the first peak to the second peak is sub-solar with and without the inclusion of neutrino captures. When comparing to the yields of low metallicity

halo stars with sub-solar Ge abundances (Roederer et al., 2014), we find that this first peak production can bring our models closer to agreement with the observed abundances of Ge, As, and Se, although the abundances are still somewhat low.

This paper is organized as follows: in Section 4.2, we present the BHNS systems we have simulated, explain how the ejected material is mapped into our smoothed particle hydrodynamics (SPH) code, and describe our nuclear reaction network. Then, in Section 4.3.1, we discuss the effect of weak interactions on the electron fraction distribution in the ejecta. In Section 4.3.2, we present the integrated nucleosynthesis from our models and discuss neutrino induced production of the first r-process peak. In Section 4.3.4, we discuss uncertainties in the results from our nucleosynthesis calculations and their possible implications for galactic chemical evolution and for abundance observations in low metallicity halo stars.

## 4.2 Methods

### 4.2.1 Relativistic merger simulations and binary systems

The BHNS merger simulations used in this work have been described in detail in our previous papers (Deaton et al., 2013; Foucart et al., 2014). Here we review the major features and error estimates of the merger simulations, referring readers to Foucart et al., 2014 for details. The fully relativistic Einstein-hydrodynamics system is evolved with the Spectral Einstein Code (SpEC) (SXS Collaboration, 2000). Neutrino cooling and lepton number evolution are incorporated through a neutrino leakage scheme (Deaton et al., 2013).

To model the NS, we employ the Lattimer-Swesty EOS (Lattimer and Swesty, 1991) with an incompressibility  $K_0 = 220$  MeV and a symmetry energy  $S_\nu = 29.3$  MeV (hereafter LS220), using the table available at <http://www.stellarcollapse.org> and described in O’Connor and Ott, 2010. This EOS yields a neutron star radius that lies within the allowed range of radii, as determined by Hebeler et al., 2013 from nuclear theory constraints and the existence of neutron stars of mass  $\sim 2M_\odot$  (Demorest et al., 2010; Antoniadis et al., 2013). For LS220, a  $1.2$  ( $1.4$ ) $M_\odot$  neutron star has a radius  $R_{\text{NS}}$  of  $12.8$  ( $12.7$ ) km and a compactness  $C = GM_{\text{NS}}/(R_{\text{NS}}c^2)$  of  $0.139$  ( $0.163$ ).

During the SpEC simulations, the dynamical ejecta is tracked for only about 5 ms before it exits the computational grid. However, during this time, the specific energy ( $u_i$ ) of fluid elements becomes nearly constant, so it is often possible to confidently identify unbound material. Convergence of our SpEC simulations was

observed to be faster than second-order. Assuming second order convergence gives a conservative relative error of up to 60% in the mass and kinetic energy of ejected material. Even if the true error were this large, which is unlikely, it would not affect the results of the present investigation. As we will see, variations of ejecta properties between different binary systems, which are of similar magnitude, have negligible effect on the final nuclear abundances.

In the simulations of Deaton et al., 2013 and Foucart et al., 2014, we considered BHNS binary systems with multiple masses and spins. The BH mass  $M_{\text{BH}}$  was taken to be  $5.6M_{\odot}$ ,  $7M_{\odot}$ , or  $10M_{\odot}$ , covering most of the estimated mass distribution for stellar mass black holes (Özel et al., 2010; Farr et al., 2011). The neutron star gravitational mass  $M_{\text{NS}}$  was taken to be  $1.2M_{\odot}$  or  $1.4M_{\odot}$ , which is typical for NSs (Kiziltan et al., 2013). For these masses, ejecta is produced only for at least moderately high BH spins, meaning that for most cases the Kerr spin parameter must be  $\chi_{\text{BH}} > 0.7$  (Foucart, 2012).

For this study, we use the ejecta from three systems. The first, called “M12-7-S9”, with parameters  $M_{\text{NS}} = 1.2M_{\odot}$ ,  $M_{\text{BH}} = 7M_{\odot}$ ,  $\chi_{\text{BH}} = 0.9$ , produces a very large ejecta mass of  $0.16M_{\odot}$ . The second, “M14-7-S8”, with  $M_{\text{NS}} = 1.4M_{\odot}$ ,  $M_{\text{BH}} = 7M_{\odot}$ ,  $\chi_{\text{BH}} = 0.8$ , has ejecta mass  $0.06M_{\odot}$ , one of our lower ejecta mass cases. The third case, “M14-5-S9”, has parameters  $M_{\text{NS}} = 1.4M_{\odot}$ ,  $M_{\text{BH}} = 5.6M_{\odot}$ ,  $\chi_{\text{BH}} = 0.9$  and ejects a mass of  $0.084M_{\odot}$ .

#### 4.2.2 SPH evolution of ejecta

After  $\sim 5$  ms, the ejecta has detached from the merger remnant and is moving for the most part ballistically. However, the outflow is not yet homologous. Also, it is possible that pressure forces will subsequently become important again because of recombination heating or collision of streams of matter (although this turns out not to be the case). Therefore, we continue the hydrodynamic evolution of the outflow using an SPH code, *StarSmasher* (Gaburov et al., 2010; Ponce et al., 2012). The SPH code is Newtonian, but since the flow is only mildly relativistic ( $v/c \approx 0.2$ ), and from the beginning somewhat far from the black hole ( $> 10M_{\text{BH}}$ ), this is probably adequate for our purposes. (See check on this below.)

The *StarSmasher* code is the successor to the earlier *StarCrash* code (Lombardi et al., 2006). It represents fluids in the standard SPH way, using a finite number of fluid elements or “particles.” In its current implementation, the particles may have different masses (Gaburov et al., 2010), which simplifies the construction of initial

data from finite volume representations. *StarSmasher* uses variable smoothing lengths to maximize resolution, using a formalism derived consistently from a particle-based Lagrangian to ensure proper energy and entropy evolution (Lombardi et al., 2006; Springel and Hernquist, 2002; Monaghan, 2002).

Stable shock evolution is achieved using artificial viscosity with a Balsara switch (Balsara, 1995) to suppress artificial viscosity in shear layers; fortunately, accurate shock evolution is not important for our application. Self-gravity forces are neglected, so the gravitational force is simply a function of position given by the black hole potential and it is implemented in the Newtonian and Paczyński-Wiita approximations (Ponce et al., 2012; Paczyński and Wiita, 1980). In order to avoid small time steps due to rapid motion, particles are removed if they come too close to the BH. These particles would eventually fall into the BH anyway, so this procedure does not affect the ejecta properties.

As initial data to the SPH simulation, hydrodynamic data from a snapshot of the SpEC merger simulation (taken after tidal disruption but before the tidal tail hits the outer boundary) are output on a uniform Cartesian mesh. *StarSmasher* reads these data, reflects them to add the lower hemisphere not evolved by SpEC, interpolates to an hexagonal close-packed lattice, and assigns a particle of appropriate density to each nonvacuum lattice point. The evolution is then continued in *StarSmasher* using the LS220 EOS with no neutrino effects. The electron fraction  $Y_e$  of each particle is constant during the SPH evolution, and no neutrino cooling or absorption is considered. If a particle falls below the LS220 density or temperature table range, the entropy  $S$  is henceforth set to be constant, and a  $S \propto \rho T^3$ ,  $P \propto \rho^{4/3}$  extrapolation of the EOS is used. This only happens when pressure is negligible, and the entropy evolution in *StarSmasher* is not used in our post-processing nucleosynthesis calculations (see below).

Although relativistic effects are not expected to be important, the translation from relativistic to Newtonian physics must account for two subtleties. First, the late-time behavior of an ejecta fluid element is most sensitive to its energy, especially whether it is bound or unbound, so it is important that this be appropriately translated. We therefore rescale the velocity vector so that the specific kinetic plus potential energy of each particle in the Newtonian framework is equal to its relativistic specific energy  $-u_t - 1$  in the SpEC simulation. Second, there is no a priori guarantee that the coordinate system in which the numerical relativity simulation evolves will be close to any known coordinates. Fortunately, SpEC’s “damped harmonic” coordinates lead the

spacetime to settle nearly in harmonic coordinates, so we transform in *StarSmasher* to Schwarzschild coordinates (ignoring the BH’s spin, whose effects will not be important far from the hole), with a simple radial transformation  $r \rightarrow r + M_{\text{BH}}$ . In the region of interest, the numerically evolved spacetime is nearly Minkowski, and the deviation from Minkowski is mostly Schwarzschild and so can be adequately modeled by a Paczyński-Wiita potential. Lastly, one must distinguish between the rest frame baryon density used in the EOS and the mass integrand density used to assign the mass of the SPH particle, which is the rest frame baryon density times a Lorentz factor and a metric determinant factor. Because SPH particle mass is a constant, the mass integrand density only needs to be calculated and integrated over at the initial time.

A straightforward evolution of the fluid equations produces a generally realistic evolution but with some clearly unphysical artifacts. Namely, matter on the upper and lower surfaces of the ejected tidal tail blow away from the equator, something unexpected given the overall weakness of pressure forces and not indicated in the SpEC evolution. This vertical expansion has no influence on the energy distribution or nucleosynthesis results, but it does affect the shape of the outflow. Convergence tests show that it is not a transient caused by an insufficient number of particles, so it is likely an artifact of the transition to Newtonian physics. It can be removed by reducing pressure forces near the black hole. In our simulations labeled “P1”, we turn off pressure forces within  $10M_{\text{BH}}$  of the black hole, while within  $100M_{\text{BH}}$ , pressure is reduced by a factor varying linearly with distance between zero (at  $10M_{\text{BH}}$ ) and one (at  $100M_{\text{BH}}$ ). Within this range, the specific entropy is held constant, because otherwise the pressure reduction would keep the fluid from adiabatically cooling. Simulations labeled “P2” have full pressure forces everywhere.

We check that our evolved results are insensitive to the time at which we transition from SpEC/relativistic to *StarSmasher*/Newtonian physics by starting from two different snapshots 1.6 ms apart and finding negligible variation in the evolved energy histograms, which are shown in Figure 4.1. In fact, even the initial energy histograms are not very different, so after the first  $\approx 2$  ms the influence of pressure on the kinematics of the ejecta is negligible. The codes’ main function is to provide the density evolution as particles follow their ballistic trajectories.

Our interest is only in unbound matter. The bound matter for the most part orbits the black hole in an accretion disk or is “eaten” when it comes within the prescribed distance from the central point mass. Both because of the exclusion of full relativity

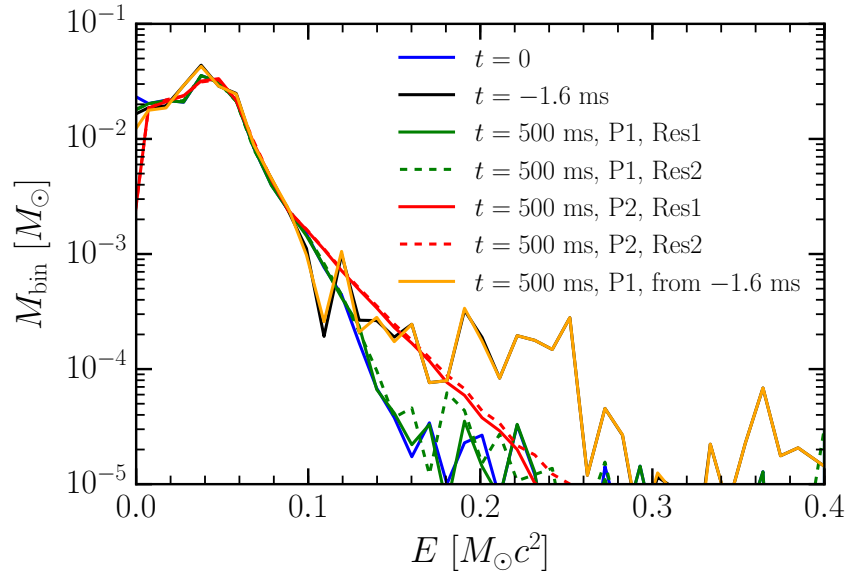


Figure 4.1: The distribution of specific kinetic plus potential energy in the unbound post-merger matter, shown for system M12-7-S9 at a time shortly after the disruption of the NS ( $t = 0$ ) and 500ms later, long after the distribution has settled. For each energy bin, we integrate the density of all particles with energy inside that bin, giving a Newtonian mass for each energy bin. We show 2 resolutions, “Res1” and “Res2”, corresponding to around 79,000 and 175,000 particles, respectively. We evolve using two methods: “P1” turns off pressure forces and imposes adiabatic internal energy evolution within a radius of about  $100M_{\text{BH}}$ . “P2” includes pressure forces everywhere but removes bound particles after 10 ms. Another SPH run begun 1.6 ms earlier in the merger has nearly stationary energy distribution if evolved with P1. A simulation using P2 with a Paczyński-Wiita potential gives results almost identical to P2 with the standard Newtonian point potential.

and the lack of a transport process to drive accretion, the disk evolution cannot be regarded as believable. We find that, for P2 evolutions, if we allow the disk to evolve for long periods of time, some fraction of the mass becomes weakly unbound. This is not perhaps incorrect given the physics included, but it cannot be regarded as physical, so we remove this contamination by eliminating bound particles after 10 ms of SPH evolution. For P1 evolutions, this removal is not necessary.

Our standard evolutions use roughly 75,000 particles. The mass profile of the ejecta M12-7-S9 is shown in Figure 4.2. Figure 4.3 shows snapshots of the SPH particles and fluid density after  $\approx 0.5$  s of starting the SPH evolution.

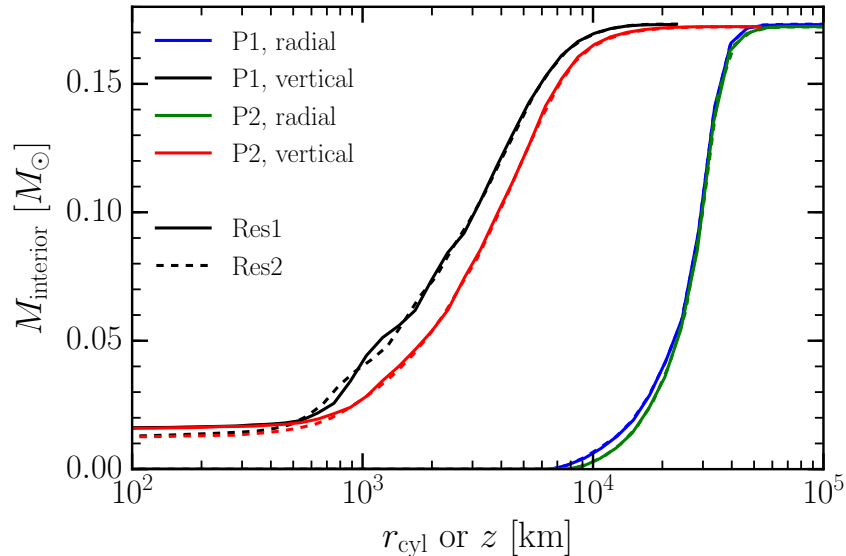


Figure 4.2: The mass (computed by density integral) interior to a given cylindrical radius  $r_{\text{cyl}}$  or vertical height  $|z|$  for binary ejecta M12-7-S9. Profiles are computed at a time 500 ms after merger, by which point the ejecta profile has settled and will thereafter spread nearly homologously. The vertical interior mass appears to asymptote to a nonzero value on the left, indicating that a significant number of particles remain near the equator. We show results for two resolutions with two ways of handling pressure forces. Simulations with pressure forces completely turned off give profiles nearly the same as P1 profiles.

### 4.2.3 Nuclear reaction network and weak interactions

To calculate the composition of a Lagrangian fluid element in the ejecta, we require the evolution of its density as a function of time as well as its initial composition and entropy. To allow evolution at very late times, we extrapolate the density histories of the particles taken from the SPH simulation assuming homology,  $\rho \propto t^{-3}$ , which accurately describes the long term evolution of the flow. In addition to the density, we extract the entropy and electron fraction along these trajectories. The extracted electron fraction is constant due to the neglect of weak reactions during the SPH evolution. The LS220 EOS is only valid for baryon densities and temperatures above  $\rho = 10^8 \text{ g cm}^{-3}$  and  $T \approx 1 \text{ GK}$ , which does not include the entire region in the temperature density plane in which neutron capture occurs. Since corrections to the EOS due to nuclear interaction become negligible below  $\rho \sim 10^{12} \text{ g cm}^{-3}$ , we switch from LS220 to a multi-species non-degenerate ideal gas EOS consistent with the nuclei included in our network along with the electron EOS of Timmes and Arnett, 1999 for our network evolutions. When keeping the entropy fixed and assuming an initial nuclear statistical equilibrium (NSE) composition—with

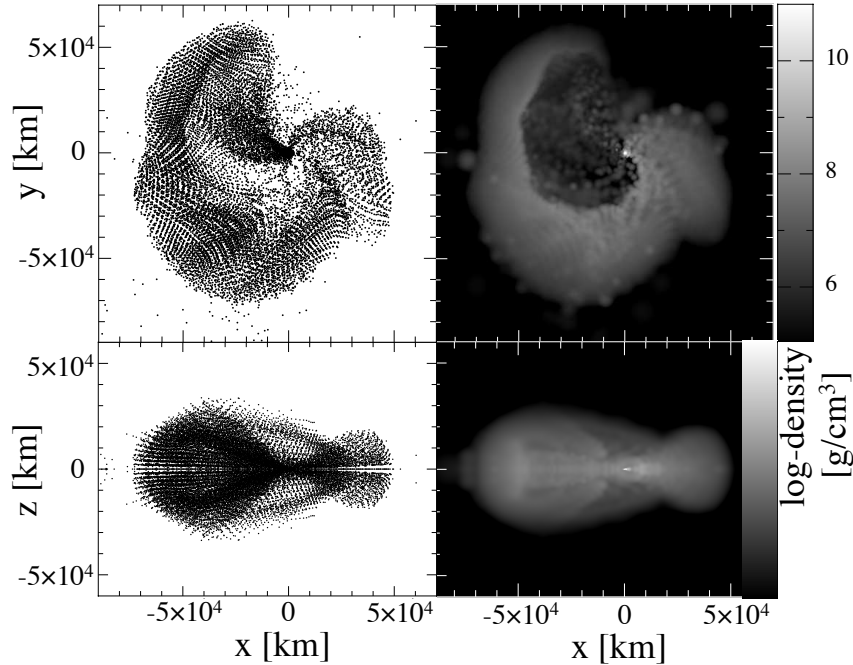


Figure 4.3: Outflow’s profile at a representative snapshot from the SPH evolution of M12-7-S9. Upper/bottom-left panels:  $xy/xz$ -projection of SPH-particles; upper/bottom-right panels: density (in log-scale  $[\text{g cm}^{-3}]$ ) views in the  $xy/xz$ -planes respectively.

the modified Helmholtz EOS described in Lippuner and Roberts, 2015—we find temperature differences less than a few percent between the two EOS in the region where they overlap. Because the single nucleus approximation of LS220 predicts different nuclei than a full NSE calculation, there is a mismatch between the total internal energies of  $\sim 0.1$  MeV/baryon when switching between the two EOSs. This level of error is unlikely to significantly impact the nucleosynthesis calculations because the total energy released per baryon during the nucleosynthesis is of order ten MeV.

Once the density evolution of the Lagrangian particles has been extracted and extrapolated, we evolve the composition of the particles using the nuclear reaction network code *SkyNet* (Lippuner and Roberts, 2015) and the network described therein. The entropy generated via nuclear transmutations is self-consistently included in the evolution, similarly to Freiburghaus et al., 1999. At 3 ms after merger—the time at which the SpEC simulations are mapped to *StarSmasher*—the particles are typically at temperatures over 10 GK and densities are below  $10^{12} \text{ g cm}^{-3}$ . At these temperatures and densities, NSE holds, but weak interactions are generally far from equilibrium over the short timescales encountered during the merger. To follow

changes in the electron fraction at high temperature, *SkyNet* includes an NSE evolution mode where strong interactions are assumed to be in equilibrium and only weak interactions are tracked. This mode is used until the temperature drops below 7 GK, at which point the full nuclear reaction network is evolved. Because inverse strong reactions are calculated via detailed balance, the transition between the two *SkyNet* evolution modes is smooth.

To track the potential importance of neutrino irradiation of the ejecta, electron neutrino capture, electron antineutrino capture, electron capture, and positron capture by free nucleons are included in both evolution modes. The neutrino capture rates are given by

$$\lambda_\nu = \frac{G_F^2(1 + 3g_A^2)}{2\pi^2\hbar^7c^6} \int_{\tilde{Q}}^{\infty} d\epsilon_e p_e \epsilon_e (\epsilon_e - Q)^2 \bar{f}_\nu(\epsilon_e - Q) (1 - f_e(\epsilon_e)), \quad (4.1)$$

where  $f_e$  is the electron distribution function,  $G_F$  is the Fermi coupling constant,  $g_A$  is the weak axial vector coupling constant,  $\epsilon_e$  is the electron energy,  $p_e$  is the electron momentum,  $Q$  is the energy transfer from the nucleons to the final state electron, and  $\bar{f}_\nu$  is the angle-averaged neutrino distribution function. The  $Q$ -value is defined in the direction of electron or positron capture and  $\tilde{Q} = \max(Q, m_e c^2)$ . The electron and positron capture rates,  $\lambda_{e^+}$  and  $\lambda_{e^-}$ , are calculated from similar expressions with the distribution functions interchanged. This expression assumes there is no momentum transfer to the nucleons and neglects weak magnetism corrections. Although these corrections are potentially significant in the case of neutrino driven winds (Horowitz, 2002), they are unlikely to significantly affect the evolution of the electron fraction in BHNS merger ejecta. The  $\alpha$ -effect locks free protons in heavy nuclei and thereby prevents significant competition from electron antineutrino capture (Fuller and Meyer, 1995). We assume that the neutrino distribution has a Fermi-Dirac shape in energy space and neutrinos of all energies are emitted from a single spherical surface, which results in the distribution function

$$f_\nu(\epsilon, \mu, r) = \frac{\theta(\mu - \mu_0(r))}{\exp(\epsilon/T_\nu) + 1}, \quad (4.2)$$

where  $\mu$  is the cosine of the angle of neutrino propagation relative to the radial direction,  $\mu_0 = \sqrt{1 - (r_\nu/r)^2}$ ,  $T_\nu$  defines the neutrino spectral temperature,  $\theta$  is the Heaviside step function,  $\epsilon$  is the neutrino energy, and  $r_\nu$  is the radius of neutrino emission. Inside of  $r_\nu$ ,  $\mu_0$  is assumed to smoothly approach negative one over a tenth of  $r_\nu$ . The value of  $r_\nu$  can be fixed by choosing a neutrino luminosity,  $L_\nu$ , and spectral temperature. This model is crude, considering the disk like geometry

of the neutrino emitting region, but it is sufficient for this study given that we are parameterizing the properties of the neutrino field anyway. In the following sections, we consider models with fixed electron neutrino luminosities of  $L_{\nu_e} = \{0, 0.2, 1, 5, 25\} \times 10^{52} \text{ erg s}^{-1}$ . The electron antineutrino luminosity is always fixed to be  $L_{\bar{\nu}_e} = 1.5L_{\nu_e}$ , but our results are insensitive to this choice due to the  $\alpha$ -effect. These values are in the range found in the simulations of Foucart et al., 2016a and the difference between the values accounts for re-leptonization of the disk. Since only charged current interactions are included in the nuclear network, the properties of the heavy flavored neutrino fields do not affect our results. We employ constant luminosities to reduce the number of parameters affecting our nucleosynthesis calculations.

We perform nucleosynthesis postprocessing for all of the ejected SPH trajectories. The nuclear evolution is followed until  $10^{13}$  s after the merger, which allows for the decay of all but a handful of long lived unstable isotopes.

### 4.3 Results and discussion

#### 4.3.1 The electron fraction of the ejecta

The electron fraction of the material ejected during the BHNS merger is the most important parameter in determining the nucleosynthesis that occurs within the outflow (e.g., Lippuner and Roberts, 2015). Given the short dynamical timescales and the lack of a hypermassive central NS after the merger, it has often been assumed that the electron fraction of the dynamical ejecta from BHNS mergers is set solely by the initial beta-equilibrium electron fraction of the NS from which the material was ejected (Just et al., 2015). If there are not a substantial number of weak interactions during and after the merger, the electron fraction will be low enough that an r-process involving a significant number of fission cycles will occur: the outer layers of a NS have  $Y_e < 0.1$  and the critical value for producing r-process material at low entropy is  $Y_e \approx 0.25$  (e.g. Kasen et al., 2015; Lippuner and Roberts, 2015). Neutrinos can impact the electron fraction of the ejecta of binary NS mergers (Wanajo et al., 2014; Goriely et al., 2015; Foucart et al., 2016a; Palenzuela et al., 2015; Radice et al., 2016). In binary NS mergers, a large fraction of the prompt ejecta comes from the shock heated material in the interaction region of the two NSs (Palenzuela et al., 2015). The increased temperatures and the large neutrino fluences near this material increases  $Y_e$  significantly and can sometimes drastically alter the character of nucleosynthesis in the outflow. In the BHNS case, there is no interaction region during the tidal disruption of the NS, and matter ejection when the tidal stream

self-intersects is very subdominant (Foucart et al., 2015). The case M14-5-S9 has the most massive ejection from the tidal stream collision (Deaton et al., 2013) of these BHNS, but even for this case the imprint of this secondary ejecta source on the overall outflow composition is small. Therefore, the ejected material has a lower average entropy and electron fraction than neutron star–neutron star (NSNS) merger ejecta and there is no significant neutrino emission until a disk has formed around the BH. Here, we consider the extent to which neutrino interactions can alter the distribution of  $Y_e$  just before r-process nucleosynthesis begins in the ejecta.

We estimate the effect of neutrino captures on the BHNS outflows by considering the maximum disk neutrino luminosities found by Foucart et al., 2014. The neutrino luminosity coming from the disk in both electron neutrinos and antineutrinos is around  $10^{53}$  erg s<sup>-1</sup>. Although the simulations of Foucart et al., 2014 used a gray leakage approximation, we can get some estimate of the average neutrino energies from the temperature of the emission region which was around 5 MeV, which suggests average neutrino energies around  $\epsilon_\nu \approx 3.15T \sim 15$  MeV (e.g., Foucart et al., 2015). We can then estimate the neutrino processing timescale as

$$\tau_\nu(r) \approx 67.8 \text{ ms} \left( \frac{r}{250 \text{ km}} \right)^2 L_{\nu_e,53}^{-1} T_{\nu_e,5}^{-1}, \quad (4.3)$$

where  $r$  is the radius of the fluid element,  $L_{\nu_e,53}$  is the electron neutrino luminosity in units of  $10^{53}$  erg s<sup>-1</sup>, and  $T_{\nu_e,5}$  is the electron neutrino spectral temperature in units of 5 MeV. Electron antineutrinos are unlikely to contribute significantly to the neutrino interaction timescale. This is because in the low entropy outflows of BHNS mergers almost all protons are locked in heavy nuclei and thus have very low neutrino capture cross-sections.

The change in  $Y_e$  due to neutrino interactions can be estimated by assuming that the tidal ejecta has a constant velocity  $v$ , the neutrino luminosity is constant, electron and positron capture are unimportant, protons are locked into heavy nuclei, and there is a finite time after merger at which neutrinos start being emitted from the disk. With these assumptions, the evolution of  $Y_e$  as a function of radius is given by

$$\frac{dY_e}{dr} = \frac{\theta(r - vt_{\nu,\text{on}})}{v\tau_\nu(r)Y_{e,\text{eq}}} (Y_{e,\text{eq}} - Y_e), \quad (4.4)$$

where  $Y_{e,\text{eq}} = \langle Z \rangle_{\text{nuclei}} / \langle A \rangle_{\text{nuclei}}$ , and  $t_{\nu,\text{on}}$  is the time after merger at which the neutrino luminosities reach their saturation value.

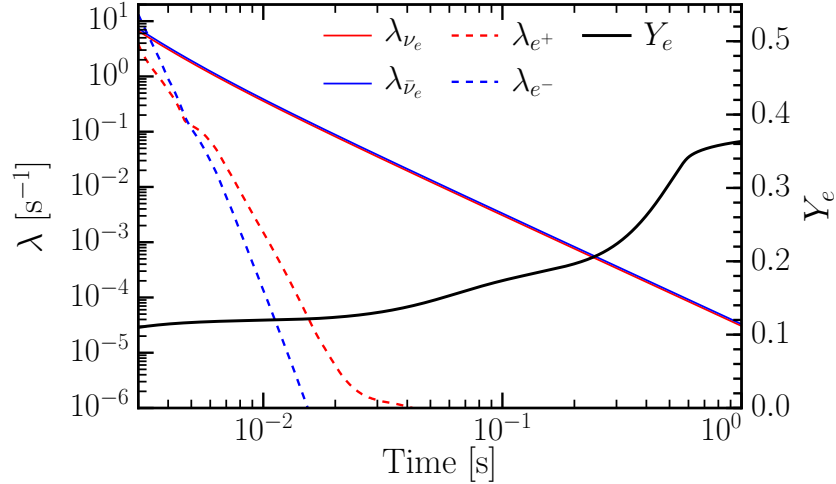


Figure 4.4: Evolution of the electron fraction and weak rates as a function of time for a characteristic fluid element. The electron neutrino luminosity is assumed to be  $10^{53}$  erg  $s^{-1}$ . Because of the relatively low entropy of the BHNS ejecta and because of the low initial density of our calculations, neutrino interaction rates dominate the electron and positron capture rates but neither have a large impact on the electron fraction of the outflow. The increase in  $Y_e$  seen after around 100 ms is due to beta-decay during the r-process.

Assuming a constant average proton and neutron numbers of the heavy nuclei, this can easily be integrated to large radius to find the final electron fraction

$$Y_{e,f} \approx Y_{e,\text{eq}} \left[ 1 - \exp\left(-\frac{r_0}{v\tau_\nu(r_0)Y_{e,\text{eq}}}\right) \right] + Y_{e,i} \exp\left(-\frac{r_0}{v\tau_\nu(r_0)Y_{e,\text{eq}}}\right), \quad (4.5)$$

where  $r_0 = t_{\nu,\text{on}}v$ . Using the outflow velocity and neutrino luminosities calculated in the M12-7-S9 model of Foucart et al., 2014 ( $v \approx 0.25 c$ ,  $L_{\nu_e} \approx 10^{53}$  erg  $s^{-1}$ , and  $t_{\nu,\text{on}} \approx 3$  ms) we find that the post neutrino interaction electron fraction is  $Y_{e,f} \approx 0.07$  if the  $Y_{e,\text{eq}}$  is close to a half. Given that the r-process is robustly produced below  $Y_e \approx 0.25$ , this suggests that neutrino interactions are much less likely to play a significant role in determining the composition of the ejecta in BHNS mergers relative to binary NS mergers, although this estimate is sensitive to  $t_{\nu,\text{on}}$  and the velocity of the outflow.

To make this more concrete, we run nucleosynthesis calculations for the M12-7-S9 model including neutrino interactions induced by a constant neutrino luminosity, modeled as described above. Similar results are found for the other two models discussed in Section 4.2.1. In Figure 4.4, the weak interaction rates and the electron fraction are shown for a single particle. Because our Lagrangian trajectories start at 3 ms after the merger, the initial density in the ejected material is below about

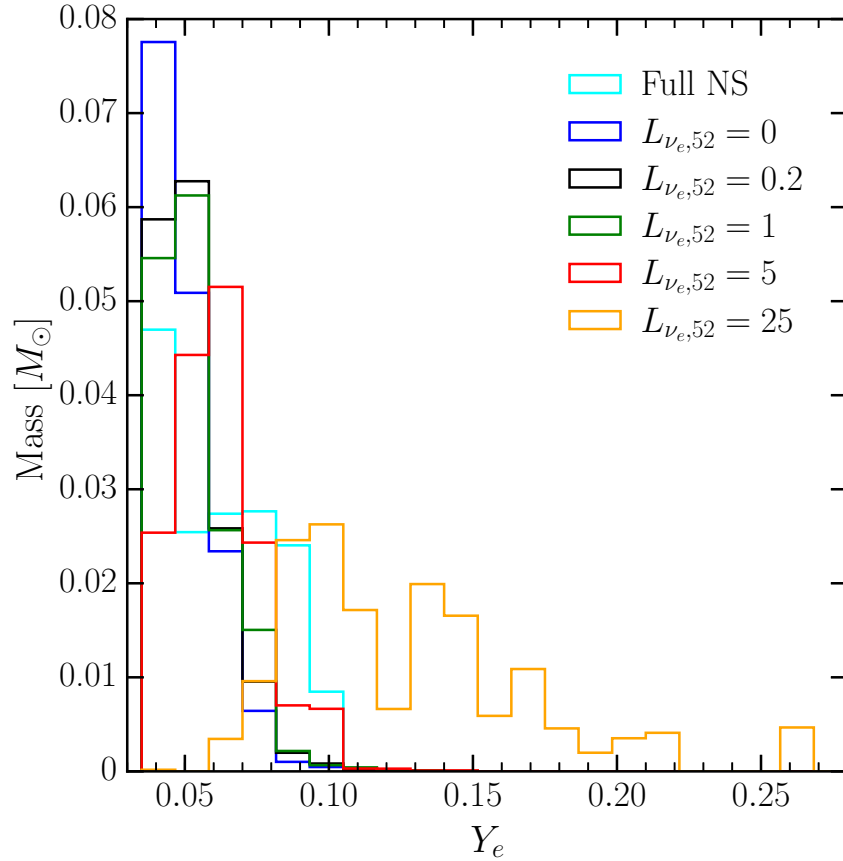


Figure 4.5: Mass weighted histogram of the electron fraction in the ejecta from model M12-7-S9 assuming fixed electron neutrino luminosities of  $\{0, 0.2, 1, 5, 25\} \times 10^{52} \text{ erg s}^{-1}$ . For comparison, we also show the electron fraction histogram in a  $1.2 M_{\odot}$  LS neutron star (cyan line).

$10^{10} \text{ g cm}^{-3}$  and lepton captures are dominated by neutrino captures for neutrino luminosities above about  $10^{52} \text{ erg s}^{-1}$ . The neutrino interaction rates fall off as a power law in time, since this particular particle is moving away from the merger site at constant velocity in a nearly radial direction. Other particles can deviate from power law behavior at early times, but not strongly. As was expected from our estimates above, the neutrino interaction timescale is long compared to the outflow timescale and very little evolution of the electron fraction occurs during the first 10 ms. The evolution of  $Y_e$  after about 20 ms is driven by beta-decays occurring during the r-process.

To look at the effect of weak interactions globally, the distribution of  $Y_e$  in the material ejected in model M12-7-S9 is shown in Figure 4.5 for a range of assumed neutrino luminosities. The GRHD simulations described in Section 4.2.1 include electron

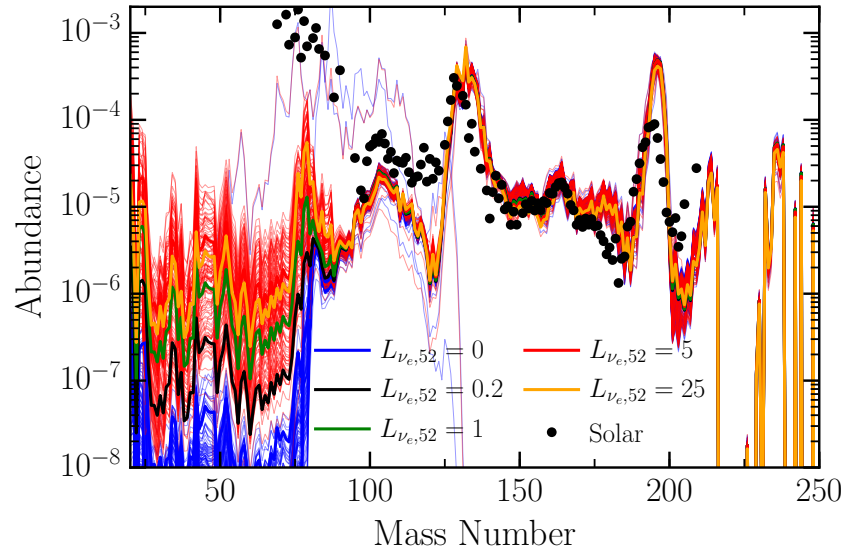


Figure 4.6: Comparison of the integrated nuclear abundances in model M12-7-S9 assuming different fixed neutrino irradiation from the nascent accretion disk. We also include the classical scaled solar abundance r-process distribution from Arlandini et al., 1999 for comparison. The abundances for a selection of single particles from the  $L_{\nu_e} = 0$  and  $L_{\nu_e,52} = 5$  runs are also shown as light lines. For all runs, we assume  $L_{\bar{\nu}_e} = 1.5L_{\nu_e}$ .

and positron captures, but do not include neutrino captures. The SPH simulations which follow the long term evolution of the ejecta include no weak interactions. Therefore, we include weak interactions in our post-processing nucleosynthesis calculations to assess their impact on  $Y_e$ . As we expect, the ejected material is very neutron-rich, but becomes slightly less neutron rich with increasing electron neutrino luminosity. The distribution of the electron fraction in the whole NS is also shown to emphasize that the ejecta in the absence of neutrinos has a significantly lower  $Y_e$  than the average  $Y_e$  of a cold  $1.2 M_\odot$  NS calculated using the LS220 EOS. The beta-equilibrium value of  $Y_e$  increases with density, so that the outer layers of the NS—which comprise most of the ejecta—have a lower electron fraction. The average electron fraction in the ejecta is 0.053, 0.053, 0.054, 0.062, and 0.127, for neutrino luminosities of  $\{0, 0.2, 1, 5, 25\} \times 10^{52} \text{ erg s}^{-1}$ .

### 4.3.2 Nucleosynthesis and neutrino induced production of the first r-process peak

We now consider the detailed nucleosynthesis in the ejecta of model M12-7-S9, both with and without neutrinos. We focus on the effect neutrinos can have on the isotopic abundances of the ejecta. In Figure 4.6, the integrated nucleosynthesis from model

M12-7-S9 is shown. Since the neutrino emission from the accretion torus formed after the BHNS merger is uncertain, we calculate the final nucleosynthetic yields of M12-7-S9 assuming the range of electron neutrino luminosities listed above. In all cases, the electron antineutrino luminosity is fixed at  $1.5L_{\nu_e}$  to very approximately account for re-leptonization of the neutrino emitting disk (Foucart et al., 2016a). Because of the  $\alpha$ -effect, the results are insensitive to the chosen electron antineutrino luminosity. The electron neutrino and antineutrino average energies are fixed at 12 MeV and 15 MeV, respectively. The results for the other two simulated binary systems are similar and they are discussed briefly below. We also find that in the case of zero neutrino luminosity, the nucleosynthesis results are not significantly altered when we use parameterized density histories with a fixed dynamical timescale for all particles. This is not surprising, given the low electron fraction encountered in the ejecta, which gives rise to robust r-process nucleosynthesis across a wide range of dynamical timescales. Nevertheless, the position history of the particles provided by our SPH code is necessary for estimating the amount of neutrino irradiation the particles undergo.

In general, we confirm previous work that has shown BHNS mergers dynamically eject a large amount of r-process rich material (e.g. Roberts et al., 2011; Korobkin et al., 2012; Just et al., 2015). Both the second and third r-process peaks are robustly produced, independent of the neutrino luminosity. Given the low electron fractions found in the ejecta at the start of neutron capture, robust production of the r-process is not surprising (Lippuner and Roberts, 2015). In all of the models, reactive flow proceeds past the third peak before neutron exhaustion occurs in the vast majority of the simulated fluid elements and they undergo fission cycling. We find that fission cycles occur in the ejecta and the number of cycles is weakly dependent on the neutrino luminosity (for the luminosities considered here). Therefore, the abundance pattern above mass number  $\sim 90$  is likely to be robust to variations in the total neutrino luminosity and the properties of the merging system. In all models, the third r-process peak is over produced relative to the second peak. This is discussed further in Section 4.3.4.

We find that the abundance of the first r-process peak at mass number 78 depends on the neutrino luminosity, in contrast to the second and third peaks which are independent of the neutrino luminosity. Nonetheless, in all cases it is under-produced relative to the solar abundance when normalizing to the second and third peaks. This first peak production is driven by low mass r-process seed production after material

falls out of NSE. This material is composed of heavy nuclei and free neutrons when strong equilibrium ceases to hold. Since the material is still relatively close to the accretion torus a few milliseconds after it is ejected, a significant number of electron neutrinos can be captured by the free neutrons. The produced protons then rapidly capture neutrons and form deuterium, which can then capture another deuteron to form an alpha particle. These alpha particles can then undergo a neutron-catalyzed triple-alpha reaction, similar to what occurs in neutron-rich neutrino driven winds (Delano and Cameron, 1971; Hoffman et al., 1997), to produce low mass seed nuclei for the r-process (Meyer et al., 1998). This non-equilibrium neutrino induced seed production creates a distinct set of seed nuclei that can undergo neutron capture, since the seeds produced by the NSE distribution tend to be between mass 78 and 100. A large number of the low mass seeds do not get processed past the  $N = 50$ ,  $Z = 28$  point in the r-process path before neutron exhaustion occurs because of the long beta-decay half lives in that region of the chart of the nuclides. Therefore, these neutrino produced seed nuclei are responsible for producing the first peak r-process nucleosynthesis seen in our simulations. This effect of neutrino irradiation of the outflow is distinct from the one discussed by Wanajo et al., 2014 and Goriely et al., 2015, where the neutrino luminosities are high enough to push the electron fraction over  $\sim 0.25$  and stop production of the second and third peaks.

### 4.3.3 Details of the first peak production mechanism

We now consider the details of the process by which abundances in the first peak are indirectly produced by electron neutrino captures by neutrons. The total number fraction of heavy nuclei produced by neutrino induced seed production can be estimated by using the results from Section 4.3.1 as follows. Low mass seed production proceeds via the neutron catalyzed triple alpha process, so it takes six protons to make a seed nucleus. The rate of proton production is just  $\dot{Y}_e$ , so the total number of low mass seed nuclei produced by neutrino interactions is

$$Y_{s,\nu} \approx \frac{Y_{e,f} - Y_{e,i}}{6} = \frac{Y_{e,\text{eq}} - Y_{e,i}}{6} \left[ 1 - \exp\left(-\frac{r_0}{\nu\tau_\nu(r_0)Y_{e,\text{eq}}}\right) \right]. \quad (4.6)$$

This estimate implies that around  $2 \times 10^{-3}$  seed nuclei per baryon are produced by this process, assuming the neutrino luminosity is  $10^{53}$  erg  $\text{s}^{-1}$ . This number is in good agreement with the values extracted from our nucleosynthesis calculations. Comparing this to the total final abundance of the first peak for a single ejecta particle shown in Figure 4.7, it is clear that only about 10% of this material gets trapped in the first peak.

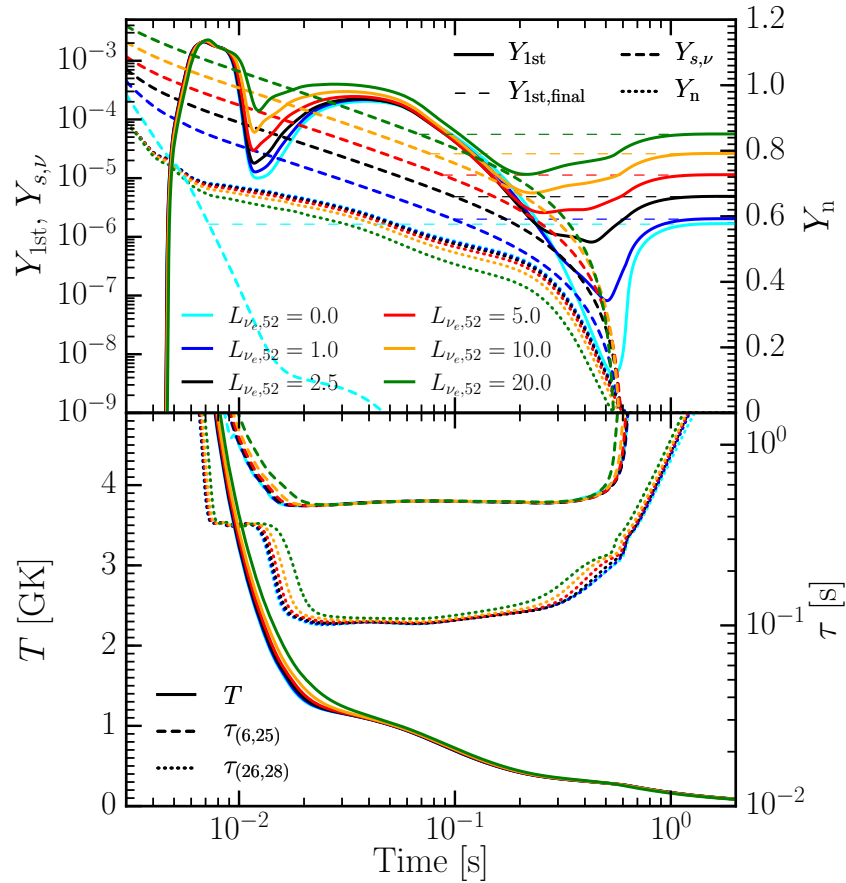


Figure 4.7: Illustration of how the first r-process peak is produced by electron neutrino captures on neutrons for a single SPH particle. This SPH particle had initial  $Y_e = 0.11$ , initial entropy  $s = 9.7 k_B$  baryon $^{-1}$ , and an asymptotic velocity  $v/c = 0.5$ . *Top panel:* The solid lines show the abundance of material in the first r-process peak,  $Y_{1st}$ , as a function of time (i.e. material with  $72 \leq A \leq 79$ ), the dashed lines show the integrated number of protons produced by weak interactions after time  $t$  divided by six,  $Y_{s,\nu} = \int_t^\infty dt Y_n / 6(\lambda_{\nu_e} + \lambda_{e^+})$ , and the dotted lines show the neutron abundance  $Y_n$ .  $Y_{s,\nu}$  gives the number of low mass seed nuclei produced by neutrino interactions. The neutrino seed nuclei produced at early times are burned past the first r-process peak, but the seed nuclei produced after the time when  $Y_{s,\nu} = Y_{1st,final}$  do not get burned passed the first peak before neutrons are exhausted, and so they will end up in the first peak. *Bottom panel:* The solid lines show the temperature of the particle as a function of time, the dashed lines show the timescale to process material to the first peak,  $\tau_{(6,25)}$ , and the dotted lines show the destruction timescale of the first peak,  $\tau_{(26,28)}$ , which are defined in the text. In this particle, there is no significant variation with neutrino luminosity of the temperature or the r-process path. Therefore, the two timescales do not change with the amount of neutrino irradiation.

Seed nuclei indirectly produced by neutrinos are not processed past the  $N = 50$  closed shell rapidly. If such rapid processing were the case, the final amount of mass in the first peak would be set by the number of seed nuclei produced after a time just before neutron exhaustion. To illustrate when the nuclei trapped in the first peak are produced, we show the total number of seed nuclei produced by neutrino interactions after time  $t$

$$Y_{s,\nu}(t) = \frac{1}{6} \int_t^\infty Y_n(\lambda_{\nu_e} + \lambda_{e^+}) dt \quad (4.7)$$

in Figure 4.7, along with the time dependence of the first peak abundance,  $Y_{1st}$ , and the neutron abundance  $Y_n$ .  $Y_{s,\nu}$  is just the number fraction of protons produced by weak interactions after time  $t$  divided by six, since it requires six protons to produce a seed nucleus that can capture neutrons. Material will be processed through the first peak on some timescale  $\tau_{1st}$ . Let  $t_{ex}$  be the time at which neutrons are exhausted and  $t_{prod}$  be the time after which neutrino produced seed nuclei get trapped in the first peak. Seed nuclei produced at times earlier than  $t_{prod} = t_{ex} - \tau_{1st}$  will be burned past the first peak, while seed nuclei produced within a time  $\tau_{1st}$  of neutron exhaustion will end up in the first peak. We can estimate  $\tau_{1st}$  by looking for solutions of  $Y_{s,\nu}(t_{prod}) = Y_{1st,final}$ . Inspecting Figure 4.7, we find  $t_{prod}$  is 70 to 100 ms and  $t_{ex}$  is 520 to 600 ms for  $L_{\nu_e,52}$  ranging from 20 to 1. Thus we estimate that  $\tau_{1st}$ , the time it takes for seed nuclei to be processed to the  $N = 50$  closed shell of the first peak, is between 450 and 500 ms for this particular fluid element. For reference, the final abundances of this particle are shown in Figure 4.8.

We now attempt to explain what sets this timescale. Assuming the waiting point approximation (c.f. Kratz et al., 1993), the timescale to go from charge  $Z_1$  to charge  $Z_2$  is given by

$$\tau_{(Z_1, Z_2)}(t) = \sum_{Z=Z_1}^{Z_2} \frac{\sum_N Y_{(Z,N)}}{\sum_N Y_{(Z,N)} \tau_{\beta^-, (Z,N)}^{-1}}. \quad (4.8)$$

Here,  $\tau_{\beta^-, (Z,N)}^{-1}$  is the beta-decay timescale of a nucleus with  $N$  neutrons and  $Z$  protons. When  $(n, \gamma)$  reactions are in equilibrium with  $(\gamma, n)$  reactions—such that  $\mu_n + \mu_{(Z,N)} = \mu_{(Z,N+1)}$ —these timescales are only functions of the density, temperature, and neutron abundance, i.e.  $\tau_{(Z_1, Z_2)} = \tau_{(Z_1, Z_2)}(\rho, T, Y_n)$ . This is often the case at the high temperatures encountered during r-process nucleosynthesis in these outflows, but the equilibrium can start to break down at lower temperatures (Kratz et al., 1993). This makes it clear that changing the temperature and electron fraction of a particular fluid element can change the path of the r-process and alter the time it takes material to be processed from one charge number to another. The quantities  $\tau_{(6,25)}$

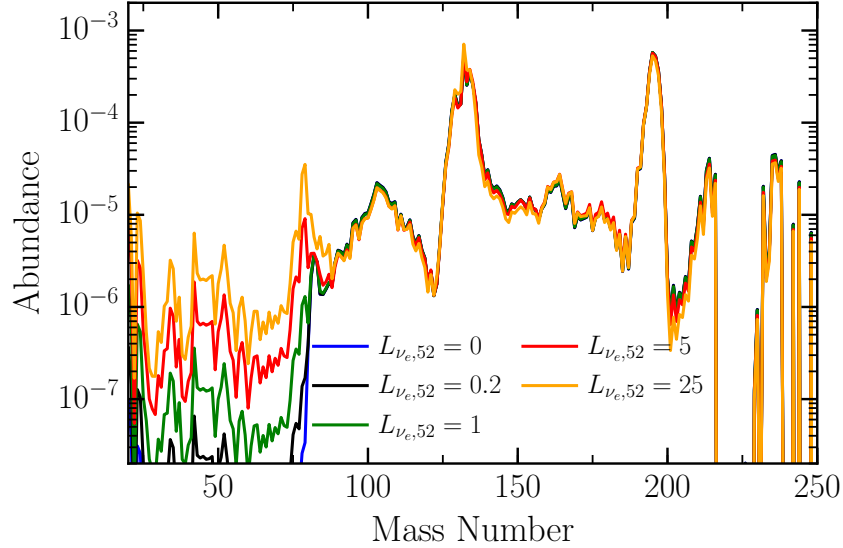


Figure 4.8: Final abundances as a function of neutrino luminosity for the single Lagrangian particle shown in Figure 4.7.

and  $\tau_{(26,28)}$  are shown in the bottom panel of Figure 4.7. Note that  $\tau_{(6,25)} + \tau_{(26,28)}$  is approximately the time it takes a seed nucleus to get to the start of the first peak and then get processed through the first peak, which we called  $\tau_{1st}$  above. We see from the bottom panel of Figure 4.7 that  $\tau_{(6,25)}$  is constant throughout the period during which the r-process is occurring and its value is in good agreement with our 450 to 500 ms estimate for  $\tau_{1st}$ . Because this timescale is determined by beta decay, the final first peak abundance goes linearly with the neutrino luminosity. The lifetimes of isotopes along the  $N = 50$  closed shell are 40 ms, 110 ms, and 110 ms, for the reactions  $^{76}\text{Fe}(\beta^-, n)^{75}\text{Co}$ ,  $^{77}\text{Co}(\beta^-, n)^{76}\text{Ni}$ , and  $^{78}\text{Ni}(\beta^-)^{78}\text{Cu}$ . These are consistent with the  $\tau_{(26,28)} \approx 100$  ms we find in Figure 4.7. We also note that at around 600 ms into the calculation—which is after neutron exhaustion—there is a further increase in the first peak abundance. This is driven by the reaction  $^{80}\text{Ni}(\beta^-, n)^{79}\text{Cu}$ . Significant production of  $^{80}\text{Ni}$  occurs just before neutron freeze-out and it has a half-life of 175 ms.

This suggests that the neutrino flux between times  $t_1 = t_{\text{ex}} - \tau_{(6,25)} - \tau_{(26,28)}$  and  $t_2 = t_{\text{ex}} - \tau_{(6,25)}$  will determine the amount of neutrino induced first peak production that occurs. Seed nuclei produced before time  $t_1$  will get beyond the first peak before neutrons are exhausted, while seed nuclei produced after time  $t_2$  will not reach the first peak before neutron exhaustion occurs. Therefore, the important quantity for understanding neutrino induced production of the first peak will be the neutrino luminosity centered at a time around 70 ms after merger, within a window of around 100 ms.

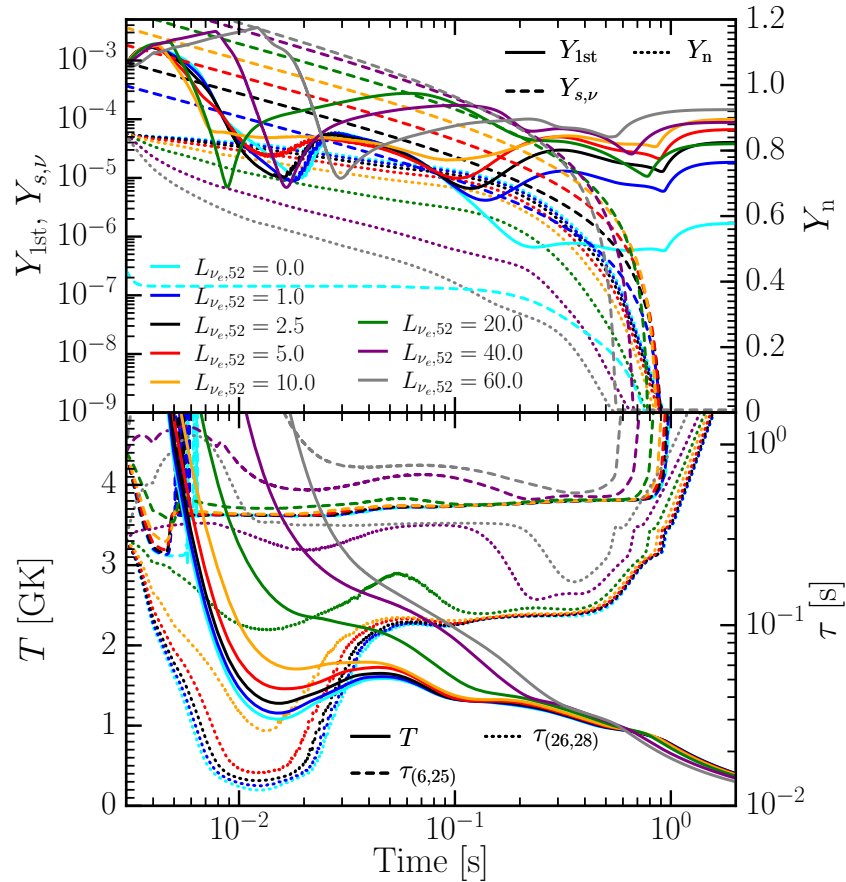


Figure 4.9: The same as Figure 4.7, except for a different thermodynamic trajectory. This SPH particle had initial  $Y_e = 0.05$ , initial entropy  $s = 4.33 k_B \text{ baryon}^{-1}$ , and an asymptotic velocity  $v/c = 0.29$ . Because of the lower velocity, lower initial entropy, and lower  $Y_e$  present in this particle relative to the particle shown in Figure 4.7, neutrino interactions significantly alter the thermodynamic state of the material and  $\tau_{(6,25)}$ . This causes the first peak abundance to vary non-monotonically with the neutrino luminosity.

We have shown that the production of first peak nuclei goes linearly with the electron neutrino luminosity for the specific Lagrangian particle shown in Figure 4.7, but Figure 4.6 shows that production of the first peak appears to saturate at luminosities above  $\sim 5 \times 10^{52} \text{ erg s}^{-1}$ . Below this luminosity, the dependence of first peak production on luminosity is approximately linear as expected. In Figure 4.9, we show a different Lagrangian particle that exhibits non-monotonic behavior of the first peak abundance with the neutrino luminosity. The first peak abundance increases at low luminosity, decreases with luminosity around  $L_{\nu_e} = 10^{53} \text{ erg s}^{-1}$ , and then increases with luminosity again. This particle has a lower asymptotic velocity than the particle shown in Figure 4.7 and therefore experiences more neutrino irradiation.

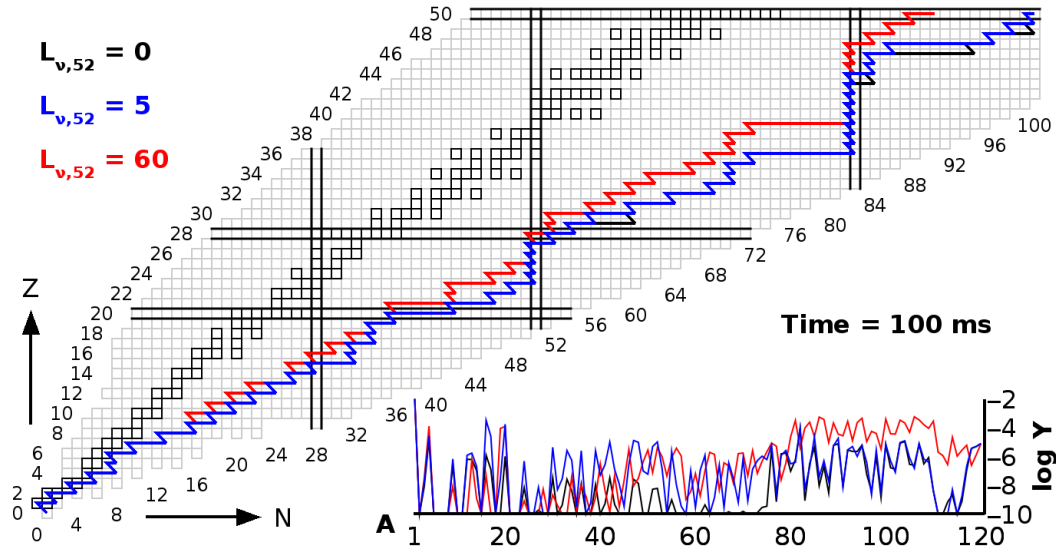


Figure 4.10: The r-process path for the SPH particle shown in Figure 4.9 for different neutrino luminosities at 100 ms into the calculation. The inset shows the mass summed abundances at the same time. Notice how the path differs for different neutrino luminosities.

Additionally, it has lower initial entropy and  $Y_e$ , which means neutrino interactions can have a larger effect on its thermodynamic state.

The lower panel of Figure 4.9 clearly shows that neutrinos significantly alter the thermodynamic state of the considered particle and that the low mass r-process path is shifted by the inclusion of neutrino interactions. In particular,  $\tau_{(26,28)}$  and  $\tau_{(6,25)}$  increase with the neutrino luminosity. Figure 4.10 shows how the r-process path varies with the neutrino luminosity 100 ms into the calculation, giving rise to the processing timescales dependence on neutrino luminosity. The total number of seeds increases with initial  $Y_e$  and temperature, corresponding to larger neutrino luminosities in this fluid element. Additionally, increasing the entropy of the outflow reduces the rate at which material can bypass the  $A = 8$  stability gap. The large difference in the first peak processing timescale,  $\tau_{(26,28)}$ , seen in Figure 4.9 is due to the r-process path shifting from being far beyond the  $N = 50$ ,  $Z = 28$  closed shells at lower temperatures (and lower neutrino luminosities) to proceeding through closed shells at higher temperatures (and higher neutrino luminosities). This significantly alters how first peak nuclei are produced throughout the calculation and breaks the linear dependence on the neutrino luminosity.

Even in the absence of neutrinos, there is some production of first peak nuclei. As we have mentioned, this material is produced by fission of heavy nuclei. Since

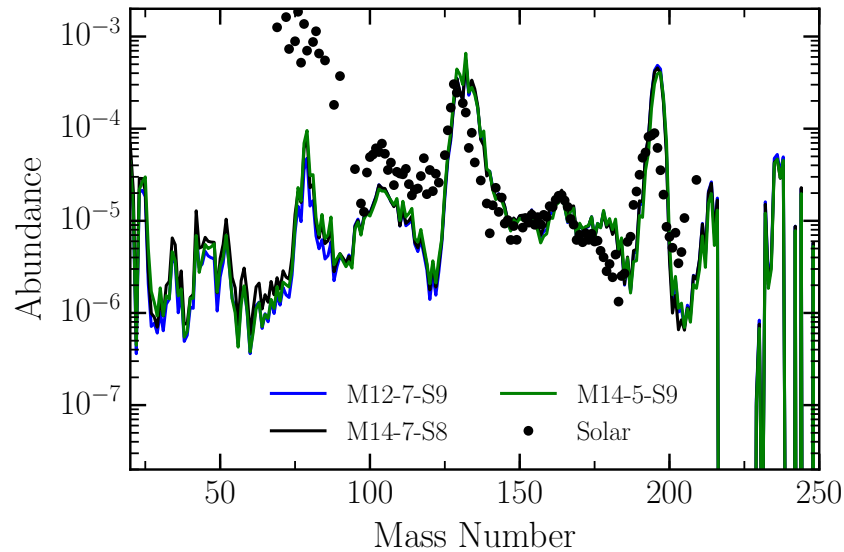


Figure 4.11: The integrated nuclear abundances of the dynamical ejecta in the models M12-7-S9, M14-7-S8, and M14-5-S9 assuming an electron neutrino luminosity of  $10^{53} \text{ erg s}^{-1}$ . The low electron fraction of all the ejecta results in production of a robust r-process, independent of the dynamics of the merger and parameters of the binary system.

we are employing symmetric fission fragment distributions, it is likely that more realistic fission fragment distributions will result in a broader distribution of fission daughters and more material being left behind in this region. Nonetheless, it seems likely that there will be at least some production of the first peak even in the very neutron-rich outflows of BHNS mergers, as long as neutrino luminosities from the post merger remnant are above about  $10^{52} \text{ erg s}^{-1}$  within a hundred milliseconds of the merger. We also emphasize that neutrino induced production of the first peak does not produce enough material in our models to agree with the solar r-process abundances when they are normalized to the second peak. Instead, the abundance is around an order of magnitude too low.

#### 4.3.4 Isotopic and elemental abundances, galactic chemical evolution, and low metallicity halo stars

In Figure 4.11, the integrated abundances from the models M12-7-S9, M14-7-S8, and M14-5-S9 are shown for a fixed neutrino luminosity of  $10^{53} \text{ erg s}^{-1}$  (and  $L_{\bar{\nu}_e} = 1.5L_{\nu_e}$ ). Clearly, there is little discernible difference between the predicted nucleosynthesis from these models. The electron fraction in almost all of the ejecta in all three models is below the threshold for fission cycling to occur (Lippuner and Roberts, 2015) and the entropy of the ejecta is quite low. These are conditions that

result in a second and third peak nuclear abundance pattern that is quite insensitive to the detailed properties of the ejecta (e.g., Lippuner and Roberts, 2015). Interestingly, the neutrino produced first peak is also very insensitive to the binary parameters if the same neutrino luminosities are assumed. A priori, it would seem that different dynamics during the merger could give rise to different dynamics of the ejecta and alter the radius at which neutron exhaustion occurs. Of course, the important parameter will be the velocity of the ejecta. Larger velocities will result in lower local neutrino densities around the time that neutrons are exhausted in the ejected material.

Although there is reasonable qualitative agreement with the solar r-process abundance pattern above  $A \sim 100$  in all of our models, there are significant quantitative differences. Most clearly, the third peak is significantly over produced and has an offset with respect to the observed solar pattern. Uncertainties in the ejecta abundance pattern can come from two sources, uncertainties in the properties of the ejecta and uncertainties in the nuclear data that serves as input for our nucleosynthesis calculations. Given how robust the r-process pattern in our models is above  $A \sim 100$  to variations in the binary parameters and neutrino irradiation, it seems unlikely—for our chosen nuclear data—that BHNS mergers can make a pattern that agrees exactly with the r-process pattern found in the Sun and low metallicity halo stars. Strictly following this argument to its conclusion, BHNS mergers would be ruled out as the dominant contributor to the galactic chemical evolution of r-process elements. This would put a significant constraint on the combined merger rate, the BH spin distribution, and the BH mass distribution in these binaries (Bauswein et al., 2014b). Of course, it is easy to imagine scenarios where the galactic r-process nucleosynthesis is produced by multiple types of events, so strongly ruling out a single r-process production channel on the basis of inexact agreement with the solar pattern seems premature at best.

The second possible source of uncertainty in our results is the input nuclear physics data. The nuclear masses, beta-decay rates, neutron capture rates, fission barrier heights, and fission fragment distributions in the r-process path, which lies far from nuclear stability, have, on the whole, not been experimentally determined but are instead determined from models that are in part constrained by data from nuclei closer to stability (e.g. Möller et al., 1997; Goriely et al., 2009). For instance, different nuclear mass models can give significantly different abundance patterns for the same thermodynamic histories (e.g. Arcones and Martínez-Pinedo, 2011;

Martin et al., 2015; Mendoza-Temis et al., 2015). By varying masses within a particular mass model within the expected uncertainty, Mumpower et al., 2015 have shown that the uncertainties in the final r-process abundance pattern solely due to nuclear physics uncertainties can be as large as a factor of ten. We have also not included neutrino-induced fission in our nuclear network (Qian, 2002; Kolbe et al., 2004), which could change the nuclei that undergo fission and potentially alter the low mass r-process pattern. Nevertheless, the neutrino irradiation in these outflows is rather weak so it would be surprising if neutrino induced fission drastically changed our results. Therefore, given the level of agreement we find with the solar r-process isotopic abundance pattern, our results seem wholly consistent with BHNS mergers contributing to the galactic budget of heavy r-process nuclei.

For confrontation with observations of abundances in low metallicity halo stars, it is more instructive to examine the *elemental* abundance pattern of the ejecta (i.e.  $Y_Z = \sum_i \delta_{Z_i,Z} Y_i$ ), since only elemental abundances are easily determined in these stars. In Figure 4.12, we show the final elemental abundances in the ejecta of model M12-7-S9 for a variety of assumed neutrino luminosities. In the region  $51 < Z < 81$ , most of the abundances agree with the solar pattern to within a factor of three. The notable exceptions are gold and platinum in the third peak and cesium in the second peak, all of which are over-produced by a factor of around ten. Although the agreement is not perfect, our patterns above Mo are within the errors due to uncertainties in the nuclear physics input (Mumpower et al., 2015).

For elements below Mo, there are a number of primary nucleosynthesis processes that can contribute to these abundances, even in low metallicity stars (Travaglio et al., 2004; Montes et al., 2007; Qian and Wasserburg, 2008; Arcones and Montes, 2011; Hansen et al., 2014). Therefore, it is hard to rule out our models because they fail to produce certain abundances below Mo. As can be seen in the bottom panel of Figure 4.12, the abundances below Mo are significantly under-produced relative to solar in all of our models. Nevertheless, neutrino induced r-process seed production brings these abundances up much closer to the solar value.

Since many processes contribute to the solar abundances, it is more reasonable to compare our abundances with those measured in the atmospheres of low metallicity halo stars. In Figure 4.12, we show the abundances of four low metallicity halo stars with sub-solar Ge abundances. The abundance data are taken from Westin et al., 2000, Roederer et al., 2012, and Roederer et al., 2014 for the stars HD 115444, 122563, 108317, and 128279, which have metallicities of  $[\text{Fe}/\text{H}] = -3.0, -2.7,$

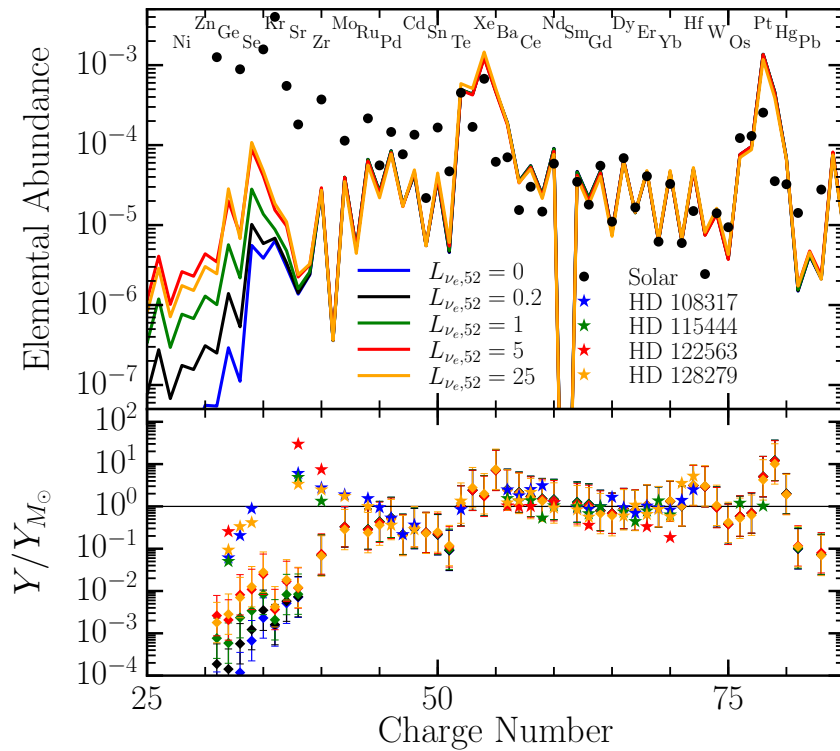


Figure 4.12: *Top Panel:* The integrated elemental abundances in the ejecta of model M12-7-S9 for a range of imposed neutrino luminosities compared to arbitrarily scaled solar r-process abundances. We include the name of every other element to guide the eye. *Bottom Panel:* Ratio of the calculated abundances to the solar abundances (from Arlandini et al., 1999). In the lower panel, factor of three error bars are included on our calculated abundance patterns to approximately account for errors in the input nuclear physics. The solar r-process abundances have been transformed by an overall scaling factor to minimize the residuals in log space in the region  $40 < Z < 81$ . We also include abundances from the low metallicity halo stars HD 115444 and 122563 (Westin et al., 2000) and HD 108317 and 128279 (Roederer et al., 2012, 2014), with  $[\text{Fe}/\text{H}]$  of  $-3.0$ ,  $-2.7$ ,  $-2.5$ , and  $-2.5$ , respectively. The observational error bars are smaller than the plotted symbols and the abundances patterns have been scaled by a factor to minimize the deviation from the solar r-process in the range  $40 < Z < 81$ .

$-2.5$ , and  $-2.5$ , respectively. These metallicities are low enough such that s-process contamination from low mass stars is highly unlikely (e.g., Simmerer et al., 2004). Nonetheless, it is possible that the s-process in massive stars may have contributed to these abundances (e.g., Woosley et al., 2002).

We can compare our predicted abundances with observed abundances of Ge, As, and Se in low metallicity halo stars. For these elements, neutrino induced r-process seed production of the first peak brings the abundances of Ge, As, and Se closer to agreement with the observed values for larger values of the electron neutrino luminosity, even though the abundances are still small by close to a factor of ten. Given the significant uncertainties in the level of neutrino irradiation and the properties of nuclei far from stability near and below the first peak, the actual amount of first peak material created by neutrino induced seed production is highly uncertain. If first peak production could be increased by around an order of magnitude, certain low metallicity halo star abundance patterns above Zn can possibly be explained by only invoking nucleosynthesis in the dynamical ejecta of BHNS mergers, although there are clearly a number of other possible ways to produce the first peak in the material ejected from the disk e.g. Just et al., 2015. This contrasts with the results of Wanajo et al., 2014 for binary NS mergers, where they find that the first peak nuclei are produced with a ratio to the second and third peak that is close to the ratio observed in the sun and therefore are over producing the first peak by about a factor of ten relative to the low metallicity halo star abundances. In contrast to Ge, As, and Se, all the BHNS merger outflows under-produce Sr by orders of magnitude and the final abundances of Sr and Zr are insensitive to the level of neutrino irradiation.

#### 4.4 Conclusions

In this work, we have considered nucleosynthesis in the ejecta of BHNS mergers including the effect of neutrino interactions. Starting from general relativistic hydrodynamic simulations of BHNS mergers with reasonably high BH spins, we have extracted the unbound material and mapped it into a Newtonian SPH code, *StarSmasher*. We then evolved the ejecta over a long enough time to reach homologous expansion. Using the Lagrangian histories of the SPH particles, we then performed post-processing calculations of nucleosynthesis in the neutron-rich ejecta with *SkyNet*. In particular, we focused on the influence of neutrinos on the nucleosynthesis in these outflows by parameterizing the neutrino luminosity coming from the disk.

As is expected from previous work (e.g. Lattimer et al., 1977; Freiburghaus et al., 1999; Roberts et al., 2011; Korobkin et al., 2012; Foucart et al., 2014; Bauswein et al., 2014b), we find that the second and third r-process peaks are robustly produced in the outflow. In contrast to the case of NSNS mergers (Wanajo et al., 2014; Goriely et al., 2015; Sekiguchi et al., 2015), we find that—for reasonable luminosities of  $L_{\nu_e} = \{0, 0.2, 1, 5, 25\} \times 10^{52} \text{ erg s}^{-1}$ —neutrinos are unable to significantly shift the distribution of the pre-r-process electron fraction in the ejecta and almost all of the ejected mass elements produce the full r-process. This is due to the rapid outflow timescales of the tidal ejecta and the relatively low expected neutrino luminosities of the disk formed around the remnant BH. Additionally, we find that there are negligible differences between the nucleosynthesis calculated for different BHNS binary parameters.

Although weak interactions have no gross effect on the electron fraction distribution, we find they do alter nucleosynthesis in more subtle ways. Once r-process neutron captures have begun, electron neutrino captures can turn a small fraction of the neutrons into protons due to the  $\alpha$ -effect (Fuller and Meyer, 1995). These protons form alpha particles which rapidly combine to form  $^{12}\text{C}$ . This provides a source of low mass seed nuclei for the r-process (Meyer et al., 1998) and results in nuclear flow below mass 78 that is not present in low entropy outflows when neutrinos are neglected. In the few hundred milliseconds before neutron exhaustion, this flow can build up a significant amount of material in the first r-process peak at mass 78. This process is likely to operate both in the dynamical ejecta of BHNS mergers and binary NS mergers, as well as in material that is ejected from the disks left over in these events, which we did not consider in this work.

Although this neutrino induced seed production produces the first peak, we find that it does not produce enough material to bring the final abundance distributions into agreement with the solar r-process distribution below mass 80. Nonetheless, this first peak production will be interesting when comparing with the abundance patterns of low metallicity halo stars. In particular, it can significantly increase the abundance of the elements Ge, As, and Se present in these outflows.

Further work is required to determine how robust neutrino induced r-process seed production is to variations in beta-decay lifetimes and neutron capture rates around the  $N = 50$  closed shell. Additionally, employing more realistic fission fragment distributions than the ones employed here may also effect the abundances found just above the first r-process peak. Of course, this process is sensitive to the electron

neutrino flux in the outflow. Here, we have chosen to parameterize the neutrino luminosity. Therefore, better models of the electron neutrino irradiation of the outflow are required to determine if neutrino induced r-process seed production is robust in nature. The results are likely to be somewhat sensitive to the beta-decay rates away from stability below  $Z = 28$ , so better measurements of decays along the r-process path could shed significant light on whether or not this process is important in the ejecta of BHNS mergers. It will also be interesting to investigate if this process operates in other environments with low  $Y_e$  outflows, namely the ejecta of binary NS mergers and material ejected from disks formed after compact object mergers.

### **Acknowledgements**

LR acknowledges Yongzhong Qian and Projjwal Banerjee for useful discussions relating to this work.

Support for this work was provided by NASA through Einstein Postdoctoral Fellowship grants numbered PF3-140114 (LR) and PF4-150122 (FF) awarded by the Chandra X-ray Center, which is operated by the Smithsonian Astrophysical Observatory for NASA under contract NAS8-03060. JL and CDO are partially supported by the NSF under award Nos. TCAN AST-1333520, CAREER PHY-1151197, and AST-1205732, and by the Sherman Fairchild Foundation. JCL is supported by NSF grant number AST-1313091. This work also benefitted from NSF support through award No. PHY-1430152 (JINA Center for the Evolution of the Elements). M.D.D. acknowledges support through NSF Grant PHY-1402916.

## NUCLEOSYNTHESIS IN HMNS DISK WINDS

*This chapter has been accepted for publication in the Monthly Notices of the Royal Astronomical Society and a preprint version was published on the arXiv ([1703.06216 \[astro-ph.HE\]](https://arxiv.org/abs/1703.06216)). I am the primary author, wrote the majority of the text, performed all nucleosynthesis calculations and data analysis of the nucleosynthesis, and I created all the figures.*

© 2017 Jonas Lippuner and coauthors

## Signatures of hypermassive neutron star lifetimes on r-process nucleosynthesis in the disk ejecta from neutron star mergers

**Jonas Lippuner<sup>1</sup>, Rodrigo Fernández<sup>2,3,4</sup>, Luke F. Roberts<sup>5,6</sup>, Francois Foucart<sup>7,8</sup>, Daniel Kasen<sup>3,4,8</sup>, Brian D. Metzger<sup>9</sup>, Christian D. Ott<sup>1,10</sup>**

<sup>1</sup> TAPIR, Walter Burke Institute for Theoretical Physics, MC 350-17, California Institute of Technology, Pasadena, California 91125, USA

<sup>2</sup> Department of Physics, University of Alberta, Edmonton, AB T6G 2E1, Canada

<sup>3</sup> Department of Physics, University of California, Berkeley, CA 94720, USA

<sup>4</sup> Department of Astronomy & Theoretical Astrophysics Center, University of California, Berkeley, CA 94720, USA

<sup>5</sup> National Superconducting Cyclotron Laboratory, Michigan State University, East Lansing, MI 48824, USA

<sup>6</sup> Department of Physics and Astronomy, Michigan State University, East Lansing, MI 48824, USA

<sup>7</sup> NASA Einstein Fellow

<sup>8</sup> Nuclear Science Division, Lawrence Berkeley National Laboratory, Berkeley, CA 94720, USA

<sup>9</sup> Columbia Astrophysics Laboratory, Columbia University, New York, NY 10027, USA

<sup>10</sup> Center for Gravitational Physics and International Research Unit of Advanced Future Studies, Yukawa Institute for Theoretical Physics, Kyoto University, Kyoto, Kyoto Prefecture 606-8317, Japan

### Abstract

We investigate the nucleosynthesis of heavy elements in the winds ejected by accretion disks formed in neutron star mergers. We compute the element formation in disk outflows from hypermassive neutron star (HMNS) remnants of variable lifetime, including the effect

of angular momentum transport in the disk evolution. We employ long-term axisymmetric hydrodynamic disk simulations to model the ejecta, and compute r-process nucleosynthesis with tracer particles using a nuclear reaction network containing  $\sim 8000$  species. We find that the previously known strong correlation between HMNS lifetime, ejected mass, and average electron fraction in the outflow is directly related to the amount of neutrino irradiation on the disk, which dominates mass ejection at early times in the form of a neutrino-driven wind. Production of lanthanides and actinides saturates at short HMNS lifetimes ( $\lesssim 10$  ms), with additional ejecta contributing to a blue optical kilonova component for longer-lived HMNSs. We find good agreement between the abundances from the disk outflow alone and the solar r-process distribution only for short HMNS lifetimes ( $\lesssim 10$  ms). For longer lifetimes, the rare-earth and third r-process peaks are significantly under-produced compared to the solar pattern, requiring additional contributions from the dynamical ejecta. The nucleosynthesis signature from a spinning black hole (BH) can only overlap with that from a HMNS of moderate lifetime ( $\lesssim 60$  ms). Finally, we show that angular momentum transport not only contributes with a late-time outflow component, but that it also enhances the neutrino-driven component by moving material to shallower regions of the gravitational potential, in addition to providing additional heating.

*Subject headings:* accretion, accretion disks — dense matter — gravitational waves — hydrodynamics — neutrinos — nuclear reactions, nucleosynthesis, abundances

## 5.1 Introduction

The astrophysical origin of chemical elements formed through the rapid neutron capture process (r-process) remains an open problem in nuclear astrophysics. Observed abundances in metal-poor Galactic halo stars demand a mechanism that produced a robust abundance pattern – mirroring that in the Solar System – for elements with mass number  $A \gtrsim 130$  (e.g., Sneden et al., 2008). This mechanism must also have operated since early on in cosmic history, since r-process elements are found in very old metal-poor stars (e.g., Cowan et al., 1999; Ji et al., 2016). In contrast, observed abundances of light r-process elements in metal-poor stars show deviations from the solar system pattern relative to heavier elements (e.g., Montes et al., 2007). Meteoritic abundances point to different formation timescales for light and heavy r-process elements, suggesting that there might be more than one dominant formation site (Wasserburg et al., 1996).

Core-collapse supernovae may be able to produce light r-process elements ( $A \lesssim 130$ ), but recent work indicates that they are most likely not the dominant source of heavy r-process elements (e.g., Roberts et al., 2010; Fischer et al., 2010; Hudepohl

et al., 2010; Martínez-Pinedo et al., 2012; Wanajo, 2013). On the other hand, mergers of binaries containing two neutron stars (NSNS) or a neutron star and a black hole (NSBH) have long been considered as candidate r-process sites, given the highly neutron-rich conditions achieved in the ejected material (Lattimer and Schramm, 1974). The study of NSNS/NSBH mergers has intensified in recent years given that (1) they are likely to be detected in gravitational waves by Advanced LIGO/Virgo within the next few years (e.g., LIGO Scientific Collaboration, 2010; LIGO Scientific Collaboration et al., 2015), (2) recent developments in numerical relativity have enabled merger simulations consistent with Einstein’s equations of general relativity (e.g., Lehner and Pretorius, 2014; Paschalidis, 2017), and (3) the electromagnetic signal from these events can aid with the localization of these sources and provide information complementary to that carried by gravitational waves (e.g., Rosswog, 2015; Fernández and Metzger, 2016; Tanaka, 2016).

Recent work has shown that the dynamical ejecta from NSNS/NSBH mergers can produce a robust Solar abundance pattern for  $A \gtrsim 130$  by virtue of *fission cycles* (e.g., Goriely et al., 2005), with little sensitivity to binary parameters or the equation of state (e.g., Goriely et al., 2011; Korobkin et al., 2012; Bauswein et al., 2013), depending instead on nuclear physics properties such as the fission fragment distribution (e.g., Eichler et al., 2015). When neutrino absorption is included in the calculations, a larger fraction of lighter elements ( $A < 130$ ) can be obtained (e.g., Wanajo et al., 2014; Goriely et al., 2015; Sekiguchi et al., 2015; Radice et al., 2016; Foucart et al., 2016a,b; Roberts et al., 2017).

In addition to the dynamical ejecta, the accretion disk formed in NSNS/NSBH mergers can eject a significant amount of material on timescales longer than the dynamical time (e.g., Ruffert et al., 1997; Lee et al., 2009; Metzger et al., 2009b). The neutron-to-seed ratio of this material is lower than that in the dynamical ejecta, because the longer evolutionary timescales allow weak interactions to modify the composition more significantly (e.g., Dessart et al., 2009; Fernández and Metzger, 2013; Perego et al., 2014). Matter can be ejected on the thermal timescale of the disk ( $\sim 30$  ms, Section 5.2.3) by neutrino energy deposition, or on much longer timescales ( $\sim 1$  s, Section 5.2.3) by a combination of angular momentum transport processes and nuclear recombination. The amount of mass ejected by the disk on the longer timescale can be comparable to that in the dynamical ejecta e.g., Fernández and Metzger, 2016, while the neutrino-driven component is significant only when a hypermassive neutron star (HMNS) phase precedes black hole (BH) formation

(Dessart et al., 2009; Fernández and Metzger, 2013; Metzger and Fernández, 2014; Just et al., 2015).

Early work on nucleosynthesis from NSNS/NSBH merger disks focused on neutrino-driven outflows and used a parametric treatment to obtain thermodynamic trajectories for composition analysis (e.g., Surman et al., 2008; Wanajo and Janka, 2012), finding that conditions for both light and heavy r-process elements are possible in these outflows. More recent work has employed tracer particles from long-term hydrodynamic simulations of the disk when a BH is the central object (Just et al., 2015; Wu et al., 2016). These studies have found that the outflow generates a robust abundance of elements around  $A = 130$ , with significant production of lighter elements, and a variable yield of heavy r-process elements that depends on binary properties and disk physics. The case of a HMNS at the center was studied by Martin et al., 2015 using tracer particles from a time-dependent simulation that considered the neutrino-driven wind phase (Perego et al., 2014). The resulting outflow generates primarily nuclei with  $A < 130$ , with a significant dependence of the yield on latitude and ejection time. The long-term (viscous) outflow was not captured, however, and the lifetime of the HMNS was accounted for only by looking at subsets of particles that were ejected before a certain time.

In this study, we analyze the nucleosynthesis yields from the long-term outflow generated by an accretion disk around a HMNS of variable lifetime. Following the approach of Metzger and Fernández, 2014, we conduct a number of long-term disk simulations in which the HMNS transforms into a BH at different times. This parameterized approach does not require the assumption of a particular equation of state of dense matter. It is also independent of the complex processes that determine transport of angular momentum and cooling, all of which set the survival time of the HMNS (e.g., Paschalidis et al., 2012; Kaplan et al., 2014). In order to obtain nucleosynthesis yields, tracer particles are injected in the disk initially, and the resulting thermodynamic trajectories are analyzed with the nuclear reaction network *SkyNet* (Lippuner and Roberts, 2015, 2017).

This paper is structured as follows. Section 5.2 describes the numerical method employed and the models studied. Results are presented and discussed in section 5.3, and we conclude in section 5.4. The appendix contains further details about our numerical implementation.

## 5.2 Methods

### 5.2.1 Disk outflow simulations and thermodynamic trajectories

The long-term evolution of the accretion disk is computed using the approach described in Metzger and Fernández (2014). In short, the equations of Newtonian hydrodynamics and lepton number conservation are solved with the FLASH code (Fryxell et al., 2000; Dubey et al., 2009) assuming axisymmetry (2D). Source terms include gravity via a pseudo-Newtonian potential, shear viscosity with an  $\alpha$  prescription (Shakura and Sunyaev, 1973), and contributions due to neutrino absorption and emission to the lepton number and energy equations. A pseudo-Newtonian potential, such as that from Artemova et al. (1996), approximates the effect of a Schwarzschild or Kerr metric by providing an innermost stable circular orbit (ISCO) in an otherwise Newtonian hydrodynamic simulation. Other aspects, such as the angular dependence of the Kerr metric, are not captured.

Neutrinos are implemented in a leakage scheme for cooling and a disk light-bulb approximation for self-irradiation. Only charged-current interactions are included, since they have the largest cross-section, exchange energy with matter, and drive the evolution of the electron fraction. The HMNS is approximated as a reflecting sphere with a radius of 30 km and a rotation period of 1.5 ms. A time-dependent, isotropic outward neutrino flux is imposed on the HMNS surface with a constant value up to 10 ms and a time dependence  $t^{-1/2}$  (e.g., Pons et al., 1999) thereafter, with  $t$  being the physical simulation time. The electron neutrino and antineutrino luminosities have the same magnitude, which we normalize to  $2 \times 10^{52}$  erg s<sup>-1</sup> at 30 ms, roughly matching the results of Dessart et al. (2009):

$$L_\nu = L_{\bar{\nu}} = 2\sqrt{3} \times 10^{52} \left[ \max \left( 1, \frac{t}{10 \text{ ms}} \right) \right]^{-1/2} \text{ erg s}^{-1}. \quad (5.1)$$

The neutrino and antineutrino temperatures are different, however, chosen to be 4 and 5 MeV, respectively, which roughly corresponds to the values found in proto-neutron stars in core-collapse supernovae (e.g., Janka, 2001). Thus, the mean neutrino energies from the HMNS are fixed at  $\langle E_\nu \rangle = 12.6$  MeV and  $\langle E_{\bar{\nu}} \rangle = 15.8$  MeV (assuming a Fermi-Dirac distributions of neutrinos, the mean energy is given by  $\langle E_\nu \rangle = 3.151 k_B T_\nu$ , where  $k_B$  is the Boltzmann constant and  $T_\nu$  is the neutrino temperature). These mean neutrino energies from the HMNS are broadly consistent with results from numerical relativity simulations that include neutrino transport (Foucart et al., 2016a). The HMNS is transformed into a BH by switching the inner radial boundary from reflecting to absorbing and setting the HMNS neutrino

luminosities to zero. The viscous stress is also set to zero at this boundary when the BH forms. See Metzger and Fernández (2014) for more details.

The initial condition for most models is an equilibrium torus obtained by solving the Bernoulli equation with constant specific angular momentum and electron fraction  $Y_e = 0.1$  (e.g., Papaloizou and Pringle, 1984; Fernández and Metzger, 2013). Outside the torus, the computational domain is filled with a low-density ambient medium that follows a power-law in radius, with an initial normalization  $\sim 9$  orders of magnitude below the maximum torus density ( $\rho_{\text{max}} \sim 10^{11} \text{ g cm}^{-3}$ ). The density floor inside 200 km decreases with time toward a constant asymptotic value of  $10 \text{ g cm}^{-3}$  over a timescale of  $\sim 100$  ms. In addition, one model initializes the disk using a snapshot from a general-relativistic NSBH simulation reported in Foucart et al. (2015). Details about the mapping procedure can be found in Fernández et al. (2017). Improvements to the code relative to Metzger and Fernández (2014) include the use of separate neutrino temperatures for disk self-irradiation, and a correction to the weak interaction rates; details are provided in the Appendix.

Passive tracer particles record thermodynamic quantities as a function of time, and the resulting information is used as input for the nuclear reaction network calculations (Section 5.2.2). The initial particle locations are randomly sampled to follow the mass distribution in the disk. We place 10,000 particles initially in all simulations. If there is a BH at the center, particles can fall into it, which then reduces the total number of tracer particles. Fluid quantities are obtained at each time step from the grid by linear interpolation. When a HMNS is at the center, the reflecting boundary for particles is placed one cell outside the inner radial boundary to prevent particle trapping in a ‘trench’ of small-magnitude negative radial velocity that forms in the active cells adjacent to this boundary. The small size of this innermost radial cell relative to the inner boundary radius ( $\Delta r/r \approx 1.8\%$ ) ensures that the effect on the particle dynamics is minimal considering all other approximations being made.

Most hydrodynamic simulations are evolved up to about 10 s of physical time (Section 5.2.3), which is sufficient for r-process nucleosynthesis that takes place within a few seconds. To obtain the final abundances, however, the nuclear reaction network needs to be evolved for tens of years, since some of the isotopes produced by the r-process have very long half-lives. One caveat with this post-processing approach is that the energy released by the nuclear reactions does not feed back into the hydrodynamic evolution of the fluid. Nuclear heating may slightly change the morphology of the ejecta at late times (see, e.g., figure 8 of Fernández et al., 2015b)

and influence specific features of the nucleosynthesis indirectly via the amount of convection in the outflow (Wu et al., 2016, see also Section 5.3.4.1).

### 5.2.2 Nuclear reaction network: *SkyNet*

We employ the nuclear reaction network *SkyNet* for the r-process nucleosynthesis calculations (Lippuner and Roberts, 2015). For each thermodynamic trajectory (Section 5.2.1), we begin the reaction network evolution once the temperature falls below 10 GK or reaches its maximum, if the maximum is less than 10 GK. Since the composition is given by nuclear statistical equilibrium (NSE) at temperatures above 10 GK, there is no need to start the reaction network evolution at higher temperatures.

*SkyNet* includes the specific viscous heating and neutrino heating/cooling rates recorded by the thermodynamic trajectories, and adds to these a self-consistent calculation of heating from nuclear reactions. In addition to the neutrino heating/cooling rate, the associated rates of neutrino interactions with free neutrons and protons are also given by the thermodynamic trajectories and evolved in *SkyNet*. The included reactions are electron (anti) neutrino emission ( $p + e^- \rightarrow n + \nu_e$ ,  $n + e^+ \rightarrow p + \bar{\nu}_e$ ) and neutrino absorption ( $n + \nu_e \rightarrow p + e^-$ ,  $p + \bar{\nu}_e \rightarrow n + e^+$ ).

*SkyNet* evolves the abundances of 7843 nuclides, ranging from free neutrons and protons to  $^{337}\text{Cn}$ , and includes over 140,000 nuclear reactions. The strong reaction rates are taken from the JINA REACLIB database (Cyburt et al., 2010), but only the forward rates are used and the inverse rates are computed from detailed balance. Spontaneous and neutron-induced fission rates are taken from Frankel and Metropolis (1947), Panov et al. (2010), Mamdouh et al. (2001), and Wahl (2002). Most of the weak rates come from Fuller et al., 1982, Oda et al., 1994, and Langanke and Martínez-Pinedo, 2000 whenever they are available, and otherwise the REACLIB weak rates are used. The nuclear masses and partition functions used in *SkyNet* are taken from the WebNucleo XML file distributed with REACLIB, which contains experimental data where available and finite-range droplet macroscopic model (FRDM, see, e.g., Möller et al., 2016) data otherwise.

### 5.2.3 Investigated models

Table 5.1 summarizes the properties of all investigated models. The main focus of this study is the outflow from a disk around a HMNS of variable lifetime. Our baseline sequence follows the parameter choices of Metzger and Fernández (2014): a HMNS mass of  $3 M_\odot$  arising from an NSNS merger, with an initial disk mass

Table 5.1: List of investigated models. Columns from left to right show the model name, the compact central object (CCO) type (HMNS or BH), mass  $M_c$  of the CCO, lifetime  $\tau$  of the HMNS, dimensionless spin  $\chi$  of the BH (the HMNSs all spin at 1.5 ms), radius  $R_d$  of the initial disk density peak, and viscosity parameter  $\alpha$ .

Model	CCO	$M_c$ ( $M_\odot$ )	$\tau$ (ms)	$\chi$	$R_d$ (km)	$\alpha$
H000	HMNS	3	0	0	50	0.03
H010			10			
H030			30			
H100			100			
H300			300			
Hinf			$\infty$			
B070	BH	3	0	0.7	50	0.03
B090				0.9		
BF15	BH	8.1	0	0.86	55	0.03
HinfNoVisc	HMNS	3	$\infty$	0	50	0

$M_d = 0.03 M_\odot$  chosen as a representative case of disk masses obtained in NSNS mergers (e.g., Hotokezaka et al., 2013b). We prescribe the lifetime  $\tau$  of the HMNS to be 0, 10, 30, 100, or 300 ms, after which the HMNS collapses to a non-spinning BH. We also run one case, denoted by  $\tau = \infty$ , in which the HMNS does not collapse. The HMNS models are denoted by H000, H010, H030, H100, H300, and Hinf, according to their lifetime. Other disk parameters are: density peak radius  $R_d = 50$  km, viscosity parameter  $\alpha = 0.03$ , constant initial entropy of  $8 k_B$  baryon $^{-1}$ , constant initial  $Y_e = 0.1$ , and maximum evolution time of 8.7 s. These choices are motivated to be broadly compatible with results from dynamical merger simulations (e.g., Ruffert et al., 1997; Oechslin and Janka, 2006; Foucart et al., 2016a) and from studies of angular momentum transport in fully-ionized accretion disks (e.g., Davis et al., 2010).

There are three important timescales in the problem: the orbital time at the initial disk density peak,

$$t_{\text{orb}} \simeq 3 \left( \frac{R_d}{50 \text{ km}} \right)^{3/2} \left( \frac{3 M_\odot}{M_c} \right)^{1/2} \text{ ms}, \quad (5.2)$$

where  $M_c$  is the mass of the central object (HMNS or BH); the initial thermal time in the disk,

$$t_{\text{th}} \simeq 30 \left( \frac{M_d}{0.03 M_\odot} \right) \left( \frac{e_{i,d}}{10^{19} \text{ erg g}^{-1}} \right) \left( \frac{2}{L_{v,52}} \right) \text{ ms}, \quad (5.3)$$

where  $e_{i,d}$  is the initial specific internal energy of the disk (a byproduct of shock heating during the dynamical phase of the merger) and  $L_{v,52}$  is a typical neutrino luminosity from the disk in units of  $10^{52}$  erg s<sup>-1</sup> (neutrino cooling is in approximate balance with viscous heating at early times); and the initial viscous time of the disk,

$$t_{\text{visc}} \simeq 200 \left( \frac{0.03}{\alpha} \right) \left( \frac{0.3}{H/R} \right)^2 \left( \frac{R_d}{50 \text{ km}} \right)^{3/2} \left( \frac{3 M_\odot}{M_c} \right)^{1/2} \text{ ms}, \quad (5.4)$$

where  $H/R$  is the height-to-radius ratio of the disk. Outflows driven primarily by neutrino energy deposition are expected to be launched on the thermal timescale (equation 5.3), whereas long-term outflows are launched on the viscous timescale (equation 5.4). The latter becomes longer with time, as the disk spreads out and most of the mass in the disk resides at an increasingly larger radius (e.g., Metzger et al., 2009a). Therefore, the length of the simulations has to be several viscous timescales, which translates into thousands of orbits. We define convergence in mass ejection from the disk as a saturation in the cumulative mass crossing some radius far away from the disk ( $10^9$  cm). This way, we generally require  $3000 t_{\text{orb}}$ , or about  $\sim 10$  s for each simulation.

In order to examine the impact of the central compact object on the nucleosynthesis, we evolve two additional models with spinning BHs at the center, following the approach of Fernández et al. (2015a). The BH mass is  $M_c = 3 M_\odot$  in both cases and the dimensionless spin parameter  $\chi = Jc/(GM_c^2)$  is 0.7 or 0.9, where  $J$  is the BH angular momentum,  $c$  is the speed of light, and  $G$  is the gravitational constant. These models are labeled B070 and B090, according to their spin. Other parameters are the same as in the HMNS models. In addition, we investigate the effect of the disk compactness (mass of the central compact object divided by the disk density peak radius,  $M_c/R_d$ , which measures the strength of the gravitational field) by evolving a model in which the initial condition is taken from a snapshot of a general-relativistic simulation of a NSBH merger from Foucart et al. (2015), including only the remnant accretion disk. This model has a BH mass of  $8.1 M_\odot$  and a disk density peak radius of 55 km, resulting in a gravitational potential that is 2.5 times stronger than our fiducial case (which better approximates the remnant of an NSNS merger). The model is denoted by BF15, and the mapping details are described in Fernández et al. (2017).

Finally, we evolve a test model that mirrors the case of a HMNS with  $\tau = \infty$ , but with the viscosity parameter set to zero, in order to eliminate angular momentum transport and viscous heating. This model, denoted by HinfNoVisc, experiences an

outflow driven solely by neutrino heating (possibly aided by nuclear recombination), and is evolved in order to compare results with Martin et al. (2015). The model is evolved for a longer time (14.5 s) since mass ejection converges more slowly with time relative to the viscous case.

### 5.3 Results and discussion

#### 5.3.1 Overview of disk evolution

The evolution of the disk and especially the neutrino interactions occurring in the disk set the stage for the outflow and determine its properties. In this section, we present a brief summary of the disk evolution, which was described in detail in Fernández and Metzger (2013) and Metzger and Fernández (2014).

When a HMNS is present, transport of angular momentum causes accreting material to form a boundary layer around the reflecting stellar surface. The outer regions of the disk expand on a thermal timescale (equation 5.3) due to energy injection by neutrino heating and viscous heating. Upon collapse of the HMNS to a BH, the boundary layer is swallowed, and a rarefaction wave moves outward from the inner boundary, quenching the thermal outflow (cf. Figure 3 of Metzger and Fernández, 2014). The disk re-adjusts on a thermal timescale, and joins the evolutionary path of a BH accretion disk, which changes on a viscous timescale (equation 5.4).

The high densities achieved on the equatorial plane of HMNS disks ( $\sim 10^{11} \text{ g cm}^{-3}$ ) are enough to locally trap neutrinos, resulting in two emission hot spots at mid latitudes and adjacent to the HMNS surface. The high densities in the midplane also result in shadowing of the outer disk, with neutrino irradiation concentrated at latitudes  $\sim 30^\circ$  away from the equator (cf. Figure 2c of Metzger and Fernández, 2014). This general neutrino irradiation geometry is also found when better (Monte Carlo) radiation transport is performed on snapshots of HMNS disk models (Richers et al., 2015).

The high densities near the boundary layer cause the electron fraction in the inner regions of the HMNS disk ( $r < 10^7 \text{ cm}$ , and within  $\sim 30^\circ$  from the equatorial plane) to remain low ( $Y_e \sim 0.1 - 0.2$ ) relative to the outer regions. Away from the midplane, the weak interaction timescale becomes shorter, and material that enters the boundary layer at high latitude reaches  $Y_e \sim 0.5$  within an orbital timescale, as it transits through the hot spot in neutrino emission. Material ejected within  $\sim 45^\circ$  of the rotation axis has therefore high electron fraction relative to the rest of the outflow. At  $t = t_{\text{th}}$ , most of the disk material within  $r = 10^7 \text{ cm}$  is close to beta

equilibrium, with  $Y_e \sim 0.2 - 0.3$  in the outer regions. As the disk approaches a viscous timescale, the density in the inner disk gradually decreases, resulting in two effects: (1) the equilibrium  $Y_e$  of the inner disk increases as the degeneracy of the material decreases, and (2) the strength of the weak interactions decreases, until weak interactions become slow relative to the viscous time (e.g., Metzger et al., 2009a). These two effects combine to leave material close to the HMNS with  $Y_e \sim 0.4$ . As long as the HMNS does not collapse, most of this material will eventually be ejected.

The BH accretion disk is such that the inner regions ( $r < 10^7$  cm) also approach beta equilibrium, but most of the material that reaches high  $Y_e$  is accreted onto the BH (cf. Figure 6 of Fernández and Metzger, 2013). The fraction of the high- $Y_e$  material that is ejected is a function of the spin of the BH, since a smaller ISCO slows down accretion and allows material to reach regions where weak interactions are stronger, before being ejected (Fernández et al., 2015a). Upon collapse of the HMNS into a BH, a low density funnel of width  $\sim 45^\circ$  around the rotation axis is created as material that has not yet been unbound is swallowed. Boundary layer material reaches the highest  $Y_e$  as it crosses the emission hot spots of the HMNS disk before being ejected, hence formation of the BH precludes further ejection of material with  $Y_e \sim 0.5$ . For the disk masses simulated, the material becomes optically thin within a few orbits if a BH is at the center, therefore hot spots also disappear upon collapse of the HMNS.

### 5.3.2 Neutrino emission

The total electron neutrino and antineutrino luminosities from the disk and the HMNS (if present) as a function of time are shown in the left panel of Figure 5.1. The disk luminosities are very similar to the luminosity from the HMNS as long as the latter does not collapse, because the disk absorbs and re-radiates the neutrinos emitted by the HMNS. When the HMNS collapses, the disk luminosities undergo a sudden decrease, and then follow a broken powerlaw as the disk re-adjusts and continues to evolve on the viscous timescale. Thereafter,  $L_{\bar{\nu}_e}$  starts to dominate over  $L_{\nu_e}$  in all models because the initial neutron-rich ( $Y_e = 0.1$ ) composition of the disk causes weak interactions to leptonize it, with more positron captures than electron captures (the gradual drop in density over the viscous timescale increases the equilibrium  $Y_e$  of the disk; Section 5.3.1). As long as the HMNS is present, the disk neutrino luminosities are approximately the same in all cases, consistent with re-radiation of the HMNS luminosities, and the different models are separated by a

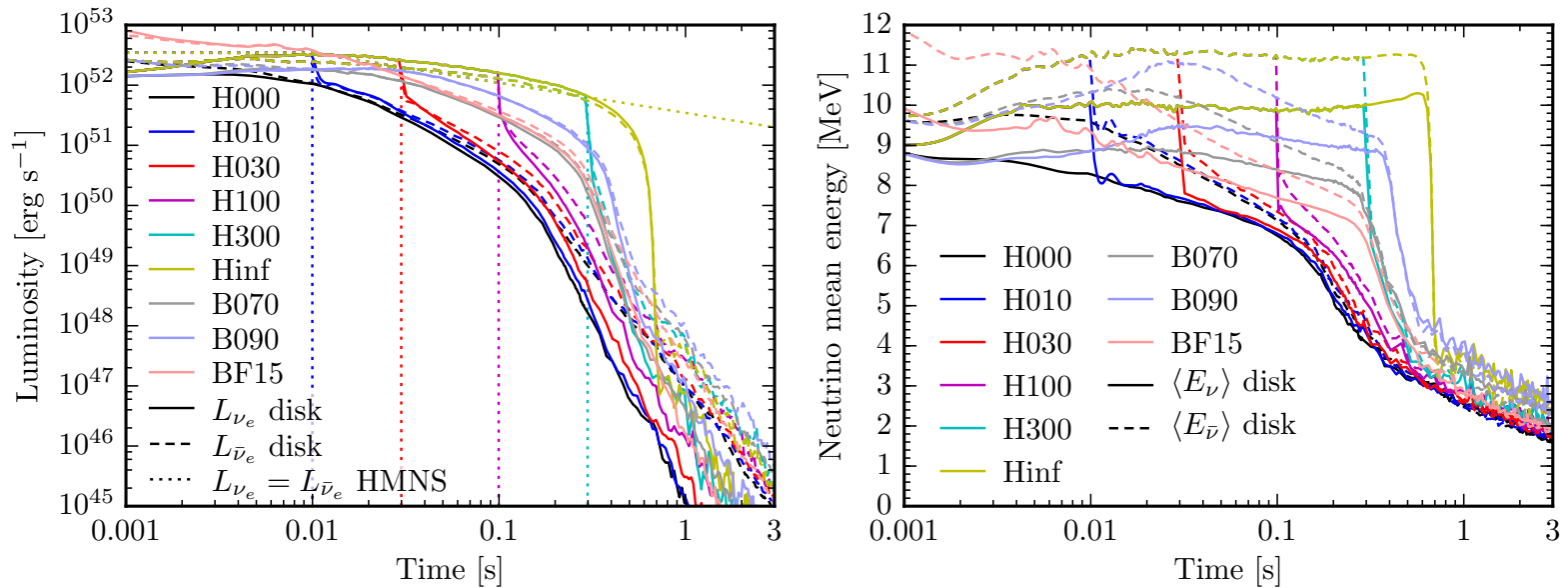


Figure 5.1: **Left:** Neutrino luminosities as a function of time for most models studied in this paper (see Table 5.1 for a summary). Shown are electron neutrinos (solid lines) and electron antineutrinos (dashed lines) emitted by the disk, as well as the imposed neutrino/antineutrino emission from the HMNS surface (dotted lines, equation 5.1). Sharp drops in the dotted lines mark the collapse of the HMNS into a BH. **Right:** Mean energies of electron neutrinos (solid lines) and electron antineutrinos (dashed lines) emitted by the disk. The mean energies of neutrinos and antineutrinos emitted by the HMNS are fixed at 12.6 MeV and 15.8 MeV, respectively.

shift in time depending on the lifetime of the HMNS.

The mean neutrino energies emitted by the disk are shown in the right panel of Figure 5.1. Given the low initial abundance of protons, the optical depth for antineutrinos is initially low, and antineutrino energies are higher by  $\sim 10\%$  than neutrino energies until  $t \sim t_{\text{visc}}$ , by which time the decrease in disk density has gradually lifted the degeneracy and weak interactions have driven the inner disk close to  $Y_e \sim 0.4$ . The neutrino/antineutrino energies are the same between HMNS models until the HMNS collapses, each following the same general evolution pattern but shifted in time. Since the disk mostly re-radiates neutrinos from the HMNS, the mean neutrino energies drop sharply when the HMNS collapses.

In the models that start out with a BH at the center (B070, B090, BF15, and H000, which has  $\chi = 0$ ), a more rapidly spinning BH results in higher neutrino luminosities and mean neutrino energies. This occurs because larger spins are associated with smaller ISCO radii. Hence the disk material can convert more gravitational energy into thermal energy, resulting in more intense neutrino emission with higher mean energies. In model BF15, the central BH is more massive ( $8.1 M_\odot$  compared to  $3 M_\odot$  in H000, B070, and B090), which results in a larger ISCO radius. The disk has nearly the same density peak radius as the other models, but the initial condition is not in equilibrium. Therefore, accretion proceeds more intensely at early times than in the other BH models, speeding up the disk evolution despite its slightly longer initial viscous time (smaller  $H/R$  in equation 5.4, which overcomes the effect of a larger BH mass).

### 5.3.3 Ejecta properties

In order to associate the thermodynamic properties of the disk with the nucleosynthesis outcome from each trajectory, we use the value of the electron fraction ( $Y_{e,5\text{GK}}$ ) and specific entropy ( $s_{5\text{GK}}$ ) at the last time when the temperature of the tracer particle drops below 5 GK. For the rare cases in which the temperature of the trajectory is always below 5 GK, we use the initial values of  $Y_e$  and  $s$  for  $Y_{e,5\text{GK}}$  and  $s_{5\text{GK}}$ , respectively. Once the temperature drops below approximately 5 GK, the composition moves out of NSE and a full network evolution is required to evolve the abundances. Therefore  $Y_{e,5\text{GK}}$  and  $s_{5\text{GK}}$  are the initial conditions for nucleosynthesis. Note that the reaction network evolution starts when the temperature drops below 10 GK, but *SkyNet* can also evolve the composition while NSE holds.

The distribution of mass ejected as a function of  $Y_{e,5\text{GK}}$  is shown in Figure 5.2 for

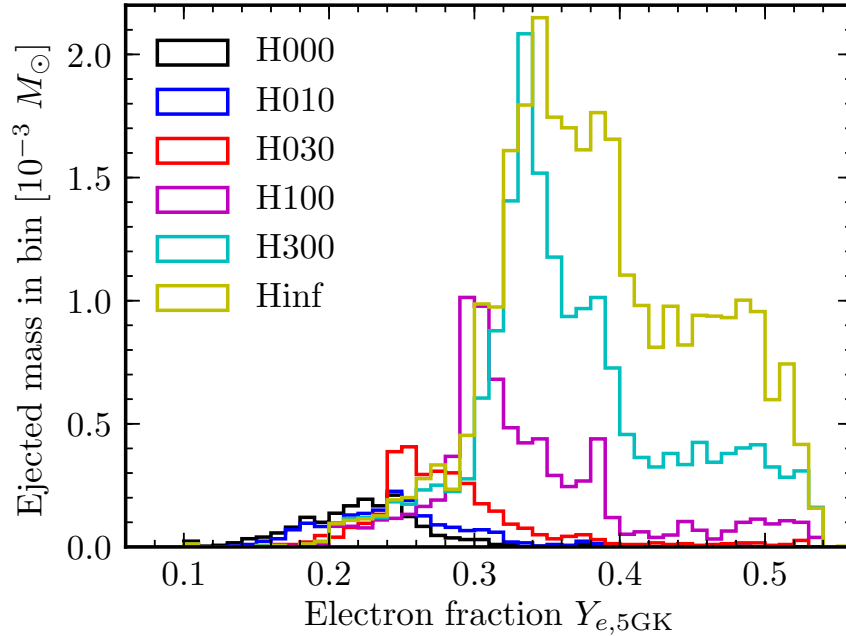


Figure 5.2: Mass distribution of the ejecta electron fraction for HMNS models at the time when the temperature is  $\geq 5$  GK for the last time for each tracer particle.

all HMNS models with non-zero viscosity. A trajectory is considered to have been ejected when it crosses the surface  $r = 10^9$  cm. There is a strong correlation between the HMNS lifetime and both the amount of mass ejected and the mean  $Y_{e,5GK}$  of the distribution (Metzger and Fernández, 2014). The disk ejecta ranges from 6 to nearly 100% of the initial disk mass. The longer the HMNS lives, the longer the disk material is subject to strong neutrino heating, which combines with viscous heating and nuclear recombination to eject material on the viscous timescale. A longer HMNS lifetime also allows more material from the inner disk to be ejected instead of being swallowed by the BH. That material from the inner disk reaches beta equilibrium and hence its ejection results in a higher mean electron fraction. Table 5.2 shows the number of ejected particles (out of the initial 10,000 particles in each model) and the total ejected mass. Also shown is the amount of mass ejected with  $Y_{e,5GK} \leq 0.25$ , which is neutron-rich enough to robustly make the full r-process (see next section and, e.g., Lippuner and Roberts, 2015).

We note that the amount of mass ejected with  $Y_{e,5GK} \leq 0.25$  is roughly constant between  $(0.5 - 0.8) \times 10^{-3} M_{\odot}$  once the HMNS lives for 30 ms or longer, despite the total ejecta mass differing by an order of magnitude. This is the result of two competing effects: a longer HMNS lifetime increases the total ejecta mass, but it also increases the average electron fraction of the ejecta, thus reducing the fraction

Table 5.2: Summary of nucleosynthesis results.  $N_{\text{ej}}$  is the number of tracer particles that reach a radius  $r = 10^9$  cm by the end of the hydrodynamic simulation (every simulation starts with 10,000 particles);  $M_{\text{ej}}$  is the total ejected mass in  $10^{-3} M_{\odot}$  at the same radius;  $M(Y_e \leq 0.25)$  is the ejected mass with  $Y_{e,5\text{GK}} \leq 0.25$ ;  $M_{\nu\text{-driv}}$  is the amount of ejected mass that is driven by neutrino interactions;  $[Y_{1\text{st}}/Y_{2\text{nd}}]$  is the  $\log_{10}$  of the ratio of the first r-process peak to the second r-process peak, normalized to the solar value, see Equation (5.5) for details;  $[Y_{\text{RE}}/Y_{2\text{nd}}]$  and  $[Y_{3\text{rd}}/Y_{2\text{nd}}]$  are the same quantities for the rare-earth and third peaks;  $\langle X_{\text{La}} \rangle$  and  $\langle X_{\text{Ac}} \rangle$  are the lanthanide and actinide mass fractions averaged over all ejecta particles; and  $\epsilon_{\text{tot}} 1 \text{ d}$  and  $\epsilon_{\text{tot}} 7 \text{ d}$  are the total heating rates of the entire ejecta at 1 and 7 days, respectively.

Model	$N_{\text{ej}}$	$M_{\text{ej}}$ ( $M_{-3\odot}$ )	$M(Y_e \leq 0.25)$ ( $M_{-3\odot}$ )	$M_{\nu\text{-driv}}$ ( $M_{-3\odot}$ )	$[Y_{1\text{st}}/Y_{2\text{nd}}]$	$[Y_{\text{RE}}/Y_{2\text{nd}}]$	$[Y_{3\text{rd}}/Y_{2\text{nd}}]$	$\langle X_{\text{La}} \rangle$	$\langle X_{\text{Ac}} \rangle$	$\epsilon_{\text{tot}} 1 \text{ d}$ ( $\text{erg s}^{-1}$ )	$\epsilon_{\text{tot}} 7 \text{ d}$ ( $\text{erg s}^{-1}$ )
H000	527	1.8	1.4	0.013	-1.3	-0.28	-0.30	$4.6 \times 10^{-2}$	$6.4 \times 10^{-3}$	$9.0 \times 10^{40}$	$1.4 \times 10^{40}$
H010	557	1.9	1.1	0.027	-1.1	-0.40	-0.50	$3.3 \times 10^{-2}$	$2.0 \times 10^{-3}$	$8.9 \times 10^{40}$	$1.3 \times 10^{40}$
H030	989	3.3	0.83	0.20	-0.64	-1.0	-1.2	$5.1 \times 10^{-3}$	$2.9 \times 10^{-4}$	$1.2 \times 10^{41}$	$1.5 \times 10^{40}$
H100	2408	7.8	0.52	1.3	-0.0053	-0.91	-1.2	$2.1 \times 10^{-3}$	$1.7 \times 10^{-4}$	$1.8 \times 10^{41}$	$1.4 \times 10^{40}$
H300	5610	18	0.67	6.4	+0.25	-0.88	-1.2	$1.1 \times 10^{-3}$	$6.7 \times 10^{-5}$	$3.3 \times 10^{41}$	$3.2 \times 10^{40}$
Hinf	9587	30	0.69	28*	+0.41	-0.86	-1.1	$7.1 \times 10^{-4}$	$4.2 \times 10^{-5}$	$5.2 \times 10^{41}$	$5.4 \times 10^{40}$
B070	1465	5.4	1.8	0.022	-0.73	-0.65	-0.67	$1.3 \times 10^{-2}$	$1.6 \times 10^{-3}$	$2.0 \times 10^{41}$	$2.4 \times 10^{40}$
B090	2363	7.9	1.6	0.070	-0.54	-0.77	-0.80	$7.6 \times 10^{-3}$	$9.7 \times 10^{-4}$	$2.7 \times 10^{41}$	$2.6 \times 10^{40}$
BF15	910	4.9	0.011	0.022	-0.26	-1.4	-1.3	$1.4 \times 10^{-3}$	$7.7 \times 10^{-5}$	$7.8 \times 10^{40}$	$6.7 \times 10^{39}$

\* Since the HMNS persists forever in model Hinf, virtually all trajectories experience significant neutrino interactions and our method becomes inadequate to isolate the component of the ejecta that is driven by neutrino interactions.

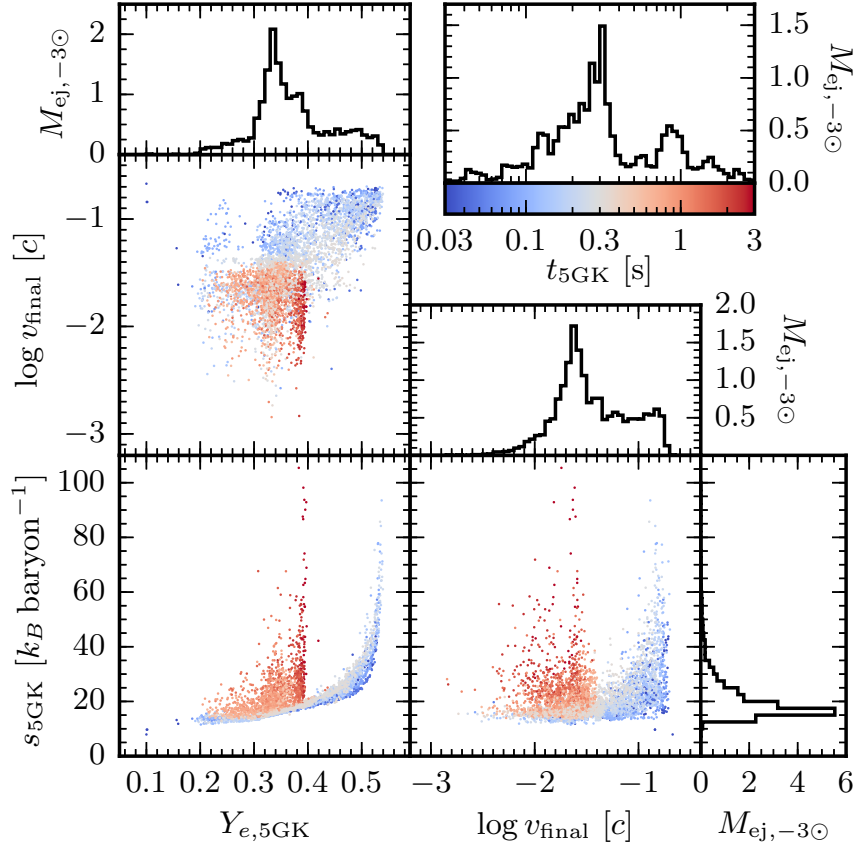


Figure 5.3: Properties of the ejecta of model H300 (central HMNS that collapse after 300 ms).  $Y_{e,5\text{GK}}$  and  $s_{5\text{GK}}$  are the electron fraction and specific entropy at the time  $t_{5\text{GK}}$ , when the temperature of the trajectory is 5 GK for the last time, while  $v_{\text{final}}$  is the final velocity of the trajectory. The scatter plot points are color coded by  $t_{5\text{GK}}$ , which marks the nucleosynthesis starting time. Blue and gray points ( $t_{5\text{GK}} \lesssim 300$  ms) start their nucleosynthesis while the HMNS is present, and are thus influenced by the neutrino irradiation from the HMNS. The strong correlation between electron fraction and entropy is similar to what is obtained in a neutrino-driven outflow. The red points ( $t_{5\text{GK}} \gtrsim 300$  ms) start nucleosynthesis after the HMNS has collapsed to a BH. Hence this component is subject primarily to the action of viscous processes and nuclear recombination in the disk. See the text for details.  $M_{\text{ej}, -3\odot}$  means the amount of ejecta mass in units of  $10^{-3} M_{\odot}$ .

of the ejected mass that has  $Y_{e,5\text{GK}} \leq 0.25$ . These two effects counteract each other, leaving the absolute amount of mass ejected with  $Y_{e,5\text{GK}} \leq 0.25$  roughly constant.

The thermodynamic properties of the ejecta for model H300 (HMNS with lifetime  $\tau = 300$  ms) are illustrated in Figure 5.3 through the electron fraction  $Y_{e,5\text{GK}}$ , specific entropy  $s_{5\text{GK}}$ , final velocity  $v_{\text{final}}$ , ejecta mass, and the time  $t_{5\text{GK}}$  when the temperature is 5 GK for the last time. Two ejecta components stand out from the scatter plot of  $Y_{e,5\text{GK}}$  versus  $s_{5\text{GK}}$ . The larger component is ejected before the HMNS

collapses, i.e.  $t_{5\text{GK}} \lesssim 300$  ms, and it exhibits a tight correlation between the entropy and electron fraction up to  $Y_{e,5\text{GK}} \sim 0.5$ . This is indicative of a neutrino-driven wind, and indeed we would expect the asymptotic  $Y_e$  to be  $\sim 0.55$  based on the neutrino properties shown in Figure 5.1 (Qian and Woosley, 1996). Note that the vast majority of the ejecta with  $Y_{e,5\text{GK}} \gtrsim 0.4$  or  $v_{\text{final}} \gtrsim 0.03 c$  is part of this early wind-like ejecta, with a much smaller group of particles extending to low velocities and low electron fractions.

The second component is ejected after the HMNS has collapsed to a BH, i.e.  $t_{5\text{GK}} \gtrsim 300$  ms, and it has only a weak correlation between  $Y_{e,5\text{GK}}$  and  $s_{5\text{GK}}$ . This component is associated with mass ejection as the disk reaches the advective state (very weak or no neutrino cooling/heating) and is driven primarily by heat injection from angular momentum transport processes and nuclear recombination (Metzger and Fernández, 2014). Mass ejection in this state is accompanied by vigorous convective activity in the disk.

In order to quantitatively disentangle the wind-like ejecta component seen in Figure 5.3 from the other component, we compute the contributions to  $s_{5\text{GK}}$  arising from neutrino and viscous heating. While all trajectories experience some degree of viscous heating, only a subset of tracer particles experience an entropy change due to neutrino heating that is larger than  $0.1 k_B \text{ baryon}^{-1}$  (ignoring any neutrino cooling). And that subset exactly exhibits the tight, boomerang-shaped correlation between  $Y_{e,5\text{GK}}$  and  $s_{5\text{GK}}$  that the early, wind-like ejecta exhibits (cf. the blue and gray dots in the lower left panel of Figure 5.3). The mass of this neutrino-driven ejecta component is shown in Table 5.2 under  $M_{\nu\text{-driv}}$ . This component is absent for HMNS lifetimes shorter than 30 ms and also in the BH models, but once the HMNS lifetime becomes longer, the neutrino-driven component becomes as large or even the dominant fraction of the total ejecta (such as in model Hinf, in which almost the entire ejecta is neutrino-driven). For very long-lived HMNSs all trajectories experience some degree of neutrino interactions, and it becomes difficult to distinguish the wind-like from the viscous component. We emphasize that even the neutrino-driven component experiences significant viscous heating and the entropy change due to viscous heating can be of the same order as that due to neutrino absorption.

One interesting feature of the late-time component is the sharp upper limit of  $Y_{e,5\text{GK}} \sim 0.38 - 0.40$ , regardless of entropy. These trajectories experience late-time fall back due to large convective eddies in the disk. They get sucked deep inside the disk where the density is much higher than in the outflow, and then they are

ejected again almost immediately. This creates a spike in their density profile that results in significant heating, as evidenced by the fact that they all have  $T \geq 5$  GK at  $t \sim 2$  s. However, before this late-time heating occurs, r-process nucleosynthesis has already taken place in these trajectories, and all free neutrons have been captured onto seed nuclei. Thus, the composition before the heating spike consists of heavy elements with  $\beta$ -decay half-lives of milliseconds to seconds. These elements decay and raise the overall electron fraction of the material to  $Y_e \sim 0.38 - 0.40$ , which is the characteristic  $Y_e$  at 1 – 3 seconds after neutron exhaustion for the r-process, for a wide range of initial  $Y_e$ . The late-time heating then simply pushes the material back into NSE, but the electron fraction remains unchanged. The resulting entropy depends on the amount of heating received by each trajectory, as determined by how far the material falls back into the disk. This class of trajectories therefore ends up with electron fractions  $Y_{e,5\text{GK}} \sim 0.38 - 0.40$  and nucleosynthesis start times of  $t_{5\text{GK}} \sim 2$  s, with uncorrelated entropies.

### 5.3.4 Nucleosynthesis

#### 5.3.4.1 Final abundances

The mass-averaged composition of the ejecta for all models with non-zero viscosity is shown in Figure 5.4. The abundances are multiplied by the total ejecta mass to emphasize their relative contributions to the different r-process regions. Models H000 and H010 (prompt non-spinning BH and shortest-lived HMNS, respectively) agree most closely with the Solar System r-process abundances (Arnould et al., 2007), which have been scaled to match the second peak at  $A = 130$  (the abundances from our models have not been scaled). The abundances around the third r-process peak in these two models approach the solar values, whereas in all other models production of the third peak is too low compared to solar. H000 and H010 also have the best agreement with the solar rare-earth peak around  $A \sim 165$ . While these two models under-produce the first r-process peak ( $A \sim 80$ ), they agree rather well with the feature around  $A \sim 100$ , in contrast to all other models which over-produce it.

While the good agreement between models H000/H010 and the solar r-process abundances could be taken as an indication of short HMNSs lifetimes being more common, one has to keep in mind that Figure 5.4 assumes that the entire second solar r-process peak is due to the disk outflow. Other sources such as the dynamical ejecta from NSNS/NSBH mergers and core-collapse supernovae can also produce significant amounts of r-process elements. The expected abundance patterns are

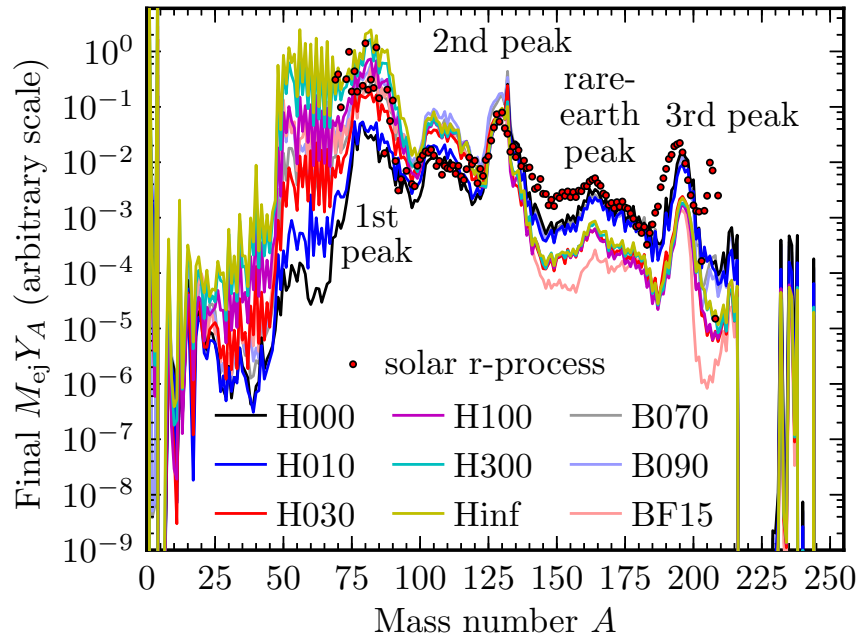


Figure 5.4: Final trajectory-averaged abundances as a function of mass number, scaled by the total ejecta mass, for all models with non-zero viscosity. The observed solar r-process abundances (Arnould et al., 2007) are scaled to match the second peak of the HMNS models at  $A = 130$  (none of the abundances from our models have been scaled).

weighted toward the third peak for the dynamical ejecta (e.g., Goriely et al., 2011; Wanajo et al., 2014; Roberts et al., 2017) and toward the first peak for core-collapse supernovae (e.g., Wanajo, 2013; Shibagaki et al., 2016; Vlasov et al., 2017). The solar r-process abundance is thus the outcome of the contribution from each source weighted by their rate and yield per event.

In all models, the third peak is shifted to slightly higher mass numbers, which is a well-known shortcoming of the FRDM mass model (e.g., Mendoza-Temis et al., 2015; Mumpower et al., 2016). We also see an abundance spike at  $A = 132$  in all models. This spike is due to some trajectories experiencing late-time heating that photodissociates neutrons from synthesized heavy elements. This results in additional neutron capture and a pile up of material at the doubly magic nucleus  $^{132}\text{Sn}$  ( $N = 82$  and  $Z = 50$ ). Wu et al. (2016) also observed this phenomenon and described it in detail.

The models with longer HMNS lifetimes have less neutron-rich ejecta (Figure 5.2) and hence synthesize a greater fraction of first peak material. Once the HMNS lifetime is longer than 100 ms, the first peak ( $70 \leq A \leq 90$ ) is over-produced with

respect to the solar values, when the abundances are normalized to the second peak. Again, we emphasize that the r-process yield from disk outflows is complementary to that from the dynamical ejecta, which tends to produce more neutron-rich nuclei.

We quantify the relative contribution of each model to the different regions of the r-process distribution by computing average abundances around the peaks and normalizing them to the solar values. The abundance of the second peak  $Y_{2\text{nd}}$  is computed as the sum of the abundances in the range  $125 \leq A \leq 135$ , excluding  $A = 132$  to avoid the spike at that mass number. For the first peak abundance  $Y_{1\text{st}}$ , we use the sum of abundances in the range  $70 \leq A \leq 90$ . For the rare-earth peak  $Y_{\text{RE}}$ , we use  $160 \leq A \leq 166$  and for the third peak we use  $186 \leq A \leq 203$ . The quantity  $[Y_{1\text{st}}/Y_{2\text{nd}}]$  shown in Table 5.2 is defined as

$$[Y_{1\text{st}}/Y_{2\text{nd}}] = \log_{10} \frac{Y_{1\text{st}}}{Y_{2\text{nd}}} - \log_{10} \frac{Y_{1\text{st},\odot}}{Y_{2\text{nd},\odot}}, \quad (5.5)$$

where  $Y_{1\text{st},\odot}$  and  $Y_{2\text{nd},\odot}$  are the abundances of the first and second peak as observed in the solar system, respectively. The same procedure is used to compute  $[Y_{\text{RE}}/Y_{2\text{nd}}]$  and  $[Y_{1\text{st}}/Y_{2\text{nd}}]$ . Using the solar r-process abundances from Arnould et al. (2007), we find  $\log Y_{1\text{st},\odot}/Y_{2\text{nd},\odot} = +1.3$ ,  $\log Y_{\text{RE},\odot}/Y_{2\text{nd},\odot} = -1.1$ , and  $\log Y_{3\text{rd},\odot}/Y_{2\text{nd},\odot} = -0.42$ , which we use to normalize the values shown in Table 5.2.

The different peak ratios shown in Table 5.2 quantify the trends apparent in Figure 5.4. For models H000 and H010, the rare-earth and third peaks are under-produced by only a third to one half of an order of magnitude. But the first peak is under-produced by slightly more than an order of magnitude compared to the second peak in those models. As we go to longer HMNS lifetimes, the rare-earth and third peaks are under-produced by about an order of magnitude regardless of the HMNS lifetime. At the same time, the first peak increases from an under-production of 2/3 of an order of magnitude at  $\tau = 30$  ms to an over-production of a factor of 2.6 at  $\tau = \infty$ .

The spinning BH models under-produce the first, rare-earth, and third peaks in roughly the same amounts, namely between about half to 3/4 of an order of magnitude compared to the second peak. The compact disk model BF15 under-produces the third peak by a similar amount as the HMNS models with long lifetimes. But it also has the lowest rare-earth peak abundance relative to solar, with an under-production factor of about 1.5 orders of magnitude. The first peak, on the other hand, is only under-produced by a factor of  $\sim 2$ .

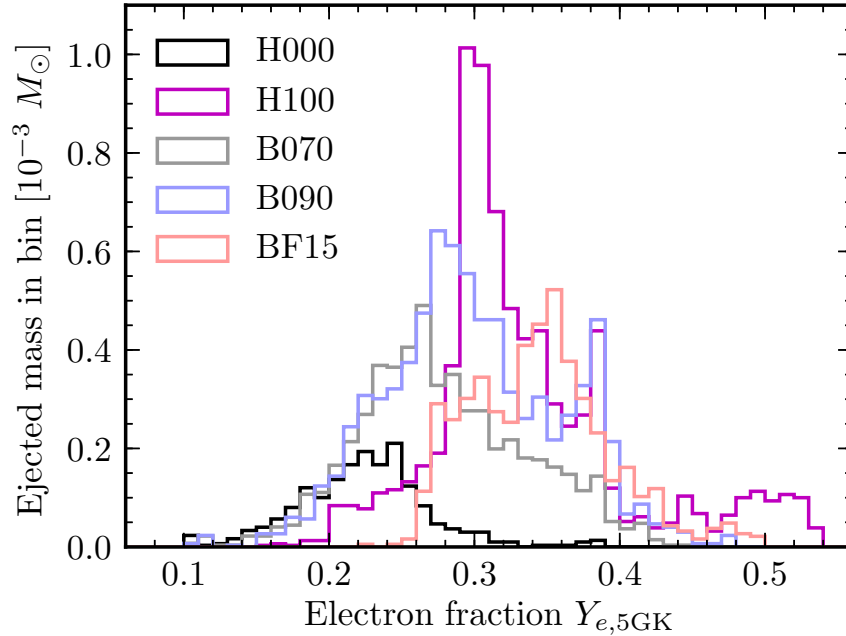


Figure 5.5: Mass histograms of electron fraction for the ejecta from BH models. We include the HMNS model H100 for comparison.

#### 5.3.4.2 BH spin mimicking HMNS lifetime

Metzger and Fernández (2014) proposed using the relative amount of blue optical emission in the kilonova as an observational test of the HMNS lifetime, given that the latter correlates with the amount of high- $Y_e$  material ejected in the disk outflow. Given that high- $Y_e$  material also correlates with BH spin (Fernández et al., 2015a), the kilonova signature of the two types of central objects can overlap. Here we investigate whether the nucleosynthesis signature offers additional information that can break the degeneracy. We consider the BH models H000, B070, and B090, which have the same mass and varying spins  $\chi = 0, 0.7, \text{ and } 0.9$ , respectively, as well as model BF15, which has a larger mass and  $\chi = 0.86$ . Figure 5.5 shows the electron fraction distributions of these BH models.

While a larger BH spin has a similar overall effect on the disk ejecta composition as a longer HMNS lifetime, even a spin  $\chi = 0.9$  does not reach the same amount of ejecta mass and average value of  $Y_{e,5GK}$  as a HMNS with a lifetime  $\tau = 100$  ms (cf. Figure 5.5). At best, a rapidly spinning BH can mimic a HMNS of modest lifetime. This can also be seen in Figure 5.4 and in the peak ratio values in Table 5.2. Models B070 and B090 have values of  $[Y_{1st}/Y_{2nd}]$  that are similar or slightly smaller than in model H030, while the values of  $[Y_{RE}/Y_{2nd}]$  and  $[Y_{3rd}/Y_{2nd}]$  from models B070 and B090 fall between those from models H010 and H030. Thus, a BH with a spin

$\chi = 0.7 - 0.9$  produces a disk outflow with a similar final abundance pattern as a HMNS with a lifetime of  $\tau \sim 15 - 20$  ms. Therefore, the fact that we assume a non-spinning BH after collapse of the HMNS only has a very small impact on the nucleosynthesis. Model BF15, on the other hand, looks more like a HMNS with a lifetime  $\tau \sim 60$  ms, judging from the under-production of the first and third peaks relative to the second peak. Nonetheless, the rare-earth peak is under-produced by almost half an order of magnitude more in the disk ejecta by BF15 than by the HMNS models with long lifetimes.

### 5.3.4.3 Lanthanides, actinides, and heating rates

The energy released by the radioactive decay of heavy elements synthesized by the r-process can power an optical or infrared transient called a kilonova (also called macronova in the literature; Li and Paczyński, 1998; Kulkarni, 2005; Metzger et al., 2010; Roberts et al., 2011; Kasen et al., 2013). The two most important microphysical components that determine the light curve and spectrum of kilonovae are the opacity of the material and the radioactive heating rate. Lanthanides ( $58 \leq Z \leq 71$ ) and actinides ( $90 \leq Z \leq 103$ ) have open f-shells, which gives them a very complex atomic line structure that leads to broadband opacities that are more than an order of magnitude larger than opacities from iron-group elements (Kasen et al., 2013; Tanaka and Hotokezaka, 2013; Fontes et al., 2015).

The trajectory-averaged lanthanide  $\langle X_{La} \rangle$  and actinide  $\langle X_{Ac} \rangle$  mass fractions of the ejecta for all models are summarized in Table 5.2. For HMNS lifetimes  $\tau \leq 10$  ms, the lanthanide mass fraction is a few times  $10^{-2}$ , which will result in opacities about an order of magnitude larger than iron group opacities (see Figure 10 in Kasen et al., 2013). Note that the actinide mass fractions are on the order of  $10^{-3}$ , which is still a significant contribution to the opacity. Once the HMNS lifetime is longer than about 10 ms, the lanthanide fraction  $\langle X_{La} \rangle \sim 10^{-3}$  monotonically decreases as the lifetime increases. In these models, the lanthanides and actinides will increase the opacity only by a factor of a few relative to iron group opacities. In the BH models, increasing the spin from 0.7 to 0.9 reduces the lanthanide and actinide mass fractions by roughly a factor of two from around  $10^{-2}$ . The compact disk model BF15 has very similar lanthanide and actinide mass fractions as H300. These results apply to the disk outflow component alone; the color of a kilonova depends also on the spatial distribution and composition of the dynamical ejecta, which tends to be more neutron-rich and hence may contain significant amounts of lanthanides/actinides.

Figure 5.6 shows the combined lanthanide and actinide mass fraction of each ejected trajectory as a function of  $Y_{e,5\text{GK}}$  for models H010, Hinf, B090, and BF15. For most trajectories, the lanthanide and actinide fraction plummets as the initial electron fraction increases from 0.2 to 0.25 (see also Lippuner and Roberts, 2015; Kasen et al., 2015). Particles with  $Y_{e,5\text{GK}} \leq 0.25$  have low entropies, because a higher entropy requires either significant neutrino heating, which increases  $Y_e$ , or viscous heating over timescales comparable to the thermal time, which gives weak interactions enough time to increase  $Y_e$  toward its equilibrium value. This correlation between  $Y_{e,5\text{GK}}$  and  $s_{5\text{GK}}$  at  $Y_{e,5\text{GK}} \lesssim 0.3$  can be seen in Figure 5.3.

Figure 5.6 also shows that there is a separate population of particles that contain significant amounts of lanthanides and actinides for electron fractions in the range  $0.25 \lesssim Y_{e,5\text{GK}} \lesssim 0.3$ , particularly in models B090, BF15, and to a lesser extent in model H010. This group of trajectories has higher entropies ( $s_{5\text{GK}} \gtrsim 30 k_B \text{ baryon}^{-1}$ ) relative to those which do not make lanthanides or actinides for  $Y_{e,5\text{GK}} \geq 0.25$ . We can understand this population by considering the strong dependence of the lanthanide/actinide abundance on the neutron-to-seed ratio  $Y_n/Y_{\text{seed}}$ , where  $Y_{\text{seed}} = \sum_{A \geq 12} Y_A$ . In general, a neutron-to-seed ratio  $Y_n/Y_{\text{seed}} \sim 40$  is necessary to produce a significant amount of lanthanides and actinides: as  $Y_n/Y_{\text{seed}}$  increases from about 35 to about 45,  $X_{\text{La}} + X_{\text{Ac}}$  increases from  $\sim 10^{-5}$  to  $\sim 10^{-2}$ . This effect is illustrated in Figure 5.7 for model B090, where the different particle populations are shown in different colors. The trajectories in the range  $Y_{e,5\text{GK}} = 0.25 - 0.30$  lie on both sides of the  $Y_n/Y_{\text{seed}} = 35$  boundary for the range of entropies encountered in the disk ejecta, with a critical entropy for lanthanide production  $s_{5\text{GK}} \sim 30 - 40 k_B \text{ baryon}^{-1}$ . Outside of this range of  $Y_e$ , lanthanide production is insensitive to  $s_{5\text{GK}}$ . The neutron-to-seed ratio increases with increasing entropy because a higher entropy prefers a larger number of particles, and thus the composition contains more lighter particles such as free neutrons.

The population of trajectories with  $Y_{e,5\text{GK}} = 0.25 - 0.30$  and  $s_{5\text{GK}} \gtrsim 30 k_B \text{ baryon}^{-1}$  is absent in model Hinf (cf. Figure 5.6). In order to achieve such entropies at modest electron fraction, neutrino irradiation cannot be too strong. In model Hinf, the weak interaction timescale is comparable to the viscous heating timescale, raising  $Y_e$  above 0.3. Since the HMNS is the strongest source of neutrinos while it persists, this population of trajectories can only exist if there is either no HMNS or if the HMNS collapses to a BH quickly. The eight trajectories in model Hinf that produce lanthanides and actinides at  $Y_{e,5\text{GK}} \gtrsim 0.4$  are an extreme case. They all have

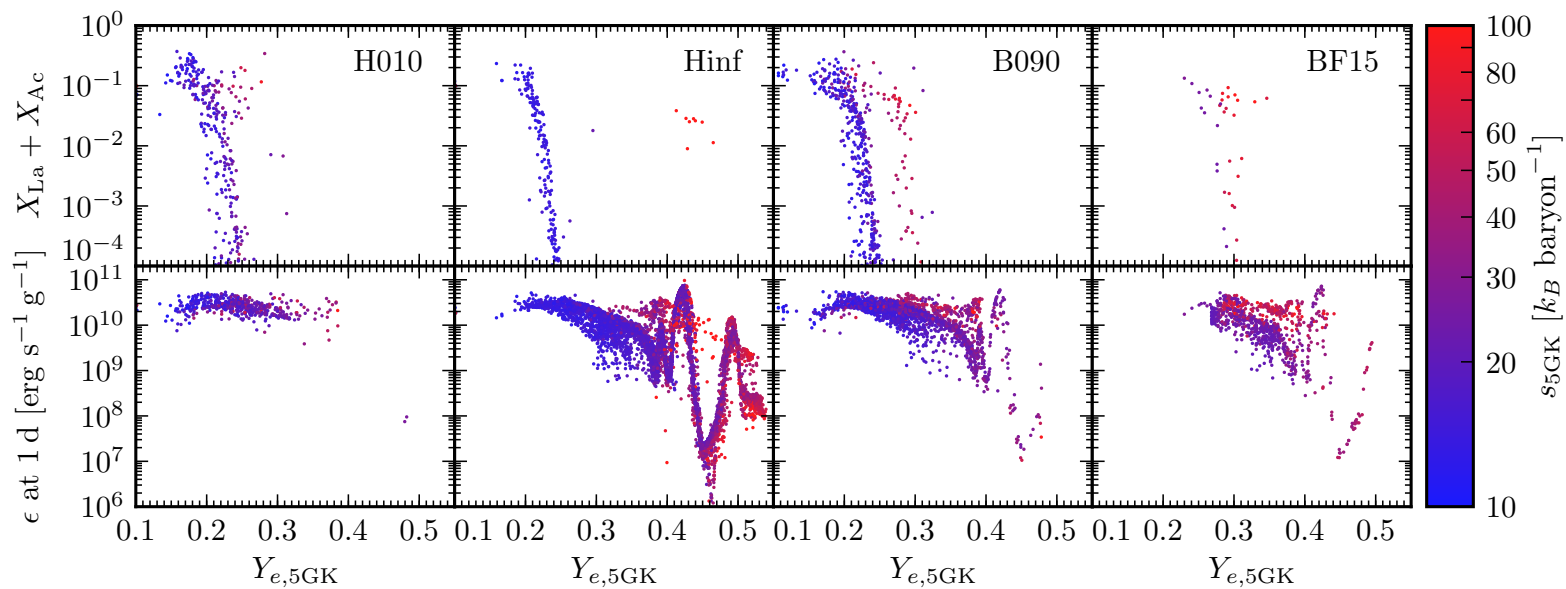


Figure 5.6: **Top:** Scatter plots of final lanthanide and actinide mass fraction in each trajectory as a function of the electron fraction  $Y_{e,5GK}$ , for selected models. Points are color-coded by the initial entropy  $s_{5GK}$ . **Bottom:** Radioactive heating rate  $\epsilon$  at one day as a function of  $Y_{e,5GK}$ , also color-coded by  $s_{5GK}$ .

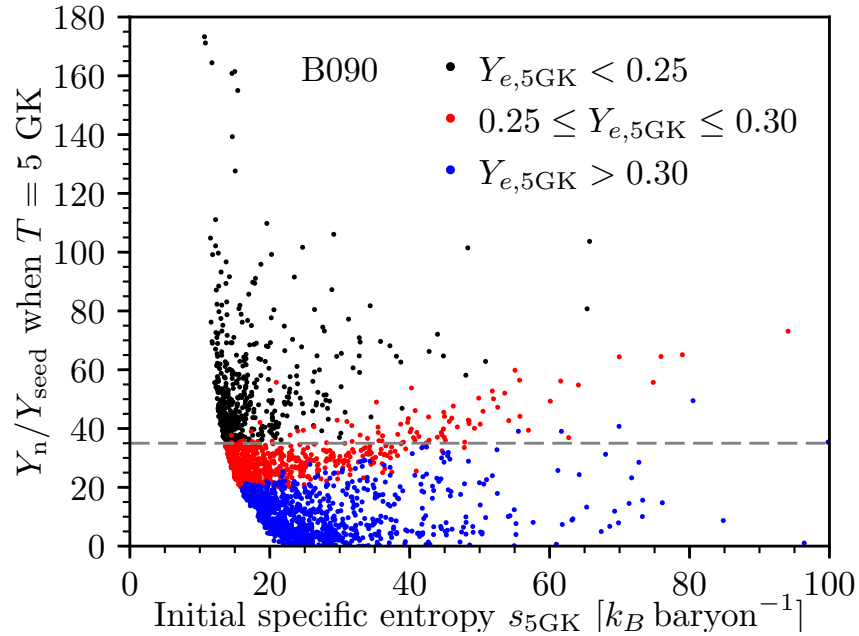


Figure 5.7: Neutron-to-seed ratio at the time when the temperature  $T \geq 5$  GK for the last time, versus the specific entropy at that time, for ejected trajectories from model B090. Nuclides with  $A \geq 12$  are counted as seeds. The gray dashed line indicates the minimum value of  $Y_n/Y_{\text{seed}} = 35$  that is required to make lanthanides and actinides. All trajectories with  $Y_{e,5\text{GK}} < 0.25$  (black dots) are above the minimum neutron-to-seed ratio regardless of initial entropy, while almost all trajectories with  $Y_{e,5\text{GK}} > 0.30$  (blue dots) are below it. The remaining trajectories ( $0.25 \leq Y_{e,5\text{GK}} \leq 0.30$ , red dots) can produce lanthanides or actinides if the initial entropy is  $\gtrsim 30 - 40 k_B \text{ baryon}^{-1}$ .

$s_{5\text{GK}} > 200 k_B \text{ baryon}^{-1}$ , which allows the neutron-to-seed ratio to be high enough to make lanthanides and actinides even at  $Y_e > 0.4$ . These particles attain this high entropy because of late-time fallback into (and then rapid ejection from) the innermost part of the disk, where they experience significant heating past 5 GK.

Table 5.2 gives the total radioactive heating rate in the ejecta  $\epsilon_{\text{tot}}$  at 1 day and at 7 days for all models. The quantity scales with the total ejecta mass. When considering the contribution of the disk outflow to a radioactively-powered kilonova, we need to keep in mind the contribution of the dynamical ejecta, which is not simply additive as in the case of nucleosynthesis. The larger fraction of lanthanides and actinides expected for the dynamical ejecta means that its optical opacity is likely to be larger than that of the disk outflow. The geometry of the dynamical ejecta depends on the type of merger involved: quasi-spherical for NSNS mergers (e.g., Hotokezaka et al., 2013b), or confined to the equatorial plane for NSBH mergers (e.g., Kawaguchi et

al., 2015; Foucart et al., 2017). In the former case, the disk ejecta can be obstructed in all directions by high-opacity material, whereas in the latter a long-lasting blue optical component from the disk ejecta can be detectable from some directions (Kasen et al., 2015). A short-lived blue optical component should be detectable in most cases since the lanthanide-rich material goes through a high-temperature phase and its outer layers let photons escape more freely (Barnes and Kasen, 2013; Fernández et al., 2017)

If we only consider the heating rates and lanthanide/actinide content from the disk outflow, we expect models H000 and H010 to make dim infrared kilonovae, while all other models should make bright blue optical kilonovae. The exception is B070, which has about 1.5% lanthanides and actinides by mass and a fairly large heating rate, so this model could make a brighter infrared kilonova. The heating rates reported here are upper limits to the bolometric luminosities of kilonovae from the disk outflow, since the conversion of energy from radioactive decay products into thermal energy of the ejecta has a limited efficiency (e.g., Metzger et al., 2010; Hotokezaka et al., 2016; Barnes et al., 2016).

The bottom row of Figure 5.6 shows the heating rates of the individual trajectories at  $t = 1$  day as a function of  $Y_{e,5\text{GK}}$ . The heating rate decreases slowly with increasing electron fraction for  $Y_{e,5\text{GK}} \lesssim 0.3$ . For higher initial  $Y_e$ , the decrease steepens until large oscillations start around  $Y_{e,5\text{GK}} \sim 0.4$ . This general behavior is consistent with the findings of the parametrized r-process nucleosynthesis study of Lippuner and Roberts (2015). The oscillations are due to the initial NSE composition, which can be dominated by a small number of individual nuclei that match the electron fraction of the material. If there is a nuclide with a matching  $Y_e$  that has a half-life of about a day, there will be strong heating at  $t \sim 1$  day as this nuclide decays, but if there is no such nuclide, then there will be significantly less heating. The peak in the heating rate at  $Y_{e,5\text{GK}} \sim 0.425$ , visible in all but the first column of Figure 5.6, is caused by  $^{66}\text{Ni}$ , which has  $Y_e = 28/66 \sim 0.424$  and is a dominant nuclide in the initial NSE composition.  $^{66}\text{Ni}$  decays to  $^{66}\text{Cu}$  with a half-life of 55 hours, which then decays to stable  $^{66}\text{Zn}$  with a half-life of 5 minutes. Around  $Y_{e,5\text{GK}} \sim 0.45$ , there is a large dip in the heating rate because the initial composition is dominated by  $^{62}\text{Ni}$  and  $^{66}\text{Zn}$ , both of which are stable and have  $Y_e = 0.45$ . The little neutron capture that takes place mainly builds up  $^{88}\text{Sr}$ , which is also stable and has  $Y_e = 0.43$ . At  $Y_{e,5\text{GK}} \sim 0.49$  there is another peak in the heating rate due to  $^{62}\text{Zn}$ ,  $^{61}\text{Cu}$ , and  $^{57}\text{Ni}$ , which are all unstable and very abundant since they have electron fractions between

0.48 and 0.49. At higher entropies, the initial neutron to seed ratio is enhanced, which will generally produce unstable nuclei and thus possibly break the oscillatory pattern of heating rate versus  $Y_{e,5\text{GK}}$ .

The morphology of the ejecta for all models with non-zero viscosity is shown in Figure 5.8, with the top row showing final lanthanide and actinide mass fractions. Since the material is close to homologous expansion, Figure 5.8 essentially shows the velocity space distribution of the ejected particles. In all models, most of the particles are concentrated in a central blob. When the HMNS persists for 100 ms or more, some particles attain higher velocities ( $v \sim 0.1 c$ ) and organize themselves into multiple shells (which arise from *shock trains* in the gas; e.g., Matsuo et al., 1999). Since particles are accelerated to high velocities predominantly by neutrino irradiation, there are more high-velocity particles the longer the HMNS persists.

In some models (H000, H010, and B070) there appears to be little structure in the distribution of lanthanides and actinides. In others there is a clear preference for the high-lanthanide trajectories to be at low velocities and clustered in the equatorial plane. Model BF15 is an exception in that the few particles that make a significant amount of lanthanides and actinides achieve the highest velocities, because they experienced a significant amount of heating (cf. Figure 5.6). The few high-entropy trajectories in model Hinf that make lanthanides and actinides at  $Y_{e,5\text{GK}} \gtrsim 0.4$  are the high-velocity points moving predominantly in the polar direction, i.e., they have a large absolute  $y$  coordinate and a small  $x$  coordinate in Figure 5.8. For the heating rates, on the other hand, there is no strong spatial correlation between heating magnitude and trajectory location in any of the models. Models H300 and Hinf are the only ones which have a significant component of low heating rate trajectories, although these particles follow the same velocity distribution as those with high heating rates. Note that the low-heating particles are easier to see in the outer part of the ejecta because the lower particle density, but they are also present in the central blob.

#### 5.3.4.4 Comparison with r-process abundances in metal-poor halo stars

Metal-poor galactic halo stars that show r-process elements in their spectra are thought to have been enriched by a single or few r-process nucleosynthesis events (Cowan et al., 1999). Figure 5.9 shows the final elemental abundances (at  $t \sim 10$  Myr) of our investigated models, along with the solar r-process abundances from Arnould et al. (2007) and from four metal-poor halo stars as reported in Westin

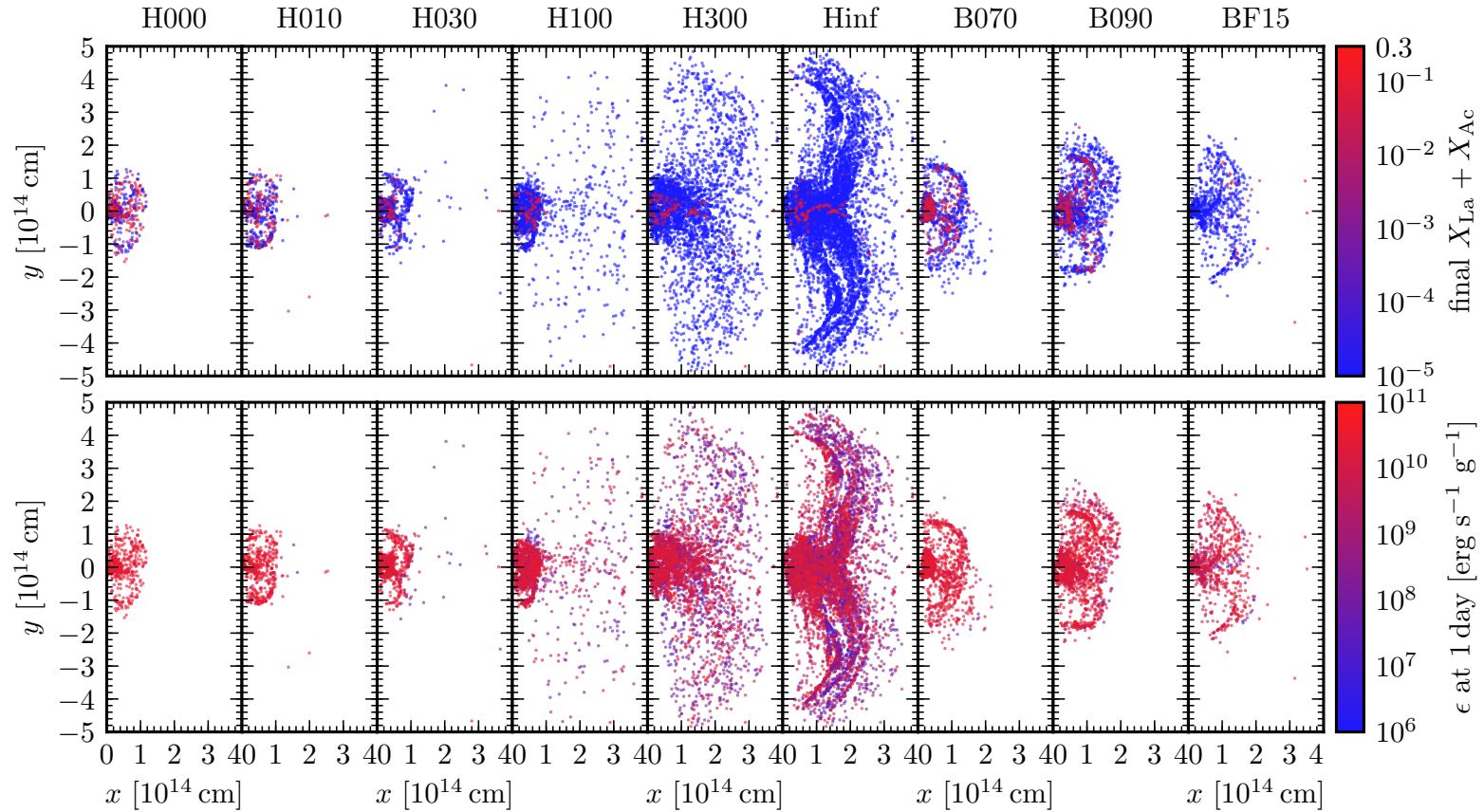


Figure 5.8: Spatial distribution of ejected trajectories at time  $t = 1$  day, for all HMNS and BH models with non-zero viscosity. Positions are computed by assuming that the velocity of each particle at the end of the simulation ( $\sim 10$  s) remains constant at later times. Aside from smoothing of sharp features by radioactive heating at late times (Rosswog et al., 2014; Fernández et al., 2015b), this extrapolation  
*(figure caption continued on next page)*

*(continued caption of Figure 5.8)*

of trajectories yields a good first approximation to the morphology of the homologously expanding disk wind ejecta. **Top:** Final lanthanide and actinide mass fraction. Because the high-lanthanide component of the ejecta is very small in most models, the points with  $X_{\text{La}} + X_{\text{Ac}} \geq 10^{-3}$  are plotted above all other points with lower mass fractions (except for models H000 and H010). The lanthanide and actinide mass fractions stop changing a few seconds after neutrons are exhausted. Therefore, the final mass fractions are the same as the ones prevailing during the kilonova emission phase. **Bottom:** Radioactive heating rate at one day. In this row, the points for the different trajectories are drawn in a random order for all models.

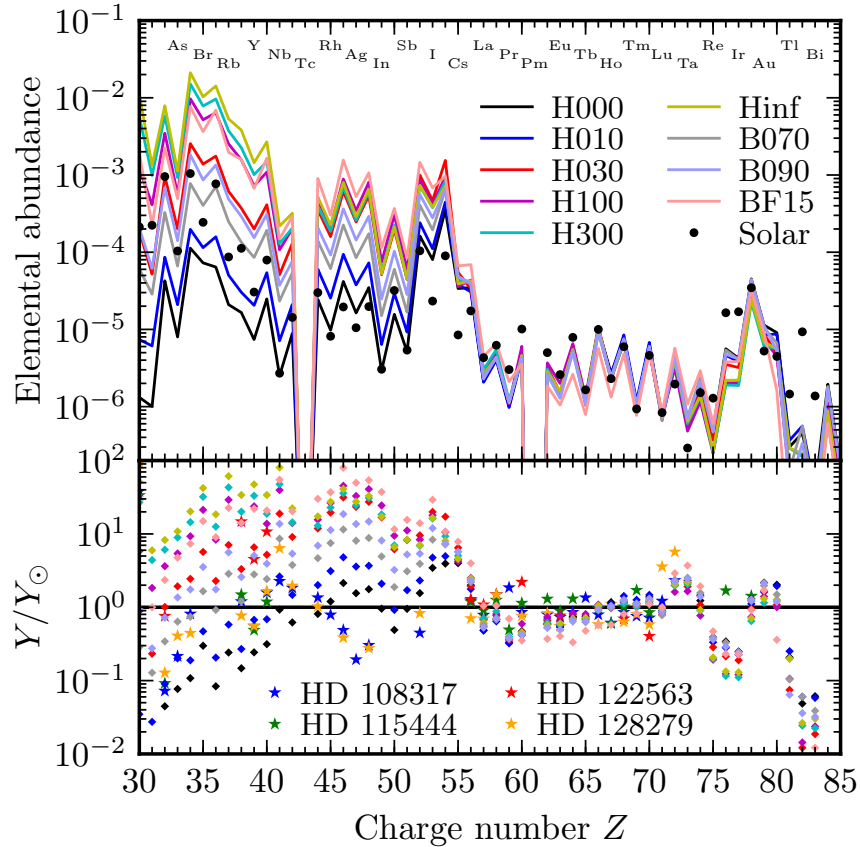


Figure 5.9: **Top:** Final elemental abundances for all models with non-zero viscosity. In each case, abundances are scaled so that  $\sum(\log Y_Z/Y_{Z,\odot})^2$  is minimized for  $55 \leq Z \leq 75$ . Black dots show solar system r-process abundances (Arnould et al., 2007). **Bottom:** Ratio of model abundances to solar system r-process abundances (diamonds). Also shown are the observed abundances of four metal-poor halo stars (shown as stars, from Westin et al., 2000; Roederer et al., 2012), scaled to the solar system values in the same way as model abundances.

et al. (2000) and Roederer et al. (2012). Abundances are scaled to give the best possible match to the solar values in the range  $56 \leq Z \leq 75$ . There is little variation between the different models in this range, and a generally good match to solar and metal-poor star abundances. While Eu ( $Z = 63$ ) is under-produced by a factor of a few with respect to solar in our models, the metal-poor halo stars also exhibit slightly sub-solar Eu abundances.

Regarding elements in the range  $44 \leq Z \leq 55$ , Figure 5.9 shows that they are overproduced relative to the solar values by all models except H000. In the range  $Z = 30 - 42$ , our disk outflow models do not match the solar abundances, but nonetheless agree with the overall increase in abundances with  $Z$  (compared to solar) exhibited by metal-poor halo stars. From  $Z = 44$  to 47, the metal-poor halo

stars have a declining abundance trend compared to solar, which none of our models reproduce. In fact, the disk outflow generates an increasing trend from  $Z = 44$  to 47. Thus, we can conclude that both the solar and metal-poor halo stars' abundance patterns are inconsistent with pure disk outflow nucleosynthesis. This means that the nucleosynthesis event (or events) that enriched these metal-poor halo stars in heavy r-process elements could not have been the r-process in merger disk outflow alone. There must have been contributions from additional types of ejecta, or perhaps a different kind of nucleosynthesis event altogether. Contributions from very neutron-rich dynamical ejecta that produces mainly second to third peak material ( $Z \gtrsim 55$ ) could make the combined final abundance pattern consistent with the metal-poor halo star observations (cf. Just et al., 2015). For  $Z \lesssim 42$ , we expect supernovae to contribute to the nucleosynthesis, thus making it difficult to draw any conclusions from the disk outflow nucleosynthesis alone.

### 5.3.5 Impact of angular momentum transport

Neutrino irradiation from a HMNS is strong enough that significant amounts of material can in principle be ejected by neutrino energy deposition alone (Ruffert et al., 1997). Therefore, it is useful to clarify the contribution of angular momentum transport processes to the overall mass ejection from the disk. Transport of angular momentum modifies the evolution of the disk in two ways: (1) it causes part of the disk to accrete and part to spread outward as the local contribution of centrifugal forces to hydrostatic balance is modified, and (2) it dissipates energy in the form of heat, increasing the local entropy of the gas. While the detailed form of these two effects depends on the way the process is modeled (i.e.  $\alpha$  viscosity), the overall contribution to the disk evolution is generic (e.g., magnetohydrodynamic turbulence also heats up the gas, but with a different spatial distribution than shear viscosity; e.g., Hirose et al., 2006).

We focus here on two models of a HMNS which does not collapse: one including angular momentum transport through  $\alpha$  viscosity like all other models (Hinf), and another in which the viscosity is set to zero (HinfNoVisc). Figure 5.10 shows the distribution of the ejected particles as a function of initial electron fraction  $Y_{e,5GK}$ , initial specific entropy  $s_{5GK}$ , and nucleosynthesis start time ( $t_{5KG}$ ).

A non-zero viscosity increases the total ejecta mass from  $5.5 \times 10^{-3} M_{\odot}$  (HinfNoVisc) to  $29.6 \times 10^{-3} M_{\odot}$  (Hinf), which corresponds to 18% and 99% of the initial disk mass, respectively. Not all of this additional mass is directly ejected by angular

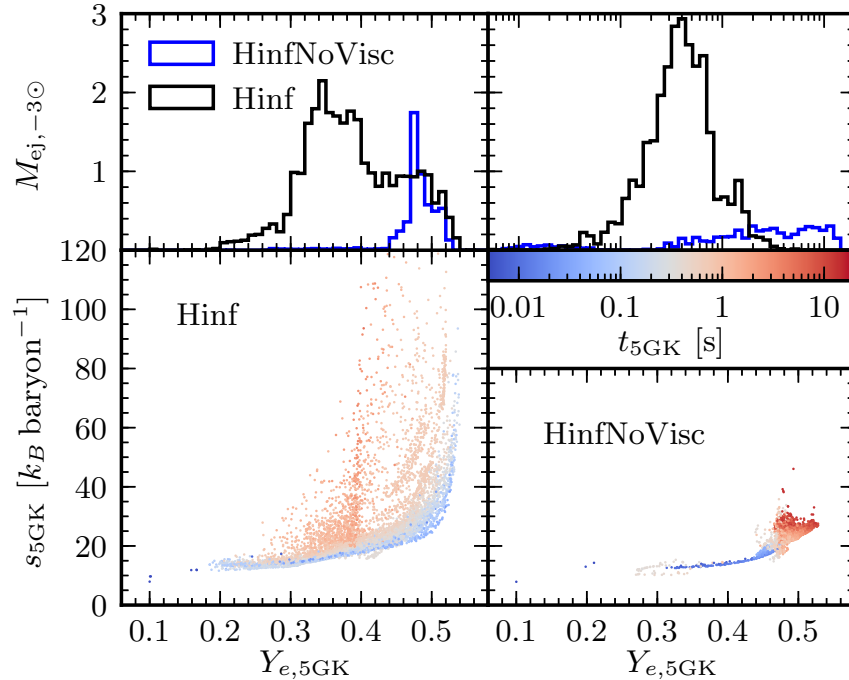


Figure 5.10: Properties of the disk wind ejecta from a HMNS that does not collapse, including and excluding the effect of viscosity on angular momentum transport and heating (models Hinf and HinfNoVisc, respectively). **Top:** Histograms of the ejected mass in units of  $10^{-3} M_{\odot}$  as a function of  $Y_{e,5\text{GK}}$  (left) and as a function of the time  $t_{5\text{GK}}$  when each particle has cooled to 5 GK (right). **Bottom:** Scatter plot of  $Y_{e,5\text{GK}}$  versus  $s_{5\text{GK}}$ , color-coded by  $t_{5\text{GK}}$  for model Hinf (left) and HinfNoVisc (right).

momentum transport, however. The scatter plot of  $Y_{e,5\text{GK}}$  versus  $s_{5\text{GK}}$  in Figure 5.10 shows a clear neutrino-driven wind pattern for part of the ejecta from model Hinf (see also Section 5.3.3 and Figure 5.3). This pattern is associated primarily with the early ejecta ( $t_{5\text{GK}} \lesssim 0.2$  s), which covers the range  $Y_{e,5\text{GK}} = 0.2 - 0.54$ . Some particles that start nucleosynthesis later ( $t_{5\text{GK}} \sim 0.5$  s), with electron fractions in the range  $Y_{e,5\text{GK}} = 0.4 - 0.54$ , also exhibit strong correlations between  $Y_{e,5\text{GK}}$  and  $s_{5\text{GK}}$ . This later ejecta could thus also be neutrino-driven, but the different thermodynamic conditions prevailing at later times alter the exact relationship between  $Y_{e,5\text{GK}}$  and  $s_{5\text{GK}}$ . Ejecta that begins nucleosynthesis at later times ( $t_{5\text{GK}} \gtrsim 0.8$  s), with  $Y_{e,5\text{GK}} = 0.3 - 0.4$ , shows a much larger dispersion in  $s_{5\text{GK}}$  for a given  $Y_{e,5\text{GK}}$ . This dispersion is associated with convective motions in the advective phase of the disk, in which mass ejection is driven exclusively by viscous heating and nuclear recombination (Section 5.3.3).

In contrast, Figure 5.10 shows that the model with zero viscosity ejects almost exclu-

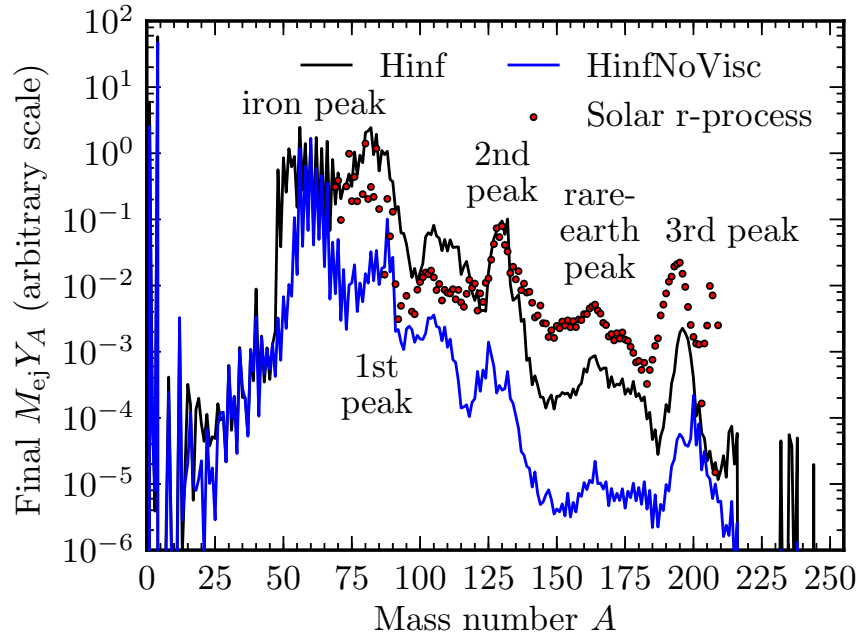


Figure 5.11: Final abundances of non-collapsing HMNS models with and without viscosity (Hinf and HinfNoVisc, respectively). Model abundances are scaled by the total ejecta mass of each model, while the solar system r-process abundances (Arnould et al., 2007) are scaled to match the second peak of model Hinf.

sively material with  $Y_{e,5\text{GK}} = 0.47 - 0.52$ , with ejection happening predominantly at late times ( $t_{5\text{GK}} \gtrsim 1$  s). All of the trajectories in model HinfNoVisc exhibit the characteristic neutrino-driven wind correlation between electron fraction and entropy. Given that the model with viscosity has more neutrino-driven wind ejecta than model HinfNoVisc, we infer that angular momentum transport not only adds an additional late-time ejecta component, but it also enhances the neutrino-driven wind itself. This enhancement arises from two effects. First, spreading of the outer regions of the disk due to angular momentum transport moves material into shallower regions of the gravitational potential, where thermal unbinding requires less energy injection. Second, viscous heating also acts on the neutrino-driven wind ejecta, increasing the rate of internal energy gain. This also explains why the neutrino-driven component is delayed in the case without viscosity: particles are more tightly bound, requiring energy deposition for a longer time in order to be ejected.

Figure 5.11 shows the final abundances for models Hinf and HinfNoVisc. Without viscosity, most of the ejecta has  $Y_{e,5\text{GK}} \sim 0.5$ , and so the final abundance is dominated by the iron peak ( $A \sim 56$ ) and  $^4\text{He}$ . Note that HinfNoVisc produces the same iron peak and  $^4\text{He}$  abundance as Hinf despite its total ejecta mass being more than a

factor of five lower. For elements significantly heavier than the iron peak, the final abundance of model HinfNoVisc is one to two orders of magnitude lower than in model Hinf. While model HinfNoVisc can still make the third r-process peak, the material is produced by just a handful of particles that have  $Y_{e,5\text{GK}} \leq 0.25$ .

The nucleosynthesis in the disk outflow from a HMNS has also been studied by Martin et al. (2015), who focused on the neutrino-driven wind without the contribution from angular momentum transport. In their study, they use the ejection time of a particle as a proxy for the HMNS lifetime. Martin et al. find that the total ejecta mass increases with increasing HMNS ejection time, and that the ejecta also becomes less neutron-rich at later times. These results are broadly consistent with what we find in model HinfNoVis.

A more detailed comparison between the results from Martin et al. and ours shows that the initial disk mass can have a significant impact on the properties of this ejecta component. Martin et al. find most of the ejecta having  $Y_e \sim 0.3-0.4$ , and a majority of the particles ejected on a timescale of 100 ms, whereas model HinfNoVisc has  $Y_e \sim 0.5$  and most trajectories begin nucleosynthesis after 1 s. The initial condition in Martin et al. is the output of a three-dimensional neutron star merger simulation by Perego et al. (2014), with a disk that is more than six times as massive as in our model ( $0.19 M_\odot$  compared to  $0.03 M_\odot$ ). Different physical and thermodynamic conditions in the disk can lead to different results in the nucleosynthesis (e.g., compare the output of our models B070 with BF15). Another source for the differences in the ejecta properties can be the different hydrodynamic methods used, which can have different amounts of numerical viscosity. Finally, one similarity between the results of Martin et al. and ours is the characteristic values for the entropy in the neutrino-driven wind ( $\sim 20 k_B \text{ baryon}^{-1}$ ; compare the bottom right panel of Figure 5.10 and Figure 5 in Martin et al., 2015).

## 5.4 Conclusions

We have performed nucleosynthesis calculations in the outflow from a neutron star merger accretion disk when the central object is a HMNS or a BH. We used long-term hydrodynamic simulations of accretion disks to model the ejecta, and detailed nucleosynthesis calculations were carried out on tracer particles using a nuclear reaction network. We have systematically varied the lifetime of the central HMNS to study its impact on the nucleosynthesis. Our simulations continued after the HMNS collapses to a BH, thus allowing us to investigate the long-term effects on

the disk and nucleosynthesis. We have also performed some simulations that start with central BHs with different spins, to explore similarities and differences with the HMNS case.

Our results are consistent with previous findings regarding the monotonic increase in mass ejection and mean electron fraction of the disk outflow for longer HMNS lifetimes (Figure 5.2; see also Metzger and Fernández, 2014). This correlation results in the amount of ejecta that has initial  $Y_e \leq 0.25$  being almost constant once the HMNS lifetime is  $\tau \gtrsim 30$  ms. The final abundance pattern at large mass numbers ( $A \gtrsim 100$ ), normalized by the total ejecta mass, is thus independent of the HMNS lifetime, because only material with  $Y_e \lesssim 0.25$  can make those heavy elements (Figure 5.4). For very short HMNS lifetimes ( $\tau \lesssim 10$  ms), there is more neutron-rich ejecta and thus the rare-earth and third r-process abundance peaks are about half an order of magnitude larger. For these short lifetimes, the disk outflow abundances alone are almost consistent with the solar r-process abundances.

For other cases, the inconsistency between the final abundances from the disk outflow and the solar values is not in itself problematic. In most neutron star mergers, we also expect a dynamical ejecta component that tends to be more neutron-rich. This means it could easily synthesize the heavy r-process material that the disk ejecta may be under-producing. If the dynamical ejecta is consistent with the solar r-process abundances between the second and third peak, then our results indicate a preference for short HMNS lifetimes, since abundances from these models are broadly consistent with solar r-process abundances between the second and third peak. If, on the other hand, the dynamical ejecta over-produces the third peak relative to the second peak, then we would require longer HMNS lifetimes, which result in under-production of the third peak compared to the second, in order to make the combined abundance pattern consistent with solar. We draw similar conclusions from comparing the nucleosynthesis in our disk models to the observed abundances in metal-poor halo stars (Figure 5.9).

If the HMNS lifetime is  $\tau \geq 30$  ms, most of the ejected material has  $Y_e \gtrsim 0.25$  and so only a small amount of lanthanides and actinides are synthesized. Thus we expect that the disk outflow to produce a kilonova that peaks in the optical band on a timescale of a day. However, this optical kilonova component may be obscured by lanthanides and actinides that were synthesized in the more neutron-rich dynamical ejecta; the effect might be viewing-angle dependent (cf. Kasen et al., 2015). If the HMNS lifetime is 10 ms or less, then the disk outflow contains substantial amounts

of lanthanides and actinides. This would also produce an infrared kilonova on a timescale of a week and would probably be indistinguishable from the dynamical ejecta contribution. The properties of the radioactive heating rates from our tracer particles (Figure 5.6) are consistent with the findings of Lippuner and Roberts (2015). We find no strong spatial correlation between radioactive heating and particle location in the ejecta (Figure 5.8).

By comparing the disk outflow abundances when a spinning BH or a HMNS is the central object, we find that a BH of spin  $0.7 - 0.9$  can mimic a HMNS with lifetime  $\tau \sim 15$  ms. If the central BH is more massive (and the disk is compact, such as in a NSBH remnant), then it can mimic a longer-lived HMNS with  $\tau \sim 60$  ms. For longer HMNS lifetimes ( $\tau \gtrsim 100$  ms), we find no possible overlap between the amounts of mass ejected or the nucleosynthesis signatures. Determining whether this difference translates into the kilonova signature requires more detailed radiation transport calculations using realistic initial conditions for the central object, disk, and dynamical ejecta.

Regarding the disk outflow dynamics, we find that when a HMNS is present, two types of ejecta are clearly distinguishable: one driven primarily by neutrino energy deposition, showing a clear correlation between electron fraction and entropy, and another driven primarily by viscous heating and nuclear recombination, in which no such correlation exists (Figure 5.3). We evolved a test model with no explicit angular momentum transport, and found that the contribution of viscosity is not limited to the late-time neutrino-independent outflow. Angular momentum transport also aids the ejection of the neutrino-driven component by moving material to shallower regions of the gravitational potential, and by accelerating thermal ejection through additional heating of the gas (Figure 5.10). Thus, excluding angular momentum transport in the HMNS disk evolution can severely underestimate the amount of mass ejected.

Neutrino interactions in the disk play a crucial role in setting the electron fraction and specific entropy distributions of the outflow. Likewise, the dominance of the HMNS irradiation in driving the early outflow requires a realistic treatment of the merger remnant instead of its approximation as a reflecting boundary. Hence our approximate treatment of the HMNS surface and neutrino interactions are the most important limitations of this study. While we are confident that the results and trends found in this study are robust, we nevertheless plan to use more sophisticated neutrino radiation transport methods in future work. Incorporating an  $\alpha$  viscosity

prescription into our disk simulations is a significant step forward from simulations with no physical viscosity. Ultimately, however, accretion disk simulations with more realistic physical viscosity (e.g., provided by magnetoturbulence driven by the magnetorotational instability) need to be performed. Furthermore, due to the extreme computational complexity of fully general-relativistic hydrodynamics simulations, no self-consistent simulations of neutron star mergers with subsequent long-term accretion disk evolution have been carried out to date. Our approach of assuming an initial equilibrium torus is thus a necessary approximation in order to investigate nucleosynthesis in merger accretion disks. Mapping the early accretion disk structure found in merger simulations into another code for the disk evolution (as we have done for model BF15) is a more accurate approach, but it is still not fully self-consistent. With next generation general-relativistic hydrodynamics codes, we hope to be able to perform completely self-consistent simulations of neutron star mergers and accretion disk outflows in the future. Finally, we only use the FRDM nuclear mass model for the nucleosynthesis calculations in this study. In future work, we plan to investigate and compare other nuclear mass models for r-process nucleosynthesis in disk outflows.

### **Acknowledgments**

JL and CDO acknowledge support from NSF grant AST-1333520. RF acknowledges support from the University of California Office of the President, from NSF grant AST-1206097, and from the Faculty of Science at the University of Alberta. DK is supported in part by a Department of Energy Office of Nuclear Physics Early Career Award, and by the Director, Office of Energy Research, Office of High Energy and Nuclear Physics, Divisions of Nuclear Physics, of the U.S. Department of Energy under Contract No. DE-AC02-05CH11231. The software used in this work was in part developed by the DOE NNSA-ASC OASCR Flash Center at the University of Chicago. This research used resources of the National Energy Research Scientific Computing Center (NERSC), which is supported by the Office of Science of the U.S. Department of Energy under Contract No. DE-AC02-05CH11231. Some computations were performed on the *Edison* compute cluster (repository m2058). Some of the calculations were performed on the *Zwicky* compute cluster at Caltech, supported by NSF under MRI award PHY-0960291 and by the Sherman Fairchild Foundation. This work was supported in part by NSF grant PHY-1430152 (JINA Center for the Evolution of the Elements). CDO thanks the Yukawa Institute for

Theoretical Physics for support and hospitality. This article has been assigned Yukawa Institute report number YITP-17-26.

### 5.A Improvements to the hydrodynamic disk simulations

We have corrected an error in the weak interaction rates used since Fernández and Metzger (2013). The error involved the absence of the neutron-proton mass difference in the argument of the Fermi-Dirac integrals for all the electron neutrino rates (but not in the antineutrino rates). After correction of this error, the electron neutrino emission rates decrease by a factor of up to two in regions with temperatures  $\gtrsim 1$  MeV. The most significant change in the result is an increase in the fraction of matter ejected with  $Y_e > 0.25$  for the non-spinning BH case from a few percent to  $\sim 30\%$  of the outflow, resulting in an increase of  $\sim 10\%$  in the average  $Y_e$  of the outflow. A similar increase in the mean  $Y_e$  of the wind is observed for the long-lived HMNS case. In terms of the amount of mass ejected, the effects are strongest for a non-spinning BH, which ejects up to  $\sim 10\%$  more mass than before the correction is applied (i.e. an additional  $\sim 0.5\%$  of the initial disk mass). For a long-lived HMNS, the mass ejection increases by  $\sim 0.2\%$ .

Relative to Metzger and Fernández (2014), we also account for separate neutrino and antineutrino temperatures for absorption. The mean energy for each neutrino species is calculated by taking the ratio of the globally-integrated energy to number emission rates, as in Ruffert et al. (1996). The temperatures are then obtained through the relation  $kT_{\nu,i} = F_4(0)/F_5(0)\langle\varepsilon_{\nu,i}\rangle$ , where  $F_i$  are the Fermi-Dirac functions of integer argument,  $F_5(0)/F_4(0) \simeq 5.065$ , and  $\langle\varepsilon_{\nu,i}\rangle$  is the neutrino mean energy. When using the updated weak interaction tables, this change translates into an *increase* of  $\sim 10\%$  in mass ejection for a non-spinning BH, and a *decrease* of  $0.4\%$  in mass ejection for a long-lived HMNS.

To put the effect of these modifications in perspective for the non-spinning BH case, doubling the resolution of the simulations in each dimension can change mass ejection by  $\sim 10\%$  (Fernández et al., 2015b), and a change in the  $\alpha$  viscosity parameter leads to an almost directly proportional change in mass ejection (i.e., a factor ten when going from  $\alpha = 0.01$  to  $\alpha = 0.1$ , Wu et al., 2016).

*Chapter VI*

## OTHER WORK

This chapter briefly summarizes other papers I contributed to during my PhD. These papers are related to my PhD research but not directly part of my thesis.

*This paper was published in February 2016 in Physical Review D, 93, 044019, doi:10.1103/PhysRevD.93.044019.*

**Low mass binary neutron star mergers: Gravitational waves and neutrino emission**

**Francois Foucart, Roland Haas, Matthew D. Duez, Evan O'Connor, Christian D. Ott, Luke F. Roberts, Lawrence E. Kidder, Jonas Lippuner, Harald P. Pfeiffer, and Mark A. Scheel**

The Laser Interferometer Gravitational Wave Observatory (LIGO) has recently directly observed the gravitational waves emitted from a binary black hole (BBH) merger event. Mergers of binary neutron star (BNS) or black hole–neutron star (BHNS) systems are also targets for LIGO (LIGO Scientific Collaboration et al., 2015). Contrary to BBH mergers, a compact object merger involving at least one neutron star is expected to produce electromagnetic emission in addition to gravitational waves. The most promising such counterparts are short gamma ray bursts (sGRBs, e.g., Mochkovitch et al., 1993; Janka et al., 1999; Fong and Berger, 2013) and kilonovae (e.g., Lattimer and Schramm, 1976; Li and Paczyński, 1998; Metzger, 2017). The neutrinos emitted from a BNS merger impact the subsequent nucleosynthesis (see Chapter V). In this paper, we study the merger of two low-mass ( $1.2 M_{\odot}$ ) neutron stars and we focus in particular on the gravitational wave and neutrino emissions. We perform the merger simulation using three different nuclear equations of state, in order to quantify the impact of the equation of state (EOS). We also use two different approximate neutrino transport methods: a leakage scheme which has been widely used before, and a more accurate gray two-moment method.

After the merger, the remnant compact object is excited and emits gravitational waves at characteristic frequencies that depend on the nuclear EOS. Observations of these gravitational waves could help constrain the EOS of nuclear matter in the

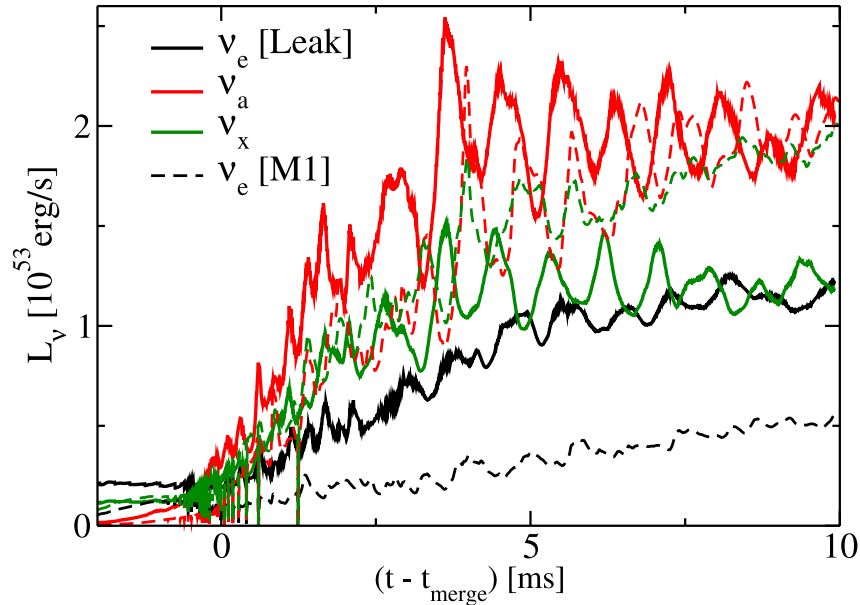


Figure 6.1: The total luminosity as function of time of the electron neutrinos (black), electron antineutrinos (red), and heavy-lepton neutrinos (green). The results of the neutrino leakage treatment are shown in solid lines and the results of the M1 two-moment scheme are shown in thin dashed lines. The choice of neutrino treatment has a big impact on the neutrino luminosity and hence on the composition of the disk and subsequent nucleosynthesis therein. Figure 23 from Foucart et al. (2016a); see that reference for details. © 2016 American Physical Society

future (e.g., Takami et al., 2014; Bauswein et al., 2014b). We find that the frequency peaks in the postmerger gravitational wave signal agree well with the results obtained from previous simulations that use an approximate gravity treatment. However, in our fully general-relativistic simulations, only the fundamental mode of the remnant is excited for an extended period of time. Thus we are less optimistic about the detection prospects of the higher-order frequency peaks in future observations of gravitational waves from neutron star mergers. We also find that there are significant differences in the total neutrino luminosities of the different neutrino species depending on the neutrino transport scheme. Figure 6.1 (Figure 23 from Foucart et al., 2016a) shows the luminosities of the electron neutrinos, electron antineutrinos, and heavy-lepton neutrinos as a function of time for the leakage and two-moment (M1) neutrino transport scheme. The differences between the two methods are up to a factor of two, which highlights the importance of using accurate neutrino treatment. The neutrino transport scheme has a large impact on the composition of the disk and its outflows, which can alter the subsequent nucleosynthesis significantly. The hydrodynamics of the merger remnant are not significantly affected by the neutrino treatment, however.

*This paper was published in February 2016 in Physical Review D, 93, 044064,  
doi:10.1103/PhysRevD.93.044064.*

## **Gravitational waveforms for neutron star binaries from binary black hole simulations**

**Kevin Barkett, Mark A. Scheel, Roland Haas, Christian D. Ott, Sebastiano Bernuzzi, Duncan A. Brown, Béla Szilágyi, Jeffrey D. Kaplan, Jonas Lippuner, Curran D. Muhlberger, Francois Foucart, and Matthew D. Duez**

LIGO is actively looking for gravitational wave signals from BNS mergers. To find such signals in the very noisy data, accurate waveform templates are required for the matched-filtering search pipeline (LIGO Scientific Collaboration, 2010). Since the tidal deformability of the neutron stars is imprinted on the gravitational wave signal, detections of BNS merger waveforms can help constrain the EOS of nuclear matter (e.g., Flanagan and Hinderer, 2008; Hinderer et al., 2010; Del Pozzo et al., 2013). However, computing these waveforms with large-scale, fully general-relativistic hydrodynamics simulations is extremely costly. There are some approximate analytic models using post-Newtonian expansions (e.g., Vines et al., 2011). In this paper, we present a new method to obtain BNS inspiral waveforms from full numerical relativity simulations of BBH systems. Numerical BBH simulations are much cheaper than BNS simulations because the BBH system contains no matter and thus no hydrodynamics have to be evolved.

While the neutron stars are far apart, they do not experience tidal deformation and can be treated as point particles. In that phase, the gravitational waveform is identical to that of a BBH system with the same masses since the black holes can also be treated as point particles. As the two stars get closer, tidal effects become stronger and need to be accounted for. We account for the tidal effect by adding the post-Newtonian expression for the tidal effects to the numerical relativity BBH waveform. Figure 6.2 (Figure 1 in Barkett et al., 2016) shows the gravitational wave phase difference between the different waveforms. The difference between the BBH waveform plus tidal terms and the numerical BNS waveform is smaller by a factor of about 3 than the difference between the original BBH and BNS waveforms. This demonstrates that we can mimic a BNS waveform at a fraction of the cost of the full simulation by adding post-Newtonian tidal corrections to a BBH waveform. However, the large numerical error in the numerical BNS waveforms prevents us from fully measuring the accuracy of this method.

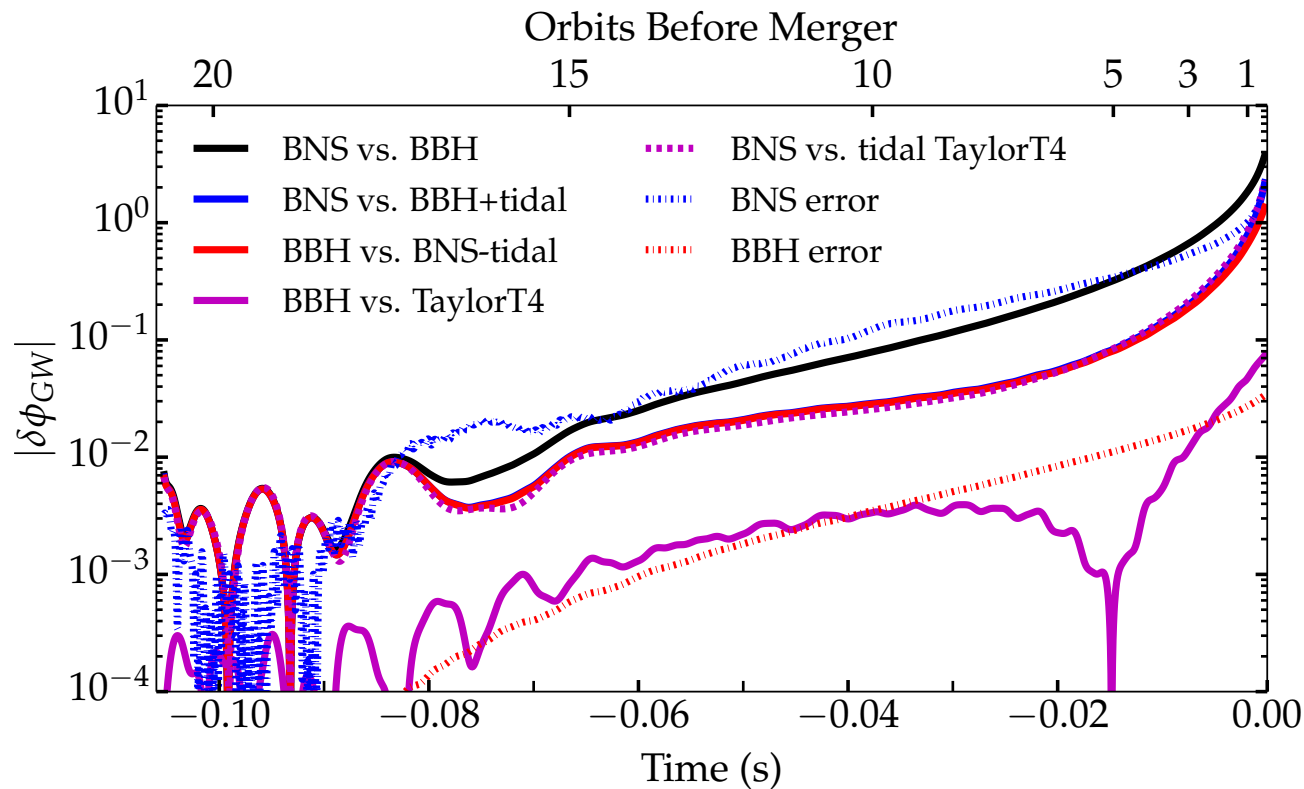


Figure 6.2: Phase difference between different gravitational waveforms. The difference between the BBH waveform plus post-Newtonian tidal terms and the full numerical relativity BNS waveform (blue) is smaller by a factor of about 3 than the difference between the BBH and BNS waveforms (black). Furthermore, the difference between the BNS waveform with the tidal terms subtracted and the BBH waveform (red) is almost exactly on top of BBH+tidal vs. BNS. This demonstrates that our method of mimicking the BNS waveform with BBH plus tidal terms works. However, the numerical BNS simulation has large errors (dashed blue), which makes it impossible to quantify the error of our method. Figure 1 from Barkett et al. (2016); see that reference for details. © 2016 American Physical Society

*This paper was published in May 2016 in the Monthly Notices of the Royal Astronomical Society, 460, 3255, doi:10.1093/mnras/stw1227.*

## **Dynamical mass ejection from binary neutron star mergers**

**David Radice, Filippo Galeazzi, Jonas Lippuner, Luke F. Roberts, Christian D. Ott, and Luciano Rezzolla**

Most previous studies of neutron star mergers have considered quasi-circular binaries. If a binary system slowly inspirals due to gravitational wave emission over hundreds of millions of years, then the orbit at merger will indeed be quasi-circular because gravitational wave emission also removes eccentricity from the system. However, in dense stellar environments, such as globular clusters, it is possible for binaries to form dynamically, which can lead to eccentric mergers. In this paper, we develop a comprehensive understanding of the physics that drives the dynamical mass ejection in binary neutron star mergers. We consider both quasi-circular and eccentric binaries of varying degrees. We also investigate the effect of the neutrino treatment on the mass ejection and the r-process nucleosynthesis in the ejecta.

We find that the eccentricity of the binary has a large effect on the ejecta. An eccentric binary can eject orders of magnitude more mass than a quasi-circular one and the ejecta tends to be more neutron-rich in the eccentric case, which has important implications for the r-process nucleosynthesis (see Chapter III). The dynamical ejecta mass is so much larger in eccentric mergers because the two neutron stars experience multiple close encounters before actually coalescing. Each encounter is associated with an episode of tidal mass ejection. Figure 6.3 (Figure 1 from Radice et al., 2016) shows the density in the orbital plane at different times. The panels show the stars immediately before and after each encounter. Our finding that the ejecta is more neutron-rich for eccentric binaries is different from what studies using Newtonian gravity found (e.g., Rosswog, 2013). This discrepancy can be explained by known shortcomings of Newtonian simulations and it highlights the importance of using full general relativity for neutron star merger simulations. Finally, we find that the different neutrino treatments have a significant impact on the basic properties of the electromagnetic counterparts of the merger. However, r-process nucleosynthesis results show very little dependence on the neutrino treatment.

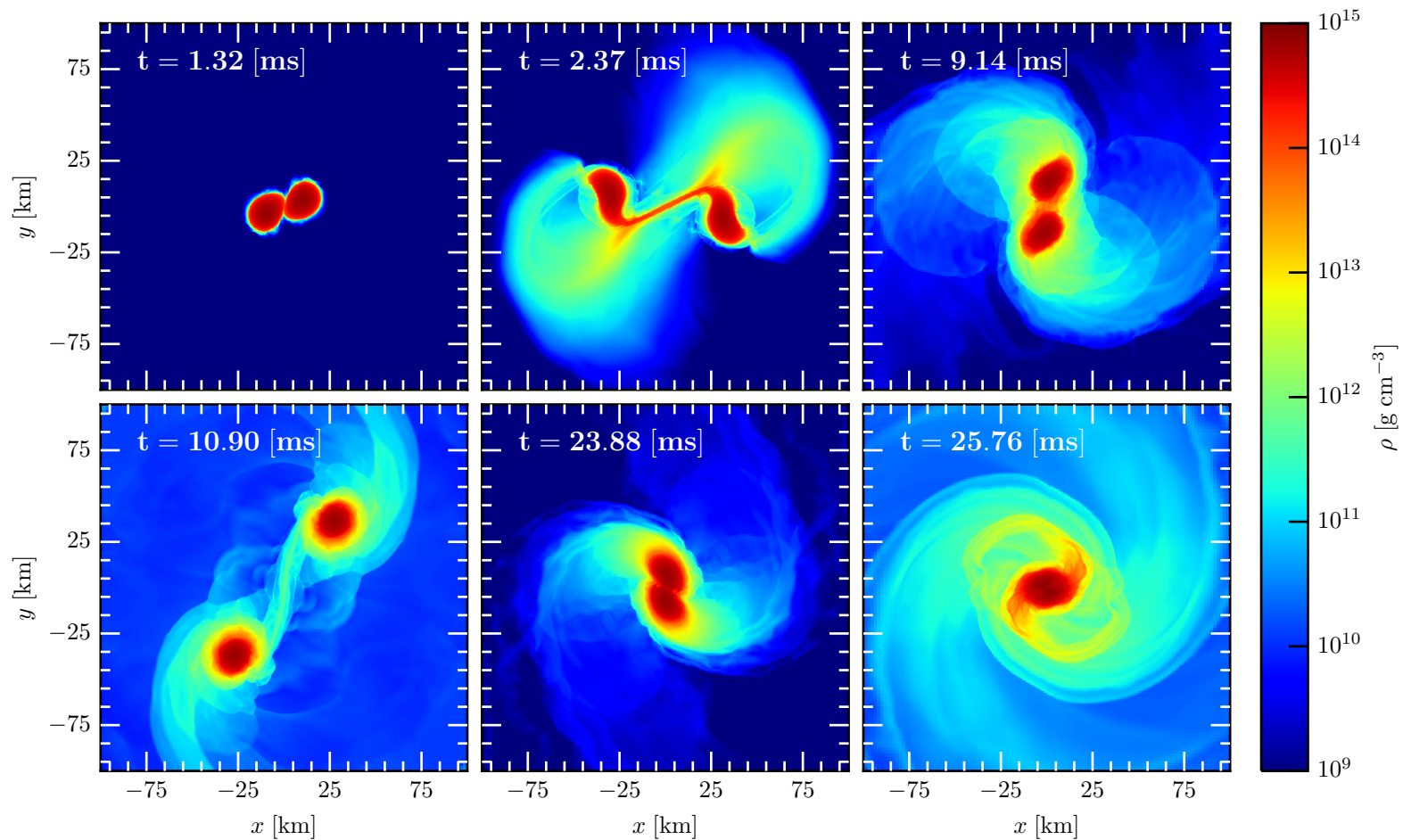


Figure 6.3: Density in the orbital plane of an eccentric binary neutron star merger. The different panels are snapshots at different times. The two neutron stars experience three close encounters before merging in the last panel. The snapshots shown are before and after each encounter. Figure 1 from Radice et al. (2016); see that reference for details. © 2016 David Radice and coauthors

*This paper was published in June 2016 in Physical Review D, 93, 124062,  
[doi:10.1103/PhysRevD.93.124062](https://doi.org/10.1103/PhysRevD.93.124062).*

## **Simulations of inspiraling and merging double neutron stars using the Spectral Einstein Code**

**Roland Haas, Christian D. Ott, Béla Szilágyi, Jeffrey D. Kaplan,  
Jonas Lippuner, Mark A. Scheel, Kevin Barkett, Curran D.  
Muhlberger, Tim Dietrich, Matthew D. Duez, Francois Foucart,  
Harald P. Pfeiffer, Lawrence E. Kidder, and Saul A. Teukolsky**

Fully general-relativistic numerical simulations of BNS inspirals, mergers, and postmerger remnants are needed to calibrate and validate approximate gravitational waveform models. These models are either fully analytic using post-Newtonian expansions or they are semi-analytic and calibrated against numerical simulations such as the effective one body model (e.g., Buonanno and Damour, 1999; Damour and Vilenkin, 2001). Since the post-Newtonian expansion is in powers of  $v/c$ , where  $v$  is the orbital velocity of the neutron stars and  $c$  is the speed of light, the expansion is only valid when the neutron stars move much slower than the speed of light. This is the case long before the merger, but as the neutron stars get closer and approach merger, their orbital velocities increase to a significant fraction of the speed of light. Thus long numerical relativity simulations are needed that start with the neutron stars being sufficiently far apart in the post-Newtonian regime.

We present the first BNS merger simulations with the hybrid pseudospectral-finite volume Spectral Einstein Code (SpEC). With  $\sim 22$  orbits, our simulation is the longest BNS inspiral and merger simulation to date. Figure 6.4 (Figure 6 from Haas et al., 2016) shows the computed gravitational waveform. Each orbit produces two cycles in the waveform. We discuss the numerical relativity implementation in SpEC and how the spacetime is evolved using a spectral method while the fluid is evolved on a different grid with a high-resolution, shock-capturing finite-volume method. The SpEC code employs a comoving coordinate system and mesh refinement. Using a spectral method to evolve the spacetime reduces the computational cost of the simulation, which allows us to evolve such a long inspiral phase. We compare our result with a shorter BNS merger waveform obtained with another code and find excellent agreement.

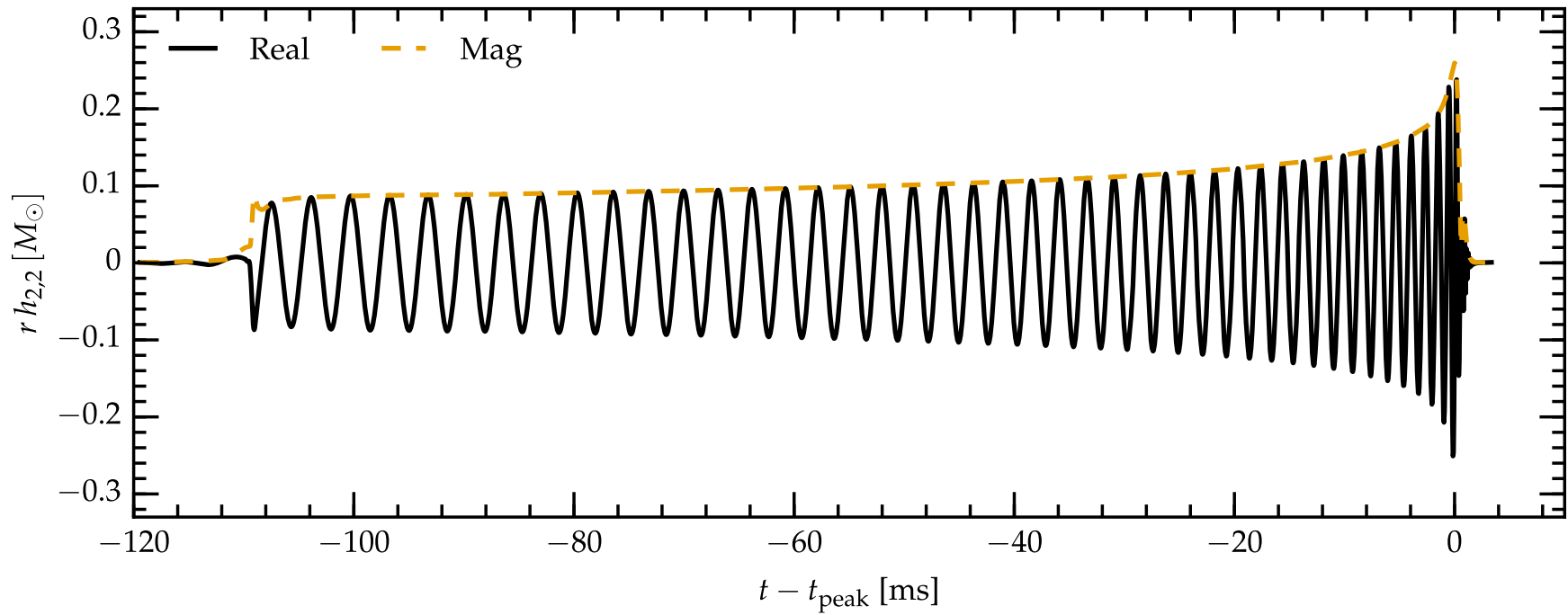


Figure 6.4: The longest ( $\sim 22$  orbits) fully general-relativistic BNS inspiral and merger gravitational waveform to date. Each orbit produces two gravitational wave cycles. We obtained this waveform from a BNS merger simulation with the Spectral Einstein Code (SpEC). Figure 6 from Haas et al. (2016); see that reference for details. © 2016 American Physical Society

*This paper was published in December 2016 in the The Astrophysical Journal Letters, 834, L2, doi:10.3847/2041-8213/834/1/L2.*

## **Post-outburst radio observations of the high magnetic field pulsar PSR J1119-6127**

**Walid A. Majid, Aaron B. Pearlman, Tatyana Dobрева, Shinji Horiuchi, Jonathon Kocz, Jonas Lippuner, and Thomas A. Prince**

Radio pulsars are spinning neutron stars that emit periodic radio pulses with extreme regularity. The periods range from several milliseconds to several seconds. See Lorimer (2008) for a recent review. The precise mechanism of the radio emission is still being debated (e.g., Sedrakian and Hayrapetyan, 2015; Melrose and Yuen, 2016). X-ray and gamma-ray emissions have also been seen from some pulsars. Some pulsars exhibit the peculiar feature that their spin period suddenly changes by a significant amount. This is termed a glitch and the mechanism that causes it remains to be understood (e.g., Espinoza et al., 2011; Chamel, 2013).

In this paper, we report high-frequency radio observations at 2.3 GHz and 8.4 GHz of the high magnetic field pulsar PSR J1119-6127 following an X-ray outburst. PSR J1119-6127 is a young radio pulsar known to glitch with a period of 410 ms, a 1.6 kyr characteristic age, one of the highest spin down rates of any pulsar with  $\dot{P} = 4.0 \times 10^{-12}$ , and an unusually high surface magnetic field of  $4.1 \times 10^{13}$  G. In late July of 2016, the *Fermi* Gamma-Ray Burst Monitor (GBM) detected a short, magnetar-like gamma-ray emission from the position of PSR J1119-6127. About twelve hours later, the *Swift* Burst Alert Telescope (BAT) detected another such gamma-ray emission from the same location. Shortly thereafter, the *Swift* X-ray Telescope (XRT) detected pulsed X-ray emission with a period of 410 ms from the pulsar's location. Our radio observations with the 70 m Deep Space Network antenna in Canberra, Australia of the pulsar a few days after the outburst revealed that the radio emission had turned off. The absence of radio emission was also reported by the Parkes radio telescope two days before our first observation. However, about three weeks after the outburst, we detected the pulsar again at 2.3 GHz and 8.4 GHz, but with a drastically different pulse profile than before the outburst. Over the next few weeks, we continued to see radio emission from PSR J1119-6127 with a continually evolving pulse profile. We thus find that PSR J1119-6127 is a highly unusual pulsar that is normally a rotation-powered radio pulsar but exhibits transient magnetar-like behavior. PSR J1846-0258 is the only other such pulsar currently known.

*This paper was published in February 2017 in the Monthly Notices of the Royal Astronomical Society, 468, 1522, doi:10.1093/mnras/stx478.*

## Neutrino-heated winds from millisecond protomagnets as sources of the weak r-process

Andrey D. Vlasov, Brian D. Metzger, Jonas Lippuner, Luke F. Roberts, and Todd A. Thompson

While it is thought that the neutrino-driven wind from proto-neutron stars (PNSs) in core-collapse supernovae (CCSNe) is not neutron-rich enough to produce the full-process (e.g., Arcones et al., 2007; Roberts et al., 2010; Martínez-Pinedo et al., 2012), it is possible that a weak version of the r-process operates in PNS winds (e.g., Wanajo, 2013). This scenario has been proposed to be the source of the lighter r-process elements ( $A \lesssim 130$  or  $Z \sim 41 - 55$ , see e.g., Arcones and Montes, 2011). However, r-process elements with  $Z \lesssim 56$  show much greater star-to-star abundance scatter than the heavier ( $Z \gtrsim 56$ ) r-process elements (e.g., Honda et al., 2006; Sneden et al., 2008; Roederer et al., 2010) and it is unclear whether r-process nucleosynthesis in standard PNS neutrino-driven winds from ordinary CCSNe can account for this scatter.

In this paper, we investigate a variation of the canonical neutrino-driven wind picture. We consider the nucleosynthesis in the neutrino-driven wind from a PNS that is rapidly rotating and has an ultrastrong magnetic field  $B \gtrsim 10^{14} - 10^{15}$  G. Similar properties are exhibited by galactic magnetars and a PNS with these characteristics is sometimes called a millisecond protomagnetar (e.g., Thompson, 2004). Since the magnetic field can be dynamically important for the supernova explosion, it can also significantly influence the neutrino-driven wind from the PNS and alter the nucleosynthesis outcome. We compute r-process nucleosynthesis with *SkyNet* in protomagnetar wind trajectories from Vlasov et al. (2014). Contemporary models for the electron fraction evolution in the wind are used. Although we find that no rotation periods can synthesize the second or third r-process peaks, we do find that rapid rotation (periods of  $\sim 1 - 5$  ms) can enhance the production of some heavy elements by two to three orders of magnitude. The nucleosynthesis pattern depends on the magnetic field strength and rotation of the protomagnetar, and thus natural variation of these properties in different CCSN could account for the observed abundance scatter of the light r-process elements.

This paper was published in April 2017 in the *Journal of Computational Physics*, 335, 84, [doi:10.1016/j.jcp.2016.12.059](https://doi.org/10.1016/j.jcp.2016.12.059).

## **SpECTRE: A task-based discontinuous Galerkin code for relativistic astrophysics**

**Lawrence E. Kidder, Scott E. Field, Francois Foucart, Erik Schnetter, Saul A. Teukolsky, Andy Bohn, Nils Deppe, Peter Diener, François Hébert, Jonas Lippuner, Jonah Miller, Christian D. Ott, Mark A. Scheel, and Trevor Vincent**

Large-scale hydrodynamics simulations of astrophysical phenomena, such as neutron star mergers and core-collapse supernovae, are computationally very intensive. These simulations need to be run on large supercomputers and spread out among thousands to hundreds of thousand of cores. One of the limiting factors of the scalability of such simulations is the communication between the different cores. With finite difference and finite volume methods, increasing the order of the numerical method requires larger stencil sizes that have to overlap at subdomain boundaries. If subdomains are processed by different cores, these large overlap regions need to be constantly communicated between the cores. To overcome this communication bottleneck, we developed *SpECTRE*, the first general relativistic magnetohydrodynamics code using the discontinuous Galerkin (DG) method and task-based parallelism.

The DG method (e.g., Hesthaven and Warburton, 2008; Cockburn and Shu, 1998) is a hybrid between the finite volume and finite element method. The large domain is subdivided into relatively small elements containing  $N^3$  points where  $N \sim 2 - 4$  is the order of the DG method. Within each element, the solution is represented with an  $N$ -degree polynomial but the elements only communicate boundary fluxes to their nearest neighbors. Furthermore, the solution is not required to be continuous at the element boundaries, which allows the DG method to handle shocks quite easily. Within an element, the DG method provides exponential convergence in the number of basis points, like a spectral method. The DG method allows refinements in both the number of points in an individual element and the size of the elements, making it extremely adaptive to many different astrophysical scenarios where shocks and hard boundaries occur alongside large regions of vacuum where the solution is trivial. Finally, local time stepping is also possible with the DG method.

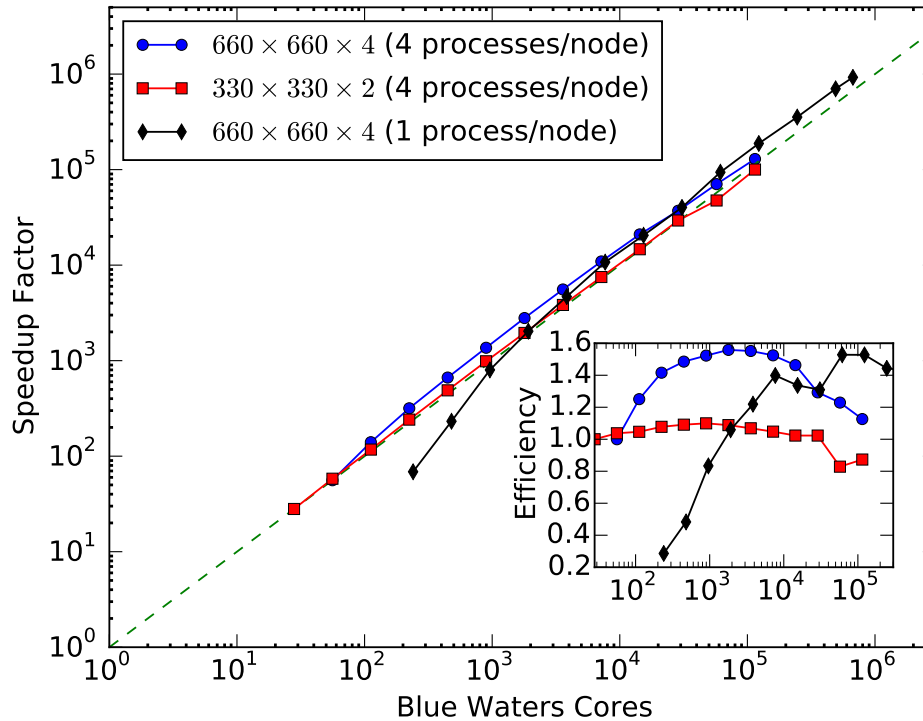


Figure 6.5: Strong scaling measures how much the simulation speeds up when more cores are used but the total problem size is fixed. With perfect strong scaling (green dashed line), the speedup factor using  $N$  cores over a single core would be  $N$ . We observe nearly perfect strong scaling for three different execution configurations. The inset shows the efficiency, which is the deviation of the observed scaling from perfect scaling. We see better-than-perfect scaling in some cases because the speedup factor is defined relative to a hypothetical single-core simulation that needs to be estimated and our estimate is not perfect. Figure 5 from Kidder et al. (2017); see that reference for details. © 2017 Elsevier Inc.

In this paper, we present the details of how the general relativistic magnetohydrodynamics system is implemented in *SpECTRE* using the DG method. We describe how the DG algorithm is mapped into a task-based parallelism framework that provides automatic load-balancing and excellent scaling performance. Finally, we perform standard performance and benchmark tests and demonstrate outstanding strong scaling to 22,380 nodes with 671,400 threads on the NCSA Blue Waters supercomputer. The scaling results are shown in Figure 6.5 (Figure 5 from Kidder et al., 2017).

*This paper has been accepted for publication in June 2017 in Classical and Quantum Gravity, doi:10.1088/1361-6382/aa7a77.*

## **Dynamics, nucleosynthesis, and kilonova signature of black hole–neutron star merger ejecta**

**Rodrigo Fernández, Francois Foucart, Daniel Kasen, Jonas Lippuner, Dhruv Desai, and Luke F. Roberts**

The two ejecta components, dynamical tidal tail and disk outflow, of a neutron star merger have different nucleosynthetic signatures. The tidal tail ejecta tends to be very neutron-rich and easily produces the full r-process (see Chapter IV). The disk outflow, on the other hand, is less neutron-rich and full r-process nucleosynthesis up to the third peak may or may not occur. The nucleosynthesis outcome in the disk outflow is sensitive to whether the central compact object is a black hole (BH) or a hypermassive neutron star (HMNS), and if it is a HMNS, the nucleosynthesis depends on how long it persists before collapsing to a BH. See Chapter V for details. If the disk outflow does not produce the full r-process, the final composition may be lanthanide-free, which would result in a bright, short, blue kilonova transient (e.g., Kasen et al., 2013). However, since the earlier tidal ejecta is neutron-rich, it undergoes a full r-process that produces a significant amount of lanthanides, which increases the opacity and produces a dim, infrared kilonova on the timescale of a week. Thus, depending on the viewing angle, the tidal ejecta could obscure a brighter, blue transient from the disk outflow (e.g., Kasen et al., 2015).

In this paper, we investigate the interaction between the tidal tail and disk outflow in a BHNS merger. We map the disk and tidal tail ejecta from a general-relativistic merger simulation into a 2D Newtonian simulation. We follow the interaction between the disk and dynamical ejecta, compute r-process nucleosynthesis with *SkyNet* using tracer particles, and finally calculate accurate kilonova light curves with a sophisticated radiative transfer code. Figure 6.6 (top panel of Figure 1 from Fernández et al., 2017) shows the initial setup with the disk, bound dynamical ejecta (fallback), and unbound tidal ejecta. We find that the total ejecta mass increases as the fallback-to-disk mass ratio increases, which also lowers the mean electron fraction of the disk outflow. In most cases, the nucleosynthesis is dominated by heavy r-process elements synthesized in the unbound tail. However, a solar-like abundance pattern can be obtained if the total dynamical ejecta mass is comparable to the disk outflow mass.

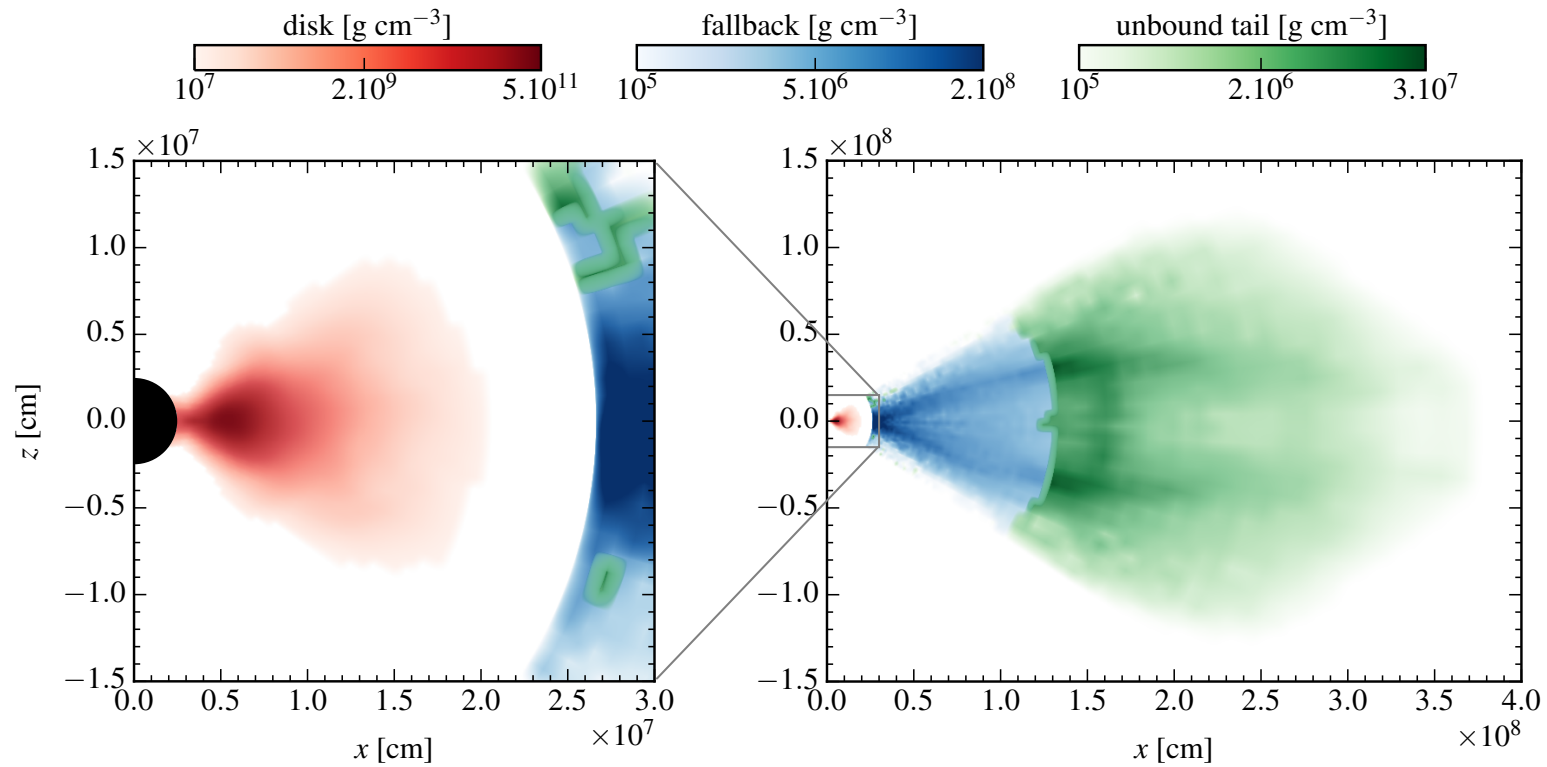


Figure 6.6: The initial setup for the simulation of the interaction between the tidal ejecta and accretion disk in a BHNS merger. The density of the accretion disk is shown in red, the fallback component (unbound tidal tail ejecta) in blue, and the unbound tidal ejecta in green. The disk configuration comes from a fully general-relativistic merger simulation that evolved the disk up to 20 ms after merger. The tidal ejecta is reconstructed from tracer particles from an earlier snapshot of that simulation, since it has left the simulation domain at  $t = 20$  ms. Both ejecta components are mapped into a 2D Newtonian code that can evolve them together for longer times. The gap between the two components gets filled in within a fraction of a millisecond. Top panel of Figure 1 from Fernández et al. (2017); see that reference for details. © 2017 IOP Publishing Ltd.

*This is a project I worked on in the summer of 2015 as a CUDA DevTech intern at NVIDIA Corporation. I developed the original prototype code but it has been significantly expanded since then. This project did not result in a peer-reviewed publication, but some slides<sup>1</sup> and a blog post<sup>2</sup> are publicly available.*

## Fast and efficient multi-GPU collective communication

**Nathan Luehr, Jonas Lippuner, Cliff Woolley, Przemek Tredak,  
Sylvain Jeaugey, Natalia Gimelshein, Simon Layton**

Large-scale parallel calculations are performed on graphics processing units (GPUs) to solve problems in a variety of academic and industrial applications. Some of these applications include large artificial neural networks (Deep Learning), parallel Fast Fourier Transforms (FFTs), molecular dynamics simulations, and graph analytics. In many cases, the problems are too big for a single GPU and so they have to be spread across multiple GPUs. Collective communication operations, such as broadcast, scatter, gather, all-reduce, etc., are commonly used in parallel applications. These communication primitives are described in the Message Passing Interface (MPI) standard and various implementations of it are used on supercomputers. Until now, however, there was no standard implementation of collective communication primitives for communication between multiple GPUs.

In this project, we developed a new library for fast and efficient multi-GPU collective communication called NCCL (pronounced “nickel”). The implementation assumes a unidirectional ring topology, which can be shown to be optimal for most collective communication operations. The data is divided into small messages to reduce latency, but the message size cannot be too small because otherwise the full communication bandwidth will not be utilized. Figure 6.7 shows that we achieve near-optimal or optimal bandwidth for communication among four GPUs. NCCL has been made available as open-source at <https://github.com/NVIDIA/ncccl>. Leading deep learning frameworks such as Caffe2 (Facebook), Microsoft Cognitive Toolkit, MXNet (Amazon Web Services), PyTorch (Facebook), and TensorFlow (Google) use NCCL to deliver near-linear scaling of deep learning training on multi-GPU systems.<sup>3</sup>

---

<sup>1</sup><https://images.nvidia.com/events/sc15/pdfs/NCCL-Woolley.pdf>

<sup>2</sup><https://devblogs.nvidia.com/parallelforall/fast-multi-gpu-collectives-ncccl>

<sup>3</sup><https://developer.nvidia.com/ncccl> retrieved 2017-06-07

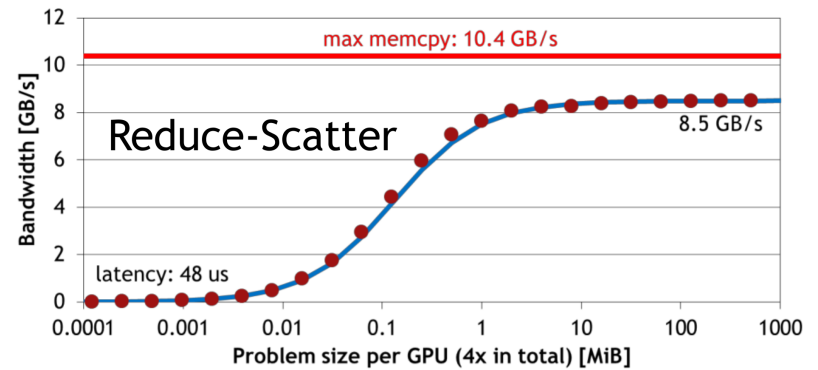
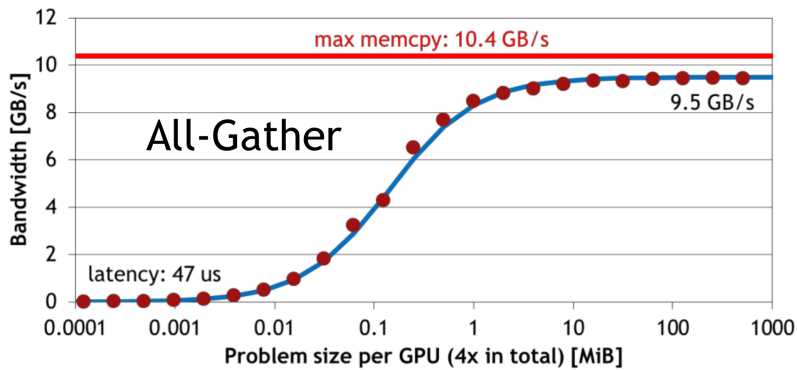
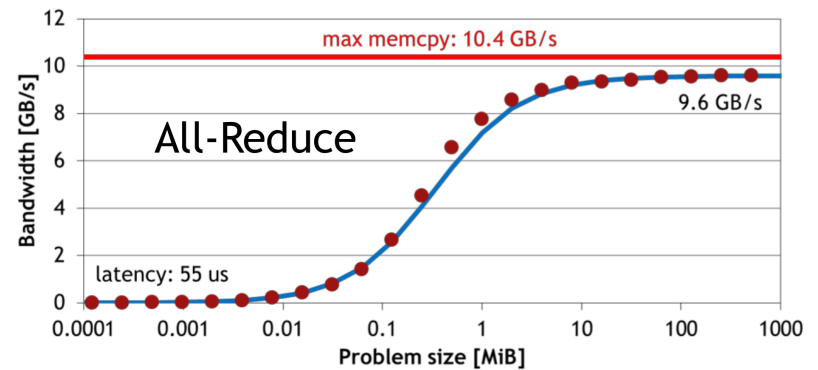
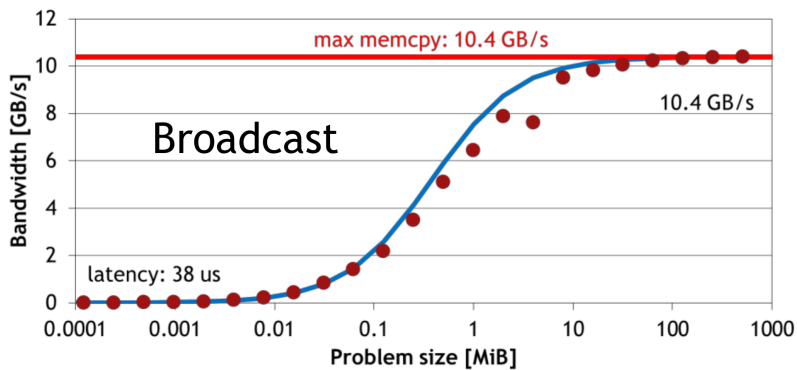


Figure 6.7: Performance test of some collective communication operations implemented in NCCL. The total communication bandwidth is measured (red dots) as function of the problem size and compared to a theoretical calculation (blue lines). For small problem sizes, the communication is inefficient because there is too little data to saturate the communication links. But for large problems, we achieve communication bandwidths that are close to the maximum achieved memory copy bandwidth between the GPUs. These tests were run on four Maxwell GPUs. © 2015 NVIDIA Corporation

## SUMMARY AND OUTLOOK

Progress has been made in understanding r-process nucleosynthesis in different astrophysical environments. While the site of the r-process remains an open question, there is a growing body of evidence that points to neutron star mergers as the dominant source of the heavy r-process elements. Such evidence includes (i) recent core-collapse supernova (CCSN) simulations that fail to produce the third r-process peak in the neutrino-driven wind; (ii) measurements of the short-lived radioactive isotope  $^{244}\text{Pu}$  in the deep sea crust and early solar system, which are not compatible with a steady-state production of  $^{244}\text{Pu}$  in CCSNe; (iii) observations of highly r-process enhanced stars in one of about ten known ultrafaint dwarf galaxies, which suggests that the r-process is a rare event with a high yield; and (iv) tentative observations of infrared kilonova transients accompanying short gamma ray bursts (sGRBs), which are thought to be the result of a neutron star merger.

I have developed *SkyNet*, a new nuclear reaction network that is easy to use and flexible. *SkyNet* is publicly available at <https://bitbucket.org/jlippuner/skyenet> as open-source software. *SkyNet* tracks the abundances of an arbitrary list of nuclear species undergoing an arbitrary set of nuclear reactions. *SkyNet* can seamlessly switch between the full network evolution and an equilibrium evolution, based on the thermodynamic conditions. Thanks to the modularity of *SkyNet*, it is easy to add additional physics or change parts of the existing physics implementation. *SkyNet* is actively being used by multiple researchers at several institutions and I hope that *SkyNet* will be a useful tool to the broader nuclear astrophysics community. In Chapter II, I present in detail the physics that is implemented in *SkyNet* and I perform comprehensive code tests and comparisons. I find that *SkyNet* produces results that are compatible with other reaction network codes.

I have used *SkyNet* to contribute to our understanding of r-process nucleosynthesis in different neutron star merger contexts. In Chapter III, I systematically investigate the dependence of the r-process on the initial electron fraction, initial entropy, and expansion timescale of the fluid. I show which regions of parameter space are lanthanide-rich and which are lanthanide-free and I find that the amount of lanthanides synthesized does not strongly correlate with the heating rate in the ejecta.

I use these results to quantitatively study the impact on kilonova light curves with a simple radiative transfer model. In Chapter IV, I present r-process nucleosynthesis calculations with *SkyNet* in the dynamical ejecta of a black hole–neutron star (BHNS) merger. I systematically vary the neutrino luminosity from the remnant disk to study its impact on the nucleosynthesis. I find that the r-process easily synthesizes the third peak and the final abundance pattern above  $A \sim 80$  does not depend on the neutrino luminosity. At lower masses, however, neutrinos can significantly enhance the production of the first peak via a newly described mechanism. In Chapter V, I use *SkyNet* to investigate r-process nucleosynthesis in the wind ejected from accretion disks formed in neutron star mergers. I vary the lifetime of the central hypermassive neutron star (HMNS) before it collapses to a black hole and quantify its impact on the nucleosynthesis. I find that a short ( $\lesssim 10$  ms) HMNS lifetime is required to produce a third r-process peak that matches the solar abundances with the disk outflow alone. For longer lifetimes, the disk ejecta is less neutron-rich and does not synthesize a significant amount of lanthanides. Finally, in Chapter VI, I summarize my minor contributions to other projects, such as binary neutron star (BNS) inspiral and merger simulations, observations of a high magnetic field radio pulsar that exhibits magnetar-like behavior, r-process nucleosynthesis in protomagnetars, and the development of a new large-scale parallel code for relativistic astrophysics.

In the future, I plan to continue the development of *SkyNet* and improve some of the physics. Specifically, I plan to add higher order integration methods and investigate other electron screening prescriptions. An extended screening implementation that includes screening corrections in the equation of state (EOS) is also planned. I intend to parallelize *SkyNet* so that it can run on GPUs. This will allow me to couple *SkyNet* to large hydrodynamics simulation where nuclear reactions play an important role, such as CCSN simulations. The capability of computing in-situ nucleosynthesis yields in CCSN will enable the detailed study of neutrino interactions in CCSNe and their impact on the nucleosynthesis, leading to new insights into the CCSN engine physics and nuclear reaction rates from yield observations. It will also advance our understanding of the origin of the elements and the chemical evolution history of our galaxy.

With the first detection of gravitational waves from binary black hole (BBH) mergers by the Laser Interferometer Gravitational Wave Observatory (LIGO), we are entering an exciting era of gravitational wave and nuclear astrophysics. Before long, LIGO and other gravitational wave detectors will see the gravitational waves from neutron

star mergers, which will allow us to constrain the merger rate, learn more about the nuclear EOS of neutron stars, and clarify the connection between sGRBs and neutron star mergers. The GROWTH Global Network of Observatories is poised to perform rapid electromagnetic (EM) follow-up observations of gravitational wave sources and will enable the routine detection of kilonovae in the near future or place stringent upper limits on EM counterparts to neutron star mergers. Many large-sky spectroscopic surveys, such as LEGUE and SDSS, have recently been conducted or are planned. These surveys find the most metal-poor stars known to date, which put important constraints on galactic chemical evolution models, and they map out the chemical composition of the galaxy. Finally, next-generation radioactive beam facilities, such as FRIB, ARIEL, and SPIRAL2, will measure nuclear properties of a host of exotic nuclei that have never before been created in a lab. These measurements are desperately needed to improve our nuclear mass models and nucleosynthesis calculations. Given the precise abundance measurements available today, more accurate nuclear data may even shed light on the site of the r-process.

To keep up with these expected advances in observational astronomy and experimental nuclear physics, the next generation of large-scale, multiphysics simulations of astrophysical phenomena will be required to be more detailed, more sophisticated, and include even more different physics coupled together. This will necessarily require a more detailed treatment of nuclear reactions coupled to the hydrodynamics evolution and I believe that a future version of *SkyNet* will be able to provide this capability.

## BIBLIOGRAPHY

- Abbott, B. P. et al. (2016a). “Observation of Gravitational Waves from a Binary Black Hole Merger”. In: *Physical Review Letters* 116.6, p. 061102. DOI: [10.1103/PhysRevLett.116.061102](https://doi.org/10.1103/PhysRevLett.116.061102). arXiv: [1602.03837 \[gr-qc\]](https://arxiv.org/abs/1602.03837).
- Abbott, B. P. et al. (2016b). “Prospects for Observing and Localizing Gravitational-Wave Transients with Advanced LIGO and Advanced Virgo”. In: *Liv. Rev. Rel.* 19. DOI: [10.1007/lrr-2016-1](https://doi.org/10.1007/lrr-2016-1). arXiv: [1304.0670 \[gr-qc\]](https://arxiv.org/abs/1304.0670).
- Acernese, F., M. Agathos, K. Agatsuma, D. Aisa, N. Allemandou, et al. (2015). “Advanced Virgo: a second-generation interferometric gravitational wave detector”. In: *Classical and Quantum Gravity* 32.2, p. 024001. DOI: [10.1088/0264-9381/32/2/024001](https://doi.org/10.1088/0264-9381/32/2/024001). arXiv: [1408.3978 \[gr-qc\]](https://arxiv.org/abs/1408.3978).
- Akiyama, S., J. C. Wheeler, D. L. Meier, and I. Lichtenstadt (2003). “The Magnetorotational Instability in Core-Collapse Supernova Explosions”. In: *Astrophysical Journal* 584, p. 954. DOI: [10.1086/344135](https://doi.org/10.1086/344135).
- Aleklett, K., D. J. Morrissey, W. Loveland, P. L. McGaughey, and G. T. Seaborg (1981). “Energy dependence of  $^{209}\text{Bi}$  fragmentation in relativistic nuclear collisions”. In: *Physical Review C* 23, p. 1044. DOI: [10.1103/PhysRevC.23.1044](https://doi.org/10.1103/PhysRevC.23.1044).
- Alpher, R. A., H. Bethe, and G. Gamow (1948). “The Origin of Chemical Elements”. In: *Physical Review* 73, p. 803. DOI: [10.1103/PhysRev.73.803](https://doi.org/10.1103/PhysRev.73.803).
- Alpher, R. A. and R. C. Herman (1950). “Theory of the Origin and Relative Abundance Distribution of the Elements”. In: *Reviews of Modern Physics* 22, p. 153. DOI: [10.1103/RevModPhys.22.153](https://doi.org/10.1103/RevModPhys.22.153).
- Anders, E. and N. Grevesse (1989). “Abundances of the elements - Meteoritic and solar”. In: *Geochimica Cosmochimica Acta* 53, p. 197. DOI: [10.1016/0016-7037\(89\)90286-X](https://doi.org/10.1016/0016-7037(89)90286-X).
- Antoniadis, J., P. C. C. Freire, N. Wex, T. M. Tauris, R. S. Lynch, et al. (2013). “A Massive Pulsar in a Compact Relativistic Binary”. In: *Science* 340, p. 448. DOI: [10.1126/science.1233232](https://doi.org/10.1126/science.1233232). arXiv: [1304.6875 \[astro-ph.HE\]](https://arxiv.org/abs/1304.6875).
- Arcones, A., C. Fröhlich, and G. Martínez-Pinedo (2012). “Impact of Supernova Dynamics on the  $\nu p$ -process”. In: *Astrophysical Journal* 750, p. 18. DOI: [10.1088/0004-637X/750/1/18](https://doi.org/10.1088/0004-637X/750/1/18). arXiv: [1112.4651 \[astro-ph.SR\]](https://arxiv.org/abs/1112.4651).
- Arcones, A., H.-T. Janka, and L. Scheck (2007). “Nucleosynthesis-relevant conditions in neutrino-driven supernova outflows. I. Spherically symmetric hydrodynamic simulations”. In: *Astronomy and Astrophysics* 467, p. 1227. DOI: [10.1051/0004-6361:20066983](https://doi.org/10.1051/0004-6361:20066983).

- Arcones, A. and G. Martínez-Pinedo (2011). “Dynamical r-process studies within the neutrino-driven wind scenario and its sensitivity to the nuclear physics input”. In: *Physical Review C* 83.4, p. 045809. DOI: [10.1103/PhysRevC.83.045809](https://doi.org/10.1103/PhysRevC.83.045809). arXiv: [1008.3890](https://arxiv.org/abs/1008.3890) [[astro-ph.SR](#)].
- Arcones, A., G. Martínez-Pinedo, L. F. Roberts, and S. E. Woosley (2010). “Electron fraction constraints based on nuclear statistical equilibrium with beta equilibrium”. In: *Astronomy and Astrophysics* 522, A25. DOI: [10.1051/0004-6361/201014276](https://doi.org/10.1051/0004-6361/201014276). arXiv: [1002.3854](https://arxiv.org/abs/1002.3854) [[astro-ph.SR](#)].
- Arcones, A. and F. Montes (2011). “Production of Light-element Primary Process Nuclei in Neutrino-driven Winds”. In: *Astrophysical Journal* 731, p. 5. DOI: [10.1088/0004-637X/731/1/5](https://doi.org/10.1088/0004-637X/731/1/5). arXiv: [1007.1275](https://arxiv.org/abs/1007.1275) [[astro-ph.GA](#)].
- Arcones, A. and F.-K. Thielemann (2013). “Neutrino-driven wind simulations and nucleosynthesis of heavy elements”. In: *Journal of Physics G Nuclear Physics* 40.1, p. 013201. DOI: [10.1088/0954-3899/40/1/013201](https://doi.org/10.1088/0954-3899/40/1/013201). arXiv: [1207.2527](https://arxiv.org/abs/1207.2527) [[astro-ph.SR](#)].
- Argast, D., M. Samland, F.-K. Thielemann, and Y.-Z. Qian (2004). “Neutron star mergers versus core-collapse supernovae as dominant r-process sites in the early Galaxy”. In: *Astronomy and Astrophysics* 416, p. 997. DOI: [10.1051/0004-6361:20034265](https://doi.org/10.1051/0004-6361:20034265). arXiv: [astro-ph/0309237](https://arxiv.org/abs/astro-ph/0309237).
- Arlandini, C., F. Käppeler, K. Wisshak, R. Gallino, M. Lugaro, M. Busso, and O. Straniero (1999). “Neutron Capture in Low-Mass Asymptotic Giant Branch Stars: Cross Sections and Abundance Signatures”. In: *Astrophysical Journal* 525, p. 886. DOI: [10.1086/307938](https://doi.org/10.1086/307938). arXiv: [astro-ph/9906266](https://arxiv.org/abs/astro-ph/9906266).
- Arnett, D. (1996). *Supernovae and Nucleosynthesis*. Princeton NJ, United States: Princeton University Press. ISBN: 978-0-691-01147-9.
- Arnett, W. D. (1977). “Neutrino trapping during gravitational collapse of stars”. In: *Astrophysical Journal* 218, p. 815. DOI: [10.1086/155738](https://doi.org/10.1086/155738).
- Arnett, W. D. and J. W. Truran (1969). “Carbon-Burning Nucleosynthesis at Constant Temperature”. In: *Astrophysical Journal* 157, p. 339. DOI: [10.1086/150072](https://doi.org/10.1086/150072).
- Arnould, M. and S. Goriely (2003). “The p-process of stellar nucleosynthesis: astrophysics and nuclear physics status”. In: *Physics Reports* 384, p. 1. DOI: [10.1016/S0370-1573\(03\)00242-4](https://doi.org/10.1016/S0370-1573(03)00242-4).
- Arnould, M., S. Goriely, and K. Takahashi (2007). “The r-process of stellar nucleosynthesis: Astrophysics and nuclear physics achievements and mysteries”. In: *Physics Reports* 450, p. 97. DOI: [10.1016/j.physrep.2007.06.002](https://doi.org/10.1016/j.physrep.2007.06.002). arXiv: [0705.4512](https://arxiv.org/abs/0705.4512).
- Artemova, I. V., G. Björnsson, and I. D. Novikov (1996). “Modified Newtonian Potentials for the Description of Relativistic Effects in Accretion Disks around Black Holes”. In: *ApJ* 461, p. 565. DOI: [10.1086/177084](https://doi.org/10.1086/177084).

- Avogadro, L. R. A. C. (1811). “Essay on Determining the Relative Masses of the Elementary Molecules of Bodies and the Proportions by Which They Enter These Combinations”. In: *Journal de Physique* 73, p. 58.
- Bader, G. and P. Deuffhard (1983). “A semi-implicit mid-point rule for stiff systems of ordinary differential equations”. In: *Numerische Mathematik* 41.3, p. 373. DOI: [10.1007/BF01418331](https://doi.org/10.1007/BF01418331).
- Bailey, C. (1928). *The Greek atomists and Epicurus*. Oxford, United Kingdom: Clarendon Press.
- Balsara, D. S. (1995). “von Neumann stability analysis of smooth particle hydrodynamics—suggestions for optimal algorithms”. In: *Journal of Computational Phys.* 121, p. 357. DOI: [10.1016/S0021-9991\(95\)90221-X](https://doi.org/10.1016/S0021-9991(95)90221-X).
- Barkett, K., M. A. Scheel, R. Haas, C. D. Ott, S. Bernuzzi, et al. (2016). “Gravitational waveforms for neutron star binaries from binary black hole simulations”. In: *Physical Review D* 93.4, p. 044064. DOI: [10.1103/PhysRevD.93.044064](https://doi.org/10.1103/PhysRevD.93.044064). arXiv: [1509.05782 \[gr-qc\]](https://arxiv.org/abs/1509.05782).
- Barnes, J. and D. Kasen (2013). “Effect of a High Opacity on the Light Curves of Radioactively Powered Transients from Compact Object Mergers”. In: *Astrophysical Journal* 775, p. 18. DOI: [10.1088/0004-637X/775/1/18](https://doi.org/10.1088/0004-637X/775/1/18). arXiv: [1303.5787 \[astro-ph.HE\]](https://arxiv.org/abs/1303.5787).
- Barnes, J., D. Kasen, M.-R. Wu, and G. Martínez-Pinedo (2016). “Radioactivity and Thermalization in the Ejecta of Compact Object Mergers and Their Impact on Kilonova Light Curves”. In: *Astrophysical Journal* 829, p. 110. DOI: [10.3847/0004-637X/829/2/110](https://doi.org/10.3847/0004-637X/829/2/110). arXiv: [1605.07218 \[astro-ph.HE\]](https://arxiv.org/abs/1605.07218).
- Bauswein, A., R. Ardevol Pulpillo, H.-T. Janka, and S. Goriely (2014a). “Nucleosynthesis Constraints on the Neutron Star-Black Hole Merger Rate”. In: *Astrophysical Journal, Letters* 795, p. L9. DOI: [10.1088/2041-8205/795/1/L9](https://doi.org/10.1088/2041-8205/795/1/L9). arXiv: [1408.1783 \[astro-ph.SR\]](https://arxiv.org/abs/1408.1783).
- Bauswein, A., S. Goriely, and H.-T. Janka (2013). “Systematics of Dynamical Mass Ejection, Nucleosynthesis, and Radioactively Powered Electromagnetic Signals from Neutron-star Mergers”. In: *Astrophysical Journal* 773, p. 78. DOI: [10.1088/0004-637X/773/1/78](https://doi.org/10.1088/0004-637X/773/1/78). arXiv: [1302.6530 \[astro-ph.SR\]](https://arxiv.org/abs/1302.6530).
- Bauswein, A., N. Stergioulas, and H.-T. Janka (2014b). “Revealing the high-density equation of state through binary neutron star mergers”. In: *Physical Review D* 90.2, p. 023002. DOI: [10.1103/PhysRevD.90.023002](https://doi.org/10.1103/PhysRevD.90.023002). arXiv: [1403.5301 \[astro-ph.SR\]](https://arxiv.org/abs/1403.5301).
- Bellm, E. (2014). “The Zwicky Transient Facility”. In: *The Third Hot-wiring the Transient Universe Workshop*. Ed. by P. R. Wozniak, M. J. Graham, A. A. Mahabal, and R. Seaman, p. 27. arXiv: [1410.8185 \[astro-ph.IM\]](https://arxiv.org/abs/1410.8185).

- Berger, E., W. Fong, and R. Chornock (2013). “An r-process Kilonova Associated with the Short-hard GRB 130603B”. In: *Astrophysical Journal, Letters* 774, p. L23. DOI: [10.1088/2041-8205/774/2/L23](https://doi.org/10.1088/2041-8205/774/2/L23). arXiv: [1306.3960](https://arxiv.org/abs/1306.3960) [[astro-ph.HE](#)].
- Bertolli, M. G., F. Herwig, M. Pignatari, and T. Kawano (2013). “Systematic and correlated nuclear uncertainties in the i-process at the neutron shell closure  $N = 82$ ”. In: *ArXiv e-prints*. arXiv: [1310.4578](https://arxiv.org/abs/1310.4578) [[astro-ph.SR](#)].
- Bethe, H. A. (1939). “Energy Production in Stars”. In: *Physical Review* 55, p. 434. DOI: [10.1103/PhysRev.55.434](https://doi.org/10.1103/PhysRev.55.434).
- Blinnikov, S. I. and I. V. Panov (1996). “A kinetic model for rapid nucleosynthesis”. In: *Astronomy Letters* 22, p. 39.
- Bodansky, D., D. D. Clayton, and W. A. Fowler (1968). “Nuclear Quasi-Equilibrium during Silicon Burning”. In: *Astrophysical Journal, Supplement* 16, p. 299. DOI: [10.1086/190176](https://doi.org/10.1086/190176).
- Boyd, R. N. (2008). *An Introduction to Nuclear Astrophysics*. Chicago IL, United States: University of Chicago Press. ISBN: 978-0-226-06971-5.
- Boyle, R. W. (1661). *The Sceptical Chymist*. London, United Kingdom: J. Cadwell.
- Bressan, A., P. Marigo, L. Girardi, B. Salasnich, C. Dal Cero, S. Rubele, and A. Nanni (2012). “PARSEC: stellar tracks and isochrones with the PAdova and TRieste Stellar Evolution Code”. In: *Monthly Notices of the RAS* 427, p. 127. DOI: [10.1111/j.1365-2966.2012.21948.x](https://doi.org/10.1111/j.1365-2966.2012.21948.x). arXiv: [1208.4498](https://arxiv.org/abs/1208.4498) [[astro-ph.SR](#)].
- Brett, S., I. Bentley, N. Paul, R. Surman, and A. Aprahamian (2012). “Sensitivity of the r-process to nuclear masses”. In: *European Physical Journal A* 48, p. 184. DOI: [10.1140/epja/i2012-12184-4](https://doi.org/10.1140/epja/i2012-12184-4). arXiv: [1211.7310](https://arxiv.org/abs/1211.7310) [[nucl-th](#)].
- Brock, B., A. Belt, J. J. Billings, and M. Guidry (2015). “Explicit integration with GPU acceleration for large kinetic networks”. In: *Journal of Computational Phys.* 302, p. 591. DOI: [10.1016/j.jcp.2015.09.013](https://doi.org/10.1016/j.jcp.2015.09.013). arXiv: [1409.5826](https://arxiv.org/abs/1409.5826) [[physics.comp-ph](#)].
- Brown, L. S. and R. F. Sawyer (1997). “Nuclear reaction rates in a plasma”. In: *Reviews of Modern Physics* 69, p. 411. DOI: [10.1103/RevModPhys.69.411](https://doi.org/10.1103/RevModPhys.69.411). arXiv: [astro-ph/9610256](https://arxiv.org/abs/astro-ph/9610256).
- Buonanno, A. and T. Damour (1999). “Effective one-body approach to general relativistic two-body dynamics”. In: *Physical Review D* 59.8, p. 084006. DOI: [10.1103/PhysRevD.59.084006](https://doi.org/10.1103/PhysRevD.59.084006). arXiv: [gr-qc/9811091](https://arxiv.org/abs/gr-qc/9811091).
- Burbidge, E. M., G. R. Burbidge, William A. Fowler, and F. Hoyle (1957). “Synthesis of the Elements in Stars”. In: *Reviews of Modern Physics* 29 (4), p. 547. DOI: [10.1103/RevModPhys.29.547](https://doi.org/10.1103/RevModPhys.29.547).

- Burden, R. L., J. D. Faires, and A. M. Burden (2015). *Numerical analysis*. 10th ed. Boston, MA, United States: Cengage Learning, Inc. ISBN: 1305253663.
- Burrows, A., L. Dessart, E. Livne, C. D. Ott, and J. Murphy (2007). “Simulations of Magnetically Driven Supernova and Hypernova Explosions in the Context of Rapid Rotation”. In: *Astrophysical Journal* 664, p. 416. DOI: [10.1086/519161](https://doi.org/10.1086/519161). arXiv: [astro-ph/0702539](https://arxiv.org/abs/astro-ph/0702539).
- Buss, O., T. Gaitanos, K. Gallmeister, H. van Hees, M. Kaskulov, O. Lalakulich, A. B. Larionov, T. Leitner, J. Weil, and U. Mosel (2012). “Transport-theoretical description of nuclear reactions”. In: *Physics Reports* 512, p. 1. DOI: [10.1016/j.physrep.2011.12.001](https://doi.org/10.1016/j.physrep.2011.12.001). arXiv: [1106.1344](https://arxiv.org/abs/1106.1344) [hep-ph].
- Cameron, A. G. W. (1973). “Abundances of the Elements in the Solar System”. In: *Space Science Reviews* 15, p. 121. DOI: [10.1007/BF00172440](https://doi.org/10.1007/BF00172440).
- Cescutti, G., D. Romano, F. Matteucci, C. Chiappini, and R. Hirschi (2015). “The role of neutron star mergers in the chemical evolution of the Galactic halo”. In: *Astronomy and Astrophysics* 577, A139. DOI: [10.1051/0004-6361/201525698](https://doi.org/10.1051/0004-6361/201525698). arXiv: [1503.02954](https://arxiv.org/abs/1503.02954).
- Chadwick, J. (1932). “The Existence of a Neutron”. In: *Proceedings of the Royal Society of London Series A* 136, p. 692. DOI: [10.1098/rspa.1932.0112](https://doi.org/10.1098/rspa.1932.0112).
- Chamel, N. (2013). “Crustal Entrainment and Pulsar Glitches”. In: *Physical Review Letters* 110.1, p. 011101. DOI: [10.1103/PhysRevLett.110.011101](https://doi.org/10.1103/PhysRevLett.110.011101). arXiv: [1210.8177](https://arxiv.org/abs/1210.8177) [astro-ph.HE].
- Chen, Y. C., C. E. Simien, S. Laha, P. Gupta, Y. N. Martinez, P. G. Mickelson, S. B. Nagel, and T. C. Killian (2004). “Electron Screening and Kinetic-Energy Oscillations in a Strongly Coupled Plasma”. In: *Physical Review Letters* 93.26, p. 265003. DOI: [10.1103/PhysRevLett.93.265003](https://doi.org/10.1103/PhysRevLett.93.265003).
- Chevalier, R. A. and N. Soker (1989). “Asymmetric envelope expansion of supernova 1987A”. In: *Astrophysical Journal* 341, p. 867. DOI: [10.1086/167545](https://doi.org/10.1086/167545).
- Chugunov, A. I., H. E. Dewitt, and D. G. Yakovlev (2007). “Coulomb tunneling for fusion reactions in dense matter: Path integral MonteCarlo versus mean field”. In: *Physical Review D* 76.2, p. 025028. DOI: [10.1103/PhysRevD.76.025028](https://doi.org/10.1103/PhysRevD.76.025028). arXiv: [0707.3500](https://arxiv.org/abs/0707.3500).
- Clayton, D. D. (1968). *Principles of stellar evolution and nucleosynthesis*. Chicago IL, United States: University of Chicago Press. ISBN: 0-226-10953-4.
- Coc, A., S. Goriely, Y. Xu, M. Saimpert, and E. Vangioni (2012). “Standard Big Bang Nucleosynthesis up to CNO with an Improved Extended Nuclear Network”. In: *Astrophysical Journal* 744, p. 158. DOI: [10.1088/0004-637X/744/2/158](https://doi.org/10.1088/0004-637X/744/2/158). arXiv: [1107.1117](https://arxiv.org/abs/1107.1117).

- Coc, A., J.-P. Uzan, and E. Vangioni (2013). “Mirror matter can alleviate the cosmological lithium problem”. In: *Physical Review D* 87.12, p. 123530. DOI: [10.1103/PhysRevD.87.123530](https://doi.org/10.1103/PhysRevD.87.123530). arXiv: [1303.1935](https://arxiv.org/abs/1303.1935).
- Cockburn, B. and C.-W. Shu (1998). “The Runge-Kutta Discontinuous Galerkin Method for Conservation Laws V. Multidimensional Systems”. In: *Journal of Computational Phys.* 141, p. 199. DOI: [10.1006/jcph.1998.5892](https://doi.org/10.1006/jcph.1998.5892).
- Couch, R. G., A. B. Schmiedekamp, and W. D. Arnett (1974). “S-PROCESS Nucleosynthesis in Massive Stars: Core Helium Burning”. In: *Astrophysical Journal* 190, p. 95. DOI: [10.1086/152851](https://doi.org/10.1086/152851).
- Cowan, J. J., B. Pfeiffer, K.-L. Kratz, F.-K. Thielemann, C. Sneden, S. Burles, D. Tytler, and T. C. Beers (1999). “R-Process Abundances and Chronometers in Metal-poor Stars”. In: *Astrophysical Journal* 521, p. 194. DOI: [10.1086/307512](https://doi.org/10.1086/307512). arXiv: [astro-ph/9808272](https://arxiv.org/abs/astro-ph/9808272).
- Cowan, J. J. and W. K. Rose (1977). “Production of C-14 and neutrons in red giants”. In: *Astrophysical Journal* 212, p. 149. DOI: [10.1086/155030](https://doi.org/10.1086/155030).
- Cyburt, R. H., A. M. Amthor, R. Ferguson, Z. Meisel, K. Smith, et al. (2010). “The JINA REACLIB Database: Its Recent Updates and Impact on Type-I X-ray Bursts”. In: *Astrophysical Journal, Supplement* 189.1. REACLIB is available at <https://groups.nsl.msu.edu/jina/reaclib/db/>, p. 240. DOI: [10.1088/0067-0049/189/1/240](https://doi.org/10.1088/0067-0049/189/1/240).
- Cyburt, R. H., B. D. Fields, K. A. Olive, and T.-H. Yeh (2016). “Big bang nucleosynthesis: Present status”. In: *Reviews of Modern Physics* 88.1, p. 015004. DOI: [10.1103/RevModPhys.88.015004](https://doi.org/10.1103/RevModPhys.88.015004). arXiv: [1505.01076](https://arxiv.org/abs/1505.01076).
- Dalton, J. (1808). *A New System of Chemical Philosophy*. London, United Kingdom: Rickerstaff.
- Damour, T. and A. Vilenkin (2001). “Gravitational wave bursts from cusps and kinks on cosmic strings”. In: *Physical Review D* 64.6, p. 064008. DOI: [10.1103/PhysRevD.64.064008](https://doi.org/10.1103/PhysRevD.64.064008). arXiv: [gr-qc/0104026](https://arxiv.org/abs/gr-qc/0104026).
- Danielewicz, P. and G. F. Bertsch (1991). “Production of deuterons and pions in a transport model of energetic heavy-ion reactions”. In: *Nuclear Physics A* 533, p. 712. DOI: [10.1016/0375-9474\(91\)90541-D](https://doi.org/10.1016/0375-9474(91)90541-D).
- Davis, S. W., J. M. Stone, and M. E. Pessah (2010). “Sustained Magnetorotational Turbulence in Local Simulations of Stratified Disks with Zero Net Magnetic Flux”. In: *ApJ* 713, p. 52. DOI: [10.1088/0004-637X/713/1/52](https://doi.org/10.1088/0004-637X/713/1/52). arXiv: [0909.1570](https://arxiv.org/abs/0909.1570) [[astro-ph.HE](https://arxiv.org/abs/astro-ph.HE)].
- De Donder, E. and D. Vanbeveren (2004). “The influence of binaries on galactic chemical evolution”. In: *New Astronomy Review* 48, p. 861. DOI: [10.1016/j.newar.2004.07.001](https://doi.org/10.1016/j.newar.2004.07.001). arXiv: [astro-ph/0410024](https://arxiv.org/abs/astro-ph/0410024).
- de Lavoisier, A.-L. (1789). *Traité Élémentaire de Chimie*. Paris, France: Cuchet.

- Deaton, M. B., M. D. Duez, F. Foucart, E. O'Connor, C. D. Ott, L. E. Kidder, C. D. Muhlberger, M. A. Scheel, and B. Szilagyi (2013). "Black Hole-Neutron Star Mergers with a Hot Nuclear Equation of State: Outflow and Neutrino-cooled Disk for a Low-mass, High-spin Case". In: *Astrophysical Journal* 776, p. 47. DOI: [10.1088/0004-637X/776/1/47](https://doi.org/10.1088/0004-637X/776/1/47). arXiv: [1304.3384](https://arxiv.org/abs/1304.3384) [[astro-ph.HE](#)].
- Del Pozzo, W., T. G. F. Li, M. Agathos, C. Van Den Broeck, and S. Vitale (2013). "Demonstrating the Feasibility of Probing the Neutron-Star Equation of State with Second-Generation Gravitational-Wave Detectors". In: *Physical Review Letters* 111.7, p. 071101. DOI: [10.1103/PhysRevLett.111.071101](https://doi.org/10.1103/PhysRevLett.111.071101). arXiv: [1307.8338](https://arxiv.org/abs/1307.8338) [[gr-qc](#)].
- Delano, M. D. and A. G. W. Cameron (1971). "Nucleosynthesis in Neutron Rich Supernova Ejecta". In: *Astrophysics and Space Science* 10, p. 203. DOI: [10.1007/BF00704083](https://doi.org/10.1007/BF00704083).
- Democritus (ca. 420 BC). *Lesser World-Order*.
- Demorest, P. B., T. Pennucci, S. M. Ransom, M. S. E. Roberts, and J. W. T. Hessels (2010). "A two-solar-mass neutron star measured using Shapiro delay". In: *Nature* 467, p. 1081. DOI: [10.1038/nature09466](https://doi.org/10.1038/nature09466). arXiv: [1010.5788](https://arxiv.org/abs/1010.5788) [[astro-ph.HE](#)].
- Dessart, L., C. D. Ott, A. Burrows, S. Rosswog, and E. Livne (2009). "Neutrino Signatures and the Neutrino-Driven Wind in Binary Neutron Star Mergers". In: *ApJ* 690, p. 1681. DOI: [10.1088/0004-637X/690/2/1681](https://doi.org/10.1088/0004-637X/690/2/1681). arXiv: [0806.4380](https://arxiv.org/abs/0806.4380).
- Dewitt, H. E., H. C. Graboske, and M. S. Cooper (1973). "Screening Factors for Nuclear Reactions. I. General Theory". In: *Astrophysical Journal* 181, p. 439. DOI: [10.1086/152061](https://doi.org/10.1086/152061).
- Dewitt, H. and W. Slattery (1999). "Screening enhancement of thermonuclear reactions in high density stars." In: *Contributions to Plasma Physics* 39, p. 97. DOI: [10.1002/ctpp.2150390124](https://doi.org/10.1002/ctpp.2150390124).
- Dominik, M., K. Belczynski, C. Fryer, D. E. Holz, E. Berti, T. Bulik, I. Mandel, and R. O'Shaughnessy (2012). "Double Compact Objects. I. The Significance of the Common Envelope on Merger Rates". In: *Astrophysical Journal* 759, p. 52. DOI: [10.1088/0004-637X/759/1/52](https://doi.org/10.1088/0004-637X/759/1/52). arXiv: [1202.4901](https://arxiv.org/abs/1202.4901) [[astro-ph.HE](#)].
- Dubey, A., L. B. Reid, K. Weide, K. Antypas, M. K. Ganapathy, K. Riley, D. Sheeler, and A. Siegal (2009). "Extensible Component Based Architecture for FLASH, A Massively Parallel, Multiphysics Simulation Code". In: *Parallel Comput.* 35, p. 512. DOI: [10.1016/j.parco.2009.08.001](https://doi.org/10.1016/j.parco.2009.08.001). arXiv: [0903.4875](https://arxiv.org/abs/0903.4875) [[cs.SE](#)].
- Duez, M. (2015). Private communication.
- Edvardsson, B., J. Andersen, B. Gustafsson, D. L. Lambert, P. E. Nissen, and J. Tomkin (1993). "The Chemical Evolution of the Galactic Disk - Part One - Analysis and Results". In: *Astronomy and Astrophysics* 275, p. 101.

- Eichler, M., A. Arcones, A. Kelic, O. Korobkin, K. Langanke, et al. (2015). “The Role of Fission in Neutron Star Mergers and Its Impact on the r-Process Peaks”. In: *Astrophysical Journal* 808, p. 30. DOI: [10.1088/0004-637X/808/1/30](https://doi.org/10.1088/0004-637X/808/1/30). arXiv: [1411.0974](https://arxiv.org/abs/1411.0974) [astro-ph.HE].
- Engstler, S., A. Krauss, K. Neldner, C. Rolfs, U. Schröder, and K. Langanke (1988). “Effects of electron screening on the  $^3\text{He}(d, p)^4\text{He}$  low-energy cross sections”. In: *Physics Letters B* 202, p. 179. DOI: [10.1016/0370-2693\(88\)90003-2](https://doi.org/10.1016/0370-2693(88)90003-2).
- Ensmann, L. (1994). “Test problems for radiation and radiation-hydrodynamics codes”. In: *Astrophysical Journal* 424, p. 275. DOI: [10.1086/173889](https://doi.org/10.1086/173889).
- Espinoza, C. M., A. G. Lyne, B. W. Stappers, and M. Kramer (2011). “A study of 315 glitches in the rotation of 102 pulsars”. In: *Monthly Notices of the RAS* 414, p. 1679. DOI: [10.1111/j.1365-2966.2011.18503.x](https://doi.org/10.1111/j.1365-2966.2011.18503.x). arXiv: [1102.1743](https://arxiv.org/abs/1102.1743) [astro-ph.HE].
- Farr, W. M., N. Sravan, A. Cantrell, L. Kreidberg, C. D. Bailyn, I. Mandel, and V. Kalogera (2011). “The Mass Distribution of Stellar-mass Black Holes”. In: *Astrophysical Journal* 741, p. 103. DOI: [10.1088/0004-637X/741/2/103](https://doi.org/10.1088/0004-637X/741/2/103). arXiv: [1011.1459](https://arxiv.org/abs/1011.1459) [astro-ph.GA].
- Feger, E. D. (2011). “Evaluating Explicit Methods for Solving Astrophysical Nuclear Reaction Networks”. [http://trace.tennessee.edu/utk\\_graddiss/1048](http://trace.tennessee.edu/utk_graddiss/1048). PhD thesis. University of Tennessee.
- Fermi, E. (1934). “Versuch einer Theorie der  $\beta$ -Strahlen. I”. In: *Zeitschrift für Physik* 88, p. 161. DOI: [10.1007/BF01351864](https://doi.org/10.1007/BF01351864).
- Fernández, R., F. Foucart, D. Kasen, J. Lippuner, D. Desai, and L. F. Roberts (2017). “Dynamics, nucleosynthesis, and kilonova signature of black hole - neutron star merger ejecta”. In: *Classical and Quantum Gravity, in press*. DOI: [10.1088/1361-6382/aa7a77](https://doi.org/10.1088/1361-6382/aa7a77). arXiv: [1612.04829](https://arxiv.org/abs/1612.04829) [astro-ph.HE].
- Fernández, R., D. Kasen, B. D. Metzger, and E. Quataert (2015a). “Outflows from accretion discs formed in neutron star mergers: effect of black hole spin”. In: *MNRAS* 446, p. 750. DOI: [10.1093/mnras/stu2112](https://doi.org/10.1093/mnras/stu2112). arXiv: [1409.4426](https://arxiv.org/abs/1409.4426) [astro-ph.HE].
- Fernández, R. and B. D. Metzger (2013). “Delayed outflows from black hole accretion tori following neutron star binary coalescence”. In: *Monthly Notices of the RAS* 435, p. 502. DOI: [10.1093/mnras/stt1312](https://doi.org/10.1093/mnras/stt1312). arXiv: [1304.6720](https://arxiv.org/abs/1304.6720) [astro-ph.HE].
- Fernández, R. and B. D. Metzger (2016). “Electromagnetic Signatures of Neutron Star Mergers in the Advanced LIGO Era”. In: *Annual Review of Nuclear and Particle Science* 66, p. 23. DOI: [10.1146/annurev-nucl-102115-044819](https://doi.org/10.1146/annurev-nucl-102115-044819). arXiv: [1512.05435](https://arxiv.org/abs/1512.05435) [astro-ph.HE].

- Fernández, R., E. Quataert, J. Schwab, D. Kasen, and S. Rosswog (2015b). “The interplay of disc wind and dynamical ejecta in the aftermath of neutron star-black hole mergers”. In: *MNRAS* 449, p. 390. DOI: [10.1093/mnras/stv238](https://doi.org/10.1093/mnras/stv238). arXiv: [1412.5588](https://arxiv.org/abs/1412.5588) [[astro-ph.HE](#)].
- Fields, B. D. (2011). “The Primordial Lithium Problem”. In: *Annual Review of Nuclear and Particle Science* 61, p. 47. DOI: [10.1146/annurev-nucl-102010-130445](https://doi.org/10.1146/annurev-nucl-102010-130445). arXiv: [1203.3551](https://arxiv.org/abs/1203.3551) [[astro-ph.CO](#)].
- Fischer, T., S. C. Whitehouse, A. Mezzacappa, F.-K. Thielemann, and M. Liebendörfer (2010). “Proton-neutron star evolution and the neutrino-driven wind in general relativistic neutrino radiation hydrodynamics simulations”. In: *Astronomy and Astrophysics* 517, A80. DOI: [10.1051/0004-6361/200913106](https://doi.org/10.1051/0004-6361/200913106). arXiv: [0908.1871](https://arxiv.org/abs/0908.1871) [[astro-ph.HE](#)].
- Fisker, J. L., H. Schatz, and F.-K. Thielemann (2008). “Explosive Hydrogen Burning during Type I X-Ray Bursts”. In: *Astrophysical Journal, Supplement* 174, p. 261. DOI: [10.1086/521104](https://doi.org/10.1086/521104).
- Flanagan, É. É. and T. Hinderer (2008). “Constraining neutron-star tidal Love numbers with gravitational-wave detectors”. In: *Physical Review D* 77.2, p. 021502. DOI: [10.1103/PhysRevD.77.021502](https://doi.org/10.1103/PhysRevD.77.021502). arXiv: [0709.1915](https://arxiv.org/abs/0709.1915).
- Fong, W. and E. Berger (2013). “The Locations of Short Gamma-Ray Bursts as Evidence for Compact Object Binary Progenitors”. In: *Astrophysical Journal* 776, p. 18. DOI: [10.1088/0004-637X/776/1/18](https://doi.org/10.1088/0004-637X/776/1/18). arXiv: [1307.0819](https://arxiv.org/abs/1307.0819) [[astro-ph.HE](#)].
- Fontes, C. J., C. L. Fryer, A. L. Hungerford, P. Hakel, J. Colgan, D. P. Kilcrease, and M. E. Sherrill (2015). “Relativistic opacities for astrophysical applications”. In: *High Energy Density Physics* 16, p. 53. DOI: [10.1016/j.hedp.2015.06.002](https://doi.org/10.1016/j.hedp.2015.06.002).
- Foucart, F. (2012). “Black-hole-neutron-star mergers: Disk mass predictions”. In: *Physical Review D* 86.12, p. 124007. DOI: [10.1103/PhysRevD.86.124007](https://doi.org/10.1103/PhysRevD.86.124007). arXiv: [1207.6304](https://arxiv.org/abs/1207.6304) [[astro-ph.HE](#)].
- Foucart, F., M. B. Deaton, M. D. Duez, L. E. Kidder, I. MacDonald, C. D. Ott, H. P. Pfeiffer, M. A. Scheel, B. Szilagyi, and S. A. Teukolsky (2013). “Black-hole-neutron-star mergers at realistic mass ratios: Equation of state and spin orientation effects”. In: *Physical Review D* 87.8, p. 084006. DOI: [10.1103/PhysRevD.87.084006](https://doi.org/10.1103/PhysRevD.87.084006). arXiv: [1212.4810](https://arxiv.org/abs/1212.4810) [[gr-qc](#)].
- Foucart, F., M. B. Deaton, M. D. Duez, E. O’Connor, C. D. Ott, R. Haas, L. E. Kidder, H. P. Pfeiffer, M. A. Scheel, and B. Szilagyi (2014). “Neutron star-black hole mergers with a nuclear equation of state and neutrino cooling: Dependence in the binary parameters”. In: *Physical Review D* 90.2, p. 024026. DOI: [10.1103/PhysRevD.90.024026](https://doi.org/10.1103/PhysRevD.90.024026). arXiv: [1405.1121](https://arxiv.org/abs/1405.1121) [[astro-ph.HE](#)].

- Foucart, F., D. Desai, W. Brege, M. D. Duez, D. Kasen, D. A. Hemberger, L. E. Kidder, H. P. Pfeiffer, and M. A. Scheel (2017). “Dynamical ejecta from precessing neutron star-black hole mergers with a hot, nuclear-theory based equation of state”. In: *Classical and Quantum Gravity* 34.4, p. 044002. DOI: [10.1088/1361-6382/aa573b](https://doi.org/10.1088/1361-6382/aa573b). arXiv: [1611.01159](https://arxiv.org/abs/1611.01159) [astro-ph.HE].
- Foucart, F., R. Haas, M. D. Duez, E. O’Connor, C. D. Ott, L. Roberts, L. E. Kidder, J. Lippuner, H. P. Pfeiffer, and M. A. Scheel (2016a). “Low mass binary neutron star mergers : gravitational waves and neutrino emission”. In: *Physical Review D* 93, p. 044019. DOI: [10.1103/PhysRevD.93.044019](https://doi.org/10.1103/PhysRevD.93.044019). arXiv: [1510.06398](https://arxiv.org/abs/1510.06398) [astro-ph.HE].
- Foucart, F., E. O’Connor, L. Roberts, M. D. Duez, R. Haas, L. E. Kidder, C. D. Ott, H. P. Pfeiffer, M. A. Scheel, and B. Szilagyí (2015). “Post-merger evolution of a neutron star-black hole binary with neutrino transport”. In: *Physical Review D* 91.12, p. 124021. DOI: [10.1103/PhysRevD.91.124021](https://doi.org/10.1103/PhysRevD.91.124021). arXiv: [1502.04146](https://arxiv.org/abs/1502.04146) [astro-ph.HE].
- Foucart, F., E. O’Connor, L. Roberts, L. E. Kidder, H. P. Pfeiffer, and M. A. Scheel (2016b). “Impact of an improved neutrino energy estimate on outflows in neutron star merger simulations”. In: *Physical Review D* 94.12, p. 123016. DOI: [10.1103/PhysRevD.94.123016](https://doi.org/10.1103/PhysRevD.94.123016). arXiv: [1607.07450](https://arxiv.org/abs/1607.07450) [astro-ph.HE].
- Frankel, S. and N. Metropolis (1947). “Calculations in the Liquid-Drop Model of Fission”. In: *Physical Review* 72, p. 914. DOI: [10.1103/PhysRev.72.914](https://doi.org/10.1103/PhysRev.72.914).
- Fraunhofer, J. R. von (1817). “Bestimmung des Brechungs-und des Farbenzerstreungs-Vermögens verschiedener Glasarten, in Bezug auf die Vervollkommnung achromatischer Fernröhre”. In: *Annalen der Physik* 56.7, p. 264.
- Freeman, K. (1946). *The Pre-Socratic Philosophers*. Oxford, United Kingdom: B. Blackwell.
- Freiburghaus, C., S. Rosswog, and F.-K. Thielemann (1999). “R-Process in Neutron Star Mergers”. In: *Astrophysical Journal, Letters* 525, p. L121. DOI: [10.1086/312343](https://doi.org/10.1086/312343).
- Fröhlich, C., P. Hauser, M. Liebendörfer, G. Martínez-Pinedo, F.-K. Thielemann, et al. (2006). “Composition of the Innermost Core-Collapse Supernova Ejecta”. In: *Astrophysical Journal* 637, p. 415. DOI: [10.1086/498224](https://doi.org/10.1086/498224).
- Fryxell, B., K. Olson, P. Ricker, F. X. Timmes, M. Zingale, D. Q. Lamb, P. MacNeice, R. Rosner, J. W. Truran, and H. Tufo (2000). “FLASH: An Adaptive Mesh Hydrodynamics Code for Modeling Astrophysical Thermonuclear Flashes”. In: *Astrophysical Journal, Supplement* 131, p. 273. DOI: [10.1086/317361](https://doi.org/10.1086/317361).

- Fuller, G. M., W. A. Fowler, and M. J. Newman (1982). “Stellar weak interaction rates for intermediate mass nuclei. III - Rate tables for the free nucleons and nuclei with  $A = 21$  to  $A = 60$ ”. In: *Astrophysical Journal, Supplement* 48, p. 279. DOI: [10.1086/190779](https://doi.org/10.1086/190779).
- Fuller, G. M. and B. S. Meyer (1995). “Neutrino Capture and Supernova Nucleosynthesis”. In: *Astrophysical Journal* 453, p. 792. DOI: [10.1086/176442](https://doi.org/10.1086/176442).
- Gaburov, E., J. C. Lombardi Jr., and S. Portegies Zwart (2010). “On the onset of runaway stellar collisions in dense star clusters - II. Hydrodynamics of three-body interactions”. In: *Monthly Notices of the RAS* 402, p. 105. DOI: [10.1111/j.1365-2966.2009.15900.x](https://doi.org/10.1111/j.1365-2966.2009.15900.x). arXiv: [0904.0997](https://arxiv.org/abs/0904.0997) [[astro-ph.SR](https://arxiv.org/abs/0904.0997)].
- Gatu Johnson, M., A. B. Zylstra, A. Bacher, C. R. Brune, D. T. Casey, et al. (2017). “Development of an inertial confinement fusion platform to study charged-particle-producing nuclear reactions relevant to nuclear astrophysics”. In: *Physics of Plasmas* 24.4, p. 041407. DOI: [10.1063/1.4979186](https://doi.org/10.1063/1.4979186).
- Gehrels, N., E. Ramirez-Ruiz, and D. B. Fox (2009). “Gamma-Ray Bursts in the Swift Era”. In: *Annual Review of Astronomy and Astrophysics* 47, p. 567. DOI: [10.1146/annurev.astro.46.060407.145147](https://doi.org/10.1146/annurev.astro.46.060407.145147).
- Goriely, S., A. Bauswein, and H.-T. Janka (2011). “r-process Nucleosynthesis in Dynamically Ejected Matter of Neutron Star Mergers”. In: *Astrophysical Journal, Letters* 738, p. L32. DOI: [10.1088/2041-8205/738/2/L32](https://doi.org/10.1088/2041-8205/738/2/L32). arXiv: [1107.0899](https://arxiv.org/abs/1107.0899) [[astro-ph.SR](https://arxiv.org/abs/1107.0899)].
- Goriely, S., A. Bauswein, O. Just, E. Pllumbi, and H.-T. Janka (2015). “Impact of weak interactions of free nucleons on the r-process in dynamical ejecta from neutron star mergers”. In: *Monthly Notices of the RAS* 452, p. 3894. DOI: [10.1093/mnras/stv1526](https://doi.org/10.1093/mnras/stv1526). arXiv: [1504.04377](https://arxiv.org/abs/1504.04377) [[astro-ph.SR](https://arxiv.org/abs/1504.04377)].
- Goriely, S., N. Chamel, and J. M. Pearson (2009). “Skyrme-Hartree-Fock-Bogoliubov Nuclear Mass Formulas: Crossing the 0.6MeV Accuracy Threshold with Microscopically Deduced Pairing”. In: *Physical Review Letters* 102.15, p. 152503. DOI: [10.1103/PhysRevLett.102.152503](https://doi.org/10.1103/PhysRevLett.102.152503). arXiv: [0906.2607](https://arxiv.org/abs/0906.2607) [[nucl-th](https://arxiv.org/abs/0906.2607)].
- Goriely, S., P. Demetriou, H.-T. Janka, J. M. Pearson, and M. Samyn (2005). “The r-process nucleosynthesis: a continued challenge for nuclear physics and astrophysics”. In: *Nuclear Physics A* 758, p. 587. DOI: [10.1016/j.nuclphysa.2005.05.107](https://doi.org/10.1016/j.nuclphysa.2005.05.107). arXiv: [astro-ph/0410429](https://arxiv.org/abs/astro-ph/0410429).
- Goriely, S., S. Hilaire, and A. J. Koning (2008). “Improved predictions of nuclear reaction rates with the TALYS reaction code for astrophysical applications”. In: *Astronomy and Astrophysics* 487, p. 767. DOI: [10.1051/0004-6361:20078825](https://doi.org/10.1051/0004-6361:20078825). arXiv: [0806.2239](https://arxiv.org/abs/0806.2239).

- Graboske, H. C., H. E. Dewitt, A. S. Grossman, and M. S. Cooper (1973). “Screening Factors for Nuclear Reactions. II. Intermediate Screen-Ing and Astrophysical Applications”. In: *Astrophysical Journal* 181, p. 457. DOI: [10.1086/152062](https://doi.org/10.1086/152062).
- Grevesse, N. and A. J. Sauval (1998). “Standard Solar Composition”. In: *Space Science Reviews* 85, p. 161. DOI: [10.1023/A:1005161325181](https://doi.org/10.1023/A:1005161325181).
- Grossman, D., O. Korobkin, S. Rosswog, and T. Piran (2014). “The long-term evolution of neutron star merger remnants - II. Radioactively powered transients”. In: *Monthly Notices of the RAS* 439, p. 757. DOI: [10.1093/mnras/stt2503](https://doi.org/10.1093/mnras/stt2503). arXiv: [1307.2943](https://arxiv.org/abs/1307.2943) [astro-ph.HE].
- Guidry, M. (2012). “Algebraic stabilization of explicit numerical integration for extremely stiff reaction networks”. In: *Journal of Computational Phys.* 231, p. 5266. DOI: [10.1016/j.jcp.2012.04.026](https://doi.org/10.1016/j.jcp.2012.04.026). arXiv: [1112.4778](https://arxiv.org/abs/1112.4778) [astro-ph.SR].
- Guidry, M. W., J. J. Billings, and W. R. Hix (2013a). “Explicit integration of extremely stiff reaction networks: partial equilibrium methods”. In: *Computational Science and Discovery* 6.1, p. 015003. DOI: [10.1088/1749-4699/6/1/015003](https://doi.org/10.1088/1749-4699/6/1/015003). arXiv: [1112.4738](https://arxiv.org/abs/1112.4738) [astro-ph.SR].
- Guidry, M. W., R. Budiardja, E. Feger, J. J. Billings, W. R. Hix, O. E. B. Messer, K. J. Roche, E. McMahon, and M. He (2013b). “Explicit integration of extremely stiff reaction networks: asymptotic methods”. In: *Computational Science and Discovery* 6.1, p. 015001. DOI: [10.1088/1749-4699/6/1/015001](https://doi.org/10.1088/1749-4699/6/1/015001). arXiv: [1112.4716](https://arxiv.org/abs/1112.4716) [astro-ph.SR].
- Guidry, M. W. and J. A. Harris (2013). “Explicit integration of extremely stiff reaction networks: quasi-steady-state methods”. In: *Computational Science and Discovery* 6.1, p. 015002. DOI: [10.1088/1749-4699/6/1/015002](https://doi.org/10.1088/1749-4699/6/1/015002). arXiv: [1112.4750](https://arxiv.org/abs/1112.4750) [astro-ph.SR].
- Haas, R., C. D. Ott, B. Szilagyi, J. D. Kaplan, J. Lippuner, et al. (2016). “Simulations of inspiraling and merging double neutron stars using the Spectral Einstein Code”. In: *Physical Review D* 93.12, p. 124062. DOI: [10.1103/PhysRevD.93.124062](https://doi.org/10.1103/PhysRevD.93.124062). arXiv: [1604.00782](https://arxiv.org/abs/1604.00782) [gr-qc].
- Hansen, C. J., S. D. Kawaler, and V. Trimble (2004). *Stellar interiors : physical principles, structure, and evolution*. New York: Springer-Verlag.
- Hansen, C. J., F. Montes, and A. Arcones (2014). “How Many Nucleosynthesis Processes Exist at Low Metallicity?” In: *Astrophysical Journal* 797, p. 123. DOI: [10.1088/0004-637X/797/2/123](https://doi.org/10.1088/0004-637X/797/2/123). arXiv: [1408.4135](https://arxiv.org/abs/1408.4135) [astro-ph.SR].
- Harris, J. A. (2017). Private communication.

- Harris, J. A., W. R. Hix, M. A. Chertkow, C.-T. Lee, E. J. Lentz, and O. E. B. Messer (2017). “Implications for Post-Processing Nucleosynthesis of Core-Collapse Supernova Models with Lagrangian Particles”. In: *ArXiv e-prints*. arXiv: [1701.08876](https://arxiv.org/abs/1701.08876) [[astro-ph.SR](#)].
- Harris, J., W. R. Hix, M. A. Chertkow, S. Bruenn, E. Lentz, O. E. B. Messer, A. Mezzacappa, J. Blondin, P. Marronetti, and K. N. Yakunin (2014). “Advancing Nucleosynthesis in Self-consistent, Multidimensional Models of Core-Collapse Supernovae”. In: *Proceedings of XIII Nuclei in the Cosmos (NIC XIII)*. 7-11 July, 2014. Debrecen, Hungary. P. 99. arXiv: [1411.0037](https://arxiv.org/abs/1411.0037) [[astro-ph.SR](#)].
- Hauser, W. and H. Feshbach (1952). “The Inelastic Scattering of Neutrons”. In: *Physical Review* 87, p. 366. doi: [10.1103/PhysRev.87.366](https://doi.org/10.1103/PhysRev.87.366).
- Hayashi, C., R. Hōshi, and D. Sugimoto (1962). “Evolution of the Stars”. In: *Progress of Theoretical Physics Supplement* 22, p. 1. doi: [10.1143/PTPS.22.1](https://doi.org/10.1143/PTPS.22.1).
- Hebeler, K., J. M. Lattimer, C. J. Pethick, and A. Schwenk (2013). “Equation of State and Neutron Star Properties Constrained by Nuclear Physics and Observation”. In: *Astrophysical Journal* 773, p. 11. doi: [10.1088/0004-637X/773/1/11](https://doi.org/10.1088/0004-637X/773/1/11). arXiv: [1303.4662](https://arxiv.org/abs/1303.4662) [[astro-ph.SR](#)].
- Heger, A. and S. E. Woosley (2010). “Nucleosynthesis and Evolution of Massive Metal-free Stars”. In: *Astrophysical Journal* 724, p. 341. doi: [10.1088/0004-637X/724/1/341](https://doi.org/10.1088/0004-637X/724/1/341). arXiv: [0803.3161](https://arxiv.org/abs/0803.3161).
- Herwig, F., M. Pignatari, P. R. Woodward, D. H. Porter, G. Rockefeller, C. L. Fryer, M. Bennett, and R. Hirschi (2011). “Convective-reactive Proton-<sup>12</sup>C Combustion in Sakurai’s Object (V4334 Sagittarii) and Implications for the Evolution and Yields from the First Generations of Stars”. In: *Astrophysical Journal* 727, p. 89. doi: [10.1088/0004-637X/727/2/89](https://doi.org/10.1088/0004-637X/727/2/89). arXiv: [1002.2241](https://arxiv.org/abs/1002.2241) [[astro-ph.SR](#)].
- Hesthaven, J. S. and T. Warburton (2008). *Nodal Discontinuous Galerkin Methods*. New York NY, United States: Springer-Verlag. ISBN: 978-0-387-72065-4. doi: [10.1007/978-0-387-72067-8](https://doi.org/10.1007/978-0-387-72067-8).
- Hillebrandt, W., M. Kromer, F. K. Röpke, and A. J. Ruiter (2013). “Towards an understanding of Type Ia supernovae from a synthesis of theory and observations”. In: *Frontiers of Physics* 8, p. 116. doi: [10.1007/s11467-013-0303-2](https://doi.org/10.1007/s11467-013-0303-2). arXiv: [1302.6420](https://arxiv.org/abs/1302.6420) [[astro-ph.CO](#)].
- Hinderer, T., B. D. Lackey, R. N. Lang, and J. S. Read (2010). “Tidal deformability of neutron stars with realistic equations of state and their gravitational wave signatures in binary inspiral”. In: *Physical Review D* 81.12, p. 123016. doi: [10.1103/PhysRevD.81.123016](https://doi.org/10.1103/PhysRevD.81.123016). arXiv: [0911.3535](https://arxiv.org/abs/0911.3535) [[astro-ph.HE](#)].

- Hirose, S., J. H. Krolik, and J. M. Stone (2006). “Vertical Structure of Gas Pressure-dominated Accretion Disks with Local Dissipation of Turbulence and Radiative Transport”. In: *Astrophysical Journal* 640, p. 901. DOI: [10.1086/499153](https://doi.org/10.1086/499153). arXiv: [astro-ph/0510741](https://arxiv.org/abs/astro-ph/0510741).
- Hix, W. R. and B. S. Meyer (2006). “Thermonuclear kinetics in astrophysics”. In: *Nuclear Physics A* 777, p. 188. DOI: [10.1016/j.nuclphysa.2004.10.009](https://doi.org/10.1016/j.nuclphysa.2004.10.009). arXiv: [astro-ph/0509698](https://arxiv.org/abs/astro-ph/0509698).
- Hix, W. R. and F. K. Thielemann (1999). “Computational methods for nucleosynthesis and nuclear energy generation”. In: *J. Comput. Appl. Math.* 109.1–2, p. 321. DOI: [10.1016/S0377-0427\(99\)00163-6](https://doi.org/10.1016/S0377-0427(99)00163-6).
- Hoffman, R. D., S. E. Woosley, and Y.-Z. Qian (1997). “Nucleosynthesis in Neutrino-driven Winds. II. Implications for Heavy Element Synthesis”. In: *Astrophysical Journal* 482, p. 951. DOI: [10.1086/304181](https://doi.org/10.1086/304181). arXiv: [astro-ph/9611097](https://arxiv.org/abs/astro-ph/9611097).
- Hofmeister, E., R. Kippenhahn, and A. Weigert (1964). “Sternentwicklung I. Ein Programm zur Lösung der zeitabhängigen Aufbaugleichungen. Mit 3 Textabbildungen”. In: *Zeitschrift fuer Astrophysik* 59, p. 215.
- Hogg, D. W. (1999). “Distance measures in cosmology”. In: *ArXiv Astrophysics e-prints*. arXiv: [astro-ph/9905116](https://arxiv.org/abs/astro-ph/9905116).
- Honda, S., W. Aoki, Y. Ishimaru, S. Wanajo, and S. G. Ryan (2006). “Neutron-Capture Elements in the Very Metal Poor Star HD 122563”. In: *Astrophysical Journal* 643, p. 1180. DOI: [10.1086/503195](https://doi.org/10.1086/503195). arXiv: [astro-ph/0602107](https://arxiv.org/abs/astro-ph/0602107).
- Horowitz, C. J. (2002). “Weak magnetism for antineutrinos in supernovae”. In: *Physical Review D* 65.4, p. 043001. DOI: [10.1103/PhysRevD.65.043001](https://doi.org/10.1103/PhysRevD.65.043001). arXiv: [astro-ph/0109209](https://arxiv.org/abs/astro-ph/0109209).
- Hotokezaka, K., K. Kiuchi, K. Kyutoku, T. Muranushi, Y.-i. Sekiguchi, M. Shibata, and K. Taniguchi (2013a). “Remnant massive neutron stars of binary neutron star mergers: Evolution process and gravitational waveform”. In: *Physical Review D* 88.4, p. 044026. DOI: [10.1103/PhysRevD.88.044026](https://doi.org/10.1103/PhysRevD.88.044026). arXiv: [1307.5888](https://arxiv.org/abs/1307.5888) [[astro-ph.HE](https://arxiv.org/abs/astro-ph.HE)].
- Hotokezaka, K., K. Kiuchi, K. Kyutoku, H. Okawa, Y.-i. Sekiguchi, M. Shibata, and K. Taniguchi (2013b). “Mass ejection from the merger of binary neutron stars”. In: *Physical Review D* 87.2, p. 024001. DOI: [10.1103/PhysRevD.87.024001](https://doi.org/10.1103/PhysRevD.87.024001). arXiv: [1212.0905](https://arxiv.org/abs/1212.0905) [[astro-ph.HE](https://arxiv.org/abs/astro-ph.HE)].
- Hotokezaka, K., K. Kyutoku, M. Tanaka, K. Kiuchi, Y. Sekiguchi, M. Shibata, and S. Wanajo (2013c). “Progenitor Models of the Electromagnetic Transient Associated with the Short Gamma Ray Burst 130603B”. In: *Astrophysical Journal, Letters* 778, p. L16. DOI: [10.1088/2041-8205/778/1/L16](https://doi.org/10.1088/2041-8205/778/1/L16). arXiv: [1310.1623](https://arxiv.org/abs/1310.1623) [[astro-ph.HE](https://arxiv.org/abs/astro-ph.HE)].

- Hotokezaka, K., T. Piran, and M. Paul (2015). “Short-lived  $^{244}\text{Pu}$  points to compact binary mergers as sites for heavy r-process nucleosynthesis”. In: *Nature Physics* 11, p. 1042. DOI: [10.1038/nphys3574](https://doi.org/10.1038/nphys3574). arXiv: [1510.00711](https://arxiv.org/abs/1510.00711) [[astro-ph.HE](#)].
- Hotokezaka, K., S. Wanajo, M. Tanaka, A. Bamba, Y. Terada, and T. Piran (2016). “Radioactive decay products in neutron star merger ejecta: heating efficiency and  $\gamma$ -ray emission”. In: *MNRAS* 459, p. 35. DOI: [10.1093/mnras/stw404](https://doi.org/10.1093/mnras/stw404). arXiv: [1511.05580](https://arxiv.org/abs/1511.05580) [[astro-ph.HE](#)].
- Hüdepohl, L., B. Müller, H.-T. Janka, A. Marek, and G. G. Raffelt (2010). “Neutrino Signal of Electron-Capture Supernovae from Core Collapse to Cooling”. In: *Physical Review Letters* 104.25, p. 251101. DOI: [10.1103/PhysRevLett.104.251101](https://doi.org/10.1103/PhysRevLett.104.251101). arXiv: [0912.0260](https://arxiv.org/abs/0912.0260) [[astro-ph.SR](#)].
- Hulse, R. A. and J. H. Taylor (1975). “Discovery of a pulsar in a binary system”. In: *Astrophysical Journal, Letters* 195, p. L51. DOI: [10.1086/181708](https://doi.org/10.1086/181708).
- Ichimaru, S. and K. Utsumi (1984). “Screening potential and enhancement of thermonuclear reaction rate due to relativistic degenerate electrons in dense multi-ionic plasmas”. In: *Astrophysical Journal* 278, p. 382. DOI: [10.1086/161802](https://doi.org/10.1086/161802).
- Iliadis, C., A. Champagne, J. José, S. Starrfield, and P. Tupper (2002). “The Effects of Thermonuclear Reaction-Rate Variations on Nova Nucleosynthesis: A Sensitivity Study”. In: *Astrophysical Journal, Supplement* 142, p. 105. DOI: [10.1086/341400](https://doi.org/10.1086/341400). arXiv: [astro-ph/0206020](https://arxiv.org/abs/astro-ph/0206020).
- Ishimaru, Y., S. Wanajo, and N. Prantzos (2015). “Neutron Star Mergers as the Origin of r-process Elements in the Galactic Halo Based on the Sub-halo Clustering Scenario”. In: *Astrophysical Journal, Letters* 804, p. L35. DOI: [10.1088/2041-8205/804/2/L35](https://doi.org/10.1088/2041-8205/804/2/L35). arXiv: [1504.04559](https://arxiv.org/abs/1504.04559).
- Itoh, N., H. Totsuji, and S. Ichimaru (1977). “Enhancement of thermonuclear reaction rate due to strong screening”. In: *Astrophysical Journal* 218, p. 477. DOI: [10.1086/155701](https://doi.org/10.1086/155701).
- Itoh, N., H. Totsuji, S. Ichimaru, and H. E. Dewitt (1979). “Enhancement of thermonuclear reaction rate due to strong screening. II - Ionic mixtures”. In: *Astrophysical Journal* 234, p. 1079. DOI: [10.1086/157590](https://doi.org/10.1086/157590).
- Iwamoto, K., F. Brachwitz, K. Nomoto, N. Kishimoto, H. Umeda, W. R. Hix, and F.-K. Thielemann (1999). “Nucleosynthesis in Chandrasekhar Mass Models for Type IA Supernovae and Constraints on Progenitor Systems and Burning-Front Propagation”. In: *Astrophysical Journal, Supplement* 125, p. 439. DOI: [10.1086/313278](https://doi.org/10.1086/313278). arXiv: [astro-ph/0002337](https://arxiv.org/abs/astro-ph/0002337).
- Janka, H.-T. (2001). “Conditions for shock revival by neutrino heating in core-collapse supernovae”. In: *Astronomy and Astrophysics* 368, p. 527. DOI: [10.1051/0004-6361:20010012](https://doi.org/10.1051/0004-6361:20010012). arXiv: [astro-ph/0008432](https://arxiv.org/abs/astro-ph/0008432).

- Janka, H.-T., T. Eberl, M. Ruffert, and C. L. Fryer (1999). “Black Hole-Neutron Star Mergers as Central Engines of Gamma-Ray Bursts”. In: *Astrophysical Journal, Letters* 527, p. L39. doi: [10.1086/312397](https://doi.org/10.1086/312397). arXiv: [astro-ph/9908290](https://arxiv.org/abs/astro-ph/9908290).
- Ji, A. P., A. Frebel, A. Chiti, and J. D. Simon (2016). “R-process enrichment from a single event in an ancient dwarf galaxy”. In: *Nature* 531, p. 610. doi: [10.1038/nature17425](https://doi.org/10.1038/nature17425). arXiv: [1512.01558](https://arxiv.org/abs/1512.01558).
- Jin, Z.-P., K. Hotokezaka, X. Li, M. Tanaka, P. D’Avanzo, Y.-Z. Fan, S. Covino, D.-M. Wei, and T. Piran (2016). “The Macronova in GRB 050709 and the GRB-macronova connection”. In: *Nature Communications* 7, p. 12898. doi: [10.1038/ncomms12898](https://doi.org/10.1038/ncomms12898). arXiv: [1603.07869](https://arxiv.org/abs/1603.07869) [[astro-ph.HE](#)].
- Jin, Z.-P., X. Li, Z. Cano, S. Covino, Y.-Z. Fan, and D.-M. Wei (2015). “The Light Curve of the Macronova Associated with the Long-Short Burst GRB 060614”. In: *Astrophysical Journal, Letters* 811, p. L22. doi: [10.1088/2041-8205/811/2/L22](https://doi.org/10.1088/2041-8205/811/2/L22). arXiv: [1507.07206](https://arxiv.org/abs/1507.07206) [[astro-ph.HE](#)].
- Jones, S., R. Hirschi, M. Pignatari, A. Heger, C. Georgy, N. Nishimura, C. Fryer, and F. Herwig (2015). “Code dependencies of pre-supernova evolution and nucleosynthesis in massive stars: evolution to the end of core helium burning”. In: *Monthly Notices of the RAS* 447, p. 3115. doi: [10.1093/mnras/stu2657](https://doi.org/10.1093/mnras/stu2657). arXiv: [1412.6518](https://arxiv.org/abs/1412.6518) [[astro-ph.SR](#)].
- José, J. and M. Hernanz (1998). “Nucleosynthesis in Classical Novae: CO versus ONe White Dwarfs”. In: *Astrophysical Journal* 494, p. 680. doi: [10.1086/305244](https://doi.org/10.1086/305244). arXiv: [astro-ph/9709153](https://arxiv.org/abs/astro-ph/9709153).
- Just, O., A. Bauswein, R. A. Pulpillo, S. Goriely, and H.-T. Janka (2015). “Comprehensive nucleosynthesis analysis for ejecta of compact binary mergers”. In: *Monthly Notices of the RAS* 448, p. 541. doi: [10.1093/mnras/stv009](https://doi.org/10.1093/mnras/stv009). arXiv: [1406.2687](https://arxiv.org/abs/1406.2687) [[astro-ph.SR](#)].
- Kaplan, J. D., C. D. Ott, E. P. O’Connor, K. Kiuchi, L. Roberts, and M. Duez (2014). “The Influence of Thermal Pressure on Equilibrium Models of Hypermassive Neutron Star Merger Remnants”. In: *Astrophysical Journal* 790, p. 19. doi: [10.1088/0004-637X/790/1/19](https://doi.org/10.1088/0004-637X/790/1/19). arXiv: [1306.4034](https://arxiv.org/abs/1306.4034) [[astro-ph.HE](#)].
- Käppeler, F., R. Gallino, S. Bisterzo, and W. Aoki (2011). “The s process: Nuclear physics, stellar models, and observations”. In: *Reviews of Modern Physics* 83, p. 157. doi: [10.1103/RevModPhys.83.157](https://doi.org/10.1103/RevModPhys.83.157). arXiv: [1012.5218](https://arxiv.org/abs/1012.5218) [[astro-ph.SR](#)].
- Käppeler, F., M. Wiescher, U. Giesen, J. Goerres, I. Baraffe, et al. (1994). “Reaction rates for O-18(alpha, gamma)Ne-22, Ne-22(alpha, gamma)Mg-26, and Ne-22(alpha, n)Mg-25 in stellar helium burning and s-process nucleosynthesis in massive stars”. In: *Astrophysical Journal* 437, p. 396. doi: [10.1086/175004](https://doi.org/10.1086/175004).

- Karypis, G. and V. Kumar (1998). “A Fast and High Quality Multilevel Scheme for Partitioning Irregular Graphs”. In: *SIAM Journal on Scientific Computing* 20.1, p. 359. DOI: [10.1137/S1064827595287997](https://doi.org/10.1137/S1064827595287997).
- Kasen, D. (2015). Private communication.
- Kasen, D., N. R. Badnell, and J. Barnes (2013). “Opacities and Spectra of the r-process Ejecta from Neutron Star Mergers”. In: *Astrophysical Journal* 774, p. 25. DOI: [10.1088/0004-637X/774/1/25](https://doi.org/10.1088/0004-637X/774/1/25). arXiv: [1303.5788](https://arxiv.org/abs/1303.5788) [[astro-ph.HE](#)].
- Kasen, D., R. Fernández, and B. D. Metzger (2015). “Kilonova light curves from the disc wind outflows of compact object mergers”. In: *Monthly Notices of the RAS* 450, p. 1777. DOI: [10.1093/mnras/stv721](https://doi.org/10.1093/mnras/stv721). arXiv: [1411.3726](https://arxiv.org/abs/1411.3726) [[astro-ph.HE](#)].
- Kasliwal, M. M., S. B. Cenko, L. P. Singer, A. Corsi, Y. Cao, et al. (2016). “iPTF Search for an Optical Counterpart to Gravitational-wave Transient GW150914”. In: *Astrophysical Journal, Letters* 824, p. L24. DOI: [10.3847/2041-8205/824/2/L24](https://doi.org/10.3847/2041-8205/824/2/L24). arXiv: [1602.08764](https://arxiv.org/abs/1602.08764) [[astro-ph.IM](#)].
- Kawaguchi, K., K. Kyutoku, H. Nakano, H. Okawa, M. Shibata, and K. Taniguchi (2015). “Black hole-neutron star binary merger: Dependence on black hole spin orientation and equation of state”. In: *Physical Review D* 92.2, p. 024014. DOI: [10.1103/PhysRevD.92.024014](https://doi.org/10.1103/PhysRevD.92.024014). arXiv: [1506.05473](https://arxiv.org/abs/1506.05473) [[astro-ph.HE](#)].
- Kidder, L. E., S. E. Field, F. Foucart, E. Schnetter, S. A. Teukolsky, et al. (2017). “SpECTRE: A task-based discontinuous Galerkin code for relativistic astrophysics”. In: *Journal of Computational Phys.* 335, p. 84. DOI: [10.1016/j.jcp.2016.12.059](https://doi.org/10.1016/j.jcp.2016.12.059). arXiv: [1609.00098](https://arxiv.org/abs/1609.00098) [[astro-ph.HE](#)].
- Kiziltan, B., A. Kottas, M. De Yoreo, and S. E. Thorsett (2013). “The Neutron Star Mass Distribution”. In: *Astrophysical Journal* 778, p. 66. DOI: [10.1088/0004-637X/778/1/66](https://doi.org/10.1088/0004-637X/778/1/66). arXiv: [1011.4291](https://arxiv.org/abs/1011.4291).
- Kolbe, E., K. Langanke, and G. M. Fuller (2004). “Neutrino-Induced Fission of Neutron-Rich Nuclei”. In: *Physical Review Letters* 92.11, p. 111101. DOI: [10.1103/PhysRevLett.92.111101](https://doi.org/10.1103/PhysRevLett.92.111101). arXiv: [astro-ph/0308350](https://arxiv.org/abs/astro-ph/0308350).
- Korobkin, O., S. Rosswog, A. Arcones, and C. Winteler (2012). “On the astrophysical robustness of the neutron star merger r-process”. In: *Monthly Notices of the RAS* 426, p. 1940. DOI: [10.1111/j.1365-2966.2012.21859.x](https://doi.org/10.1111/j.1365-2966.2012.21859.x). arXiv: [1206.2379](https://arxiv.org/abs/1206.2379) [[astro-ph.SR](#)].
- Kratz, K.-L., J.-P. Bitouzet, F.-K. Thielemann, P. Moeller, and B. Pfeiffer (1993). “Isotopic r-process abundances and nuclear structure far from stability - Implications for the r-process mechanism”. In: *Astrophysical Journal* 403, p. 216. DOI: [10.1086/172196](https://doi.org/10.1086/172196).

- Kulkarni, S. R. (2005). “Modeling Supernova-like Explosions Associated with Gamma-ray Bursts with Short Durations”. In: *preprint, astro-ph/0510256*. arXiv: [astro-ph/0510256](https://arxiv.org/abs/astro-ph/0510256).
- Kyutoku, K., K. Ioka, H. Okawa, M. Shibata, and K. Taniguchi (2015). “Dynamical mass ejection from black hole-neutron star binaries”. In: *Physical Review D* 92.4, p. 044028. doi: [10.1103/PhysRevD.92.044028](https://doi.org/10.1103/PhysRevD.92.044028). arXiv: [1502.05402](https://arxiv.org/abs/1502.05402) [[astro-ph.HE](https://arxiv.org/abs/1502.05402)].
- Langanke, K. and G. Martínez-Pinedo (2000). “Shell-model calculations of stellar weak interaction rates: II. Weak rates for nuclei in the mass range  $A=45-65$  in supernovae environments”. In: *Nucl. Phys. A* 673, p. 481. doi: [10.1016/S0375-9474\(00\)00131-7](https://doi.org/10.1016/S0375-9474(00)00131-7). arXiv: [nucl-th/0001018](https://arxiv.org/abs/nucl-th/0001018).
- Lattimer, J. M., F. Mackie, D. G. Ravenhall, and D. N. Schramm (1977). “The decompression of cold neutron star matter”. In: *Astrophysical Journal* 213, p. 225. doi: [10.1086/155148](https://doi.org/10.1086/155148).
- Lattimer, J. M. and M. Prakash (2005). “Ultimate Energy Density of Observable Cold Baryonic Matter”. In: *Physical Review Letters* 94.11, p. 111101. doi: [10.1103/PhysRevLett.94.111101](https://doi.org/10.1103/PhysRevLett.94.111101). arXiv: [astro-ph/0411280](https://arxiv.org/abs/astro-ph/0411280).
- Lattimer, J. M. and D. N. Schramm (1974). “Black-hole-neutron-star collisions”. In: *ApJ* 192, p. L145. doi: [10.1086/181612](https://doi.org/10.1086/181612).
- Lattimer, J. M. and D. N. Schramm (1976). “The tidal disruption of neutron stars by black holes in close binaries”. In: *Astrophysical Journal* 210, p. 549. doi: [10.1086/154860](https://doi.org/10.1086/154860).
- Lattimer, J. M. and F. D. Swesty (1991). “A generalized equation of state for hot, dense matter”. In: *Nuclear Physics A* 535, p. 331. doi: [10.1016/0375-9474\(91\)90452-C](https://doi.org/10.1016/0375-9474(91)90452-C).
- Law, N. M., S. R. Kulkarni, R. G. Dekany, E. O. Ofek, R. M. Quimby, et al. (2009). “The Palomar Transient Factory: System Overview, Performance, and First Results”. In: *Publications of the ASP* 121, p. 1395. doi: [10.1086/648598](https://doi.org/10.1086/648598). arXiv: [0906.5350](https://arxiv.org/abs/0906.5350) [[astro-ph.IM](https://arxiv.org/abs/0906.5350)].
- Lee, W. H. and E. Ramirez-Ruiz (2007). “The progenitors of short gamma-ray bursts”. In: *New Journal of Physics* 9, p. 17. doi: [10.1088/1367-2630/9/1/017](https://doi.org/10.1088/1367-2630/9/1/017). arXiv: [astro-ph/0701874](https://arxiv.org/abs/astro-ph/0701874).
- Lee, W. H., E. Ramirez-Ruiz, and D. López-Cámara (2009). “Phase Transitions and He-Synthesis-Driven Winds in Neutrino Cooled Accretion Disks: Prospects for Late Flares in Short Gamma-Ray Bursts”. In: *Astrophysical Journal, Letters* 699, p. L93. doi: [10.1088/0004-637X/699/2/L93](https://doi.org/10.1088/0004-637X/699/2/L93). arXiv: [0904.3752](https://arxiv.org/abs/0904.3752) [[astro-ph.HE](https://arxiv.org/abs/0904.3752)].
- Lehner, L. and F. Pretorius (2014). “Numerical Relativity and Astrophysics”. In: *ARA&A* 52, p. 661. doi: [10.1146/annurev-astro-081913-040031](https://doi.org/10.1146/annurev-astro-081913-040031). arXiv: [1405.4840](https://arxiv.org/abs/1405.4840) [[astro-ph.HE](https://arxiv.org/abs/1405.4840)].

- Leucippus (ca. 430 BC). *The Great World-Order*.
- Leung, S.-C., M.-C. Chu, and L.-M. Lin (2015). “A new hydrodynamics code for Type Ia supernovae”. In: *Monthly Notices of the RAS* 454, p. 1238. DOI: [10.1093/mnras/stv1923](https://doi.org/10.1093/mnras/stv1923). arXiv: [1507.08549](https://arxiv.org/abs/1507.08549) [astro-ph.HE].
- Li, L.-X. and B. Paczyński (1998). “Transient Events from Neutron Star Mergers”. In: *Astrophysical Journal, Letters* 507, p. L59. DOI: [10.1086/311680](https://doi.org/10.1086/311680). arXiv: [astro-ph/9807272](https://arxiv.org/abs/astro-ph/9807272).
- LIGO Scientific Collaboration (2010). “TOPICAL REVIEW: Predictions for the rates of compact binary coalescences observable by ground-based gravitational-wave detectors”. In: *Classical and Quantum Gravity* 27.17, p. 173001. DOI: [10.1088/0264-9381/27/17/173001](https://doi.org/10.1088/0264-9381/27/17/173001). arXiv: [1003.2480](https://arxiv.org/abs/1003.2480) [astro-ph.HE].
- LIGO Scientific Collaboration, J. Aasi, B. P. Abbott, R. Abbott, T. Abbott, et al. (2015). “Advanced LIGO”. In: *Classical and Quantum Gravity* 32.7, p. 074001. DOI: [10.1088/0264-9381/32/7/074001](https://doi.org/10.1088/0264-9381/32/7/074001). arXiv: [1411.4547](https://arxiv.org/abs/1411.4547) [gr-qc].
- Limongi, M. and A. Chieffi (2003). “Evolution, Explosion, and Nucleosynthesis of Core-Collapse Supernovae”. In: *Astrophysical Journal* 592, p. 404. DOI: [10.1086/375703](https://doi.org/10.1086/375703). arXiv: [astro-ph/0304185](https://arxiv.org/abs/astro-ph/0304185).
- Lippuner, J., R. Fernández, L. F. Roberts, F. Foucart, D. Kasen, B. D. Metzger, and C. D. Ott (2017). “Signatures of hypermassive neutron star lifetimes on r-process nucleosynthesis in the disk ejecta from neutron star mergers”. In: *accepted by Monthly Notices of the RAS*. arXiv: [1703.06216](https://arxiv.org/abs/1703.06216) [astro-ph.HE].
- Lippuner, J. and L. F. Roberts (2015). “r-Process Lanthanide Production and Heating Rates in Kilonovae”. In: *Astrophysical Journal* 815, p. 82. DOI: [10.1088/0004-637X/815/2/82](https://doi.org/10.1088/0004-637X/815/2/82). arXiv: [1508.03133](https://arxiv.org/abs/1508.03133) [astro-ph.HE].
- Lippuner, J. and L. F. Roberts (2017). “SkyNet: A modular nuclear reaction network library”. In: *submitted to Astrophysical Journal, Supplement*. arXiv: [1706.06198](https://arxiv.org/abs/1706.06198) [astro-ph.HE].
- Lodders, K. (2003). “Solar System Abundances and Condensation Temperatures of the Elements”. In: *Astrophysical Journal* 591, p. 1220. DOI: [10.1086/375492](https://doi.org/10.1086/375492).
- Lombardi Jr., J. C., Z. F. Proulx, K. L. Dooley, E. M. Theriault, N. Ivanova, and F. A. Rasio (2006). “Stellar Collisions and Ultracompact X-Ray Binary Formation”. In: *Astrophysical Journal* 640, p. 441. DOI: [10.1086/499938](https://doi.org/10.1086/499938). arXiv: [astro-ph/0509511](https://arxiv.org/abs/astro-ph/0509511).
- Longland, R., D. Martin, and J. José (2014). “Performance improvements for nuclear reaction network integration”. In: *Astronomy and Astrophysics* 563, A67. DOI: [10.1051/0004-6361/201321958](https://doi.org/10.1051/0004-6361/201321958). arXiv: [1401.5762](https://arxiv.org/abs/1401.5762) [astro-ph.SR].
- Lorimer, D. R. (2008). “Binary and Millisecond Pulsars”. In: *Living Reviews in Relativity* 11. DOI: [10.12942/lrr-2008-8](https://doi.org/10.12942/lrr-2008-8). arXiv: [0811.0762](https://arxiv.org/abs/0811.0762).

- Lunney, D., J. M. Pearson, and C. Thibault (2003). “Recent trends in the determination of nuclear masses”. In: *Reviews of Modern Physics* 75, p. 1021. DOI: [10.1103/RevModPhys.75.1021](https://doi.org/10.1103/RevModPhys.75.1021).
- Mamdouh, A., J. M. Pearson, M. Rayet, and F. Tondeur (2001). “Fission barriers of neutron-rich and superheavy nuclei calculated with the ETFSI method”. In: *Nuclear Physics A* 679, p. 337. DOI: [10.1016/S0375-9474\(00\)00358-4](https://doi.org/10.1016/S0375-9474(00)00358-4). arXiv: [nuc1-th/0010093](https://arxiv.org/abs/nuc1-th/0010093).
- Martin, D., A. Arcones, W. Nazarewicz, and E. Olsen (2016). “Impact of Nuclear Mass Uncertainties on the r Process”. In: *Physical Review Letters* 116.12, p. 121101. DOI: [10.1103/PhysRevLett.116.121101](https://doi.org/10.1103/PhysRevLett.116.121101). arXiv: [1512.03158 \[nucl-th\]](https://arxiv.org/abs/1512.03158).
- Martin, D., A. Perego, A. Arcones, F.-K. Thielemann, O. Korobkin, and S. Rosswog (2015). “Neutrino-driven Winds in the Aftermath of a Neutron Star Merger: Nucleosynthesis and Electromagnetic Transients”. In: *Astrophysical Journal* 813, p. 2. DOI: [10.1088/0004-637X/813/1/2](https://doi.org/10.1088/0004-637X/813/1/2). arXiv: [1506.05048 \[astro-ph.SR\]](https://arxiv.org/abs/1506.05048).
- Martínez-Pinedo, G., T. Fischer, A. Lohs, and L. Huther (2012). “Charged-Current Weak Interaction Processes in Hot and Dense Matter and its Impact on the Spectra of Neutrinos Emitted from Protoneutron Star Cooling”. In: *Physical Review Letters* 109.25, p. 251104. DOI: [10.1103/PhysRevLett.109.251104](https://doi.org/10.1103/PhysRevLett.109.251104). arXiv: [1205.2793 \[astro-ph.HE\]](https://arxiv.org/abs/1205.2793).
- Mathews, G. J. and J. J. Cowan (1990). “New insights into the astrophysical r-process”. In: *Nature* 345, p. 491. DOI: [10.1038/345491a0](https://doi.org/10.1038/345491a0).
- Matsuo, K., Y. Miyazato, and H.-D. Kim (1999). “Shock train and pseudo-shock phenomena in internal gas flows”. In: *Progress in Aerospace Sciences* 35, p. 33. DOI: [10.1016/S0376-0421\(98\)00011-6](https://doi.org/10.1016/S0376-0421(98)00011-6).
- Matteucci, F. (2012). *Chemical Evolution of Galaxies*. Berlin/Heidelberg, Germany: Springer. ISBN: 978-3-642-22490-4. DOI: [10.1007/978-3-642-22491-1](https://doi.org/10.1007/978-3-642-22491-1).
- Matteucci, F., D. Romano, A. Arcones, O. Korobkin, and S. Rosswog (2014). “Europium production: neutron star mergers versus core-collapse supernovae”. In: *Monthly Notices of the RAS* 438, p. 2177. DOI: [10.1093/mnras/stt2350](https://doi.org/10.1093/mnras/stt2350). arXiv: [1311.6980](https://arxiv.org/abs/1311.6980).
- Melrose, D. B. and R. Yuen (2016). “Pulsar electrodynamics: an unsolved problem”. In: *Journal of Plasma Physics* 82.2, p. 635820202. DOI: [10.1017/S0022377816000398](https://doi.org/10.1017/S0022377816000398). arXiv: [1604.03623 \[astro-ph.HE\]](https://arxiv.org/abs/1604.03623).
- Mendoza-Temis, J. d. J., M.-R. Wu, K. Langanke, G. Martínez-Pinedo, A. Bauswein, and H.-T. Janka (2015). “Nuclear robustness of the r process in neutron-star mergers”. In: *Physical Review C* 92.5, p. 055805. DOI: [10.1103/PhysRevC.92.055805](https://doi.org/10.1103/PhysRevC.92.055805). arXiv: [1409.6135 \[astro-ph.HE\]](https://arxiv.org/abs/1409.6135).

- Metzger, B. (2015). Private communication.
- Metzger, B. D. (2017). “Kilonovae”. In: *Living Reviews in Relativity* 20, p. 3. DOI: [10.1007/s41114-017-0006-z](https://doi.org/10.1007/s41114-017-0006-z). arXiv: [1610.09381](https://arxiv.org/abs/1610.09381) [astro-ph.HE].
- Metzger, B. D., A. Bauswein, S. Goriely, and D. Kasen (2015). “Neutron-powered precursors of kilonovae”. In: *Monthly Notices of the RAS* 446, p. 1115. DOI: [10.1093/mnras/stu2225](https://doi.org/10.1093/mnras/stu2225). arXiv: [1409.0544](https://arxiv.org/abs/1409.0544) [astro-ph.HE].
- Metzger, B. D. and E. Berger (2012). “What is the Most Promising Electromagnetic Counterpart of a Neutron Star Binary Merger?” In: *Astrophysical Journal* 746, p. 48. DOI: [10.1088/0004-637X/746/1/48](https://doi.org/10.1088/0004-637X/746/1/48). arXiv: [1108.6056](https://arxiv.org/abs/1108.6056) [astro-ph.HE].
- Metzger, B. D. and R. Fernández (2014). “Red or blue? A potential kilonova imprint of the delay until black hole formation following a neutron star merger”. In: *Monthly Notices of the RAS* 441, p. 3444. DOI: [10.1093/mnras/stu802](https://doi.org/10.1093/mnras/stu802). arXiv: [1402.4803](https://arxiv.org/abs/1402.4803) [astro-ph.HE].
- Metzger, B. D., G. Martínez-Pinedo, S. Darbha, E. Quataert, A. Arcones, D. Kasen, R. Thomas, P. Nugent, I. V. Panov, and N. T. Zinner (2010). “Electromagnetic counterparts of compact object mergers powered by the radioactive decay of r-process nuclei”. In: *Monthly Notices of the RAS* 406, p. 2650. DOI: [10.1111/j.1365-2966.2010.16864.x](https://doi.org/10.1111/j.1365-2966.2010.16864.x). arXiv: [1001.5029](https://arxiv.org/abs/1001.5029) [astro-ph.HE].
- Metzger, B. D., A. L. Piro, and E. Quataert (2009a). “Neutron-rich freeze-out in viscously spreading accretion discs formed from compact object mergers”. In: *MNRAS* 396, p. 304. DOI: [10.1111/j.1365-2966.2008.14380.x](https://doi.org/10.1111/j.1365-2966.2008.14380.x). arXiv: [0810.2535](https://arxiv.org/abs/0810.2535).
- Metzger, B. D., A. L. Piro, and E. Quataert (2009b). “Nickel-rich outflows from accretion discs formed by the accretion-induced collapse of white dwarfs”. In: *MNRAS* 396, p. 1659. DOI: [10.1111/j.1365-2966.2009.14909.x](https://doi.org/10.1111/j.1365-2966.2009.14909.x). arXiv: [0812.3656](https://arxiv.org/abs/0812.3656).
- Meyer, B. S. and D. C. Adams (2007). “Libnucnet: A Tool for Understanding Nucleosynthesis”. In: *Meteoritics and Planetary Science Supplement* 42, p. 5215.
- Meyer, B. S., G. C. McLaughlin, and G. M. Fuller (1998). “Neutrino capture and r-process nucleosynthesis”. In: *Physical Review C* 58, p. 3696. DOI: [10.1103/PhysRevC.58.3696](https://doi.org/10.1103/PhysRevC.58.3696). arXiv: [astro-ph/9809242](https://arxiv.org/abs/astro-ph/9809242).
- Mihalas, D. and B. Weibel-Mihalas (1999). *Foundations of Radiation Hydrodynamics*. Mineola, NY, USA: Dover Publications.
- Mochkovitch, R., M. Hernanz, J. Isern, and X. Martin (1993). “Gamma-ray bursts as collimated jets from neutron star/black hole mergers”. In: *Nature* 361, p. 236. DOI: [10.1038/361236a0](https://doi.org/10.1038/361236a0).

- Möller, P., J. R. Nix, and K.-L. Kratz (1997). “Nuclear Properties for Astrophysical and Radioactive-Ion Beam Applications”. In: *Atomic Data and Nuclear Data Tables* 66, p. 131. DOI: [10.1006/adnd.1997.0746](https://doi.org/10.1006/adnd.1997.0746).
- Möller, P., J. R. Nix, W. D. Myers, and W. J. Swiatecki (1995). “Nuclear Ground-State Masses and Deformations”. In: *Atomic Data and Nuclear Data Tables* 59, p. 185. DOI: [10.1006/adnd.1995.1002](https://doi.org/10.1006/adnd.1995.1002). arXiv: [nuc1-th/9308022](https://arxiv.org/abs/nuc1-th/9308022).
- Möller, P., B. Pfeiffer, and K.-L. Kratz (2003). “New calculations of gross  $\beta$ -decay properties for astrophysical applications: Speeding-up the classical  $r$  process”. In: *Physical Review C* 67 (5), p. 055802. DOI: [10.1103/PhysRevC.67.055802](https://doi.org/10.1103/PhysRevC.67.055802).
- Möller, P., A. J. Sierk, T. Ichikawa, and H. Sagawa (2016). “Nuclear ground-state masses and deformations: FRDM(2012)”. In: *Atomic Data and Nuclear Data Tables* 109, p. 1. DOI: [10.1016/j.adt.2015.10.002](https://doi.org/10.1016/j.adt.2015.10.002). arXiv: [1508.06294 \[nucl-th\]](https://arxiv.org/abs/1508.06294).
- Monaghan, J. J. (2002). “SPH compressible turbulence”. In: *Monthly Notices of the RAS* 335, p. 843. DOI: [10.1046/j.1365-8711.2002.05678.x](https://doi.org/10.1046/j.1365-8711.2002.05678.x). arXiv: [astro-ph/0204118](https://arxiv.org/abs/astro-ph/0204118).
- Montes, F., T. C. Beers, J. Cowan, T. Elliot, K. Farouqi, et al. (2007). “Nucleosynthesis in the Early Galaxy”. In: *Astrophysical Journal* 671, p. 1685. DOI: [10.1086/523084](https://doi.org/10.1086/523084). arXiv: [0709.0417](https://arxiv.org/abs/0709.0417).
- Mösta, P., C. D. Ott, D. Radice, L. F. Roberts, R. Haas, and E. Schnetter (2015). “A Large-Scale Dynamo and Magnetoturbulence in Rapidly Rotating Core-Collapse Supernovae”. In: *Nature* 528.7582, p. 376. DOI: [10.1038/nature15755](https://doi.org/10.1038/nature15755).
- Mösta, P., S. Richers, C. D. Ott, R. Haas, A. L. Piro, K. Boydston, E. Abdikamalov, C. Reisswig, and E. Schnetter (2014). “Magnetorotational Core-collapse Supernovae in Three Dimensions”. In: *Astrophysical Journal, Letters* 785, p. L29. DOI: [10.1088/2041-8205/785/2/L29](https://doi.org/10.1088/2041-8205/785/2/L29). arXiv: [1403.1230 \[astro-ph.HE\]](https://arxiv.org/abs/1403.1230).
- Müller, E. (1986). “Nuclear-reaction networks and stellar evolution codes - The coupling of composition changes and energy release in explosive nuclear burning”. In: *Astronomy and Astrophysics* 162, p. 103.
- Mumpower, M. R., G. C. McLaughlin, and R. Surman (2012). “Formation of the rare-earth peak: Gaining insight into late-time  $r$ -process dynamics”. In: *Physical Review C* 85.4, p. 045801. DOI: [10.1103/PhysRevC.85.045801](https://doi.org/10.1103/PhysRevC.85.045801). arXiv: [1109.3613 \[nucl-th\]](https://arxiv.org/abs/1109.3613).
- Mumpower, M. R., R. Surman, D.-L. Fang, M. Beard, P. Möller, T. Kawano, and A. Aprahamian (2015). “Impact of individual nuclear masses on  $r$ -process abundances”. In: *Physical Review C* 92.3, p. 035807. DOI: [10.1103/PhysRevC.92.035807](https://doi.org/10.1103/PhysRevC.92.035807). arXiv: [1505.07789 \[nucl-th\]](https://arxiv.org/abs/1505.07789).

- Mumpower, M. R., R. Surman, G. C. McLaughlin, and A. Aprahamian (2016). “The impact of individual nuclear properties on r-process nucleosynthesis”. In: *Progress in Particle and Nuclear Physics* 86, p. 86. DOI: [10.1016/j.pnpnp.2015.09.001](https://doi.org/10.1016/j.pnpnp.2015.09.001). arXiv: [1508.07352](https://arxiv.org/abs/1508.07352) [nucl-th].
- Myers, W. D. and W. J. Swiatecki (1966). “Nuclear masses and deformations”. In: *Nuclear Physics A* 81, p. 1. DOI: [10.1016/S0029-5582\(66\)80001-9](https://doi.org/10.1016/S0029-5582(66)80001-9).
- Nakar, E. (2007). “Short-hard gamma-ray bursts”. In: *Physics Reports* 442, p. 166. DOI: [10.1016/j.physrep.2007.02.005](https://doi.org/10.1016/j.physrep.2007.02.005). arXiv: [astro-ph/0701748](https://arxiv.org/abs/astro-ph/0701748).
- Nakar, E. and T. Piran (2011). “Detectable radio flares following gravitational waves from mergers of binary neutron stars”. In: *Nature* 478, p. 82. DOI: [10.1038/nature10365](https://doi.org/10.1038/nature10365). arXiv: [1102.1020](https://arxiv.org/abs/1102.1020) [astro-ph.HE].
- Neilsen, David, Steven L. Liebling, Matthew Anderson, Luis Lehner, Evan O’Connor, and Carlos Palenzuela (2014). “Magnetized neutron stars with realistic equations of state and neutrino cooling”. In: *Physical Review D* 89.10, p. 104029. DOI: [10.1103/PhysRevD.89.104029](https://doi.org/10.1103/PhysRevD.89.104029). arXiv: [1403.3680](https://arxiv.org/abs/1403.3680).
- Nishimura, N., R. Hirschi, T. Rauscher, A. S. J. Murphy, and G. Cescutti (2017). “Uncertainties in s-process nucleosynthesis in massive stars determined by Monte Carlo variations”. In: *Monthly Notices of the RAS* 469.2, p. 1752. DOI: [doi:10.1093/mnras/stx696](https://doi.org/10.1093/mnras/stx696). arXiv: [1701.00489](https://arxiv.org/abs/1701.00489) [astro-ph.SR].
- Nishimura, N., T. Takiwaki, and F.-K. Thielemann (2015). “The r-process Nucleosynthesis in the Various Jet-like Explosions of Magnetorotational Core-collapse Supernovae”. In: *Astrophysical Journal* 810, p. 109. DOI: [10.1088/0004-637X/810/2/109](https://doi.org/10.1088/0004-637X/810/2/109). arXiv: [1501.06567](https://arxiv.org/abs/1501.06567) [astro-ph.SR].
- Nollett, K. M. and S. Burles (2000). “Estimating reaction rates and uncertainties for primordial nucleosynthesis”. In: *Physical Review D* 61.12, p. 123505. DOI: [10.1103/PhysRevD.61.123505](https://doi.org/10.1103/PhysRevD.61.123505). arXiv: [astro-ph/0001440](https://arxiv.org/abs/astro-ph/0001440).
- Nomoto, K., K. Iwamoto, N. Nakasato, F.-K. Thielemann, F. Brachwitz, T. Tsujimoto, Y. Kubo, and N. Kishimoto (1997). “Nucleosynthesis in type Ia supernovae”. In: *Nuclear Physics A* 621, p. 467. DOI: [10.1016/S0375-9474\(97\)00291-1](https://doi.org/10.1016/S0375-9474(97)00291-1). arXiv: [astro-ph/9706025](https://arxiv.org/abs/astro-ph/9706025).
- O’Connor, E. and C. D. Ott (2010). “A new open-source code for spherically symmetric stellar collapse to neutron stars and black holes”. In: *Class. Quantum Grav.* 27.11, p. 114103. DOI: [10.1088/0264-9381/27/11/114103](https://doi.org/10.1088/0264-9381/27/11/114103). arXiv: [0912.2393](https://arxiv.org/abs/0912.2393) [astro-ph.HE].
- Oda, T., M. Hino, K. Muto, M. Takahara, and K. Sato (1994). “Rate Tables for the Weak Processes of sd-Shell Nuclei in Stellar Matter”. In: *Atomic Data and Nuclear Data Tables* 56, p. 231. DOI: [10.1006/adnd.1994.1007](https://doi.org/10.1006/adnd.1994.1007).
- Oechslin, R. and H.-T. Janka (2006). “Torus formation in neutron star mergers and well-localized short gamma-ray bursts”. In: *MNRAS* 368, p. 1489. DOI: [10.1111/j.1365-2966.2006.10238.x](https://doi.org/10.1111/j.1365-2966.2006.10238.x). arXiv: [astro-ph/0507099](https://arxiv.org/abs/astro-ph/0507099).

- Orlov, A. V., A. V. Ivanchik, and D. A. Varshalovich (2000). “Primordial nucleosynthesis: Effects of possible variations of fundamental physical constants”. In: *Astronomical and Astrophysical Transactions* 19, p. 375. DOI: [10.1080/10556790008238584](https://doi.org/10.1080/10556790008238584).
- Özel, F., D. Psaltis, R. Narayan, and J. E. McClintock (2010). “The Black Hole Mass Distribution in the Galaxy”. In: *Astrophysical Journal* 725, p. 1918. DOI: [10.1088/0004-637X/725/2/1918](https://doi.org/10.1088/0004-637X/725/2/1918). arXiv: [1006.2834](https://arxiv.org/abs/1006.2834).
- Paczynski, B. and P. J. Wiita (1980). “Thick accretion disks and supercritical luminosities”. In: *Astronomy and Astrophysics* 88, p. 23.
- Palenzuela, C., S. L. Liebling, D. Neilsen, L. Lehner, O. L. Caballero, E. O’Connor, and M. Anderson (2015). “Effects of the microphysical equation of state in the mergers of magnetized neutron stars with neutrino cooling”. In: *Physical Review D* 92.4, p. 044045. DOI: [10.1103/PhysRevD.92.044045](https://doi.org/10.1103/PhysRevD.92.044045). arXiv: [1505.01607 \[gr-qc\]](https://arxiv.org/abs/1505.01607).
- Panov, I. V., S. I. Blinnikov, and F.-K. Thielemann (2001). “Nucleosynthesis of Heavy Elements: Computational Experiment”. In: *Astronomy Letters* 27, p. 239. DOI: [10.1134/1.1358381](https://doi.org/10.1134/1.1358381).
- Panov, I. V., I. Y. Korneev, T. Rauscher, G. Martínez-Pinedo, A. Kelić-Heil, N. T. Zinner, and F.-K. Thielemann (2010). “Neutron-induced astrophysical reaction rates for translead nuclei”. In: *Astronomy and Astrophysics* 513, A61. DOI: [10.1051/0004-6361/200911967](https://doi.org/10.1051/0004-6361/200911967). arXiv: [0911.2181 \[astro-ph.SR\]](https://arxiv.org/abs/0911.2181).
- Panov, I. V., D. A. Ptitsyn, and V. M. Chechetkin (1995). “Formation of elements beyond the iron peak: the rbc-process”. In: *Astronomy Letters* 21, p. 185.
- Papaloizou, J. C. B. and J. E. Pringle (1984). “The dynamical stability of differentially rotating discs with constant specific angular momentum”. In: *Monthly Notices of the RAS* 208, p. 721. DOI: [10.1093/mnras/208.4.721](https://doi.org/10.1093/mnras/208.4.721).
- Parikh, A., J. José, G. Sala, and C. Iliadis (2013). “Nucleosynthesis in type I X-ray bursts”. In: *Progress in Particle and Nuclear Physics* 69, p. 225. DOI: [10.1016/j.pnpnp.2012.11.002](https://doi.org/10.1016/j.pnpnp.2012.11.002). arXiv: [1211.5900 \[astro-ph.SR\]](https://arxiv.org/abs/1211.5900).
- Paschalidis, V. (2017). “General relativistic simulations of compact binary mergers as engines for short gamma-ray bursts”. In: *Classical and Quantum Gravity* 34.8, p. 084002. DOI: [10.1088/1361-6382/aa61ce](https://doi.org/10.1088/1361-6382/aa61ce). arXiv: [1611.01519 \[astro-ph.HE\]](https://arxiv.org/abs/1611.01519).
- Paschalidis, V., Z. B. Etienne, and S. L. Shapiro (2012). “Importance of cooling in triggering the collapse of hypermassive neutron stars”. In: *Physical Review D* 86.6, p. 064032. DOI: [10.1103/PhysRevD.86.064032](https://doi.org/10.1103/PhysRevD.86.064032). arXiv: [1208.5487 \[astro-ph.HE\]](https://arxiv.org/abs/1208.5487).

- Paxton, B., L. Bildsten, A. Dotter, F. Herwig, P. Lesaffre, and F. Timmes (2011). “Modules for Experiments in Stellar Astrophysics (MESA)”. In: *Astrophysical Journal, Supplement* 192, p. 3. DOI: [10.1088/0067-0049/192/1/3](https://doi.org/10.1088/0067-0049/192/1/3). arXiv: [1009.1622](https://arxiv.org/abs/1009.1622) [astro-ph.SR].
- Payne, C. H. (1925). “Stellar Atmospheres; a Contribution to the Observational Study of High Temperature in the Reversing Layers of Stars.” PhD thesis. Radcliffe College.
- Perego, A., S. Rosswog, R. M. Cabezón, O. Korobkin, R. Käppeli, A. Arcones, and M. Liebendörfer (2014). “Neutrino-driven winds from neutron star merger remnants”. In: *Monthly Notices of the RAS* 443, p. 3134. DOI: [10.1093/mnras/stu1352](https://doi.org/10.1093/mnras/stu1352). arXiv: [1405.6730](https://arxiv.org/abs/1405.6730) [astro-ph.HE].
- Peskin, M. E. and D. V. Schroeder (1995). *An Introduction to Quantum Field Theory*. Boulder CO, United States: Westview Press. ISBN: 978-0-201-50397-5.
- Peters, J. G. (1968). “Nucleosynthesis by the s-PROCESS in Stars of 9 and 15 Solar Masses”. In: *Astrophysical Journal* 154, p. 225. DOI: [10.1086/149753](https://doi.org/10.1086/149753).
- Planck Collaboration, P. A. R. Ade, N. Aghanim, M. Arnaud, M. Ashdown, et al. (2016). “Planck 2015 results. XIII. Cosmological parameters”. In: *Astronomy and Astrophysics* 594, A13. DOI: [10.1051/0004-6361/201525830](https://doi.org/10.1051/0004-6361/201525830). arXiv: [1502.01589](https://arxiv.org/abs/1502.01589).
- Ponce, M., J. A. Faber, and J. C. Lombardi (2012). “Accretion Disks around Kicked Black Holes: Post-kick Dynamics”. In: *Astrophysical Journal* 745, p. 71. DOI: [10.1088/0004-637X/745/1/71](https://doi.org/10.1088/0004-637X/745/1/71). arXiv: [1107.1711](https://arxiv.org/abs/1107.1711).
- Pons, J. A., S. Reddy, M. Prakash, J. M. Lattimer, and J. A. Miralles (1999). “Evolution of Proto-Neutron Stars”. In: *Astrophysical Journal* 513, p. 780. DOI: [10.1086/306889](https://doi.org/10.1086/306889). arXiv: [astro-ph/9807040](https://arxiv.org/abs/astro-ph/9807040).
- Prantzos, N., M. Hashimoto, and K. Nomoto (1990). “The s-process in massive stars - Yields as a function of stellar mass and metallicity”. In: *Astronomy and Astrophysics* 234, p. 211.
- Press, William H., Saul A. Teukolsky, William T. Vetterling, and Brian P. Flannery (2007). *Numerical Recipes, 3rd. edition*. Cambridge, U. K.: Cambridge University Press.
- Price, D. J. and S. Rosswog (2006). “Producing Ultrastrong Magnetic Fields in Neutron Star Mergers”. In: *Science* 312, p. 719. DOI: [10.1126/science.1125201](https://doi.org/10.1126/science.1125201). arXiv: [astro-ph/0603845](https://arxiv.org/abs/astro-ph/0603845).
- Pruet, J., R. D. Hoffman, S. E. Woosley, H.-T. Janka, and R. Buras (2006). “Nucleosynthesis in Early Supernova Winds. II. The Role of Neutrinos”. In: *Astrophysical Journal* 644, p. 1028. DOI: [10.1086/503891](https://doi.org/10.1086/503891). arXiv: [astro-ph/0511194](https://arxiv.org/abs/astro-ph/0511194).

- Qian, Y.-Z. (2000). “Supernovae versus Neutron Star Mergers as the Major R-Process Sources”. In: *Astrophysical Journal, Letters* 534, p. L67. DOI: [10.1086/312659](https://doi.org/10.1086/312659). arXiv: [astro-ph/0003242](https://arxiv.org/abs/astro-ph/0003242).
- Qian, Y.-Z. (2002). “Neutrino-induced Fission and r-Process Nucleosynthesis”. In: *Astrophysical Journal, Letters* 569, p. L103. DOI: [10.1086/340643](https://doi.org/10.1086/340643). arXiv: [astro-ph/0203194](https://arxiv.org/abs/astro-ph/0203194).
- Qian, Y.-Z. and G. J. Wasserburg (2008). “Abundances of Sr, Y, and Zr in Metal-Poor Stars and Implications for Chemical Evolution in the Early Galaxy”. In: *Astrophysical Journal* 687, p. 272. DOI: [10.1086/591545](https://doi.org/10.1086/591545). arXiv: [0807.0809](https://arxiv.org/abs/0807.0809).
- Qian, Y.-Z. and S. E. Woosley (1996). “Nucleosynthesis in Neutrino-driven Winds. I. The Physical Conditions”. In: *Astrophysical Journal* 471, p. 331. DOI: [10.1086/177973](https://doi.org/10.1086/177973). arXiv: [astro-ph/9611094](https://arxiv.org/abs/astro-ph/9611094).
- Radice, D., F. Galeazzi, J. Lippuner, L. F. Roberts, C. D. Ott, and L. Rezzolla (2016). “Dynamical mass ejection from binary neutron star mergers”. In: *Monthly Notices of the RAS* 460, p. 3255. DOI: [10.1093/mnras/stw1227](https://doi.org/10.1093/mnras/stw1227). arXiv: [1601.02426](https://arxiv.org/abs/1601.02426) [[astro-ph.HE](https://arxiv.org/abs/astro-ph.HE)].
- Ramirez-Ruiz, E., M. Trenti, M. MacLeod, L. F. Roberts, W. H. Lee, and M. I. Saladino-Rosas (2015). “Compact Stellar Binary Assembly in the First Nuclear Star Clusters and r-process Synthesis in the Early Universe”. In: *Astrophysical Journal, Letters* 802, p. L22. DOI: [10.1088/2041-8205/802/2/L22](https://doi.org/10.1088/2041-8205/802/2/L22). arXiv: [1410.3467](https://arxiv.org/abs/1410.3467).
- Rauscher, T. and F.-K. Thielemann (2000). “Astrophysical Reaction Rates From Statistical Model Calculations”. In: *Atomic Data and Nuclear Data Tables* 75, p. 1. DOI: [10.1006/adnd.2000.0834](https://doi.org/10.1006/adnd.2000.0834). arXiv: [astro-ph/0004059](https://arxiv.org/abs/astro-ph/0004059).
- Reddy, S., M. Prakash, and J. M. Lattimer (1998). “Neutrino interactions in hot and dense matter”. In: *Physical Review D* 58.1, p. 013009. DOI: [10.1103/PhysRevD.58.013009](https://doi.org/10.1103/PhysRevD.58.013009). arXiv: [astro-ph/9710115](https://arxiv.org/abs/astro-ph/9710115).
- Reichl, L. E. (1980). *A Modern Course in Statistical Physics*. Austin TX, United States: University of Texas Press. ISBN: 029275051X.
- Richers, S., D. Kasen, E. O’Connor, R. Fernandez, and C. D. Ott (2015). “Monte Carlo Neutrino Transport through Remnant Disks from Neutron Star Mergers”. In: *Astrophysical Journal* 813, p. 38. DOI: [10.1088/0004-637X/813/1/38](https://doi.org/10.1088/0004-637X/813/1/38). arXiv: [1507.03606](https://arxiv.org/abs/1507.03606) [[astro-ph.HE](https://arxiv.org/abs/astro-ph.HE)].
- Roberts, L. F., D. Kasen, W. H. Lee, and E. Ramirez-Ruiz (2011). “Electromagnetic Transients Powered by Nuclear Decay in the Tidal Tails of Coalescing Compact Binaries”. In: *Astrophysical Journal, Letters* 736, p. L21. DOI: [10.1088/2041-8205/736/1/L21](https://doi.org/10.1088/2041-8205/736/1/L21). arXiv: [1104.5504](https://arxiv.org/abs/1104.5504) [[astro-ph.HE](https://arxiv.org/abs/astro-ph.HE)].

- Roberts, L. F., J. Lippuner, M. D. Duez, J. A. Faber, F. Foucart, J. C. Lombardi Jr., S. Ning, C. D. Ott, and M. Ponce (2017). “The influence of neutrinos on r-process nucleosynthesis in the ejecta of black hole-neutron star mergers”. In: *Monthly Notices of the RAS* 464, p. 3907. DOI: [10.1093/mnras/stw2622](https://doi.org/10.1093/mnras/stw2622). arXiv: [1601.07942](https://arxiv.org/abs/1601.07942) [[astro-ph.HE](#)].
- Roberts, L. F., S. E. Woosley, and R. D. Hoffman (2010). “Integrated Nucleosynthesis in Neutrino-driven Winds”. In: *Astrophysical Journal* 722, p. 954. DOI: [10.1088/0004-637X/722/1/954](https://doi.org/10.1088/0004-637X/722/1/954). arXiv: [1004.4916](https://arxiv.org/abs/1004.4916) [[astro-ph.HE](#)].
- Roederer, I. U., J. J. Cowan, A. I. Karakas, K.-L. Kratz, M. Lugaro, J. Simmerer, K. Farouqi, and C. Sneden (2010). “The Ubiquity of the Rapid Neutron-capture Process”. In: *Astrophysical Journal* 724, p. 975. DOI: [10.1088/0004-637X/724/2/975](https://doi.org/10.1088/0004-637X/724/2/975). arXiv: [1009.4496](https://arxiv.org/abs/1009.4496) [[astro-ph.SR](#)].
- Roederer, I. U., J. E. Lawler, J. S. Sobeck, T. C. Beers, J. J. Cowan, A. Frebel, I. I. Ivans, H. Schatz, C. Sneden, and I. B. Thompson (2012). “New Hubble Space Telescope Observations of Heavy Elements in Four Metal-Poor Stars”. In: *Astrophysical Journal, Supplement* 203, p. 27. DOI: [10.1088/0067-0049/203/2/27](https://doi.org/10.1088/0067-0049/203/2/27). arXiv: [1210.6387](https://arxiv.org/abs/1210.6387) [[astro-ph.SR](#)].
- Roederer, I. U., H. Schatz, J. E. Lawler, T. C. Beers, J. J. Cowan, A. Frebel, I. I. Ivans, C. Sneden, and J. S. Sobeck (2014). “New Detections of Arsenic, Selenium, and Other Heavy Elements in Two Metal-poor Stars”. In: *Astrophysical Journal* 791, p. 32. DOI: [10.1088/0004-637X/791/1/32](https://doi.org/10.1088/0004-637X/791/1/32). arXiv: [1406.4554](https://arxiv.org/abs/1406.4554) [[astro-ph.SR](#)].
- Rolfs, C. E. and W. S. Rodney (1988). *Cauldrons in the cosmos: Nuclear astrophysics*. Chicago IL, United States: University of Chicago Press. ISBN: 0-226-72456-5.
- Rolfs, C. and E. Somorjai (1995). “Status report on electron screening”. In: *Nuclear Instruments and Methods in Physics Research B* 99, p. 297. DOI: [10.1016/0168-583X\(95\)00225-1](https://doi.org/10.1016/0168-583X(95)00225-1).
- Rosswog, S. (2013). “The dynamic ejecta of compact object mergers and eccentric collisions”. In: *Philosophical Transactions of the Royal Society of London Series A* 371, p. 20272. DOI: [10.1098/rsta.2012.0272](https://doi.org/10.1098/rsta.2012.0272). arXiv: [1210.6549](https://arxiv.org/abs/1210.6549) [[astro-ph.HE](#)].
- Rosswog, S. (2015). “The multi-messenger picture of compact binary mergers”. In: *International Journal of Modern Physics D* 24, p. 1530012. DOI: [10.1142/S0218271815300128](https://doi.org/10.1142/S0218271815300128). arXiv: [1501.02081](https://arxiv.org/abs/1501.02081) [[astro-ph.HE](#)].
- Rosswog, S., O. Korobkin, A. Arcones, F.-K. Thielemann, and T. Piran (2014). “The long-term evolution of neutron star merger remnants - I. The impact of r-process nucleosynthesis”. In: *Monthly Notices of the RAS* 439, p. 744. DOI: [10.1093/mnras/stt2502](https://doi.org/10.1093/mnras/stt2502). arXiv: [1307.2939](https://arxiv.org/abs/1307.2939) [[astro-ph.HE](#)].

- Ruffert, M., H.-T. Janka, and G. Schaefer (1996). “Coalescing neutron stars - a step towards physical models. I. Hydrodynamic evolution and gravitational-wave emission.” In: *Astronomy and Astrophysics* 311, p. 532. arXiv: [astro-ph/9509006](https://arxiv.org/abs/astro-ph/9509006).
- Ruffert, M., H.-T. Janka, K. Takahashi, and G. Schaefer (1997). “Coalescing neutron stars - a step towards physical models. II. Neutrino emission, neutron tori, and gamma-ray bursts.” In: *A&A* 319, p. 122. arXiv: [astro-ph/9606181](https://arxiv.org/abs/astro-ph/9606181).
- Russell, H. N. (1934). “Molecules in the Sun and Stars”. In: *Astrophysical Journal* 79, p. 317. DOI: [10.1086/143539](https://doi.org/10.1086/143539).
- Rutherford, E. (1911). “The scattering of  $\alpha$  and  $\beta$  particles by matter and the structure of the atom”. In: *Philosophical Magazine Series 6* 21.125, p. 669. DOI: [10.1080/14786440508637080](https://doi.org/10.1080/14786440508637080).
- Salpeter, E. E. (1954). “Electrons Screening and Thermonuclear Reactions”. In: *Australian Journal of Physics* 7, p. 373. DOI: [10.1071/PH540373](https://doi.org/10.1071/PH540373).
- Schatz, H. (2013). “Nuclear masses in astrophysics”. In: *International Journal of Mass Spectrometry* 349, p. 181. DOI: [10.1016/j.ijms.2013.03.016](https://doi.org/10.1016/j.ijms.2013.03.016).
- Schatz, H. (2016). “Trends in nuclear astrophysics”. In: *Journal of Physics G Nuclear Physics* 43.6, p. 064001. DOI: [10.1088/0954-3899/43/6/064001](https://doi.org/10.1088/0954-3899/43/6/064001). arXiv: [1606.00485](https://arxiv.org/abs/1606.00485) [nucl-ex].
- Schatz, H., A. Aprahamian, V. Barnard, L. Bildsten, A. Cumming, M. Ouellette, T. Rauscher, F.-K. Thielemann, and M. Wiescher (2001). “End Point of the rp Process on Accreting Neutron Stars”. In: *Physical Review Letters* 86, p. 3471. DOI: [10.1103/PhysRevLett.86.3471](https://doi.org/10.1103/PhysRevLett.86.3471). arXiv: [astro-ph/0102418](https://arxiv.org/abs/astro-ph/0102418).
- Schenk, O. and K. Gärtner (2004). “Solving unsymmetric sparse systems of linear equations with {PARDISO}”. In: *Future Generation Computer Systems* 20.3, p. 475. DOI: [10.1016/j.future.2003.07.011](https://doi.org/10.1016/j.future.2003.07.011).
- Schenk, O. and K. Gärtner (2006). “On fast factorization pivoting methods for sparse symmetric indefinite systems”. In: *Electronic Transactions on Numerical Analysis* 23, p. 158.
- Sedrakian, D. M. and M. V. Hayrapetyan (2015). “Mechanism for Radio Emission of Pulsars”. In: *Astrophysics* 58, p. 131. DOI: [10.1007/s10511-015-9371-z](https://doi.org/10.1007/s10511-015-9371-z).
- Seitenzahl, I. R., F. Ciaraldi-Schoolmann, F. K. Röpke, M. Fink, W. Hillebrandt, M. Kromer, R. Pakmor, A. J. Ruiter, S. A. Sim, and S. Taubenberger (2013). “Three-dimensional delayed-detonation models with nucleosynthesis for Type Ia supernovae”. In: *Monthly Notices of the RAS* 429, p. 1156. DOI: [10.1093/mnras/sts402](https://doi.org/10.1093/mnras/sts402). arXiv: [1211.3015](https://arxiv.org/abs/1211.3015) [astro-ph.SR].
- Seitenzahl, I. R., D. M. Townsley, F. Peng, and J. W. Truran (2009). “Nuclear statistical equilibrium for Type Ia supernova simulations”. In: *Atomic Data and Nuclear Data Tables* 95, p. 96. DOI: [10.1016/j.adt.2008.08.001](https://doi.org/10.1016/j.adt.2008.08.001).

- Sekiguchi, Y., K. Kiuchi, K. Kyutoku, and M. Shibata (2011). “Gravitational Waves and Neutrino Emission from the Merger of Binary Neutron Stars”. In: *Physical Review Letters* 107.5, p. 051102. DOI: [10.1103/PhysRevLett.107.051102](https://doi.org/10.1103/PhysRevLett.107.051102). arXiv: [1105.2125](https://arxiv.org/abs/1105.2125) [gr-qc].
- Sekiguchi, Y., K. Kiuchi, K. Kyutoku, and M. Shibata (2015). “Dynamical mass ejection from binary neutron star mergers: Radiation-hydrodynamics study in general relativity”. In: *Physical Review D* 91.6, p. 064059. DOI: [10.1103/PhysRevD.91.064059](https://doi.org/10.1103/PhysRevD.91.064059). arXiv: [1502.06660](https://arxiv.org/abs/1502.06660) [astro-ph.HE].
- Shakura, N. I. and R. A. Sunyaev (1973). “Black holes in binary systems. Observational appearance.” In: *Astronomy and Astrophysics* 24, p. 337.
- Shaviv, G. (2012). *The Synthesis of the Elements*. New York NY, United States: Springer. ISBN: 978-3-642-28384-0.
- Shaviv, G. and N. J. Shaviv (2000). “Is There a Dynamic Effect in the Screening of Nuclear Reactions in Stellar Plasmas?” In: *Astrophysical Journal* 529, p. 1054. DOI: [10.1086/308290](https://doi.org/10.1086/308290).
- Shaviv, N. J. and G. Shaviv (1996). “The Electrostatic Screening of Thermonuclear Reactions in Astrophysical Plasmas. I.” In: *Astrophysical Journal* 468, p. 433. DOI: [10.1086/177702](https://doi.org/10.1086/177702).
- Shen, S., R. J. Cooke, E. Ramirez-Ruiz, P. Madau, L. Mayer, and J. Guedes (2015). “The History of R-Process Enrichment in the Milky Way”. In: *Astrophysical Journal* 807, p. 115. DOI: [10.1088/0004-637X/807/2/115](https://doi.org/10.1088/0004-637X/807/2/115). arXiv: [1407.3796](https://arxiv.org/abs/1407.3796).
- Shibagaki, S., T. Kajino, G. J. Mathews, S. Chiba, S. Nishimura, and G. Lorusso (2016). “Relative Contributions of the Weak, Main, and Fission-recycling r-process”. In: *Astrophysical Journal* 816, p. 79. DOI: [10.3847/0004-637X/816/2/79](https://doi.org/10.3847/0004-637X/816/2/79). arXiv: [1505.02257](https://arxiv.org/abs/1505.02257) [astro-ph.SR].
- Siegel, D. M. and B. D. Metzger (2017). “Three-dimensional GRMHD simulations of the remnant accretion disks from neutron star mergers: outflows and r-process nucleosynthesis”. In: *ArXiv e-prints*. arXiv: [1705.05473](https://arxiv.org/abs/1705.05473) [astro-ph.HE].
- Simmerer, J., C. Sneden, J. J. Cowan, J. Collier, V. M. Wolf, and J. E. Lawler (2004). “The Rise of the s-Process in the Galaxy”. In: *Astrophysical Journal* 617, p. 1091. DOI: [10.1086/424504](https://doi.org/10.1086/424504). arXiv: [astro-ph/0410396](https://arxiv.org/abs/astro-ph/0410396).
- Singer, L. P., L. R. Price, B. Farr, A. L. Urban, C. Pankow, et al. (2014). “The First Two Years of Electromagnetic Follow-up with Advanced LIGO and Virgo”. In: *Astrophysical Journal* 795, p. 105. DOI: [10.1088/0004-637X/795/2/105](https://doi.org/10.1088/0004-637X/795/2/105). arXiv: [1404.5623](https://arxiv.org/abs/1404.5623) [astro-ph.HE].
- Sneden, C., J. J. Cowan, and R. Gallino (2008). “Neutron-Capture Elements in the Early Galaxy”. In: *Annual Review of Astronomy and Astrophysics* 46, p. 241. DOI: [10.1146/annurev.astro.46.060407.145207](https://doi.org/10.1146/annurev.astro.46.060407.145207).

- Snedden, C., J. E. Lawler, J. J. Cowan, I. I. Ivans, and E. A. Den Hartog (2009). “New Rare Earth Element Abundance Distributions for the Sun and Five r-Process-Rich Very Metal-Poor Stars”. In: *Astrophysical Journal, Supplement* 182, p. 80. DOI: [10.1088/0067-0049/182/1/80](https://doi.org/10.1088/0067-0049/182/1/80). arXiv: [0903.1623](https://arxiv.org/abs/0903.1623) [[astro-ph.SR](#)].
- Springel, V. and L. Hernquist (2002). “Cosmological smoothed particle hydrodynamics simulations: the entropy equation”. In: *Monthly Notices of the RAS* 333, p. 649. DOI: [10.1046/j.1365-8711.2002.05445.x](https://doi.org/10.1046/j.1365-8711.2002.05445.x). arXiv: [astro-ph/0111016](https://arxiv.org/abs/astro-ph/0111016).
- Starrfield, S., C. Iliadis, and W. R. Hix (2016). “The Thermonuclear Runaway and the Classical Nova Outburst”. In: *Publications of the ASP* 128.5, p. 051001. DOI: [10.1088/1538-3873/128/963/051001](https://doi.org/10.1088/1538-3873/128/963/051001). arXiv: [1605.04294](https://arxiv.org/abs/1605.04294) [[astro-ph.SR](#)].
- Straniero, O., R. Gallino, and S. Cristallo (2006). “s process in low-mass asymptotic giant branch stars”. In: *Nuclear Physics A* 777, p. 311. DOI: [10.1016/j.nuclphysa.2005.01.011](https://doi.org/10.1016/j.nuclphysa.2005.01.011). arXiv: [astro-ph/0501405](https://arxiv.org/abs/astro-ph/0501405).
- Strohmayer, T. E. and E. F. Brown (2002). “A Remarkable 3 Hour Thermonuclear Burst from 4U 1820-30”. In: *Astrophysical Journal* 566, p. 1045. DOI: [10.1086/338337](https://doi.org/10.1086/338337). arXiv: [astro-ph/0108420](https://arxiv.org/abs/astro-ph/0108420).
- Suda, T., Y. Katsuta, S. Yamada, T. Suwa, C. Ishizuka, Y. Komiya, K. Sorai, M. Aikawa, and M. Y. Fujimoto (2008). “Stellar Abundances for the Galactic Archeology (SAGA) Database — Compilation of the Characteristics of Known Extremely Metal-Poor Stars”. In: *Publications of the ASJ* 60, p. 1159. DOI: [10.1093/pasj/60.5.1159](https://doi.org/10.1093/pasj/60.5.1159). arXiv: [0806.3697](https://arxiv.org/abs/0806.3697).
- Suess, H. E. and H. C. Urey (1956). “Abundances of the Elements”. In: *Reviews of Modern Physics* 28, p. 53. DOI: [10.1103/RevModPhys.28.53](https://doi.org/10.1103/RevModPhys.28.53).
- Surman, R., G. C. McLaughlin, and W. R. Hix (2006). “Nucleosynthesis in the Outflow from Gamma-Ray Burst Accretion Disks”. In: *Astrophysical Journal* 643, p. 1057. DOI: [10.1086/501116](https://doi.org/10.1086/501116). arXiv: [astro-ph/0509365](https://arxiv.org/abs/astro-ph/0509365).
- Surman, R., G. C. McLaughlin, M. Ruffert, H.-T. Janka, and W. R. Hix (2008). “r-Process Nucleosynthesis in Hot Accretion Disk Flows from Black Hole-Neutron Star Mergers”. In: *Astrophysical Journal, Letters* 679, p. L117. DOI: [10.1086/589507](https://doi.org/10.1086/589507). arXiv: [0803.1785](https://arxiv.org/abs/0803.1785).
- SXS Collaboration (2000). *Spectral Einstein Code*. <http://www.black-holes.org/SpEC.html>.
- Takami, K., L. Rezzolla, and L. Baiotti (2014). “Constraining the Equation of State of Neutron Stars from Binary Mergers”. In: *Physical Review Letters* 113.9, p. 091104. DOI: [10.1103/PhysRevLett.113.091104](https://doi.org/10.1103/PhysRevLett.113.091104). arXiv: [1403.5672](https://arxiv.org/abs/1403.5672) [[gr-qc](#)].

- Tanaka, M. (2016). “Kilonova/Macronova Emission from Compact Binary Mergers”. In: *Advances in Astronomy* 2016, p. 634197. DOI: [10.1155/2016/6341974](https://doi.org/10.1155/2016/6341974). arXiv: [1605.07235](https://arxiv.org/abs/1605.07235) [[astro-ph.HE](#)].
- Tanaka, M. and K. Hotokezaka (2013). “Radiative Transfer Simulations of Neutron Star Merger Ejecta”. In: *Astrophysical Journal* 775, p. 113. DOI: [10.1088/0004-637X/775/2/113](https://doi.org/10.1088/0004-637X/775/2/113). arXiv: [1306.3742](https://arxiv.org/abs/1306.3742) [[astro-ph.HE](#)].
- Tanvir, N. R., A. J. Levan, A. S. Fruchter, J. Hjorth, R. A. Hounsell, K. Wiersema, and R. L. Tunnicliffe (2013). “A ‘kilonova’ associated with the short-duration  $\gamma$ -ray burst GRB 130603B”. In: *Nature* 500, p. 547. DOI: [10.1038/nature12505](https://doi.org/10.1038/nature12505). arXiv: [1306.4971](https://arxiv.org/abs/1306.4971) [[astro-ph.HE](#)].
- Thielemann, F.-K., A. Arcones, R. Käppeli, M. Liebendörfer, T. Rauscher, et al. (2011). “What are the astrophysical sites for the r-process and the production of heavy elements?” In: *Progress in Particle and Nuclear Physics* 66, p. 346. DOI: [10.1016/j.ppnp.2011.01.032](https://doi.org/10.1016/j.ppnp.2011.01.032).
- Thielemann, F.-K., K. Nomoto, and K. Yokoi (1986). “Explosive nucleosynthesis in carbon deflagration models of Type I supernovae”. In: *Astronomy and Astrophysics* 158, p. 17.
- Thompson, T. A. (2004). “Protoneutron Star Winds”. In: *Astrophysics and Space Science Library*. Ed. by C. L. Fryer. Vol. 302. Astrophysics and Space Science Library, p. 175. DOI: [10.1007/978-0-306-48599-2\\_6](https://doi.org/10.1007/978-0-306-48599-2_6). arXiv: [astro-ph/0309111](https://arxiv.org/abs/astro-ph/0309111).
- Thompson, T. A., A. Burrows, and B. S. Meyer (2001). “The Physics of Proto-Neutron Star Winds: Implications for r-Process Nucleosynthesis”. In: *Astrophysical Journal* 562, p. 887. DOI: [10.1086/323861](https://doi.org/10.1086/323861). arXiv: [astro-ph/0105004](https://arxiv.org/abs/astro-ph/0105004).
- Thomson, J. J. (1897). “Cathode rays”. In: *Philosophical Magazine* 44.269, p. 293.
- Timmes, F. X. (1999). “Integration of Nuclear Reaction Networks for Stellar Hydrodynamics”. In: *Astrophysical Journal, Supplement* 124, p. 241. DOI: [10.1086/313257](https://doi.org/10.1086/313257).
- Timmes, F. X. and D. Arnett (1999). “The Accuracy, Consistency, and Speed of Five Equations of State for Stellar Hydrodynamics”. In: *Astrophysical Journal, Supplement* 125, p. 277. DOI: [10.1086/313271](https://doi.org/10.1086/313271).
- Timmes, F. X., R. D. Hoffman, and S. E. Woosley (2000). “An Inexpensive Nuclear Energy Generation Network for Stellar Hydrodynamics”. In: *Astrophysical Journal, Supplement* 129, p. 377. DOI: [10.1086/313407](https://doi.org/10.1086/313407).
- Timmes, F. X. and F. D. Swesty (2000). “The Accuracy, Consistency, and Speed of an Electron-Positron Equation of State Based on Table Interpolation of the Helmholtz Free Energy”. In: *Astrophysical Journal, Supplement* 126, p. 501. DOI: [10.1086/313304](https://doi.org/10.1086/313304).

- Timmes, F. X., S. E. Woosley, and T. A. Weaver (1996). “The Neutron Star and Black Hole Initial Mass Function”. In: *Astrophysical Journal* 457, p. 834. DOI: [10.1086/176778](https://doi.org/10.1086/176778). arXiv: [astro-ph/9510136](https://arxiv.org/abs/astro-ph/9510136).
- Travaglio, C., R. Gallino, E. Arnone, J. Cowan, F. Jordan, and C. Sneden (2004). “Galactic Evolution of Sr, Y, And Zr: A Multiplicity of Nucleosynthetic Processes”. In: *Astrophysical Journal* 601, p. 864. DOI: [10.1086/380507](https://doi.org/10.1086/380507). arXiv: [astro-ph/0310189](https://arxiv.org/abs/astro-ph/0310189).
- Truran, J. W., W. D. Arnett, and A. G. W. Cameron (1967). “Nucleosynthesis in supernova shock waves”. In: *Canadian Journal of Physics* 45, p. 2315. DOI: [10.1139/p67-184](https://doi.org/10.1139/p67-184).
- Truran, J. W., A. G. W. Cameron, and A. Gilbert (1966). “The approach to nuclear statistical equilibrium”. In: *Canadian Journal of Physics* 44, p. 563. DOI: [10.1139/p66-049](https://doi.org/10.1139/p66-049).
- Tsujimoto, T., T. Yokoyama, and K. Bekki (2017). “Chemical evolution of  $^{244}\text{Pu}$  in the solar vicinity and its implications for the properties of r-process production”. In: *Astrophysical Journal, Letters* 835, p. L3. DOI: [10.3847/2041-8213/835/1/L3](https://doi.org/10.3847/2041-8213/835/1/L3). arXiv: [1701.02323](https://arxiv.org/abs/1701.02323).
- Tytler, D., J. M. O’Meara, N. Suzuki, and D. Lubin (2000). “Review of Big Bang Nucleosynthesis and Primordial Abundances”. In: *Physica Scripta Volume T* 85, p. 12. DOI: [10.1238/Physica.Topical.085a00012](https://doi.org/10.1238/Physica.Topical.085a00012). arXiv: [astro-ph/0001318](https://arxiv.org/abs/astro-ph/0001318).
- van de Voort, F., E. Quataert, P. F. Hopkins, D. Kereš, and C.-A. Faucher-Giguère (2015). “Galactic r-process enrichment by neutron star mergers in cosmological simulations of a Milky Way-mass galaxy”. In: *Monthly Notices of the RAS* 447, p. 140. DOI: [10.1093/mnras/stu2404](https://doi.org/10.1093/mnras/stu2404). arXiv: [1407.7039](https://arxiv.org/abs/1407.7039) [[astro-ph.GA](https://arxiv.org/abs/astro-ph.GA)].
- Vines, J., É. É. Flanagan, and T. Hinderer (2011). “Post-1-Newtonian tidal effects in the gravitational waveform from binary inspirals”. In: *Physical Review D* 83.8, p. 084051. DOI: [10.1103/PhysRevD.83.084051](https://doi.org/10.1103/PhysRevD.83.084051). arXiv: [1101.1673](https://arxiv.org/abs/1101.1673) [[gr-qc](https://arxiv.org/abs/gr-qc)].
- Vlasov, A. D., B. D. Metzger, J. Lippuner, L. F. Roberts, and T. A. Thompson (2017). “Neutrino-heated winds from millisecond protomagnetars as sources of the weak r-process”. In: *Monthly Notices of the RAS* 468, p. 1522. DOI: [10.1093/mnras/stx478](https://doi.org/10.1093/mnras/stx478). arXiv: [1701.03123](https://arxiv.org/abs/1701.03123) [[astro-ph.HE](https://arxiv.org/abs/astro-ph.HE)].
- Vlasov, A. D., B. D. Metzger, and T. A. Thompson (2014). “Neutrino-heated winds from rotating protomagnetars”. In: *Monthly Notices of the RAS* 444, p. 3537. DOI: [10.1093/mnras/stu1667](https://doi.org/10.1093/mnras/stu1667). arXiv: [1405.7043](https://arxiv.org/abs/1405.7043) [[astro-ph.HE](https://arxiv.org/abs/astro-ph.HE)].
- Wagoner, R. V. (1973). “Big-Bang Nucleosynthesis Revisited”. In: *Astrophysical Journal* 179, p. 343. DOI: [10.1086/151873](https://doi.org/10.1086/151873).
- Wahl, A. C. (2002). *Systematics of Fission-Product Yields*. Tech. rep. LA-13928. Los Alamos, NM: Los Alamos National Laboratory. DOI: [10.2172/809946](https://doi.org/10.2172/809946).

- Wallner, A., T. Faestermann, J. Feige, C. Feldstein, K. Knie, et al. (2015). “Abundance of live  $^{244}\text{Pu}$  in deep-sea reservoirs on Earth points to rarity of actinide nucleosynthesis”. In: *Nature Communications* 6, p. 5956. DOI: [10.1038/ncomms6956](https://doi.org/10.1038/ncomms6956). arXiv: [1509.08054](https://arxiv.org/abs/1509.08054) [astro-ph.SR].
- Wanajo, S. (2006). “The r-Process in Proto-Neutron Star Winds with Anisotropic Neutrino Emission”. In: *Astrophysical Journal, Letters* 650, p. L79. DOI: [10.1086/508568](https://doi.org/10.1086/508568). arXiv: [astro-ph/0608539](https://arxiv.org/abs/astro-ph/0608539).
- Wanajo, S. (2013). “The r-process in Proto-neutron-star Wind Revisited”. In: *Astrophysical Journal, Letters* 770, p. L22. DOI: [10.1088/2041-8205/770/2/L22](https://doi.org/10.1088/2041-8205/770/2/L22). arXiv: [1305.0371](https://arxiv.org/abs/1305.0371) [astro-ph.SR].
- Wanajo, S. and H.-T. Janka (2012). “The r-process in the Neutrino-driven Wind from a Black-hole Torus”. In: *Astrophysical Journal* 746, p. 180. DOI: [10.1088/0004-637X/746/2/180](https://doi.org/10.1088/0004-637X/746/2/180). arXiv: [1106.6142](https://arxiv.org/abs/1106.6142) [astro-ph.SR].
- Wanajo, S., H.-T. Janka, and S. Kubono (2011). “Uncertainties in the  $\nu p$ -process: Supernova Dynamics Versus Nuclear Physics”. In: *Astrophysical Journal* 729, p. 46. DOI: [10.1088/0004-637X/729/1/46](https://doi.org/10.1088/0004-637X/729/1/46). arXiv: [1004.4487](https://arxiv.org/abs/1004.4487) [astro-ph.SR].
- Wanajo, S., Y. Sekiguchi, N. Nishimura, K. Kiuchi, K. Kyutoku, and M. Shibata (2014). “Production of All the r-process Nuclides in the Dynamical Ejecta of Neutron Star Mergers”. In: *Astrophysical Journal, Letters* 789, p. L39. DOI: [10.1088/2041-8205/789/2/L39](https://doi.org/10.1088/2041-8205/789/2/L39). arXiv: [1402.7317](https://arxiv.org/abs/1402.7317) [astro-ph.SR].
- Wasserburg, G. J., M. Busso, and R. Gallino (1996). “Abundances of Actinides and Short-lived Nonactinides in the Interstellar Medium: Diverse Supernova Sources for the r-Processes”. In: *ApJL* 466, p. L109. DOI: [10.1086/310177](https://doi.org/10.1086/310177).
- Weaver, T. A., G. B. Zimmerman, and S. E. Woosley (1978). “Presupernova evolution of massive stars”. In: *Astrophysical Journal* 225, p. 1021. DOI: [10.1086/156569](https://doi.org/10.1086/156569).
- Wehmeyer, B., M. Pignatari, and F.-K. Thielemann (2015). “Galactic evolution of rapid neutron capture process abundances: the inhomogeneous approach”. In: *Monthly Notices of the RAS* 452, p. 1970. DOI: [10.1093/mnras/stv1352](https://doi.org/10.1093/mnras/stv1352). arXiv: [1501.07749](https://arxiv.org/abs/1501.07749).
- Weiss, A. and J. W. Truran (1990). “Na-22 and Al-26 production and nucleosynthesis in novae explosions”. In: *Astronomy and Astrophysics* 238, p. 178.
- Weizsäcker, C. F. V. (1935). “Zur Theorie der Kernmassen”. In: *Zeitschrift für Physik* 96, p. 431. DOI: [10.1007/BF01337700](https://doi.org/10.1007/BF01337700).
- Westin, J., C. Sneden, B. Gustafsson, and J. J. Cowan (2000). “The r-Process-enriched Low-Metallicity Giant HD 115444”. In: *Astrophysical Journal* 530, p. 783. DOI: [10.1086/308407](https://doi.org/10.1086/308407). arXiv: [astro-ph/9910376](https://arxiv.org/abs/astro-ph/9910376).

- Wheeler, J. C., I. Yi, P. Höflich, and L. Wang (2000). “Asymmetric Supernovae, Pulsars, Magnetars, and Gamma-Ray Bursts”. In: *Astrophysical Journal* 537, p. 810. DOI: [10.1086/309055](https://doi.org/10.1086/309055).
- Winteler, C. (2013). “Light element production in the big bang and the synthesis of heavy elements in 3D MHD jets from core-collapse supernovae”. PhD thesis. University of Basel. DOI: [10.5451/unibas-006194131](https://doi.org/10.5451/unibas-006194131).
- Winteler, C., R. Käppeli, A. Perego, A. Arcones, N. Vasset, N. Nishimura, M. Liebendörfer, and F.-K. Thielemann (2012). “Magnetorotationally Driven Supernovae as the Origin of Early Galaxy r-process Elements?” In: *Astrophysical Journal, Letters* 750, p. L22. DOI: [10.1088/2041-8205/750/1/L22](https://doi.org/10.1088/2041-8205/750/1/L22). arXiv: [1203.0616 \[astro-ph.SR\]](https://arxiv.org/abs/1203.0616).
- Wollaeger, R. T., O. Korobkin, C. J. Fontes, S. K. Rosswog, W. P. Even, C. L. Fryer, J. Sollerman, A. L. Hungerford, D. R. van Rossum, and A. B. Wollaber (2017). “Impact of ejecta morphology and composition on the electromagnetic signatures of neutron star mergers”. In: *ArXiv e-prints*. arXiv: [1705.07084 \[astro-ph.HE\]](https://arxiv.org/abs/1705.07084).
- Wollaston, W. H. (1802). “A Method of Examining Refractive and Dispersive Powers, by Prismatic Reflection”. In: *Philosophical Transactions of the Royal Society of London Series I* 92, p. 365.
- Woosley, S. E., W. D. Arnett, and D. D. Clayton (1973). “The Explosive Burning of Oxygen and Silicon”. In: *Astrophysical Journal, Supplement* 26, p. 231. DOI: [10.1086/190282](https://doi.org/10.1086/190282).
- Woosley, S. E., A. Heger, A. Cumming, R. D. Hoffman, J. Pruet, T. Rauscher, J. L. Fisker, H. Schatz, B. A. Brown, and M. Wiescher (2004). “Models for Type I X-Ray Bursts with Improved Nuclear Physics”. In: *Astrophysical Journal, Supplement* 151, p. 75. DOI: [10.1086/381533](https://doi.org/10.1086/381533). arXiv: [astro-ph/0307425](https://arxiv.org/abs/astro-ph/0307425).
- Woosley, S. E., A. Heger, and T. A. Weaver (2002). “The evolution and explosion of massive stars”. In: *Reviews of Modern Physics* 74, p. 1015. DOI: [10.1103/RevModPhys.74.1015](https://doi.org/10.1103/RevModPhys.74.1015).
- Woosley, S. E. and R. D. Hoffman (1992). “The alpha-process and the r-process”. In: *Astrophysical Journal* 395, p. 202. DOI: [10.1086/171644](https://doi.org/10.1086/171644).
- Woosley, S. E., J. R. Wilson, G. J. Mathews, R. D. Hoffman, and B. S. Meyer (1994). “The r-process and neutrino-heated supernova ejecta”. In: *Astrophysical Journal* 433, p. 229. DOI: [10.1086/174638](https://doi.org/10.1086/174638).
- Wu, M.-R., R. Fernández, G. Martínez-Pinedo, and B. D. Metzger (2016). “Production of the entire range of r-process nuclides by black hole accretion disc outflows from neutron star mergers”. In: *Monthly Notices of the RAS* 463, p. 2323. DOI: [10.1093/mnras/stw2156](https://doi.org/10.1093/mnras/stw2156). arXiv: [1607.05290 \[astro-ph.HE\]](https://arxiv.org/abs/1607.05290).

- Yang, B., Z.-P. Jin, X. Li, S. Covino, X.-Z. Zheng, K. Hotokezaka, Y.-Z. Fan, T. Piran, and D.-M. Wei (2015). “A possible macronova in the late afterglow of the long-short burst GRB 060614”. In: *Nature Communications* 6, p. 7323. DOI: [10.1038/ncomms8323](https://doi.org/10.1038/ncomms8323). arXiv: [1503.07761](https://arxiv.org/abs/1503.07761) [[astro-ph.HE](#)].
- Yukawa, H. (1935). “On the Interaction of Elementary Particles. I”. In: *Proceedings of the Physico-Mathematical Society of Japan. 3rd Series* 17, p. 48. DOI: [10.11429/ppmsj1919.17.0\\_48](https://doi.org/10.11429/ppmsj1919.17.0_48).